# ELECTRON AND ION BEAM SCIENCE AND TECHNOLOGY

## THIRD INTERNATIONAL CONFERENCE

Edited by

Robert A. Bakish
Bakish Materials Corp.
Englewood, New Jersey

*ELECTROTHERMICS AND METALLURGY DIVISION*

THE ELECTROCHEMICAL SOCIETY, INC., 30 East 42 Street, New York, N. Y. 10017

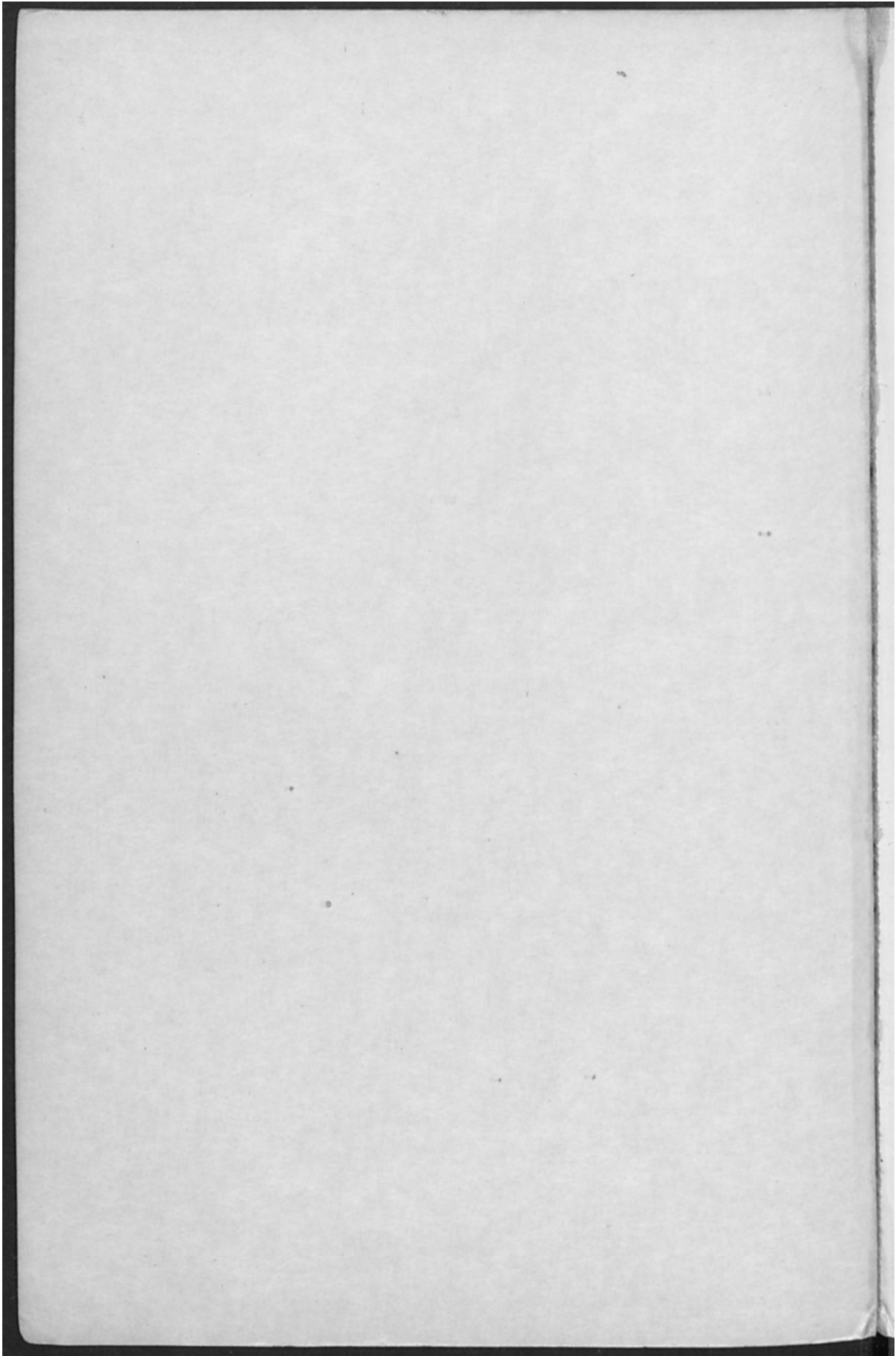

# ELECTRON AND ION BEAM SCIENCE AND TECHNOLOGY

## THIRD INTERNATIONAL CONFERENCE

Edited by

Robert A. Bakish
Bakish Materials Corp.
Englewood, New Jersey

*ELECTROTHERMICS AND METALLURGY DIVISION*
THE ELECTROCHEMICAL SOCIETY, INC., 30 East 42 Street, New York, N. Y. 10017

Copyright 1968
by
The Electrochemical Society, Incorporated

*Papers contained herein may not be reprinted and may not be digested by publications other than those of The Electrochemical Society in excess of 1/6 of the material presented.*

Library of Congress Catalog Card Number: 65-14260
Printed in the United States of America

CONTENTS

Page

SECTION 1. ELECTRON AND ION BEAM PHYSICS AND RELATED TOPICS


An Electronic Analog of Relativistic Space
Homer B. Tilton .......... 3

New Space-Charge Flow Solutions Useful for Gun Design
B. Komatsu, H. Hamada, and M. Terada .......... 15

Some Aspects of Flow Visualization and Local Density Measurements in Rarefied Gases by Means of Electron Beam Probes
B. W. Schumacher .......... 31

Power Density Limits for the Particle Penetration Laws and the Onset of Energy Phenomena in Electron Beam Targets
B. W. Schumacher .......... 74

Characteristic Properties of Duoplasmatron-Type Ion Sources, and of Extracted Beams
G. Gautherin, C. Lejeune, and A. Septier .......... 94

Backscattering of Kilovolt-Electron Beams
Claude A. Klein .......... 113

An Experimental Investigation of a High-Voltage Electron-Bombardment Ion Thruster
David C. Byers .......... 122

Composite Ion Accelerator Grids
Bruce Banks .......... 163

Alkali Metal Ion Sources
Julius Perel .......... 184

Current Density Distribution in Beams from Cold Hollow Cathodes
L. H. Stauffer .......... 206

High Output Plasma Electron Beam
Seiichiro Kashu, Shuji Nishino, and Chikara Hayashi .......... 221

Some Observations on High Power Electron Beams Under Water
B. W. Schumacher .......... 236

Page

Recent Developments in the Application of Laser-Surface Interactions
A. S. Gilmour, Jr. and R. J. Clark, Jr. .................... 254

SECTION 2. ELECTRON BEAMS IN MATERIALS PROCESSING:
PART A: ELECTRON BEAM WELDING
PART B: MELTING, REFINING AND EVAPORATION

Effect of Electron Scattering in the Metal Vapor on the Energy Dissipation in the Cavity Present During Electron Beam Welding
D. C. Schubert and B. W. Schumacher .................... 269

Energy Considerations in Electron Beam Welding
Paul G. Klemens .................... 291

Present Knowledge of the Fundamental Processes of Electron Beams as Material Working Tools
Helmut Schwarz .................... 301

Basic Research on Welding with Electron Beams of High Intensity
A. Matting and G. Sepold .................... 318

Materials Removal Processes in Laser and Electron Beam Machining
G. Pahlitzsch and A. Visser .................... 335

The Influence of Electron Beam Focusing on the Shape and Dimensions of Welds in the Electron Beam Welding Process
M. Boncoeur, J. Y. Marhic, and M. Rapin .................... 358

Metal Mixing During Electron Beam Welding
P. Shahinian, J. T. Atwell, and E. J. Brooks .................... 384

Penetration Variations in Electron Beam Welding
G. K. Hicken and W. G. Booco .................... 398

New Developments in Electron Beam Welding Technique of Nuclear Reactor Structure Components
P. Thomé and R. Roudier .................... 412

Short Term Production Applications for Electron Beam Welding
M. M. Schwartz .................... 433

Electron Beam Cutting of Rocks and Concrete
B. W. Schumacher .................... 447

Page

Ultrahigh-Vacuum Zone Purification of Zirconium with Analysis of Partial Pressures
D. S. Easton and J. O. Betterton .......................... 469

New Electron Beam Optics for the Preparation of Insulating Crystals by the Floating Zone Method
Charles E. Ryan, Dennis P. Considine, John J. Hawley, and Robert C. Marshall .................................... 501

Sources of Contamination during Electron-Beam Melting
R. E. Reed, C. W. Dean, R. E. McDonald, and J. F. Emery .... 516

Evaporation of Isotopically Enriched Stable and Radioactive Materials by Electron Bombardment Heating
H. L. Adair, E. H. Kobisk, and F. R. O'Donnell ............ 530

Application of Vapor Deposition Technique in the Metallurgical Industry
S. Schiller, H. Förster, P. Lenk, and B. Wenzel ............ 539

Measuring Thin Aluminum Coatings on Steel by Means of an Electron Probe
Eldon L. Keller and Berthold W. Schumacher ................. 551

SECTION 3. ELECTRON AND ION BEAMS IN MICROELECTRONICS

High Resolution Electron Beam Techniques for Transistor Fabrication
J. M. S. Schofield, H. N. G. King, and R. A. Ford .......... 561

Rapid Direct Formation of Siliceous Diffusion Barriers by Electron Beams
E. D. Roberts.............................................. 571

Application of Electron-Beam-Induced Conductivity to Measurement of Resistivity, Electric Field and Potential Distributions in GaAs
Chusuke Munakata .......................................... 580

The Transport of Excess Carriers in Diffused Silicon Diodes During Electron Beam Irradiation
G. J. Sprokel and J. Chin .................................. 590

An Electron Beam Digital Recorder
Kenneth E. Haughton ........................................ 624

Page

Requirements on Beam Techniques and Systems for Ion Implantation Doping of Semiconductor Materials and Devices
R. G. Wilsom, R. R. Hart, D. M. Jamba, and S. A. Thompson ........ 640

An Ion Implantation System Which Employs a Velocity Filter for Mass Separation
J. D. Macdougall, F. W. Anderson, K. E. Manchester, and P. E. Roughan ........ 649

Implantation of Boron and Phosphorus into Silicon Substrate and Its Application to Range Measurement
Takashi Tsuchimoto ........ 656

SECTION 4. APPENDIX: AUTHORS' SUMMARIES

On the Measurement of Impurity Atom Distributions Arising From Ion Implantation in High-Resistivity Silicon
D. P. Kennedy, P. C. Murley, and W. Kleinfelder

Introduction of Diffusion Sources by Implantation
P. E. Roughan, A. H. Clark, J. D. Macdougall, K. E. Manchester, and F. W. Anderson

Evaluation of Ion Implantations into Silicon by Hall Measurements
G. A. Shifrin, R. Baron, O. J. Marsh, and J. W. Mayer

Electrical Characteristics of Ion Implanted Gallium Arsenide
R. G. Hunsperger and O. J. Marsh

Advantages of Electron-Beam Heating in a Metallurgical Heat-Treating Furnace
J. C. Wilson

Poisoning of $LaB_6$ Cathodes
H. E. Gallagher

Cold Cathode as a Metalworking Tool
Marvin L. Kohn

Some Recent Developments in E.B. Welding Equipment and Its Applications
J. Sommeria

Dynamic Voltage Contrast Display Using the Stroboscopic Scanning Electron Microscope
G. S. Plows and W. C. Nixon

Examination of Metal-Insulator-Semiconductor Structures by Scanning Electron Microscopy
D. V. Sulway and P. R. Thornton

Detection of Compositional Variations using the Scanning Electron Microscope
D. A. Shaw and P. R. Thornton

Time Resolved Scanning Electron Microscopy of Electric Fields in CdS Oscillators
N. C. MacDonald and R. M. White

Factors Covering Contrast in Scanning Electron Micrographs of Thin Oxide Layers
David Green

Electron Microprobe Investigation of Integrated Circuit Metallization
James E. Cline, Rosemary P. Beatty, and Jon Gerhard

The Application of Electron Beam Fabrication to Large Scale Integration
M. W. Larkin, R. K. Matta, and P. R. Malmberg

Electron Beam Techniques for High Resolution Circuit and Mask Fabrication
M. Hatzakis

Design of Anastigmatic Coils for Deflecting Micron Size Electron Beams
A. Speth ...........

A 10 Kev, 0.5 Ampere Rocket-Borne Electron Accelerator
W. C. Beggs, R. Elcox, R. Harrison, and F. McCoy

## CONFERENCE COMMITTEE AND SESSION CHAIRMEN

Dr. Robert Bakish, Chairman, Bakish Materials Corp., 171 Sherwood Place, Englewood, N. J.

Dr. F. Benesowski, Metalwerk Plansee, Reutte/Tyrol, Austria

Prof. A. E. Jenkins, University of New South Wales, N.S.W., Australia

Prof. L. Habraken, CNRM, Liege, Belgium

Prof. J. Cabelka, Slovak Academy of Scienes, The Institute of Physical Metallurgy, Bratislava, Czechoslovakia

M. Boston, Esq., Torvac Ltd., Histon, Cambridge, England

Dr. J. Nielson, Micro Electro Division, Royal Radar Establishment, St. Andrews Road, Malvern, England

Prof. M. von Ardenne, am Weisen Hirsch, Dresden, East Germany

Prof. E. Rexer, Institute for Applied Physics of Pure Metals, Dresden, East Germany

Dr. J. A. Stohr, Centre d'Etudes Nucleaires, Saclay, France

Dr. A. Septier, Director of Research, S.N.R.S., Institute for Electronics, Faculty of Sciences, 91 Orsay (S&O), France

Dr. J. G. Siekman, Philips Research Laboratories, Eindhoven, Holland

Dr. S. Namba, The Institute of Physical & Chemical Research, Tokyo, Japan

Dr. C. Hayashi, Japan Vacuum Engineering Co., Ltd., Yokohama, Japan

Dr. O. Winkler, Balzers AG, Balzers, Lichtenstein

Dr. E. Bas, Swiss Federal Polytechnic Institute, Zurich, Switzerland

Prof. G. Molenstedt, University Tubingen, Tubingen, West Germany

Dr. W. Dietrich, W. C. Heraeus, Hanau/Main, West Germany

Prof. N. A. Olshanski, Moscow Power Institute, Moscow, U.S.S.R.

Dr. B. Paton, Director, Institute for Electro-Welding, Kiev, U.S.S.R.

B. W. Schumacher, Westinghouse Research Laboratories, Pittsburgh, Pa.

E. C. Mully, National Research Council, Cambridge, Mass.

CONFERENCE COMMITTEE AND SESSION CHAIRMEN CONTINUED

K. Amboss, Hughes Aircraft Co., Malibu Beach, Calif.

David Medved, Electro-Optical Systems Inc., 300 N. Halsted St., Pasadena, Calif.

F. L. Vogel, Sprague Electric Co., North Adams, Mass.

A. Lawley, Drexel Institute, Philadelphia, Pa.

R. E. Reed, Oak Ridge National Laboratories, Oak Ridge, Tenn.

George Brewer, Hughes Aircraft Co., Malibu Beach, Calif.

Oliver Wells, Watson Research Center, International Business Machines Corp., Yorktown Heights, N. Y.

Ch. Spitzer, Ampex Corp., Redwood City, Calif.

E. S. Barrekette, Watson Research Center, International Business Machines Corp., Yorktown Heights, N. Y.

S. V. Nablo, Ion Physics Corp., P.O. Box 98, Burlington, Mass.

R. Worlock, Electro-Optical Systems, Pasadena, Calif.

Ernest Foti, Central Research Institute for Physics, Budapest, Hungary

# PREFACE

This volume contains the papers presented at the Third International Conference on Electron and Ion Beam in Science and Technology. The papers have been edited by the writer with the assistance of Drs. F. Lincoln Vogel and E. C. Mully whose help has been invaluable and is herewith gratefully acknowledged. Thanks are also due to Dr. K. Manchester for his special effort in rewriting one of the contributions.

An editor is always torn between speedy publication on one hand and a complete conference record on the other. Believing the sooner this material is available the more valuable it becomes, the editor has stressed promptness over completeness. Where an author failed to meet manuscript submission deadline, an author's summary replaced the material presented. Those who wish to obtain the complete papers are advised to address the authors for full manuscripts.

The order of presentations in the conference has been altered in this volume in the hope of making it more coherent. The papers further have been grouped in three sections: The first section consists of papers dealing with the physics of related problems including physics of sources of particular beams, subject of the conference. The second section deals with the application of these beams to materials processing tasks including welding. The third section deals with electron and ion beams in microelectronics applications including recording and information storage.

In view of the continuing growth of the field and breadth of application of electron and ion beam, the writer has omitted introductory remarks to the three sections, a custom established in the proceedings of the two earlier conferences. Newcomers to the field are referred to the proceedings of the past two conferences will materially help their introduction to the field.

I would like to take the opportunity to thank all contributors for their willingness to share their experience with us and to assist the Electrothermics and Metallurgy Division of the Society in their desire to disseminate information about this field with ever increasing scientific and technological importance. Thanks are also due to The Electrochemical Society for sponsoring this event. Last but not least, the writer wishes to express his personal thanks to Charles Moore, Director of Publications of the Society and his staff at the ECS Headquarters for the support they rendered to the writer during the conference organization, at the meeting itself, and in the publication of this volume.

In closing, let me say that the Electrothermics and Metallurgy Division of the Society is planning to be your host again for the Fourth Conference in the Spring of 1970 in Los Angeles. We would like this Fourth International Electron and Ion Beam Conference to provide you with most if not all requirements that you wish such a conference should meet. Would you drop a line addressed to the writer or to Charles Moore at The Electrochemical Society, Inc., and tell us how we could serve you better.

R. Bakish,
Englewood, N. J., July 1, 1968

INTRODUCTORY REMARKS

Ladies and Gentlemen:

It gives me a great pleasure to welcome you here to Boston on the behalf of the Electrothermics and Metallurgy Division of The Electrochemical Society on the occasion of the Third International Conference on Electron and Ion Beam in Science and Technology. This meeting by strange coincidence takes place in Boston where practically ten years ago I became intimately involved with the subject of electron beams. At that time, for most practical purposes, we were essentially dealing with laboratory curiosities in virtually all areas of electron beam applications.

Today Electron and Ion Beams are an accepted industrial tool in a number of technological areas and are about to become so accepted in several others. Our sessions hopefully reflect these developments.

At this time I wish to make several announcements:

First: The proceedings of the last conference are still blocked by a legal tanglement among Gordon and Breach, its type setter and the AIME. This unfortunate development has been entirely beyond my control; yet it has been a cause of great aggravation to me as I am sure it has been to many contributors to that event.

Second: The few program changes which invariably accompany a meeting such as this will be announced by the session chairmen preceding each session.

Third: On registration you received cards requesting your comments on the planning of future meetings of this conference. These comments will be most valuable to the conference organization committee in their attempts to further improve this event in the future.

As there is much of interest that you will rather hear than listen to my introductory remarks, I will without further delay turn the session over to Dr. Schumacher who will chair the planary session.

Before I do so however, I wish to thank all who have made this conference a reality: the Society for sponsoring the event, the conference committee for helping with the selection of the speakers, and last but not least the speakers themselves, without whose participation we would not find it worthy of getting together here today.

R. Bakish,
Boston, May 6, 1968

# SECTION I

# ELECTRON AND ION BEAM PHYSICS

# AND

# RELATED TOPICS

# INTRODUCTORY REMARKS

Ladies and Gentlemen:

It gives me a great pleasure to welcome you here to Boston on the behalf of the Electrothermics and Metallurgy Division of The Electrochemical Society on the occasion of the Third International Conference on Electron and Ion Beam Science and Technology. This meeting by strange coincidence takes place in Boston where practically ten years ago I became intimately involved with the subject of electron beams. At that time, for most practical purposes, we were essentially dealing with laboratory curiosities in virtually all areas of electron beam applications.

Today Electron and Ion Beams are an accepted industrial tool in a number of technological areas and are about to become so accepted in several others. Our meetings have faithfully reflected these developments.

At this time I wish to make several announcements:

First: The proceedings of the last conference are still blocked by a legal tangle among [illegible] the type setter and the [illegible]. This unfortunate development has been entirely beyond my control; yet it has been a cause of great [illegible] to me as I am sure it has been to many contributors to [illegible].

Second: The [illegible] this accompany a meeting such as this will be announced by the session chairman preceding each session.

Third: On registration [illegible] requesting your comments on the planning of future [illegible]. These comments will be most valuable to the [illegible] committee in their attempts to further improve [illegible] in the future.

As there is much of interest that you will rather hear than listen to my introductory remarks, I will without further delay turn the session over to Dr. [illegible] who will chair the plenary session.

Before I do so however, I wish to thank all who have made this conference a reality: the Society for sponsoring the event, the conference committee for helping with the selection of the speakers, and last but not least the speakers themselves, without whose participation we would not find it worthy of getting together here today.

R. Bakish,
Boston, May [illegible], 1968

AN ELECTRONIC ANALOG OF RELATIVISTIC SPACE

Homer B. Tilton
Lockheed Electronics Co., Plainfield, N. J. 07061

ABSTRACT

Einstein's theory of relativity reveals the existence of an infinitely-high barrier at the velocity of light to acceleration of particles traveling in free space and at constant velocity; but the parallel cases for movement in material media and non-constant velocities are not treated in either the special or general theories. An analogy developed herein suggests that the barrier may not be infinitely high for those two cases.

The purpose of this paper is to examine the widely-held supposition that the theory of relativity and the concept of super-relativistic particle velocities are incompatible. Our primary concern will be with the mathematical aspects of the theory, although the philosophical aspects will not be completely ignored. We do not question the validity of the mathematical theory of relativity as it now stands.

Nearly all of the objections to the concept of super-relativistic particle velocities are based on the strange form which the equation

$$\gamma = 1/\sqrt{1-\beta^2} \qquad (1)$$

assumes in that case.[1] It becomes imaginary. Equation (1) is the well established law describing various relativistic effects for particle travel in free space at constant velocity. For example, the effective mass of a particle is increased over its at-rest value by the factor $\gamma$ when it is traveling at the normalized velocity $\beta$ relative to the observer.

Another basis which has been used to object to the concept involves the law which shows that no compounding of sub-relativistic velocities can lead to a super-relativistic velocity.[2] But this law simply indicates to us one way in which we cannot achieve the desired goal; it does not rule out the possibility that some other method might work.

Finally, philosophical arguments have been brought to bear. One of these - causality reversal - is discussed in Appendix 1.

The method chosen for examining the super-relativistic domain is the method of analogy. Two purposes of reasoning by analogy which

will be useful in the present investigation are: (1) To permit us to think in terms which are more familiar or more visual; and (2) To facilitate an extension of the boundaries of the problem under investigation.

It is of course true that analogy does not constitute proof. But analogy does indicate possibilities and promising direction of inquiry. In particular the analogy to be developed will give us a new and novel way of thinking about some important relativistic phenomena.

An analog of certain mathematical aspects of the theory of relativity will be developed in terms of electronic circuit theory. A detailed examination in terms of the analogy will then be made of equation (1) over the entire spectrum of velocities. Also, possible forms of $\gamma$ for material media and non-constant velocities will be examined by means of the analogy.

### The Analogy

The analogy is a further development of one which is already in widespread use, two elements of which are the intrinsic impedance of space (the analog of the characteristic impedance of a network) and the Q of a medium (the analog of the Q of a network).[3] Other analogous pairs are given in Table 1.

The concept of impedance, and its inverse admittance, will play a significant role in the analogy. The characteristic impedance of any two-port network is[4]

$$Z_c = \sqrt{Z_{oc}\, Z_{sc}} \qquad (2)$$

where $Z_{oc}$ is the open-circuit impedance (the impedance measured across the input terminals) and $Z_{sc}$ is the short-circuit impedance (the impedance measured across the input terminals with the output terminals shorted together).

The analogy could have been developed in terms of distributed circuit constants such as are found in transmission lines. We chose instead to work in terms of lumped constants primarily because of the resulting ease of graphical representation.

Consider the simple LC circuit in Fig. 1A. Its characteristic impedance is

$$Z_c = \sqrt{L_o/C_o}\,\sqrt{1-\Omega^2} \qquad (3).$$

At zero frequency this is $\sqrt{L_o/C_o}$ which is the analog of $\sqrt{\mu_o/\epsilon_o}$, the expression for the intrinsic impedance of free space. It follows that the circuit of Fig. 1A represents free space for zero velocity

(zero frequency).

It can be shown (see Appendix 2) that the apparent intrinsic impedance of free space under certain conditions is given by

$$\eta = \sqrt{\mu_o/\epsilon_o}\sqrt{1-\beta^2} \qquad (4)$$

when the source of the electromagnetic disturbance is moving at normalized velocity $\beta$. Equations (3) and (4) are analogs. Therefore the circuit of Fig. 1A is an analog of free space even when velocity (frequency) is not zero.

The function in equation (1) can be formed by taking the ratio of $\sqrt{\mu_o/\epsilon_o}$ (intrinsic impedance for zero velocity) to equation (4). This is the normalized intrinsic admittance.

In circuit theory, one method often used to examine a network admittance in detail is by means of magnitude and phase plots. The plots corresponding to the circuit of Fig. 1A and applying to equation (1) are shown in curve nos. 1 and 2 of Fig. 2. It is seen that the magnitude curve rises towards infinity as $\beta$ approaches unity from either direction. Also, the phase angle is zero below "resonance" and -90° above resonance.

In the circuit, the phase angle is just the angle between the current and voltage vectors, in time. If we let the analog of electric field E be voltage V and the analog of magnetic field H be current I, then phase angle in free space must be interpreted in the nature of a shift (probably spatial and temporal) which will occur between magnetic and electric vectors if the subject particle has an electric field; or in the nature of a shift between some as yet unspecified dynamic and static quantities if the particle has some other type of field instead, such as gravitational.

When a high-energy electron beam impinges on a material medium such as glass, some of the electrons exceed the local velocity of light as they traverse the medium (which is less than the free-space velocity of light) and Cerenkov radiation is produced.[5] Are we to assume that there is no light barrier in the medium? Or that there still is a barrier at the free-space velocity of light? Just what is the picture in this case?

Some answers will be given to these questions after more groundwork has been laid in the following section.

## Extending the Analogy

In order to find the form of the light barrier in material media and for non-constant particle velocities, it is necessary to extend

the analogy. This extension takes the form of a generalized definition of $\gamma$.

In the development of the analogy up to this point, it was found for the case of free space and constant velocity that $\gamma$ is equal to the normalized intrinsic admittance of space. We now will assume that this holds in general; and that $\gamma$ is known when the normalized intrinsic admittance is known for any case.

We could just as well have defined $\gamma$ as the normalized mass of a body; or as the normalized time; or as any of a number of other normalized quantities. The admittance definition is chosen for the reason that it lends itself to a direct transfer to the circuit domain whereas the others do not.

Consider the network in Fig. 1B. The characteristic impedance of that network is

$$Z_c = \sqrt{\frac{L}{C}} \sqrt{\frac{1 - \Omega^2 n^2 (1 - jD)}{1 - jD}} \qquad (5)$$

where $j = \sqrt{-1}$, n is analogous to the index of refraction of the medium being represented so that $\Omega n = \omega / \omega_r$, and D is the dissipation factor, representing the losses associated with the medium. At zero frequency equation (5) becomes

$$Z_c{}^o = \sqrt{\frac{L}{C}} \frac{1}{\sqrt{1 - jD^o}} \qquad (6)$$

which is the analog of the expression given by Schelkunoff[6] for the intrinsic impedance of a lossy medium. Therefore, by reasoning which is parallel to that given in connection with equations (3) and (4), we would expect that the analog of the ratio of equation (6) to equation (5) is $\gamma$ for a lossy medium. This is, if $D^o = D$,

$$\gamma = \frac{1}{\sqrt{1 - \beta^2 n^2 (1 - jD)}} \qquad (7)$$

which reduces to equation (1) when n = 1 and D = 0, as it should.

Magnitude and phase plots of equation (7) are shown in curve nos. 3 and 4 of Fig. 2. It is seen that the resonance peak - the "barrier" - is not infinitely high as long as D is not zero. Note also the phase angle characteristic.

It is now apparent that an electron projected into a material medium with a large but finite amount of energy - such as it would

have at Point A on curve no. 1 of Fig. 2 - can be expected to exceed the local velocity of light in the medium and thereby cross over into the Cerenkov region, just as it is known to do.

But Cerenkov radiation can also be produced in materials having essentially no loss. The following paragraphs will reveal a possible mechanism for this.

The case of a non-constant particle velocity is now considered. This is the most difficult case so far considered to analyze by means of the electronic circuit analogy because the concept impedance assumes in its definition that the signal in the network does not have a varying frequency.

The usual way of treating frequency modulation is to work in terms of ordinary impedances, which then requires the introduction of Bessel functions into the analysis.[7] The present analysis could be carried out in that manner; however, another method is used instead which permits a much simpler treatment of our particular problem. We return to the basic current-voltage relationships for capacitors, resistors, and inductors; and define a generalized impedance valid for varying frequency and reducing to ordinary impedance when the frequency is constant.

This development is given in Appendix 3. It reveals that the generalized impedance of a capacitor is still capacitively reactive (in the -j direction) with $\omega + \dot{\omega} t$ replacing $\omega$ and now serving in the role of frequency; that of a resistor is still real and equal to its ordinary resistance; and that of an inductor now effectively has a resistive component.

This effective resistive component does not produce a loss; but it does have the effect of lowering the resonance peak of the circuit of Fig. 1A so that it can no longer store an infinite amount of energy.

The characteristic impedance (generalized) of the free-space analog (Fig. 1A) is given by

$$Z_c = \sqrt{\frac{L_o}{C_o}} \sqrt{(1-\Omega^2 n^2 + \Psi^2 n^2/\Omega^2) - j(\Psi/\Omega^2 - 2\Psi n^2)} \quad (8)$$

where

$$\Omega = \frac{\omega + \dot{\omega} t}{\omega_{ro}}, \qquad \Psi = \frac{2\dot{\omega} + \ddot{\omega} t}{\omega_{ro}^2} \quad (9).$$

If we let $\Omega$ be the analog of $\beta$ where

$$\beta = \frac{v + \dot{v}t}{c_o} = \beta + \dot{\beta}t \tag{10}$$

and $\Psi$ be the analog of $\psi$ where

$$\psi = \frac{2\dot{v} + \ddot{v}t}{c_o^2} = \frac{2\dot{\beta} + \ddot{\beta}t}{c_o} \tag{11}$$

then $\gamma$ for the case of free space and non-constant velocity is seen to be given by

$$\gamma = \frac{1}{\sqrt{(1-\beta^2 n^2+\psi^2 n^2/\beta^2) - j(\psi/\beta^2 - 2\psi n^2)}} \tag{12}.$$

The general form which the curves assume is the same as those of Fig. 2. Curve nos. 1 and 2 being obtained when the parameter $(2\dot{\beta}+\ddot{\beta}t)/c_o$ is zero, and curve nos. 3 and 4 being obtained when the parameter has some value greater than zero. The parameter has the dimensions of acceleration. The independent variable is now $\beta + \dot{\beta}t$ instead of $\beta$. It is seen that as the particle acceleration becomes greater, the resonance peak (and hence the light barrier) becomes lower.

As a result of this it is not surprizing to find that a high-energy electron impinging on a medium having no loss and an index of refraction greater than unity can "cross the barrier" due to the very abrupt increase in the velocity of the particle relative to the ambient or local velocity of light as it encounters the boundary of the medium. The barrier is effectively lowered at the instant of contact, allowing the particle to "cross over."

## Comment and Analysis

The analog which has been generated is consistent with the theory of relativity, while at the same time describing a possible mechanism whereby electrons are able to cross the local light barrier in a material medium. An important implication which can be drawn from the analogy is that

> Conceptually, there is no difference between crossing the light barrier in a material medium and crossing the light barrier in free space.

Further, we are so bold as to suggest that once an electron has crossed the light barrier in a material medium, it will encounter no further barrier to acceleration as long as it is in the medium; that there is no upper limit to the velocity which it can attain; and that it can by this means find itself traveling faster than the free-space velocity of light when it re-enters free space at which time it may be still further accelerated to any desired velocity.

It is not as yet clear precisely how the phase angle characteristics of free space or a material medium should be interpreted when dealing with particle movement. Perhaps the 90° phase angle found in free space above "resonance" indicates that no energy or information can be carried in that region. Numerous examples have been given of faster-than-light phenomena.[8] In all of these, it was found that no energy or information can be transmitted faster than light velocity. Perhaps we have simply found another such example.

But Cerenkov electrons do carry energy and information, leading us to believe that there is some hope. Some new experimental evidence is needed at this point. Attempts to further accelerate Cerenkov electrons while they are in the medium should be most enlightening.

## Appendix 1. Causality Reversal

The possibility of any body traveling faster than light under any circumstances whatsoever has been objected to on the basis that the normal cause-effect relationship would thereby be violated.[9] The reasoning being that effect is linked to cause by the velocity of light and that we therefore could conceivably see effect preceding cause.

The key word here is "see." Relativistic effects have been referred to as a sort of kinematical perspective[10] which does not show the actual state of affairs.[11] It has also been said that the philosophical difficulties encountered in finding a way to synchronize two remotely separated clocks would disappear if a ball could be thrown with infinite velocity between the two stations.[12]

A cause and effect relationship linked by the velocity of sound does not suffer a real reversal when we fly at supersonic speed even though there may be an apparent reversal. It has been argued that the difference between these two cases is that the velocity of light is the ultimate velocity at which an effect can be propagated whereas the velocity of sound is not.

But this leads to a circular argument wherein it is necessary to assume that the velocity of light is ultimate in order to prove that it is ultimate.

## Appendix 2. The Apparent Intrinsic Impedance of Free Space for the Case of a Moving Source

It is generally believed that the intrinsic impedance of free space is determined only by $\mu_0$ and $\epsilon_0$, and is independent of any movement of the source of electromagnetic effects. But just as effective mass depends on motion of the source body, it can be shown that the effective or apparent intrinsic impedance of free space can vary with the source velocity. The nature of the variation is dependent on the relative orientations of electric, magnetic, and velocity vectors. In the case where the magnetic and velocity vectors of the source are aligned, and are perpendicular to the electric vector, the apparent intrinsic impedance of space can be shown to be given by equation (4) by use of equations (111) in Stratton.[13]

## Appendix 3. Generalized Impedance

Impedance is defined as the opposition - not to the scalar current of the form sin $\omega t$ - but to the vector current of the form $\exp(j\omega t)$ where $\omega$ is constant. In general, the impedance of a two-terminal component or network is defined as the vector voltage across it times the inverse of the vector current through it.

Although it is customary to specify a vector current generator in the derivation of impedance, it is more convenient in the derivation of generalized impedance to specify a vector charge generator. This is permissible since the generalized impedance so obtained reduces to ordinary impedance when $\omega$ is constant. Specifying a charge generator removes the necessity to integrate the current - a simple enough task when $\omega$ is constant, but one which is not so simple when $\omega$ is allowed to vary.

Table 2 gives the relationships necessary to the derivation. Use of those relationships gives for the generalized impedances of C, R, and L

$$\begin{aligned} Z_C &= -j/FC \\ Z_R &= R \\ Z_L &= (G/F)L + j\,FL \end{aligned} \qquad (3\text{-}1).$$

$Z_L$ is composed of an inductively reactive term plus a term which is effectively resistive. When $\omega$ is constant, $Z_C$ and $Z_L$ reduce to the familiar pure reactance $X_C$ and $X_L$, where

$$\begin{aligned} X_C &= -j/\omega C \\ X_L &= j\omega L \end{aligned} \qquad (3\text{-}2).$$

References


1. Albert Einstein, Relativity - The Special and General Theory, English translation; Crown Publishers, New York, 1931, page 43.

2. Robert B. Leighton, Principles of Modern Physics, McGraw-Hill, New York, 1959, page 14.

3. S. A. Schelkunoff, "The Impedance Concept and Its Application to Problems of Reflection, Refraction, Shielding, and Power Absorption", The Bell System Technical Journal, Vol. XVII, No. 1, January 1938, pages 17-48.

4. R. W. Landee et al, Electronic Designers' Handbook, McGraw-Hill, 1957, Section 16, page 2.

5. J. V. Jelley, Cerenkov Radiation and Its Applications, Pergamon Press, New York, 1958.

6. Reference 3, page 24.

7. Reference 4, Section 5, pages 27-32.

8. Milton A. Rothman, "Things that go Faster than Light", Scientific American, Vol. 203, July 1960, page 142.

9. Edward Gerjuoy, "Causality", McGraw-Hill Encyclopedia of Science and Technology, Vol. 2, 1960, page 571.

10. F. K. Richtmyer and E. H. Kennard, Introduction to Modern Physics, McGraw-Hill, New York, 1947, page 123.

11. Max Born, Einstein's Theory of Relativity, Revised Edition, Dover Publications, New York, 1965, page 254.

12. Reference 10, page 119.

13. J. A. Stratton, Electromagnetic Theory, McGraw-Hill, New York, 1941, page 79.

Table 1. Analogous Pairs

| Relativistic Space | | | Electronic Circuit | | |
|---|---|---|---|---|---|
| permittivity | $\epsilon$ | farads/m | capacitance | C | farads |
| permittivity of free space | $\epsilon_o$ | farads/m | capacitance of ref. circuit | $C_o$ | farads |
| permeability | $\mu$ | hy/m | inductance | L | henries |
| permeability of free space | $\mu_o$ | hy/m | inductance of ref. circuit | $L_o$ | henries |
| linear velocity | v | m/sec | angular frequency | $\omega$ | rd/sec |
| velocity of light | c | m/sec | resonant frequency | $\omega_r$ | rd/sec |
| velocity of light in free space | $c_o = \frac{1}{\sqrt{\mu_o \epsilon_o}}$ | | resonant frequency of ref. circuit | $\omega_{ro} = \frac{1}{\sqrt{L_o C_o}}$ | |
| normalized velocity | $\beta = v/c_o$ | | normalized freq. | $\Omega = \omega/\omega_{ro}$ | |
| figure of merit | Q | (ratio) | figure of merit | Q | (ratio) |
| dissipation factor | $D = 1/Q$ | | dissipation factor | $D = 1/Q$ | |
| index of refraction | $n = c_o/c$ | | an index | $n = \omega_{ro}/\omega_r$ | |
| intrinsic impedance | $\eta$ | ohms | charac. impedance | $Z_c$ | ohms |
| intrinsic admittance | $1/\eta$ | siemens | characteristic admittance | $Y_c$ | siemens |
| electric field | E | V/m | voltage | V | volts |
| magnetic field | H | A/m | current | I | amperes |
| the relativistic factor | $\gamma$ | (ratio) | normalized charac. admit. | $Y_c/Y_c^o$ | (ratio) |

Sub o refers to free space or reference conditions.
Super o refers to zero velocity or zero frequency.

Table 2. Impedance Equations

A. Basic equations which apply to both ordinary impedance and generalized impedance:

| | | | |
|---|---|---|---|
| Driving charge | $q = Q\,e^{j\omega t}$ | where | $e = 2.71828...$ |
| Resulting current | $i = dq/dt$ | | $j = \sqrt{-1}$ |
| Resulting voltage across: | | | $Q$ = const. charge |
| capacitance C | $V = (1/C)\,q$ | | $\omega$ = angular freq. |
| resistance R | $V = R\,i$ | | $t$ = time |
| inductance L | $V = L(di/dt)$ | | |

Definition of the impedance of a component or network: $Z = V\,i^{-1}$

B. Further equations which apply to ordinary impedance only (A special case of generalized impedance):

$$i = j\omega q$$

$$di/dt = -\omega^2 q$$

Angular frequency is constant

C. Further equations which apply to generalized impedance:

$$i = j F q$$

$$di/dt = -(F^2 - jG)\,q$$

$$\text{where } F = \omega + \dot{\omega} t$$

$$\text{and } G = 2\dot{\omega} + \ddot{\omega} t$$

Dots indicate differentiation with respect to time

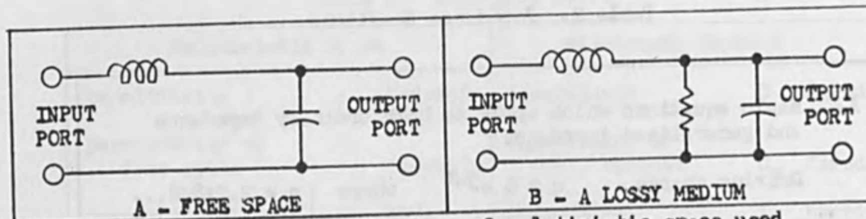


Fig. 1. Electronic circuit analogs of relativistic space used to determine $\gamma$. Inductors represent permeabilities, capacitors represent permittivities, and the resistor represents losses.

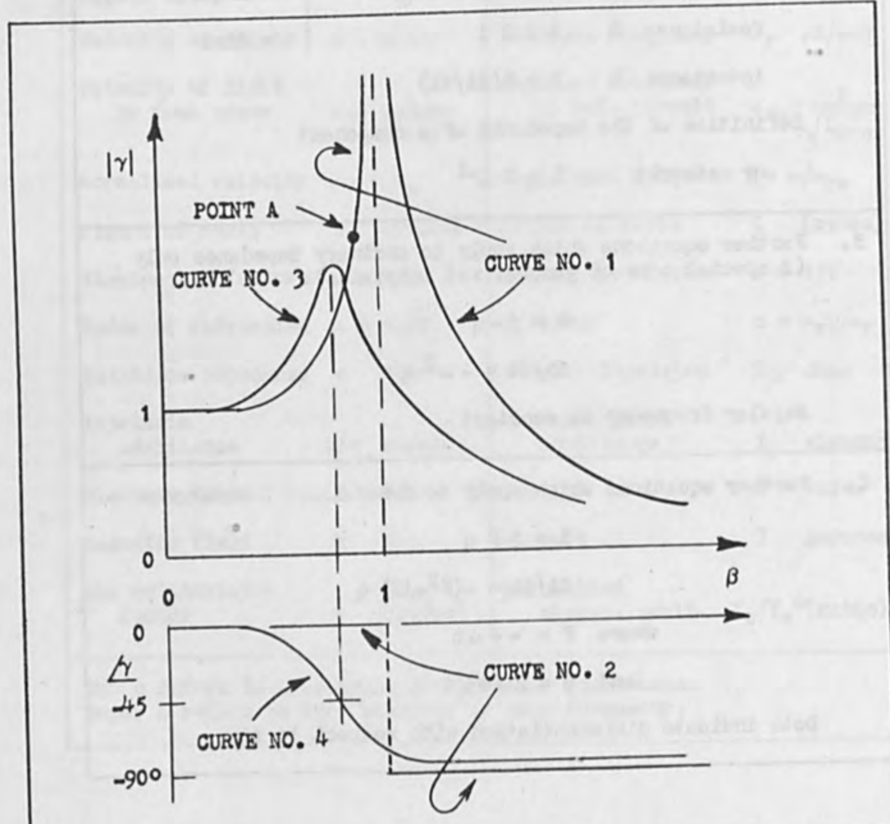


Fig. 2. Curves of magnitude and phase for free space and for a lossy medium.

# NEW SPACE-CHARGE FLOW SOLUTIONS
# USEFUL FOR GUN DESIGN

B. Komatsu, H. Hamada and M. Terada

Faculty of Engineering, Osaka University
Higashinoda, Miyakojimaku, Osaka
JAPAN

ABSTRACT

New self-consistent space-charge flow solutions for the design of conical flow Pierce guns are presented which take into consideration the effect of the anode hole. The flow solutions are found by solving the space-charge flow equations under the initial condition which is specified on the axis in such a manner that the potential rises as that of the cospherical space-charge limited diode until it reaches a certain value, after which it almost levels off to a constant value. We propose one form of mathematical expression for the potential distribution of this nature. Before the actual calculation, we develop a numerical method for solving stably the problem, which is a kind of composite of the finite difference method and the power series expansion method. Finally the flow solutions thus obtained are presented; the cathode shapes, the cathode current densities, the flow lines and the equipotentials. The resulting space-charge flows behave themselves satisfactorily for the application to gun design.

## 1. INTRODUCTION

Pierce's method[1] has widely been applied to the design of high-current electron or ion guns. It begins with finding a solution to the space-charge flow equations useful for gun design. So far only a small number of such flow solutions,[2][3] obtained analytically, have been available. They all have a potential variation increasing unboundedly along each flow line. In the design of practical guns, which are required to produce drifting beams, therefore, they must be truncated somewhere to be joined to some other flow solutions with potential constant along the flow lines. This procedure is rigorously correct so long as the acceleration region is perfectly shielded from the drift space with the anode. This is practically impossible, however, because an anode hole must be cut out to bring the beam into the drift space. If the gun perveance is low, the only effect to be considered may be its lens action. In high-perveance guns, however, the flow in the gun region is appreciably disturbed by the presence of the anode hole. As a result, the gun once designed is compelled to be modified by trial and error through analysis using an analogue or digital computer, or through test on the experimental tubes.

The most direct way to avoid such cumbersome procedures is to design guns originally on the basis of such flow solutions that the potential approaches a definite value along each flow line far from the cathode. It is unlikely to find such flow solutions analytically, so that we shall rely on a numerical method. In this method, we designate, at first, a certain trajectory, called central trajectory, and specify an appropriate potential distribution on it. Then, we numerically solve the equations for space-charge flow under the initial conditions above prescribed. Such numerical method for the initial value problem of space-charge flow equations has been developed by Colburn, Harker and Kino.[4] We shall start with the basic equations of theirs, which will be rewritten in a slightly modified form in Sec. 2.

We shall develop in Sec. 3 a new method, which is a kind of composite of the finite difference method and the power series expansion method, for the actual computation, while Colburn et al. used the method, originated by Garabedian and first applied to the gun design problem by Harker[5][6]; the equations forming an elliptic system, whose solutions would be unstable if they were solved by finite difference technique, are continued into the complex domain so that they become hyperbolic, before they are

calculated by usual finite difference technique. Our method may also be applied to obtain stable solutions to the initial value problem of any elliptic system of equations, having the advantage of short time of computation, economical utility of memory capacity and high accuracy of computation on a digital computer.

Using this method, we shall solve the equations for space-charge flow in the absence of magnetic field applicable to the design of axially-symmetric solid beam guns. The initial conditions under which the equations are solved are so specified along the axis of symmetry that the potential varies as $p^{4/3}$ (p: the distance from the cathode along the axis of symmetry) in the vicinity of the cathode to make the flow space-charge limited and approaches a constant value far from the cathode. We shall propose a mathematical expression of such potential distribution along the axis in Sec. 4. Finally in Sec. 5 we shall present the results of computation and make some descriptions on the nature of the flow solutions.

## 2. BASIC EQUATIONS

The basic equations that we use are almost the same that Colburn et al. developed, except that the paraxial ray equation along the axis slightly different from that along the path off the axis is added to theirs, which is necessary in our case to find the space-charge flow satisfying the initial conditions specified along the axis of symmetry.

We describe the basic equations in the (p, q) coordinate system as Colburn et al. did. In this coordinate system, shown in Fig. 1, p and q are defined in such a manner that each surface of p = const. is a surface of constant action and each surface of q = const. corresponds to a particular trajectory, and in addition the cathode surface has the coordinate p = 0, where q is equal to the cathode arc length measured from the cathode center, and the axis of symmetry the coordinate q = 0, where p the distance from the cathode. Let h and x be the metric coefficients in the (p, q) coordinate system and the basic equations for irrotational space-charge flow without magnetic field are

$$v = \frac{1}{h}\frac{dW}{dp} \quad , \quad v^2 = 2\eta\phi \quad , \qquad (1)$$

$$\frac{1}{hxr}\left[\frac{\partial}{\partial p}\left(\frac{rx}{h}\frac{\partial\phi}{\partial p}\right) + \frac{\partial}{\partial q}\left(\frac{rh}{x}\frac{\partial\phi}{\partial q}\right)\right] = -\frac{\rho}{\varepsilon_0} \quad , \qquad (2)$$

$$\frac{1}{hxr}\frac{\partial}{\partial p}(rxJ) = 0 \qquad (J = \rho v) \quad , \tag{3}$$

$$\frac{\partial}{\partial p}\left(\frac{1}{h}\frac{\partial x}{\partial p}\right) + \frac{\partial}{\partial q}\left(\frac{1}{x}\frac{\partial h}{\partial q}\right) = 0 \quad , \tag{4}$$

$$\frac{1}{x}\frac{\partial r}{\partial q} = \frac{1}{h}\frac{\partial z}{\partial p} \quad , \tag{5}$$

$$\frac{1}{x}\frac{\partial z}{\partial q} = -\frac{1}{h}\frac{\partial r}{\partial p} \quad , \tag{6}$$

where $-\eta$ is the ratio of charge to mass of an electron, $\varepsilon_0$ the dielectric constant of vacuum, v the velocity, W the action function, $\phi$ the potential, $\rho$ the space-charge density and J the current density. Eq. (1) are the equations of motion, Eq. (2) Poisson's equation and Eq. (3) the equation of continuity. The metric coefficients are required to satisfy Eq. (4) if the coordinate surface is a plane. Eqs. (5) and (6) hold for any orthogonal coordinate system. These equations are to be solved under the initial conditions specified along the axis (q = 0) as follows:

$$r = 0 \ , \quad z = p \ , \quad h = 1 \ , \quad \psi = 0 \text{ and } \quad \phi = \phi_0(p), \tag{7}$$

where $\psi$ is the angle of a trajectory with respect to the axis and related to the curvature K of the path and the metric coefficients as

$$\frac{1}{h}\frac{\partial \psi}{\partial p} = K = -\frac{1}{hx}\frac{\partial h}{\partial q} \quad . \tag{8}$$

Before we seek numerical solutions to the basic equations, we shall put them into the form convenient to numerical calculation. After some integration, we obtain the equations

$$\phi(p, q) = \frac{\phi_0(p)}{h^2} \quad , \tag{9}$$

and

$$\rho = \frac{r_0 J_0}{rx\sqrt{2\eta\phi}} \quad , \tag{10}$$

where $r_0$ and $J_0$ are the values of r and J on the cathode

respectively. It follows from Eq. (9) that one has only to know the value of h in order to evaluate the potential at any point. Substituting Eq. (10) into Eq. (2), we obtain

$$\frac{1}{hxr}\left[\frac{\partial}{\partial p}\left(\frac{rx}{h}\frac{\partial\phi}{\partial p}\right) + \frac{\partial}{\partial q}\left(\frac{rh}{x}\frac{\partial\phi}{\partial q}\right)\right] = \frac{r_0(-J_0)}{rx\varepsilon_0\sqrt{2\eta\phi}} \quad . \tag{11}$$

We may put the basic equations into more convenient form by the following normalization. Hereafter r, z, p and q are measured in terms of a certain distance d, the cathode current density $J_0$ in terms of that in the center of the cathode and the potential $\phi$ in terms of the unit

$$\left(\frac{9d^2[-J_0]_{q=0}}{4\varepsilon_0\sqrt{2\eta}}\right)^{\frac{2}{3}} \quad .$$

By doing this we can reduce Eq. (11) into the normalized form

$$\frac{1}{hxr}\left[\frac{\partial}{\partial p}\left(\frac{rx}{h}\frac{\partial\phi}{\partial p}\right) + \frac{\partial}{\partial q}\left(\frac{rh}{x}\frac{\partial\phi}{\partial q}\right)\right] = \frac{4r_0(-J_0)}{9rx\sqrt{\phi}} \quad . \tag{12}$$

If we let the potential on the axis

$$\phi_0(p) = p^{\frac{4}{3}}V(p) \quad , \tag{13}$$

then V(p) is reduced to a function analytic at p = 0, because we are concerned with space-charge limited flows. Substitution of Eq. (13) into Eq. (9) yields

$$\phi(p,\ q) = \frac{p^{\frac{4}{3}}V(p)}{[h(p,\ q)]^2} \quad . \tag{14}$$

Substituting Eq. (14) into Eq. (12) and replacing

$$\frac{\partial}{\partial q}\left(\frac{1}{x}\frac{\partial h}{\partial q}\right) \qquad \text{by} \qquad -\frac{\partial}{\partial p}\left(\frac{1}{h}\frac{\partial x}{\partial p}\right)$$

with the use of Eq. (4) and

$$\frac{1}{x}\frac{\partial h}{\partial q} \qquad \text{by} \qquad -\frac{\partial\psi}{\partial p}$$

with the use of Eq. (8), we obtain the extended paraxial trajectory equation for x:

$$Ap^2x_{pp} + Bpx_p + Cx + D = 0 \tag{15}$$

with

$$\left.\begin{aligned} A &= 18rh^2V^{\frac{3}{2}} , \\ B &= \{9rh^2p\dot{V} + (12rh^2 - 36rhph_p)V\}V^{\frac{1}{2}} , \\ C &= [9rh^2p^2\ddot{V} + (24rh^2 - 45rhph_p + 9pr_ph^2)p\dot{V} \\ &\quad + \{4rh^2 - 60rhph_p + 12pr_ph^2 - 18rhp^2h_{pp} \\ &\quad - 18pr_phph_p + 72r(ph_p)^2 + 18pz_ph^2p\psi_p \\ &\quad + 36rh^2(p\psi_p)^2\}V]V^{\frac{1}{2}} , \\ D &= -4r_0h^7(-J_0) , \end{aligned}\right\} \tag{16}$$

where the suffix p denotes partial differentiation with respect to p and the dot ($\dot{}$) denotes ordinary differentiation with respect to p. The paraxial ray equation on the axis is slightly different from that off the axis. It may be shown that the limiting values of r, h, $h_p$, $r_p$, $h_{pp}$, $z_p$, $\psi_p$ and $-J_0$ for $q \to 0$ are given as

$$r \to xq , \quad h \to 1 , \quad h_p \to 0 , \quad r_p \to x_pq ,$$

$$h_{pp} \to 0 , \quad z_p \to 1 , \quad \psi_p \to x_{pp} , \quad -J_0 \to 1 .$$

Thus, the paraxial trajectory equation on the axis can be formed to be

$$A'p^2x_{pp} + B'px_p + C'x + \frac{D'}{x} = 0 \tag{17}$$

with

$$
\left.
\begin{aligned}
A' &= 36V^{\frac{3}{2}} , \\
B' &= (18p\dot{V} + 24V)V^{\frac{1}{2}} , \\
C' &= (9p^2\ddot{V} + 24p\dot{V} + 4V)V^{\frac{1}{2}} , \\
D' &= -4 .
\end{aligned}
\right\} \quad (18)
$$

Eqs. (15) and (17), together with the partial differential equations

$$\frac{\partial h}{\partial q} = -x\frac{\partial \psi}{\partial p} , \quad (19)$$

$$\frac{\partial \psi}{\partial q} = \frac{1}{h}\frac{\partial x}{\partial p} , \quad (20)$$

$$\frac{\partial r}{\partial q} = \frac{x}{h}\frac{\partial z}{\partial p} , \quad (21)$$

$$\frac{\partial z}{\partial q} = -\frac{x}{h}\frac{\partial r}{\partial p} , \quad (22)$$

form the complete set of basic equations for numerical solution of the initial value problem of space-charge flow.

## 3. METHOD FOR NUMERICAL SOLUTION

A set of basic equations derived in the previous section is elliptic and therefore has unstable nature when solved as the initial value problem with the direct application of finite difference technique. In order to obtain stable solutions, Colburn et al. have converted the space-charge flow equations into a set of hyperbolic equations by making analytic continuation into the complex domain and then integrated them by finite difference technique. In place of their method, we shall develop here a method in which the finite difference method and the power series expansion method are compounded.

First, we express all the variables as power series of p:

$$h = h_0(q) + h_1(q)p + h_2(q)p^2 + \cdots , \tag{23}$$

$$\psi = \psi_0(q) + \psi_1(q)p + \psi_2(q)p^2 + \cdots , \tag{24}$$

$$r = r_0(q) + r_1(q)p + r_2(q)p^2 + \cdots , \tag{25}$$

$$z = z_0(q) + z_1(q)p + z_2(q)p^2 + \cdots , \tag{26}$$

$$x = x_0(q) + x_1(q)p + x_2(q)p^2 + \cdots . \tag{27}$$

All the coefficients of these power series are functions of q only. Thus, the problem is reduced to solve a set of ordinary differential equations for the coefficients. The coefficients for $q = 0$ are specified by the initial conditions (7) as follows:

$$\left.\begin{array}{ll} h_0(0) = 1 , \quad h_1(0) = h_2(0) = \cdots & = 0 , \\ \psi_0(0) = \psi_1(0) = \psi_2(0) = \cdots & = 0 , \\ r_0(0) = r_1(0) = r_2(0) = \cdots & = 0 , \\ z_0(0) = 0 , \quad z_1(0) = 1 , \; z_2(0) = z_3(0) = \cdots & = 0 . \end{array}\right\} \tag{28}$$

The coefficients of x for $q = 0$ are obtained by solving successively a series of algebraic equations resulting from substituting Eq. (27) with $A'$, $B'$, $C'$ and $D'$ expanded in power series into Eq. (17) and then equating coefficients of each power of p to zero in the resulting power series. Now that we know all the variables for $q = 0$ in the form of power series in p, we can find the coefficients of those except x for $q = \Delta q$ approximately by the aid of Taylor's expansion:

$$h_k(\Delta q) = h_k(0) + h_k'(0)\Delta q + \tfrac{1}{2}h_k''(0)\Delta q^2 , \tag{29}$$

$$\psi_k(\Delta q) = \psi_k(0) + \psi_k'(0)\Delta q + \tfrac{1}{2}\psi_k''(0)\Delta q^2 , \tag{30}$$

$$r_k(\Delta q) = r_k(0) + r_k'(0)\Delta q + \tfrac{1}{2}r_k''(0)\Delta q^2 , \tag{31}$$

$$z_k(\Delta q) = z_k(0) + z_k'(0)\Delta q + \tfrac{1}{2}z_k''(0)\Delta q^2 , \tag{32}$$

with

$$
\left.
\begin{aligned}
&h_k(0) = \begin{cases} 1 & \text{for } k = 0 \\ 0 & \text{for } k \neq 0 \end{cases} \quad , \quad h_k'(0) = 0 \quad , \\
&h_k''(0) = -\sum_{j=0}^{k} (k-j+2)(k-j+1)x_j(0)x_{k-j+2}(0) \quad , \\
&\psi_k(0) = 0 \quad , \quad \psi_k'(0) = (k+1)x_{k+1}(0) \quad , \\
&\psi_k''(0) = 0 \quad , \\
&r_k(0) = 0 \quad , \quad r_k'(0) = x_k(0) \quad , \quad r_k''(0) = 0 \quad , \\
&z_k(0) = \begin{cases} 1 & \text{for } k = 1 \\ 0 & \text{for } k \neq 1 \end{cases} \quad , \quad z_k'(0) = 0 \quad , \\
&z_k''(0) = -\sum_{j=0}^{k} (k+1-j)x_j(0)x_{k+1-j}(0) \quad ,
\end{aligned}
\right\} \quad (33)
$$

where (′) denotes differentiation with respect to q. The values of $h_k(0)$, $\psi_k(0)$, $r_k(0)$ and $z_k(0)$ follow from Eq. (28), those of $h_k'(0)$, $z_k'(0)$, $\psi_k''(0)$ and $r_k''(0)$ from the symmetry and antisymmetry of these variables about the axis and those of $h_k''(0)$, $\psi_k'(0)$, $r_k'(0)$ and $z_k''(0)$ from Eqs. (19), (20), (21) and (22) respectively. With the knowledge of the coefficients above described, we can solve Eq. (15) in the same manner that Eq. (17) has been done and obtain x for $q = \Delta q$ in a power series.

Now we have known the coefficients of all the variables for $q = 0$ and for $q = \Delta q$. They are used to give the coefficients of h, ψ, r and z for $q = 2\Delta q$. Generally the coefficients of h, ψ, r and z in $q = q_0 + \Delta q$ $(q_0 > \Delta q)$ are calculated from those in $q = q_0 - \Delta q$ and the derivatives of those with respect to q in $q = q_0$ with the help of Taylor's expansion as follows:

$$h_k(q_0 + \Delta q) = h_k(q_0 - \Delta q) + 2h_k'(q_0)\Delta q \quad , \qquad (34)$$

$$\psi_k(q_0 + \Delta q) = \psi_k(q_0 - \Delta q) + 2\psi_k'(q_0)\Delta q \quad , \qquad (35)$$

$$r_k(q_0 + \Delta q) = r_k(q_0 - \Delta q) + 2r_k'(q_0)\Delta q \quad , \qquad (36)$$

$$z_k(q_0 + \Delta q) = z_k(q_0 - \Delta q) + 2z_k'(q_0)\Delta q \quad . \tag{37}$$

Substitution of Eqs. (23)-(27) into Eqs. (19)-(22) yields the ordinary differential equations for the coefficients of h, $\psi$, r and z, which are used for calculating $h_k'$, $\psi_k'$, $r_k'$ and $z_k'$ in the above equations with the coefficients of h, $\psi$, r, z and x. In the actual computation on a digital computer, the programming is so devised that this calculation of $h_k'$, $\psi_k'$, $r_k'$ and $z_k'$, together with that of the coefficients of x by using Eqs. (15) and (17), is numerically manipulated within the computer without giving their mathematical forms explicitly. Now, knowing the coefficients in $q = \Delta q$ and in $q = 0$, we obtain those in $q = 2\Delta q$, using above equations with $q_0 = \Delta q$. Again, Eq. (15) is solved in the form of power series of p to obtain x for $q = 2\Delta q$. Similarly Eqs. (34)-(37), together with Eqs. (19) -(22), and Eq. (15) are used to determine the coefficients of h, $\psi$, r, z and x for $q = 3\Delta q$ with those of h, $\psi$, r, z and x which have just been obtained for $q = 2\Delta q$ and those of h, $\psi$, r and z for $q = \Delta q$. This process is repeated to obtain the coefficients of the variables h, $\psi$, r, z and x for larger q. It should be noted that the cathode current density is necessarily determined in course of solution of Eq. (15) by assumption that x is analytic at $p = 0$, which is a singular point of Eq. (15), and therefore can be expanded around $p = 0$ as in Eq. (27).

In the actual calculation we should be content with retaining the terms in the power series expansion to a certain finite order. In solving the initial value problem for elliptic type of partial differential equations by our method, in general, the extent to which the desired degree of accuracy in the resulting solutions may be kept depends upon how many terms are retained in the power series. For the application to gun design, the flow solutions are generally required to be quite accurate to a fairly long range in direction of p, or in the direction of flow. In order to meet this requirement we should connect the power series solution around $p = 0$ with that around $p = p_1$ ( $>0$) in such a way that both x and its first derivative with respect to p are continuous there. The power series solution around $p = p_1$, if necessary, may be connected further with those around $p = p_2, p_3, \cdots$ successively in the same way, where $p_1 < p_2 < p_3$ . Thus, the number of terms to be retained should be decided by how far in direction of q

the solution must be sufficiently accurate. In our calculation the terms have been retained to the order 99th in power series of all the variables.

## 4. POTENTIAL DISTRIBUTION ALONG THE AXIS

It is desirable for the design of practical convergent-type gun to find such a space-charge flow that the potential on the axis rises as that of the cospherical space-charge limited diode until it reaches a certain value, after which the potential almost levels off to a constant value. Among various functions of such nature, we adopt the function expressed by

$$\phi_0(p) = \Phi(y) \tag{38}$$

and

$$y = \int_0^p \exp[-(ap)^n]\, dp \quad , \tag{39}$$

where $\Phi(y)$ is the function describing the potential distribution in the cospherical diode if y is interpreted as the distance from the cathode. Here, d, in terms of which length is measured, is chosen as the cathode radius of the cospherical diode. In actual numerical calculation the function $\phi_0(p)$ is expressed in the form of power series.

The function y involves two parameters n and a. The parameter n is to be positive integer, since otherwise y can not be expanded into power series. The parameter a is related to $y_a$, the limiting value of y for infinitely large p, as

$$y_a = \frac{1}{a}\Gamma(1 + \frac{1}{n}) \quad . \tag{40}$$

Then we may characterize the function $\phi_0(p)$ by n and $y_a$, instead of n and a. In Fig. 2 y(p) and $\phi_0(p)$ are presented with $n = 4$ and $y_a = 0.5$. As n becomes large, the curve y in Fig. 2 tends to approach the broken line segments OXY and therefore $\phi_0(p)$ comes to have a distinct knee at $p = y_a$. Thus, it may roughly be said that $p = y_a$ corresponds to the position of anode aperture of prototype Pierce's gun.

## 5. RESULTS OF THE SOLUTION

Following the method aforementioned, we have obtained the numerical solutions for the space-charge flow equations

with various values of the parameters n and $y_a$. Some examples of the solutions are presented here; the flow lines and the equipotentials in Fig. 3, the cathode current density distributions in Fig. 4 and the cathode shapes, together with the sphere of radius equal to unity for reference, in Fig. 5.

We see that the solutions may be classified into two groups, one having the parameter n of even number and the other of odd number. As for the former group, or that with $n = 2k$ ($k = 1, 2, 3, \cdots$), if k is even, the cathode tends to deviate inward from the sphere and the cathode current density to decrease with the increase of the distance from the cathode center, and if k is odd, on the contrary, the cathode tends to deviate outward and the current density to increase. On the other hand, as for the latter group, or that with $n = 2k-1$ ($k = 1, 2, 3, \cdots$), if k is even, the inward deviation of the cathode from the sphere is accompanied with the increase of the cathode current density and if k is odd the outward deviation with the decrease of the current density.

We can find in each group that the larger $y_a$ becomes with n constant or the larger n becomes with $y_a$ constant, the larger the cathode area of uniform current density becomes, and the larger $y_a$ the better the cathode approximates the sphere but the larger n it dose not necessarily. Finally it should be noted that in all the space-charge flows obtained here the flow lines tend to becomes denser away from the axis in the drift region sufficiently far from the cathode though the flows remain laminar there.

## 6. CONCLUSION

In this paper, we have dealt with two subjects; one is to develop the numerical method to solve stably the initial value problem of the space-charge flow equations which are of elliptic type, and the other to find new space-charge flows useful for electron and ion gun design by applying this method.

As for the former problem, a method, which is a composition of the finite difference method and the power series expansion method, has been developed. Use may be made of it for the initial value problem of any elliptic type of partial differential equations. Accordingly, this method is applicable to the determination of the electrode shapes of the guns utilizing the space-charge flow obtained in this paper, the next problem in gun design.

As for the latter problem we have tried to find the

irrotational space-charge flows of axial symmetry in which the potential on the axis has a limiting value sufficiently far from the cathode, in order to exclude the correction to the anode aperture effects. We have presented one mathematical form for the potential variation of this nature, and there may be many other possible ones which might give space-charge flow solutions more useful to practical gun design. The results shown in the last section suggest that, for example, the form of potential variation

$$\phi_0(p) = \Phi(y)$$

with

$$y = \int_0^p \exp[-\sum_k (a_k p)^k]\, dp$$

may give more favourable result in the uniformity of the cathode current density and the sphericity of the cathode shape if appropriate choice is made of k and $a_k$.

In practical gun design it is required to determine what values are to be chosen in the parameters characterizing the gun so as to produce the beam of given current, voltage and radius. It is of practical importance to meet such requirement with the guns using our space-charge flows. In microwave electron tubes the guns have often been made with the cathode immersed in the magnetic field for sound practical reasons. It is necessary to extend our method so as to be applicable to rotational space-charge flows with magnetic field for the design of the guns of such use. This, together with a few problems pointed out above, is to be solved in near future.

REFERENCES


1) J. R. Pierce, "Theory and design of electron beams," Van Nostrand Co., p. 173, (1954).
2) I. Langmuir and K. Blodgett, "Currents limited by space charge between concentric spheres," Phys. Rev., vol. 24, p. 49, (July, 1924).
3) P. T. Kirstein and G. S. Kino, "Solution to the equations of space-charge flow by the method of the separation of variables," J. Appl. Phys., vol. 29, p.1758, (Dec.1958).
4) D. S. Colburn, K. J. Harker and G. S. Kino, "New method for the design of high perveance guns," Proc. 4th International Congress on Microwave Tubes, p. 572, (Sept.1962).

5) K. J. Harker, "Determination of electrode shapes for axially symmetric electron guns," J. Appl. Phys., vol. 31, p. 2165, (Dec. 1960).
6) K. J. Harker, "Electrode design for axially symmetric electron guns," J. Appl. Phys., vol. 33, p. 1861, (May 1962).

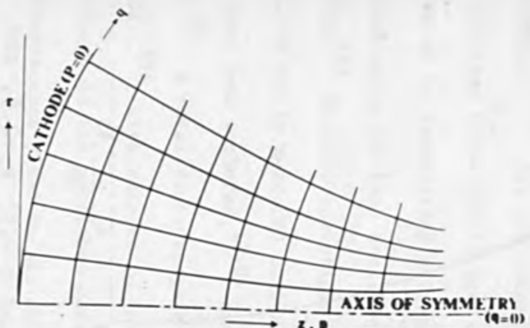


Fig.1 (r,z) and (p,q) coordinate systems

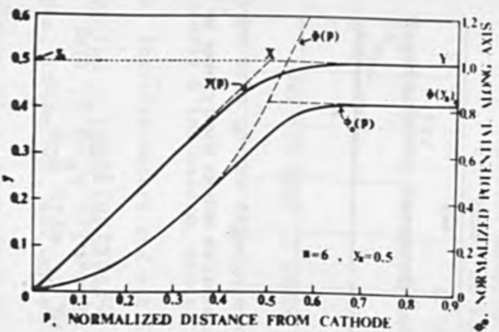


Fig.2 Function y(p) and potential on the axis $\phi_0(p)$ for n=6 and $y_a$=0.5

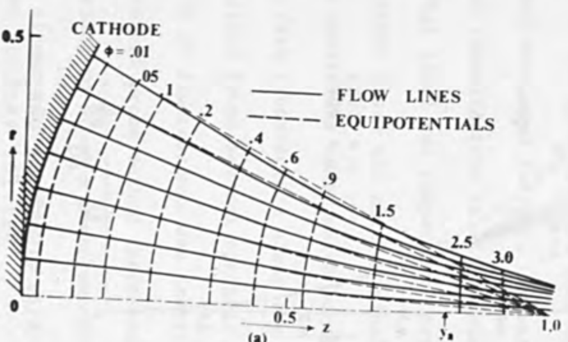


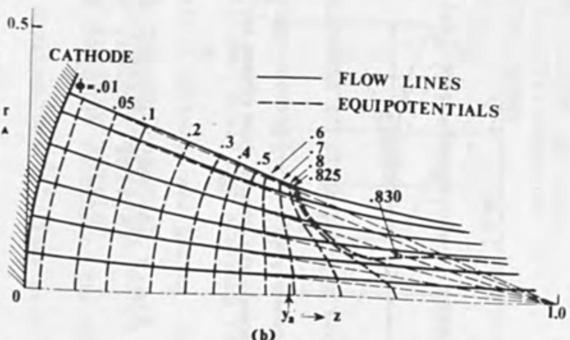


Fig.3 Cathode shapes, flow lines and equipotentials (a):for n=4 and $y_a$=0.8, and (b):for n=6 and $y_a$=0.5

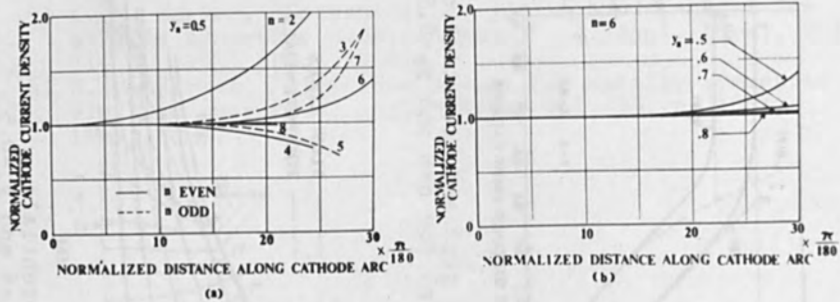


Fig.4 Cathode current density distributions
(a):for various values of n with $y_a$=0.5, and
(b):for various values of $y_a$ with n=6

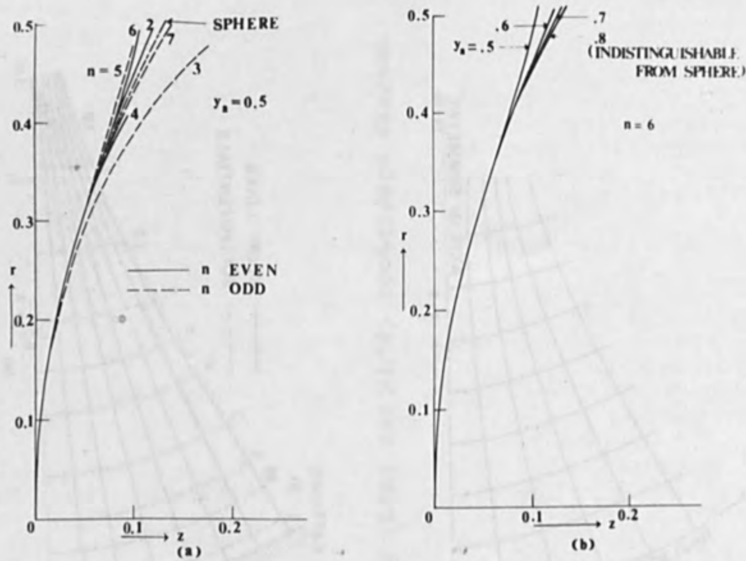


Fig.5 Cathode shapes
(a):for various values of n with $y_a$=0.5, and
(b):for various values of $y_a$ with n=6

# SOME ASPECTS OF FLOW VISUALIZATION AND LOCAL DENSITY MEASUREMENTS IN RAREFIED GASES BY MEANS OF ELECTRON BEAM PROBES

B. W. Schumacher

**Westinghouse Research Laboratories, Pittsburgh, Pa. 15235**

Over the past 15 years the development of electron beam techniques has given eyes to the aerodynamists studying rarefied gas flow, where they were nearly blind before, since the traditional tools for studying flow fields, interferometers and schlieren-optical systems, are losing their sensitivity at lower pressures. As an alternative analytical method Schopper, Schumacher, and Gruen[1-4] have therefore introduced the electron beam probes, which have since found many applications.[5] They were first used in a mode which one may call the integrating type of probe; and these early beginnings were briefly mentioned in the then standard text on density measurements.[6] But the method was soon developed further. It was shown that electron beams can be used for flow visualization in either shadowgraph systems or by stimulating afterglow. That local gas temperature can be measured using the band spectrum of diatonic gases was also originally shown by Gruen.[4] In other investigations the conditions under which local gas densities can be measured utilizing the fast fluorescence along the beam path have been explored,[7,8] and the method found several specific applications.[9] A total pressure gage based on UV-fluorescence was described by Alexeff.[10] With respect to the fluorescent probe method there remained a discrepancy in the published data; according to Gruen's measurements[11] the fluorescence yield in air should be linear with density to at least 1 Torr whereas Gadamer[9] found it to saturate towards 1 Torr. New experi-

ments reported here agree with Gruen's data. Some of the inherent difficulties with stray light have been avoided by Trochan[12] measuring the x-rays emitted by the gas in the electron beam path. In order to separate the induced fluorescence from background light we have pulsed the electron beam. With a swept beam we obtained fluorescent cross section pictures of, among others, a helium gas jet. The interpretation of these pictures poses several as yet unanswered questions.

The light and x-ray optical method is in principle capable of measuring not only density but the local gas composition, i.e., the distribution of the different species in a mixture of gases or ions.[7] In a plasma the excited spectrum of the ions (optical or soft x-ray region) should allow one to determine local ion densities, as proposed earlier,[13] but no experiments to this effect have been made to date. With the refined energy loss spectrograph of Geiger[14] composition analysis may become practical on the basis of scatter energy loss measurements. A method using ion beam scattering for composition analysis has been described some time ago (Ref. 15 Fig. 7 and Claim 6) but its performance has not been evaluated to date.

An integrating density gage based on electron single-scattering was developed by the author[15,16,17] some time ago. This method was used by Camac[18] to measure the thickness of a shock front in argon. An alternative method for determining local gas densities, based on measuring the large-angle single-scattering of the electrons from a small region of the gas, had also been suggested.[13] The results from a first experiment[19] show that it is applicable to pressure levels of up to at least 1 Torr. In the rendition of details it will probably not match the optical method, but has none of its difficulties.

While there are many more exploratory experiments which one obviously would like to see done the limited facilities which were available at the time imposed restrictions on our program. Nevertheless, the following discussions will, it is hoped, help in the understanding and use of electron probes as a measuring tool in aerodynamics and plasma diagnostics.

## THE ELECTRON BEAM FLUORESCENCE PROBE WITH PULSED AND SWEPT BEAM

### General Principles

Every interaction process of an electron with a gas molecule can be used to obtain information about the gas. This seems so obvious that it is astonishing how long it took until this possibility was exploited. However, the development of suitable instrumentation(4) played a great part in the success which electron probe techniques recently enjoyed.

In Fig. 1 an electron beam system is shown which exploits most of the interaction processes, getting simultaneously as much information about the gas as possible.

An electron gun is schematically indicated in Fig. 1 shooting a beam of electrons vertically up through a inhomogeneous gas flow field. The primary electron beam is stopped and the beam current measured by a Faraday cage F; the distance D1 between the electron gun and the Faraday cage is in the order of 4 ft. Electrons which are scattered through small angles in the forward direction by collisions with the gas molecules are measured by another ring-shaped Faraday cage designated FC. Between F and

and FC a shield SH1 is placed to avoid interaction. A second shield SH2 collects electrons which are scattered even beyond FC. A large beam stop ST can be pushed into the beam path in order to collect the total beam current $I_0$ regardless of small angle scattering.

The electron beam interacts with a gas jet in the region designated by A in Fig. 1. This gas jet can either be a wind tunnel flow, or, as in our preliminary measurements, a jet coming from a small capillary tube. The interaction region A of electron beam and gas flow is observed by a set of optical detectors, consisting of a lens, an aperture plate in the plane of the picture produced by this lens, interference filters for the various wave lengths of light placed over the various apertures, and a set of photomultiplier tubes recording the light coming from the various apertures or regions of the interaction area respectively. The optical detector set can be located inside the vacuum of a wind tunnel, or the observation can take place through a glass window in the wall of a duct as indicated in Fig. 1. Opposite to the optical detectors is a large-angle scatter detector for electrons scattered approximately 90° within the area A. This detector consists for instance of an aluminum foil, thin enough to let the scattered electrons pass, a scintillation crystal, and a photomultiplier tube registering the light pulses from the scattered electrons. Apertures in front of this detector limit its field of view to a defined narrow area.

Electronic circuits are provided which, first of all, allow to pulse the primary electron beam. For beams with less than 1 kW of power this can be done by deflecting the beam across a narrow aperture. Pulse repetition frequencies from, say, 10 kHz to 1 MHz were available. Each of

the photomultiplier tubes in the optical detector set feeds its output signal through an ac preamplifier into a phase-sensitive amplifier, synchronized with the beam pulsing circuits, and the output signal from the phase-sensitive amplifier is recorded. At the same time the dc signal from the photomultiplier tube is amplified by dc amplifiers and also recorded. The pulses registered by the phototube of the large-angle scatter detector are fed to a scaler, whereas the dc output of this phototube is fed through dc amplifiers again to a recorder. The scaler registers particles per second, whereas the dc channel registers energy flux per second. The large-angle scatter detector is completely impervious to stray light, however is somewhat sensitive to x-rays. The optical detectors are, when operating in the pulsed beam mode also little influenced by background light, in addition narrow band interference filters will reject all background light but the one in the region of the spectral line of interest. This gives the system a very good signal-to-noise ratio. The optical detectors can of course be augmented by a photographic system, or by a television pick-up tube, for instance of the SEC type [35] which permits integration. A gated light amplifier tube may be placed in front of this system and, if synchronized with the beam pulsing circuits, will permit scroboscopic observations, e.g. for flow velocity measurements.

With a system as shown in Fig. 1 we can make the following measurements simultaneously. A measurement of the primary beam current $I_F$ will give the attenuation of the beam due to the average gas density across the distance $D_1$. It is most effective in the range of .1 Torr to 10 Torr. The forward scatter current $I_{SC}$ permits to make average density measurements down to a pressure level in the order of $10^{-12}$ Torr, perhaps to $10^{-15}$ Torr

and up to .2 Torr. The ratio of scatter current $I_{SC}$ to primary current $I_F$ gives another independent measure of average gas density covering many orders of magnitude. The gaseous fluorescence, excited by the electron beam and observed by the optical detector set, permits to make local measurements of the gas composition from the intensity of the various spectral lines; it permits to make local density measurements from the intensity of certain short lived spectral lines; it permits to measure temperature in di-atomic gases from the translational and rotational band spectrum; in certain cases is may allow to discriminate between the molecular density and ion density on the basis of the different visible spectra or x-ray spectra of the molecules, atoms and ions; and in some cases it may permit to make temperature measurements on the basis of the fluorescence yield if the density is known from other measurements.[20] Finally a measurement of the doppler-broadening or shift of a spectral line can give temperature and velocity. All these spectroscopic methods were, of course, well known before they were combined with the electron probe technique.

In certain gases the electron beam will also excite long-lived fluorescence or so-called afterglow and in a high speed flow a luminous afterglow vane will be carried by the gas in the direction of the flow. Under certain conditions and using a pulsed electron beam timing marks can be impressed on this afterglow and the local flow velocity vector determined from these timing marks. The necessary scroboscopic optical observation system is not shown in Fig. 1.

All instruments shown in Fig. 1 may either be completely immersed in the vacuum, say a large free-stream wind tunnel or, for a ducted system, for instance a shock tube, the optical detectors can sit outside the glass

window, the scatter detector can operate through the thin foil window in the wall of the duct. The current measuring devices, F, FS, etc., must be inside the vacuum. The electron gun can project through the wall of the flow chamber.

Fig. 2 shows an electron gun which can be flanged to a wind tunnel, brings the beam exit nozzle close to the flow field, and fires a horizontal beam of 50 - 120 kW and 1 - 10 mA through the gas.

Fig. 3 shows an instrumentation system built for the plasma wind tunnel of the U.S. Army Missile Command, Redstone Arsenals, Huntsville, Alabama. It will be completely inside the vacuum and the electron gun and detectors can travel during operation over an area of about 1 x 2 ft. Fig. 4 shows a beam of 75 kV, 1 mA going across the 4 ft. flow field in this wind tunnel, but without flow, at a static pressure of about .1 Torr of air. So far only a few calibration runs have been made with the plasma flow.[21] The measurements reported in the following sections were made with a small test chamber, a 6" ID cross-piece of steel pipe.

## Static Calibration; Light Yield as Function of Pressure

Before local measurements in an inhomogeneous flow field can be made the instruments must be calibrated. This can be done under static conditions. The phototube currents were recorded while the pressure was varied without a gas jet present. The phototubes saw about 2" of the beam path under these conditions the signal levels were always far above the dark durrent of the tubes, stray light being excluded. One phototube

(Du Mont K1780 with S11 cathode response) recorded the total light, a second similar phototube with an interference filter in front recorded essentially the intensity of the $N_2^+(0,0)$ band. (Filter with 68A half width, centered at 3935A). The current $I_o$ changed with pressure.*) But even without measuring $I_o$, the current through the observation region is represented by $I'_{TOT}=I_F + I_{SHI} + I_{SC}$ unless the beam spread becomes too wide and the concept of a "probe" loses its meaning.

Fig. 5 shows the measured value of the currents I and the light intensities L as a function of pressure. Values for $I'_{TOT}$, $I_F$, $I_{SC}$ and $I_S$ are also shown to demonstrate how much information is indeed obtained simultaneously and must, of course, form a self-consistent set of data. The light intensities per unit beam current

$$L^* = L \times I_{oo}/I'_{TOT}$$

represent the actually desired data. $L_2^*$ refers to phototube #2, without filter, and $L_5^*$ to phototube #5, with filter. (Tubes e and f in Fig. 1). The L intensities are given in arbitrary units and should not be compared with one another. The indices ac and dc refer to the ac and dc output channels as discussed below.

The light output per unit current $L^*$ follows in each case closely the 45° line up to a pressure of nearly 1 Torr. This means it is proportional to pressure up to about 1 Torr as one would expect on the basis of Gruen's[11] measurements. The curve $L_5^*(AC)$ becomes nonlinear sooner than the curves $L_5^*(DC)$ which is at present unexplained.

*) The current $I_o$ could be kept constant by a more elaborate differential pumping system than the one we had used on this gun.

Some of the non-linearities may indicate gas focusing, especially above 1 Torr. For high voltage beams of low current gas focusing is certainly negligible. What happens at higher currents and pressures has never been studied. The "relativistic pinch"[22], forming a potential trough for the beam because of the residual gas ions, is hardly effective at beam voltages below 500 keV. The "electrostatic" pinch effect, recently studied by Halsted and Dunn[23] should not be noticeable either at the low beam perveance which we were using here.

In similar runs with helium and nitrogen the same general response of the system was confirmed. In case of helium the linear response continued beyond 2 Torr, but no detailed, comparative measurements were made.

To check on the advantages of the ac mode of operation the phototube output was split into two channels, one for the dc (average) plate current of the phototube, the other for the ac signal only. The ac signal was fed by capacitive coupling into a tuned amplifier, General Radio Type 1232A. Since the deflection pulsing produced only a quasi-sinusoidal beam current pulse, conditions were not really optimized. If then, under otherwise constant conditions, dc stray light was deliberately introduced, the dc phototube output could be increased to more than 5 times the previous (signal) value before a small change in the ac output signal would be noted. For a specific, narrower working range one could still better this result. Later, on the wind tunnel, phase-sensitive detection brought impressive further improvements in background reduction and sensitivity.[20]

## Inhomogeneous Flow Field; Resolution and Sensitivity of Probes

For any measurements in an extended, inhomogeneous gas space there is the principle requirement that the probing beam is not unduly altered, for instance attenuated, on its passage through the observation space. This may seem a condition that can not easily be fulfilled, since signals are only produced if the probe beam interacts with the gas. If it produces fluorescence, it loses energy; if it emits a current of scattered electrons, the primary probe current is diminishing steadily.

The fact that an electron probe can nevertheless be used has very deep reasons. The energy flux density in an electron beam exceeds anything we know in light or in other particle beams. The same feature makes electron microscopy possible in spite of the large aberrations of electron optical lenses. Typical values for such flux densities are:[24]

| | |
|---|---|
| Microscope Lamp | 2.5 Watts/cm$^2$, steradian |
| Sun | 350 " " |
| Electron beam, 100 kV, | $8 \times 10^9$ " " |

Even with laser beams one can not achieve a flux density similar to that in electron beams, except in single pulses. On the other hand we find only a very slight interaction of fast electrons with the gas atoms. Indeed, the interaction would not produce a useful signal were it not for the high energy flux available in the probing beam. If the field is inhomogeneous in density say, the electron beam passes through a cone shaped shock wave, one may ask whether the density discontinuity at the point of exit of the electron beam shows up in the same way as where the beam enters. In other words, one may ask whether there is an after-effect or memory-effect when the electron beam

has traversed a high density region. Again the answer is that this need not concern us as long as the interaction of probing beam and gas is weak. In our first large scale test of the electron beam fluorescence probe we have especially checked this aspect and found no "memory effect" with the high beam voltages we had used, as shown in Figs. 7 and 8 of the earlier publication.[8] We had shown an electron beam crossing a stationary shock front. Since the beam is the same (as to voltage and current) in front as well as behind the shock front, relative density measurements can be made with great accuracy, a principle later very successfully exploited by Robben and Talbot.[9]

With lower beam voltages one can obtain a higher sensitivity (greater fluorescence yield) but loses resolution. Obviously there must be a judicious choice of parameters for each applications.

For actual density measurements, - - but not for flow visualization as shall be shown later - - one must distinguish between lateral and longitudinal resolution. The visible width and spread of the beam is an immediate indication of the lateral resolution. The longitudinal resolution (along the beam axis) can in principle be made as small as desired by looking through narrow slit apertures. The practical limit is determined by the required measuring sensitivity which, in turn, is proportional to the beam current. However, the primary beam current, beam width, and angular aperture, are again interrelated. Space charge broadening or contraction due to gas focusing, which are both small for high voltage beams can be neglected. Using the above given power density figure we see that with a 100 keV beam a maximum current flux density of $0.8 \times 10^5$ amp/cm$^2$, steradian can be attained. Assuming a beam aperture of 0.005 radian half angle is required, e.g., a

cone which opens up to 0.6 cm diameter over a distance of 60 cm. This aperture is equivalent to 8 x $10^{-5}$ steradians. The maximum current density is therefore 6.4 A/$cm^2$. With a smallest beam diameter of 0.1 cm the maximum beam current is therefore 50 mA. If a higher current is required than the diameter or the angular aperture of the beam must be increased. From a less than perfect gun not even the current of 50 mA will be obtained. But already with beam currents in the order of .1 mA a longitudinal resolution near 0.1 cm can be attained, as the pictures in Fig. 11 will show. Robben and Talbot[9] estimated 0.075 mm for their measurements. This means the longitudinal resolution reaches the order of 1 mean free path of the gas molecules.

The lateral resolution is not only determined by the primary width of the beam, but by scattering in the gas. Scatter broadening due to multiple scattering can be calculated in the form of current density profiles as shown by Kessler,[25] or for single scattering one can calculate the fraction of electrons scattered into a ring-shaped area around the beam by an approximate numerical integration over scatter probability function and path length. The curves in Fig. 6 were obtained by the latter approach.[17] Since the scatter probability function per unit angle has a very steep peak at a small but finite angle in the forward direction the beam does not just broaden by increasing its diameter, but the central primary beam acquires a "skirt" of scattered electrons. Only in a later phase, at higher pressures or longer path lengths, will the current distribution become more uniform over a larger diameter; a state of conditions which is then maintained by backscattering from the "skirt" to the center. But then we have practically lost a distinct "probe" beam.

The curves of Fig. 6 give the integral scatter values over a long beam path, therefore the just mentioned peak in the forward scatter direction is not apparent. In our previous curves for $(N_{ij}/N_o)\ d\theta^{-1}$ this was not brought out either because the approximation which was used does not hold for very small angles. Since it seems so important for explaining the appearance of the beam this peaking effect is shown in Fig. 7 which shows scatter distributions measured by J. Geiger[14] as a function of angle. (Geiger's curves for $d\sigma/d\Omega$ are replotted for $d\sigma/d\theta$ by using the relation $d\Omega = 2\pi \sin\theta d\theta$, hence the curves shown the scatter probability into a cone-mantle element $d\theta$ at cone angle $\theta$). The elastic and inelastic scattered electrons peak separately. For the gross scatter distribution the elastic scatter peak (at larger angles than the inelastic!) is the more important one, as demonstrated and pointed out by Kessler et. al. For all gases shown here, as well as in Kessler's paper, this peak lies between 20 and 40 milli-radians (1.1° and 2.2°). For molecular nitrogen diffraction effects will change the scatter distribution for angles less than 30 mrad.[26]

The examples of Fig. 7 show that for the light elements the inelastic scattering dominates whereas for argon (and heavier elements) the elastic scattering is more important. Note that Fig. 7 is in logarithemic coordinates; on linear coordinates the "peaks" would, of course, appear very much steeper.

With increasing beam voltage the scatter peaks shift to smaller angles, as one would expect. Considerable information on this aspect, and also on the influence of multiple scattering, can be found in the earlier studies of the electron microscopists.[27] But at that time neither theories nor experiments gave sufficiently accurate quantitative results. As for

the progress that has been made since, it should be noted that the energy loss analysis of Geiger (loc. it.) has been developed to a point where gas composition analysis from the scattered beam seems to become practical.

For the initial scatter broadening of the probe beam Fig. 6 gives the fraction of the current going into any ring-shaped area of 1 mm in width, with mean radius r, located at a path length of 57 cm, in nitrogen ($N_2$) of 0.1 Torr, 25°C. We see, with 60 keV electrons a ring with 10 mm radius and 1 mm width receives about 2% of the beam current, assuming the primary current is all concentrated at r = 0. At 1 Torr it would be 20%; no sharply defined beam would exist anymore. It is all the more remarkable that the fluorescence light as function of pressure is proportional up to these higher pressures. In the measurements shown in Fig. 2, at the point where $I_{sc}/I_F = 1$, namely at 0.3 Torr, the beam is actually 5 cm wide, at a path length of $D_1 = 87$ cm. At the location of the light detectors the visible beam width, although hard to define, was about 1 cm. This would be the lateral resolution of a probe of 60 keV electrons at 0.3 Torr, and at a point 30 cm from the gun. For higher lateral resolution higher beam voltages must be used. From Fig. 6 one would expect going from 60 keV to 100 keV would improve resolution by a factor of slightly more than two.

Gruen[28] has shown that the light yield as a function of beam voltage is proporational to dE/ds, the energy loss per unit path length.* For higher beam voltages dE/ds reaches the well known minimum of 1.68 keV/ $mg/cm^2$ at 1.1 MeV (value for nitrogen).[29] The fluorescence probe will

---

*This was not checked for the MeV range, but is here assumed to be a valid approximation.

therefore not lack in light output when operated with higher voltages at higher pressures, but as Gruen has also shown the light yield as function of pressure becomes non-linear. To determine whether there exists an upper pressure limit on the latter account systematic studies of the light yield for each spectral line or band system, which is excited, would have to be made, as suggested by Gruen.

To predict the obtainable resolution at higher pressures the question is then to find the initial beam spread as function of voltage, up to the MeV range, from scattering theory. This has, to our knowledge, not been done in such a way that we could readily apply the results. Scaling laws for the beam spread due to scattering on which to base an estimate do not exist either. However, we may use the scaling laws for the range, and assume the reciprocal relationship to hold for the initial beam spread, at least approximately. The range of an electron beam in gas is given by a relationship of the form $R = aE^n$ with n varying from 1 to 2 as a function of $E_o$. Referring to the curves for the range as given in a previous review[30] (Fig. 46) we find for $E_o$ = 60 keV a range $R_{Air} = 6.0 \times 10^{-3}$ g/cm$^2$. In order to get a range 5 times as large, and thereby reducing the beam spread in the above example to 1/5, from 1 cm to 0.2 cm, we would need to increase the electron energy to $E_o$ = 160 keV. To maintain this resolution at a pressure of 15 Torr, a voltage of 750 keV would be required.

These higher voltages present, of course, a problem in instrumentation. The sensitivity of a probe with 750 keV as compared to one with 60 keV would be reduced by the ratio of dE/ds (750 keV) to dE/ds (60 keV) for which we find 1.71 keV cm$^2$/mg and 5.13 keV cm$^2$/mg respectively.[29] We see that the loss in sensitivity is not great but the gain in resolution is significant when going to higher voltages.

Suppose one wanted to use the electron probe at much higher pressures, for instance 1/4 atmospheres. The required voltage for keeping the resolution of 1 cm at 30 cm distance from the gun can still be found approximately by the above extrapolation; it leads us to 10 MeV. The specific energy loss would be $dE/ds = 2.2$ keV $cm^2/mg$; but now about 10% would be due to radiation losses, rather than collision losses. This makes the extrapolation questionable. Nevertheless, electron probes in the energy range of 10 MeV could probably be used for getting local density measurements in gases at 1/4 atmosphere and room temperature, the other requirement being that spectral lines be found which are not quenched within the lifetime of the excited state.

At present we must leave the discussion with these semi-quantitative considerations. Exact data for sensitivity and resolution would be very desirable but must await further experimental investigations. The justification for all these considerations and, eventually, the use of such obviously expensive instrumentation as MeV electron proves lies, of course, in the fact that the non-material electron probes can be used under conditions where material probes are unsuitable.

## Flow Visualization by Direct Local Excitation; Resolution of Cross Section Pictures

Already in our earliest studies it became obvious that the "probe" method is not necessarily the only way to get interesting information about the flow. In certain gases the probe would excite afterglow which immediately rendered the flow visible.[2] But the electron beam can be used for flow-

visualization not only where it excites afterflow. One can also use direct excitation and short-lived fluorescence if the beam is "swept" through the gas, as suggested some time ago.[7] This was recently demonstrated by Trochan.[12] Fig. 8 shows in principle how a plane across the gas flow can be "illuminated" by an electron beam. Fig. 9 shows several photographs of a He-jet obtained in this manner. Between any two pictures the plane in which the beam was sweeping was displaced, giving a series of successive cross sections of the gas flow. The camera was looking under 45° to the gas flow and the illuminated plane. One can just see in the pictures that the distance between gas jet nozzle and illuminated plane is different in each case. The illumination of the sector through which the electron beam swept is not quite uniform, the edges are brighter. This is due to a small "round" transition in the sawtooth voltage which was applied to the deflection coils. (Any non-linearity in the sawtooth deflection was also noticeable at once in the fluorescence intensity.)

The pictures of Fig. 9 represent a series of cross sections through the inhomogeneous gas density region of the gas jet. In the top picture the electron beam grazes the jet nozzle (which has a flat end face with a center hole of 1mm diameter as shown on the right). The gas jet from the central hole lights up brightly due to its higher density. From the next pictures one can see how the gas jet forms a hollow "bubble." The center of this bubble is clearly darker than the beam region below or above the jet. In the lowest picture we see a bright round spot in the center, surrounded by a darker ring-shaped region, the dark ring having about three times the diameter of the bright spot.

We can also see a faint afterglow vane following the flow from right to left. It is much clearer seen with the eye. It seems as if this afterglow comes from a region outside the dark ring area. While the photographs of Fig. 9 were taken on panchromatic black and white film, a better impression was obtained with color pictures. From these color pictures secondary black and white negatives were made using color filters, because it was immediately apparent that color differences existed between the directly excited fluorescent cross section and the afterglow. Fig. 10 shows prints from the secondary negative, a "blue" picture in the top row, and a "green" picture in the lower row. In the lower left picture (cross section of the flow at a distance of about 1" from the nozzle) the dark ring with center spot is clearly seen, but hardly any afterglow. In the picture above it the afterglow comes out bright but we see not much detail in the cross section plane. The general haze in the "blue" pictures is real and not a result of different printing of the negatives.

The different contrast at different colors is, of course, related to the difference in the excitation probability and mechanism for the different spectral lines of helium and residual air, if any. Our method of separation, Ektachrome B film copied with Wratten filter No. 50, blue, and Wratten filter No. 74, green, was very crude. Narrow-pass filters should be used in taking the picture. But a discussion of the spectroscopic details is beyond the scope of this investigation. It shall only be emphasized that with regard to the interpretation of the fluorescence and afterglow pictures caution and further studies are needed.

Geometric features of the flow appear easily, clearly, and with high resolution. The resolution which one can obtain from the pictures with

respect to localized gas parameters is of particular interest, especially since it seems to be higher than the one obtainable with probes. Another set of pictures shall illustrate this once more. In Fig. 11 the electron beam is stationary. It has a diameter of about 2 mm where it crosses a helium jet perpendicularly and through the axis. The jet comes from a capillary of 1.5 mm ID which is visible in the two photographs at the right (printed so as to show the capillary and the afterglow). The point of intersection of electron beam and gas jet is very close to the capillary in the top left picture and successively further downstream in the lower pictures. The electron beam therefore illuminates a sequence of "line cross sections" through the axis of the gas jet. In the second and third pictures from the top we see again the hollow "bubble" that has formed in the jet, as we saw it in Fig. 9. Noticeable is the sharp, narrow "wall" of this bubble, and the fact how the electron beam resolves these fine details. The thickness of this bright "wall region" is less than 0.2 mm. The Mach-disc, where the "bubble" closes, is of the same thickness, and is clearly revealed, although it is oriented parallel to the electron beam, and the beam is much wider than the disc.

A comparison of the left and right row of pictures in Fig. 11 shows the much higher intensity of the primary fluorescence as compared with the afterglow. The pictures also show a halo of luminescence around the central beam. This can be caused by fast electrons scattered about small angles (scatter-skirt of the primary beam) as well as by slow secondaries with limited range. It can also be partly due to diffusion of metastable atoms or due to radiation diffusion. Detailed studies must still be made. We note in the pictures that the fluorescence halo seems to be blown away with

the flow. This would hardly be the case if the halo were only due to scattered or secondary electrons. In the right hand pictures of Fig. 11 it can be seen that the halo continues into the afterglow vane which, as such, may not represent the flow but the mixing region (see below). The halo may then also be due to the diffusion of metastable atoms and collision processes. This could explain the observations of Robben and Talbot (loc. cit.) on the helium shock waves.

Suppose now it were possible to find a spectral line which is emitted within a few times $10^{-8}$ sec after excitation by the fast electron beam, then a direct excitation cross section picture taken in the light of this line would give the molecular density distribution, because in this short time neither flow, nor thermal movement, nor collisions will have affected the excited molecules. We know that this situation applies to the $N_2^+$ band in nitrogen ($N_2$ being ionized and excited at the same time).

Petrie[31] has discussed the influence of temperature on these density measurements, only above 1000°K will corrections become necessary. On the other hand, getting the density from scatter measurements, would allow to deduce temperatures (above 1000°K) from the fluorescence yield, if the relationships can be worked out.[20]

In Figs. 9, 10, and 11 it is not clear whether the afterglow is actually the flow region or only the boundary between the flow and the stagnating gas. The energy transfer from metastable atoms carried with the flow to others in the quiescent gas is possible as demonstrated for the Ar/CO system by Gruen,[3] and for $He/N_2$ mixtures by Sebacher.[5] With the system of Fig. 11 we pulsed the primary electron beam and tried to pick up an ac signal from the afterglow, but were unable to do so. If

it is metastable atoms in collision with others that cause the afterglow then all phase relationship to the primary beam would be lost. But turbulence may also break up all phase relations. Further investigations are planned. It is also planned to determine the local flow velocity vector by pulsed beam and stroboscopic observation techniques, as suggested earlier.

The fluorescence technique with direct excitation in bi-atomic gases gives local molecular concentrations (if local current densities are known and local, molecular luminosities are measured). The resolution is, as we have seen, very good. It has been suggested[20] that since scatter measurements give atom densities the local degree of dissociation can be determined from a comparison of the scatter reading and luminosity reading. In the next chapter the resolution of electron scatter measurements from localized areas shall be discussed.

## ELECTRON BEAM PROBE WITH LARGE-ANGLE SCATTER DETECTOR

### Sensitivity and Static Calibration

The first pictures of gas jets at low pressures were taken by the electron microscopists.[32,33] In their dark-field pictures they made use of the small-angle scattering of the electrons in order to achieve the necessary sensitivity. Typically, the environmental pressure at which the forward scattering method can be used is below $10^{-6}$ Torr. No "bright-field" picture or absorption type of measurement could be made anymore at these low pressures.

At higher pressures multiple scattering makes it impossible to get forward-scatter dark-field pictures. Absorption pictures or shadow-

graphs[4] have limited resolution and depth of field. The fluorescence probe was the only tool with which one could get local values of gas density. However, at higher pressures there are so many gas molecules present that the sensitivity or cross section of the individual interaction process with the electrons is no longer a critical factor. One such interaction that can now be utilized is large-angle scattering, as had been suggested in connection with a complete instrumentation system for measuring gas parameters,[1 essentially as shown in Fig. 1.

The scatter probability for electrons of different energy on nitrogen atoms, as a function of angle, is shown in Fig. 12. For angles larger than 5° we have only Rutherford scattering with some small correction for the Mott-factor at higher angles and energies. While the scatter probability values fall off sharply between 5° and 60°, namely over 5 orders of magnitude, they drop by only 1 order of magnitude from 60° to 120°, which means in this angular range a gaging system is not overly sensitive to changes in alignment. The scatter probability for 60 keV electrons at 90° is $8 \times 10^{-23}$ $cm^2$, $steradian^{-1}$ per atom, as compared with a figure of $9 \times 10^{-1}$ at 2°. The large-angle scattering is 6 orders of magnitude fainter than the small-angle scattering. We can also make a comparison with the attenuation coefficient; for 60 keV electrons in nitrogen it is $\alpha_J = 650$ $cm^2/g$ whereas for 90° scattering we find a cross section of only 0.1 $cm^2/g$, steradian. But since scatter measurements are a dark-field method, which is always more sensitive than a bright-field method, the above figures suggest that a large-angle scatter gage may cover the same range of gas densities as an attenuation gage.

A first set of tests[19] confirmed the above expectations. Fig. 13 shows the response of the large-angle scatter detector, looking at the electron beam under an angle of 90°, as shown in Fig. 1. The gas was helium, and the gas jet which is seen in Fig. 11, lowest photograph, could be moved in and out of the electron beam region and the field of view of the scatter detector. The detector itself consisted of a plastic scintillator with a thin aluminum window. Unfortunately this window was not completely light-tight, but we are certain that the response curves of Fig. 13 are not shifted due to light by more than 10%. The scintillation pulses were recorded with a photomultiplier, discriminator, and scaler, as well as with a dc meter measuring the average anode current of the photomultiplier tube.

In front of the detector were two square apertures which limited the section of the electron beam seen by the detector to 1 $cm^2$. Curve $J_D$ shows the dc response as function of pressure. From 0.4 Torr to well over 2 Torr it follows nearly the 45° line, which means proportionality to pressure, as expected. Below 0.4 Torr the dark current, (X-rays, stray light) of the phototube becomes noticeable.

The integral count for discriminator base line settings of 3 V, 5 V, and 7.5 V is shown by $J_3$, $J_5$, and $J_{7.5}$ respectively. All three curves rise more than proportional to pressure, because the effective discriminator base line shifted with the dc average. While this could be corrected it was not done at the time. We can assume that at 2 Torr and $J_3$ settings all scattered electrons are counted, the count rate being 21000 cps, with not more than 200 cps background. This figure agrees closely with the calculated sensitivity, as shown in more detail elsewhere.[19]

It can further be seen from Fig.13 that the large-angle scatter detector, seeing only 1 cm of the beam, begins to respond before any useful response is obtained from the attenuation detector (curve $I_F$) although the latter has a path length of 87 cm. The forward scatter (curve $I_{SC}$) at lower pressures is probably falsified by scatter from the walls and by traces of air. Beyond 2 Torr it levels off, as expected, while the large-angle scattering still increases with pressure.

After the static response curves of Fig. 13 had been determined the jet was operated at 1.9 Torr average systems pressure, which also agreed with the previously measured value of $I_{SC}/I_F = 0.32$. (The $I_{SC}/I_F$ measurements represent a built-in average density gage.) If the gas jet was moved in and out of the electron beam a response on the $J_D$ and $J_5$ readings was obtained as shown by the arrows. The average density in the jet region is higher than in the quiescent gas by approximately 20%, referred to the whole area observed by the scatter detector.

Moving the gas jet in and out of the beam did not cause any noticeable change in the readings of $I_F$ or $I_{SC}$, since the jet region is only a very small part of the total beam path. Herein lies just the weakness of any integrating type of beam probe. The gas jet could probably be seen in absorption by the shadowgraph method, with the screen close behind the gas jet.

The practical sensitivity (in terms of useful signal output) of the large-angle scatter gage as compared with the attenuation system is still remarkable. It is partly due to the fact that the scattered electrons carry high energy; the energy loss in the scatter process, the recoil energy going to the atom, is small. The detector responds to the energy, not only to

the number of the electrons, and therefore a single electron produces already a signal well above noise.

For the high pressure limit of the single-scatter method the same considerations are valid as in the case of the fluorescence probes. The scatter probability drops faster with increase in voltage than the stopping power; but this should not lead to a serious limitation. There seems to be no reason why the method should not also work with 10 MeV electrons at 1/4 atmosphere.

### Flow Visualization Using Scattered Electrons; Estimate of Resolution

If the flow field contains as many fine details as for instance the one shown in Fig. 11 it would be desirable to get also a picture by means of the scattered electrons, since scanning the field with a single detector would be impractical. A picture could obviously be obtained by means of a pinhole camera, but the small pinhole aperture would limit the sensitivity. Therefore, the system of Fig. 14 is suggested[19] and shall be briefly discussed, although it was not yet put in operation.

The scattered electrons from any one point in the gas are refocused by a magnetic lens onto the picture plane. There they can be recorded by a photographic plate or by a combination of a honeycomb scintillator and a vidicon tube. The observation plane is again defined and "illuminated" by a narrow electron beam which sweeps across this plane. It is a necessary condition that the energy of the electrons in this beam is so high as to produce little forward scattering (see the previous chapter);

however, a slight "scatter skirt" around the main beam does no great harm. Under these conditions the electrons scattered through 90° will suffer as little additional small-angle scattering as the main beam itself, because their energy is the same. The scatter picture will get only some minor background due to this superimposed small-angle scattering; most of it will appear as a halo around the "bright" spots. Of course, with increase in the average pressure of the system a state will be reached where the picture loses its contrast more and more, until it finally disappears. It will probably not be blurred or distorted by the additional scattering at higher pressures; in shadowgraphs we found we only lose contrast, the half-width of the shadow pictures remains the same.

One can compare the sensitivity of this "scatter camera" with the one of the fluorescence probe, although data are scarce. As the "practical" sensitivity, Gadamer[9] found that $2.5 \times 10^{-12}$ g/cm$^2$ of air, with an electron probe of 20 kV, 1 mA would just give a detectable signal. Let us assume with 60 keV electrons, improved collection optics and in nitrogen we can detect a fluorescence signal from the same amount of nitrogen. In comparison we find for the electron scattering at 90°: $d\theta/d\Omega = 0.1$ cm$^2$/g, sterad. A magnetic lens of 2.5 cm diameter at a distance of 22 cm from the object plane would have an aperture of 0.01 sterad. A layer of $2.5 \times 10^{-12}$ g/cm$^2$ of $N_2$ would therefore produce a scatter current $N = 2.5 \times 10^{-15} N_o$. For a primary beam current of $N_o = 1$ mA this amounts to $N = 15$ electrons/sec. This signal is as readily measured as the light signal. It should further be noted that the fluorescence yield differs widely for different gases. But although $d\theta/d\Omega$ depends upon atomic number Z, the effect is not great if data are referred to mass per unit area.

CONCLUSIONS

The electron beam fluorescence probe cannot only be used for point by point measurements but can produce density cross section pictures of any plane through a rarefied gas flow. The spatial resolution is in the order of 0.1 mm at the 1 Torr level. This means it is in the order of one mean free path. In gases with afterglow caution is necessary in the interpretation of the pictures. In so far as the fluorescence observed is a molecular property the fluorescence probe measures molecular density. The large-angle single-scattering of electrons from a narrow beam yields density measurements of approximately the same sensitivity as the fluorescence probe in nitrogen. A system has been proposed which should yield cross section pictures, again of any desired plane through a rarefied gas flow, but showing atom density. In many respects the two methods complement one another.

An analysis of the sensitivity factors show that both methods should well be applicable to higher pressures, say 15 Torr if high energy electrons are employed. There seems to be no principle obstacle to make local density measurements even up to 1/4 atmosphere, or gases above 2000°K at atmospheric pressure, if beams in the energy range of a few MeV are employed.

ACKNOWLEDGMENTS

The above investigations were supported in part by a grant received by Ontario Research Foundation from the Department of Economics and Develop-

ment of the Province of Ontario. The instrumentation system was built for the Plasma Physics Branch Physical Science Laboratory, Research and Development Directorate, U.S. Army Missile Command under Contract No. OI-01-021-D4-07170(Z).

I am indebted to the staff members of the Physics Department of Ontario Research Foundation who all in many ways have contributed and made these studies possible, and to Charles Cason of the Army Missile Command Plasma Physics Laboratory for many stimulating discussions during the installation and tests of the instruments in the plasma wind tunnel.

REFERENCES

1. Schopper,E., Schumacher, B. W., and Knapp, D., Phys. Verh. 6, 73, 1950.
   Schopper, E. and Schumacher, B. W., Z. Naturf. 6a, 700-705, 1951.

2. Gruen, A. E., Schopper, E., and Schumacher, B. W., J. Appl. Phys. 24, 1527-1528, 1953.

3. Gruen, A. E., Z. Naturf., 9a 833-836, 1954.

4. Schumacher, B. W., Ann. Physik (6), 13 404-420, 1953; OPTIK 10, 116-131, 1953; NUCLEONICS 18, 106-114, 1960; Symposium Transactions, Second International Congress on Vacuum Technology, Washington 1961, Pergamon Press, New York 1962.

5. Wada, I., in Rarefied Gas Dynamics, Vol. II, J. H. DeLeeuw, Editor, Academic Press, New York 1966. Marsden, D. J., in Rarefied Gas Dynamics, Vol. II, J. H. DeLeeuw, Editor, Academic Press, New York 1966

Schultz-Grunow, F. and Frohn, A., in Rarefied Gas Dynamics, Vol. II, J. H. DeLeeuw, Editor, Academic Press, New York 1966. Sebacher, D. I. and Duckett, R. J., NASA TR-R 214, December 1964. Sebacher, D. I., J. Chem. Phys. 42, 1368, 1965.

6. "Physical Measurements in Gas Dynamics and Combustion," R. W. Ladenburg, Editor, Vol. IX of High Speed Aerodynamics and Jet Propulsion, Princeton, 1954.

7. Schumacher, B. W. and Gruen, A. E., German Patent 1 102 442/1955; U. S. Patent 2 952 776. Also: Schumacher, B. W., U. S. Patent 2 908 821, 1955.

8. Schumacher, B. W. and Gadamer, E. O., Can. J. Phys., 36, 659-671, 1958.

9. Gadamer, E. O., UTIAS Report No. 83 (AFOSR TN 60-500), March 1962. Robben, F. and Talbot, L., Phys. Fluids, 9, 633, 1966. French, J. B., AIAA Journal 3, 993, 1965.

10. Alexeff, I., 1961 Transactions, Second International Vacuum Congress, Washington; Pergamon Press, New York 1962.

11. Gruen, A. E. , Can. J. Phys., 36, 858-862, 1958.

12. Trochan, A. M., Appl. Mech. and Phys. (In Russian), 3, 81, 1964.

13. Schumacher, B. W., Ont. Res. Foundation, Phys. Res. Report No. 6303, February 1963./German Patent 962 206, 1954 and U. S. Patent 2 908 821.

14. Geiger, J., Z. Phys. 175, 530, 1963/ 177, 138, 1964/ 181, 413, 1964.

15. Schumacher, B. W., U. S. Patent No. 3 207 895, April 1961.

16. Falckenberg, H. R. and Schumacher, B. W., Can. J. Phys., 40, 1521, 1962.

17. Schumacher, B. W., Aruja, E., and Falckenberg, H. R., Proceedings Third International Vacuum Congress, Stuttgart, 1965. Vol. 2, Part 1-3, 543-554, Pergamon Press 1966.

18. Camac, M., Phys. of Fluids, 7, 1076, 1964.

19. Schumacher, B. W. and Grodski, J. J., Ont. Res. Foundation, Phys. Res. Report No. 6601, March 1966/ ISA Transactions 6, 103-110, 1967.

20. Cason, C., private communication.

21. Cason, C., CCTS Proc. of 4th Space Congress 25, 11-26, April 3-6, 1967.

22. Budker, G. J., CERN Symposium on High Energy Accelerators, June 1956.

23. Halsted, A. S. and Dunn, D. A., J. Appl. Phys., 37, 1810, 1966.

24. Borries, B. V., OPTIK, 3, 321-380/389-412, 1948.

25. Kessler, J., Z. Physik, 155, 350, 1959; 182, 137, 1964. Jost and Kessler, Z. Physik, 176, 126, 1963. Fink and Kessler, Z. Physik 196, 1-15, 1966.

26. Fink, M. and Kessler, J: J. Chem. Phys. 47, 1780. 1967.

27. Borries, B. v., Z. Naturforsch. 4a, 51, 1949.

28. Gruen, A. E., Naturf., 12a, 89-95, 1957.

29. Berger, M. J and Seltzer, S. M., Tables of Energy Losses and Ranges of Electrons and Positrons, NASA SP-3012, (OTS N65-12506).

30. Schumacher, B. W., "A Review of the (macroscopic) Laws for Electron Penetration through Matter," in Electron and Ion Beam Science and Technology, R. Bakish, Editor; Wiley & Sons, New York 1965.

31. Petrie, S. L., AIAA Journal 4, 1679, 1966.

32. Boersch, H., Z. Physik, 107, 493-496, 1937.

33. Marton, L., Schubert, D. C. and Mielczarek, S. R., J. Appl. Phys., 27, 419, 1956; 33, 1613, 1962.

34. Wyrwich, H. and Lenz, F., Z. Naturf., 13a, 515-523, 1958.

35. Sternglass, E. J. and G. W. Goetze, IRE Transact. Nuclear Sc. NS9 No. 3, 97 June 1962; Goetze G. W. and A. H. Boerio IEEE Proceedings Sept. 1964 p. 1007.

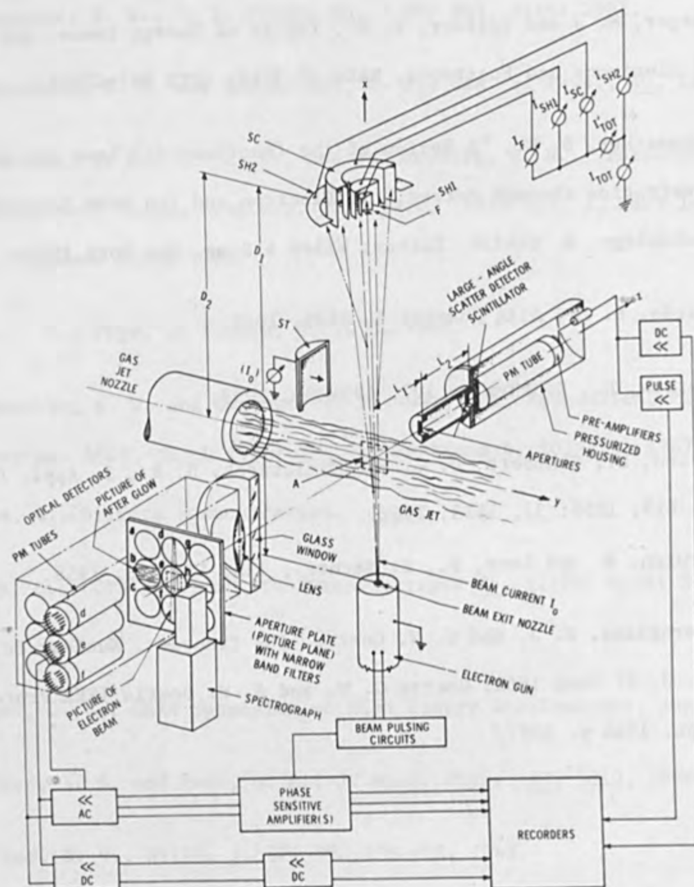


**Fig. 1. Schematic diagram of an electron beam probe with multiple read-out instrumentation. The electron beam passes through a low pressure chamber with a gas jet. Integral attenuation and forward scattering are measured by the Faraday cups F and SC. Total beam current can be measured by ST (when shifted into the beam). The optical detectors measure fluorescence. The large-angle scatter detector measures electrons scattered from a small area A at the intersection of electron beam and gas jet.**

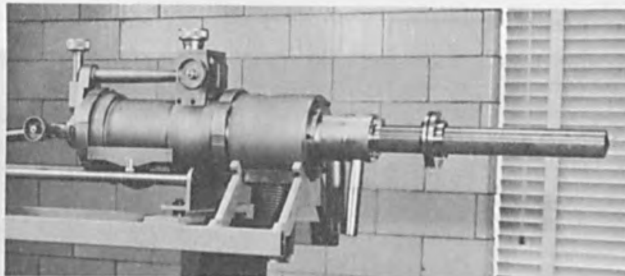

Fig. 2 Electron gun, to be located outside a wind tunnel, with long differentially pumped drift tube bringing the beam close to the flow field, and alignment devices for beam positioning. Typical beam parameters: 50 to 120 kv, 1 to 10 mA.

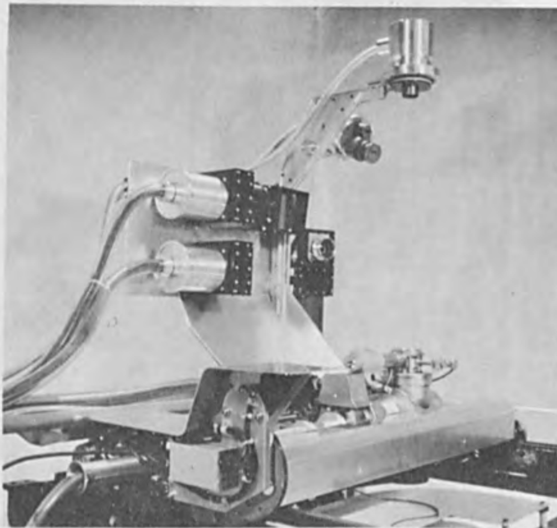

Fig. 3 Electron gun with read-out instrumentation mounted on cross slide, built for the 6 ft free-stream plasma wind tunnel of the Plasma Physics Laboratory, U. S. Army Missile Command, Redstone Arsenals, Huntsville, Ala. The electron gun is at the bottom hanging in the cross slide and fires a beam vertical up at right angles to its main axis. It can travel under operation over a field of 2 x 2 ft carrying the whole instrumentation with it.

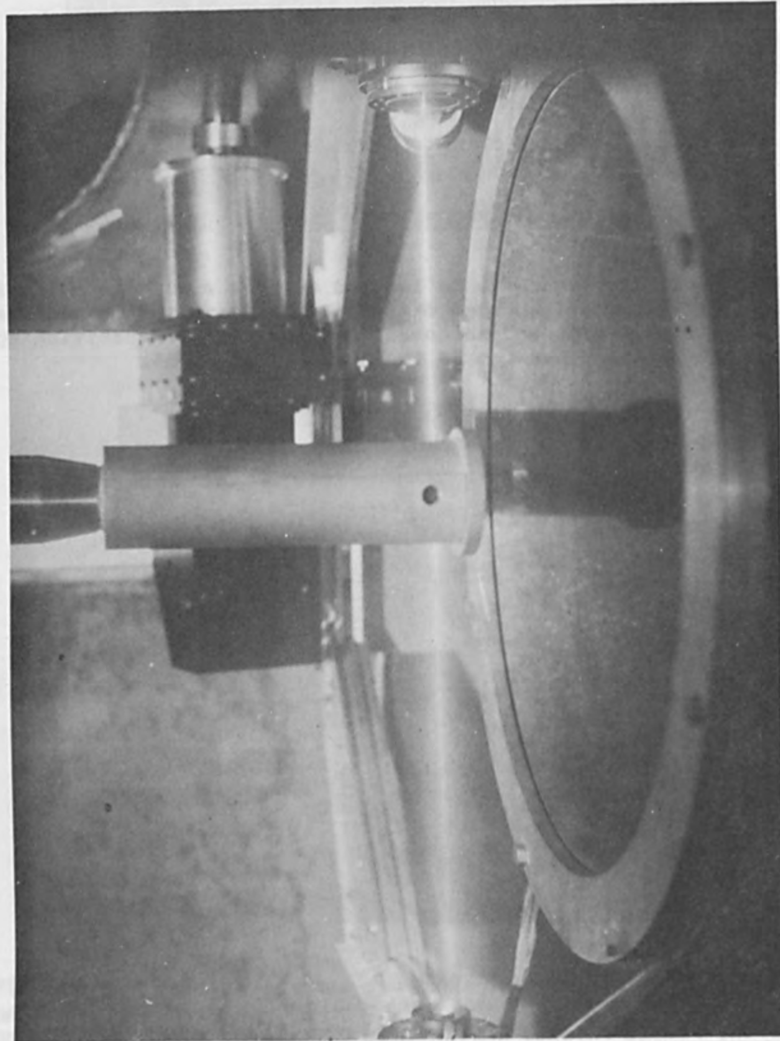

Fig. 4 Electron beam of 75 kV and 1 mA going across the 4 ft flow field of the wind tunnel, without flow, at a static pressure of about .1 Torr of air.

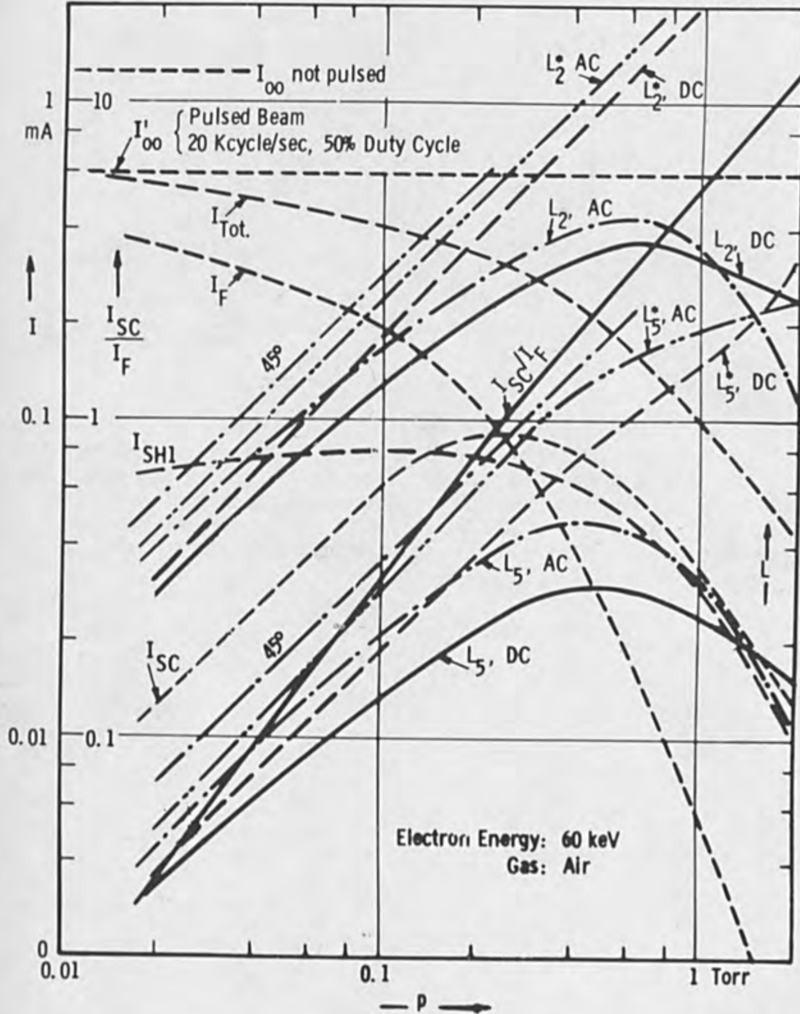


Fig. 5 Response L of the optical detectors as function of pressure, for air. $L_2$ and $L_5$ refer to phototubes d and e respectively. The beam was pulsed, and AC refers to an ac output channel, DC refers to the dc average signal. L* are the corrected values for constant total current, namely L* = L x $I'_{oo}/I_{TOT}$.

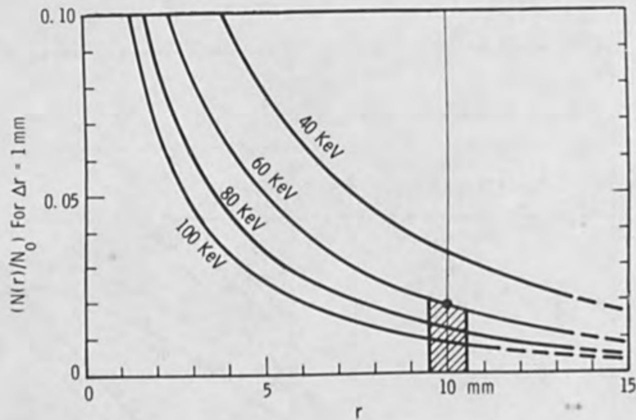


Fig. 6 Fraction of electrons $N/N_o$ scattered from a beam located at r = o into a ring-shaped area of radius r mm and width $\Delta r$ = 1 mm, after a pathlength of 57 cm in molecular nitrogen of 0.1 Torr; electron energy is parameter. Adapted from Fig. 4 of a previous publication.[17] These curves were obtained by a coarse numerical integration over the angular scatter probability functions as given by Lenz.[34]

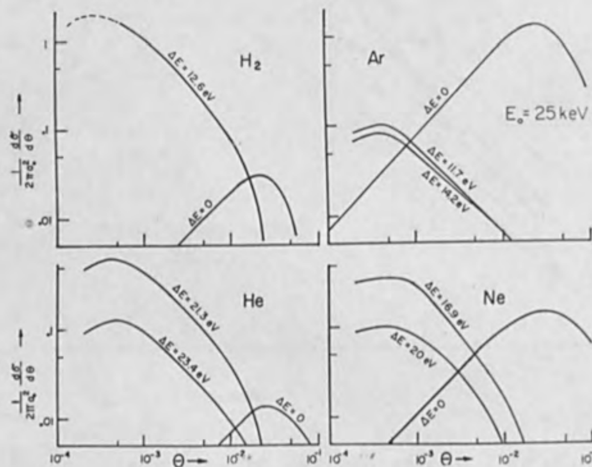


Fig. 7 Measured probabilities for elastic and inelastic single scattering; adapted from Geiger.[14]

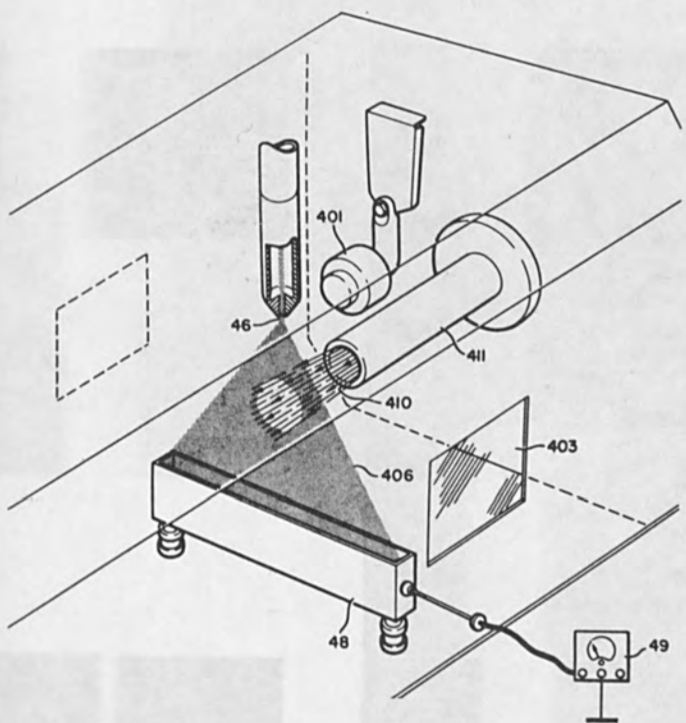


Fig. 8 A triangular section 406 of a plane perpendicular to the gas flow 410 is illuminated by the electron beam 46 which is deflected in a saw-tooth mode by the magnet 401. The Faraday cage and meter 49 measure the current. (From 7)

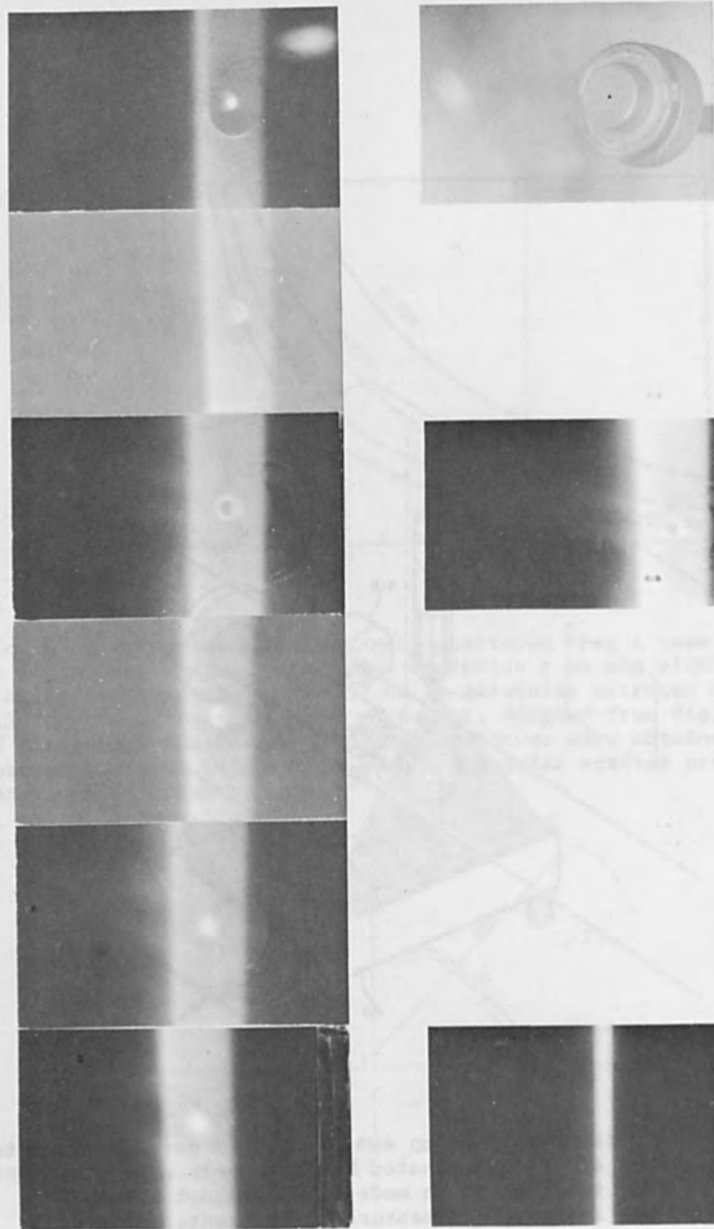

Fig. 9 Cross section pictures through a helium jet coming from a nozzle with 1 mm diameter, shown in the upper right photograph. The stationary electron beam is shown in the lower right. Photographs taken under $45^{o}$ to the gas jet and the sweep-plane of the electron beam. Average gas pressure 3.5 Torr; electron energy 60 kev, current 0.3 mA; helium flow 20 liter/sec. Kodak Plus-X film; exposure 90 seconds at f:8.

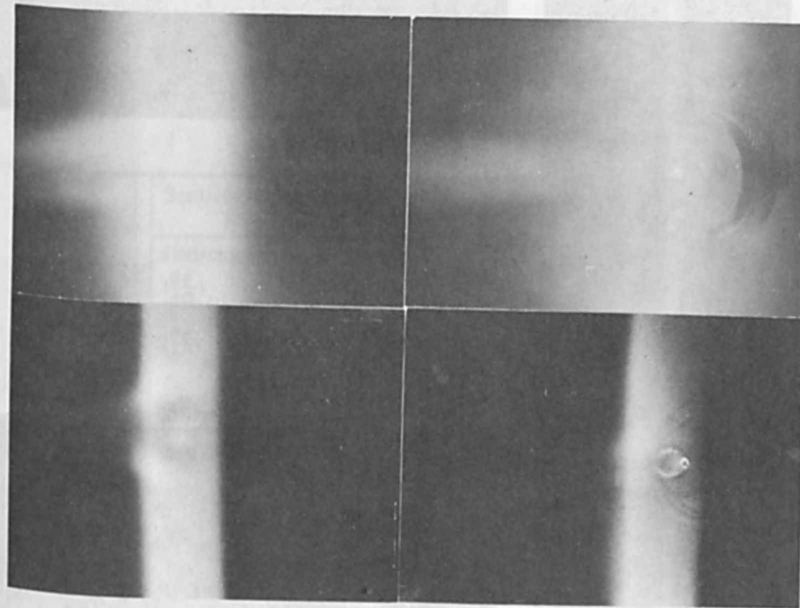

Fig. 10 As Fig. 9 but nozzle of 1.5 mm diameter; photographs on Ektachrome B, copies through blue filter (top picture) and green filter (lower picture).

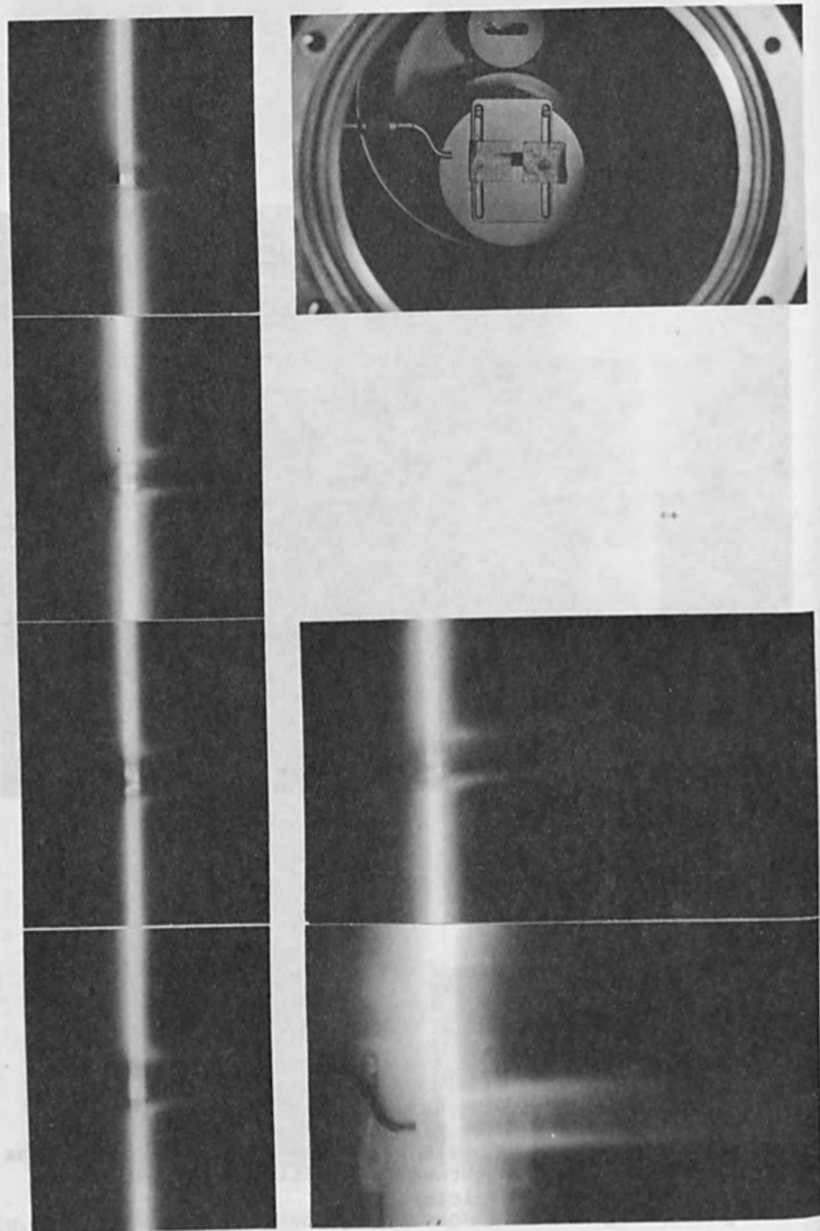

Fig. 11 Cylindrical electron beam of 2 mm diameter crossing helium gas jet from capillary with 1.5 mm ID at different positions from end of capillary. Electron beam 61 kv, 0.48 mA; static pressure 1.9 Torr; gas flow (pump speed) approximately 20 liter/sec.

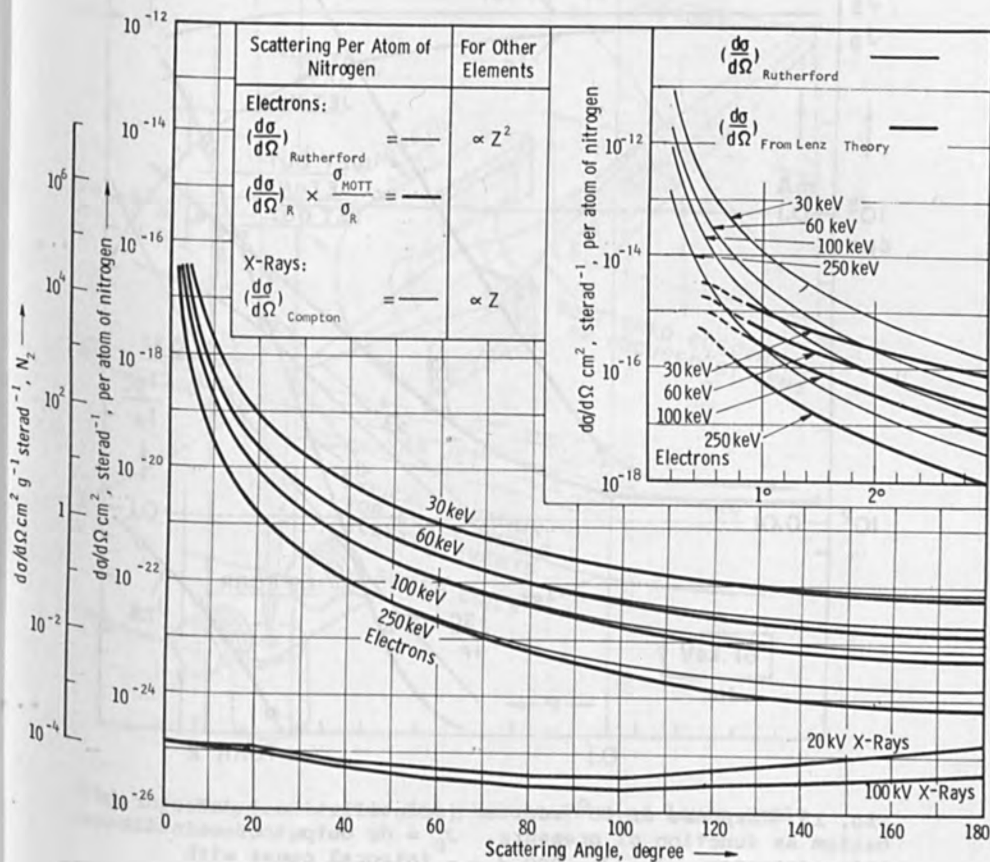


**Fig. 12 Scatter probability for electrons and X-rays in nitrogen from 0.2° to 180°.**

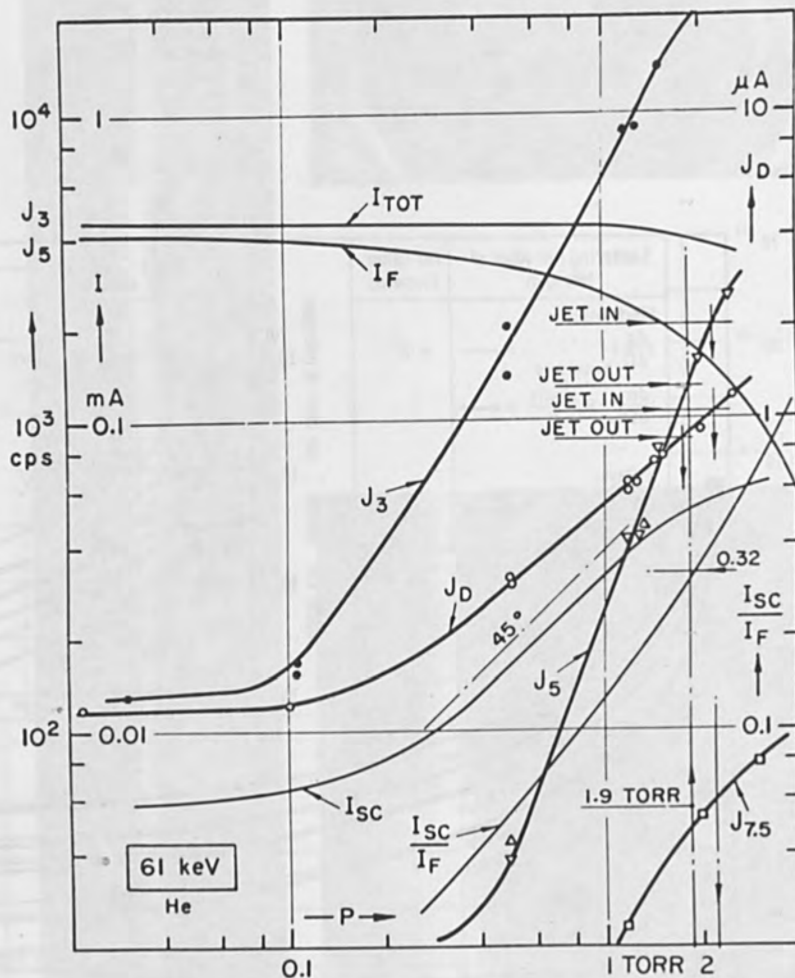


Fig. 13 Response of 90° scatter (scintillation-) detector in helium as function of pressure. $J_D$ = dc output of scintillation detector. $J_3$, $J_5$, and $J_{7.5}$ integral count with discriminator baseline at 3, 5, and 7.5 v. Arrows show response when helium jet was moved in and out of electron beam.

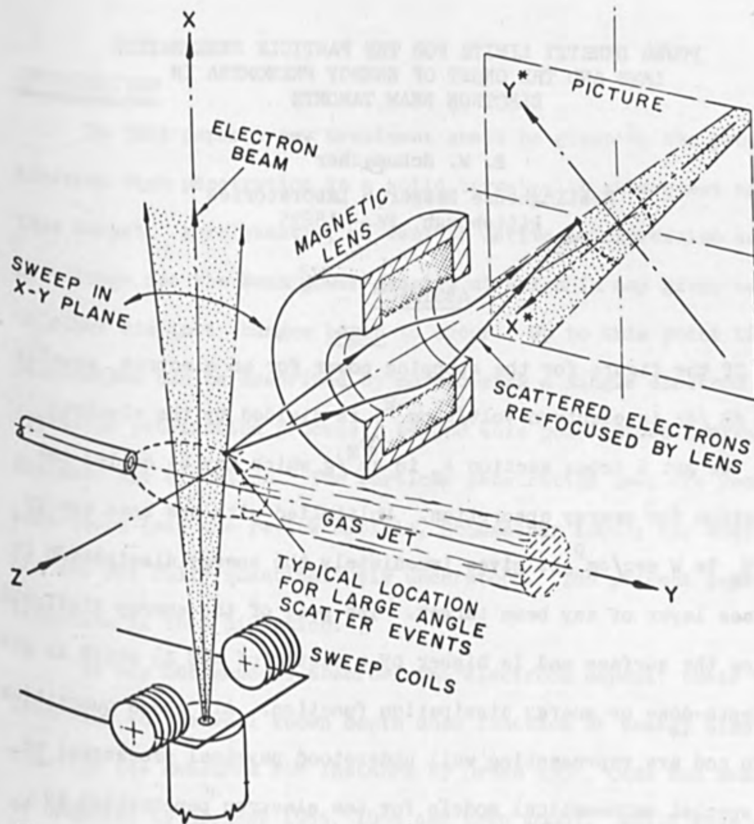


**Fig. 14 Proposed system for picture-forming large-angle scatter detector.**

# POWER DENSITY LIMITS FOR THE PARTICLE PENETRATION LAWS AND THE ONSET OF ENERGY PHENOMENA IN ELECTRON BEAM TARGETS

B. W. Schumacher

Westinghouse Research Laboratories
Pittsburgh, Pa. 15235

## ABSTRACT

If the figure for the stopping power for an electron, usually given as $dE_o/d\xi$ in electron-Volt/g $cm^{-2}$, is divided by the electron energy $E_o$ we get a cross section $A_E$ in $cm^2/g$ which may be called the cross section for energy absorption. Multiplied with the beam energy density $N_B$ in W sec/$cm^2$ it gives immediately the energy dissipation in the surface layer of any beam target. The peak of the energy dissipation lies below the surface and is higher by a factor of $a(E_oZ)$ which is given by the depth-dose or energy dissipation function. All these quantities are known and are representing well understood physical processes; we need no special mathematical models for the electron penetration to calculate target heating. No assumptions about boundary conditions are required; we are dealing with laws of physics. We find the onset of any changes in the target due to heating, the associated breakdown of the particle penetration laws and the onset of energy related phenomena as a function of beam power and thermal constants of the target.

## INTRODUCTION

In this paper a new treatment shall be given to the problem of electron beam penetration in a solid target with subsequent melting of this target. More exactly, we want to derive an expression as a function of voltage for the beam power density at which in any given target melting or other distinct changes begin to occur. Up to this point the electron penetration can be described by considering a single electron at a time (particle penetration process); beyond this point gross energy phenomena dominate the situation. The particle penetration laws are reasonably well understood (see the review article, Schumacher 1964); the energy phenomena are not yet fully quantitatively understood. The present paper is a contribution in this direction.

In any homogeneous absorber the electrons deposit their energy according to the well known depth dose function or energy dissipation function (as measured for instance by Gruen 1957, Olde and Brannen 1959, or computed by Spencer 1955, 1959 and Crew 1960). While this dissipation function $\alpha(z)$ is usually measured by means of ionization or luminosity measurements there is no reason to assume that the relative thermal energy

dose, deposited in each volume element, follows any different distribution. For electrons with energies below about 200 kV and for elements with low atomic number Z, say $Z < 20$, the shapes of all dissipation functions are closely similar if plotted over the range $R_E$ as the unit of penetration, measured in the direction z perpendicular to the surface. A detailed discussion of the definition of range and other characteristic quantities was given in an earlier paper. (Schumacher, loc. cit.). Dissipation function from Gruen and Spencer are produced in Figs. 1 and 2 as an illustration to the present discussion.

When the beam enters the absorber at $z = 0$, the intersection of the dissipation function $\alpha(z) = dE/dz$ with the axis is of special importance; it gives us $dE_o/d\xi$ which is the energy loss of an electron of energy $E_o$ along a unit element of its true zig-zag path $\xi$ (which for $\xi \rightarrow o$ coincides with the z-axis). The values for $dE_o/d\xi$ were first derived theoretically by Bethe (1930); refined, computed values were recently tabulated by Berger and Seltzer (1964); the numerical values for $dE_o/d\xi$ are known and accessible. As far as this quantity goes we are on firm, reliable ground. For our present purpose we may use as an approximation in the low energy range (< 200 keV and $Z \lesssim 20$*) the expression

$$dE_o/d\xi = 95\ E_o^{-0.7}\ \frac{\text{keV/electron}}{\text{mg/cm}^2} \quad (E_o \text{ in kV}) \qquad (1)$$

Since 1 eV = $1.602 \times 10^{-19}$ VA sec and 1 electron = $1.602 \times 10^{-19}$ A sec we can convert this to the more practical value (for unit current):

* With the exception of $H_2$ which lies about a factor of 2 higher because it has approximately twice as many electrons per unit mass than the other elements.

$$dU_o/d\xi = .95 \times 10^5 E_o^{-0.7} \frac{kV}{g/cm^2} \quad (E_o \text{ in kV}) \qquad (1')$$

This may be called the "voltage gradient" induced in the target due to the stoppage of the beam. If multiplied by the beam current density it gives the energy deposition rate in watts/g. For higher energies and heavy elements the numerical tables of Berger and Seltzer must be used instead of (1).

To get the peak value of the energy dissipation -- or energy deposition if the absorber is considered -- we have to refer to the shape or the functions of Fig. 1 and 2. The peak is higher than $dE_o/d\xi$ by a factor which we may call $a(E_o,Z)$, which for light elements and $E_o < 200$ kV is close to 2.

Hence we can write:

$$(dU/dz)_{max} = a(E_o,Z)(dU_o/d\xi) \frac{kV}{g/cm^2} \approx 2dU_o/d\xi \qquad (2)$$

$$\approx 2 \times 10^5 E_o^{-0.7} \frac{kV}{g/cm^2} \qquad (2')$$

This layer of maximum energy release is located at a depth of about $0.38R_E$, where $R_E$ is the total range of the electrons. Its definition was discussed in the earlier review paper (Schumacher, loc. cit.); we find:

$$R_E = 4.57 \times 10^{-3} E_o^{1.75} \text{ mg/cm}^2 \quad (E_o \text{ in kV}) \ (5 < E_o < 100 \text{ kV}) \ (3)$$

It may also be recalled that the dissipation functions taken along the z-axis for a thin, parallel beam (diameter small against $R_E$) and an infinitely broad beam are identical. For the thin beam the energy distribution (the electrons) spreads also to the side but about 1/2 of the energy is deposited close to the original beam axis; we will come back to

this point later. To get an exact figure Crew's curves could be evaluated, which was not done. The thin-beam case can be included in our equations by making $a(E_oZ)$ also a function of beam width $d_o$, namely $a = a(E_o, Z, d_o)$. It should also be remembered that the dissipation function already includes the effect of back scattering,(but not back-back-scattering on a boundary).

In the above analytically expressed relationships we have well defined physical quantities with a well understood physical meaning quite appropriate to the physical processes which we observe when electrons penetrate matter. We are not manipulating artificial mathematical definitions and models, as other people have done, which deal successfully with one aspect but are incompatible with other aspects of the electron penetration process.

The complete description of all particle penetration phenomena which was attempted in the above mentioned previous paper excluded all "power" or "energy" phenomena, i.e., all the situations where the beam power density becomes important because of heating and related effects on the target. The power density level where such effects begin, or at least a lower limit for it, shall now be derived in a way which is indeed compatible with the previous, analytical formulation of the "nonenergetic" electron penetration laws, at the same time establishing the energy dissipation limit up to which these laws apply. Just heating a target does not make it inhomogeneous except if it is a gas or vapor. But a solid or liquid target becomes inhomogeneous as soon as melting or vaporization occur, or a phase transition occurs like the one in quartz from beta-quartz to beta-tridymite at 876°C with a 15% increase in volume (which leads to the spallation of silica bearing rocks under electron bombardment). Even thermal stress alone, without phase transition can lead to a destruction of the target. Such a phenomenon can also determine "power limit."

## THE ONSET OF ENERGY PHENOMENA IN THE ABSORBER

The above given relationships, together with the materials parameters of the absorber, are quite sufficient to answer the following question:

> At which energy density of a short beam pulse will the peak value of the deposited energy per unit volume become so high as to (a) melt the solid or (b) vaporize a liquid target?

The stipulation of a short pulse may seem arbitrary; but it defines a very clear situation, insofar as all the interplay between energy deposition and removal by heat conduction is excluded. Making the pulse duration "short enough" leads to what may be called a quasi-adiabatic situation. This will, in general, yield a lowest limit for the energy input; no energy is lost by heat conduction. But it ignores the total power input (in contrast to power density), and therefore ignores bulk heating effects, which could well lower the permissible continuous beam power. The later case can only be treated if the boundary conditions of a specific beam/target system are known, and this is not the concern of the present paper.

Short-pulse input is not as uncommon a situation as it may seem. As examples of where this situation is closely approached, we may mention high-speed recording, high-speed radiation treatment of surfaces, beam profile scanning with fast rotating aperture discs, or thin surface layer melting, where this is desired. Beam "pulses" are also found where a beam, because of a short spurious deflection, strikes an aperture in an electron gun. Last but not least, pulsed electron guns are in use for many purposes.

(Schaaffs 1950. Schaaffs and Streich 1959, W. P. Dyke et. al. 1966. Oswald 1966, Graham and Hutchison 1967).

An estimate of the maximum pulse duration for which we still find quasi-adiabatic conditions can be readily made as shown in the Appendix. We find values for metals between .3 μsec and 8 μsec. For target materials with a lower thermal diffusivity these times get longer; for concrete we find 65 μsec. All these figures are for 100 to 150 kV beams.

The maximum "voltage gradient" according to (1'), (2) or (2') must be multiplied by the charge which is deposited by the beam to get the energy H which the absorber has taken up. Hence:

$$H = j_o \times \Delta t \times a(E_o Z)(dU_o/d\xi) \ \frac{Wsec/cm^2}{g/cm^2} \qquad (4)$$

($j_o$ in $A/cm^2$, $\Delta t$ pulse duration in sec)

Since $dU_o/d\xi$ is a function of beam voltage $E_o$ it is convenient to express equation (4) in terms of beam power density and to write:

$$H = j_o \times E_o \times \Delta t \times a(E_o Z) \ \frac{(dU_o/d\xi)}{E_o} \ \frac{Wsec/cm^2}{g/cm^2} \qquad (5)$$

$$= N_B \times a(E_o Z) \times A_E(E_o Z) \qquad (5')$$

Here $N_B$ is the beam energy in $Wsec/cm^2$ coming in, (not the dissipated energy per unit mass!).

$a(E_o Z)$ was defined in equation (2),

$$A_E(E_o Z) = \frac{dU_o/d\xi}{E_o} \ cm^2/g \qquad (6)$$

defines a cross section, which we may call the <u>cross section for energy absorption</u>. Making use of (1') we get

$$A_E = 0.95 \times 10^5 E_o^{-1.7} \quad cm^2/g \qquad (E_o \text{ in kV}) \qquad (6')$$

With this definition we have put all our calculations back on the familiar and convenient formalism of beam power density times target cross section.

We must now consider the thermal properties of the absorber; but note that the above expressions do not refer to a specific volume of the target, nor will later the target density come in, since this is indeed unnecessary for our unique conditions which were chosen to reveal relationships <u>free</u> from special boundary values, and therefore revealing actual physical relationships or laws, as one would want it.

The heat capacity per unit mass is a materials property of the absorber. Let $\lambda_S$ in cal/g degree be the average specific heat between room temperature $T_o$ and the melting point $T_1$; then the energy input needed to bring the target material to the melting point is $H_1 = \lambda_S(T_1 - T_o)$ cal/g. To melt the target the additional energy (heat of fusion) $H_2 = \lambda_F$ cal/g must be supplied. This gives a total energy of $H_{tot} = H_1 + H_2$ cal/g. Since 1 cal = 4.186 Wsec we can also write $H^*_{W,tot} = 4.186\ H_{tot}$ Wsec/g.

If the energy deposited by the beam equals $H^*_{W,tot}$ melting will begin; but also for any energy input H* which will lead to a thermal transition of any kind we have a "thermal limit." Equating H* with H in (5) will give immediately the critical beam energy $N_{B,crit}$ which will bring the target to this thermal limit; hence:

$$N_{B,crit} = \frac{H^*}{a(E_oZ)\, A_E(E_oZ)} \tag{8}$$

or:

$$N_{B,crit} = \frac{H^*}{2 \times 10^5 E_o^{-1.7}}$$

$$= 5 \times 10^{-6}\, H^* E_o^{1.7} \ \frac{\text{Wsec}}{\text{cm}^2} \tag{8'}$$

(H* in Wsec/g; $E_o$ in kV)

We now have arrived, as we had intended, at an expression for $N_{B,crit}$ with reference to only $dE_o/d\xi$, to the general shape of the dissipation function, and to the specific heat for fusion (or any other phase transition) of the target materials. No other boundary conditions influence this value except that the energy input must be in the form of a fast pulse. In any experimental verification of this relationship the infinitely short pulse can be approached by extrapolation from a series of measurements with shorter and shorter pulses. In $N_{B,crit}$ we have a true physical parameter, giving the <u>minimum</u> beam energy input that can possibly lead to melting, beginning at a layer of about 1/3 to 1/2 $R_E$ below the surface. Using (6') as well as (6) together with the tables of Berger and Seltzer we have in Fig. 3 plotted $A_E(E_oZ)$ as a function of $E_o$ with Z as parameter.

## NUMERICAL VALUE OF THE CRITICAL BEAM ENERGY

To find $N_{crit}$ for different targets we can make a list of the parameters that determine H* and then calculate $N_{crit}$ for various values of $E_0$. Table I gives selected values for H*.

We can note a few facts which may seem surprising. Beryllium has by far the highest H*. Unfortunately its toxic nature precludes its use where it could be vaporized. The next best target is graphite, although data to calculate its behavior reliably were not available (e.g. heat of sublimation). Also surprising is that iron, aluminum, and molybdenum stand a larger power pulse than copper or tungsten, which is certainly not the case for continuous power input. Melting quartz glass needs twice the energy of producing a phase change in crystalline quartz. (This may, however, not be correct if the reaction rate (time needed) for the phase transformation is considered.)

The critical beam energy for the onset of melting in molybdenum is now given according to (8) by

$$N_{B,crit} = \frac{982 \text{ Wsec/g}}{2 \times 18 \text{ cm}^2/\text{g}} = 27 \ \frac{\text{Wsec}}{\text{cm}^2}$$

where we have taken a = 2, $A_E = 18 \text{ cm}^2/\text{g}$ for a 150 kV beam, using a value between iron and tungsten.

A welding beam has typically a power of 9 kW in a $10^{-2}$ $\text{cm}^2$ spot, hence $9 \times 10^5$ $\text{W/cm}^2$. Under "adiabatic" conditions it would take this beam a time of

$$\Delta t = \frac{27}{9 \times 10^5} = 3 \times 10^{-5} \text{ sec}$$

to actually melt the molybdenum at the region of maximum energy dissipation. This figure holds for a beam which is wide compared with the range $R_E$. We see from (3) that for a 150 kV beam $R_E = 29.3 \text{ mg/cm}^2$; since $\rho_{Mo}$

$= 10.2\ g/cm^3$ the beam penetration is 0.0029 cm whereas the beam width is approximately 0.1 cm; we have a broad-beam case in spite of the beam spot being small in absolute terms. However, the above time of 30 μsec is not compatible with the adiabatic conditions, as discussed earlier. Heat is already conducted away and the total power, or the power density would have to be higher to achieve "adiabatic" melting on a molybdenum surface. A power density of $10^7\ W/cm^2$ (which can be produced) would do it. Yet adiabatic conditions would also exist if we used a foil as a target having a thickness about equal to the range $R_E$.

Let us furthermore consider that the beam of 9 kW, $10^{-2}\ cm^2$ falls on a rotating disc with a pinhole (beam scanner). Then we may define as a beam "pulse" the period of time in which an element of the disc traverses the width of the beam, i.e., 0.1 cm. If this occurs in less than $3 \times 10^{-5}$ sec, which requires a linear speed of the surface relative to the beam of $3.3 \times 10^3$ cm/sec = 33 m/sec, then we can be sure, according to the above considerations, that no melting occurs. If this beam had a finer focus, say a spot diameter of 0.03 cm ($10^{-3}\ cm^2$, $10^7$ W/cm$^2$) the critical energy $N_{B,crit}$ would be deposited in: $\Delta t = 3 \times 10^{-6}$ sec and adiabatic conditions are met. For a rotating disc the linear speed at the beam spot would have to be at least $1 \times 10^5$ cm/sec = 100 m/sec to avoid melting, without any safety margin on account of heat condution.

For graphite, since H* is at least twice that for molybdenum, we could either double the power or reduce the speed of scanning to 1/2.

In order to bring quartz to the point of phase change, for instance with the aim of spalling rocks, we require a critical energy input of H* = 655 Wsec/g. Using a = 2 and $A_E = 20\ cm^2/g$ (150 kV electrons) we find:

$$N_{B,crit} = \frac{655 \text{ Wsec/g}}{40 \text{ cm}^2/\text{g}} = 16 \frac{\text{Wsec}}{\text{cm}^2}$$

A 100 kW beam with 0.3cm$^2$ area will deliver this energy in 48 μsec, which brings us into the adiabatic range of conditions. We can use a sweeping speed of $10^4$ cm/sec or 100 m/sec, covering an area of $F = 0.6$ m$^2$/sec. This value may be over-optimistic in view of the fact that phase change in solid state needs time to proceed, not only the energy input, on the other hand we may not need to use a "dense" scan if we want to spall rocks.

It is logical, and can be easily verified, that once adiabatic conditions are reached -- which is only a condition for the power density but not for total beam power (at least in the kW range of power) -- then the maximum area $F_{max}$ which can be scanned (and for instance melted) with a focused beam is independent of any further reduction in the focal spot size (or further increase in power density) and only given by the required $N_{B,crit}$ (a target property) and the available total power $P_o$, namely:

$$F_{max} = P_o/N_{B,crit} \quad \text{cm}^2/\text{sec}$$

Staying with our approximations for the maximum energy deposition time $t_a$ which secures adiabatic conditions we see that we obviously need a minimum power density $p_m$ in the beam of

$$p_m = N_{B,crit}/t_a \quad \text{W/cm}^2 \qquad (9)$$

To see how the beam voltage will affect $p_m$ we can combine equation (8'), (3) and $t_a = (R_E/\rho)^2/(\pi\lambda/\rho c)$ from page 13, and we find

$$p_m = 2 \times 10^5 \, E_o^{-1.7} \times H^* \times \frac{\pi\lambda\rho}{c} \quad W/cm^2 \qquad (10)$$

($E_o$ in kV; $H^*$ in Wsec/g; $\rho$ in g/cm$^3$;
$\lambda$ in cal/cm sec degr.; c in cal/g degr )

Not much weight should be given to the numerical value of this $p_m$ because of the gross approximations under which $t_a$ was derived; yet equation (10) shows once more that the power density can be lower for higher beam voltages $E_o$ because of the deeper penetration. Of course, the total power required according to equation (8') will be higher since the volume over which the power is distributed increases with beam voltage.

CONCLUSIONS

With the newly introduced parameters $A_E(E_oZ)$ and $a(E_oZ)$, which give the cross section for energy dissipation and the peaking of the energy dissipation curve respectively, we can quickly calculate the onset of any bulk energy effect in any target as a function of beam power density (in Wsec/cm$^2$). The cross section $A_E(E_oZ)$ was derived from well known other electron physics data; $a(E_oZ)$ is not known in detail but is a very slowly varying function with a value between 1.5 and 2, which is available from graphs with reasonable accuracy.

The faster the energy is deposited in the target the closer we come to the theoretical minimum energy which is needed to produce any bulk effect or change in the target, because heat losses by conduction are minimized. This leads to a condition for maximum pulse duration and minimum power density in case of pulsed beams or beam

scanning. We have shown that these conditions can be met in either case, and how they depend on beam voltage.

It is hoped that these deductions contribute to an increase in logical clarity whenever electron beam target effects are discussed or computed.

APPENDIX

An estimate of the maximum pulse duration which yields quasi-adiabatic condition can be made as follows: The temperature dissipation from a plane in an infinite medium is given by the differential equation

$$\frac{dT}{dt} = \frac{\lambda}{c\rho} \frac{d^2T}{dX^2}$$

with the solution:

$$T = \frac{T_o(X)dx}{2\sqrt{\pi t\lambda/c\rho}} \; e^{-\frac{(X_o-X)}{4t\lambda/c\rho}}$$

T = temperature at (X, t); $T_o$ = temperature at t = o; $X_o$ = location of plane; t = time, λ = heat conduction in cal/cm, sec, degree C; c = heat capacity in cal/g, degree C; ρ = density in g/cm$^3$; λ/cρ in cm$^2$/sec is also called thermal diffusivity).

For X = $X_o$, the plane, which we may consider as "heat pole," and for a width of this "plane" ΔX = equal to the range $R'_E$ (in cm) of our electron beam we get a simplified expression for the temperature drop with time, namely:

$$T(t) = \frac{T_o \Delta X}{2\sqrt{\pi t\lambda/c\rho}}$$

We can now say the adiabatic conditions are no longer fulfilled when the pulse duration is longer than that in which T(t) drops to 1/2 $T_o$. The so defined "time limit for adiabatic conditions," is obviously given by

$$t_a = \frac{(\Delta X)^2}{\pi\lambda/c\rho} = \frac{R'^{\,2}_E}{\pi\lambda/c\rho} = \frac{10^{-6}\, R_E^{\,2}}{\rho\pi\lambda/c}$$

$$R'_E \text{ (in cm)} = R_E(\text{in mg/cm}^2)/10^3\rho(\text{in g/cm}^3)$$

Since we have not a plane in an infinite medium but our "heat pole" is a surface layer of thickness $R_E$, the temperature drop to $T_o/2$ will take place in a time of about $2t_a$. Nevertheless we may, by definition, consider $t_a$ the longest permissible pulse duration for which we can assume quasi-adiabatic conditions. For various materials, and $\Delta X = 10^{-3}$ cm (100 to 150 kV electrons) we find:

Cu: 0.3 μsec; Fe (pure): 1.4 μsec; Stainless Steel: 8.4 μsec; Mo: 0.6 μsec; Al: 0.3 μsec; Graphite: 0.3 μsec; Be: 0.7 μsec; W: 0.5 μsec; Quartz Glass: 40 μsec; Concrete: 65 μsec.

For larger $\Delta X$, i.e., electrons of higher voltage, these times become longer.

Electron beam pulses from typical pulsed guns have a duration of $10^{-7}$ sec or less. In this case the interaction with a target is always "adiabatic".

REFERENCES

Bethe, H., 1930, Ann. Phys. 5, 325.

Berger, M. J. and Seltzer, St. M., 1964; Tables of Energy Losses and Ranges of Electrons and Positrons NASA SP-3012 (O.T.S. N65-12506).

Crew, J. W., 1961, J. of Research N.B.S. 65A, 113.

Dyke, W. P., Barbour, J. P., Grundhauser, F. J., and Charbonnier, F. M., 1966, Proceedings of the 8th Annual Electron and Laser Beam Symposium, G. I. Haddad, Ed., University of Michigan, Dept. of El. Eng.

Graham, R. A. and Hutchison, R. E. 1967, Appl. Phys. Letters 11, 69.

Gruen, A. E., 1957, Z. Naturf, 12a, 89.

Olde, G. L. and Brannen, E., 1959, Rev. Sc. Instr. 30, 1014.

Oswald, Jr., R. B. 1966 IEEE Transactions NS-13, 63.

Shaaffs, W., 1950, Z. Naturf 5a, 132-136.

Schaaffs W., and Streich, M., 1959, Z. angew. Phys. 11, 188.

Schumacher, B. W., 1964; in "Electron and Ion Beam Science and Technology," R. Bakish, Ed., Wiley and Sons, New York 1965.

Spencer, L. V., 1955, Phys. Rev. 98, 1957.

Spencer, L. V., 1959 N.B.S. Monograph No. 1.

| Process | $H_2O$ | Graphite | Be | Al | Cu | Fe | Mo | W | Quartz | Pb |
|---|---|---|---|---|---|---|---|---|---|---|
| Bring to melting point | | 2100(?) | 2420 | 520 | 409 | 706 | 691 | 445 | 1240 (Glass) | 39.6 |
| Bring to melting point and melt | | ? | 3630 | 917 | 614 | 974 | 982 | 637 | 1324 (Glass) | 63 |
| Bring to boiling point | 420 | | 4950 | | | | | | | 330 |
| Bring to boiling point and vaporize | 2680 | | ? | | | | | | | |
| Bring to sublimation | | 2100(?) | | | | | | | | |
| Bring to phase-change | - | - | - | - | - | - | - | - | 655 (Crystal) | - |
| $t_a$, μsec | - | 0.3 | 0.7 | 0.3 | 0.3 | 1.4 to 8.4 | 0.6 | 0.5 | 40 (Glass) | - |

Table I Values for H* of various materials (Wsec/g) and maximum pulse duration $t_a$ for quasi-adiabatic conditions (150 kV beam)[a]

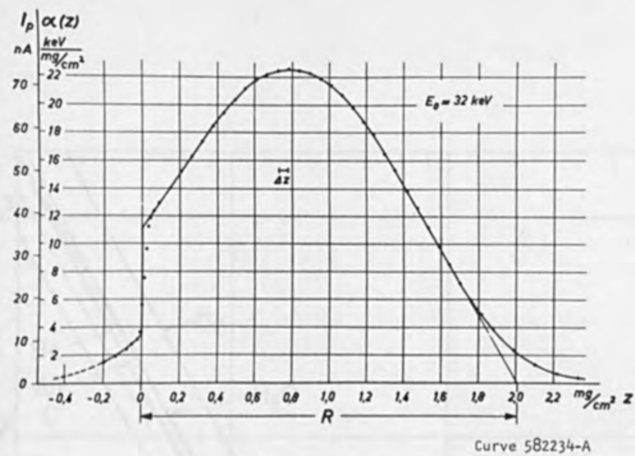


Curve 582234-A

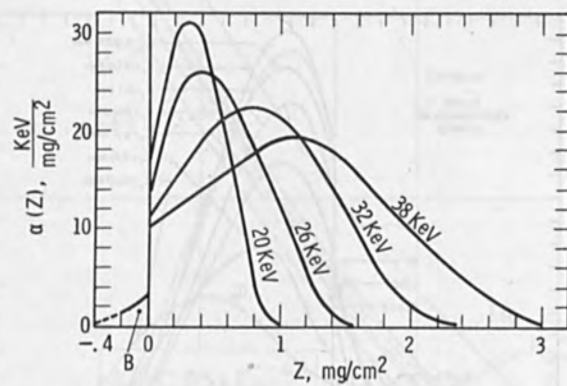


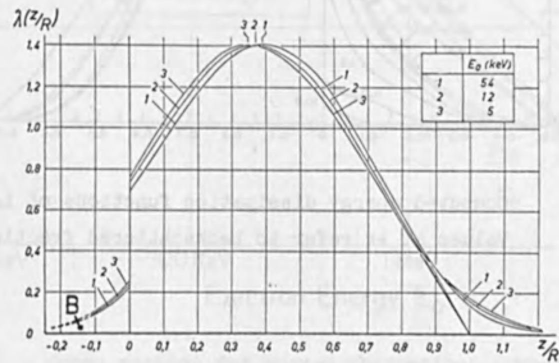


Fig. 1: Energy dissipation functions α(z) as measured by A. E. Gruen for air, using the fluorescence method. Top: measured points for 32 KeV electrons; middle: curves for various energies plotted over $z = \rho s$ scale; lower: normalized dissipation functions (range R as unit measure for penetration). B is backscattered fraction.

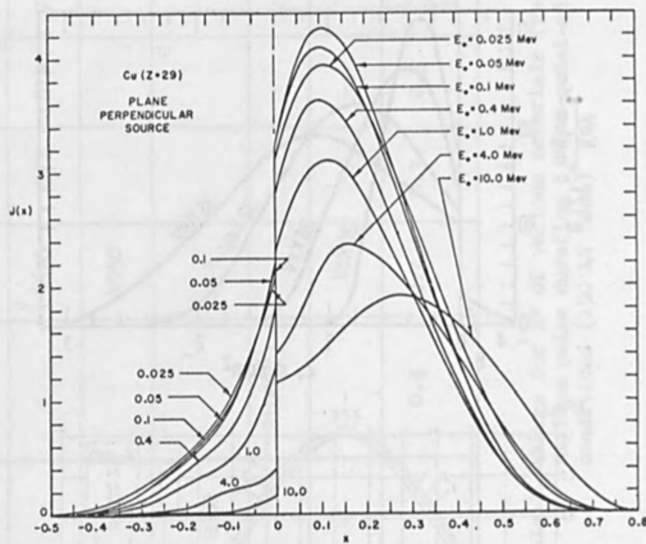


Fig. 2: Computed energy dissipation functions of L. V. Spencer. Values at -x refer to backscattered fraction of energy.

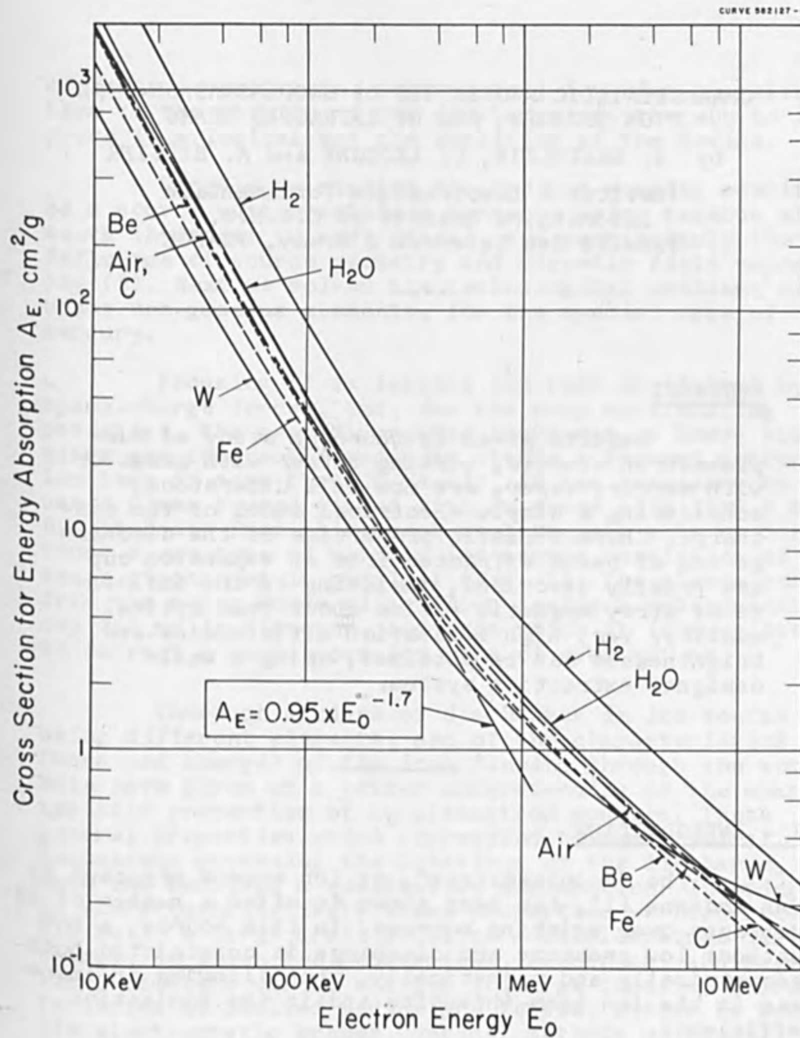


Fig. 3 Cross section for energy absorption; computed values from tables of Berger and Seltzer (1964). Values are for parallel beam (surface of target); to get peak of energy absorption in a target $A_E$ must be multiplied by $a(E_0Z)$ which represents the peaking of the differential energy dissipation as function of depth; $1.4 < a < 2$.

CHARACTERISTIC PROPERTIES OF DUOPLASMATRON-TYPE ION SOURCES, AND OF EXTRACTED BEAMS

by G. GAUTHERIN, C. LEJEUNE and A. SEPTIER

Institut d'Electronique Fondamentale
Laboratoire associé au C.N.R.S.
Faculté des Sciences d'Orsay, FRANCE

----

ABSTRACT

Results given by thorough study of Duoplasmatron sources, working either with gases or with mercury vapor, are now well understood, considering a simple electrical model of the discharge. Characteristic properties of the discharge and of beams extracted from an expansion cup are briefly described, insisting on the influence of stray magnetic fields about beam optical quality. Very high ionization efficiencies and brightnesses can be obtained, using a well-designed extraction system.

---

## I - INTRODUCTION

The "Duoplasmatron", an ion source proposed by Von Ardenne (1), has been shown to offer a number of advantages over existing sources. In this source, a hot cathode low pressure arc discharge is constricted both geometrically and magnetically, thus allowing an increase in the ion beam intensity and in the ionization efficiency.

For a certain number of years research in our Laboratory has been directed towards the following two objectives :

-to develop a source working continuously with gases or vapors and providing an intense, easily focused ion beam

- to study the source properties (beam intensity

efficiency, emittance, noise level) in order to relate them to the physics of gas discharge and thereby to improve in a logical way the qualities of the device.

Firstly we studied the optimum working conditions of a source with rotational symmetry using gaseous elements (hydrogen or rare gases), and particularly the influence of source geometry and magnetic field topography (2). Next we solved the technological problems of using non-gaseous elements, for the special case of mercury.

Focusing of an intense ion beam is limited by space-charge forces, and, for the same accelerating potential, the beam divergence increases as heavy elements are chosen. In order to obtain a focused mercury ion beam of more than 20 mA (3), it was necessary to use a plane source fitted with an anode slit 20x0.4 $mm^2$. By extension from this model we have been able to construct a new type of mercury ion source consisting of seven discharges in parallel (Fig. 1). The plasma coming from the seven anode slits flows inside a cylindrical cup 160 mm in diameter, and from which it is possible to extract a continuous ion beam of over 400 mA.

Thorough studies of discharges in ion source using different elements, and of the characteristics (mass and charge) of the ions flowing through the anode hole have given us a better understanding of the characteristic properties of duoplasmatron sources. These general properties which correspond to the physical mechanisms governing the behaviour of the discharge, have now received a qualitative explanation. In order to study quantitatively these properties we have recently built a large scale model of a duoplasmatron discharge, in which the geometrical, electrical and magnetic parameters can be changed in large domains. Characteristics of ionized medium are tested, either by movable electrostatic probes, optical methods or pencil beams of particles. In this paper, we shall describe the essential properties of duoplasmatron sources and of the extracted ion beams. To begin with, we recall the principle of the source and the particularities of the discharge.

## 2 - ELEMENTARY MODEL OF A DUOPLASMATRON DISCHARGE

### 2.1 - Principle of operation of a duoplasmatron source (Fig. 2)

The plasma from which the ions are extracted is produced by striking a low-pressure arc between a hot cathode F and an anode A. The ion beam is extracted from the plasma diffusing through a hole, situated on the symmetry axis (or plane) of the discharge and bored in the anode. In order to obtain as dense a plasma as possible at the level of the anode hole, the discharge is strongly concentrated by the action of a third electrode IE called the intermediate electrode, and the effect of a strong inhomogeneous axial magnetic field set up by an electromagnet whose poles are respectively IE and A.

### 2.2 - A discharge model (4)

The duoplasmatron arc is composed of two successive discharges separated by a constriction sheath (Fetz's sheath) :

i) - The cathode discharge, which is a classical hot cathode discharge consisting of a relatively cold homogeneous plasma ($n_e \simeq 5.10^{11}$ cm$^{-3}$ , $T_e \simeq 20{,}000°$K). The plasma potential, relative to the anode potential, increases with the intensity of the magnetic field. It strongly depends on the pressure value in the region between intermediate electrode and anode and on the nature of the gas : it increases both when the pressure and when the effective ionization cross-section of the gas are decreased.

ii) - The anode discharge consisting of a very inhomogeneous plasma extending from the constriction sheath (situated in the axial channel of the intermediate electrode) to the extraction area and having considerable axial gradients both of density and potential. This plasma is created by a beam of energetic electrons extracted from the cathode-plasma by the potential difference across the sheath and channeled along the magnetic field lines. Ionization caused by secondary electrons can

be neglected to a first approximation. The strong ionization in the region where the axial magnetic field has its maximum value, and the low rate of radial ion diffusion produce locally a high positive potential (relative to the anode) which tends to drain positive ions both towards the anode hole and towards the cathode (5).

Therefore, a true plasma beam is emitted through the anode hole. This beam contains both ions and electrons having axial energies of about the same order of magnitude (some tens of eV - see following chapters).

## 3 - ION BEAM INTENSITY

### 3.1 - Influence of the extraction potential $V_{ext}$

The ion accelerating system is composed of a non magnetic extracting electrode, facing the anode of the source, and a cylindrical collector cooled by circulating kerosene. The anode is generally fitted with an expansion cylindrical cup in which the plasma beam coming from the discharge can diffuse. Position and shape of the plasma boundary from which ions are extracted, are fixed by the values of ion density in the plasma, and applied electric field. At low voltages, the external part of the diverging beam falls on the extractor, but for voltage greater than a critical value, the beam divergence is low enough and all the ions may reach the collector situated beyond the extracting electrode. This last electrode is a few hundred volts more positive than the extractor, for avoiding secondary electron emission.

Total extracted current $I_{total}$ may be defined by

$$I_{total} = I_{collector} + I_{extractor} / (1 + \gamma)$$

$\gamma$ is the electron emission coefficient of the extractor material.

A typical experimental curve giving $I_{ext} = f(V_{ext})$ in a source without a large expansion cup is shown on Fig. 3a. The source parameters being fixed, $V_{ext}$ has no influence on the total extracted ion beam current value. When the ions are extracted from a large expansion cup, a

slight increase of I with $V_{ext}$ is observable, due to a reduction of particle losses on the cup walls (the plasma emitting surface recedes from the extractor when the accelerating voltage increases). Same phenomena occur when electrons are extracted from the plasma, by changing the polarity of $V_{ext}$. (see Fig. 3b, obtained with a large expansion cup).

Movements and deformations of the plasma boundary are well understood by considering an emitting surface working in a space-charge limited regime. Let us consider for example the Child-Langmuir expression giving the space-charge limited current between two concentric spherical electrodes.

$$\frac{I}{V_{ext}^{3/2}} = \frac{8}{9} \pi \, \mathcal{E}_o \left(\frac{2e}{m}\right)^{1/2} \left(\frac{1-\cos\theta}{2}\right)$$

$\theta$ is the half aperture angle of the beam, and $\alpha$ a function of the curvature radii of both electrodes.

I being constant, a variation of $V_{ext}$ provokes variations of $\theta$ and $\alpha$, that is to say of the shape of the beam and of the emitting surface (11). This variations has been confirmed experimentally. It can therefore be said that the discharge behaves like a constant current generator, in which the geometry of the emissive plasma surface and of the beam assumes a geometry which obeys Poisson's law taking into account the external electric fields.

As a verification, the following experiment was performed : for the same geometrical conditions in the extraction space ($\theta$ and $\alpha$ being fixed), we modify the discharge parameters in order to vary I ($V_{ext}$ must be adjusted to maintain same $\theta$ and $\alpha$ . In these conditions, the variation of the factor $(I.M^{1/2})$ as a function of $V_{ext}$ obeys the classical space-charge $V^{3/2}$ law (see fig. 4). In this example, corresponding to an Hydrogen source M is the mean value of the ion atomic mass, taking into account the relative proportions of $H_1^+$, $H_2^+$, $H_3^+$ ($M_i$ = 1, 2 or 3 respectively).

Finally, because of the high longitudinal ion velocities in the anode plasma, it should be noted that

the local extracted current density is not given (11) by the classical formula :

$$J = n_+ e \sqrt{\frac{k T_e}{2 M}}$$

which can only be used in the case of a polarized probe immersed in a thermalized plasma ($n_+$ = ionic local density, $T_e$ = electronic temperature, K = Boltzman constant, e and M = charge an mass of extracted ions).

3.2 - Role of the anode expansion cup

In order to reduce space-charge divergence in the extraction zone, and have the same total current it is useful to define the density of the emissive plasma, and increase the surface area by using an expansion cup surrounding the anode hole.

Though this process is good from the optical point of view, this solution leads to a reduction in the efficiency of the source due to ion losses on the walls. In order to reduce these losses the following two solutions were tested (6) :

- Application of an axial magnetic field in the expansion cup to reduce the radial diffusion.

- Use of walls made of insulating material which is in each point at a floating potential, and collect a noticeably smaller electronic current.

The results of these modifications are shown on Fig. 5. It is interesting to note that in the latter case the discharge characteristics are modified by the change in the conditions influencing the motion of ions towards the extraction regions (7).

3.3 - Influence of the area of the anode hole

a) - For a source of plane symmetry, the number of extracted ions is proportional to the length of the slit, in so far as the discharge is uniform along the direction of this slit. The extracted current is proportional to the width of the slit, only if this dimension is not greater than about half the thickness of the ribbon discharge.

b) - For on axially symmetric source, the

extracted current is proportional to the area of the circular extraction hole as long as the diameter of this hole is roughly less than the radius of the discharge. The discharge diameter can be evaluated either by means of a Langmuir probe or by observing the radial distribution of luminosity.

### 3.4 - Influence of the discharge parameters.

A duoplasmatron discharge has two distinct regimes, characterized by a difference in axial potential distribution, and showing themselves by a break in the curves giving variations of arc potential and of extracted ion current as functions of the arc discharge current. In Fig. 6 are shown the evolution of these quantities, the arc intensity being varied in Argon, at a given pressure and a constant magnetic field. The change in regime corresponds to a limitation in arc current due to a too weak pressure in the anode compartment. This leads to a redistribution of space charge (formation of a new sheath) and also the setting up of high frequency instabilities in the discharge.

Only the first regime corresponds to a rational use of the duoplasmatron source, and optimum results are obtained when the source is working near the regime changeover point.

The laws mentioned previously in this paper (including those schematically illustrated in Fig. 7), correspond to the first regime, and can be summarized as follows :

- The extracted current is substantially proportional to the arc discharge intensity and to the maximum magnetic induction ; it depends little on the anode pressure, decreasing slightly when the pressure increases.

- The optimum extracted current only depends on the anode pressure, these quantities being proportional. This is not surprising as the intensity of the arc at the regime changeover point is itself proportional to the pressure in the anode plasma region (for the same magnetic field configuration, and the same value of maximum magnetic induction), and inversely proportional to the maximum magnetic induction.

### 3.5 - Ionization efficiency of the source

In order to evaluate the ionization efficiency of the source, the extracted beam has been analyzed by

measuring charge and mass of the different ions (8). This analysis is necessary, on the one hand for the calculation of a focusing optics (case of magnetic lenses or prisms), and on the other for beam utilization ; in particular for an hydrogen ion source the relative proportion of protons, $H_2^+$ and $H_3^+$ ions must be examined, and it is possible to determine optimum working conditions giving a high ratio of protons (or alternatively of $H_2^+$).

Multicharged ions appear beyond a threshold arc current whose value decreases as magnetic field increases, and when the pressure is low in the anode compartment. Above the threshold value the proportion of multicharged ions increases faster when the pressure is low and the magnetic field high. (Fig. 8). The evolution of the proportion of multicharged ions or of molecular and triatomic (in the case of hydrogen) ions depends largely on the cathode plasma potential which affects the energy of the ionizing electrons (7).

Fig. 9 gives the variation of the efficiency of an argon source equipped with an expansion cup, as a function of the magnetic induction, the pressure being kept constant and the discharge being adjusted to obtain the optimum current. Variation of efficiency shows the difference of losses in the expansion cup. It is preferable to use an intense arc rather than a strong magnetic field (because of beam disturbances induced by the external stray field see later) and this ca give rise to efficiencies of the order of 80 %.

## 4 - ION ENERGY SPECTRA (7) (9)

Two basically different methods of diagnostics have been used. In the first, the beam is extracted by means of an accelerating potential of 20 - 25 kV. After deceleration and focusing the beam it sent into a 127° cylindrical electrostatic analyser of resolution about 2 eV. The second method is based on the retarding field principle and uses a polarized (150-500 V) electrode to select the components of the plasma ; a variable retarding potential V applied to a second electrode gives rise to an adjustable potential barrier which allows particle energy analysis.

Results using the two methods are in agreement both for ions and electrons, and it can therefore be deduced that the speed of the emitted particles is not modified by the extracting electric field. We shall characterize a spectrum by the most probable value of energy $W_p$ (referred to the anode potential and by the half-width $\Delta W$.

4.1 - Electron Energy Spectrum

The most probable electron energy always corresponds to the cathode plasma potential, $V_{p_1}$ , measured by means of Langmuir probes.

The average dispersion is between 20 and 50 eV according to the values of the various working parameters of the duoplasmatron.

The energy spectra, and notably the most probable energy, is modified very little by the addition of a expansion cup, whatever be its polarization. Due to considerable post-ionization in the expansion cup, however, a substantial broadening of the electronic energy spectrum may be observed.

4.2 - Ion energy Spectrum

Using an expansion cup at anode potential all the spectra obtained had the same characteristics.

The beam consists of two ion populations of different energy, the relative importance of which varies with pressure, magnetic field, and discharge intensity.

One of these populations always has a probable energy corresponding to a potential near to that of the anode : these ions are formed in the expansion cup by a "post-ionization" process. (10).

The second population seems to come from a region in which the potential is higher than that of the anodê ("potential hill"). The height of this hill seems to be more important when the flow of ions from anode space discharge to expansion cup is made more difficult (for instance an electrical polarization of the expansion cup walls may diminish this flow).

W and $W_p$ increase in harmony with the intensity of the discharge and the magnetic induction. In contrast, these quantities decrease with an increase in pressure. The energy dispersion may be between 10 and 100 eV according to the working parameters.

5 - BEAM EMITTANCE AND BRIGHTNESS IN A DUOPLASMATRON WITH EXPANSION CUP (11) (6)

This study has been performed beyond the extractor, without additional lenses. The use of a continuous

beam has made it possible to use an electrical detection in the emittance measurements. This method does not give the usual calibration difficulties of the classical photographical equipment and gives directly recording of :

- overall beam diameter
- divergence of different parts of the beam
- maximum current density in the beam

A small part of the beam passes through holes bored in a molybdenum plate positionned perpendicular to the axis ; these holes are distributed along a diameter of the beam. A movable probe, situated at a distance L beyond the plate, crosses successively all the beamlets, and the collected current is recorded, as a function of the probe position.

At the beginning of our experiments the beam density measurements gave complicated results, as shown in Fig. 10 and emittances were very different from the theoretical ellipse. After having proved that these perturbations did not come from the plasma itself we tried to relate them to the emissive plasma characteristics.

### 5.1 - Presence of drift movements in the cup

Two plane circular probes working in a ionic saturation regime and separated by a thin insulator sheet are placed respectively parallel and perpendicular to the axis of the cup (at the same point). The ratio of the currents collected by the two probes is very different from 1. This ratio varies from 0.03 (for cup walls covered with insulator) to 0.20 (for a metallic cup, at anode potential). In both cases, we are faced to a "plasma stream", very different from an isotropic plasma.

This observation confirms our measurements of energy spectra. The azimutal movements were also studied. Because of the presence of the magnetic stray field of the source, or the magnetic induction added to reduce wall losses, the following results are obtained :

- the plasma density varies slightly along a radial direction, decreasing from axis to the walls,

- an azimutal movement of charged particles exists the direction of rotation depends on those of the added induction

- ions and electrons move in the same way.

5.2 - Study of the emittance

We shall mainly consider the effects of magnetic induction on the beam emittance.

- Influence of magnetic induction at the plasma boundary

The main effect of placing the plasma boundary in a magnetic field is to create a strong radial density gradient. The emitting surface homogeneity is strongly disturbed ; corresponding radial density profiles are shown in Figure 11. Two characteristic regions ("core" and "halo") appear in the beam (12), whose origin can be explained qualitatively : Let us consider a plane diode in the space charge mode. For an isotropic plasma the current density emitted at a point M on the surface is given by $J_M = K\, V^{3/2}/d_M^2$ where $d_M$ is the distance between M and the anode (i.e. the extractor electrode). For a given voltage, V, $d_M$ is smaller on the axis if the density $n^+$ is higher in this region, due to the magnetic induction. From this axial "bump", ions are emitted in a large solid angle and form the halo on the target, as shown on Fig. 12. Ions coming from the external part of the emitting surface are concentrated in the beam central region (core).

A good emittance cannot be obtained if the magnetic field inside the expansion cup is not zero on the plasma emitting surface.

- Influence of the magnetic induction existing inside the expanded plasma

Discharge parameters and extraction voltage (20 kV) being fixed, the excitation of coils $B_1$ and $B_2$ (see fig. 2) was changed in sign and amplitude in order to obtain the same extracted current (20 mA). (The source is working at constant perveance). For different currents $I^+_{B_1}$ , $I^-_{B_1}$ , $I^+_{B_2}$ , $I^-_{B_2}$ corresponding inductions and measured values of density are shown on Fig. 13. The differences between values of $B^+$ and $B^-$ giving the same extracted current are due to the leakage flux of the source. It can be seen that an important perturbation is produced by an induction $B_1^-$ opposite in direction to the leakage induction of the source (fig. 13-2). This can be explained in this case by the shape of the

magnetic lines system, in which a zone of pure radial induction exists. Calculations using a simplified field model show a transfer of longitudinal to transversal energy, which is very important for the electrons in our experimental conditions : electrical field resulting from the rotating space-charge electron cloud will then appear and disturb the ion trajectories by increasing their radial energy. The fact that $B_2$ does not give the same emittance deformation can be explained by the following : as the distance between the coil $B_2$ and the plasma surface is small, the trajectories inside the plasma are less disturbed ; on the other hand, as the ion and electron densities decrease rapidly with the distance from the anode hole, electrical fields resulting from space charge movements are more important in the region $B_1$ than in the zone $B_2$.

In order to verify these assumptions, an isolated diaphragm was placed in the expansion cup as shown on Fig. 14. Its influence should be negligible in the case either of a laminar flow, or of an isotropic plasma. The measured values of density with and without diaphragm, by identical discharge conditions, are shown on Fig. 15 : the diaphragm has an important effect enhancing the beam quality. It seems that it stops the non paraxial trajectories which disturb the beam emittance.

### 5.3 - Emittance and brightness

Emittance is related to the area A of the diagram containing all the points representing ion trajectories for a given beam cross-section plane in a system of coordinates (r, r') by the simple relation $E = A/\pi$ ; for a beam drifting at the same velocity along the axis, or crossing linear optical systems (without aberrations), emittance is a constant. In accelerated or decelerated beams, E varies, but the product $E_n = \frac{p}{m_o c} E = \frac{m v}{m_o c} E$ is now invariant which suggest that we define a "normalized emittance" :

$$E_n = \frac{v/c}{1-(v/c)^2} . E$$

For non-relativistic particles : $E_n \simeq (v/c)E$

This definition offers a mean of comparing different sources and the various extraction systems with one another : the better source gives the smaller value of $E_n$ , the current I being fixed.

The brightness B of a source is defined as the emitted current per unit of surface and unit of solid angle aperture. For a quasi- point source of zero emittance

$$B = \frac{I(amp)}{\pi^2 r_o^2 (m^2)\ {}^2(rad^2)}$$

For a source of emittance E, B is given by the relation (13) ;

$$B = \frac{2I}{\pi^2 E^2}$$

For a comparison of different sources, it is wiser to use the "normalized brightness"(14).

$$B_n = \frac{2I}{\pi^2 E_n^2}$$

In the domain $60 < I < 400$ mA, normalized brightness as high as $1\text{-}2.10^{11}$ have been reported. In our case (continuous working sources), same values were measured in an hydrogen source, with currents varying between 20 and 40 mA, using a well adjusted extraction system. These values are obtained at a distance $Z \simeq 30$ cm beyond the extractor, in a plane where the beam is about 10-20 mm in diameter and slightly divergent.

Such brightness values which are higher that those of good electrons guns, may be explained by the large values of longitudinal velocities at the emitting plasma boundary.

## CONCLUSION

In conclusion, the Duoplasmatron source is a very interesting tool to produce high intensity ion beams. Its ionization efficiency is particularly high (80 % with $H_2$ , 90 % with Argon and Mercury) and a good design of extraction region permits to obtain beams having good optical qualities, small emittances and high brightnesses.

AKNOWLEDGMENTS

The authors would like to aknowledge the continued support of these studies by the Applied Physics Department of the French Nuclear Energy Center of Saclay.

---

REFERENCES

1 . M. Von ARDENNE
Tabellen für Elektronenphysik, Ionenphysik und Ubermikroscopie, Berlin 1956

2 . R. BECHERER, G. GAUTHERIN et A. SEPTIER
J. de Physique et le Radium, 1962, 23, 121 A

3 . A. SEPTIER, F. PRANGERE, H. ISMAIL and G. GAUTHERIN
Nucl. Instr. and Methods, 1965, 38, 41.

4 . C. LEJEUNE and F. PRANGERE
To be published in Journal de Physique

5 . C. LEJEUNE and F. PRANGERE
C.R.Ac.Sc. 1967, 264 B, 1075

6 . G. GAUTHERIN
Doctorat Thesis, Orsay, 1967

7 . G. GAUTHERIN, C. LEJEUNE and A. SEPTIER
To be published in Plasma Physics

8 . C. LEJEUNE and F. PRANGERE
C.R.Ac.Sc. 1967, 265 B, 389

9 . M. WATANABE and T. SUITA
Japanese J. of Appl. Phys. 1967, 6, 758

10. G. GAUTHERIN
C.R.Ac.Sc. 1962, 255 B, 653

11. G. GAUTHERIN
Nuclear Instruments and Methods, 1968, 59, 261

12. L.E. COLLINS and P.T. STROUD

Nuclear Instruments and Methods, 1964, 26, 157

N.B. BROOKS, P.H. ROSE, A.B. WITTKOWER and R.P.BASTIDE

R.S.I. 1964, 35, 894

13. A. SEPTIER

Focusing of Charged Particles, vol. 2, 1967, p. 123 (Acad. Press, N.Y.)

14. P. BERNARD, J. FAURE and R. VIENET

Proceedings of the Linear Accelerator Conference - Los Alamos, 1966

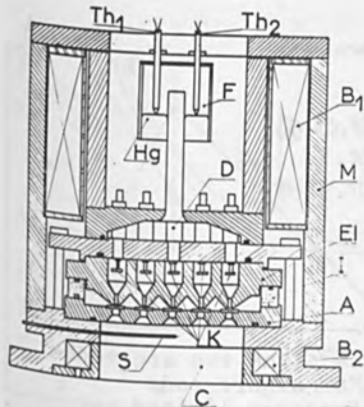


Fig.1

Duoplasmatron with seven discharges in parallel
$Th_1$-$Th_2$ : thermocouples
$B_1$ : main coil
$B_2$ : auxiliary coil
F : oven - A : anode
K : cathode
$E_I$ : intermediate electrode
I : insulator
C : expansion cup
S : Langmuir probe
D : mercury vapor distributor

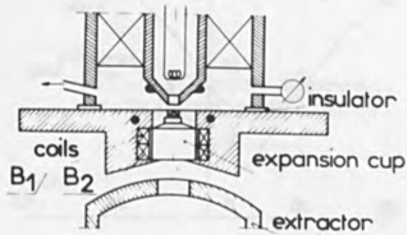


Fig.2

Schema of duoplasmatron with expansion cup and cylindrical symmetry

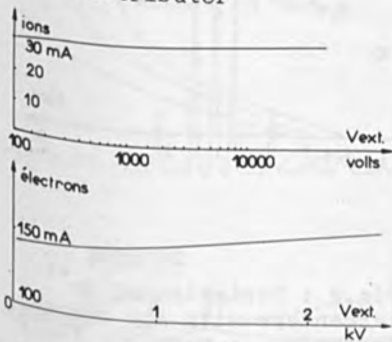


Fig.3 : Variations of extracted current versus extracting potential

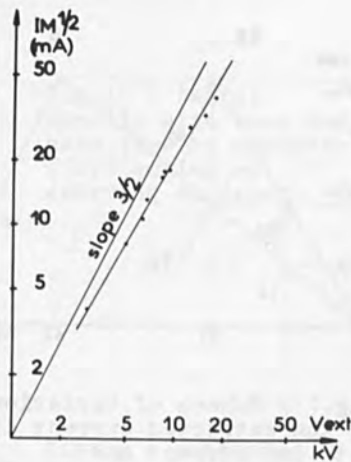


Fig. 4 : Verification of space charge emission law

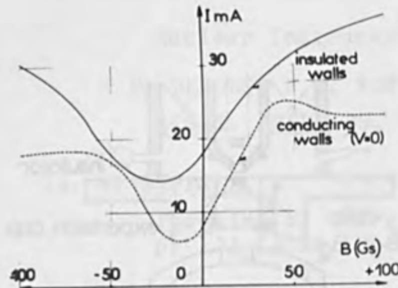


Fig.5 : Influence of the nature of the expansion cup walls and auxiliary magnetic field on extracted ion current

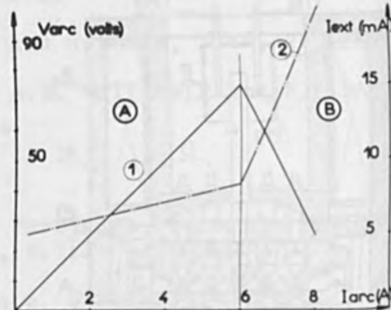


Fig.6 : The two arc modes
A Normal arc mode
B Pressure limited arc mode
1 Variation of arc voltage (cathode working in space charge limited emission)
2 Variation of ion extracted current

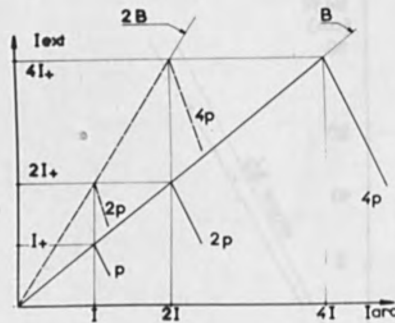


Fig.7 : Schema of variation of ion extracted current with arc current and parameters :
B : magnetic fiel maximum value
p : pressure in anode space

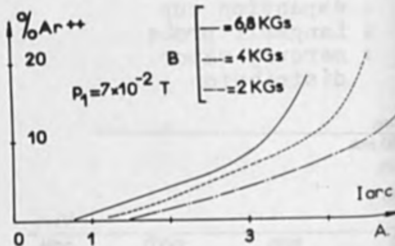


Fig.8 : Variation of $Ar^{++}$ percentage with arc current parameter : magnetic field

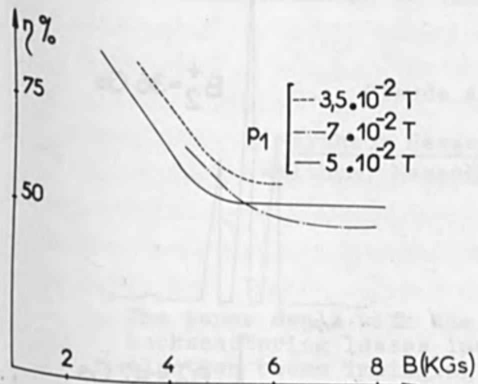

Fig.9 : Argon source ionization efficiency

Fig.10 : Perturbated radial density of current in the ion beam

Fig.11 : Radial density with core and halo (due to magnetic field acting on emitting surface)

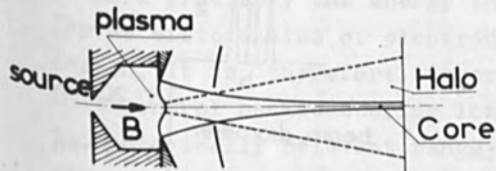

Fig.12 : Schematic beam cross-section corresponding to fig.11

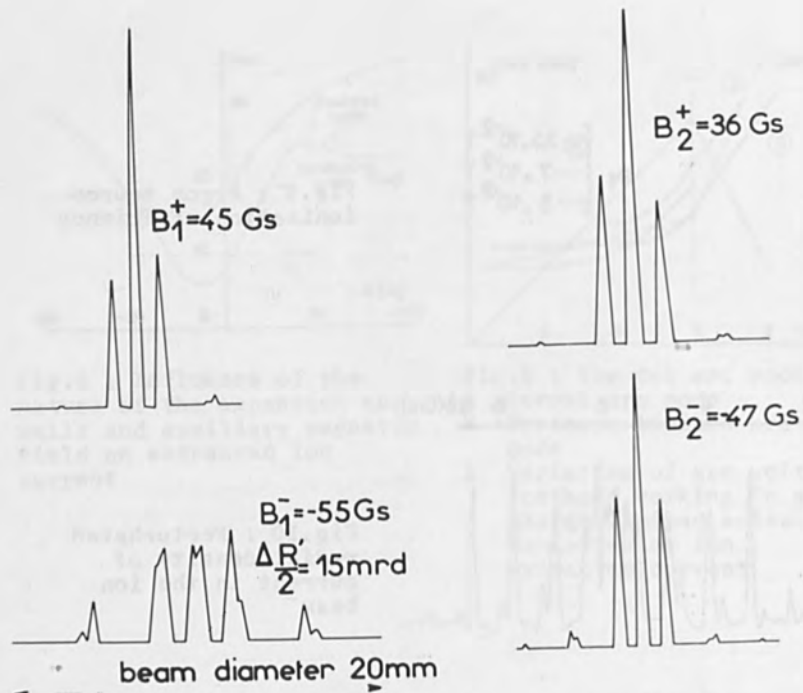


Fig.13 : Influence of auxiliary magnetic field on emittance

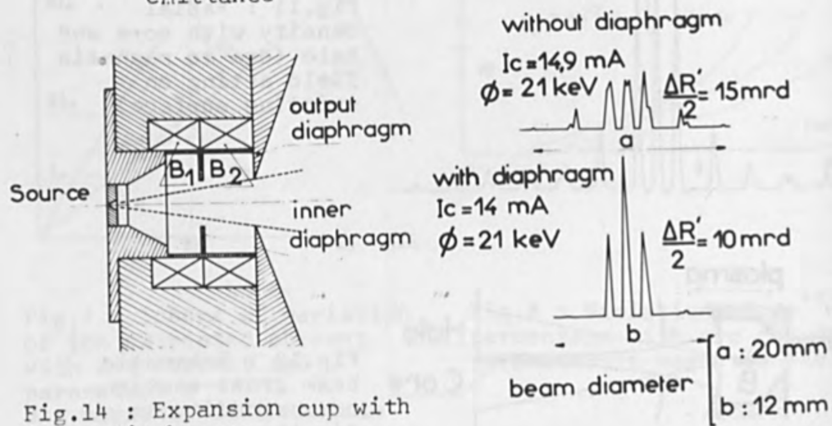


Fig.14 : Expansion cup with inner diaphragm

Fig.15

# BACKSCATTERING OF KILOVOLT-ELECTRON BEAMS

Claude A. Klein

Raytheon Research Division
Waltham, Massachusetts 02154

The paper deals with the problem of evaluating backscattering losses incurred by kilovolt-electron beams impinging on solid matter. It is proposed to bypass the usual electron-transport equation and to describe a reasonably approximate model that yields satisfactory agreement with available experimental evidence. This approach is utilized to assess the energy-balance situation in electron-beam pumped lasers.

## I. INTRODUCTION

The transfer of electron-beam energy to a solid target represents the end result of a complex sequence of events usually described in terms of the spatial distribution of specific energy losses, dE/dX, where E is the residual average primary-electron energy at a penetration depth X. A substantial fraction of the incident electrons, however, may scatter out of the target; these electrons, or more precisely the energy they carry, are "lost" insofar as efficiencies of electron-beam processes are concerned. It is, therefore, imperative to assess the factors that control backscattering losses, especially in the technologically relevant range of kiloelectronvolt energies.

Much work has been done regarding electron fluxes reflected from various targets, but few investigators have actually recorded the energy distribution of back-scattered electrons at incident energies $E_0 < 100$ keV.[1] On the theoretical side, while it is true that Spencer's work[2] provides a soundly based approach to problems involving the scattering of fast electrons in matter, in its mise en oeuvre it requires complex mathematical procedures. Besides, there is an essential difference between "zero-plane" type configurations and those considered by Spencer, who assumes the scattering medium to extend homogeneously in all directions. For this reason I propose to bypass the electron-transport equation and to seek a reasonably approximate model that would yield satisfactory agreement with the available experimental evidence.[3] In effect, I will attempt to set up a phenomenological model capable of describing relevant aspects of backscattering on the basis of empirical indications about electron trajectories and energy dissipation within the target. In addition, I wish to illustrate the relative weight of losses stemming from backscattering in the light of some recent achievements in the area of electron-beam pumped lasers.

## II. A SIMPLE MODEL

Ehrenberg and King's (E &K)[4] photographs of glows induced by a narrow bundle of kilovolt electrons penetrating into luminescent material show spherical shapes, or spherical segments, which move deeper into the material as the incident energy increases (see Fig.1 for a typical example). In addition, since luminescent intensity is a good indicator of the local energy dissipation, it can be inferred that the brightness contours reflect an exponential

distribution of energy losses along any radius vector of the sphere of excitation. This state of affairs is reminiscent of a model initially proposed by Bethe, Rose, and Smith (BRS)[5]: In a first approximation the primary electrons are presumed to travel straight into the target down to a certain distance, the "depth of complete diffusion" $X_D$, from whence they diffuse evenly in all directions to cover an over-all path equal to the Bethe range $R_B$.[6] This model gives a representation of the observed isotropic spreading of electrons, and automatically makes allowance for backscattering because some of the diffusing electrons recross the surface and cease participating in the energy-deposition process. In the following we will make use of the BRS model, in conjunction with the exponential energy-transfer law suggested by E & K's experiment, to calculate both, the backscattered energy fraction, $\Delta E/E_o$, and the differential energy loss, $dE/dX$.

Figure 2 illustrates the situation. To derive the volume density of in-target energy dissipation we consider the amount deposited in an elemental spherical shell of radius r and assume that

$$\int_o^{R_B-X_D} r^2 \exp(-\mu r)dr \approx \int_o^{\infty} r^2 \exp(-\mu r)dr. \qquad (1)$$

In other words, we take it that the macroscopic absorption coefficient $\mu$ is compatible with assuming $\mu(R_B-X_D) \gg 1$; it will be brought out, subsequently, that this holds for substances of atomic number $Z \geqslant 5$. We conclude that, in this approximation, the density of energy deposition is $(E_o \mu^3/8\pi)\exp(-\mu r)$ if $E_o$ designates the initial kinetic energy of the incident particles. The energy dissipated in an elemental shell of radius r and height h is then given by

$$S[r,h]\,dr = (E_o\mu^3/4) rh\exp(-\mu r)\,dr \quad (2)$$

so that we may obtain the total backscattered amount simply by setting $h = r - X_D$ and integrating over the range $X_D \leq r \leq R_B - X_D$:

$$\Delta E = \int_{X_D}^{R_B-X_D} S[r,r-X_D]\,dr \approx (E_o/2)(1 + \mu X_D/2)\exp(-\mu X_D). \quad (3)$$

In a similar vein, if $E(X)$ is the total energy dissipated between the surface and a given depth $X$, it follows from elementary geometrical considerations that

$$E(X) \equiv E(X_D) + E(X) - E(X_D), \quad (4)$$

where

$$E(X) - E(X_D) = \delta\left\{\int_{o}^{\delta(X-X_D)} S[r,r]\,dr + \int_{\delta(X-X_D)}^{R_B-X_D} S[r,\delta(X-X_D)]\,dr\right\} \quad (5)$$

and $\delta = (X-X_D)/|X-X_D|$. Hence, we may deduce $dE/dX$ by differentiating the two integrals in (5) with respect to $X$, which yields

$$dE/dX \approx (E_o\mu/4)\,[1 + \mu|X-X_D|]\exp[-\mu|X-X_D|]. \quad (6)$$

## III. BACKSCATTERED ENERGY FRACTION

According to (6) the differential loss distribution peaks at a depth $X = X_D$, which makes it tempting to refer to Spencer's tabulation[7] for the purpose of locating the depth of complete diffusion. The procedure is illustrated in Fig. 3 and leads to the conclusion that, for $Z \geqslant 5$, the

reduced[8] depth of complete diffusion decreases with atomic number in a manner similar to

$$X_D/R_B = 4/(Z + 4) , \qquad (7)$$

at non-relativistic energies. For the sake of comparison we should mention here that Archard[9] derived $X_D/R_B \approx 5.7/Z$ within the framework of an application of the BRS model to related problems.

Equation (7) suggests to relate backscattered energy fraction and atomic number via

$$\Delta E/E_o = \left[\tfrac{1}{2} + \mu R_B(4 + Z)^{-1}\right]\exp\left[-\mu R_B(1 + Z/4)^{-1}\right]. \qquad (8)$$

Figure 4 exhibits the dependence for values of the dimensionless "parameter" $\mu R_B$ ($\mu R_B$ = 8, 10, and 12) that are compatible with E & K's luminosity data. On the same diagram are plotted experimental points inferred from backscattering flux ($\eta$) measurements of various investigators[10] together with average backscattered electron energies ($\bar{k}$) as determined by Kuhlenkampff and Spyra.[11] The confrontation reveals that, by and large, the calculated curves reflect the experimental situation, which shows very little energy dependence in the range of interest, and thus points to an effectively Z-independent $\mu R_B$ product of 10±1. In the light of E & K's glow-luminosity data this is very gratifying albeit physical implications have not yet been clearly established.[12] At any rate, Fig.4 demonstrates - conclusively - that backscattering losses become quite substantial with targets of intermediate or high atomic number; in effect, backscattering may "remove" as much as 40% of the incident primary beam energy.

## IV. APPLICATION TO EBP LASERS

The over-all power efficiency of an electron-beam pumped (EBP) laser,[13] i.e., the ratio of the coherent optical power emitted to the power carried by the incident electron beam is best expressed as a product of three factors,

$$P_{out}/P_{in} = K(E_G/\varepsilon)\eta_{ex} \ . \qquad (9)$$

These factors are: (a) the power-retention factor, $K = 1 - \Delta E/E_o$, which reflects pump-power losses stemming from the backscatter of the incident electrons, (b) the ionization-yield factor, $E_G/\varepsilon$, which incorporates the losses originating from the phonon production associated with the creation and the thermalization of the electron-hole pairs, and (c) the external quantum efficiency, $\eta_{ex}$, which relates the power efficiency to inherent characteristics of the optical cavity. For instance, consider the case of CdS. Since $\bar{Z} = 32$, Eq. (8) with $\mu R_B = 10 \pm 1$ points to $K = 0.75 \pm .02$; the ratio $E_G/\varepsilon$ of bandgap energy and ionization energy, on the other hand, amounts to $0.325 \pm .01$.[14] Consequently, the over-all power efficiency of an electron-beam pumped CdS laser cannot possibly exceed 25 or 26%. Since both, electron backscattering and phonon generation represent intrinsic features of electron-beam pumping and will continue to impose fundamental limitations on the efficiency of this technique, it would appear that Hurwitz's CdS laser[15] with its reported power efficiency of 26.5% illustrates an essentially "ideal" operational situation ($\eta_{ex} \approx 1$) and, thus, leaves no room for further performance improvement.

## REFERENCES


1. For a bibliography, see R. W. Dressel, Phys. Rev. 144, 344 (1966).
2. L. V. Spencer, Phys. Rev. 98, 1597 (1955).
3. For a preliminary account, see C. A. Klein, Appl. Opt. 5, 1922 (1966).
4. W. Ehrenberg and D. King, Proc. Phys. Soc. (London) 81, 751 (1963).
5. H. A. Bethe, M. E. Rose, and L. P. Smith, Proc. Am. Phil. Soc. 78, 573 (1938).
6. Or integrated path length as derived from Bethe's stopping-power law (see Ref.3).
7. L. V. Spencer, NBS Monograph No.1 (1959).
8. Reduced in the sense that it is measured in units of the Bethe range.
9. G. D. Archard, J. Appl. Phys. 32, 1505 (1961).
10. R. Palluel, Compt. Rend. 224, 1492 (1947); H. Kulenkampff and K. Rüttiger, Z. Physik 137, 428 (1954); H. Kanter, Ann. Physik 20, 144 (1957).
11. H. Kulenkampff and W. Spyra, Z. Physik 137, 416 (1954).
12. Further work is in progress and will be submitted to the Journal of Applied Physics.
13. For background information, see C. A. Klein, IEEE J. Quantum Electronics (to be published).
14. C. A. Klein, J. Appl. Phys. 39, 2029 (1968).
15. C. E. Hurwitz, Appl. Phys. Letters 9, 420 (1966).

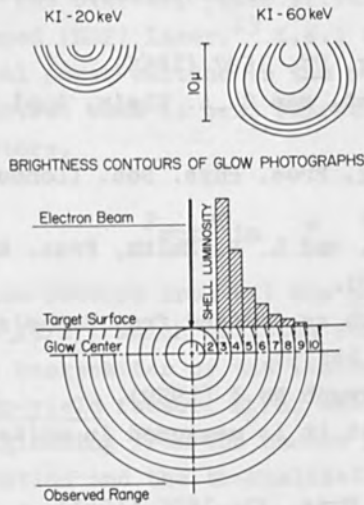


FIG.1. (a) Brightness-level contours of cathodoluminescent glows in potassium iodide. (b) Distribution of luminosity within the glow. For particulars, see Ref.4.

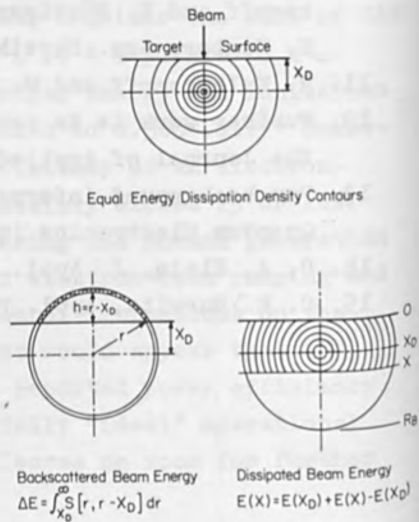


FIG.2. (a) Equal energy-dissipation density contours for an exponential distribution of specific energy losses assuming penetration à la BRS (Ref.5). (b) Model constructions for evaluating backscattered energy fraction and dissipated beam energy. For particulars, see Sec.II of Text.

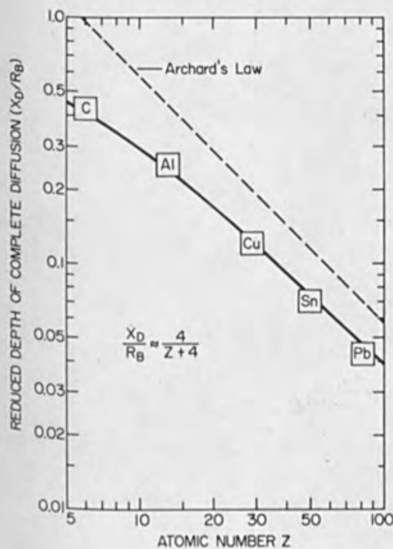


FIG.3. Reduced depth of complete diffusion plotted against the atomic number. The solid curve fits to peak energy-dissipation positions obtained from Spencer's theoretical work (Ref.7) on the assumption that these positions coincide with the depth of complete diffusion. The broken line illustrates the classic result of Archard (Ref.9).

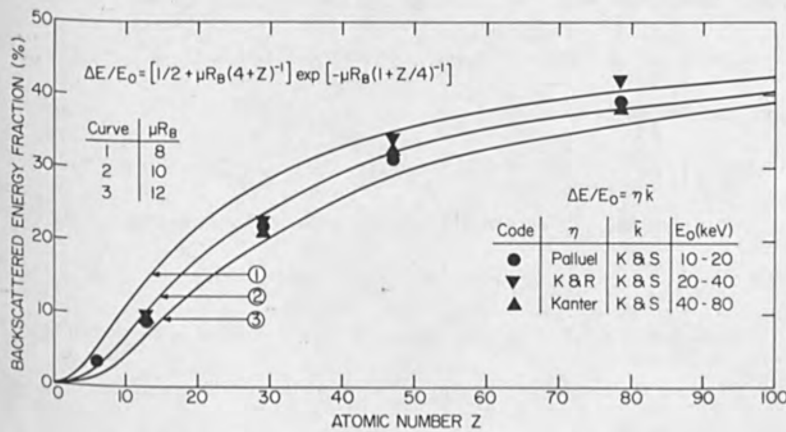


FIG.4. Backscattered energy fraction as a function of target atomic number for electron beams in the range $10 < E_0 < 100$ keV impinging at normal incidence. For particulars, see Sec.III of Text.

# AN EXPERIMENTAL INVESTIGATION OF A HIGH-VOLTAGE ELECTRON-BOMBARDMENT ION THRUSTER

by David C. Byers

Lewis Research Center
National Aeronautics and Space Administration
Cleveland, Ohio

## SUMMARY

The performance of a mercury electron-bombardment thruster at large values of net accelerating potential is described. A 20-centimeter-diameter thruster was tested at values of ion beam current and net accelerating potential up to 0.165 ampere and 70 kilovolts, respectively. A maximum beam power of about 10 kilowatts was obtained. The maximum supportable electric field strength between accelerator grids was approximately constant at $2\times10^{6}$ volts per meter for spacings between 0.5 and 3.0 centimeters. The ion chamber performance was qualitatively similar to that at low accelerating voltage. The energy dissipated per beam ion in the ion-chamber discharge was related to the percentage of Child's law ion current extracted over a wide range of accelerator spacings and potentials. The maximum percentages of Child's law current transmitted were about 60 and 80 percent for thrusters with 20 and 7.5 centimeter-diameter accelerator grids, respectively, and were essentially independent of grid spacing and thickness. Ion focusing characteristics, at ion beam current densities of about 10 amperes per square meter, indicated that the ratio of center-to-center grid spacing to

grid thickness should be between about 2.5 and 4 to avoid direct ion impingement.

Accelerator grid lifetimes up to two years were calculated for net accelerating potentials between 20 and 70 kilovolts, based on measured values of ion sputtering rates and ion impingement currents. The lifetimes were a function of the percentage of Child's law current at which the plates were operated.

The power efficiency was measured and found to be consistent with data taken with low voltage thrusters operated at similar conditions. A power efficiency of 0.8 was obtained at a net accelerating potential of 18 kilovolts and rose to 0.88 at a net accelerating potential of 36 kilovolts. Overall thruster efficiencies of about 0.80 and 0.82 were obtained at net accelerating potentials of 28 and 36 kilovolts, respectively.

## INTRODUCTION

The operation of electron-bombardment thrusters at high values of net acceleration potential has promise of increasing the overall thruster efficiency (ref. 1). Higher specific impulses (and therefore higher accelerating voltage) also become more necessary as mission difficulty increases and propulsion system specific mass decreases (ref. 2). In addition, degradation of the maximum supportable field strength at high voltages, often found in high voltage breakdown studies (ref. 3), would reduce the maximum thrust per unit area of the thrusters (ref. 4).

This investigation was carried out to determine the operating characteristics of mercury electron-bombardment thrusters at net accelerating potentials between 10,000 and 70,000 volts. Previous thruster data had been limited to a maximum potential of approximately 10,000 volts (ref. 5).

The discharge chamber efficiency and the current carrying characteristics of the high voltage grid system were investigated and compared with data obtained at low values of net accelerating potential (ref. 6). Ion impingement currents were measured and compared with an existing analysis (ref. 7) extrapolated to high voltage. Overall thruster efficiencies are discussed both as a function of propellant utilization efficiency and net accelerating potential and in addition are compared with low voltage data.

SYMBOL LIST

$A_A$ open area of accelerator on screen grid, $m^2$

$A_I$ flow area of ions, $m^2$

$A_O$ nominal thruster area, $m^2$

B magnetic field strength, $W/m^2$

D accelerator plate hole diameter, m

f(R) $1/R^{3/2} + 3/R - 4$

$I_{sp}$ specific impulse, sec

J current, A

$J_O$ current equivalent neutral flow rate, A

$j$ current density, $A/m^2$

$\ell$ grid-to-grid spacing, cm

$\ell_{\mathfrak{c}}$ center-to-center grid spacing, cm

m mass, kg

q charge of an electron, C

R ratio of net-to-total accelerating potential, $V_I/V_I + |V_A|$

t accelerator grid thickness, cm

V potential, V

$\Delta V$ potential difference, V

$\beta$ $4\epsilon_o/9\sqrt{2\,q/m} = 3.86\times10^{-9}$ mks units for $H_g^{+1}$ ions

$\epsilon_o$ permittivity of free space, $8.85\times10^{-12}\ C^2/(N)(m^2)$

$\eta$ efficiency

$\tau$ lifetime, hr

Subscripts:

A accelerator

B beam

CH Child's law

I ion chamber

n neutral

p power

T total

U utilization

## APPARATUS AND PROCEDURE

### Thruster

The electron-bombardment thruster utilized in this program is shown in figure 1. The principle of operation of the thruster has been described in many references (e.g., ref. 5). In brief, a mercury vaporizer was heated with steam slightly above atmospheric pressure to provide close thermal control of the vaporizer. Interchangeable vaporizer orifices were utilized to change propellant flow rates. The propellant flowed into the ionization chamber through an annular slot distributor. A small screen was between the vaporizer and the distributor to prevent plasma leakage to the vaporizer (ref. 8).

Electrons are emitted from the cathode and reach an energy nearly equal to the potential difference between the anode and the cathode. These electrons, which are constrained by an axial magnetic field, ionize some of the mercury. The mercury ions diffuse to the accelerator grid region and are accelerated into the exhaust beam.

For all tests, a 20-centimeter-diameter anode was used. The cathode was tantalum ribbon 0.05 millimeter thick, 40 millimeters long, and about 5 millimeters wide.

Accelerator grid system. - A typical accelerator configuration is shown in sketch (a).

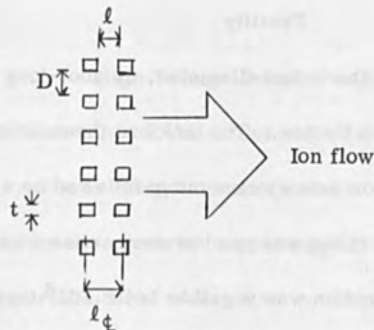

(a)

The value of the ratio of center-to-center grid spacing to hole diameter, $\ell_{℄}/D$, was varied between 0.5 to 3.0 by insertion of shims between the downstream insulators and the screen grid extensions (fig. 1). The screen and accelerator grids were of equal thickness unless otherwise stated. All the data presented in the figures of this report were taken with accelerator grids with hole diameters of 2.2 centimeters because, as will be later explained, the use of larger holes, 5 centimeters, led to undesirable thruster performance.

Insulators. - The high voltage thruster was initially designed with spherical insulators scaled from insulators used successfully up to about 10 kilovolts. The 5-centimeter-diameter aluminum oxide spheres were capable of supporting 22 kilovolts before severe flashover occurred. Insulators utilizing shielded negative terminals were also fabricated and tested. These tests are presented in the RESULTS AND DISCUSSION. The final design, shown in figure 2, was capable of withstanding potentials up to 250 kilovolts in vacuum.

## Facility

The facility was one of the 5-foot-diameter, 16-foot-long vacuum tanks at the NASA Lewis Research Center. The tank has three 32-inch oil diffusion pumps feeding into a common ejector pump followed by a mechanical pump. Cryogenic pumping ($LN_2$) was used in conjunction with the diffusion pumps so that thruster operation was possible in the $10^{-6}$ torr pressure range. A more complete description of this facility is included in reference 9.

## Measurements

All electrical measurements in this program were made with standard meters with an accuracy of about 3 percent at full scale deflection. The propellant utilization efficiency could not be fixed to much better than 5 percent. This accuracy was estimated from measured variation in neutral propellant flow rate from several tests where the same orifice size was utilized.

# RESULTS AND DISCUSSION

The results of the high voltage breakdown characteristics over insulators and between accelerator grids are described first. The ion chamber performance is considered next. The effects of accelerator parameters on the maximum attainable ion current are then presented followed by a discussion of the accelerator lifetimes to be expected at high voltage. Finally a discussion of overall thruster efficiencies at high voltage is presented.

## High Voltage Breakdown Studies

The maximum value of the thrust per unit area of a Child's law current limited system is directly proportional to the square of the electric field supported by the accelerator grid system (ref. 4). The value of the maximum supportable field strength in vacuum has, in general, been found to decrease with increasing spacing (ref. 3). The voltage breakdown characteristics of accelerator grids at spacings of interest in this program (roughly 0.5 to 5 cm) were therefore studied.

In addition, initial tests indicated that spherical insulators were unacceptable for use at the intended voltage levels. A test program was carried out to find a suitable insulator design.

Insulator studies. - Spherical insulators (such as utilized in low voltage thrusters), 5 centimeters in diameter, were found to breakdown at 22 kilovolts. A program was carried out to improve the insulator design to meet the voltage requirements of the study. The guideline for this program was the data of references 12 and 13 which indicated that the primary cause of insulator flashover was electron emission initiating at the negative metal-dielectric junction.

The program consisted of three phases. Initial tests utilized small bakelite samples (for convenience in fabrication) in a small bell jar facility with total potentials up to 50 kilovolts available. Intermediate studies

were conducted on full size insulators, fabricated from various ceramic materials, in the thruster vacuum facility. Tests on the final design (fig. 2), fabricated from aluminum oxide, were performed in a high voltage bell jar facility with total applied potentials up to 400 kilovolts. The final insulator was found to eliminate insulator flashover breakdown up to voltages of 250 kilovolts, at which point the insulator failed due to puncture through the dielectric. The design increased the flashover voltage for two reasons. First, the electric fields which can liberate electrons are reduced near the negative junction, as suggested by reference 12. Secondly, the discharge at the negative junction was constrained to the hollowed out section of the insulator. As in most high voltage tests, occasional breakdowns occur during initial testing. For example, in one test two flashover breakdowns occurred as the voltage was being raised to 250 kilovolts. The insulator then held for three hours at this potential without breakdown. This voltage level was sufficient because the total accelerating potential available for thruster operation was about 125 kilovolts.

Plate breakdown studies. - Breakdown tests between simulated accelerator grids were carried out in a bell jar facility. The effects of spacing and surface conditioning on the maximum supportable electric field strength were investigated at voltages up to 285,000 volts. The grids were attached to independent holders which were connected to high voltage feed throughs at opposite ends of the bell jar. This mounting technique eliminated the need

of spacing insulators and allowed comparison of grid-to-grid breakdown separate from insulator flashover.

Stainless steel plates 0.31 centimeter thick and 25 centimeters in diameter were fabricated. Plain plates and plate sets with up to 37 holes (all holes 2.54-cm diam) were utilized. The edges of one side of each of the plates were left unfinished while the edges of the opposite side were machined to approximately 0.06 centimeter radius.

The results of these tests are presented in figure 3, where the maximum supportable field strength is plotted against the face-to-face spacing between the plates. Above the maximum field strength the breakdowns would become nearly continuous. In addition, this field strength was the highest that could be supported without breakdowns for times greater than about five minutes after prolonged conditioning (i.e., repeated breakdowns). A breakdown was defined as a discharge between the plates greater than 1 milliampere (which tripped the power supplies).

Figure 3 shows that the maximum supportable electric field does decrease with increasing spacing as expected. The fields are, however, considerably greater than the maximum supportable fields for low voltage thruster operation, which are generally from 2 to $3\times10^6$ volts per meter (ref. 7). Figure 3 also shows that the maximum field is somewhat dependent on the number of holes. In general, the voltage breakdown level decreased with the number of holes drilled in the plates. Although not shown, the critical electric

field was larger when rounded edges rather than square edges faced each other. This difference in critical electric field was, however, always less than 20 percent. It is seen that the data agrees relatively well with the data of reference 10, which was taken with unpolished stainless steel plates.

It was found that the characteristics of the breakdowns which occurred at spacings less than 1 centimeter spacing differed substantially from those breakdowns at spacings greater than 1 centimeter. At the smaller spacings the breakdowns were localized, data were quite repeatable, and the current between the plates approached zero at the maximum voltage difference after conditioning for a few minutes. At larger spacings, however, breakdowns were not localized, the leakage current did not decrease significantly with time near the maximum field strength, and the data were never repeatable to much closer than about 20 percent. This was true whether the data was repeated in sequence, with up to 24 hours between tests, or following an intermediate spacing change. The lack of repeatability at spacings greater than 1 centimeter precluded both the identification of sources of prebreakdown leakage currents and prediction of the maximum supportable field strengths to better than 20 percent.

Thruster breakdown tests. - Data were taken throughout the thruster program of the maximum supportable field during thruster operation (utilizing the improved insulator design previously described). The results are

shown in figure 4. Comparing these data with figure 3 it is seen that the levels of field strength are approximately a factor of 3 or 4 lower than those obtained in the bell jar tests. The data do not, however, show significant degradation from field strengths obtained previously with thrusters operating at lower voltages. The reason for the low maximum supportable field strength between grids of operating thrusters, as compared with breakdown between plates of the same physical geometry in vacuum is not certain. During operation, however, the grids of a thruster suffer ion impingement, and become heated to about $700^{\circ}$ K (ref. 7). These factors would probably tend to reduce the maximum supportable field strength.

Ion Chamber Performance

The ion chamber was tested over a large range of thruster operating conditions. In general, the qualitative trends were the same as those obtained with low voltage thrusters utilizing tantalum cathodes. This discharge energy required to form a beam ion, eV/ion, is defined as:

$$eV/ion = \frac{\Delta V_I (J_I - J_B)}{J_B} \tag{1}$$

Figure 5 shows the eV/ion as a function of the propellant utilization efficiency, net accelerating potential, ion-chamber discharge potential, and magnetic field strength. As is generally true (ref. 5) the eV/ion increased with propellant utilization efficiency, decreased with net accelerating potential, and exhibited a minimum at some value of both ion chamber potential

difference and magnetic field strength. These data are not optimum for a 20-centimeter thruster. Use of a discharge chamber configuration employing a hollow cathode (ref. 14) or different propellant introduction modes (ref. 15) would probably lower the chamber losses.

Discharge stability. - During the investigation it was found that some limits had to be placed upon various thruster parameters in order to maintain stable thruster operation. The instability of the discharge would manifest itself both by breakdowns from the thruster anode potential to ground and quenching of the ion-chamber discharge. Such instabilities are similar to those experienced during operation with short anodes (refs. 5 and 16). The factors most strongly affecting the discharge stability were the propellant utilization efficiency and the accelerator grid hole size. The grid spacing and thickness did not significantly affect stability over the range of values tested.

The discharge chamber was unstable with the 2.2 and 5.0-centimeter diameter grid holes at propellant utilization efficiencies greater than about 0.90 and 0.30, respectively. Data presented herein at propellant utilization efficiencies greater than these values (with the specified hole sizes) were taken during repeated breakdowns and/or discharge quenching.

Operation with the large hole grids was characterized by very severe breakdowns which would often destroy the cathode. When wire mesh was placed over the screen grid holes (sketch b), breakdowns from the anode

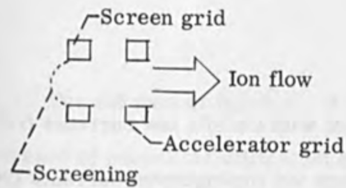


(b)

to ground were eliminated. Use of such screens proved unsatisfactory, however, because the mesh would quickly burn through. In addition, the eV/ion was 2 to 3 times that obtained without mesh screening.

The above statements indicate that the accelerator field can interact with the ion chamber plasma. The grid hole size strongly affected the maximum propellant utilization efficiency that could be attained. The data suggests that discharge quenching, at high utilization efficiencies, may be inherent with the grid geometries required at high voltage.

Accelerator spacing and net accelerating voltage. - Throughout the test it was found that the eV/ion was strongly dependent upon the accelerator geometrical and electrical parameters within the region of stable discharge operation. Accelerator grids with hole diameters of 2.2 centimeters and 7 or 37 holes were utilized for the tests discussed below. The ratios of center-to-center spacing and grid thickness to the hole diameter were varied between 0.8 to 2.5 and 0.34 to 0.86, respectively.

Figure 6 shows the energy loss per beam ion as a function of the center-to-center grid spacing. The center-to-center spacing was chosen

because it allows reasonable agreement with Child's law currents (ref. 6) and predicted values of charge-exchange ion impingement currents (ref. 7). It is seen from figure 6 that the eV/ion tends to increase with both grid spacing and thickness at fixed values of accelerating voltage and propellant utilization efficiency (the hole size was constant for the data of fig. 6).

To concisely present data over a wide variety of operating conditions, the eV/ion was plotted as a function of the ratio of beam current to the Child's law current predicted by use of the center-to-center grid spacing (ref. 6). This ratio is hereafter referred to as percentage of Child's law, and for reference is given by equation (2):

$$\left(\frac{J_B}{J_{CH}}\right) = 2.59\times10^{10} \frac{J_B l_¢^2}{A_A \Delta V_T^{3/2}} \tag{2}$$

Figure 7 shows this variation and is typical of all data taken in that the energy lost per beam ion always rose monotonically with the percentage of Child's law.

Comparison of figures 5(a) and 7 show that the eV/ion is less sensitive to the propellant utilization efficiency when the percentage of Child's law current, rather than the net accelerating potential, is held constant. This fact is more clearly demonstrated by figure 8 which presents, at one grid spacing, the variation of eV/ion with propellant utilization efficiency at three values of percentage of Child's law ion current.

For the data of figure 8, at a fixed percentage of Child's law, an increase of propellant utilization efficiency from 0.3 to 0.9 corresponded to increases of ion beam current and net accelerating potential by factors of about 3 and 2, respectively. At a fixed propellant utilization efficiency, the net accelerating potential decreased (eq. (1)) by a factor of about 1.4 as the percentage of Child's law current increased from 30 to 50 percent.

Figure 9 shows that to a good approximation the eV/ion was not a strong function of grid spacing if the accelerating voltage was adjusted to provide a constant percentage of Child's law ion current. The data of figure 6 (fixed net accelerating potential, 7 hole grid) indicate that the eV/ion nearly doubled as the spacing ratio increased from 0.8 to 2.0. The increase in eV/ion for the same spacing ratio variation at fixed percentage of Child's law current (fig. 9) was about 15 percent.

The basic energy requirement of producing a beam ion is, of course, most strongly a function of propellant type and the geometrical and electrical parameters of the ionization chamber (ref. 17). Within this framework, however, the accelerator parameters can play an important role in determining the eV/ion.

The ion extraction efficiency could be a function of either the ion sheath withdrawal area or long range extraction phenomena such as axial electric field gradients in the discharge chamber. Figures 7 and 8 of reference 18 indicate that small changes in the percentage of Child's law can

result in large variation in ion sheath withdrawal area. Reference 18 indicates, for example, that the sheath area increased by about 50 percent when the ion current was varied to decrease the percent Child's law from approximately 27 to 17 percent. On the other hand, increased extraction efficiency is almost certain to change the plasma parameters, at least near the accelerator grids. Variation of the electron temperature, for example, could affect the ion drift velocity toward the accelerator grids (ref. 17).

A consequence of the above discussion is that the eV/ion does not decrease indefinitely with increasing net accelerating potential. For a fixed grid spacing the energy expended per beam ion will decrease with increasing acceleration voltage up to the voltage limit determined by grid-to-grid breakdown. In order to further increase the acceleration potential it is necessary to increase the grid spacing. An increase in spacing has the effect (eq. (2)) of increasing the percentage of Child's law current represented by a given ion beam current density and net accelerating potential, and as previously seen, the eV/ion will increase. This implies a serious limitation in the attainable discharge power losses or beam current densities with simple two grid accelerators at large spacings.

## Beam Current Density Measurements

The value of the maximum attainable beam current density was of interest because of its direct influence upon the thrust per unit area. Calculation of the grid aperture effect (ref. 6) indicated that no decrease in the maximum

transmitted percentage of Child's law ion current would occur due to operation at high voltage (large spacings).

Grid spacing and thickness. - Figure 10 shows the variation of the maximum percentage of Child's law current as a function of the ratio of accelerator grid spacing to hole diameter. Data for both the 37 and 7 hole grids (sketch c) are included in figure 10. The maximum beam current was determined by the "knee" method of reference 6, and can contain considerable error due to the difficulty of locating the knee exactly. Briefly, the "knee" method is the determination of the total voltage between the grids at which the impingement current begins to rise rapidly when the thruster is operated at a constant beam current. For a fixed spacing the Child's law ion current can be calculated for the "knee" voltage and the data of figure 10 is the ratio of the actual ion current at the "knee" to the calculated Child's law value.

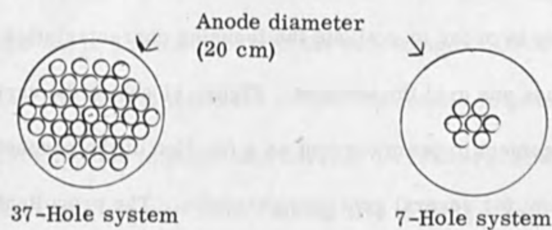


(c)

It is seen from figure 10 that the value of the maximum percentage of Child's law current does not significantly vary with grid spacing for a fixed number of holes. The general levels of maximum percentage of Child's law ion currents were higher for the 7 hole than the 37 hole system. The defining diameters, within which all holes were contained, were about 7.5 and 20 centimeters, respectively, for the 7 and 37 hole configurations. It was found that closing the central 7 holes on the 37 hole system increased the maximum transmitted percentage of Child's law ion current for the remaining 30 holes but the maximum current from the thruster was reduced.

It is likely that there was a larger variation in the discharge ion density across the 37 hole system than the 7 hole system. The radial ion number density gradient is probably most strongly affected by the basic geometry of the discharge chamber which had a constant anode diameter for both grid configurations. The presence of a large ion density gradient thus might lead to defocusing of the central holes before the outer holes become defocused as the total thruster current approaches the Child's law current limit.

Focusing characteristics. - Tests were performed with 7-hole accelerator grids in order to evaluate the focusing characteristics over a large range of spacings and grid thicknesses. Figure 11 shows the variation of the ratio of impingement to beam current as a function of the percentage of Child's law ion current for several grid configurations. The propellant utilization efficiency was low for the tests with the 7-hole grid system (0.17). As will be

discussed later, the general levels of the ratio of ion impingement to beam current will increase with decreasing propellant utilization efficiency. Focusing effects should not, however, be strongly affected by the utilization efficiency. The neutral propellant flow rate and beam current were constant for the data of figure 11 and variation in percentage of Child's law ion current reflects variation of the total accelerating potential. It is seen from figure 11 that as the percentage of Child's law increased, or the net accelerating potential decreased, the ion impingement first decreased slowly, became relatively constant, and then increased sharply at some value which is a function of grid spacing and thickness.

The effect of various geometric accelerator grid parameters on ion focusing is seen more clearly on figure 12 which shows the ratio of ion impingement to ion beam current as a function of grid spacing at three values of percentage of Child's law ion current. The data were taken at fixed values of ion beam current, ratio of net to total accelerating potential, and propellant utilization efficiency.

It is seen from figure 12 that the variation of the impingement current with spacing is a function of both the percentage of Child's law ion current and the ratio of grid thickness to hole diameter. In general, at 30 percent of Child's law the impingement current decreased slightly with increasing grid thickness and was rather insensitive to the grid spacing. At 80 percent of Child's law ion current the impingement current is, however, a rather

sensitive function of the grid geometry. The ion beam appeared to defocus at both large and small spacing for the thinner grids (data were not taken with the thickest grids at a large enough spacing for defocusing to occur). As the grid thickness increased, both the maximum and minimum spacing at which defocusing initiated increased. A crossplot of the data of figure 11 indicates that defocusing occurred when the ratio of grid spacing to thickness became less than about 2.5 and greater than about 4.0. The value of the grid spacing to thickness ratio at which the minimum impingement occurred was about 3.1 for the two thinnest grid configurations (crossplot of figs. 12(b) and (c)).

The data of figure 12 indicate that if thruster operation at a large value of percentage of Child's law is desired, care is necessary in selection of the grid geometry in order to operate at low values of impingement current. If the thruster is to be operated at a low percentage of Child's law, the impingement will be substantially constant over a wide range of grid geometries. The lack of dependence of the impingement current upon the grid configuration at low values of percent Child's law is probably due to the fact that in this region the ion beam becomes strongly focused into the center of the accelerator holes (see figs. 9 and 10 of ref. 18). As the value of the percentage of Child's law increased, the ion beam spreads, due to sheath readjustment, and the ion focusing becomes more strongly dependent upon the specific grid geometry.

Charge-exchange ion impingement. - In the region of good ion focusing the value of impingement current due to charge-exchange has been calculated in reference 7. The value of the charge-exchange currents in the present investigation will differ from those of reference 7 due to the large differences in net accelerating potential and spacings utilized. For fixed values of neutral mass flow rate, propellant utilization efficiency and open area, the values of the charge-exchange current will be considerably larger than at low voltage operation. The cross section for charge exchange does decrease somewhat with increasing voltage. Large uncertainties exist in the literature, however, regarding the exact variation. For example, figure 13 is a plot of this variation comparing values from three different sources (refs. 19 to 21). For purposes of later calculation the charge-exchange cross section will be assumed to be constant at $5\times10^{-15}$ cm$^2$ for the net accelerating potentials (15,000 to 70,000 V) used in this investigation.

Figure 14 shows the variation of the ratio of impingement to beam current as a function of grid spacing. These data were taken with the 37-hole grid system with a grid thickness to hole diameter ratio of 0.54. This grid thickness ratio was selected as it allowed operation over a wide range of percentage of Child's law ion currents and accelerator grid spacings (fig. 12). Also shown are the calculated values of the impingement to beam current ratio obtained by use of equation (B16) of reference 7. This equation is given below with the charge-exchange cross section assumed to be $5\times10^{-15}$ cm$^2$

rather than $6 \times 10^{-15}$ $cm^2$ as in reference 7.

$$\frac{J_A}{J_B} = 2.63(1 - \eta_U)J_O \left[ 1.5 \frac{\ell_{\mathrm{C\!\!\!L}}}{A_A} + \sqrt{\frac{\beta V_I^{3/2} A_I f(R)}{A_O^2 \eta_U J_O}} \right] \qquad (3)$$

It is seen from figure 14 that, in general, the values of ion impingement were within about a factor of 2 of those predicted from the calculated charge-exchange impingement current of reference 7. This agreement, approximately the same as that obtained at low voltage (ref. 7), held as long as care was taken to operate in the aforementioned region of good focusing. It is thus likely that the impingement in the good focusing region was due primarly to charge-exchange ions. The data of figures 11 and 12 (7-hole grid) also agreed with equation (3). The higher values of impingement arose primarily because the low utilization efficiencies and reduced open area at which the 7-hole grids were operated.

Accelerator grid durability. - Attempts were made to measure accelerator grid erosion rates on short term tests and the results are presented in figure 15. The value of the mass sputtering rate was 11 to 190 g/(amp)(hr) for tests ranging from 4 to 10 hours duration. Tests 1 (28 kV) and 2 (40 kV) were taken at 67 and 48 percent of Child's law current, respectively, while tests 3 (40 kV) and 4 (70 kV) were performed at 30 and 25 percent of Child's law current. It is likely that the tests at the higher percentages of Child's law current contained a larger proportion of direct ion impingement than those at the lower percentages of Child's law (figs. 11 and 12). The wide range in meas-

ured mass sputtering rates could, however, arise from a number of other reasons, such as:

(1) Variation of the mass sputtering rate with the ion incidence angle. Reference 22 indicates, for example, that the mass sputtering rate of mercury ions varies by a factor of 15 as the ion incidence angle varies from $0^{\circ}$ $90^{\circ}$.

(2) The existence of secondary electron emission.

(3) Arc damage.

(4) Inaccuracies in measurement. The ratio of the mass loss to the mass of the accelerator plate was nominally between about $10^{-4}$ and $10^{-5}$ for the data of figure 15. For mass sputtering rates less than 200 g/(amp)(hr), tests in excess of about 100 hours would have been required to produce mass losses greater than about 1 percent of the accelerator grid mass.

Although an accurate calculation of accelerator grid lifetime cannot be made from the data of figure 15 it is illustrative to make an approximate lifetime calculation based on the analysis of reference 7. The treatment of reference 7 predicted a lifetime based on the time necessary to erode the downstream accelerator web thickness to zero. An endurance test (ref. 7) indicated that the mass sputtering rate of mercury ions at 2400 volts energy was about 4 g/(amp)(hr).

It will be assumed that the mass sputtering rate of mercury ions on a thruster accelerator grid increases by about a factor of 9 as the ion energy

increases from 2400 to 40,000 volts. This increase was selected as it is in proportion to the sputtering increase for normally incident mercury ions on molybdenum (fig. 13). The fact that the web thicknesses of the plates utilized in this program were about a factor of three larger than those of the plates utilized in reference 7 then indicates that the total allowable impingement current at 40,000 volts ion energy is about a factor of three less than that utilized on reference 7 at low voltage.

Equation (6) of reference 7 gives a rough estimate of the maximum ideal lifetime of thruster accelerator grids.

$$\tau = \frac{1.35 \times 10^6}{\ell_{\mathfrak{c}} j_B^2} \left( \frac{\eta_U}{1 - \eta_U} \right) \text{ hours} \tag{4}$$

This equation contains a numerical constant which was determined on the basis of an accelerator grid lifetime test and a calculation of the charge-exchange impingement current utilizing an equation similar to equation (3). In arriving at this relation in reference 7 it was assumed that the erosion rate was radially uniform and that no charge-exchange ions were formed downstream of the accelerator grid. This equation will be utilized with the following modifications:

(1) The proportionality constant in the lifetime equation will be reduced by a factor of two. It was found experimentally in reference 7 that nonuniform radial grid erosion would reduce the lifetime by about this factor.

(2) The proportionality constant will further be divided by a factor of three to account for the increased mass sputtering rate at high voltage.

The equation for the lifetime is then:

$$\tau \approx 2.0\times10^{5}\left[\frac{\eta_U}{\ell_{\text{¢}}\, j_B^2 (1 - \eta_U)}\right] \quad \text{hours} \qquad (5)$$

where $j_B$ is based on the total thruster area, $A_O$.

Equation (5) can be reduced to a function of the propellant utilization efficiency as follows:

(1) The percentage of Child's law ion current will be assumed constant at 30 percent. Figure 15 indicates that this might be an upper limit for long lifetime. The current density in equation (5) of a 50-percent open grid system ($A_I = 0.5\ A_O$) is then, from equation (2):

$$j_B \approx 0.6\times10^{-9} \frac{\Delta V^{3/2}}{\ell_{\text{¢}}^2}$$

(2) The electric field strength, based on the center-to-center grid spacing will be assumed to be constant at $1.5\times10^{6}$ volts per meter. Equation (4) then becomes:

$$\tau \approx 1.5\times10^{3} \frac{\eta_U}{(1 - \eta_U)} \quad \text{hours} \qquad (6)$$

This expression for the accelerator grid lifetime is based on the assumptions of constancy of percentage of Child's law ion current, electric field strength, and charge-exchange cross section. Although the calculation is

approximate it does indicate that accelerator grid lifetimes of about one and two years can be obtained at propellant utilization efficiencies of 80 and 90 percent, respectively.

A major uncertainty in this calculation of charge-exchange erosion is the value of the mass sputtering rate selected. Other major sputtering factors, such as the presence of direct ion impingement at large angles, could further reduce the lifetime from that given in equation (6). An accurate evaluation of the lifetime of an accelerator grid system therefore still requires extended thruster tests at the specific conditions contemplated for space use.

Power Efficiency

One of the primary advantages of high-voltage operation is the increase to be expected in the power efficiency, or ratio of beam power to total expended power. As was previously shown (fig. 9), the value of the energy loss per beam ion does not vary substantially over a large range of spacings so that the power efficiency can be expected to reflect directly the increasing ion beam energy.

Figure 16 shows the power efficiency as a function of the net accelerating potential for three values of accelerator spacing. Power losses in the cathode, magnet, accelerator, and ion chamber were included in this data. The power efficiency is a steadily increasing function of net accelerating potential for a fixed value of propellant utilization efficiency. Unfortunately power supply limitations did not allow data to be taken in excess of approximately 70 milli-

amperes of ion beam current with net accelerating voltages in excess of 50 kilovolts. It was found that the combination of large neutral propellant flow rates and ion beam power would result in vacuum system pressure increases which would lead to anode to ground breakdown. The upper limits were neutral flow rates of about 0.2 equivalent ampere and beam power levels of approximately 7000 watts at net accelerating potentials in excess of 20 kilovolts.

The data of figure 16 indicate that the value of the power efficiency was greater than 0.80 at net accelerating potentials larger than 20 kilovolts. Reduction of the eV/ion would not appreciably affect these data. Because of the small ion beam currents (imposed by Child's law considerations) these losses were always less than 150 watts. The use of permanent magnets and hollow cathodes (ref. 15) would reduce the power losses by about 300 watts or more. The cathode power of the tantalum cathodes was typically about 12 percent of the total thruster power. That of a hollow cathode is about 2 percent. The increase in power efficiency that would result from a 300 watt saving is shown by the projected power efficiency on figure 16.

Also shown on figure 16 are data taken at low voltage with a 20-centimeter-diameter thruster (ref. 7). Magnet and cathode losses of 150 and 200 watts, respectively, were used to determine these power efficiencies. The data selected from reference 7 were those closest to 0.80 propellant utilization efficiency and which were available over some range of

net accelerating potential. The power efficiency, at a fixed net accelerating potential, is not strongly affected by variation of the propellant utilization efficiency between about 0.60 and 0.80. A comparison between the low and high voltage power efficiencies can, therefore, be made.

The extrapolated power efficiencies at high voltage best match the data of reference 7 when the value of the neutral flow rates were approximately equal. In general, the value of the power efficiency increased with the neutral flow rate at a fixed propellant utilization and net accelerating potential. This occurred because of fixed losses that did not vary significantly with ion beam current. The high and low voltage data, with the assumed savings of 300 watts, show that thruster power efficiencies in excess of 0.85 and 0.90 should be obtained at net accelerating potentials greater than about 10 and 20 kilovolts, respectively.

### Overall Thruster Efficiency

The overall thruster efficiency as a function of the net acelerating potential is shown in figure 17(a). For reference the same data is plotted as a function of specific impulse in figure 17(b). The projected power efficiencies from figure 16 were utilized in calculation of overall efficiency. It is seen that the overall efficiency should be greater than 0.80 for net accelerating potentials greater than 16 kilovolts at propellant utilization efficiencies of 0.90 or larger. To achieve this overall efficiency at lower propellant utilizations would require higher net accelerating potentials.

Data are not presented at values of propellant utilization efficiency greater than 0.91 since this was the largest value at which the thruster operated stably. From previous consideration it would appear that the maximum stable propellant utilization efficiency could probably be increased by decreasing the grid hole size. Because of the spacings required for high voltage (fig. 4), however, and the fact that there exists a maximum ratio of center-to-center spacing to hole diameter (ref. 6 and fig. 12) for good ion focusing the hole diameters could not be significantly reduced.

## CONCLUDING REMARKS

It was found that the maximum supportable electric field strength between accelerator grids of operating thrusters was about $2 \times 10^6$ volts per meter over a large range of spacings. This field strength refers to grid-to-grid breakdowns after 2 to 20 hours conditioning.

The qualitative variations in eV/ion were found to be quite similar to that at low voltage. In addition, the eV/ion was nearly independent of the net accelerating potential and center-to-center grid spacing if the propellant utilization efficiency and percent of Child's law current were held constant.

It was found that the ratio of center-to-center grid spacing to grid thickness should be between 2.5 and 4 to provide good ion focusing. The value of the grid thickness alone did not strongly affect the ion focusing, however, unless the beam current was in excess of approximately 50 percent of Child's law value.

Estimated lifetimes of accelerator electrodes were in excess of one year at net accelerating potentials between 20 and 70 kilovolts, if the value of the percentage of Child's law is less than about 30 percent and the geometric accelerator parameters are such as to avoid direct ion impingement.

The thruster power efficiency can be expected to be in excess of 0.85 at all net accelerating potentials greater than 20,000 volts. The overall thruster efficiency (the product of the power and utilization efficiencies) was limited to 0.86 in the present study because of discharge chamber stability problems and was substantially less for most conditions investigated. High current densities at high voltage probably require more complex accelerator grid systems to avoid stability problems and excessive ion chamber losses.

REFERENCES


1. H. R. Kaufman, NASA TN D-585 (1961).

2. E. Stuhlinger, "Ion Propulsion for Space Flight," McGraw-Hill, New York (1964), pp. 150-151.

3. D. Alpert, D. A. Lee, and H. E. Tomasche, Proceedings of the International Symposium on Insulation of High Voltages in Vacuum, MIT Press, Cambridge (1964), pp. 1-12.

4. H. R. Kaufman, NASA TN D-261 (1960).

5. P. D. Reader, NASA TN D-1163 (1962).

6. W. R. Kerslake, NASA TN D-1168 (1962).

7. W. R. Kerslake, NASA TN D-1657 (1963).

8. S. Nakanishi, NASA TN D-3535 (1966).

9. T. A. Keller, "Transactions of the Seventh National Symposium on Vacuum Technology," Pergamon Press, London (1960), pp. 161-167.

10. C. Germain and F. Rohrback, in "CR VI Conf. Internat. Phénomènes d'Ionisation dans les Gaz," S.E.R.M.A., Paris (1963), Vol. 2, p. 111.

11. W. R. Kerslake and E. V. Pawlik, NASA TN D-1411 (1963).

12. M. J. Kofoid, AIEE Trans., Part III, 79, 991 (1960).

13. M. J. Kofoid, AIEE Trans., Part III, 79, 999 (1960).

14. R. T. Bechtel, G. A. Csiky, and D. C. Byers, AIAA Paper 68-88 (1968).

15. P. D. Reader, NASA TN D-2587 (1965).

16. D. C. Byers, W. R. Kerslake, and J. S. Grobman, NASA TN D-2401 (1964).

17. H. R. Kaufman, NASA TN D-3041 (1965).

18. E. V. Pawlik, P. M. Margosian, and J. F. Staggs, NASA TN D-2804 (1965).

19. A. von Engel, "Ionized Gases," Clarendon Press, Oxford (1955), p. 112.

20. R. M. Kushnir, B. M. Palyukh, and L. A. Sena, Bull. Acad. Sci. USSR, 23, 995 (1959).

21. I. Popescu Iovitsu and N. Ionescu-Pallas, Soviet Phys.-Tech. Phys., 4, 781 (1960).

22. G. K. Wehner, J. Appl. Phys., 30, 1762 (1959).

23. W. R. Mickelsen and H. R. Kaufman, Brit. Interplanetary Soc. J., 19, 369 (1964).

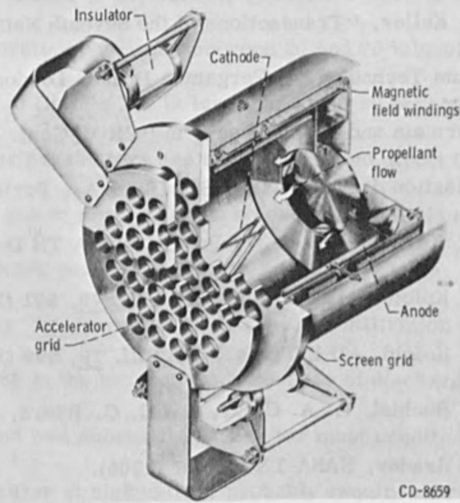


Figure 1. - 20-Centimeter Kaufman thruster.

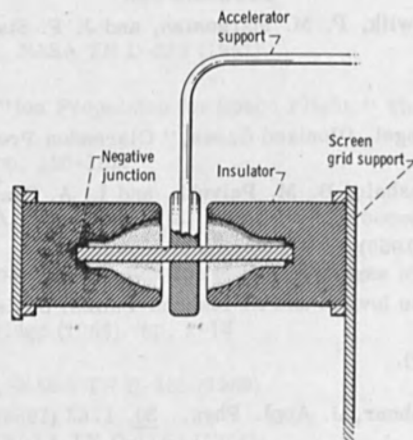


Figure 2. - Sketch of the insulator and mounts.

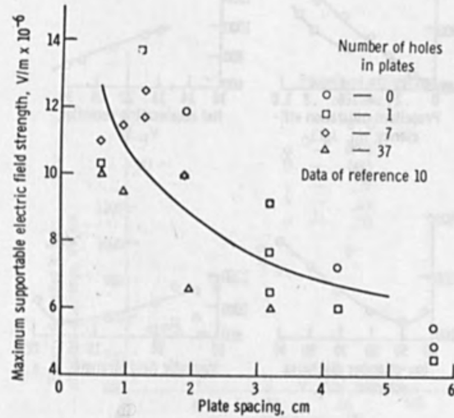

Figure 3. - Effect of spacing on the maximum supportable electric field strength between stainless steel plates. Plate diameter, 25 cm; hole size, 2.2 cm.

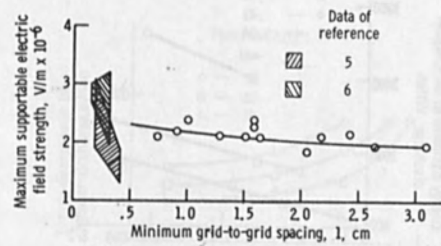

Figure 4. - Maximum supportable electric field strength between the accelerator grids of an operating electron-bombardment thruster as a function of the grid spacing. t, 1.18 cm; D, 2.2 cm; 37-hole grid.

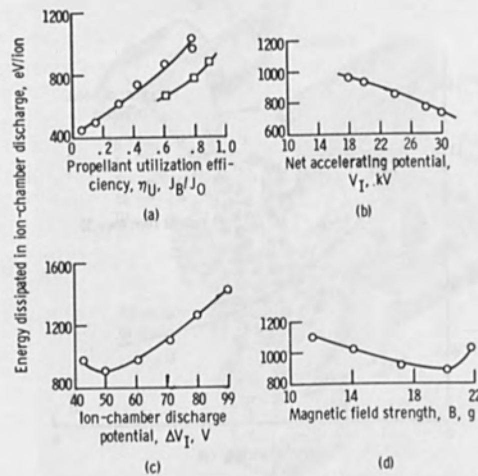


Figure 5. - Ion-chamber performance as a function of several thruster parameters. $\Delta V_I$, 50 V; $V_I$, 20 kV; $J_O$, 0.165 A; $\eta_U$, 0.79; B, 17.4 g; R, 0.8; $l_¢/D$, 1.29; D, 2.2 cm; t, 1.18 cm; 37-hole grid; unless otherwise noted.

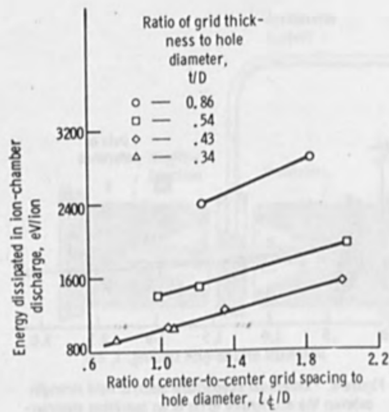


Figure 6. - Effect of center-to-center grid spacing on ion-chamber performance. $\Delta V_I$, 50 V; $V_I$, 16 kV; $J_O$, 0.165 A; $\eta_U$, 0.12; B, 17.4 g; R, 0.8; D, 2.2 cm; 7-hole grid.

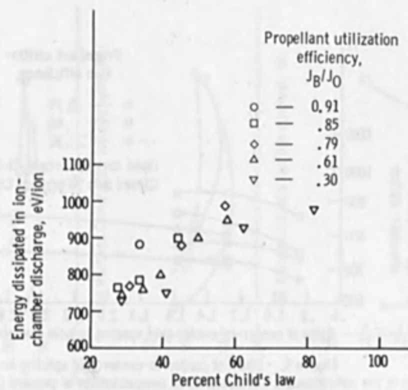


Figure 7. - Effect of percent Child's law on ion-chamber performance. $\Delta V_I$, 50 V; $J_O$, 0.165 A; B, 17.4 g; R, 0.8; $L_t/D$, 1.29; D, 2.2 cm; t/D, 0.54; 37-hole grid.

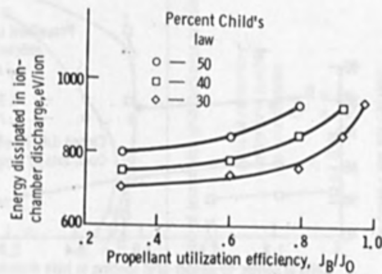


Figure 8. - Effect of propellant utilization efficiency on ion-chamber performance. $\Delta V_I$, 50 V; $J_O$, 0.165 A; B, 17.4 g; $L_t/D$, 1.29; D, 2.2 cm; t/D, 0.535; 37-hole grid.

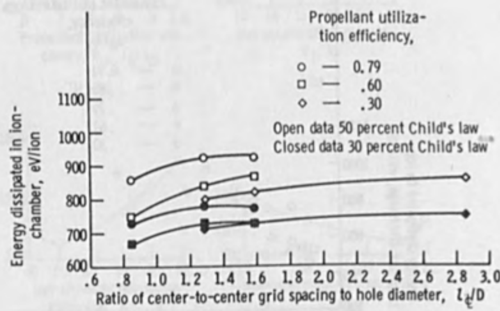


Figure 9. - Effect of center-to-center grid spacing on ion-chamber performance at several values of percent Child's law and propellant utilization efficiency. $\Delta V_I$, 50 V; $J_O$, 0.165; B, 17.4 g; R, 0.8; D, 2.2 cm; t/D, 0.54; 37-hole grid.

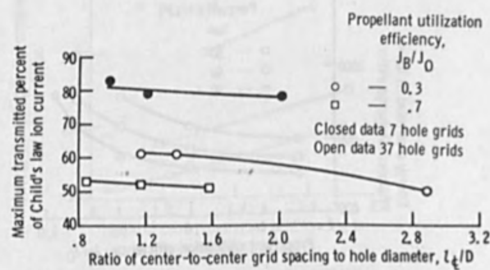


Figure 10. - Effect of spacing on the maximum percent Child's law ion current transmitted. $\Delta V_I$, 50 V; $J_O$, 0.165 A; B, 17.4 g; R, 0.8; D, 2.2 cm; t/D, 0.54.

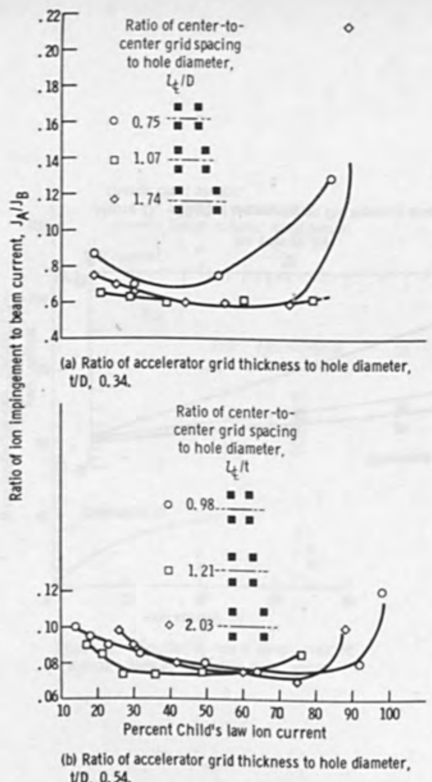


Figure 11. - Effect of the percent Child's law ion current on the ratio of ion impingement current to beam current $\Delta V_I$, 50 V; $J_O$, 0.165 A; B, 17.4 g; R, 0.8; D, 2.2 cm; 7-hole grid.

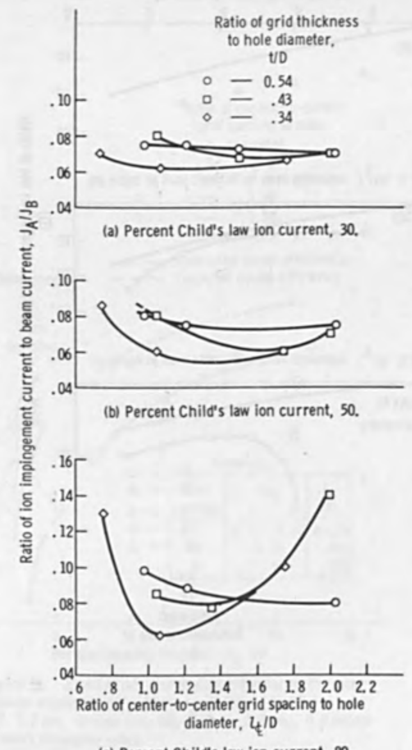


Figure 12. - Effect of grid spacing on the ratio of ion impingement current to beam current. 7-hole system $J_O$, 0.165 A; $\eta_U$, 0.12; R, 0.8.

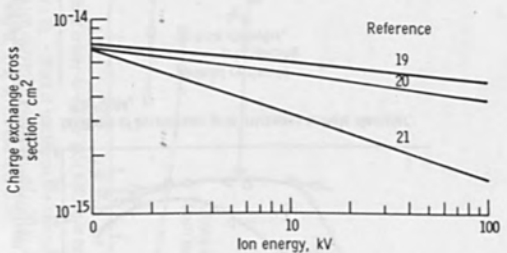


Figure 13. - Effect of ion energy on the mercury charge exchange cross section.

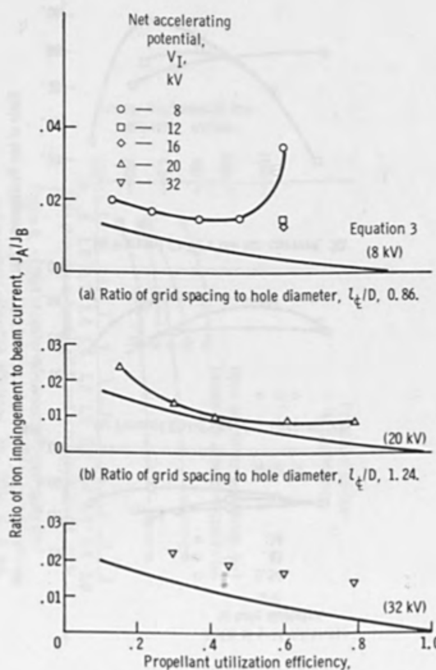


(a) Ratio of grid spacing to hole diameter, $l_\xi/D$, 0.86.

(b) Ratio of grid spacing to hole diameter, $l_\xi/D$, 1.24.

(c) Ratio of grid spacing to hole diameter, $l_\xi/D$, 1.59.

Figure 14. - Effect of propellant utilization efficiency on the ion impingement current. $\Delta V_I$, 50 V; $J_O$, 0.165 A; B, 17.4 g; R, 0.8; D, 2.2 cm; t/D, 0.54; 37-hole grid.

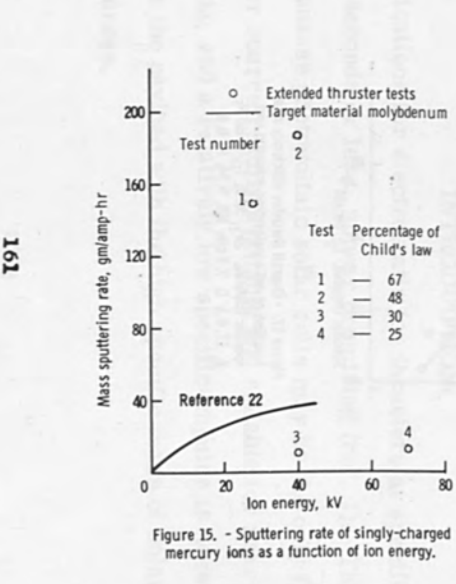


Figure 15. - Sputtering rate of singly-charged mercury ions as a function of ion energy.

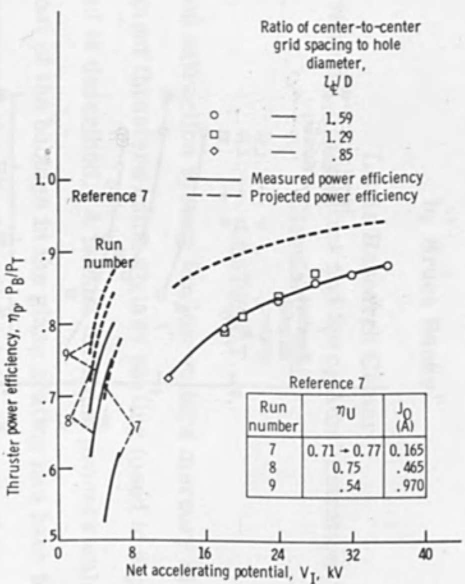


Figure 16. - Effect of net accelerating potential on thruster power efficiency $\Delta V_I$, 50 V; $J_O$, 0.165 A; B, 17.4 g; D, 2.2 cm; 37-hole grid; t/D, 0.54; R, 0.8; $\eta_U$, 0.8 except where otherwise noted.

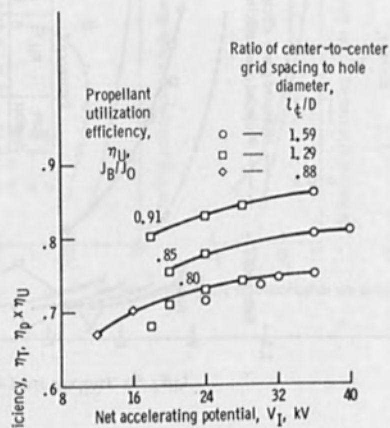


(a)

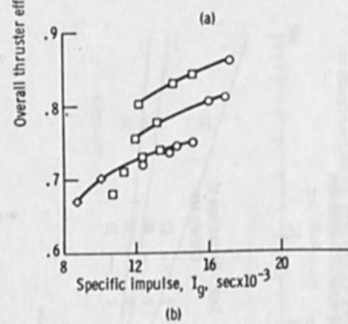


(b)

Figure 17. - Overall thruster efficiency as a function of net accelerating potential and specific impulse. $\Delta V_I$, 50 V; $J_O$, 0.165 A; B, 17.4 J; D, 2.2 cm; t/D, 0.54; R, 0.8.

# COMPOSITE ION ACCELERATOR GRIDS

by Bruce Banks

Lewis Research Center
National Aeronautics and Space Administration
Cleveland, Ohio

## ABSTRACT

An ion extraction system for low voltage mercury electron-bombardment thrusters using a glass coating fused to a perforated metal grid is described. A helium diffusion process which eliminates most of the bubbles in the glass coating has been found that greatly increases the effective dielectric strength of the glass and allows acceptable low voltage ion extraction. Grid fabrication techniques and experimental performance results are also discussed.

## INTRODUCTION

Applications for electrostatic ion thrusters at specific impulses of 3, 000 seconds or less, appear promising (ref. 1). This is mainly because photovoltaic solar cells may be the only flight qualified power source readily available and suitable for near term application, and a relatively low specific impulse is necessary to maximize the payload with the high specific mass of solar-cell power sources.

Previous Kaufman thrusters have been optimized at higher specific impulse. Some thruster modifications are required to assure optimum performance at low voltage (net accelerating voltages of 1000 volts or less). The component that would require the most redesign is the ion accelerator grid system.

Recent tests of a composite accelerator grid system indicate the possibility of substantial performance gains over the conventional double grid ion extraction system (ref. 2). A composite accelerator grid system is one in which an electrical insulator is placed in close proximity or in contact with a metallic accelerator grid. The insulator, in effect, replaces the screen grid which separates the plasma in the discharge chamber from the acceleration region in the conventional grid system.

Results of tests on composite accelerator grids are reported herein. First, background information is given with emphasis upon the fused-glass type of composite accelerator grid. Next, in the theory section a helium diffusion process is described which helps to eliminate large bubbles normally found in the fused glass coating. A brief description of the fabrication procedure for constructing a fused glass composite grid is then given followed by a discussion of experimental results.

## BACKGROUND

A section view of a Kaufman, or electron-bombardment, ion thruster is depicted in Fig. 1. Typically, mercury vapor is fed

into the ionization chamber by passing it through a distributor plate. The atoms of the vaporized gas are then bombarded by electrons emitted from the cathode. The path length traveled by electrons going from the cathode to the anode is greatly increased by the axial magnetic field thus causing much more ionization by electron-bombardment. Ions in the near vicinity of the screen grid have a high probability of being accelerated through the holes in the screen and accelerator grid because of the high electric fields present there. After the ions accelerate through the grid system (thus producing a thrust) electrons are injected to neutralize the exhaust beam. Detailed information concerning the thruster and neutralizer can be found in Refs. 3 and 4 respectively. The screen grid of the conventional double grid system shown in Fig. 1 serves the purposes of containing the discharge plasma and forming the necessary ion optics to prevent direct impingement of the accelerated ions on to the accelerator grid.

Section views of a conventional double grid system and a fused glass composite accelerator grid are compared in Figs. 2(a) and (b). In the conventional system, the plasma sheath is formed at the upstream surface of the screen grid. In the composite grid system the sheath is believed to form near the upstream surface of the insulator. Because of the high electrical resistance of the insulator, charges can build up on the surface forming a virtual screen grid. In this way the sheath is moved closer to the nega-

tive accelerator, thus increasing the field strength for a given voltage and consequently increasing the ion beam current density. A close up view of the glass coated side and uncoated side of a typical fused glass composite grid is shown in Figs. 3(a) and (b).

Some advantages of a fused glass composite grid system over the conventional double grid system for low voltage thruster operation are as follows:

1. Close spacing and accurate alinement of the screen and accelerator grids during assembly is no longer required. Also, the grids cannot become misalined by warpage during thruster operation. This leads to the possibility of large diameter accelerator systems previously considered impractical for low voltage operation.

2. The single, glass composite grid does not require match drilling of screen and accelerator holes. Therefore, prepunched sheet can be used for the metallic portion.

3. A reduction in weight of the accelerator grid system is possible with elimination of the screen grid and use of a simplified support structure.

4. The discharge chamber power loss is reduced because of the enhanced ion extraction capability (ref. 5). Two possible factors contributing to the increased ion current density for a given voltage are (a) the increased field strength previously mentioned,

and (b) an increase in the sheath area available for ion extraction.

Some of the factors that had to be considered before these potential advantages could be realized are discussed below.

For efficient thruster operation, the accelerator electrode should be as close as possible to the discharge chamber plasma to permit the highest possible ion extraction rate. As a result the composite grid glass thickness should be only as thick as needed to prevent electrical breakdown through the glass. (The electrical potential which is applied across the glass is approximately the net accelerating potential, $V_I$, plus the magnitude of the accelerator potential, $V_A$.) There is a high probability though, that bubbles formed in the glass coating during fabrication will enhance the occurrence of electrical breakdown through the glass. In fabrication the glass is slurry sprayed onto the molybdenum grid, which is then heated in an inert atmosphere to fuse the glass particles together and to the grid. The fusing of the glass particles encapsulates gas. Bubbles are thus formed which, in turn, reduce the effective electrical breakdown strength of the glass. The gas encapsulation could be reduced by vacuum fusing, but various gas liberating mechanisms tend to make the glass to boil and fill in the grid holes with the foaming glass. Alternatively, the electrical breakdown strength could be increased by applying additional glass coatings to the grid, but there is a well defined thickness beyond which grid holes will fill in if more glass is applied.

One obvious answer to this dilemma is to eliminate the bubbles in the glass coating. A procedure to accomplish this has been developed and will now be presented.

## THEORY

If the glass is applied such that the maximum glass radius, $r_{g,max}$, is greater than the hole radius, $r_h$, (see Figs. 4(a) and (b)) then the molten glass surface tension will collapse the walls of the hole during the fusing process. It was show in Ref. 6 that the maximum glass thickness, $L_{g,max}$, for stable hole walls depends on the metal hole radius, $r_m$; fraction open area, $F_m$, of the metal grid and the thickness, $L_m$, of the metal grid. The relationship can be written as

$$L_{g,max} = r_m \sqrt{\frac{\pi}{6F_m\sqrt{3}}}\left[1 + \sqrt{1 - \left(2 - \sqrt{\frac{6F_m\sqrt{3}}{\pi}}\right)^2}\right] - L_m \quad (1)$$

Figure 5 is a plot of the stability limit relationship as a function of fraction open area of the metal grid.

In addition to applying glass coatings up to the stability limit, a further increase in the electrical breakdown strength can be achieved through the use of a helium diffusion process which eliminates nearly all the bubbles. This process consists of fusing the

powdered glass in a helium environment which produces helium bubbles in the molten glass. Then, while the grid is still hot, the helium environmental gas is replaced with argon. This causes a high helium concentration gradient in the molten glass since the helium partial pressure in the bubble is atmospheric pressure plus that due to the surface tension of the bubble surface, while at the same time there is a near zero helium partial pressure above the glass surface. The rate of helium diffusion has been found to be sufficient to collapse the bubbles initially formed in the glass. The following equation, which is derived in Ref. 6, relates bubble radius and diffusing time.

$$t' = \frac{1}{2K}\left\{r_{B,0}^2 - r_{B,t}^2 - \frac{4\gamma}{3P_0}\left[r_{B,0} - r_{B,t} - \frac{2\gamma}{P_0}\ln\left(\frac{2\gamma + P_0 r_{B,0}}{2\gamma + P_0 r_{B,t}}\right)\right]\right\} \tag{2}$$

Figure 6 is theoretical plot of bubble radius, $r_{B,t}$, at time, t', for a glass temperature of 1444° K (1171° C) and a typical initial bubble radius, $r_{B,0}$, of $10^{-4}$ meters. For this calculation, the helium diffusion coefficient of Corning glass code 7052 at 1444° K is $K \cong 4.56\times10^{-11}$ m²/sec, the surface tension of Corning glass code 7052 is $\gamma \cong 2.73\times10^{-1}$ N/m, and the atmospheric pressure is $P_0 \cong 1.01\times10^5$ N/m². As the bubble radius decreases the surface tension forces greatly increase the helium bubble pres-

sure thus enhancing the rate of diffusion and the rate of bubble collapse as shown by the change in slope of the curve in Fig. 6. The time for bubble collapse to zero radius is obtained from Eq. (2) by setting $r_{B,t} = 0$ and is given by

$$t'_c = \frac{1}{2K}\left\{r^2_{B,0} - \frac{4\gamma}{3P_0}\left[r_{B,0} - \frac{2\gamma}{P_0}\ln\left(1 + \frac{P_0 r_{B,0}}{2\gamma}\right)\right]\right\} \quad (3)$$

This collapse time, $t'_c$, is plotted as a function of the initial bubble radius in Fig. 7.

The times given in Figs. 6 and 7 are for helium diffusion at 1444° K. The corresponding time, t, at other temperatures, $T_B$, is found by simply multiplying the time t' by the factor t/t' as given by Fig. 8. This figure takes into account the temperature dependence of the helium diffusion coefficient for Corning glass code 7052.

## GRID FABRICATION PROCEDURE

As a result of theoretical and experimental investigations a suitable fused glass composite grid fabrication procedure has been developed. It is given in detail in Ref. 6 and briefly described below for a molybdenum grid to be coated with Corning glass code 7052.

1. Determine stability limit from Fig. 5.

2. Deburr the grid and wash it with water then acetone.

3. Glass bead blast entire grid and oxidize it is an electric oven at $538^{\circ}$ C for 5 to 10 minutes until a blue or purple surface coloration is present.

4. Sand oxide layer off the downstream face of the molybdenum grid.

5. Slurry spray the upstream face of the grid with a solution consisting of equal parts (by volume) of water and powdered glass.

6. Set the grid on a clean oxidation resistant tray or edge support it in the oxidation resistant environmental control box as shown in Fig. 9 and put lids on the box without any sealing material in the trough. Note that the box has two lids each with its own gas feed system. This arrangement minimizes the amount of back diffusion of oxygen to the grid.

7. Fuse the glass coating following the time environment sequence given in Fig. 10 using inert gas purging rates of approximately $6 \times 10^{-4}$ $m^3$ per second per meter of lid perimeter.

8. For each additional coating repeat steps 4 to 7.

9. Sand the downstream face of the grid to expose the molybdenum surface before operation in a thruster.

EXPERIMENTAL RESULTS

The effectiveness of the bubble reduction process can be seen from a comparison of Figs. 11(a) and (b) which are photographs taken looking normal to the glass surface with the molybdenum surface underneath. The glass coating shown in Fig. 11(a) was fused in an argon atmosphere. The amount of bubble collapse is neglibile. Figure 11(b) shows a bubble-free glass coating that was fused using the helium diffusion process. The effective breakdown strength of the bubble free glass was measured to be $8.75 \times 10^7$ v/m (for glass coating thicknesses of approximately 0.4 mm) which is more than a factor of 8 improvement over the glass coatings made using only an argon environment.

Figure 12 is a close-up photograph of the glass coated side of a grid fabricated using the bubble reduction process. The photograph was taken after the grid was operated for more than 200 hours on a 5 cm diameter thruster with no degradation in performance. Operating conditions were: net accelerating potential, 400 volts; accelerator potential, -225 volts; ion beam current, 0.032 amperes; and accelerator drain currents of about 0.002 amperes.

As can be seen in Fig. 12 sputtered material accumulated in some regions where the glass surface was close to or in contact with the discharge plasma. However, even in these regions

the hole walls remained clean. Apparently the rate of mercury ion sputter-cleaning of the glass hole walls exceeded the rate of deposition of the sputtered material.

Larger diameter fused glass composite grids, such as the one shown in Fig. 13, have been fabricated. This grid is mounted on a 30 cm diameter thruster and has approximately 12, 400 prepunched holes. An optimization program for a 30 cm diameter thruster is presently being conducted at Lewis by Robert T. Bechtel. A typical thruster operating point is given below:

| Parameter | Value |
|---|---|
| Net accelerating potential | 1000 volts |
| Accelerator potential | -700 volts |
| Ion beam current | 1. 5 amperes |
| Accelerator drain current | 0. 07 amperes |
| Discharge chamber power loss | 250 electron volts per beam ion |
| Propellant utilization efficiency | 0. 80 |

The accelerator system was found to give satisfactory performance over a range of net accelerating potentials from 400 to 1100 volts. At these low net accelerating potentials at least partial neutralization of the exhaust ion beam by means of a hot wire or a plasma bridge neutralizer was found necessary for stable thruster operation in both the 5 and 30 cm thruster tests.

Vibrations developed during launch of a glass grid thruster system might easily excite drum modes of oscillation for the flat grids shown in Figs. 12 and 13. Some shake tests have been conducted and the small diameter glass coated grids for 5 cm thrusters have withstood shake tests exciting the drum modes of oscillation at levels up to 30 g's of random noise (20 to 2000 Hz) and 40's of sinusoidal oscillation (39 to 3,000 Hz). For these tests the grid was clamped rigidly at its edges beyond a 6.7 cm diameter circle. The fundamental drum mode of oscillation was found to be at 967 Hz. A considerable amount of rigidity can be added to the glass coating by dishing the molybdenum grid prior to glass coating. Figure 14 is a photograph of a dished glass coated grid for a diameter thruster. The grid has a radius of curvature of 44.6 cm and is held in place by a retaining assembly around its outer edge. Detail of the retaining assembly are shown in Fig. 15. The two molybdenum rings are fused together with glass which provides both mechanical support and electrical isolation for the grid. The glass insulation is extended into the first row of holes so that a portion can be kept clean by ion bombardment. Otherwise sputtered material would creat a breakdown path along the surface. This grid is currently being tested on an operating thruster.

## CONCLUDING REMARKS

This paper briefly described the recent results of a composite grid program for low voltage, mercury electron-bombardment ion thrusters. Major considerations and findings of the program are listed below.

1. The fused glass composite grid is a potentially attractive grid system for low voltage thrusters because it eliminates several spacing, alinement, and fabrication difficulties present in conventional double grid systems.

2. Glass can be applied to the grid up to a well defined limit that is a function of the metal grid's hole radius, thickness, and fraction open area.

3. A procedure for minimizing the occurrence of bubbles in the glass coating has been developed.

4. Fused glass grids have been successfully fabricated and operated in 5, 15, and 30 cm diameter thrusters. Tests of more than 200 hours of grid operation have given no indication of failure.

5. A fused glass composite grid for a 5 cm diameter thruster has withstood shake tests exciting the drum mode of oscillation at levels of 30 g's of random noise (20 to 2000 Hz) and 40 g's of sinusoidal oscillation (39 to 3000 Hz).

6. A glass coated grid has been fabricated which is dished for rigidity and has an electrically isolated mounting system as an integral part of the grid. It is now being tested on an operating 15 cm diameter thruster.

## REFERENCES

1. D. J. Kerrisk, and H. R. Kaufman, AIAA Paper 67-424 (1967).

2. S. Nakanishi, E. A. Richley, and B. A. Banks, AIAA Paper 67-680 (1967).

3. R. T. Bechtel, G. A. Csiky, and D. C. Byers, AIAA Paper 68-88 (1968).

4. V. K. Rawlin and E. V. Pawlik, AIAA Paper 67-670 (1967).

5. P. M. Margosian, NASA TM X-1342 (1967).

6. B. A. Banks, (Proposed NASA Technical Note in process).

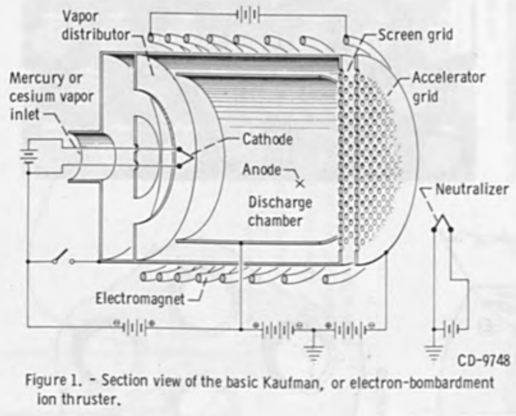


Figure 1. - Section view of the basic Kaufman, or electron-bombardment ion thruster.

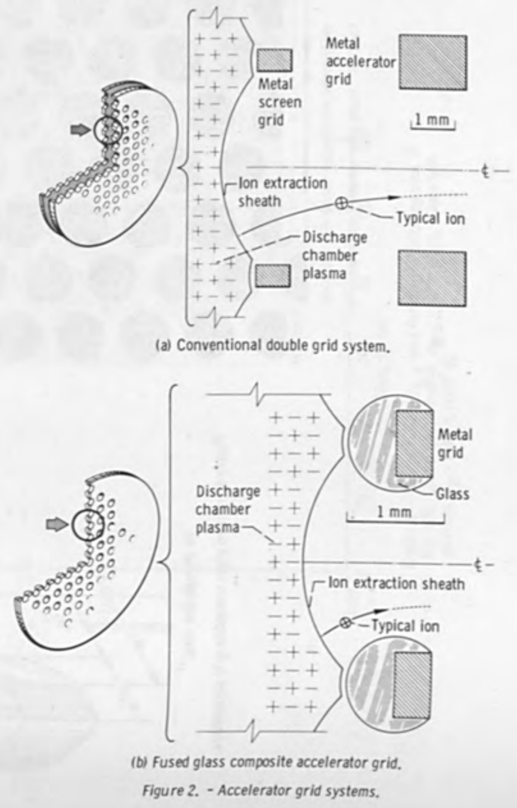


(a) Conventional double grid system.

(b) Fused glass composite accelerator grid.

Figure 2. - Accelerator grid systems.

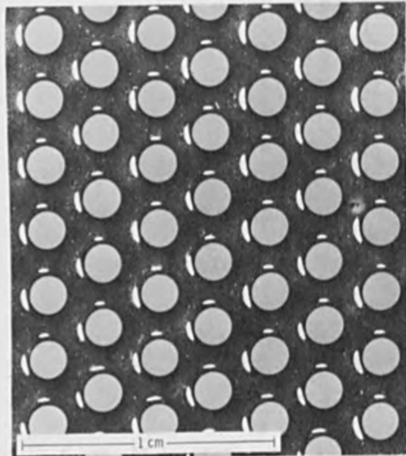


(a) Glass coated side.

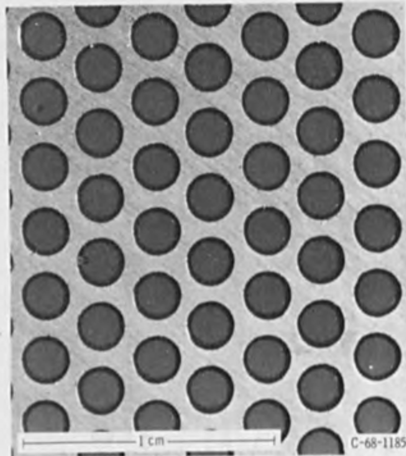


(b) Uncoated side showing molybdenum substrate.

Figure 3. - Fused glass composite accelerator grid.

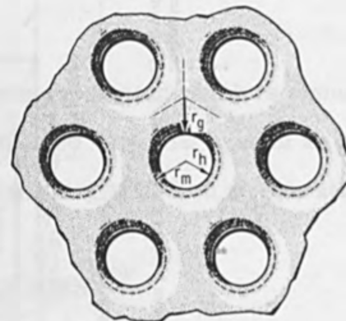


(a) Face view.

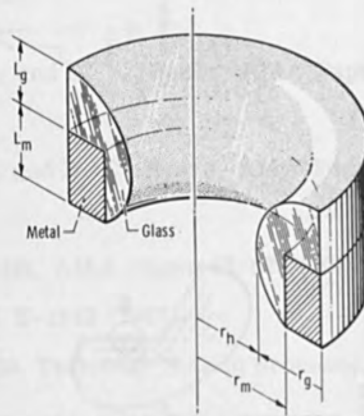


(b) Perspective view.

Figure 4. - Fused glass composite grid parameters.

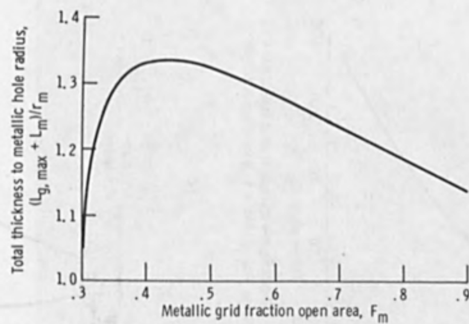


Figure 5. - Ratio of total fused glass composite grid thickness to metallic grid hole radius as a function of the metallic grid fraction open area for stability limited coatings (Eq. (1)).

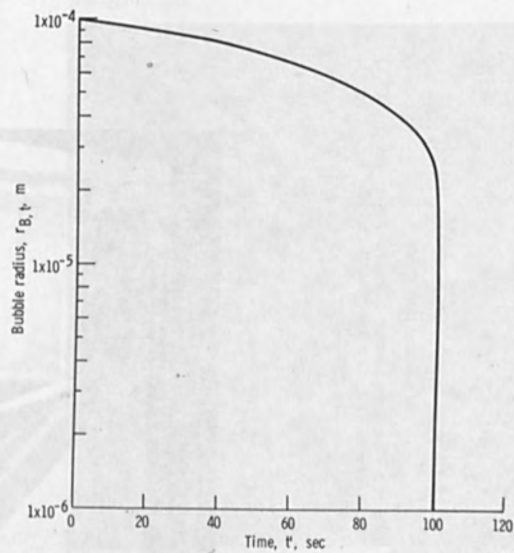


Figure 6. - Bubble radius, $r_{B,t}$, as a function of diffusing time, t' (Eq. (2)). Initial bubble radius, $r_{B,o} = 10^{-4}$ meters. Glass temperature, $T_B = 1444°$ K (2140° F).

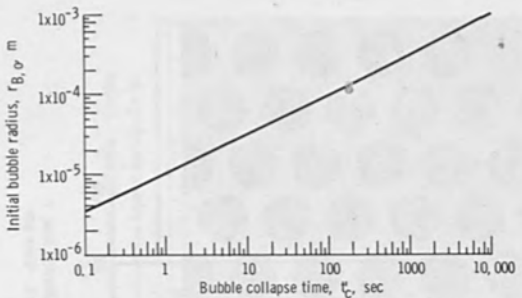


Figure 7. - Bubble collapse time, $t_c$, as a function of initial bubble radius, $r_{B,o}$, for a glass temperature of 1444° K (2140° F).

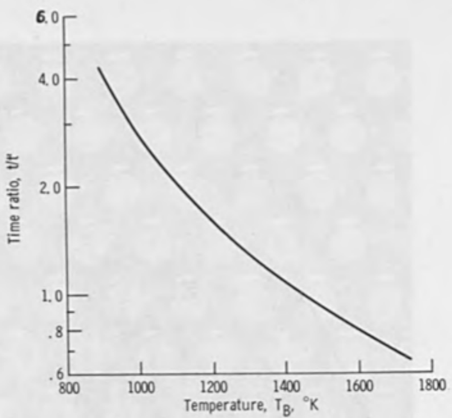


Figure 8. - Ratio of bubble collapse time at temperature $T_B$ to collapse time at 1444° K as a function of temperature.

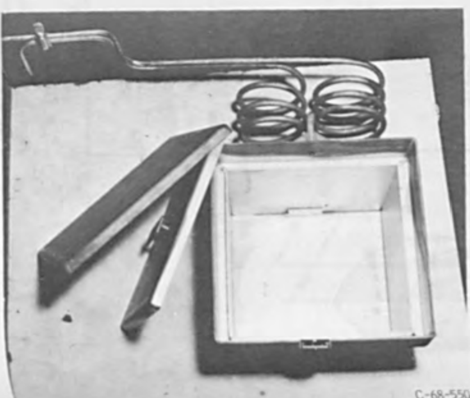


Figure 9. - 15 cm diameter grid in the box used for environmental control during fusing.

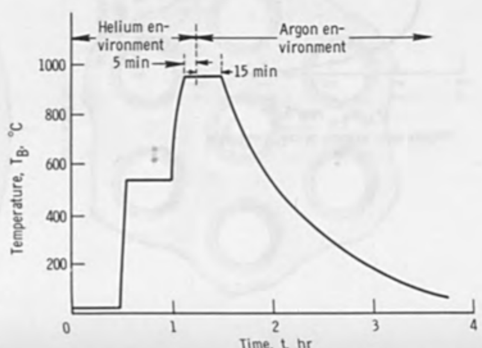


Figure 10. - Temperature-time-environment sequence for fusing powdered glass coatings on a composite accelerator grid.

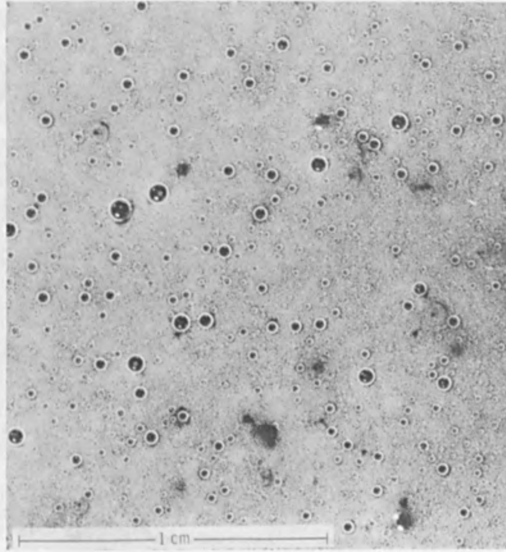


(a) Coating fused in an argon atmosphere resulting in a negligible amount of bubble collapse.

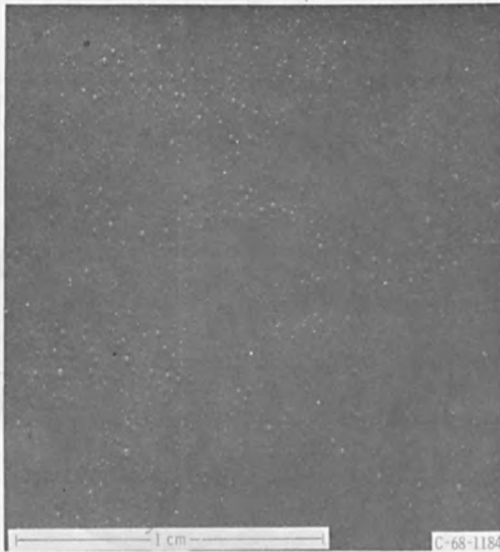


(b) Coating fused using the helium diffusion process. The dark appearance is because the glass is nearly bubble free.

Figure 11. - Photographs of 0.2 mm thick fused Corning glass code 7052 coatings on molybdenum.

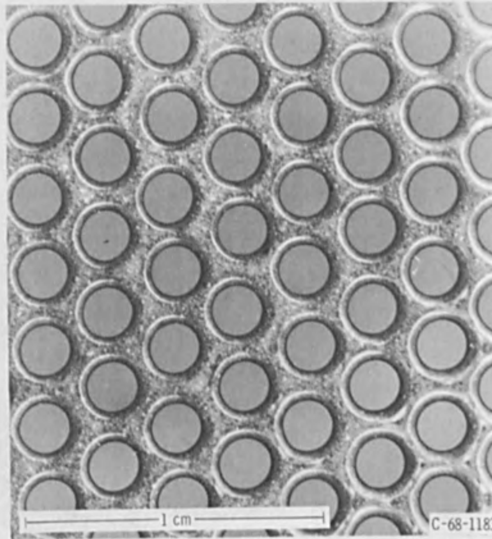


Figure 12. - Photograph of the central portion of the glass coated side of a composite accelerator grid after more than 200 hours operation in a 5 cm diameter thruster. The maximum thickness of the glass is 0.0465 cm.

Figure 13. - Fused glass composite accelerator grid mounted on a 30 cm diameter Kaufman thruster.

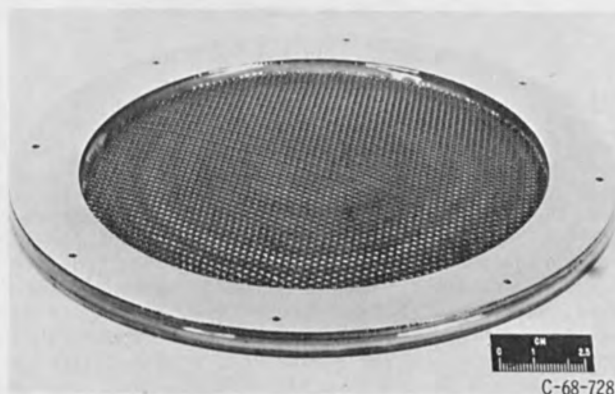


Figure 14. - Dished fused glass composite grid with integral electrically isolated retaining assembly.

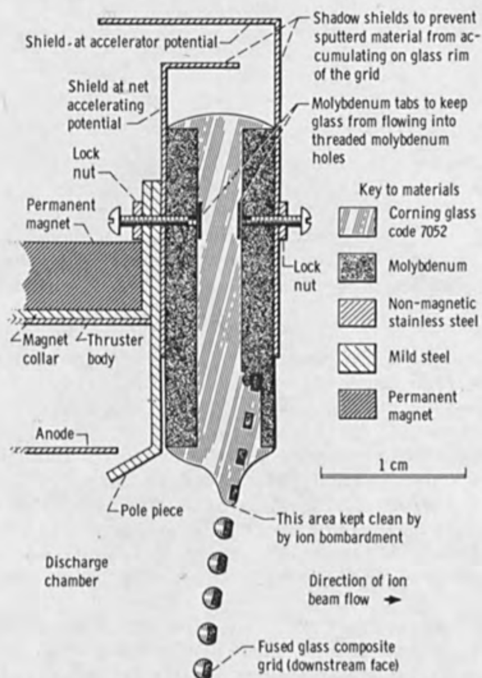


Figure 15. - Section view of the retaining assembly of the dished grid showing thruster mounting detail.

ALKALI METAL ION SOURCES

Julius Perel

Electro-Optical Systems, Inc.
Pasadena, California

ABSTRACT

The development of alkali metal ion sources has been greatly accelerated in the past decade due to the interest in these ions in basic research and more important because of cesium ion engine development for space propulsion. Three techniques used to generate alkali metal ions are described. The porous tungsten surface ionization source, highly developed for electric propulsion, has generated ion beams of over one ampere of cesium and is being used to produce other alkali metal ions. The electron bombardment engine, or low-pressure discharge source, has produced high currents of $Cs^+$, $Na^+$, and $Hg^+$ and is used to generate other ions. The liquid metal hydrodynamic spray technique, also studied as an electric propulsion thruster, is used to produce high current densities from a very small source, and generates some molecular ions. The operational levels of the various engines and their modification for use as laboratory ion sources are described.

1. INTRODUCTION

1.1 Brief Survey

Alkali metal ion source technology has been greatly advanced in order to use high-velocity ions to produce thrust from ion engines for manipulating and propelling space and orbital vehicles. The aims in the development of ion engines which do not differ greatly from those in developing ion sources are examined in this report with the emphasis placed upon the generation of alkali metal ions and the description of ion engines and their features as ion sources.

The two most used methods of generating ions for ion engines are surface ionization and electron impact ionization. Efficient surface ionization is applicable for elements having low ionization potentials such as the alkali metals. The technique of ionization by electron impact in a gaseous discharge is applicable for producing a wide range of ion species including molecular ions. A third method, discussed in this report, is the generation of charged particles from the surface of a liquid by the application of high electric fields. Heavy charged particles are generally produced from organic liquids while ions are generally produced from liquid metals, with the alkali metals being particularly suitable using this latter method.

The alkali metals comprise a family of elements each of which have a single electron in the outer or valance shell. The ease with which the single outer electron can be removed to form an ion is indicated by the low first ionization potentials which are listed in Table I. The second ionization

potentials are higher than the first by factors ranging from 15 to 5 going from Li to Cs. Therefore singly ionized alkali metals can be generated without producing an appreciable number of doubly ionized species in a low voltage discharge. First ionization potentials are in the range of refractory metal work functions, a condition required for efficient surface ionization.

Table I also contains the atomic number, atomic weight, and melting points of the alkali metals. Cs and Rb are highly reactive and must be handled under an inert atmosphere. The others can be stored in oil or kerosene and can be handled in air under relatively dry conditions with inert atmosphere handling recommended.

TABLE I

THE ALKALI METALS

| Element | Atomic Number | Atomic Weight (amu) | Melting Point ($^{o}$C) | Ionization Potential (eV) |
|---|---|---|---|---|
| Lithium | 3 | 6.94 | 186 | 5.39 |
| Sodium | 11 | 22.99 | 97.7 | 5.14 |
| Potassium | 19 | 39.1 | 63 | 4.34 |
| Rubidium | 37 | 85.48 | 39 | 4.18 |
| Cesium | 55 | 132.91 | 28 | 3.89 |

## 1.2 Ion Engine and Ion Source Characteristics

An ion engine is characterized in terms of parameters such as thrust, power, weight, efficiency, etc. Since an engine is designed to operate on a space vehicle, the emphasized features include reliability, long life, and low power consumption. Laboratory lifetime tests have shown that engines can operate reliably for thousands of hours with little degradation in performance.

Ion engine accelerating voltages are usually limited to several kV because of mission considerations and to minimize breakdown problems. At these relatively low voltages large currents are extracted electrostatically by using large ion emission areas and multibeam electrode systems. Accel-decel electrode configurations are typically used with ions generated by an ionizer at +3 kV, an accel electrode at -1 to -8 kV, and possibly a decel electrode at ground potential. The accel serves as an electron trap to prevent electrons in the ion beam from backstreaming to the ionizing region and sometimes to increase the engine perveance in order to extract high beam currents.

In space both current neutralization and beam space charge neutralization, required to obtain thrust, are achieved by electron emission. Emitted electron currents must be equal to the ion beam current to prevent excessive charging of the spacecraft. A large rise in the potential of a spacecraft with respect to the ambient potential degrades the ion emission energy and could ultimately result in beam turn-around with loss of thrust. Beam space charge causes the ions to diverge and results in a degradation of thrust.

Thus, the electrons neutralize the ion beam, which results in a highly ionized, low-density plasma ($\approx 10^8$ particles/cm$^3$). Electrons are obtained from a separate source located near the ion engine, with emission regulated by the positive potential of the ion beam.

Parameters which characterize an ion engine as a thruster system are examined in terms of ion source operational parameters. The thrust (F) produced by an ion engine is the force required to accelerate a beam of particles to a velocity (v) and is given by

$$F = \dot{m}v, \tag{1}$$

where $\dot{m}$ is the ion beam mass flow rate. The mass flow rate in terms of the ion beam current (i) is given by

$$m = \frac{m}{e} i, \tag{2}$$

where m is the ion mass and e is the charge, and e/m is the particle charge-to-mass ratio.

In terms of measurable operating parameters, the thrust is given by

$$F = (2m/e)^{1/2}\ i\ V^{1/2}, \tag{3}$$

where V is the accelerating voltage and $eV = mv^2/2$.

Equation 3 shows the advantage of using particles having a low charge-to-mass ratio such as Cs and Hg, which are $7.21 \times 10^5$ and $4.77 \times 10^5$ C/kg respectively. Even lower charge-to-mass ratios are achieved by generating heavy particles from a liquid using the electrohydrodynamic technique. Small ion engines have been developed that produce a few micropounds of thrust, with larger ones producing thrusts up to a few tenths of a pound. For example, at an accelerating voltage of 4 kV, a Cs ion engine requires an ion beam current of 42 mA to produce 1 mlb (0.454g) of thrust.

Another term used to characterize the operation of an ion engine is the specific impulse ($I_{sp}$), defined as the ratio of thrust to propellant weight flow rate ($\dot{M}g$) and given by

$$I_{sp} = \dot{m}v/\dot{M}g. \tag{4}$$

The term $\dot{M}$ is the total mass flow rate and is equal to the ion mass flow rate plus the neutral particle flow rate, with g being the gravitational acceleration at the surface of the earth. This latter term is a constant independent of operating environment such as space, and is used to relate the engine operation to the weight of the propellant on earth. For a given thrust, the power (iV) can be decreased by using particles having lower charge-to-mass ratios. This in turn lowers the specific impulse, and propellant is used at a more rapid rate. Thus, the propellant weight and power available, determined by mission requirements, are used to select the ion engine type and its operating modes.

Another important parameter is the mass utilization efficienty ($\eta$), given by $\dot{m}/\dot{M}$. When $\eta \approx 1$, as in the case for surface ionization engines, the specific impulse is proportional to the ion exhaust velocity. Using the operating parameters for the thruster example given above, the specific impulse is approximately 8000 sec, and about 4 lb of propellant is required for continuous operation during 1 year with a total impulse of $3 \times 10^4$ lb-sec.

Mass utilization efficiencies generally range from 85% to nearly 100%. This efficiency is high enough in terms of propellant usage, but low neutral fractions ($1 - \eta$) are required for long-life ion engines, since the emission of neutral particles contributes to the erosion of ion engine electrodes, which can severely limit the lifetime. A slow ion, generated in the inter-electrode region by a charge transfer collision between a fast ion and a slow atom, is likely to impinge upon an electrode and produce sputtering. This removes electrode material, weakening the electrode, and the sputtered material may form harmful deposits on sensitive surfaces such as insulators, ionizers, and cathodes.

## 2. SURFACE IONIZATION SOURCES

### 2.1 Fundamentals of Surface Ionization

The surface ionization process of ion generation depends primarily upon the difference between the work function of the surface and the ionization potential of the atoms to be ionized. The process can be illustrated by considering the metal to be a potential well filled with electrons up to an energy level called the Fermi level. The potential difference between the Fermi level and the space just outside the metal is the energy that is required to remove an electron from the metal and is known as the work function of the metal ($\phi$). The energy required to remove an electron from an atom is known as the ionization potential (I).

When the work function of the metal is greater than the ionization potential of an atom located at the metal surface (i.e., $\phi > I$), the most loosely bound electron has a high probability of remaining in the metal when the particle is desorbed from the surface. The ratio of the number of ions ($n_p$) to the number of atoms ($n_a$) desorbed is given quantitatively by the Saha-Langmuir equation[1] which may be expressed as

$$\frac{n_p}{n_a} = \left(\frac{w_p}{w_a}\right) \exp\left[(\phi - I)/kT\right] \qquad (5)$$

where the weighting factor for each state (w) is equal to $2J + 1$, with J being the inner quantum number (or total angular momentum) of the ion or atom, and T the temperature.

For alkali metal atoms $J = 1/2$, while for alkali metal ions $J = 0$ so that $w_p/w_a = 1/2$ and Eq. 5 reduces to

$$\frac{n_p}{n_a} = \frac{1}{2} \exp\left(\frac{\phi - I}{kT}\right) . \tag{6}$$

The ionization potentials of the alkali metals are well defined and are given in Table I. The work function of a metal is not so well ordered and depends upon the conditions at the surface of the metal. The work function of "clean" tungsten is about 4.6 eV, but the presence of adsorbed atoms on the surface can increase or decrease the work function depending upon the characteristics of the composite surface produced. The adsorption of alkali metal atoms on a tungsten surface tends to decrease the effective work function, the amount of decrease depending upon the concentration of alkali atoms on the surface. This concentration is defined in terms of the fraction of a monolayer coverage ($\theta$), where a monolayer on tungsten is about $4.5 \times 10^{14}$ atoms/cm$^2$. The effective work function of tungsten decreases very rapidly as the coverage exceeds a few percent of a monolayer so that the ratio of ions to atoms desorbed from the composite surface decreases greatly with small changes in coverage. The coverage is therefore quite critical and it is necessary to control it by controlling temperature and/or the rate at which alkali metal atoms are supplied to the surface.

The effect of coverage upon ion and atom emission rates from solid tungsten with cesium atoms supplied to the surface is shown in Fig. 1. The ion emission rate increases nearly linearly up to a coverage of about 1% of a monolayer with only a small increase in the atom emission rate. As the coverage increases, the effective work function of the surface decreases, with a decrease in ion emission occurring above a 2% coverage. Here an instability occurs. As the coverage increases, the ion emission rate decreases, further increasing the coverage, and so on. Thus, the emission mode changes from point a to point b, and the ion emission drops sharply. Surface ionization is inefficient at coverages above point a. With increasing temperatures the curves increase appreciably toward high emission rates, and the peak near point a shifts only slightly toward higher coverage.

Efficient and stable ion emission is obtained at or below 1% of a monolayer. In this coverage region, the mean time that a particle remains on the surface before desorption is approximately 100 times longer for the emission of an atom than an ion. The ion desorption time, $\tau_i$, decreases with increasing surface temperature (T) and is given by

$$\tau_i = \tau_o \exp (Q/kT) , \tag{7}$$

where Q is the energy required to desorb an ion, and $\tau_o$ is the extrapolated desorption time at $T^{-1} = 0$.

In this low coverage region the emitted ion current density, j, as a function of coverage, N is atoms/cm$^2$ is given by

$$j = eN/\tau_i , \tag{8}$$

where e is the charge of the ion the $\tau_i$ dependence upon the temperature is given by Eq. 7. To determine an approximate ion emission upper limit, the value of N at 1% of a monolayer is about $4.5 \times 10^{12}$ particles/$cm^2$. Desorption measurements extrapolated to 1400°K show the ion desorption time ranging from $2 \times 10^{-5}$ to $10^{-4}$ sec with variations probably due to surface contamination.[2,3] Using Eq. 8 to find j/e, the upper limit ion emission rate at this temperature ranges from $4.5 \times 10^{16}$ to $2.25 \times 10^{-15}$ ions/$cm^2$-sec, which is consistent with the curve of Fig. 1.

In the operation of a surface ionization source, currents, voltages, and temperatures are first determined for stable and efficient modes. Consider a flow of Cs atoms onto a tungsten surface whose temperature is controllable. A sufficiently high voltage is applied between the ionizer and an ion collector to assure emission-limited current flow. At a fixed atom impingement rate $\mu_1$ (atoms/$cm^2$-sec), the temperature of the ionizer is decreased from a very high value. Figure 2 illustrates a typical ion emission current variation with the surface temperature. The ion current density does not vary appreciably with temperatures down to a value $T_i$. In this plateau region where the emission is stable, the ion current is approximately equal to the atom flow rate and the coverage is below about 1%. At the knee of a given curve for a temperature $T_1$, the coverage corresponds to the peak near point a in Fig. 1. With further lowering of the temperature, the ion current decreases sharply and the atom emission rate increases corresponding to operation at point b in Fig. 1. Reversing the process and increasing the temperature from a low value gives a very similar emission curve except that the knee is shifted toward a higher temperature. The hysteresis occurs because the change from high to low coverage operation requires higher temperatures to desorb sufficient atoms. At a higher atom flow rate, $\mu_2$, the $T_1$ knee shifts toward a higher temperature ($T_2$) as illustrated in Fig. 2. The lower temperature knee ($T_1$) is the lowest temperature at which efficient surface ionization occurs for a given beam current density. The position of the knee can be estimated at each current density using Eq. 8 and desorption time data. Adsorbed contaminants such as $O_2$ or C can affect the position of the knees and/or the ionization efficiency.

An adsorbed layer of $O_2$ increases the work function of most refractory metals. The work function of tungsten can be increased to values over 6 eV with a stable layer of $O_2$. Thus, oxygenating a hot tungsten surface makes it possible to efficiently produce ions from atoms whose ionization potentials are below 6 eV and somewhat less efficiently for those slightly above this value. This includes all of the alkali metals, indium, gallium, and several other elements which are not reactive with hot tungsten.

### 2.2 Types of Surface Ionization Sources

A surface ionization source is designed and operated according to the principles discussed in Subsection 2.1 and by Worlock.[4] The ionizer temperature and the vapor feed rate are selected to maintain an adsorbed Cs coverage near 1% of a monolayer with the ion current emission limited.

Front feed techniques, in which an atom beam impinges upon a heated solid refractory surface to produce ions, were found to be inadequate for ion engines because the ion beam interaction with the atoms caused excessive electrode erosion and other problems. A porous tungsten ionizer was introduced to avoid this troublesome interaction between the two beams.[5]

The porous tungsten ionizer is made from slabs of sintered tungsten granules which are cut to shape and brazed into a crucible manifold. Cs vapor is distributed by the manifold to the rear of the porous tungsten, operated at about 1100°C. The vapor percolates through the hot ionizer and ions are formed at the surface and in the pores. Ionizers made of granules of different sizes and shapes have been fabricated and tested in an effort to obtain low neutral fraction and high performance at low power.[6,7]

In some cases ion generation was found to occur predominantly in the pores[8,9] and resulted in ion current densities in excess of those obtained from a solid tungsten surface. Other refractory metals and alloys have also been investigated to find higher ionization efficiencies.[10]

Figure 3 shows a typical surface ionization engine configuration with a zero-gravity feed system. The delivery rate is controlled by the feed rate heater, which determines the vapor pressure at the porous ionizer. The sastrugi ionizer shown in the diagram is a large slab of porous tungsten machine-ground to form spherical concavities. This shape was found to optimize focusing of the ion beam for the current densities and voltages of an operating ion engine.[11,12,13] The ionizer is operated at positive voltages from 2 to 4 kV which determine the kinetic energy of the ions (i.e., exhaust velocity). The accel electrode is maintained at several kV negative and the decel at ground potential. Individual beams are formed in the electrode region which merge to a single large beam several cm downstream. Figure 3 also shows a neutralizer which emits electrons into the ion beam to assure beam neutrality and to prevent charging of a spacecraft. Tests in vacuum chambers do not require neutralizers, since sufficient electrons for ion beam neutralization are provided by secondary emission from ion impingement upon the ion beam collector.

The reservoir and feed system shown in Fig. 3 are capable of operating on earth or under zero-gravity conditions. The reservoir is heated to above the Cs melting point, and the liquid Cs wets the radial fins which converge toward the porous rod. Since surface tension forces tend to minimize a surface area, the liquid flows toward the rod. It fills the porous rod for the same reason and is vaporized from the end by heat from the feed rate control heater. This type of feed system is used to supply Cs for the electron bombardment ion engine and for the discharge type neutralizer, both discussed in Subsection 3.2.

To provide a low neutral fraction and assure that the ion current is controlled by the feed rate, ion engines are operated in an emission-limited mode, even though many design criteria stem from analysis of space-charge-limited operation.

Space-charge-limited operation is given by the Child-Langmuir equation, which can be written as

$$j = \frac{PV^{3/2}}{d^2} , \qquad (9)$$

where d is the distance between ionizer and accel electrode and P is the perveance in units of $A/V^{3/2}$. The perveance is proportional to the square root of the ion charge-to-mass ratio.

To avoid low fields at the beam axis near the ionizer, the aspect ratio, or ratio of d to the beam aperture diameter, is limited to values equal to or greater than one. For $Cs^+$, a perveance of about $5 \times 10^{-9}$ $A/V^{3/2}$ is a practical value for the extraction and acceleration of stable beams using circular apertures. Choosing an emission surface area equal to $d^2$, the current that can be obtained through a single aperture at 4 kV is about 1 mA (from Eq. 9). At an emission current density of 2 $mA/cm^2$ the emission area is limited to about 0.5 $cm^2$ with an electrode spacing of about 0.8 cm. To achieve higher currents, a multiaperture electrode system is used to form up to several hundred beams. To obtain multiple ionizing surfaces, a single crucible is made with many porous tungsten ionizer buttons or a large-area porous tungsten slab is machined to form separate concave emitting surfaces as in the sastrugi ionizer shown in Fig. 3. To obtain a higher current through each aperture, an accel-decel electrode system is used, since the extracted current may be space-charge-limited by the potential between ionizer and ground potential. By applying a high negative voltage to the accel electrode, the extraction field is increased without increasing the net energy of the ions in the beam. Nevertheless beam focusing is affected by the accel potential.

Surface ionization engines operate typically up to 5 $mA/cm^2$, with total beam currents determined by the emission area. A single-beam microthruster generates about 1 mA, providing several μlb of thrust.[14] A large-area engine tested at EOS produced 3.8A of beam current to provide about 0.1 lb of thrust. Many engines have been developed to fill the gap between these two.

Single-beam $Cs^+$ sources have been developed to study emission characteristics and for application studies of ion beam interaction phenomena. Special ionizers composed of tungsten spherical powder were used to produce current densities up to 80 $mA/cm^2$ for an ionizer temperature just above 1200°C.[15] Charge transfer collisions, ion sputtering, secondary electron emission, and ion implantation studies were conducted using porous tungsten ion sources to generate $Cs^+$, $Rb^+$, and $K^+$.[16-19] Modification of this type source was made to permit high-temperature operation (> 1200°C), and an $O_2$ spray on the ionizer was introduced so that ion beams of the rest of the alkali metals and other species could be generated.[20,21] Total currents of about 0.3 mA of $Li^+$ were obtained from a 0.475-inch-diameter porous tungsten ionizer operated at a temperature of 1200°C and with an $O_2$ impingement rate of about $10^{15}$ particles/$cm^2$-sec. This source was operated at up to about 20 kV with little change in the current above 3 kV. A special source was constructed

and operated with reservoir and ionizer at > 1200°C to generate the required vapor pressure and ionize indium.[22] Up to 0.5 mA of $In^+$ was obtained with the current being feedrate limited.

## 3. LOW-PRESSURE DISCHARGE SOURCES

### 3.1 Fundamentals of Ion Generation

A discharge source used to produce ion beams is applicable for those species which can be introduced as gas or vapor. Ions, generated by electron bombardment, are extracted from the discharge and accelerated to produce an ion beam. When the vapor is composed of a single atomic specie, such as in the case of the alkali metals, the number of singly charged ions can be enhanced and the fraction of emitted multiple charged ions can be minimized by optimizing the discharge mode.

To sustain a gaseous discharge, electrons are emitted from a cathode into a gas and accelerated to the anode by the application of an electric field. Electrons collide with the gas atoms and some of these collisions result in ionization of the atom. The electron removed from the atom will also be accelerated and will participate in further ionization processes. Ions are accelerated toward the cathode, and the current flow through the discharge is carried by both electrons and ions. Because of their much lower mass, the current flow of electrons will greatly exceed that of the ions.

The probability that an electron will collide with and ionize an atom depends upon the procuct of the atom density, the electron path length through the gas, and the ionization collision cross section. This cross section, the effective physical area presented by the atom to the oncoming electron, depends upon the electron energy.[23] The ionization cross sections of atoms have several distinct features. Thresholds (or onset energies) occur at the ionization potential with cross sections rising rapidly to a maximum at an electron energy about five times the ionization potential, then slowly decreasing with increasing energy. Thus, as an electron is accelerated toward the anode in a gas discharge the probability that the electron undergoes an ionizing collision is affected by the gas density and the electric field. To sustain the discharge, the field and gas density must be such that the energy gained between collisions is high enough for ionization to occur. This is enhanced by increasing the field and/or increasing the mean free path (average path length between collisions) by decreasing the gas density. The number of collisions at a given gas density can be increased by lengthening the total path traversed by each electron, using a magnetic field which causes the electron to spiral and be constrained from reaching the anode. Thus, a discharge can be operated at an optimum condition for producing desired current densities by varying gas pressure, applied discharge voltage, magnetic field, etc.

Because the electrons travel more rapidly than the ions, the region where the ions are generated tends to become more positive than it would be due to the electric field between cathode and anode. Electrons escape rapidly enough to increase the potential of this region to somewhat above that of

the anode, forming a nearly field-free plasma region. Because the plasma region is at a somewhat higher potential than the anode, it also constrains the electron flow to the anode. This is a self-regulating process, since an excessive loss of electrons increases the potential of the plasma region, which in turn further constrains the electron loss to the anode.

Ions are extracted out of the edge of the plasma through a region called the plasma sheath. Figure 4 illustrates schematically a typical low-pressure discharge source. The cathode in the discharge chamber of the source is electrically connected to the enclosing cylinder, and the cylindrical anode is contained within the chamber. The magnetic field is coaxial with the cylinders. The screen electrode at the cathode potential aids in forming the plasma sheath from which the ions are extracted. Since the accel electrode is negative by several kV with respect to the screen, positive ions are accelerated and electrons are retarded. Thus, the plasma sheath shape or the meniscus at the screen aperture is affected by the ion current extracted.

The meniscus is determined by the plasma ion density, the aperture configuration, and the field between the screen and accel electrodes. Good focusing of the ion beam occurs when the meniscus is concave. This general shape and the formation of the ion beam using an accel-decel electrode system are essentially the same as described in Subsection 2.2 for the surface ionization source.

### 3.2 Electron Bombardment Ion Engines

In the electron bombardment ion engine, a low-pressure discharge is used to generate ions which are extracted and accelerated to produce a beam. This type of engine differs from the surface ionization engine only in the means of ionization, the rest of the features being nearly the same. Bombardment engines have been developed to use Cs or Hg as the propellant, with some differences in components and operating modes to accommodate the particular vapor used. Both these elements provide the heavy ions desired for propulsion. The discharges are optimized to provide a predominance of singly charged ions with a minimum of emitted neutral atoms. Cs shows some advantage over Hg because of its lower ionization potential and higher ratio of second to first ionization potentials.

An electron bombardment ion engine (Fig. 4) is composed of a reservoir for propellant storage, a feed system, a discharge chamber for producing ions, and an ion acceleration electrode system. The reservoir containing the propellant in liquid form can be either the laboratory type or the zero-gravity type discussed in Subsection 2.2. The vapor is generally delivered to the discharge at or through the cathode, depending upon the type of cathode used. The gas pressure, in a typical Cs discharge operating between 7V and 15V, is maintained between $10^{-4}$ and $10^{-3}$ torr to provide an extracted ion current density of between 1 and 10 $mA/cm^2$. The axial magnetic field, generally near $10^{-3}$ $Wb/m^2$, maintains the electrons in a long spiraling trajectory to increase the probability of ionization collisions. As the electrons collide and lose energy, they tend to drift toward the anode, where they are lost from the discharge. Ions are also lost from the discharge

when they strike a surface and reenter the discharge as atoms. Ions, atoms, and electrons drift toward the screen electrode, where the electrons are repelled, the ions are extracted by the electrode field, and the neutral atoms escape. A beam collector located at the end of the vacuum chamber is used to measure the ion beam current and absorb the beam energy. To enhance the emission of ions over that of atoms, diverging magnetic fields have been used to increase the flow of charged particles toward the screen.[24] This tends to decrease the neutral fraction and/or the discharge power by increasing the ionization efficiency.

Mass utilization efficiencies of 85% to 95% have been achieved with these engines. Beam currents, obtained by using a broad-area source having many apertures, up to 1A of $Cs^+$ and 10A of Hg, have been produced by bombardment engines.

Because a large portion of the discharge power is generally consumed in heating the cathode, attention was given to the development of low-power cathodes. As a result, several types of cathodes have been developed and used with bombardment engines. Refractory wire and oxide-coated filaments were used initially with Cs and are still used with Hg. In the early Cs engines the vapor was directed toward the cathode, the adsorbed Cs coating decreasing the electron emission work function. This lowers the cathode operating temperature with a net saving of power. In the Hg engine the vapor flow is directed away from the cathode because the adsorbed Hg coating increases the filament work function. A further improvement in cathodes was made by using an autocathode, wherein Cs vapor is fed through a refractory metal cathode which is heated by ion bombardment from the discharge.[24] The discharge is operated at low voltages (6V to 8V) so that ion sputtering of the cathode is negligibly small. This cathode is operable only over a limited range of discharge modes suitable for an ion engine stabilized by an electronic control system.

Another electron source known as the discharge cathode or discharge neutralizer is capable of emitting very large electron currents.[25,26] Cesium vapor is fed into a small enclosed chamber heated to about 600°C. The cesiated surface at this temperature is capable of emitting high electron current densities. An aperture approximately 0.02 cm in diameter allows particles to escape from the chamber. When a relatively low electric field is applied outside the chamber aperture, a discharge strikes and the plasma is emitted. Electron currents of several amps are readily drawn from this device with electron-to-atom (and electron-to-ion) emission ratios in the range of several hundred to one. When used as a cathode this discharge electron emitter is regulated to introduce Cs vapor, $Cs^+$, and electrons at rates required for the main chamber discharge. When it is used to neutralize the ion beam outside the ion engine, a plasma bridge to the ion beam is formed, resulting in good coupling with only a few volts potential difference between the beam and neutralizer.

Electron bombardment ion engines have been developed to produce ion beams of from 1 mA to 1A. A series of Cs microthrusters was developed, the smallest having a single beam aperture, to operate efficiently in the range from 10 to 100 μlb of thrust.[26] Other engines generating hundreds of mA of beam

current have been developed in investigating cathode types, discharge modes, and electrodes to increase performance efficiency.[27] Large Hg engines with source diameters up to 50 cm produce up to several amps of beam current.[28] Cs engines have been life-tested for over 8000 hours of continuous operation and terminated only because the propellant was exhausted.[29]

A 1A beam of $Na^+$ was produced at EOS by an ion engine modified to operate at somewhat higher temperatures. The source was operated with 4 kV applied to the ionizer and about 1 kV to the accel electrode. The multibeam electrode system contained over 500 apertures and was heated to about 300°C to prevent condensation and thereby obtain stable operation. Other species such as Kr, Ar, $N_2$ and $H_2$,[30] in addition to others not reported, have been used with standard ion engines.

## 4. THE ELECTROHYDRODYNAMIC ION SOURCE

Investigations conducted to generate heavy charged particles having charge-to-mass ratios a factor of approximately 100 below that of $Cs^+$ are aimed at developing a thruster which operates at a specific impulse of about 1000 sec. This type of thruster can produce a higher thrust per unit power than the two types of ion engines described above, but it requires higher mass flow rates.

Heavy charged particles are generated by the application of intense electric fields at the surface of a conducting liquid.[31,32,33] The intense electric field is achieved at nominal voltages (2 to 10 kV) by using high-curvature particle emitters such as capillary needles. Organic fluids such as glycerol, doped with salts or acids, have been used to produce charged particles over a wide range of charge-to-mass ratios up to $10^5$ C/kg. Since the charged particle beam contains a distribution of charge-to-mass ratios, time-of-flight (TOF) techniques in addition to current and voltage measurements are employed to determine thruster operational parameters. Alkali metals used as the liquid produce ions predominately at high current densities.[32] The state of the art in this field is not as advanced as those of the surface ionization and electron bombardment ion engines. For this reason generalizations are not drawn from the limited data available.

The experimental arrangement for charged particle generation and testing is shown in Fig. 5. Fluid flow to the tip of a capillary needle emitter is controlled by a pressure feed system. High voltage (2 to 10 kV) is applied to the emitter with an extractor electrode maintained at several hundred volts negative. The extractor aids in forming the electric field at the needle tip and prevents electrons in the particle beam from backstreaming to the emitter. It is important to prevent backstreaming electrons from impinging upon the emitter because they cause excessive emitter heating and also errors in measuring emitter ion current. A shielded collector is provided to measure part of the beam current and determine the charge-to-mass distribution using TOF analysis. The emitter potential is brought to ground by means of the shorting switch, and the subsequent current decay is observed on the oscilloscope. This provides the beam particle velocity distribution, from which the charge-to-mass ratio distribution can be obtained. Emitter

tips are fabricated from capillary tubing made of stainless steel, platinum, or tungsten ranging in size from $2.5 \times 10^{-3}$ to $2 \times 10^{-2}$ cm i.d. and from $7.5 \times 10^{-3}$ to $4.5 \times 10^{-2}$ cm o.d. The tips are tapered by grinding to provide a narrow, rounded rim.

The interaction between the conductive liquid and the metal surface at the emitter tip under high field conditions results in the electrohydrodynamic emission of charged particles. The electric fields at the emitter tips are somewhat below $10^6$ V/cm, which is insufficient to extract charged particles or ions by field emission. Instabilities can occur at the liquid surface which is under tension because of high field and opposing surface tension forces. As the liquid develops a surface protuberance, the electrical force at the peak increases with the distance from the average surface level. This can grow into a liquid spike with dimensions one or two orders of magnitudes below those of the emitter. With the effective electric field at these spikes greater than $10^7$ V/cm, ions can be extracted by field emission. The space charge of the emitted ions lowers the field at the spike to either limit the current flow or allow the spike to collapse to be regenerated a short time later. Conductivity, surface tension, and emitter tip size determine the applied voltage required to produce emission and also the average size of the particles emitted. Ions are generated from liquid alkali metals because of their high condutivities, high surface tension, and good wetting properties. No positive feed system pressure was required in the cesium tests, with only sufficient pressure applied initially to fill the feed system lines. The liquid metal then replenished itself at the needle tip by self-sustaining capillary and surface tension forces.

Needle currents of 270 μA at 4.4 kV were obtained using a $2.5 \times 10^{-3}$ cm i.d. needle, and 200 μA at 4.03 kV using the $10^{-2}$ cm i.d. needle with a 0.16 cm extractor aperture. In all of the tests the charged particle beam consisted almost wholly of $Cs^+$ ions. Figure 6 shows two TOF traces showing $Cs^+$, $Cs_2^+$, and $Cs_3^+$ at 4.03 kV and $Cs^+$ alone at 7.8 kV. No attempt was made to focus the beam, with the result that only a few percent of the ions impinged upon the collector. Onset of spraying occurred at about 0.9 kV for the $2.5 \times 10^{-3}$ cm i.d. needle.

In conjunction with the spraying of cesium ions, the neutral cesium yield was measured directly with neutral cesium detector used for similar measurements with ion engines. The measurements show that the neutral fraction of the total mass flow rate varied from less than 1.8% for the case where the emitter temperature was between 100° and 200°C. Above 200°C the neutral fraction was nearly 100% and the cesium spray from the emitter showed a visible glow. At the lower temperatures the spray was not visible, indicating a correlation of the neutral yield with the visible spray. The transition between the two operating conditions was abrupt and showed considerable hysteresis. The glow indicates the presence of a discharge which heats the emitter tip, evaporating copious quantities of neutral cesium.

ACKNOWLEDGEMENT

The author wishes to thank H. L. Daley for the aid and criticism he provided in the course of writing this paper.

LIST OF SYMBOLS

$F$ = thrust, newtons
$\dot{m}$ = ion mass flow rate, kgm/sec
$v$ = velocity, m/sec
$e$ = charge of ion, $1.6 \times 10^{-19}$ coul
$m$ = mass of ion, kgm
$i$ = ion beam current, A
$V$ = accelerating potential, V
$I_{sp}$ = specific impulse, sec
$\dot{M}$ = total mass flow rate, kgm/sec
$g$ = acceleration due to gravity, 9.8 m/sec$^2$
$\eta$ = mass utilization efficiency
$\phi$ = surface work function, eV
$I$ = atomic ionization potential, eV
$n_a$ = Atom emission rate, atoms/cm$^2$-sec
$n_p$ = ion emission rate, ions/cm$^2$-sec
$w_a$ = atom weighting factor, $2J + 1$
$w_p$ = ion weighting factor, $2J + 1$
$J$ = total angular momentum of ion or atom
$k$ = Boltzmann constant $1.38 \times 10^{-23}$ J/$^o$K or $8.63 \times 10^{-5}$ eV/$^o$K
$T$ = temperature, $^o$K
$\tau_i$ = ion desorption time, sec
$\tau_o$ = ion desorption time extrapolated to $T^{-1} = 0$, sec
$Q$ = ion desorption energy, eV
$j$ = ion current density, A/cm$^2$
$N$ = adsorbed atom surface coverage atoms/cm$^2$
$\theta$ = surface coverage fraction of a monolayer
$\mu$ = atom flow rate, atom/cm$^2$-sec

REFERENCES

1. J. B. Taylor and I. Langmuir, "The Evaporation of Atoms, Ions and Electrons from Cesium Films on Tungsten," The Physical Review, 44, 423 (1923).

2. J. Perel, R. H. Vernon, and H. L. Daley, "Desorption Time Measurements Using AC Modulation Techniques," J. Appl. Phys., 36, 2157 (1965).

3. M. D. Scheer and J. Fine, J. Chem. Phys., 37, 107 (1962).

4. R. M. Worlock, "The Surface Ionization Ion Engine," First International Conf. on Electron and Ion Beam Science and Technology, edited by R. Bakish, 853, (John Wiley & Sons, Inc., New York 1964).

5. A. T. Forrester and R. C. Speiser, "Cesium-Ion Propulsion," Astronautics, 4, (1959).

6. G. Kuskevics and B. L. Thompson, "Comparison of Commercial, Spherical Powder and Wire Bundle Tungsten Ionizers," AIAA J., 2, 284 (1964).

7. M. LaChance, G. Kuskevics, and B. Thompson, "High-Performance Cesium Ionizers Made from Sized Spherical Tungsten Powder," AIAA J., 3, 1498 (1965).

8. A. T. Forrester, "Analysis of the Ionization of Cesium in Tungsten Capillaries," J. Chem. Phys., 42, 972 (1965).

9. T. R. Bates and A. T. Forrester, "Coupled Molecular Flow and Surface Diffusion. Application to Cesium Transport," J. Appl. Phys., 38, 1956 (1967).

10. O. K. Husmann, "Improved Surface Ionization Efficiency by High Work Function Refractory Metals and Alloys," J. Appl. Phys., 37, 4662 (1966).

11. S. L. Eilenberg, W. Seitz, and E. Caplinger, "Evaluation of Electrode Shapes for Ion Engines," AIAA J., 3, 866 (1965).

12. S. L. Eilenberg, E. Caplinger, H. L. Daley, J. Perel and W. Seitz, "Design and Performance of Sastrugi Ion Optical Systems," J. Spacecraft and Rockets, 2, 982 (1965).

13. W. S. Seitz and S. L. Eilenberg, "Numerical Self-Consistent Field Approximation to the Interaction of an Ion Beam with a Plasma Boundary," J. Appl. Phys., 38, 276-283 (1967).

14. R. M. Worlock, P. Ramirez Jr., M. P. Ernstene, and W. E. Beasley Jr., "A Contact Ion Microthrustor System," AIAA Paper 67-80, New York, N.Y., (1967).*

15. G. Kuskevics and B. Thompson, "Surface Ionization Source of Cesium Ions," Rev. Sci. Instr., 37, 710, (1966).

16. J. Perel, R. H. Vernon, and H. L. Daley, "Measurement of Cesium and Rubidium Charge Transfer Cross Sections," Phys. Rev., 138, A937 (1965).

17. J. Perel, R. H. Vernon, and H. L. Daley, "Measurement of $K^+$ -Rb Charge Transfer Cross Sections," IVth International Conference on Physics of Electronic and Atomic Collisions, Quebec, Aug. 1965, 336 (Science Bookcrafters, Inc., Hastings-on-Hudson, N.Y.).

18. H. L. Daley and J. Perel, "Cesium Ion Sputtering of Aluminum, Copper, and Titanium," AIAA J., 5, 113, (1967) (AIAA Paper 66-203, 5th Electric Propulsion Conf., San Diego, California, March 1966).*

19. D. B. Medved, J. Perel, H. L. Daley, and G. P. Rolik, "Implantation and Channeling Effects of Alkali Ion Beams in Semiconductors," Nuclear Instr. and Meth., 38, 175 (1965) (Proceedings of Electro-Magnetic Isotope Separators Conf., Holland, 1965).

20. J. Perel and A. Y. Yahiku, "Oscillations in Total Cross Sections of $Rb^+$, $K^+$, $Na^+$ and K Charge Transfer," Fifth Int. Conf. on the Phys. of Elect. and Atomic Collisions -- Leningrad, July 1967, 400 (Publishing House "Nauka" Leningrad).

21. J. Perel and H. L. Daley, "$Li^+$ and $Na^+$ Source," (to be published).

22. H. L. Daley, J. Perel, and R. H. Vernon, "Indium Ion Source," Rev. Sci. Instr., 37, 473 (1966).

23. R. H. McFarland and J. D. Kinney, "Absolute Cross Sections of Lithium and Other Alkali Metal Atoms for Ionization by Electrons," Phys. Ref., 137, A1058 (1965).

24. G. Sohl, G. C. Reid, and R. C. Speiser, "Cesium Electron Bombardment Ion Engines," J. Spacecraft and Rockets, 3, 1093 (1966).

25. M. P. Ernstene, E. L. James, G. W. Purmal, R. M. Worlock, and A. T. Forrester, "Surface Ionization Engine Development," J. Spacecraft and Rockets, 3, 744 (1966).

26. G. Sohl, V. V. Fosnight, S. J. Goldner, and R. C. Speiser, "Cesium Electron-Bombardment Ion Microthrusters," J. Spacecraft and Rockets, 4, 1180 (1967).

27. G. Sohl, K. Wood, T. R. Dillon, and R. Vernon, "Performance of a Cesium Bombardment Ion Engine with a Self-Rectifying Discharge and Automatic Controls," AIAA Paper 67-666, Colorado Springs, Colorado, (1967).*

28. P. D. Reader, "Experimental Performance of a 50-cm Electron Bombardment Ion Rocket," AIAA Paper 64-689, Toronto, (1964)* and NASA TMX-52042 (1964).

29. V. V. Fosnight, G. Sohl, S. J. Goldner, and R. C. Speiser, "Cesium Ion Engine System Life Test Results," accepted for publication in J. Spacecraft and Rockets.

30. P. D. Reader, "The Operation of an Electron Bombardment Ion Source with Various Gases," First Inter. Conf. Electron and Ion Beam Sci. and Tech., edited by R. Bakish, (J. Wiley) 925 (1964).

31. C. Hendricks, "Classical Physics in Modern Space Propulsion: Heavy Particle Beam Formation by Electrical Spraying of Liquids," First Inter. Conf. Electron and Ion Beam Sci. and Tech., edited by R. Bakish, 915, (J. Wiley 1966).

32. J. Perel, T. Bates, J. Mahoney, R. D. Moore, and A. Y. Yahiku, "Research on a Charge Particle Bipolar Thruster," AIAA Paper 67-728, Colorado Springs, Colorado (1967).*

33. J. C. Beynon, E. Cohen, D. S. Goldin, M. N. Huberman, R. W. Kidd, and S. Zafran, "Present Status of Colloid Microthruster Technology," AIAA Paper No. 67-531, Colorado Springs, Colorado (Sept. 1967).*

34. J. Perel, R. H. Vernon, and H. L. Daley, "Ion and Atom Angular Distributions from a Multibeam Cesium Ion Engine," AIAA Paper 64-696, Philadelphia, Pa. (Aug. 1964).*

* AIAA preprints can be obtained from American Institute of Aeronautics and Astronautics, 1290 6th Avenue, New York, New York 10019.

## BIBLIOGRAPHY OF REVIEW ARTICLES ON ION ENGINES

A. R. Brewer, M. R. Currie, and R. C. Knechtli, "Ionic and Plasma Propulsion for Space Vehicles," Proceedings of the Institute of Radio Engineers, 49, 1789 (1961).

A. T. Forrester and J. M. Teem, "Advances in Electrostatic Propulsion," Astronautics, 6, 34 (1961).

D. B. Langmuir, E. Stuhlinger, and J. M. Sellen, Jr., eds., Progress in Astronautics and Rocketry; Electrostatic Propulsion, 5, (Academic Press, New York, 1961).

E. Stuhlinger, editor, Progress in Astronautics and Rocketry: Electric Propulsion Development, 9, (Academic Press, New York, 1963).

A. T. Forrester and S. L. Eilenberg, "Ion Rockets," International Sci. and Tech. (Jan. 1964).

E. Stuhlinger, Ion Propulsion for Space Flight (McGraw-Hill, New York, 1964).

G. R. Brewer, "Physical Electronics Phenomena in Ion Propulsion Engines," IEEE Spectrum, 2, 65 (1965).

M. P. Ernstene, "Progress and Prospects of Electric Propulsion," AIAA Paper 66-830, Boston (1966).*

W. R. Mickelsen, "Auxiliary and Primary Electric Propulsion, Present and Future," J. Spacecraft and Rockets, 4, 1409 (1967).

A. T. Forrester and G. Kuskevics, eds., "Ion Propulsion," AIAA Selected Preprints, Vol. III, (1968).*

R. M. Worlock, "The Surface Ionization Ion Engine," First International Conference on Electron and Ion Beam Science and Technology, edited by R. Bakish, 853 (John Wiley & Sons, Inc., New York 1964).

* AIAA preprints can be obtained from American Institute of Aeronautics and Astronautics, 1290 6th Avenue, New York, New York 10019

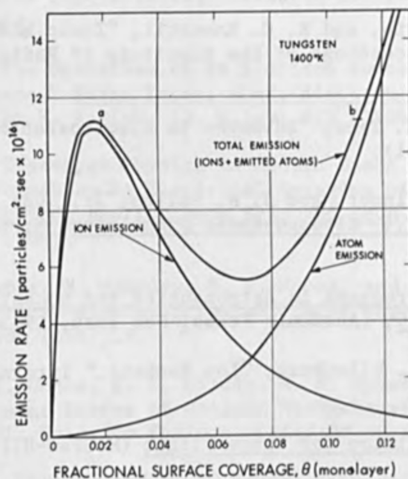


Figure 1 Cesium ion and atom emission from a tungsten surface as a function of the surface coverage in fraction of a monolayer. The region of stable and efficient ion emission operation is below 0.02 of a monolayer.

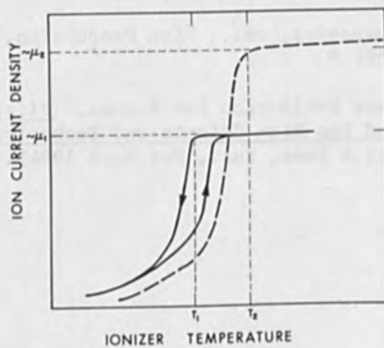


Figure 2 Ion emission current density versus ionizer temperature for two atom impingement rates $\mu_1$ and $\mu_2$. At an atom impingement $\mu_1$ a hysteresis loop occurs between the decreasing and increasing temperature cycles. The knee of the curve at $T_1$ is the lowerst temperature for stable and efficient operation. The dashed curve shows the change with a higher atom impingement rate with $T_2$ being the lowest stable and efficient operating temperature at $\mu_2$.

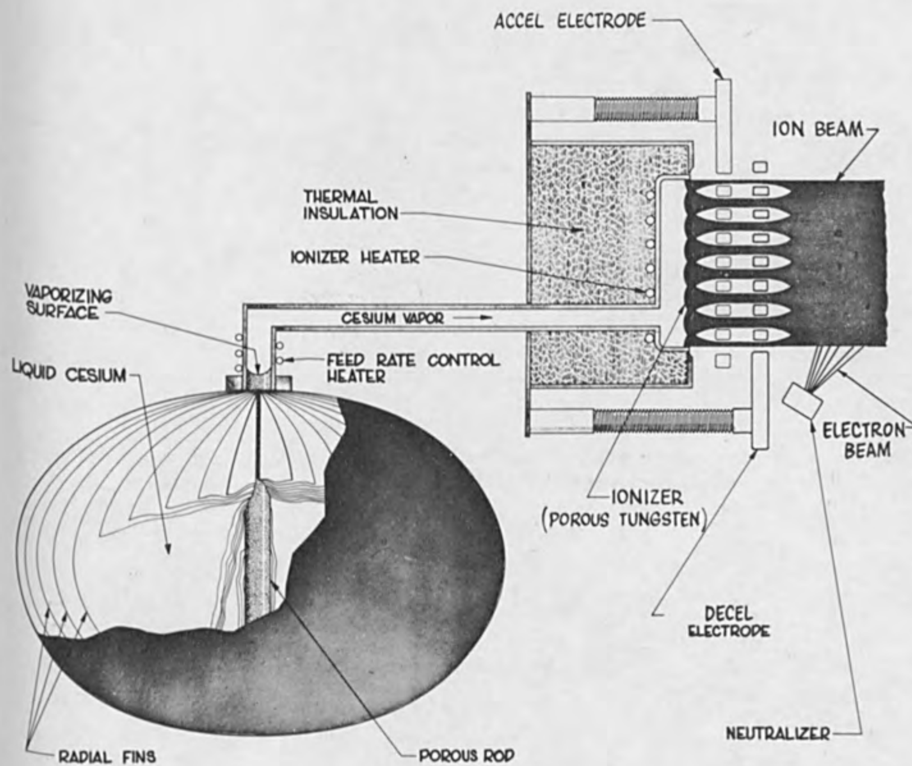


Figure 3 Schematic of a multibeam surface ionization engine with zero-gravity feed system. Ions emitted from hot porous tungsten surface are accelerated by the electrodes to form individual ion beams. These beams merge downstream into a single large beam which is neutralized by the introduction of electrons.

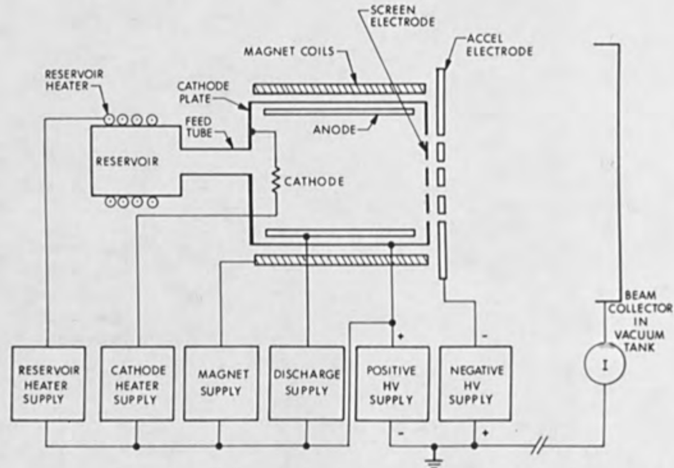


Figure 4 Schematic diagram of low pressure discharge ion source with associated power supplies.

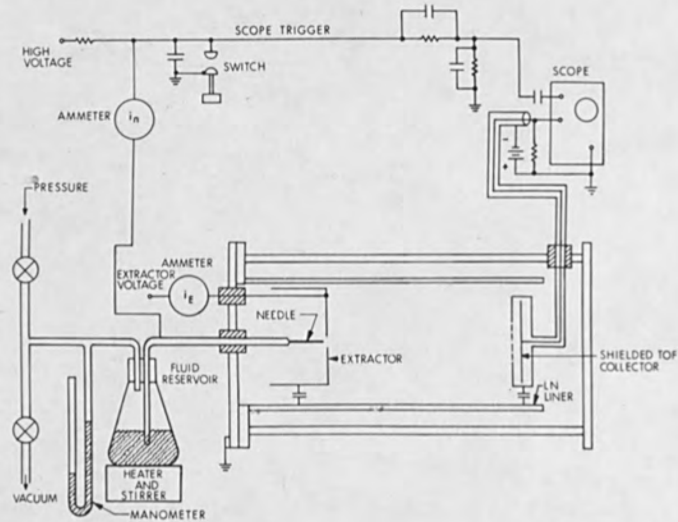


Figure 5 Schematic diagram of electrohydrodynamic ion source experiments showing the arrangement for measuring time of flight.

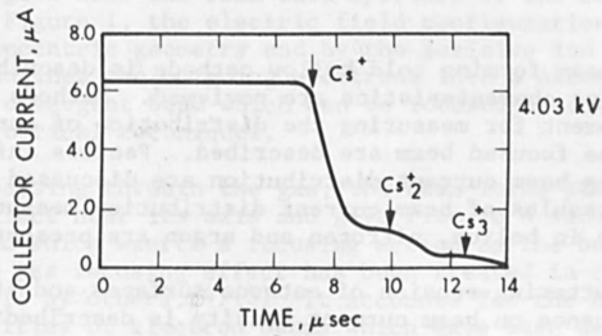


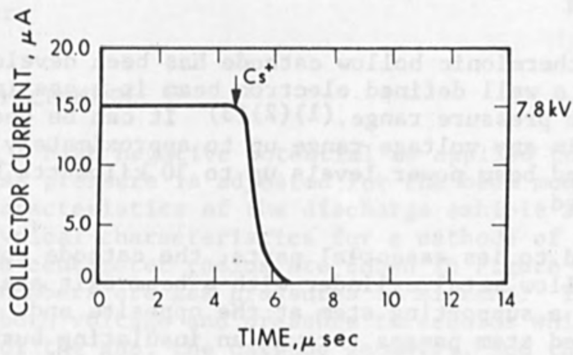


Figure 6 Time-of-flight data from cesium tests.

# CURRENT DENSITY DISTRIBUTION IN BEAMS FROM COLD HOLLOW CATHODES

L. H. Stauffer
Research & Development Center
General Electric Company
Schenectady, New York 12301

A beam forming cold hollow cathode is described and its characteristics are reviewed. Methods and equipment for measuring the distribution of current in the focused beam are described. Factors influencing beam current distribution are discussed and the results of beam current distribution measurements in helium, nitrogen and argon are presented.

Sputtering erosion of cathode surfaces and its influence on beam current density is described and cathode life data are presented.

## INTRODUCTION

A non-thermionic hollow cathode has been developed which emits a well defined electron beam in a gas in the rough vacuum pressure range.(1)(2)(3) It can be designed to operate in any voltage range up to approximately 100 kilovolts and beam power levels up to 30 kilowatts have been attained.

Reduced to its essential parts, the cathode consists of a closed hollow metal cylinder with a beam exit aperture at one end and a supporting stem at the opposite end. The axially attached stem passes through an insulating bushing mounted on the vacuum chamber. A small radial gap separates the cathode cylinder from a grounded metal shield which surrounds it, as shown in the schematic cross sectional view in Figure 1. At the operating pressure, the electron mean free path is many times the length of the gap between the cathode and the shield, or anode. For this reason, no electron avalanches take place in the gap and the discharge is forced to take a long path terminating inside the cathode. Under these conditions, a well defined beam of electrons issues from the

cathode aperture as in the photograph shown in Figure 2.

In this type of glow discharge, a region of high voltage gradient exists near the cathode. Across this so-called cathode dark space appears almost the entire applied cathode potential. Electrons leaving the cathode are accelerated to an energy corresponding to nearly the full cathode potential. In the region near the beam exit aperture of the cathode shown in Figure 1, the electric field configuration imposed by the concentric geometry and by the positive ion space charge confines the outgoing electrons into a narrow, slightly divergent beam which can be focused by conventional electron optical techniques.

In passing through the gas, the beam forms positive ions which collect near its axis and give rise to a radial electric field which exerts a focusing action on the beam. This so-called gas focusing effect has been treated in considerable detail by others.(4)(5) It accounts for the high current densities of electron beams which have been derived from the relatively diffuse plasma of this type of cathode, where the average current density at the interior surfaces does not, in most cases, exceed 10 milliamperes per square centimeter.

## EMISSION MECHANISM

When a high negative potential is applied to the cathode and the gas pressure is adjusted for the beam mode, the volt-ampere characteristics of the discharge exhibit a positive slope. Typical characteristics for a cathode of approximately one centimeter radius are shown in Figure 3. The attached numbers are gas pressures in microns. The beam mode exhibits both voltage and pressure thresholds which are a function of the gas, the cathode geometry, and the material.

Positive ions, formed by electron impacts with gas atoms, are accelerated in the strong electric field of the cathode dark space and on striking the cathode release secondary electrons which are accelerated in the opposite direction. Because the field near the end of the cathode has a strong radial component, axial focusing action directs an appreciable fraction of the ions into the cathode cavity

where they produce secondary electrons on striking the inner surfaces. Ionizing collisions with gas atoms also contribute free electrons. Upstreaming positive ions entering the cavity establish a positive space charge potential distribution near the axis which traps many of the low energy electrons until they find their way to the beam exit aperture where they are extracted by the strong external field to form the beam.

During steady state operation a glowing plasma, surrounded by a positive space charge sheath, fills the cathode cavity. Langmuir probes have been inserted into the cavity through a hollow support stem to determine the plasma potential. With argon at 6 microns pressure, the plasma potential is approximately + 400 volts with respect to the cathode when the cathode is emitting a 50 milliampere beam with 12 kilovolts applied to it. At 4 microns, the beam current and plasma potential fall to 20 milliamperes and + 180 volts respectively.

When an internal grid of fine molybdenum wire is interposed between the plasma boundary and the cathode wall, the grid assumes the plasma potential (several hundred volts) when isolated. When connected to a separate variable voltage source, the grid potential controls the beam intensity. A typical beam current versus grid potential plot for a 2.5 centimeter diameter cathode, operated at 17 kilovolts in nitrogen, is shown in Figure 4. The gas pressure was 8 microns.

From the sharp fall-off in the beam current at small negative grid potentials, it may be concluded that the internal plasma is sustained by secondary electrons having energies less than 5 or 6 electron volts. The residual beam current (about 9.5 milliamperes) arises from secondaries emitted by the grid wires and supports. At positive grid potentials, positive ions are retarded in their flight to the cathode walls. Comming from a highly excited plasma, some of these ions are multiply ionized and may have energies well above 100 electron volts due to the penetration of the strong external field into the cavity. This accounts for the high value of positive grid potential needed to suppress secondary emission. Cut-off is almost complete when ions cannot reach the cathode surface with enough energy to eject secondary electrons. A few ions enter the beam exit aperture with

energy corresponding to the full dark space potential drop while others, originating in the dark space, have less energy. Metastable atoms and photons could account for the lack of complete beam cut-off at high positive grid potentials.

These observations, together with measurements of grid and cathode input currents, suggest that most of the beam current is derived from electrons released by ionizing events within the internal plasma. Secondary emission from the cathode walls alone is insufficient to account for more than a fraction of the beam current. However, when the secondary electrons, having a few electron volts of initial energy, cross the space charge sheath surrounding the plasma, they gain several hundred electron volts. On making collisions with particles constituting the plasma, they lose energy and are constrained within the potential trap where each may ionize or excite several atoms. Thus, a single initial secondary may give rise to several plasma electrons as well as photons and metastable atoms.

Positive ions from the plasma gain energy in crossing the sheath and eject additional secondaries on impact with the cathode walls. These ions appear to account for most of the current drawn by the cathode, the balance being due to secondaries and photo-electrons. Penetration of the external field into the cathode cavity maintains the plasma at a positive potential with respect to the cathode by continuously extracting electrons from the plasma to maintain the beam current.

At low gas densities, a large proportion of the secondary electrons will traverse the cathode cavity and strike the opposite wall without contributing energy to maintain the internal plasma. As the gas pressure is increased, more collisions will occur and the electron density will rise, causing an increase in beam current. In argon, the cross sections for ionization are of the order of 10 times larger than those for helium. Consequently, the operating pressure required when helium is used is about 10 times that for argon. As the cathode is increased in diameter, the operating pressure is correspondingly less as a consequence of the increased probability of encounters with gas atoms as electrons pass through the larger plasma body.

Further evidence that the internal plasma is largely maintained by secondary electrons accelerated in the space charge sheath is obtained when an axially directed magnetic field is applied to the cathode. Electrons are thereby constrained to move in circular paths within the plasma with reduced chance of reaching a wall before losing energy by collision with plasma particles. This effect is illustrated by the data plotted in Figure 5 showing the effect of a uniform axial magnetic field on the beam current from a cathode of 3.7 centimeter diameter operated at 25 kilovolts in argon and in nitrogen. At field strengths above 80 oersteds, the measurements (in both gases) were terminated by the onset of beam instabilities.

## SURFACE EFFECTS AND THERMAL CONSIDERATIONS

In choosing cathode materials, consideration must be given to secondary emission coefficients, sputtering coefficients, and thermal characteristics. Since some parts of the cathode may reach temperatures in excess of 1000 degrees C, low melting materials are to be avoided. Carbon and molybdenum have been found to be most useful. Carbon has relatively good resistance to sputtering erosion by ion bombardment and molybdenum has a relatively high secondary emission yield. Since sputtered material from the interior walls can escape only through the small beam exit aperture, most of it is redeposited on the walls giving them a dull "frosted" appearance. A thin renewable molybdenum liner is employed in larger cathodes rated for 5 kilowatts or more.

Since sputtering erosion is most severe at the ends of the cathode where high energy ions are incident, these parts may consist of circular carbon plates which resist sputtering and whose interior surfaces become good secondary emitters when they develop a coating of sputtered metal.

A composite cathode employing a molybdenum shell and renewable liners and end plates is illustrated in Figure 6. Such a cathode, having an internal cavity 3.5 centimeters in diameter and 4.3 centimeters high with a beam exit aperture 0.8 centimeters in diameter, can develop a 250 milliampere beam of 40 kilovolt electrons from 12 kilowatts of input power. After about 50 hours at this power level, with argon at 4 to 6 microns pressure, the exit aperture becomes

enlarged and the end plates and liner become eroded by sputtering action. This causes a gradual deterioration in beam power density until the eroded parts are replaced. In nitrogen, which has a sputtering coefficient for molybdenum of about one third that of argon, the period between replacements is correspondingly longer.

Water cooling through a length of plastic tubing sufficient to isolate the cathode from ground is employed in cathodes to be operated at power input levels above one kilowatt. This protects the metal-to-ceramic seal and the rubber gasket vacuum seal from heat damage.

Any desired beam current, within the rating of the cathode, can be obtained by means of an automatic pressure regulator. This consists of an electromagnetically actuated needle valve energized by a servo amplifier which maintains constant current in a shunt placed in series with the ground return to the high voltage power supply. This method requires a small continuous flow of gas through the needle valve together with sufficient pumping capacity to insure the desired speed of response.

## BEAM CURRENT DENSITY MEASUREMENT

For some applications, such as electron beam welding, high current density in the focused beam is of prime importance. To insure a finely focused beam, the electron stream issuing from the cathode must have a narrow waist or cross-over point near the exit aperture as illustrated in the diagram of Figure 1. This cross-over is then imaged on the work piece by a magnetic lens, so positioned as to form an image two or three times smaller than the cross-over. In this way, current densities approaching 100 amperes per square centimeter have been attained. Power density, of course, increases linearly with cathode voltage.

Since the beam exit aperture separates two regions differing in electric field strength, it has the focusing properties of an electrostatic lens. This, together with the axially concentrated stream of positive ions entering the cathode, accounts for the constriction of the electron stream into a narrow waist or cross-over. The location and the diameter of the constriction are determined by the cathode

potential, the gas pressure and the diameter and thickness of the aperture plate. These factors, therefore, affect the power density in the focused beam.

Current density measurements are made by passing the focused beam successively through each of a series of holes in a water-cooled copper plate and measuring the transmitted portion. If the transmitted current is plotted as a function of the hole diameter, a curve such as that shown in Figure 7 is obtained. From the slope of this curve, the current density may be derived as follows.

Divide the beam cross section into annular zones of mean radius r and width dr. Then the current dI passing through each zone is JdA, where J is the current density and $dA = 2\pi r\ dr$ is the area of the zone. Therefore

$$dI = 2\pi r J\ dr \quad \text{and}$$

$$J = \frac{1}{2\pi r} \cdot \frac{dI}{dr}$$

Since the current density J is proportional to the slope of the curve shown in Figure 7 and inversely proportional to the radius of the zone, it falls off steeply with r as shown in Figure 8, which is derived from Figure 7. For cathode evaluation purposes, curves of the type shown in Figure 7 are adequate for obtaining peak and average power densities.

To avoid melting and vaporizing metal, the plate containing holes for current density measurements must be water-cooled and the focused beam must be swept over the holes with sufficient velocity and amplitude to avoid melting. A drawing of the beam aperture plate is shown in Figure 9. A pair of Helmholz coils energized by 60 cycle current provides a 15 centimeter sweep amplitude at the beam focus. To reduce the power density of the beam near the turn-around points, a pair of 2.5 centimeter thick water-cooled absorber plates are mounted on either side of the row of holes in the aperture plates. Underneath each plate is a carbon block 3.8 centimeters thick to elevate the absorber plate surfaces well above the focal plane of the swept beam. Photographs of the top and bottom of the absorber plate assembly are shown in Figure 10 and 11. The assembly is mounted on ways so that any one of the holes may be positioned in the beam path.

Beam tracks appearing on the surface of the absorber plates show that some local melting has occurred near the beam turn-around points. However, the beam velocity at the center, where the holes are, is high enough so that no damage is observed at that location.

From oscillograms of the beam current transmitted through the series of holes, the peak instantaneous transmission for each hole size can be obtained. This is the beam current in a circular zone of the same diameter as the hole. To facilitate the routine recording of data, an automatic curve plotter is employed in connection with the oscilloscope.

## FACTORS AFFECTING BEAM CHARACTERISTICS

In electron beam welding applications, high beam power density is an essential requirement for deep penetration. Factors which affect the initial velocity distribution, the distribution of space charge and the electric field configuration near the cathode, affect the beam coherence. Among these factors are cathode aperture diameter, plate thickness, cathode potential, beam current and gas pressure, and composition. To increase the beam power density, the influence of some of these factors on beam current distribution has been investigated.

### Gas Composition

Pure gases or mixtures of gases may be used, however, the heavier gases are preferable because they introduce less spreading of the beam than do the lighter gases. Multiple ionization in the heavier gases may be a factor affecting the efficiency of secondary electron release at the cathode as well as influencing space charge potentials in the beam region. It has been observed that operating pressures for a given beam current have an inverse dependence on the atomic number of the gas.

In a typical hollow cathode, the beam current distribution was measured by the method described in the previous section using argon, nitrogen, and helium as operating gases. For each gas, the pressure was automatically regulated to maintain an input to the cathode of 100 milliamperes at 35

kilovolts. This 3.8 centimeter diameter cathode had a 0.79 centimeter diameter aperture in a 0.28 centimeter thick molybdenum face plate. The current distribution in the beam focal spot is displayed in Figure 12 with the operating gas and its pressure in microns designated for each curve.

These curves show that the ratio of beam current to cathode input current (beam efficiency) increases with the atomic number of the operating gas. Also, it is seen that the beam current density in argon is more than twice that in helium. It is not yet clear whether the observed difference in performance is due to multiple ionization effects, or to differences in the scattering cross sections of the various gases, or to a combination of these.

Voltage and Current Effects

Current distribution curves taken at different levels of cathode potential and input current reveal that both of these operating parameters have an influence on the shape of the curves. This is illustrated by the curves of Figures 13 and 14 representing the focal spot distribution for a 2.5 centimeter diameter cathode of construction similar to that shown in Figure 6. This cathode has a 0.71 centimeter aperture in a 0.32 centimeter thick molybdenum face plate. From these curves, it is seen that the efficiency and the current density in the focal spot are dependent on the cathode voltage and input current.

To obtain 100 milliamperes at 15, 25, and 35 kilovolts (Figure 13), the corresponding gas pressures required were 4.8, 4.3, and 4.0 microns. As would be expected, the current density is less for the lower energy electrons traversing the higher density gas because of the larger scattering cross section for slower electrons. Corresponding to the 15, 25, and 35 kilovolt levels, the average power densities inside the central zone are 28, 160, and 280 kilowatts per square centimeter. By increasing the cathode voltage by a little more than a factor of two, a tenfold increase in power density results.

To increase the current (Figure 14) from 50 milliamperes to 100, the gas pressure was raised from 3.3 microns to 4.0 and finally to 4.9 microns to obtain 150 milliamperes of

input current to the cathode. This not only affects the gas density but the density of ions, and hence influences beam scattering and current density at the focal spot.

## CONCLUSIONS

The foregoing analysis of the mechanism of the shielded hollow cathode discharge is in general agreement with the experimental results reported. Results are explained in terms of a model in which the major portion of the electrons forming the beam originate from ionizing collisions made by secondary electrons accelerated in the space charge sheath surrounding the plasma inside the cathode. Penetration of the strong external electric field through the beam exit aperture maintains the high sheath drop and provides the electrostatic focusing action which is necessary to form a coherent, focusable beam.

By measuring the transmitted portion of the focused beam as it is successively swept across a series of holes of increasing diameter, the radial distribution of beam current is determined. From this, the power density in the central zone can be computed. Such measurements have been extended to power densities in excess of one megawatt per square centimeter in electromagnetically focused beams having unit magnification. Larger densities are obtainable in demagnified focal spots.

Recent applications of the beam forming hollow cathode include electron beam welding, melting of refractory alloys having volatile components, and ionization studies.

## ACKNOWLEDGEMENT

The writer wishes to thank Mr. W. R. Giard for his technical contributions in measuring beam current density.

## REFERENCES

1. Terhune, J. H. and Stauffer, L. H. - "Analysis of a Collimated Hollow Cathode Discharge", Proc. Electron Beam

Symposium - Sixth Annual Meeting, J. R. Morley, Editor April 1964.

2. Stauffer, L. H. - "Self Focusing Electron Beam Apparatus", U. S. Patent No. 3,218,431, Nov. 16, 1965.

3. Boring, K. L. - "Non-thermionic Hollow Cathode Electron Beam Apparatus", U.S. Patent No. 3,320,475 May 16, 1967.

4. Linder, E. G. and Hernquist, K. G. - "Electron Space Charge Neutralization by Positive Ions", Jour. Appl. Phys. 32, 1181, (June 1961).

5. Dunn, D. A. and Self, S. A. - "Static Theory of Density and Potential Distribution in a Beam-Generated Plasma", Jour. Appl. Phys. 35, 113, (January 1964).

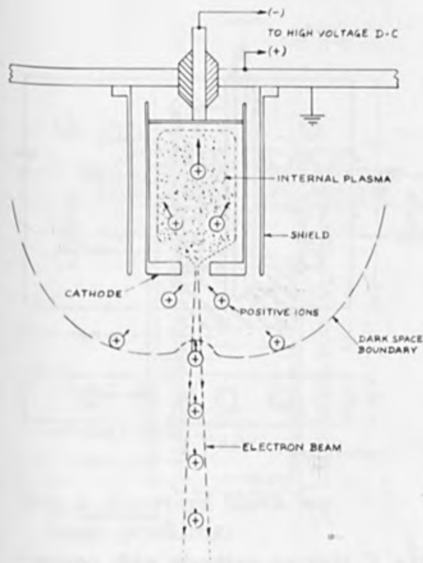


Fig. 1 Beam formation in shielded hollow cathode.

Fig. 2 Focused hollow cathode beam in hydrogen at 50 microns.

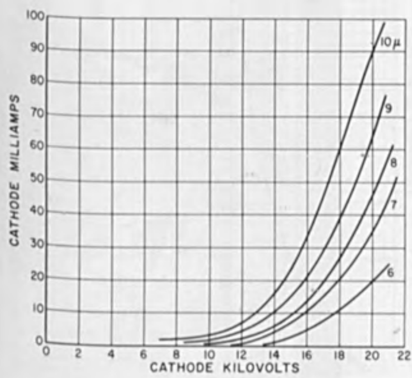


Fig. 3 Current-voltage characteristics of a shielded cathode at various argon pressures.

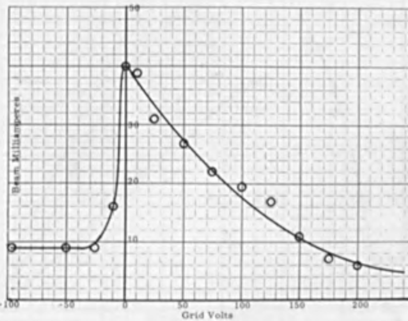

Fig. 4 Beam current response to grid voltage variations.

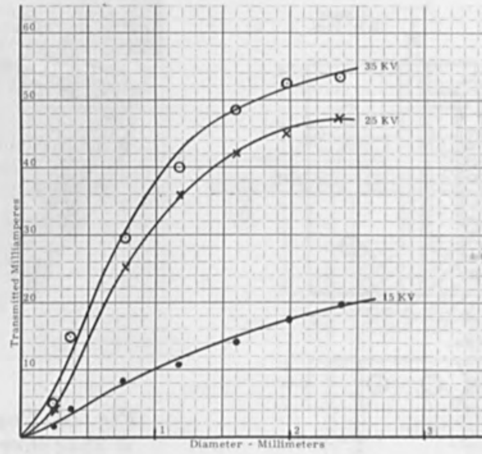


Fig. 13 Effect of cathode voltage on beam current distribution with 100 MA input in argon.

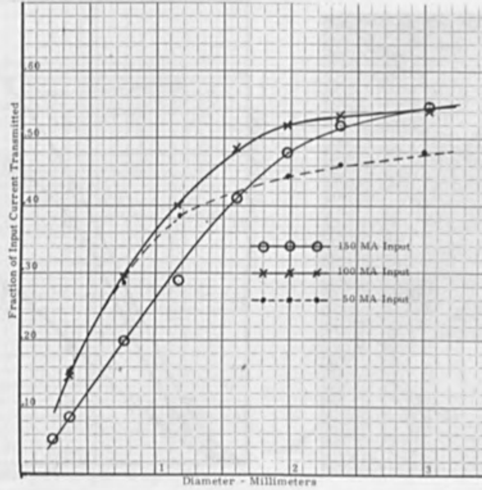


Fig. 14 Fraction of input current transmitted at 35 KV in argon.

# High Output Plasma Electron Beam

Seiichiro Kashu, Shuji Nishino and Chikara Hayashi

Japan Vacuum Engineering Co., Ltd.
2500, Hagizono, Chigasaki-shi, Japan

A characteristics of a maximum output of a 100kw plasma electron beam was investigated. With 1m 800mm cathode-to-anode distance, the plasma electron beam discharge was operated in an active gases (CO, air) atmosphere at the pressure of up to $4 \times 10^{-1}$torr. At this range, the plasma discharge showed a quite stable positive impedance.

## 1. INTRODUCTION

This paper describes some experimental results concerning hot hollow cathode discharge* operated at a large anode to cathode distance with relatively high power level. Application of the discharge as a power source for melting or heat treating of refractory or reactive metals were discussed in several papers,** but the high output, long cathode to anode distance discharge seemed worth studying in consideration of the possible application to large scale vacuum metallurgical processing.

*1)2)3)4)
**5)6)7)

## 2. APPARATUS

Schematic drawing of the apparatus used is shown in Fig. 1. Two plasma electron guns are attached to the upper cover plate of the vacuum chamber of 1.2m in diameter by 2.2m in length. The first gun is located at the centre while the second gun is about 400mm apart from and seventeen(17) degrees inclined to the first one. The two guns can be operated in parallel to study whether appreciable interfernece may occur between the two or not. Each cathode is made of a simple tantalum tube. Each gun can be moved vertically to obtain varied cathode to anode distance. The anode is made of a water cooled copper plate having 0.65m outer diameter. An auxiliary anode is equipped on the side wall of the vacuum chamber. The auxiliary anode is used for starting up the discharge at a large anode to cathode gap. Vacuum pumping system is composed of a $3500m^3$/hr roots blower and a 3000 liter/min rotary piston pump. Two independent D.C. power sources were connected each to each gun. No magnetic coil for constriction of the plasma was used.

## 3. EXPERIMENTAL RESULTS

3-1. Start up of the plasma at large cathode to anode gap. At a cathode to anode distance less than 1m the plasma could be started up with applying a high frequency ($\gtrsim$100KC) starter along with ordinary D.C. generator. For an electrode gap larger than about 1m the plasma could be started without fail by using the auxiliary anode. The plasma was at first generated between the cathode and the auxiliary anode which was inserted in the path between the cathode and anode. The plasma reaches the anode immediately when the auxiliary anode is pulled outside and the positive terminal of the power source is switched in to the anode instead of the auxiliary anode. A plasma of 1.8m in length, which was the limiting length of the apparatus used, could always be generated and maintained stationary.

3-2. Cathode temperature, consumption rate and the limiting current.

3-2-1. Outside temperature of the cathode was measured by using an optical pyrometer. The observed values are shown in Fig. 2. Apparently thin tube is raised to a higher temperature than it is for thick tube. The highest

temperature should be experienced on the inside wall of the cathode tube where ion bombardment rate is very large, but no temperature measurement could be attempted for that portion. The highest temperature on the outside wall is observed at a distance from the end tip of the cathode.

3-2-2. Consumption rate

Consumption rate of the cathode was measured by weight loss measurement. The result is shown in Table 1. It should be noted that the consumption rate at 1500 Amp is less than that at 1200 Amp.

3-2-3. Maximum current

The discharge current is practically limited by either deformation of the cathode caused by excess temperature rise or by leaping of the discharge to the cathode holder. Heat generation at the cathode should be caused by both ion bombardment and joule heating. Heat loss from the cathode will be composed of thermal radiation and the conduction loss to the cathode holder. For the thin tantalum tube cathodes having thickness between 0.5mm and 1.5mm the conduction loss is negligibly small compared to the radiation loss. The joule heat per unit length, on the otherhand, may be even larger than the heat input per unit length of the ion bombardment which is distributed for some area. Practical upper limit of the discharge current for several cathodes used were determined experimentally. The results are plotted in Fig. 4. The temperature of the cathodes operating at the limit was around 2600°K at any case.

3-3. Characteristics of the discharge

3-3-1. Current to voltage characteristics

The current to voltage characteristics are shown in Fig. 5 for four cathodes of different diameter. Anode to cathode distance was kept at 1.4m during the measurements. The current to voltage characteristics at varied anode to cathode distance were also measured and the results are shown in Fig. 6.

3-3-2. Thermal efficiency

The ratio of thermal input to the anode to electrical input measured between the anode and the cathode was calculated as the thermal efficiency. The anode is divided into two concentric copper plate, inner and outer plate, as shown in Fig. 7 so that rough estimation of radial spread of the plasma may be observed. Some results are shown in Fig. 8.

The plasma beam diverges for larger cathode to anode distance. The thermal efficiency is low for a small target as is reported by several authors.*** Constriction of the plasma by using a focussing coil seems required for a small anode. The thermal efficiency observed by using the two guns in parallel is shown in Table 2 and plotted in Fig. 8. Not any appreciable difference was observed for the thermal efficiency with the two guns in parallel compared to single gun operation at an electrical output.

3-3-3. Operation in some active gases
Operation of the cathodes in carbon monoxide gas or air was observed. These atmosphere are quite common in large scale vacuum metallurgical treatment such as melting and degassing. A protective device as shown in Fig. 9 was provided to avoide excess vaporization of the cathode material. Protective argon flow outside the tantalum tube is formed by the device. Fig. 10 shows discharge with the device. Carbon monoxide or air was filled into the chamber up to 0.4torr. The colour of the discharge was changed white immediately after introducing carbon monoxide as shown in Fig. 11. The discharge in CO was continued for 80 min but not any symptom of excess cathode disintegration was observed at the inspection after the experiment. Characteristics of the discharge in CO and air are shown in Fig. 12. Discharge at a CO pressure over 0.4torr was somewhat unstable accompanying voltage fluctuation.

## 4. SUMMARY

4-1. Conventional D.C. generator equipped with high frequency starter is useful for starting up the plasma discharge at a cathode to anode distance up to 1m. For a distance over 1m and auxiliary anode was deviced and proved satisfactory for the distance up to 1.8m which was the limit of the experimental set up used. The discharge with the electrode gap of 1.8m was quite stable.

4-2. Consumption rate of the tantalum cathode was 2 $\sim$ 3 gr/1000 Amp.hr for current of less than 1000 Amp. For a cathode the rate was over 6 gr/1000 Amp.hr at 1200 Amp but dropped to about 4 gr/1000 Amp.hr for the discharge current of 1500 Amp. The reason for the drop is not yet clarified.

***1)2)4)5)6)

4-3. Practical maximum of the discharge current is limited by cathode performance. Within the scope of this investigation using single tubular cathode made of tantalum the maximum current is roughly proportional to the diameter and the root of thickness of the tube.

4-4. Current versus voltage plot of the discharge showed positive characteristics up to 230kw of electrical output and the discharge was quite stable. Further increase in the output will be obtained by using a larger cathode.

4-5. Diversion of the plasma is experienced for a larger cathode to anode distance. For 1200 Amp, 120kw discharge with the electrode gap of 0.75m about 50% of the total input reached the central part of 0.65m in diameter of a circular disk.

4-6. Parallel operation of two hot cathode plasma guns rather closely located each other is feasible. Practically the same beam concentration was observed at the power level and with the electrode gap used in this invertigation.

4-7. Hot cathode made of tantalum tube can be usable in CO or air atmosphere up to 0.4torr, provided the cathode is protected by a reasonable argon flow. A silica tube concentric with the cathode tube is effective to formulate the protective Ar sheath outside the tantalum tube. Over 0.4torr the discharge was not stable.

The hot hollow cathode plasma discharge will be usable as heat source for medium sized or large sized vacuum metallurgical treatment.

ACKNOWLEDGEMENTS

Financial support was made by the Ministry of International Trade and Industry of Japan. The authors are indebted to Mr. Morley for the presentation of this work.

References

1) L. M. Lidsky, S.D. Rothleder, D.J. Rose and S. Yoshida
J. Appl. Phys. 33 8, (1962) p2490-2497

2) J.R. Morley
Proc. 5th Electron Beam Symp. (1963) p369-377

3) J.R. Morley et.al.
Proc. 6th Electron Beam Symp. (1964) p66-82

4) L.M. Lidsky
Proc. 6th Electron Beam Symp. (1964) p53-65

5) J.R. Morley
Trans. Vac. Metallg. Conf. (1963) p186-202

6) S. Kahsu, S. Nishino and C. Hayashi
Trans. Vac. Metallg. Conf. (1967)

7) A.G.S. Morton
Trans. Vac. Metallg. Conf. (1967)

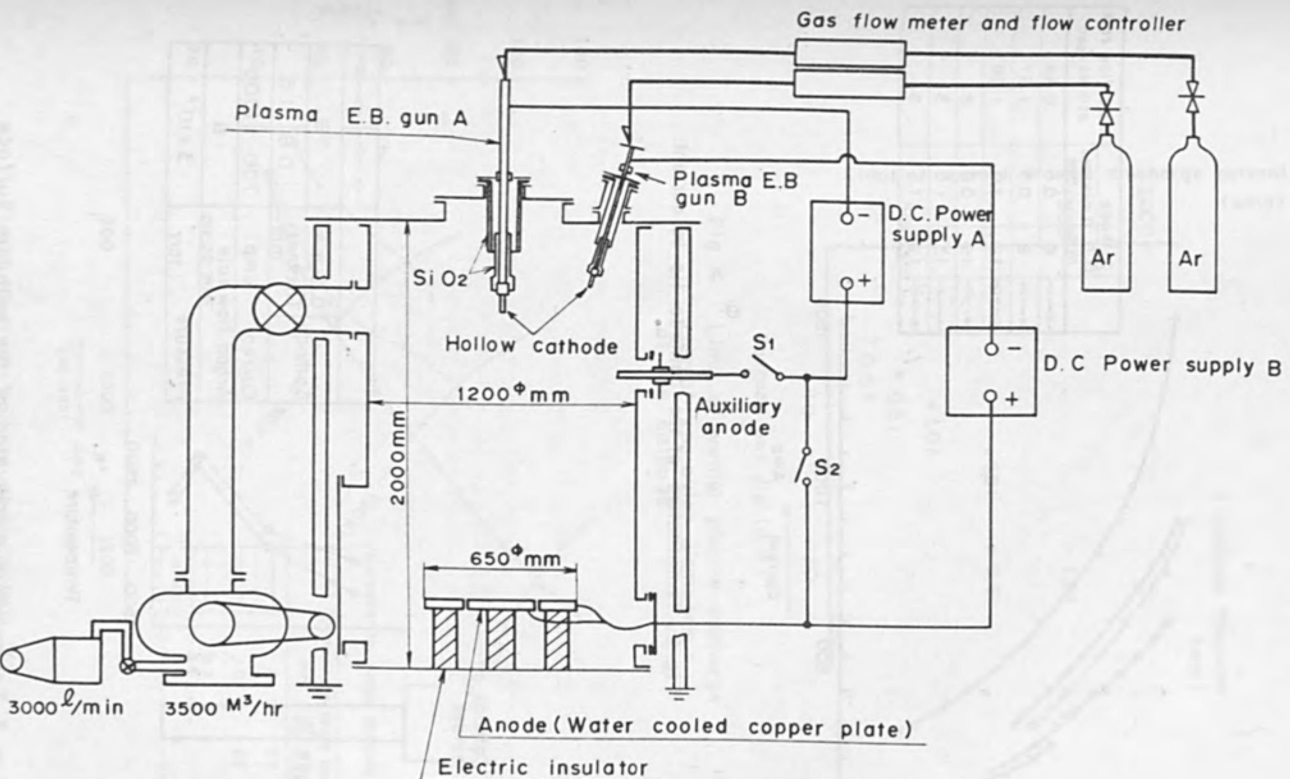


Fig. 1. Experimental arrangement of plasma electron beam guns and anodes

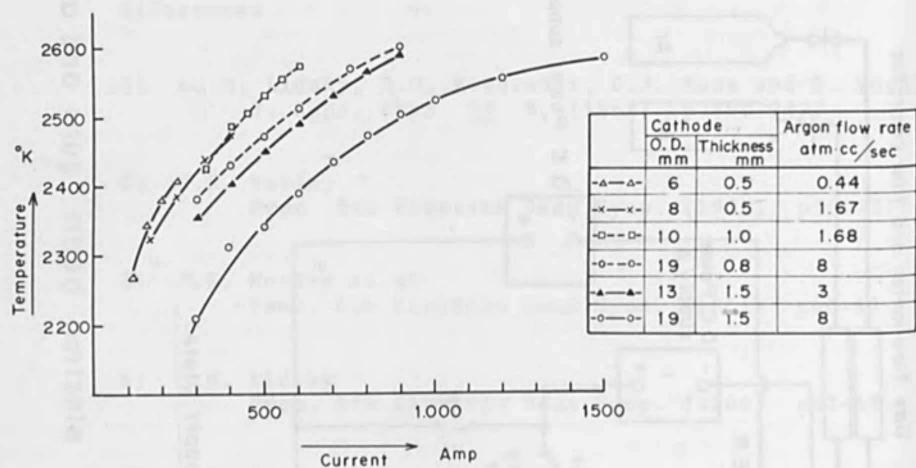


Fig. 2. Temperature of the cathode tip vs. current.

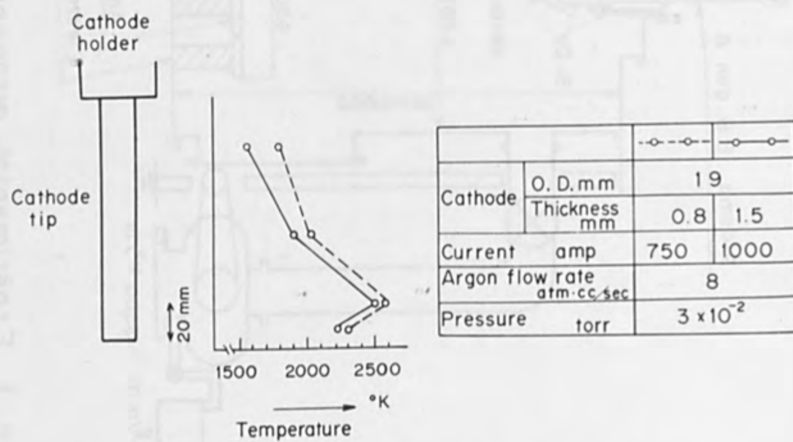


Fig. 3. Temperature distribution of the cothode surface

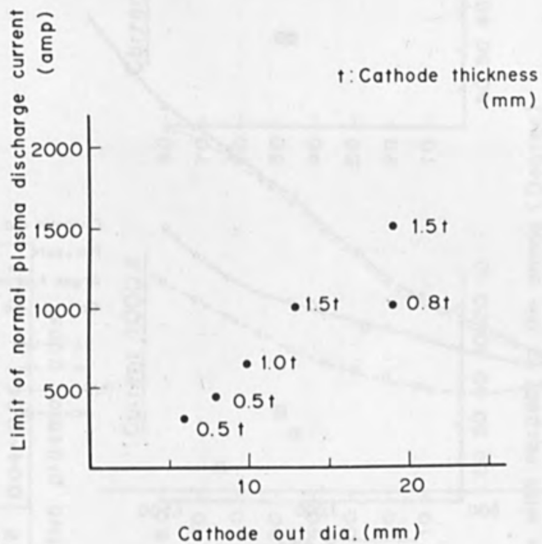


Fig. 4. Limit of normal plasma discharge current vs. outer diameter of the cathode.

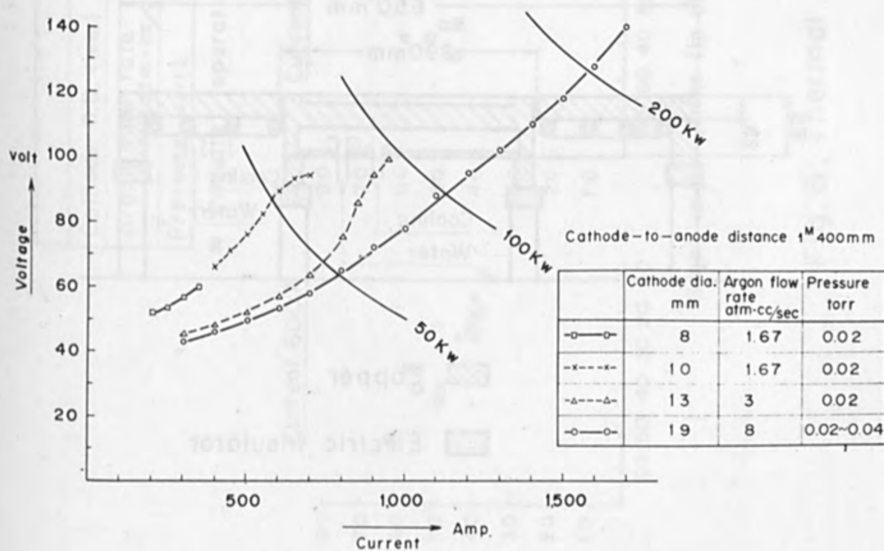


| | Cathode dia. mm | Argon flow rate atm-cc/sec | Pressure torr |
|---|---|---|---|
| -o-o- | 8 | 1.67 | 0.02 |
| -x---x- | 10 | 1.67 | 0.02 |
| -Δ---Δ- | 13 | 3 | 0.02 |
| -o—o- | 19 | 8 | 0.02~0.04 |

Fig. 5. Current-voltage characteristic (I)

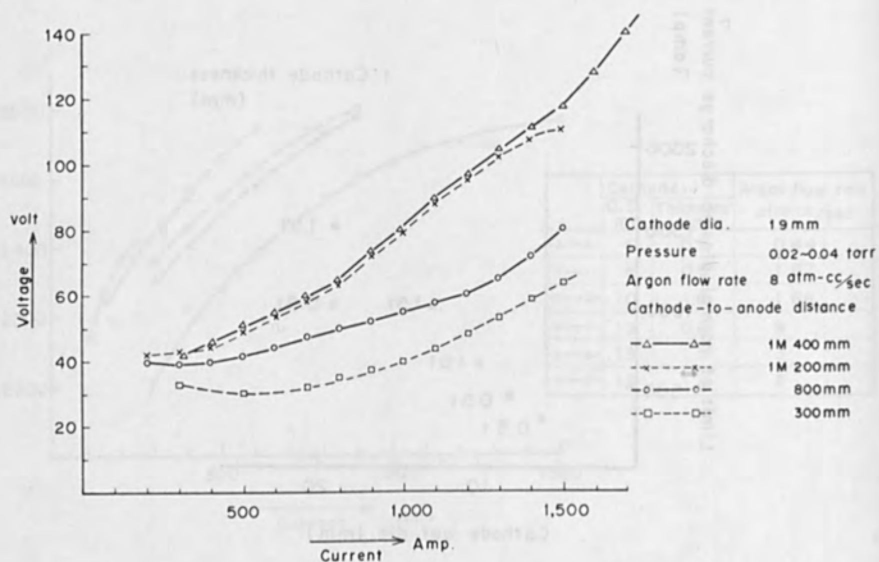


Fig. 6. Current-voltage characteristic (II)

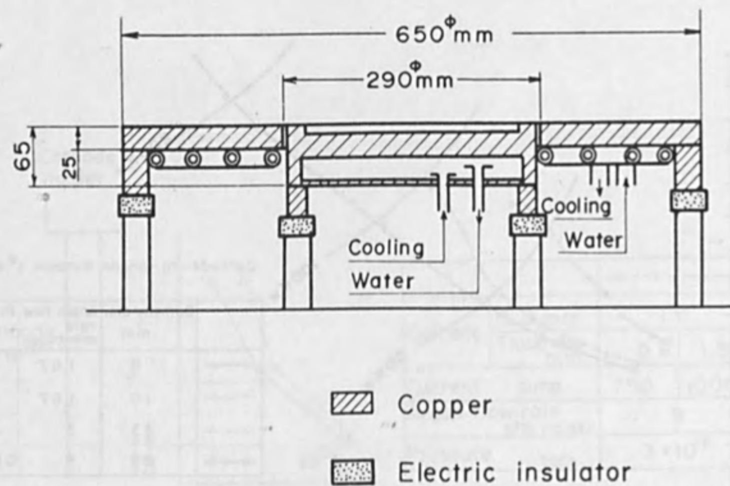


Fig. 7 Anode

| | ○ | × | □ |
|---|---|---|---|
| Cathode O.D. (mm) | 13 | 13 | 19 |
| Argon flow rate (atm-cc/sec) | 4 | 3 | 8 |
| Pressure (torr) | 0.02 | 0.04~0.06 | 0.03 |

■ Parallel operation of the two plasma guns

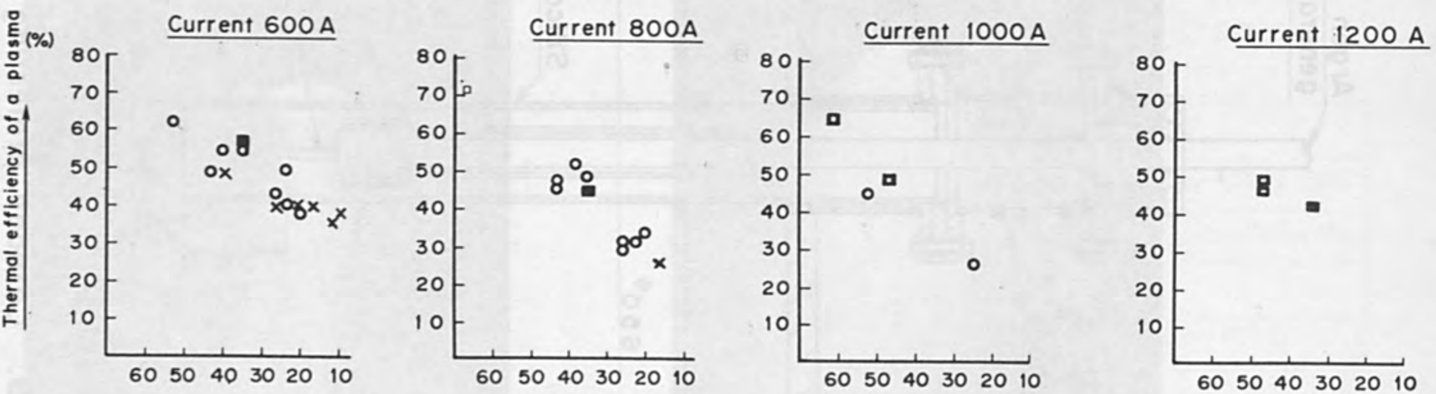


Fig. 8. Thermal efficiency of a plasma

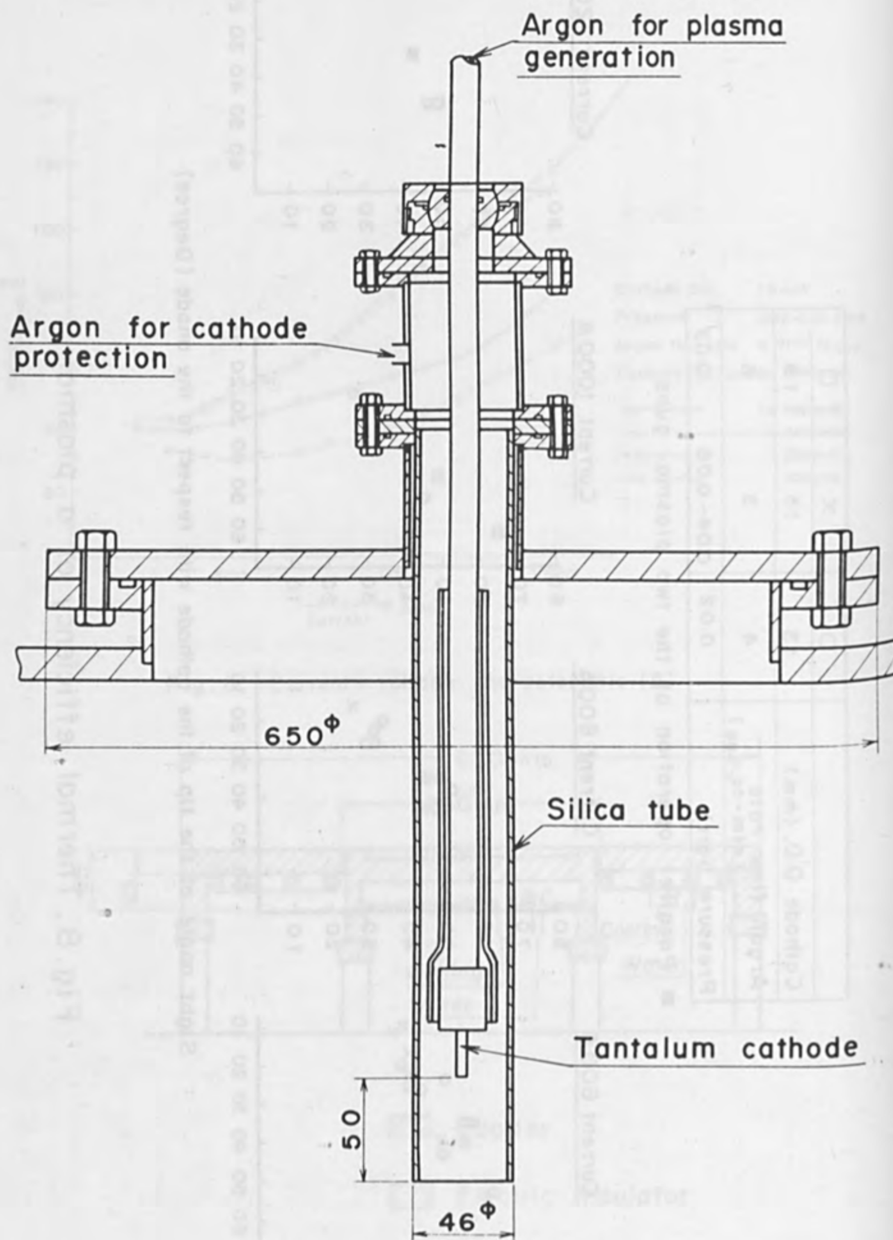


Fig. 9. Cathode protecting method

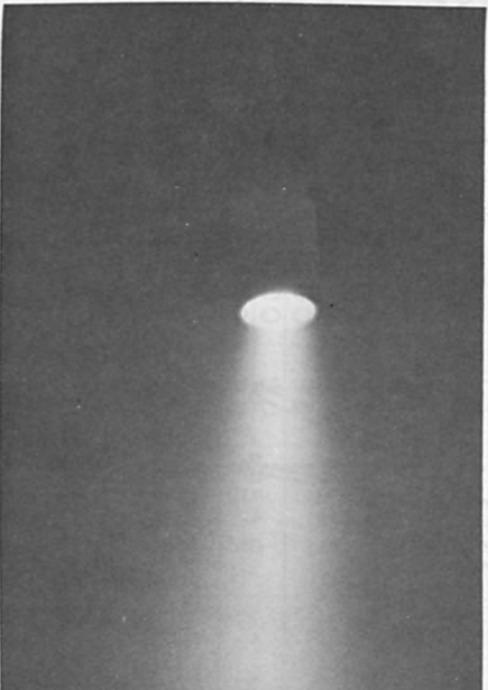

Fig. 10. Plasma discharge in argon atmosphere (with silica tube as shown in Fig. 9)

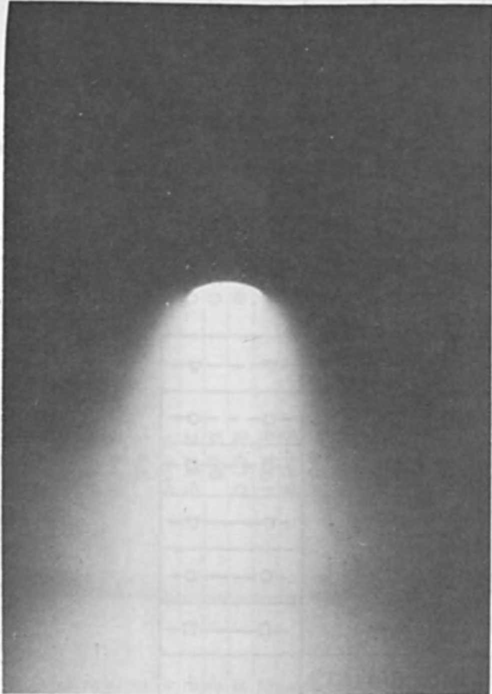

Fig. 11. Plasma discharge in carbon monoxide gas atmosphere (Protective argon flow is prepared by using the silica tube)

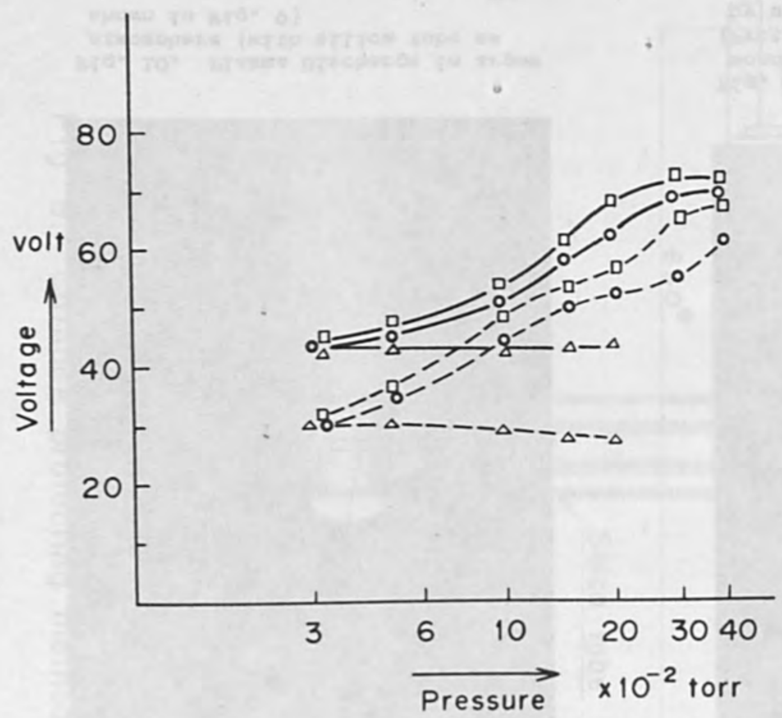


| | Current | Atmosphere |
|---|---|---|
| -□——□- | Amp | Co (P-0.03) torr |
| -o——o- | 1,000 | Air (P-0.03) torr |
| -Δ——Δ- | | Ar |
| -□---□- | | Co (P-0.03) torr |
| -o---o- | 500 | Air (P-0.03) torr |
| -Δ---Δ- | | Ar |

Ta cathode 13 mm O.D.
Argon flow rate (atm cc/sec)
For plasma generation 8
For cathode protection 10

Fig. 12. Characteristic of plasma E.B. in active gas atmosphere

Table. I Consumption of the Tantalum Cathode

| Cathode O.D. (mm) | Current (amp) | Discharging time (hr) | Decrease of the weight of the cathode (gr) | Consumption rate of the cathode A(gr) / 1000(amp) × 1(hr) |
|---|---|---|---|---|
| 8 | 200 | 7.0 | 3.205 | 2.28 |
| | | 10.5 | 4.566 | 2.17 |
| | 300 | 8.0 | 8.344 | 3.48 |
| | 400 | 15.5 | 15.988 | 2.76 |
| 10 | 300 | 6.0 | 5.459 | 3.03 |
| | 400 | 8.0 | 8.751 | 2.73 |
| | 500 | 7.0 | 9.410 | 2.68 |
| | 600 | 5.0 | 8.28 | 2.76 |
| 13 | 500 | 2.0 | 2.215 | 2.215 |
| | 700 | 1.03 | 1.685 | 2.33 |
| | 800 | 0.8 | 1.46 | 2.28 |
| | 850 | 0.5 | 0.877 | 2.06 |
| | 900 | 0.76 | 1.593 | 2.32 |
| | 950 | 0.63 | 1.962 | 3.27 |
| 19 | 1200 | 0.33 | 2.445 | 6.11 |
| | 1500 | 0.25 | 1.565 | 4.16 |

Table II Parallel operation of the two plasma guns

| Operation (No.) | Plasma gun | Current (amp) | Voltage (V) | Electrical out put (Kw) | Thermal efficiency (%) |
|---|---|---|---|---|---|
| P-1 | A | 300 | 50 | 28.5 | 55.5 |
| | B | 300 | 45 | | |
| P-2 | A | 500 | 41 | 31.3 | 45 |
| | B | 300 | 36 | | |
| P-3 | A | 800 | 50 | 55.6 | 42 |
| | B | 400 | 39 | | |
| P-4 | A | 1.000 | 70 | 95 | 38 |
| | B | 500 | 50 | | |

Cathode Dia.
Gun A 19 mm
Gun B 13 mm

Cathode-to-Anode Distance 1 M
Anode Dia. 650 mm

SOME OBSERVATIONS ON HIGH POWER ELECTRON
BEAMS UNDER WATER*

B. W. Schumacher
Westinghouse Research Laboratories
Pittsburgh, Pa. 15235

ABSTRACT

A beam of 145 kV electrons with 9 kW beam power and about 1.5 mm diameter was fired into water from a submerged electron gun. A narrow vapor cavity formed within which the beam energy was dissipated. Its fluctuating appearance was recorded in a motion picture. The average shape, as recorded in long exposure photographs, is pear-shaped, about 2" deep and 1/2" at its widest point. An x-ray picture taken with a pinhole camera shows that the major energy dissipation takes place at the bottom of the vapor cavity. To the eye the color of the "beam" under water is bluish-green. A survey spectrogram which was taken shows a few lines, no bands, but a considerable continuum. The various gas-focusing and pinch effects which may contribute to the deep penetration phenomena, in addition to vapor formation in the beam path, are discussed in a qualitative manner.

INTRODUCTION

At high power levels electron beam penetration into a target is no longer governed by simple particle scattering but rather energy controlled processes dominate.* An initially homogeneous target will become inhomogeneous, as was first pointed out a long time ago.[1] All deep penetration processes in electron beam cutting and welding are based on this phenomenon: the electron beam heats the gas or vapor through which it travels, thereby reducing the density to such a degree that the beam travels in a rarefied gas space (produced by heating rather than reduction of pressure). Scattering and energy loss are reduced accordingly and the "range" at the electrons increases. This is also true for "solid" targets because of the high power density levels in the commonly used beams every solid is melted and vaporized within a few milli-seconds.

While energy controlled phenomena like vaporization and super-heating of the vapor by the beam reduce the electron scattering and thereby can more

---------

*The criteria for the onset of the energy controlled processes are discussed elsewhere.[2]

or less account for the deep penetration phenomenon** there may be, in addition, focusing mechanisms which keep the unscattered electrons together. But observations or measurements on the beam generated vapor plasma are very difficult because of the narrow confinement and the extreme temperatures between 10,000° and 100,000°K. In fact this beam generated, high pressure plasma has hardly received the attention which, I believe,[4] this new and unique phenomenon deserves.

Since water is a transparent target and one can see what happens we thought it interesting to fire a high power electron beam of 9 kW at 145 kV into water from a submerged gun; the following is a discussion of some preliminary observations.

EXPERIMENTAL

The Westinghouse atmospheric electron beam gun has a small overpressure chamber between the vacuum column and the atmosphere to prevent debris from being sucked into the vacuum. Therefore, it can also be submerged under water to moderate depth. Gas emerging from the over-pressure chamber forms bubbles in the water; to reduce disturbances by these gas bubbles an additional baffle plate with a 1/32" hole was mounted in the water a small distance from the gun orifice, as shown in Fig. 1. The water below this baffle stayed quiescent. As for the electron gun, a description can be found elsewhere.[5,6]

---------

** A quantitative appraisal of the importance of electron scattering in the super-heated vapor path was attempted in another paper.[3]

OBSERVATIONS AND DISCUSSIONS

The moment the beam is switched on a bluish-green glow appears in the water throughout a vapor cavity which is formed by the beam and which is about 2" long and 1/2" wide at its widest point. Fig. 2 shows the appearance of this glow in a selection of frames from a motion picture. These short exposure photographs show the continuous fluctuation and variation in the shape of the vapor cavity. In contrast Fig. 3 shows a long exposure photograph of the electron beam under water. The random fluctuations of the cavity are evened out and a surprisingly symmetrical shape appears. At the bottom of the cavity the fluorescence outside the bright core assumes a conical shape with nearly straight boundaries. This is an averaging effect over the "wings" which one can see in some frames of Fig. 2. It is probably a hydrodynamic phenomenon.

In size and shape this vapor cavity in the water is surprisingly similar to the cavity which a stationary electron beam will drill in a piece of rock, for instance in a sandstone as shown for comparison in Fig. 4. Both, water and sandstone are elements of low atomic number. Why this shape may differ for targets of high atomic number is being discussed in another paper.[3]

The luminescence of the electron beam region in the water is surprisingly faint compared with the similar fluorescence produced by the same beam in atmospheric air. The bluish-green color is also different from the blue color one sees in air. To get some idea about the composition of the fluorescence in the water we took a spectrum with a 1.5 meter grating spectrograph. The water basin had a Lucite window, and quartz lenses were

used to collimate the light that we might see as much of the ultra-violet region as possible. The light collection efficiency was not very good and the luminosity was weak, as mentioned, therefore exposure times of 30 minutes were needed to record a spectrum. Its character was completely different from what one usually sees in air or in metal vapors. A number of distinct lines appeared, but none very intense,at first glance no bands were visible, such as are very prominent in the air spectrum, but some band heads could later be identified. Surprising was a relatively strong continuum stretching from 3750 A to 4700 A. (Orthochromatic film was used)

Several explanations for the continuum are possible but none can be proven at present. A black body (thermal) continuum would be more intense in the red. It cannot be Cerenkov radiation because the speed of the electrons is just marginal to produce Cerenkov radiation in water. It is possible that the continuum is the visible end of the brems-radiation spectrum which should continue from the x-ray range into the visible and infrared regions with roughly equal intensity per frequency interval. However, not much information seems to exist concerning the visible region. The fact that the spectrum showed no continuum below 3700 can be explained by absorption of the shorter wave lengths. That a continuous spectrum of this nature should look bluish-green to the eye could be explained on the basis of the sensitivity function of the human eye.

Of the lines found in the spectrum the following were tentatively identified: the whole Balmer series appeared due to the hydrogen atoms from the disassociated water vapor. Intensities were roughly as follows: $H_\beta$ medium strong, $H_\gamma$ medium strong, $H_\delta$ very weak, $H_\xi$ medium, $H_\zeta$ strong. Of

the He II lines only the strongest of the Fowler series showed, namely 4685 Å, medium intensity. Other helium lines were as follows: 5016 Å medium strong, 3665 Å medium, 4922 Å medium, 4388 Å medium, 4472 Å strong. Of the band heads of the $N_2^+$ system, the ionized molecule of nitrogen, the bands of which show very prominently in air, only the following showed up: 3914 Å weak, 4278 Å weak, 4709 Å weak, 4652 Å weak, 4600 Å weak. Of the $N_2$ second positive system only the following showed: 4417 Å weak. The following lines attributed to the nitrogen atom appeared: 4100 Å and 4112 Å very weak, 4447 Å weak, 4642 Å weak. The only line which may be attributed to the oxygen atom was 3947 Å very weak. But the spectral range of the spectrograph did not cover the oxygen lines and others in the red and infrared region, which one may expect to find.

In passing it should be mentioned that with NaCl added to the water the yellow sodium lines appeared, as one would expect.

Information about the energy dissipation of the electrons can be obtained from an x-ray pinhole camera picture as shown in Fig. 5. A long exposure was chosen, 12 minutes, to record even the regions where only a few x-rays are produced. The right-hand picture of Fig. 5 is a short exposure copy from the x-ray film. The left picture in Fig. 5 is a long exposure copy from the same x-ray film. The outline of the cavity in each picture is an isodensity curve. In the left picture one can see the somewhat higher x-ray intensity in and along the central axis of the cavity, along the electron beam path. However most of the intensity comes from the bottom third of the cavity. The bright region at the very top is probably produced by x-rays from the metal aperture through which the beam passes. On the other

photograph taken with visible light, Fig. 3, this bright beam core can be seen at the top of the cavity. However, in the light-picture there is no indication of the high energy dissipation at the bottom of the cavity.

A few general observations may be added here. The 9 kW of beam power going into the water will of course heat the water; this was quite noticeable although we used a basin with a volume of about 25 liter. While no boiling or bubbling of any kind was seen beneath the orifice plate as long as the electron beam was off, boiling occured as soon as the electron beam was on. To vaporize the amount of water in the visible cavity, having initially a volume of roughly 2.5 $cm^3$ requires an energy of 6 kW seconds, which the 9 kW beam can supply in 0.7 seconds.

While initially the cavity may be slimmer, and therefore form faster, a noticeable time is required. Checking the movie films which contained several turn-on sequences, one frame was found where the cavity was only about half formed, as shown in Fig. 6. In other sequences the first frame showed a cavity at least 3/4 formed or fully developed. Since the film speed was 8 frames per second this places the formation time for the vapor cavity also in the order of 0.2 seconds.

From the depths of the cavity and the maximum range which a 145 kV electron can possibly travel one can arrive at another estimate about the conditions in the cavity. Let us assume some electrons go straight down the center of the cavity and have a residual energy of 45 kV left when they hit the water surface, which means they suffer an energy loss of 100 kV in the vapor. The range $R_\xi$ of 145 keV electrons in a light element such as water is .030 $g/cm^2$, the residual range of 45 keV electrons is .0042 $g/cm^2$ hence

the energy loss of 100 keV would require a layer density of .026 g/cm$^2$. Since the depths of the cavity is 6 cm the average density $\rho_{av}$ would have to be 4.3 mg/cm$^3$. This would be four times the density of air, which seems rather high. The assumption that electrons lose 100 keV is probably wrong, they may lose much less energy before they hit the water surface; hence the high brems-radiation which is evident from Fig. 5 as coming from the bottom of the vapor cavity, where the electrons hit the water. This is consistent with what Schwarz[7] found for metals. It is reasonable to expect that the electrons must give most of their energy directly to the water because heat transfer rates from the vapor to the water would hardly be high enough to sustain this big energy flux. Little of this energy goes to the walls of the vapor cavity, at least in targets of low atomic number.[3]

In this connection a brief analysis of the focusing forces which we may expect to hold the beam together in spite of electrons scattering is also of interest. At least in some cases it seems the beam remains confined to a much larger degree than electron optical considerations, for instance the initial angular aperture of the beam, would suggest. Such focusing phenomena have variously been named pinch effect or gas focusing. There is more than one phenomenon which produces a pinch action on a beam of charged particles and it may or may not be essential that residual gas ions are present. The various situations which may exist shall be discussed with reference to Fig. 7. In Fig. 7(a) a current flowing through a metallic conductor is shown schematically. Only the electrons move, however we have complete charge neutrality outside, as well as inside the conductor; we find a magnetic field $\vec{H}$; its annular field lines produce a pressure towards the

center of the conductor, as is well known.

Probably the first discussion of this magnetic pinch action is the one by E. F. Northrup[8] at the New York meeting of the Physical Society in March 1907; he already called it a pinch phenomenon. One can build electromagnetic pumps for liquid metal on this basis, and the effect is often shown in the better experimental physics lectures.[9]

If we have a gaseous conductor, a plasma, the positive ions as well as the negative electrons move, in opposite directions, and we find again complete charge neutralization. The electron current and the ion current are equal and parallel in the conventional sense for the current flow which is that of the positive ions. It was pointed out by W. H. Bennett[11] that the annular magnetic field around this current can constrict the discharge, and this is usually meant when the pinch effect is mentioned today. A numerical analysis shows that currents in the order of 1000 A or more are needed to produce a noticeable pinch, large enough to overcome the gas pressure. Pinch discharges are therefore typically of the short duration type.

In Fig. 8(c) it is indicated what may occur if a beam of fast electrons, say 1 keV or more, travels through a rarefied gas. The fast electrons ionize the residual gas molecules; the electrons which are knocked off the atoms and which move rather slowly compared with the beam electrons (but still much faster than the heavy ions), are projected out of the beam. If they can reach the anode or a wall at anode potential then the beam region is left with an excess charge of positive ions. These positive ions of course attract the electrons of the original electron beam towards the center of the beam path. This is commonly called gas focusing and

was utilized in some of the old-fashioned cathode ray tubes. The focusing effect is lost either if the primary electron beam has a much higher energy, and produces consequently much less ions per centimeter path length, or if the primary electron beam is deflected rapidly so that the rather inert ion column cannot follow the beam. The conditions which must be fulfilled to observe this kind of gas focusing at higher beam voltages have recently been discussed by Halsted and Dunn.[12] It seems from these discussions that typical welding beams never have the necessary perveance to fulfill the conditions for simple gas focusing, as long as they travel through a vacuum chamber. However, as soon as a beam of, say, 50 mA passes through a narrow capillary the "knock-off electrons" from the ionization processes can reach the walls immediately and a strong plasma sheath field could develop. The quantitative aspects of this process, a high-power electron beam going through a narrow capillary with residual gas present, should be analyzed in detail. No such analysis is known to the writer.

The situation which we encounter if an electron beam of high speed electrons travels in a good vacuum is shown in Fig. 7(d). Simplifying the picture somewhat we may say; two rows of electrons are moving along in the same direction and parallel to one another. This represents two parallel currents. There is no space charge neutralization and the two rows of electrons, representing negatively charged cylinders, repulse one another. On the other hand, since the electrons move, the corresponding annular magnetic fields $\vec{H}$ produce an attraction. The magnitude of the electric field is determined by the number of electrons present, the magnitude of the magnetic field, which is proportional to current, is not only determined by the

number of electrons but also by their speed. The magnitude of the electrostatic repulsion being known and the magnitude of the magnetic attraction being known, Wilhelm Weber, in 1856, has asked himself at what speed of the electrons the forces would cancel one another. In modern terms when would $\vec{v} \times \vec{H} = \vec{E}$? The numerical result of Weber's calculation yielded $\vec{v} = \vec{c}$, the velocity of light.[10] This was historically a first hint for the connection of electrical and optical phenomena. For practical purposes it is important to note that $\vec{v}$ comes close to $\vec{c}$ for electron energies in the order of only 1 MeV. The so-called space charge spread, which is so troublesome for low energy electron beams, is therefore already considerably reduced for beams in the 1 MeV range. If now in addition, just a few gaseous ions are present in the beam path, the residual space charge repulsion is easily compensated and the beam kept together.[13] This is called the relativistic pinch effect. It becomes noticeable with already very weak beams and is in this respect completely different in its behavior from the Bennett pinch. A discussion of the relativistic pinch can be found in the better physics textbooks; recently Meltzer[14] has pointed out its importance for beams in the 100 keV region.

Finally a pinching mechanism shall be mentioned which, to the writer's knowledge, has not been discussed before. It may be called "image force pinch." When a high speed electron beam travels through a capillary in a conductor and off-center to the axis an image charge travels parallel to it in the conductor wall which is closest to the beam. There is an electrostatic attraction between image charge (which is positive) and beam electrons, but there is also a magnetic repulsion. The electrostatic attraction can be shielded by the presence of a few ions, yet the magnetic

repulsion remains, as found previously in the relativistic pinch. Besides, the magnetic repulsion by the image force has the tendency to push the beam to the center of the capillary.

One may ask the question whether the image charge is really moving; a stationary negative charge along a wire inside the capillary would certainly not be repulsed. But this is not a good analogy for an electron beam of fast electrons. A simple calculation can show the difference:

A current of $I = 0.1$ A corresponds to a flow rate of $n_e = 6.3 \times 10^{17}$ electrons/sec. At about 130 keV the electrons possess a velocity of $v_e = 1.8 \times 10^{10}$ cm/sec. This means the number of electrons per cm path length is $n_1 = n_e/v_e = 3.3 \times 10^7$ electrons/cm. If the beam cross section is $A = .01$ cm$^2$ the space occupied per electron is $V_{e1} = A/n_1 = 3 \times 10^{-10}$ cm$^3$/electron, which means that the electrons are spaced at an average distance of $D_e = .67 \times 10^{-3}$ cm. As soon as the edge of the electrom beam approaches the capillary wall to a distance in the order of $10^{-3}$ cm the beam electrons will indeed appear as separate entities and will be accompanied by moving image charges.

Still another curious aspect of electron beam currents deserves to be mentioned. If 1 A of current is carried in the beam by $6.3 \times 10^{18}$ electrons/sec at speeds of $10^{10}$ cm/sec and passing into a metal conductor, then it will require $10^{10}$ times this number of electrons at the marginal possible speed of 1 cm/sec to carry this current in the metal. How does the transition proceed in detail? One may also ask how image-charges could flow as fast as the electrons. Can image charges flow in a plasma? What can image-current forces do to a beam passing through a plasma where the "conductive wall" could by infinitely close to the moving beam electrons if the beam creates steep density gradients ?

Yet another aspect of beam passage through conductive narrow ducts (capillary or vapor channel) should be mentioned: if, by a sudden movement the beam (or in this case any filament of current, e.g., a wire) is pushed toward the wall, then this displacement produces eddy currents which tend to counteract the movement.

A quantitative treatment of image current focusing or beam centering will be rather involved. A simple experiment is planned, namely to pass a slim beam through a capillary (an aperture will not do) and move it mechanically to see whether the beam follows. One hint that these forces exist is available in the observation that electron beams can be more easily aligned at capillaries with a conical entrance than with a sharp edge.

These last questions were mainly raised to show that we are far from a full understanding of electron beams. It is hoped that the observations and discussions which were presented here will stimulate further interest in electron beam physics.

ACKNOWLEDGMENTS

I want to thank Mr. C. R. Taylor for his able help with the experiments.

REFERENCES

1. B. W. Schumacher, Am. Phys. (6) 13, 404, 1953.

2. B. W. Schumacher. This conference, Paper and Abstract No. 116.

3. D. C. Schubert and B. W. Schumacher. This conference, Paper and Abstract No. 127.

4. B. W. Schumacher, Can. J. Phys. 35, 239, 1957.

5. B. W. Schumacher. This conference, Paper and Abstract 151; also "1961 Transactions of the Eighth Vacuum Symposium and Second International Congress" Pergamon Press, N.Y. 1962, p 1192.

6. J. Lempert, IEEE Electric Welding Conference, Nov. 15-17, 1966 Detroit, Michigan. IEEE Transact. on Industr. General Applic., Vol. IGA-3.

7. H. Schwarz, "Mechanism of high-power-density electron beam penetration in metal," in: Electron and Ion Beam Science and Technology (R. Bakish, Ed.) p. 138, J. Wiley and Sons, New York 1965.

8. E. F. Northrup, Phys. Rev. 24, 474, 1907.

9. R. W. Pohl, Introduction to Electricity, 11th Ed. Springer-Verlag, Berlin 1944, p. 190. (In German.)

10. ibid; p. 88.

11. W. H. Bennett, Phys. Rev. 45, 890, 1934.

12. A. S. Halsted and D. A. Dunn, J. Appl. Phys. 37, 1810, 1966.

13. J. J. Budker, CERN Symposium on High Energy Accelerators and Pion Physics, Proceedings, Geneva 1956, p. 68.

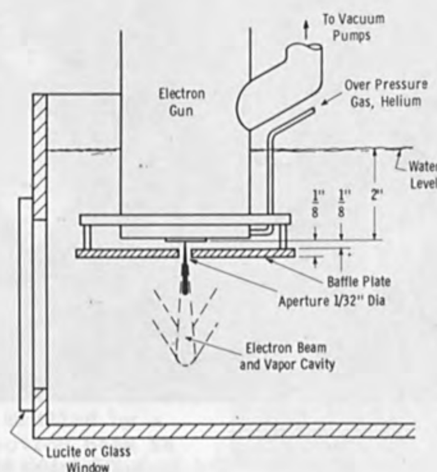


Fig. 1 Experimental arrangement for observing 9 kW electron beam in water

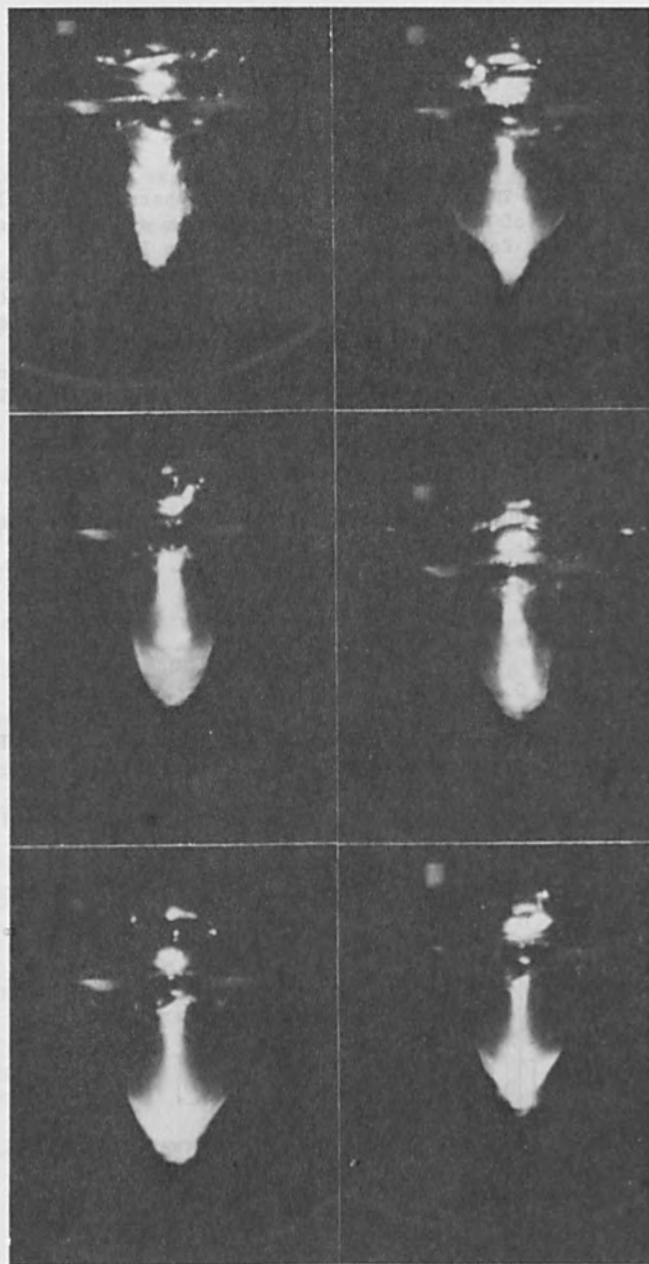

Fig. 2 Luminous vapor cavity produced by a 9 kW 145 kV electron beam in water. Random selection of frames from a movie film taken at 8 frames per second, with f:1.4 on Kodachrome II, Type A.

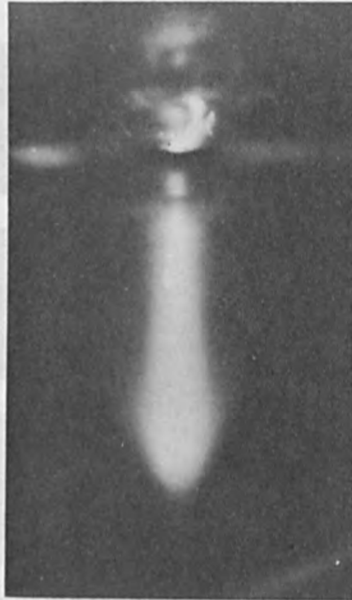

Fig. 3 Long-exposure picture on Polaroid color film; fluctuations of the cavity's shape are evened out.

Fig. 4 Cavity drilled by a 145 kv 9 kW electron beam in a piece of sandstone, having the same shape as the water vapor cavity.

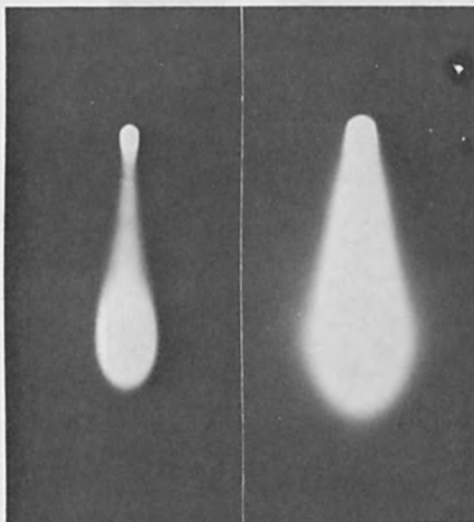

Fig. 5 X-ray picture taken with pinhole camera; pinhole .06" diameter, distance beam-pinhole 6-1/4" (including 3" of water), pinhole-film 6-1/4", exposure 12 minutes. Left picture a short exposure copy from the same negative.

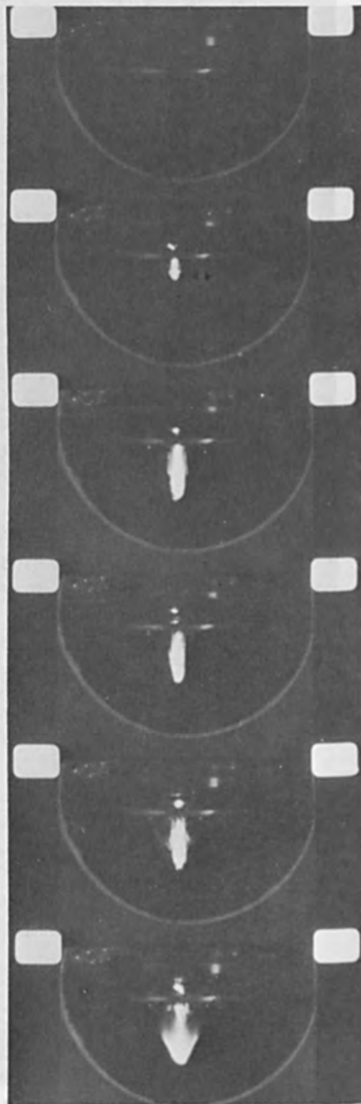

Fig. 6 Frame sequence showing the turn-on of the electron beam; a partly formed cavity can be seen on the second frame, film speed 8 frames per second.

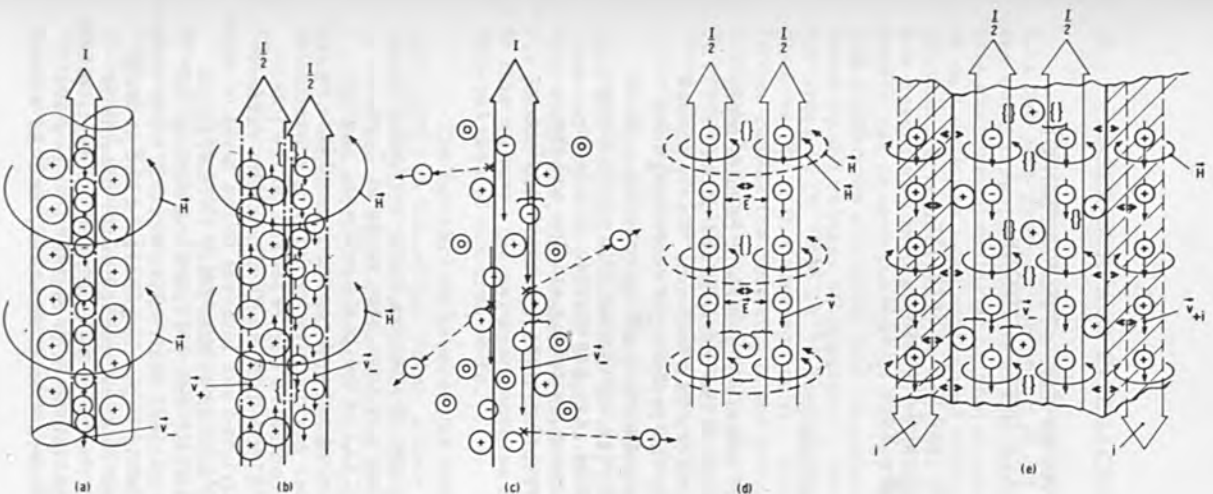


Fig. 7

The various pinch and self-focusing mechanisms in electric currents; $v_+$ and $v_-$ indicate the velocity of the positive and negative carriers respectively; $n_-$ and $n_+$ is number density; the sign ≪≫ denotes repulsion, the sign {} denotes attraction between particles or currents.

(a) Current through solid or liquid metal $v_+ = 0$, $v_-$ low, $n_-$ high; complete charge neutrality. Pinch for large values of current.

(b) Current through plasma (electric arc), $v_+$ and $v_-$ low, $n_+$ high, and complete charge neutrality. Pinch for large values of current.

(c) Electron beam in rarefied gas (poor vacuum); $v_-$ high (.1c), $n_-$ moderately high, no charge neutrality, atomic electrons ejected; $v_+ = 0$ ion column in beam path leading to "Gas Focusing" if certain conditions are fulfilled.

(d) Electron beam in good vacuum; $v_-$ very high (.6c), $n_-$ low, $n_+$ very low, $v_+ = 0$, residual E compensated by $\vec{v}_- \times \vec{H}$; "Relativistic Pinch.

(e) Electron beam passing through metal capillary. In addition to gas focusing and relativistic pinch "Image -Current-Focusing" due to $\vec{v}_+ \times \vec{H}$ ($v_+$ being the velocity of the positive image charge, produced by the electrons, in the metal).

# RECENT DEVELOPMENTS IN THE APPLICATION OF LASER-SURFACE INTERACTIONS

A.S. Gilmour, Jr. and R.J. Clark, Jr.
Cornell Aeronautical Laboratory, Inc.
Buffalo, New York 14221

## ABSTRACT

A review is given of selected, pertinent results from more than four years of study of the interactions between laser light and metallic surfaces in a vacuum. Early phases of the study concentrated on the problem of extracting ions from the metallic plasma produced by the interaction. More recent studies, which have been concerned with applications of the laser generated plasma, are presented. These include high-power, high-current switching studies and the development of pulsed plasma thrustors for space applications.

## I. INTRODUCTION

It is the purpose of this paper to discuss laser-surface interaction and some of the applications that have been made at Cornell Aeronautical Laboratory, Inc. (CAL) of the basic process. Laser-surface interaction is a rather broad area of research, and it is necessary to put this work in the proper perspective by defining a particular region of interest. We have concentrated our research on the interaction of focused radiation from a ruby laser with a metallic surface in vacuum, and have further restricted our interest to the level of incident radiation that is sufficiently intense to that there is interaction between the radiation and the material emitted from the surface but below the level where major mechanical destruction occurs. The interaction is thus one in which a metallic vapor is generated and at least partially ionized, and in which the internal energy of the plasma is increased to several tens of electron volts by continued interaction with the radiation. The rest of this presentation is divided into two sections — the first describing the interaction phenomena, and the second discussing applications.

II. LASER-SURFACE INTERACTION

The interaction of the laser radiation with the target material is a two step process composed of the removal of target material from the solid target surface by evaporation and the addition of energy to this evaporated material by photon-particle interaction. Since much of our work has been performed with a laser pulse length of 30 nanoseconds, it is necessary to consider only evaporation processes which are essentially instantaneous. The mechanism by which the target lattice can absorb the optical energy is through the excitation of valence and conduction electrons and the subsequent relaxation of these electrons by the release of phonons.[1] The relaxation time is rapid -- on the order of $10^{-10}$ to $10^{-11}$ seconds for the generation of acoustic phonons ($E_p \sim 0.1$ electron volt). The energy thus added to the crystal lattice causes the breaking of the lattice bonds, and the target material instantly becomes a high density fluid. The threshold optical energy to produce a sufficiently high rate of electron excitation is estimated to be about $10^3$ to $10^4$ joules per cubic centimeter, a level easily achieved with low-power ruby lasers and simple optics.

The expanding vapor is assumed to be partially ionized by surface and thermal ionization, so that there are free electrons in the blow-off vapor to provide a means of further energy absorption. The free electrons, in conjunction with the metallic ions, provide the means for photon absorption through the inverse bremsstrahlung mechanism. In this manner, the particle energies in the plasma are elevated to several tens of electron volts.

The interaction between the optical radiation and the plasma is terminated in one of two ways: either the optical radiation is removed (laser radiation is terminated) or the plasma becomes too diffuse to to maintain an appreciable level of photon-particle interaction. The energy and particle content of the resultant plasma is the basis for any uses to which this interaction product might be put.

### Characterization of the Laser-Generated Plasma

The typical laser-generated plasma plume has been found to have high energy ions (and sometimes a high percentage ionization), to have have a high expansion velocity and to expand in an anisotropic fashion. When a large area probe was placed in a tungsten plasma generated during long-pulse ruby laser illumination of a cold tungsten target, the current-voltage characteristic shown in Figure 1 was obtained. The average electron saturation current during the laser pulse was found to correspond to the value of thermionic emission

---

[1] H. T. Yura, "The Interaction of Laser Light with Metals," Rand Corp. Memorandum RM-3560-PR, March 1963.

predicted by the Richardson-Dushman equation for tungsten, extrapolated to a temperature approximately equal to the boiling point. The laser-generated tungsten plasma has been examined by a Paul-type mass filter (quadrupole mass spectrometer)[2] and found to consist of only singly ionized tungsten ions and to be better than ninety-nine percent ionized; and the multiapertured hemispherical collector shown in Figure 2 was used to determine the spatial distribution of ion energy and number density.[3] The construction of the energy sampling probe used in this collector is shown in Figure 3. The distribution of ion density obtained with a tungsten emitter, which is typical of the several materials tested, is shown in Figure 4. In one series of experiments, an axial magnetic field was applied to the experiment, with the results shown.

The investigation of the electron and ion energy distribution proved to be more complicated than resolving the density distribution. Very energetic electrons were present in sufficient quantity to prevent the direct measurement of the quantity of ions with a given energy. It was necessary to correct all ion charge measurements for the presence of the electrons; thus, the ion energy distribution shown in Figure 5 represents measurements made with the mass spectrometer as well as the hemispherical collector system.

The properties of six metals used as laser targets were investigated with the quadrupole spectrometer, and four of these were also placed in the hemispherical collector experiment. Tungsten, tantalum, rhenium and thorium were completely investigated; chromium and lead were excluded from the hemispherical collector experiments because they were found to produce large quantities of neutral particles and a relatively small percentage of ions. Of the six materials, only tantalum and rhenium were found to produce doubly charged ions. We also found that although the absolute number of ions emitted increased rapidly with increasing laser power density, the ion energy distribution became more concentrated about the lower energies. The average ion velocity for thorium and tungsten, determined by time of flight measurements, was found to be about $0.7 \times 10^6$ centimeters per second. The existence of ions with energies in excess of 100 electron volts and the relatively high mean ion energy (about 15 electron volts) substantiates the belief that a significant amount of plasma heating occurs after the initial vaporization phase.

---

[2] A.S. Gilmour, Jr., and F.A. Giori, "The Use of the Quadrupole Mass Spectrometer for Laser-Surface Studies," Presented at the Thirteenth Annual Conference on Mass Spectrometry and Allied Topics, May 1965.

[3] R.E. Biss and A.S. Gilmour, Jr., Pulsed Laser Ion Generator Study, NASA Report NASA CR-54154 (CAL Report UB-1989-E-4), October 1965.

## III. APPLICATIONS OF LASER-SURFACE INTERACTION

Some of the possible applications of laser-surface interaction become obvious once the properties of the interaction are known. For example, the vaporization of materials to permit spectrographic analysis and for use in the formation of thin films has been investigated in our laboratory[4] and in others.[5]

A major part of the program that generated the data presented above was oriented toward the determination of the reaction forces generated at the target surface by the directed expulsion of material. The purpose of such investigation was to explore the possible utility of these forces in the production of attitude correction moments on a spacecraft where forces of the magnitude anticipated would be desirable.

### Electric Propulsion

Electric propulsion schemes have received a significant amount of attention because they are ideally suited for long life, low thrust applications such as synchronous satellite station keeping and attitude control. To be practical, the electric rocket must have an exhaust beam with a high, directed velocity that contains few, if any, neutral or slow particles (although the beam leaving the spacecraft must be completely neutral).

The diagnostic experiments described above showed that laser generated ions in general met many of the requirements of electric propulsion. The average laser-generated ion energy lies between 10 and 40 electron volts; this corresponds to ion velocities on the order of 3 to 6 kilometers per second, and provides a specific impulse[6] of 600 seconds without employing additional ion acceleration mechanisms. (Cesium and mercury ion engines which employ high voltage electrostatic acceleration, operate with specific impulses of 2000 to 5000.)

---

[4] See Reference 2 and R.J. Clark, "Investigation of the Laser-Stimulated Deposition of Thin Films," CAL Report UD-2037-E-1, March 1966.

[5] For example, H.M. Smith and A.F. Turner, "Vacuum Deposited Thin Films using a Ruby Laser," Appl. Opt., 4, pp. 147-148; and N.C. Fenner and N.R. Daly, "Laser Used for Mass Analysis," Rev. Sci, Inst., 37, pp. 1068-1070, August 1966.

[6] Specific impulse, a commonly used parameter to describe any rocket exhaust velocity, is defined as the developed impulse per unit weight of propellant. It is a measure of propellant utilization efficiency.

During this program, no experiments were performed on accelerating the ions; however, there is no theoretical reason why additional acceleration cannot be employed.

The spatial distribution of the ion emission was determined to be cosinusoidal about the axis of the emitter in the absence of a magnetic field (using the hemispherical collector described above). The percentage of thrust that is axially directed (the nozzle efficiency) is therefore only 67 percent. The application of the axial magnetic field modified the distribution enough to increase this efficiency to about 85 to 90 percent.

Ballistic pendulum experiments were performed to get absolute impulse-per-pulse measurements. These data were reduced to give average thrust during the laser pulse to remove the pulse length dependency. The results are shown in the next figure (Figure 6). Low laser power levels were used because they would be more representative of the power levels that should become available from future compact, high efficiency, high average power lasers.

Even though the ionization efficiency (energy expended per emitted ion) of the laser-surface interaction process is quite low -- from $10^4$ to $10^6$ electron volts per ion -- if reasonably efficient lasers are developed (40 to 50 percent conversion efficiency) then this method of thrust production will be quite reasonable for low total impulse applications such as attitude control. It is impractical for the higher impulse requirements, such as station keeping, unless an auxiliary acceleration means is employed to raise the specific impulse by a factor of 50 to 100. Without the additional acceleration, the power consumption and weight of fuel required are excessive compared to existing ion engines.

A possible configuration for a laser-stimulated thrustor is shown in Figure 7.

The present difficulty in this scheme is the low efficiency of existing high-power, low-divergence, high-coherence lasers. The type of optical pumping system used in these studies -- a flash lamp which emits a wide frequency spectrum of light -- is inherently a low efficiency system. The solid-state laser, here ruby, can only use discrete energy levels to excite electrons into higher order states. Thus, a large percentage of the flash lamp energy is wasted, and in fact causes a further decrease in the system efficiency by heating the ruby rod.

## High-Power Switching Triggered by a Laser

Early in our studies of laser-surface interaction, we noted that there were many similarities between the laser-generated blow-off and the expulsion of material from the cathode of a vacuum arc. In particular, since most of our measurements were electrical, we normally applied a low-voltage electrical bias between the metallic target and a separate electrode positioned to intercept part of the ejected material. We noticed that, under certain conditions, it was possible to initiate

a sustained, externally powered electrical discharge between two electrodes in a vacuum when one electrode was illuminated by a high-power laser.

This arc initiation phenomenon has been separately investigated in our laboratory as a means of triggering a high-vacuum (ambient pressure $\sim 10^{-8}$ torr) spark gap. In addition to determining the characteristics of the switch as seen by the external circuit, we have also gained significant knowledge about the interaction process.

The experimental geometry for the laser-triggered switch is shown in Figure 8. Using this simple geometry with the electronics shown, we have been able to investigate the triggering process for sensitivity to electrode shape and composition, electrode spacing, applied potential, and laser power level. When the target electrode is negative with respect to the collector, the laser pulse initiates a vacuum arc[7] by heating a small area of the target. Only a very small amount of ionized material is required in the interelectrode space to permit breakdown, and it has been possible to use a "Q"-switched laser for triggering. A 40 nanosecond (full width at half amplitude) pulse containing 40 to 50 millijoules of energy at 694.3 nanometers has been used for most of the study. The vacuum-arc breakdown is characterized by conduction across the interelectrode gap which begins essentially coincident with the trigger pulse. The rise of the conduction current to peak amplitude is governed by the development of a metallic plasma conducting medium within the interelectrode volume. A sample of this form of conduction buildup is shown in Figure 9. The current through the switch rises to a peak value determined by the external circuit, and the voltage drop across the switch, after saturation has been achieved, depends only upon the electrode composition and geometry. Typical conduction voltage drops for switches capable of several kilovolts stand-off and several kiloampere peak currents are a few hundred volts.

When the target polarity was changed to positive with respect to the collector, there was a significant change in the operation of the switch, as evidenced by the current waveforms shown in Figure 10. Investigation of the turn-on process for this case leads us to believe that a two-state build-up occurs and that a vacuum-arc-type discharge is not formed. We know from basic studies that the creation of the high energy plasma is instantaneous and coincident with the laser pulse. This plasma propagates outward from the target, as was described above, with a leading edge velocity between $10^6$ and about $4 \times 10^6$ centimeters per second. The interception of the high energy particles by the collector results in the generation of free electrons by secondary emission. The free electrons stream back to the target electrode along the field lines, and a self-sustaining discharge develops between the two electrodes.

---

[7] No attempt to describe a vacuum arc will be made here. For further information, refer to the extensive American, British and Russian literature on the subject.

An important feature of this argument is the point that a vacuum-arc-type discharge is not involved. This has developed through an examination of the visible emission characteristics and the rate of electrode erosion. When a vacuum arc is struck on the surface of an electrode, an intensely bright emission spot is created. If the laser is used to trigger a vacuum arc, there is a noticeable increase in the brightness of the laser-heated spot when an external energy source is connected to the electrode pair to power the arc. This brightness change does not occur when the target is at a positive potential. When a vacuum arc is formed on the surface of a negative electrode (cathode), that electrode erodes at a rate proportional to the amount of charge that passes through the arc. This rate of erosion is not observed when the positive electrode is the laser target. In a test with the tungsten target electrode shown in Figure 11, only about 10 micrograms were removed by 100 arcs having a charge-per-arc of $3.3 \times 10^{-3}$ coulombs. This is approximately an order of magnitude less than would be expected if the conventional vacuum-arc mechanisms were involved.

Certain features of the laser-triggered conduction process held the promise of permitting the development of a practical device based upon the laser-stimulated plasma generation in a high vacuum. This device would be fundamentally a high-vacuum diode, and therefore could be a high voltage switch, but would retain the favorable conduction characteristics of the plasma switch (i.e., the ignitron). Because the plasma would be generated by the vaporization and ionization of a low vapor pressure metal, the plasma would be removed from the interaction region by the natural processes of recombination and condensation after the conduction period had been terminated by the removal of the electrode voltage. Replacing the common electrical triggering of the conduction by a light beam also offers some system advantages, especially where it is desirable or necessary that both electrodes be "floated" away from ground by a high voltage.

A high voltage test vehicle was designed as a completely demountable tube to facilitate inspection and modification of the internal elements. A sectional view of the device is shown in Figure 12. The first complete high-voltage switch is shown photographically in Figure 13. This device was tested for d-c stand-off capability and found to be operable to 300 kilovolts, the design limit. Low voltage versions of the switch have conducted pulse currents in excess of 2000 amperes, which is twice the design value of the high voltage unit.

Experiments were performed, primarily with tungsten targets, to obtain data from which estimates could be made of the life of the laser-triggered switch. It was determined that about 0.1 microgram of material was removed from the target per laser shot. If this rate of material removal was maintained throughout the life of the switch, then, during 1000 hours of operation at a repetition rate of 300 pulses per second, a total of 5 cubic centimeters of emitter material would be consumed. Although we do not have sufficient experimental confirmation, it appears that the erosion rates for all materials are about the same.

ACKNOWLEDGEMENT

The data upon which the paper is based are the products of several programs. The authors would like to acknowledge the support of these programs by the Cornell Aeronautical Laboratory, Inc., the National Aeronautics and Space Administration - Lewis Research Center, and the United States Air Force - Rome Air Development Center.

The contributions and assistanceof many co-workers is also greatfully acknowledged.

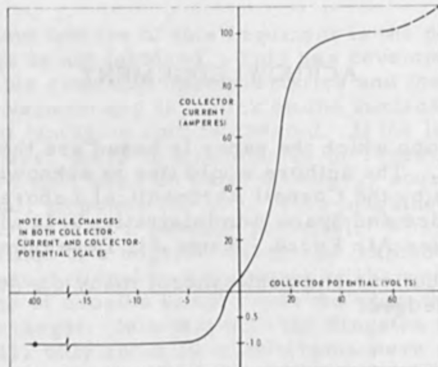


Figure 1 COLLECTOR CURRENT vs COLLECTOR POTENTIAL FOR LASER EXCITED DIODE (Laser Energy: 3.2 joules)

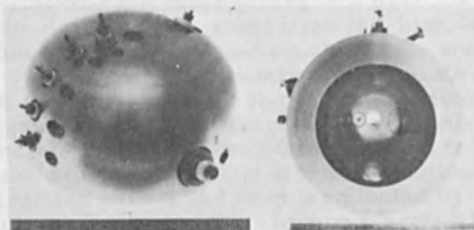

Figure 2 EIGHT-APERTURE HEMISPHERICAL COLLECTOR

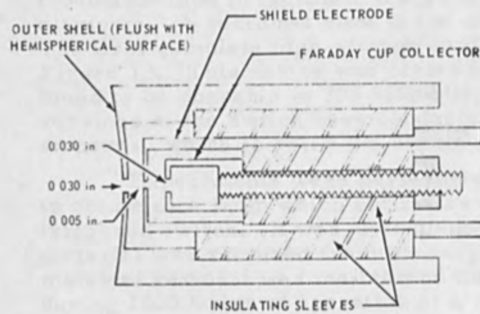


Figure 3a CROSS SECTION SKETCH OF COLLECTOR PROBE FOR ION ENERGY MEASUREMENT

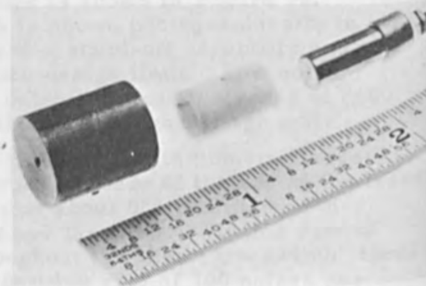

Figure 3b EXPLODED VIEW OF COLLECTOR PROBE FOR ION ENERGY MEASUREMENT

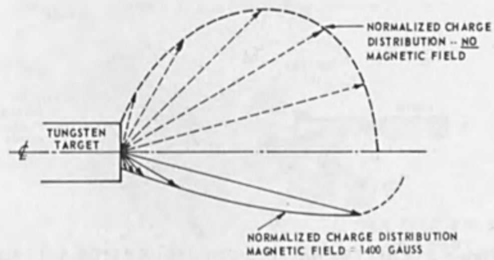


Figure 4a NORMALIZED DENSITY DISTRIBUTION OF LASER-GENERATED IONS

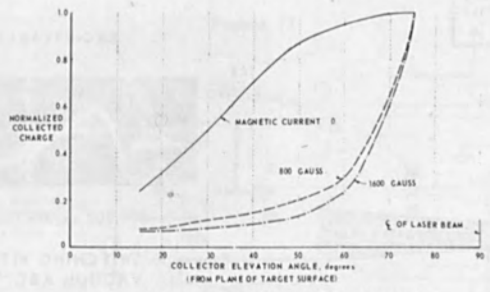


Figure 4b CHARGE DISTRIBUTION

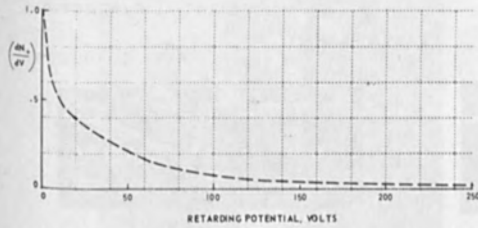


Figure 5 NORMALIZED ION ENERGY DISTRIBUTION

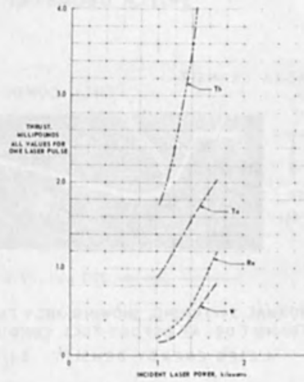


Figure 6 THRUST OUTPUT AS A FUNCTION OF LASER POWER

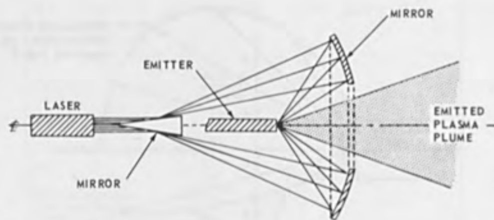


Figure 7 EMITTER-OPTICS CONFIGURATION SUITABLE FOR THRUSTOR APPLICATIONS

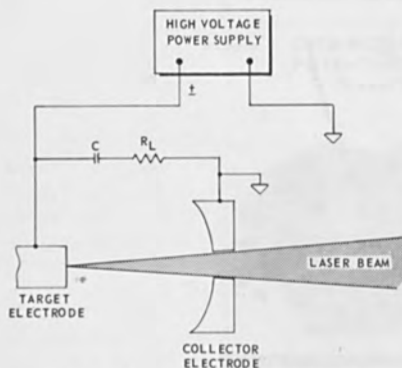


Figure 8 LASER-TRIGGERED SWITCH GEOMETRY

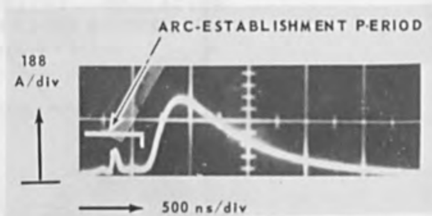


Figure 9 SWITCHING WITH TRIGGERED VACUUM ARC

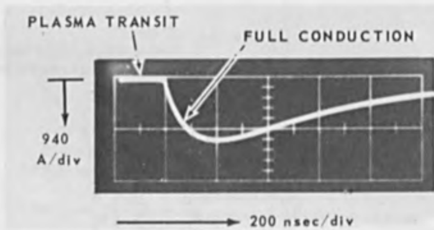


NORMAL SWITCHING, SHOWING ONLY PLASMA TRANSIT DELAY BEFORE FULL CONDUCTION

LASER ENERGY DENSITY: 3 j/cm$^2$

Figure 10a NORMAL SWITCHING

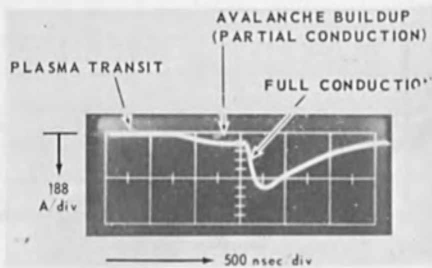


SWITCHING WHEN LASER-GENERATED PLASMA DENSITY IS INSUFFICIENT TO CAUSE IMMEDIATE FULL CONDUCTION

LASER ENERGY DENSITY: 1.3 j/cm$^2$

Figure 10b DELAYED SWITCHING

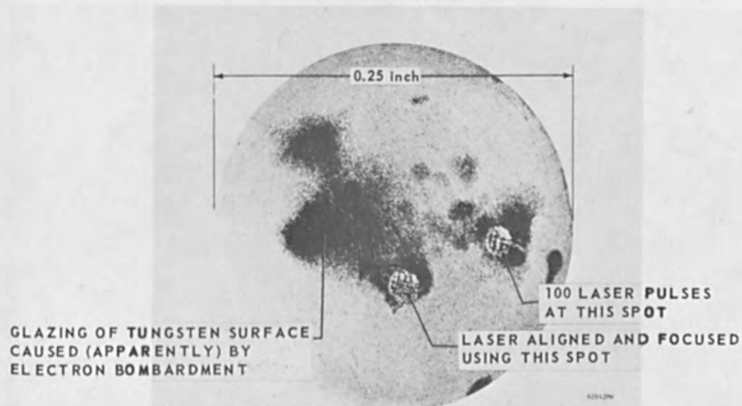


Figure 11

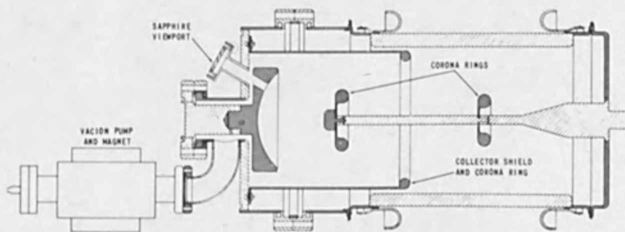


Figure 12 HIGH VOLTAGE SWITCH

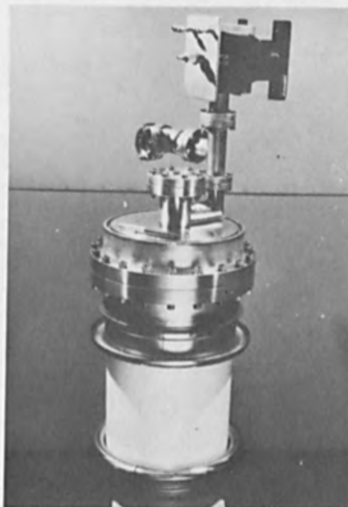

Figure 13

HIGH VOLTAGE SWITCH

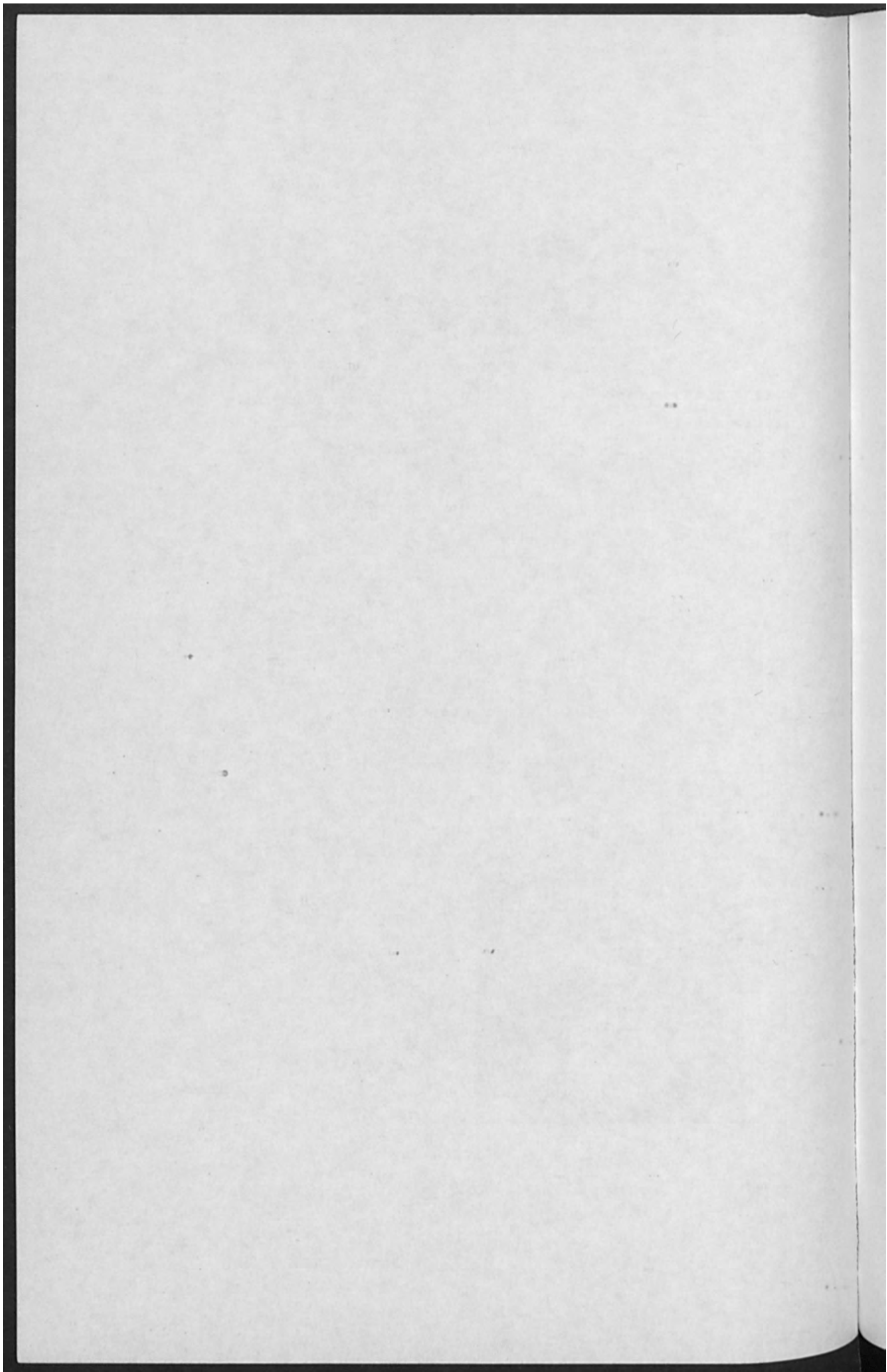

SECTION 2
ELECTRON BEAMS IN MATERIALS PROCESSING

PART A: ELECTRON BEAM WELDING
PART B: MELTING, REFINING AND EVAPORATION

EFFECT OF ELECTRON SCATTERING IN THE METAL VAPOR
ON THE ENERGY DISSIPATION IN THE CAVITY PRESENT
DURING ELECTRON BEAM WELDING*

D. C. Schubert and B. W. Schumacher

Westinghouse Research Laboratories
Pittsburgh, Pa. 15235

ABSTRACT

High energy density electron beams, as used in electron beam welders, pass through long, narrow, vapor-filled cavities in the metal. Energy is transferred to the vapor in the beam by inelastic collisions associated with small scattering angles. Large angle collisions which do not heat the vapor appreciably provide a supply of high energy electrons which bombard and heat the cavity walls. Analysis of the collision process has been carried out to derive general quasi-empirical formulae for the energy division in the cavity for beam voltages in the range of 10 - 150 kV.

The large angle scattering to the walls was calculated using the Rutherford formula, and the Bethe stopping power formula was used for calculating the energy degradation of the central beam with depth. Although scattering sets an upper limit on depth of the weld at a given voltage, it is shown that the bulk of the energy is always deposited in the last 25% of the cavity depth. The atomic number of the metal plays an important role in the detailed energy distribution and also affects the maximum depth. These results are independent of the conductivity and heat capacity of the metal but dependent on the vaporization temperature.

INTRODUCTION

A typical electron beam as used for welding has an energy density of $10^6$ watts/cm$^2$. If all of this energy were used simply to heat the metal in the beam path to the melting temperature and melt it, the solid-liquid interface could advance into the metal at speeds of the order of 100 cm/sec. On the other hand the conduction of this energy density through a typical metal (aluminum) would produce a temperature gradient of $4.5 \cdot 10^{5}$ °K/cm. It is thus evident that by the time the melt had advanced even 0.1 millimeter into the metal, the exposed liquid surface would have reached temperatures at least 1000° greater than the melting temperature. Even before this point is reached rapid vaporization sets in, developing vapor pressures of the order of 1 atmosphere. If we are welding in air the atmospheric pressure balances this vapor pressure; in vacuum a thin liquid metal film on top of the cavity may confine the vapor at nearly this pressure as Schwarz[1] has shown. It is generally believed that the vapor thus generated keeps most of the liquid out of the way of the electron beam. Thus a substantial portion of the beam energy density remains available for melting at the bottom of a cavity in the liquid. With high power, as well as high power density, a narrow, deep cavity is formed. The sides of this cavity are lined with a thin coating of liquid metal, and the metal vapor streams

out of the cavity at velocities in the neighborhood of the speed of sound. The pressure of this escaping stream squeezes the liquid against the walls formed by the solid liquid interface, overriding hydrostatic pressure and surface tension which would otherwise close the cavity. Of course, this can only occur under ideally balanced conditions; in reality every so often hydrodynamic instabilities may cause waves of liquid metal to intercept the electron beam diverting beam energy to regions where it is not useful. The properties of such waves are influenced by the thickness of the layer of liquid metal along the cavity walls, and this thickness is in turn influenced by the energy flow at the metal-vapor interface. Even when the path is free of obstruction from liquid, not all electrons proceed by straight paths to the bottom of the cavity. The liquid lining the cavity walls is heated to some extent by electrons scattered to the walls from the main beam by collisions with the vapor atoms. Electrons which remain in the main beam lose energy to the escaping vapor by inelastic collisions. This dissipation of beam energy along the cavity walls and in the vapor places an upper limit on weld depth independently of all parameters except vapor density and scattering cross section. The above limitations are completely independent of heat conduction parameters of the metal which, however, will pose another set of limits on weld depth, speed, etc.[2] From the following study we can see which limits are dominant in a given situation and what has to be done to get deeper welds or greater depth in cutting.

In the regime of narrow welds and cuts, electrons scattered through large angles by the gas atoms are lost to the walls within a few millimeters of the point where scattering occurred. Thus at any

point in the beam, the majority of the electrons still in the beam have traveled essentially straight paths. This fact greatly simplifies the computation of mean kinetic energy of the beam electrons at any depth in the cavity. In Appendix A it is thus shown that to an accuracy sufficient for engineering purposes, a simple quadratic function gives the ratio of retained energy to initial energy, for those electrons which are still in the main beam, as a function of relative depth (taking the full depth of the cavity as unity). Through the use of this function and the cross section for large angle scattering (as a function of energy) we can deduce with fair accuracy the energy imparted to the vapor and to the cavity walls as a function of distance from the surface. In the present study, a crude model of scattering to the walls is used in the interest of simplicity and the results give rather a lower limit to this energy than a precise value.

Electron Energy Loss in the Beam

In Appendix A it is shown that those electrons going nearly straight and initially accelerated through $U_o$ kilovolts, and having an ultimate range $R_\xi$ in a scattering gas[3] retain energy approximately equivalent to

$$U = U_o \, (1-x/R_\xi)^{1/2} \tag{1}$$

where x is the distance of penetration into the gas. The power remaining in the beam is then

$$W(x) = U(x) \, I(x) \tag{2}$$

where I(x) is the current represented by the surviving electrons, the ones which go straight. This current is attenuated in accord with

$$dI = -I(x)F'dx \tag{3}$$

where F'dx is the probability that, while traveling the distance dx in the vapor, the electron strikes the cavity wall. The precise determination of F' is an exceedingly complicated problem in transport theory, since the effects of successive scattering events cause the electron to move about the yz plane in a random walk. We take as a lower limit for F' the probability of the electron being scattered through angles in the range from 60-120°. Such electrons can be expected to strike the walls after traveling an additional distance $\Delta x$ which is of the order of 1/2 the cavity radius. Calculations by computer program of scattering in this range gave results which fit the empirical equation.*

$$F = \frac{0.221Z^2p}{U^2T} \tag{4}$$

where Z is atomic number of the gas or vapor, p is pressure in Torr and T is the Kelvin temperature. Setting F' = F in (3) and making use of (1) and (4) we obtain a differential equation for I(x)

$$\frac{dI}{I} = \frac{-0.221Z^2p}{U_o^2T(1-x/R_\xi)}\,dx \tag{5}$$

---

*Details of the calculation are described in Appendix B.

which has the solution

$$I = I_o\left(1 - \frac{x}{R_\xi}\right)^{\frac{0.221Z^2pR_\xi}{U_o^2T}} = I_o\left(1 - \frac{x}{R_\xi}\right)^{\frac{\eta}{2}} \qquad (5a)$$

The exponent $\frac{\eta}{2} = F \cdot R_\xi = \frac{0.221Z^2R_\xi}{U_o^2T}$ affects several quantities of interest to us and is discussed separately in Appendix B. Using the derivatives

$$\frac{dI}{dx} = -\frac{I_o\eta}{2R_\xi}\left(1 - \frac{x}{R_\xi}\right)^{\frac{\eta}{2} - 1} \qquad (6a)$$

and

$$\frac{dU}{dx} = -\frac{U_o}{2R_\xi}\left(1 - \frac{x}{R_\xi}\right)^{-\frac{1}{2}} \qquad (6b)$$

we can readily calculate the power per unit length dissipated into the vapor:

$$\frac{dW_{vap}}{dx} = -I(x)\,\frac{dU}{dx} = \frac{I_oU_o}{2R_\xi}\left(1 - \frac{x}{R_\xi}\right)^{\frac{\eta-1}{2}} \qquad (7a)$$

and power directed to the walls:

$$\frac{dW_w}{dx} = -U(x)\,\frac{dI}{dx} = \frac{U_oI_o\eta}{2R_\xi}\left(1 - \frac{x}{R_\xi}\right)^{\frac{\eta-1}{2}} \qquad (7b)$$

Comparing (7a) and (7b) we find the remarkable result that the ratio of power directed to the walls to that dissipated in the vapor is independent of x and equal to the parameter η defined above. Finally the power left in the beam at each point is

$$W = I(x)\ U(x) = I_o U_o (1 - x/R_\xi)^{\frac{\eta+1}{2}} \quad (8)$$

The functions describing power loss from the main beam and power retained in the beam thus have the normalized forms:

$$W' = \text{Const} \cdot (1-x/R_\xi)^{\frac{\eta\pm1}{2}} \quad (9)$$

where $\eta$ and $R_\xi$ are functions of density (which is mainly but not exclusively determined by temperature and pressure in the cavity) and of beam voltage and atomic number of the vapor. We get as derived in Appendix A:

$$\eta = \frac{0.060Z^{1.177}}{U_o^{0.29}} \quad (10a)$$

$$R_\xi = 0.136\ \frac{U_o^{1.71}T}{Z^{0.823}p} = 10^{19} \cdot \frac{U_o^{1.71}}{NZ^{0.823}} \quad (10b)$$

(N = number of vapor atoms per $cm^3$.)

The normalized functions W(x), $\frac{dW_{vap}}{dx}$ and $\frac{dW_w}{dx}$ are shown in Figure 1 for several values of $\eta$ corresponding to $U_o$ vs Z relationships given in Figure 2. It was assumed, however, that the vapor density is uniform throughout the cavity, which is only an approximation. (Uniformity of temperature is not decisive, since vapor-jets may be present which alter the vapor density regardless of temperature.)

The four curves drawn correspond to a typical element in each of the four groups shown in Table 1, and to a 50 kV beam. For the lightest elements the power retained in the beam W(x) remains high until nearly the end of the range $R_\xi$ when this retained power drops precipitously with a corresponding increase in the rate of power delivery to the vapor and to the walls,* while the heaviest elements display the opposite behavior. Two intermediate groups display less marked behavior on either side of uniform linear power loss ($\eta = 1.0$).

TABLE 1

Element Arranged According to Parameter $\eta$

| Group | A | B | C | D |
|---|---|---|---|---|
| $\eta_{50\ kV}$ | 0.4 | 0.8 | 1.70 | 2.70 |
| Members | Mg, Al | Ti, V, Cr | Mo, Rh, Pd | Ta, W, |
| | Si | F, Co, Ni | Ag, Cd, In | Ir, Pt, |
| | | Cu, Zn | Sn | Au, Pb |

The $\eta$-value depends upon the atomic number Z as well as on $R_\xi$ which is determined by the mean ionization potential of the vapor atoms, which can be approximated as a function of atomic number also. Finally the dependence of $\eta$ on voltage (as well as atomic number) is shown in Figure 2.

*This is very evident from the x-ray pinhole pictures of an electron beam under water, a light element, as shown by B. W. Schumacher (in print, this conference).

Increasing the beam voltage to 150 kV would divide each $\eta$ value by 1.375, i.e., not quite enough to move each element one column to the left. Likewise a corresponding reduction of beam voltage would move each element one column to the right.

Since the elements of greatest interest for deep welding are in the first two columns we conclude that increase of wall temperature with depth will be the general rule in deep welding; but it will not lead to large thermal gradients for any elements except aluminum, magnesium, and silicon.

Some of the energy given up from the beam to the vapor is ultimately carried by the vapor atoms to the walls and out of the cavity. This does not concern us here. However from the large amounts of energy thus deposited in the vapor for conditions corresponding to, say $\eta = 1.0$, it seems likely that the vapor itself will quickly be heated to temperatures in the order of $10^4$ °K. This in turn increases the value of $R_\xi$ until an equilibrium is reached.

The increase of range $R_\xi$ with beam voltage and decrease with atomic number is striking (see Figure 3). This suggests that higher voltages will be necessary for deep welding of materials such as tungsten and tantalum.

The indicated values of $\eta$ show that most of the energy lost from the beam by electron scattering is transferred to the walls in the case of the heavy elements, but not for the light elements regardless of vapor temperature. This result is shaded somewhat by our limitation of interest to scattering between 60 and 120°. If we had included smaller angles,

the calculated values of $\eta$ would have been considerably larger and the wall heating would have exceeded vapor heating for all elements. The forward component of velocity of many electrons scattered through small angles to the walls would provide wall heating at higher values of x than where the scattering occurred, providing some deviation from the universal curves of Figure 1 in the direction of enhanced wall heating at the larger values of x. Energy transfer would then have shifted toward the bottom of the cavity. Thus the concentration of heat at the bottom of the cavity for the lighter elements would be accented further (without the upper walls getting any less!) The width of the cavity will obviously affect this calculation; in a wider cavity the 60° cut-off angle used for scattering "to the wall" would be sufficient.

To test this hypothesis that the vapor is super-heated, we note that the average rate of energy absorption per vapor atom is

$$\frac{d\overline{E}}{dt} = \frac{1}{\pi r^2 N} \frac{dW_{vap}}{dx} \tag{11}$$

where r is the cavity radius. Allowing kinetic energy $\frac{kT}{2}$ per degree of freedom, then the rate of temperature rise is

$$\frac{dT}{dt} = \frac{2}{nk} \frac{d\overline{E}}{dt} \tag{12}$$

where n is the assigned number of degrees of freedom per atom.

Now if $\lambda(\frac{x}{R_\xi})$ is the ordinate of the $W_{vap}$ curve in Figure 1a, then

$$\frac{dW_{vap}}{dx} \frac{erg}{cm\ sec} = \frac{\lambda U_o I_o \cdot 10^{10}}{R_\xi} \tag{13}$$

Combining equations (11), (12), and (13) above, with (10b) finally yields

$$\frac{dT_{vap}}{dt} = 4.55 \cdot 10^7 \frac{\lambda I_o Z^{0.823}}{nU_o^{.71} r^2} \quad (14)$$

Inserting a realistic set of conditions into this equation, i.e., $\lambda = 0.3$, $I_o = 0.1A$, $Z = 13$, $n = 3$, $U_o = 150$, $r = 0.1$ yields a typical rate of temperature rise

$$\frac{dT}{dt} \approx 1.2 \cdot 10^7 \text{ deg/sec} \quad (15)$$

In determining the degree of super-heating that takes place we are handicapped by lack of knowledge of the mean length of time which a vapor atom spends in the cavity before either recondensing or escaping out the top. Velocity and distance considerations place this time somewhere between $10^{-5}$ and $10^{-3}$ sec leading to superheating in the range

$$100 < \Delta T < 10^4 \ {}^\circ K \quad (16)$$

Since 11,600 °K corresponds to an energy of one electron volt, and ionization potentials are of the order of 10 volts, the vapor is only weakly (thermally) ionized. The energy retained by the vapor is initially in the form of excitation and (collision) ionization, but plasma interactions may transform some of that energy into kinetic energy.

Our graphs show what would happen if the vapor atoms had kinetic energy corresponding to T = 3000°K. As we have just seen, uncertainties of mean lifetime of atoms in the cavity and of conversion of excitation and ionization energy into thermal energy leave us quite unsure of the actual vapor temperature, but 3000°K seems a fair mean value.

The large values of $R_\xi$ for, say, 150 kV electrons in a hot, high-pressure metal vapor may seem surprising. An electron can travel 100 cm and more before its energy has been dissipated. This clearly suggests that the electron "range" is not the factor limiting deep welding and cutting with electron beams. It is the fact that the vapor temperature, and preferably the super-heated vapor temperature must be maintained by the electron beam. For deep penetration to occur the power density in the central beam must remain high enough at large values of x, so as still to super-heat the vapor, and the beam must remain narrow so as not to be lost to the walls. If we look for 50 to 100 cm of penetration then this calls not only for an initially high power and power density but also for small beam angles. This is more easily obtained at higher voltages. We hope to have quantitative data on this aspect (mainly governed by small-angle scattering) shortly.

The energy balance, as discussed in the accompanying paper by Klemens[2], sets another limit for penetration. This limit will also reach the order of 100 cm for elements with low thermal diffusivity (e.g. rocks). That in practice we have not yet reached this depth is probably due to lower temperature than 3000°K in part of the vapor zone where power density is lost. (But note, vapor temperature and beam voltages do not enter into Klemens' calculations which deal exclusively with energy transport in the beam target). Initial beam cone angle could also be a contributing factor but only another quantitative analysis can show this.

We believe our present calculations indicate that much greater depth than we see today can be attained in e.b. welding and cutting if power and power-density is increased and beam angles kept small. No limit is imposed by the large angle scattering of the electrons at the sufficiently high voltages which allow us to fulfill the above conditions also. Some of the depth limits in present welding and cutting practice may be due to scattering or beam spread near the end of the range, and some may be due to the overall energy balance especially in metals which are good thermal conductors.

## REFERENCES


1. H. J. Schwarz, "Mechanism of High-Power-Density Electron-Beam Penetration in Metal," in Electron and Ion Beam Science and Technology, R. Bakish, Ed., Wiley and Sons, New York 1965.

2. P. G. Klemens, "Energy Considerations in Electron Beam Welding," in print, this conference.

3. For definition of $R_\xi$ see B. W. Schumacher, "A Review of the Macroscopic Laws for Electron Penetration through Matter," in Electron and Ion Beam Science and Technology, R. Bakish, Ed., Wiley and Sons, New York 1965.

4. F. Rohrlich and B. C. Carlson, Phys. Rev. 93, 38 (1954).

5. M. J. Berger and S. M. Seltzer, "Tables of Energy Losses and Ranges of Electrons and Positrons" NASA SP-3012.

6. B. W. Schumacher, Ann. Phys. 13, 404-420, 1953 (see p. 405).

## APPENDIX A

### AVERAGE ENERGY RETAINED BY THE ELECTRONS REMAINING IN THE CENTRAL BEAM AS A FUNCTION OF DEPTH IN THE CAVITY

In the process of passing through matter a high energy electron suffers many collisions involving small energy losses and small changes of direction. Less frequently a large angular deflection due to elastic scattering occurs.

A formula exists for the average energy loss per unit distance along the actual zigzag electron path. Ordinarily it must be used with caution since the line from the source to a point reached by an electron may be considerably shorter than the actual electron path. In the case of an electron beam passing through the cavity in a weld, however, any electron scattered through a large angle hits the cavity walls in the next millimeter or two of travel and is thus lost from the beam. Thus, at any point within the long narrow cavity, the overwhelming majority of the electrons are moving essentially parallel to the axis of the cavity and we can confidently equate the element of true path length $dR_\xi$ to distance along the cavity axis dx. The Bethe stopping power formula as revised by Rohrlich and Carlson[4,5] may then be expressed as:

$$\frac{d\tau}{dx} = \frac{-2\pi r_o^2 NZ(1+\tau)^2}{\tau(\tau+2)} \left[\ln\left[\frac{\tau^2(\tau+2)}{2I^{*2}}\right] + F(\tau) - \delta\right] \qquad (A1)$$

where $\tau$ = the electron energy in units of $mc^2 = \frac{U}{511}$, $r_o^2 = \left(\frac{e^2}{mc^2}\right)^2$ $= 7.94 \cdot 10^{-26}\ cm^2$,

$N$ = number of atoms/cm$^3$, $Z$ = atomic number

$I^*$ = excitation energy in units of $mc^2$ and

$$F(\tau) = 1-\beta^2 + \frac{\tau^2/8-(2\tau+1)\ln 2}{(\tau+1)^2} = \frac{1+\tau^2/8-(2\tau+1)\ln 2}{(\tau+1)^2} \qquad (A2)$$

and $\delta$ is a correction for polarization of the medium, which does not take effect at beam voltages lower than 210 KV; $\beta = v/c$.

The excitation potential in volts, $I = 5.11\cdot 10^5 I^*$, is tabulated[5] for elements of atomic number up to 10 and is given by the emperical formula:

$$I = 9.76Z + 58.8/Z^{0.19}$$

for elements where $Z \geqq 13$.

The most interesting features of the energy of the electrons remaining in the beam, $\tau(x)$, may be obtained by approximating the portion of equation (A1) within the brackets by a constant $K(\tau,Z) = K(\tau_o,Z)$, where $\tau_o = \frac{U_o}{511}$ is the initial beam potential in units of $mc^2$, and

$$K(\tau,Z) = \ln[(\frac{\tau}{I^*})^2(1+\tau/2)]+F(\tau) \qquad (A3)$$

Straightforward integration of equation (A1) with this approximation yields:

$$\int_o^x N(x)dx = \frac{\tau_o^2}{2\pi r_o^2 Z(1+\tau_o)} \cdot \frac{(1-\nu^2)}{K(\tau_o,Z)} \cdot \frac{1+\tau_o\frac{\nu}{1+\nu}}{1+\tau_o\nu} \qquad (A4)$$

where N(x) is the gas particle density as a function of the x coordinate, and

$$\nu = \frac{\tau(x)}{\tau_o} = \frac{U(x)}{U_o}$$

If the density of metal vapor atoms is assumed a constant, $N_o$, then the maximum distance which can be traveled is obtained by setting $\nu = o$ in equation (A4).

$$R_\xi = \frac{\tau_o 2}{2\pi r_o^2 Z(1+\tau_o)K(\tau_o,Z)N_o} \qquad \text{(A5)}$$

and

$$\Delta x = R_\xi(1-\nu^2) \cdot \frac{1+\tau_o\frac{\nu}{1+\nu}}{1+\tau_o\nu} \qquad \text{(A5.1)}$$

Remembering that $(1 - \nu^2) = 1 - \frac{U^2}{U_o 2}$, it is seen that equation (A5.1) can be rearranged to become equation (1) if unity is substituted for the fraction involving $\tau_o$ and $\nu$. The value of this quantity differing most from unity is $\frac{1+\tau_o/2}{1+\tau_o} \geq 0.887$ for the most energetic beam ( $U_o$ = 150 kV) which we are considering.

At smaller values of $U_o$ and of U, the error due to neglect of this term is correspondingly smaller.

Equation (A5.1) is, of course, in error to the extent $K(\tau,Z)$ differs from the constant $K(\tau_o,Z)$, which was used to simplify the integration. If we write $K(\tau)$ as a function of $= \tau_o\nu$, i.e.,

$$K(\tau) = \ln\frac{\tau_o^2\nu^2\ \tau_o\nu+2}{2I^{*2}} + \frac{1+\frac{1}{8}\tau_o^2\nu^2 - (2\tau_o\nu+1)\ln 2}{(1+\tau_o\nu)^2} \qquad \text{(A6)}$$

we see that

$$K(\tau) - K(\tau_o) \cong 2\ln\nu + \ln \frac{2+\tau_o\nu}{2+\tau_o} + 0(\tau_o) \qquad (A7)$$

The dominant term, 2 ln$\nu$, remains moderate in size unless we let $\nu$ approach zero. It is reasonable, however, for us to limit our interest in the integral to the range $\nu \geqq 1/2$, since by (A5.1) this includes the range $0 < x < 3/4\ R_\xi$ .

The creation of a cavity that close to the limiting depth in the face of other limitations such as energy loss by thermal conductions, is not very likely, and the details of energy distribution in such a small dimensional range could have only a very localized effect. Setting $\nu_{min} = 1/2$ the largest relative error in $\frac{dU}{dX}$ becomes

$$\left| \frac{K(\tau)-K(\tau_o)}{K(\tau_o)} \right| \cong \frac{\ln 2}{\ln\left\{\frac{\tau_o}{I^*}\right\}} \qquad (A8)$$

at the bottom of the cavity and much less elsewhere. With beam voltages above 20 kV and base materials having $Z < 30$, the fraction in equation (A8) ranges downward from 0.167. For the purpose of this report, namely a general survey of trends in energy distribution over the whole range of beam voltages and target materials, this accuracy is more than adequate. In most cases of practical interest the fractional error in the depth at which $U = U_o/2$ proves to be 8% or less.

The actual ranges reported in the literature run slightly larger than $R_\xi$ as given by equation (A5) because they are based on numerical integration using the exact expression for $K(\tau)$. We prefer to insert the value computed in equation (A5) into equation (1), however,

since it is consistent with the behavior of $\frac{dU}{dX}$ in the region $\frac{U}{U_o} \approx 1$, where equation (A4) and hence equation (1) are most accurate.

The difference between our value of $R_\xi$ and those in the literature turn out to be speculative, since if equation (A1) is taken literally, $\frac{dX}{d\tau}$ becomes infinite at $\tau = I^*$.

This singularity is a departure from reality due to failure of the Born Approximation at low voltages. The behavior of $\frac{dx}{d\tau}$ is essentially unknown in this region, but it is believed to approach zero as $\tau$ approaches zero. To handle this situation, authors of range tables have used equation (A1) for voltages down to some arbitrary figure, such as 1 kV and let $\frac{dX}{d\tau}$ go linearly to zero with $\tau$ from that point.

The variation of $R_\xi$ with voltages and atomic number for conditions reasonably close to what one way encounter in e.b. welding practice, (p = 1000 Torr, T = 3000°K) is plotted in Figure 3. In the range which applies to most target materials ($10 < Z < 30$), this is well represented by the simplified emperical equation

$$R_\xi = \frac{.306}{Z^{.823}} \left(\frac{U_o}{50}\right)^{1.71+(20-Z)/364}$$
$$\simeq .409 \frac{U_o^{1.71}}{Z^{.823}} \qquad \text{(A9)}$$

In its most general form, this simplified formula becomes

$$R_\xi = 0.136 \frac{U_o^{1.71}}{Z^{.823}} \frac{T}{P}$$
$$= 1.02 \cdot 10^{19} \frac{U_o^{1.71}}{NZ^{.823}} \qquad \text{(A10)}$$

(N = number of atoms per $cm^3$).

APPENDIX B

# COMPUTATION OF SCATTERING PROBABILITY TO THE CAVITY WALLS

A digital computer program has been developed for the study of current density distributions resulting from the scattering of electrons by all kinds of gas atoms. At the present stage of development, the program makes use of known x-ray form factors to calculate cross section in the small angle region by means of the Born Approximation. In the large angle region, cross section is determined by the classical Rutherford formula with the Mott corrections for spin and relativistic effects.

For the purposes of this report, a table was made of $\int_{60°}^{120°} 2\pi\sigma(\theta)d\theta$ where $\sigma(\theta)$ is the differential cross section at the angle $\theta$, for all of the elements. With better than 1% accuracy these results were found to fit the empirical relationship.

$$\int_{60°}^{120°} 2\pi\sigma(\theta)d\theta = \frac{0.0737Z^2}{U^2} \qquad \text{(B1)}$$

Using the laws of perfect gases, this is readily shown to imply

$$F = -\frac{dI}{Idx} = \frac{0.221Z^2p}{U^2T} \qquad \text{(B2)}$$

where, p is pressure in Torr and T is the Kelvin temperature.

The scatter-losses from the center of the beam decrease as pressure is lowered which is of significance for comparisons of electron beam welding in air and in vacuum. But even in vacuum a vapor pressure of up to 1 atm is assumed by various authors. Losses are inversely proportional to the temperature T, and this is most important. T will increase with power density, therefore the losses will be lower for higher power density, leading to an increase in "range" of the high power electron beam over the range of single electrons of the same voltage, as it was mentioned and observed some time ago[6]. The essential mechanism which leads to deep drilling, cutting, and welding is the heating of the vapor by the electron beam.

Inserting the value of $R_\xi$ from equation (A10) into the definition of $\eta$ in Equation (5a), yields

$$\eta = F \cdot R_\xi = \frac{0.442 Z^2 p}{U_o^2 T} \cdot \frac{0.136 U_o^{1.71} T}{Z^{0.823} p}$$

$$= \frac{0.060 Z^{1.177}}{U_o^{0.29}}$$

The shape of the energy dissipation curves (Figure 1) and the ratio of wall heating to vapor heating is thus seen to be a property of vapor atomic number and beam voltage, independent of the pressure and temperature of the vapor.

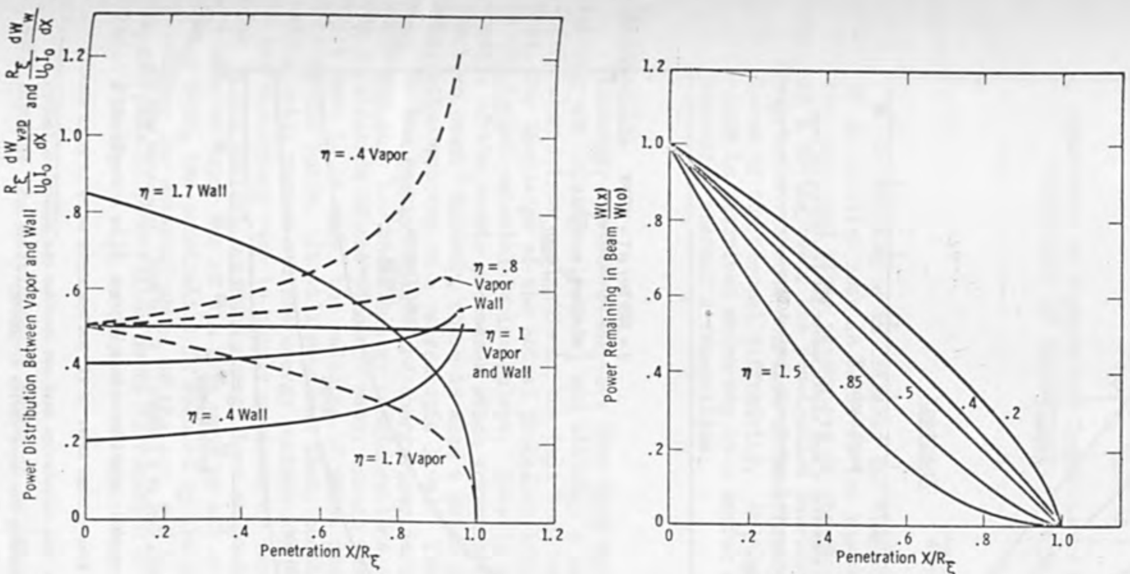


Figure 1. (a) Normalized distributions of power dissipation to the vapor and to the cavity walls.
(b) Corresponding values of power remaining in the central beam.

Variation of behavior depend upon the value of $\eta = \frac{0.060Z^{1.177}}{U_o^{0.29}}$ as explained in the text. The power transfer curves to the cavity walls and to the vapor have the same shape, but $\frac{dW_{wall}}{dx} = \eta \frac{dW_{vapor}}{dx}$. For $\eta = 1.0$ wall and vapor share the energy everywhere equally. The values $\eta = .4, .8, 1.70, 3.0$ correspond to $U_o = 50kV$, and Z values central to the characteristic materials grouping A, B, C, D of Table 1. For other voltages multiply by $(50kV/U_o kV)^2$.

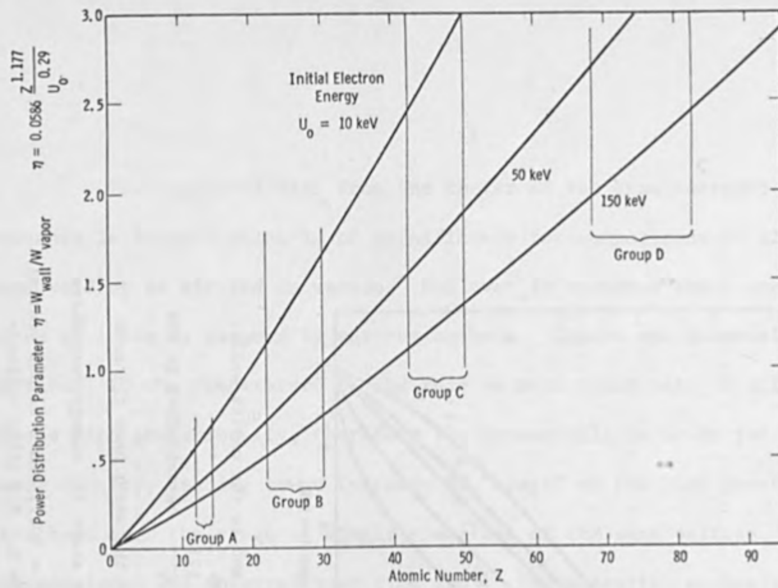


Figure 2. Variation of shape parameter η with atomic number for representative beam potentials. The ranges in Z marked with vertical bars correspond to the groups of materials in Table 1.

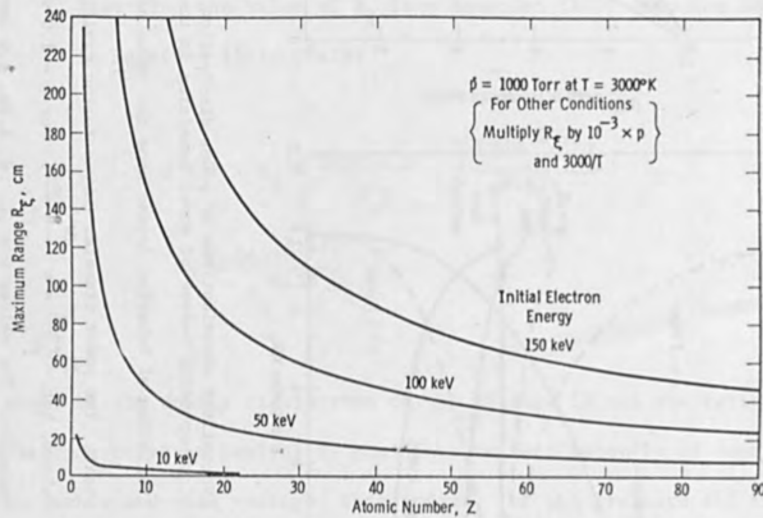


Figure 3. Range $R_\zeta$ for the plausible case of T = 3000°K, p = 1000 Torr. In contrast with the shape parameter η, the range is sensitive to beam voltage. $R_\zeta$ is evidently not a serious limitation for beam voltage above 50 kV, but operation below 10 kV is clearly impractical. Note that this calculation does not consider the conditions (energy requirements) for maintaining the vapor cavity at 3000°K.

# ENERGY CONSIDERATIONS IN ELECTRON BEAM WELDING+

Paul G. Klemens

Department of Physics and Institute of Materials Science
University of Connecticut, Storrs, Conn. 06268

Abstract

An expression is obtained for the depth of penetration of an electron beam in terms of the thermal conductivity of the solid and other parameters of the material. In the case of a moving beam, the penetration decreases with speed; an expression for the decrease of penetration is obtained in terms of the thermal diffusivity. An electron beam technique is described which may be a useful method for measuring thermal diffusivities.

## Introduction

Although electron beams have been used successfully as a tool in cutting and welding materials, and although a large body of empirical information is now available on how this tool can be used to good advantage, our knowledge of the actual processes induced by the electron beam in the target material is incomplete. Ideally we would like to know the details of the atomic processes which govern the penetration of the electron beam:[1] however, there is also a prior need to understand the penetration process on a macroscopic level. The present paper will consider the energy balance and energy loss mechanisms on a macroscopic basis and show how these energy considerations govern to a large extent the penetration of the electron beam, though there are some assumptions which have to be made, the validity of which can only be examined on a microscopic basis. It will be shown that, provided the beam is sufficiently narrow and its energy content high enough, the penetration in the stationary case is mainly governed by thermal conduction. If the beam is not narrow, a second energy loss mechanism becomes important - the flow of vapor out of the hole made by the beam. In the case of a moving beam, the penetration is reduced by the extra energy requirement of melting the material ahead of the cut, and an expression is found for the decrease of penetration depth as function of the forward speed of the beam. Finally it will be pointed out that since the loss of penetration

+ Work done at the Westinghouse Research Laboratories, Pittsburgh, Pa. 15235

depth depends upon the thermal diffusivity, an electron beam technique may be a convenient way of measuring thermal diffusivity in circumstances when measurements of temperature gradients or temperature variations inside a solid are difficult.

The present treatment depends mainly on energy flow considerations. It applies not only to electron beams, but to any other method which delivers a high flux of energy in a beam of narrow cross-section. It may, in particular, apply under appropriate circumstances to laser welding.

Stationary Beam

Consider a narrow beam impinging on a surface. Let the voltage be $V$, the current $J$, so that the energy flow is $W = VJ$. Suppose in the steady state the beam has cut a deep hole, of depth $D$, and diameter $\ell$, and let $D \gg \ell$. Let $T_m$ be the melting point of the material, and let the vapor inside the hole be of temperature $T_v$. Presumably there is a sheath of molten material between the vapor core and the surrounding solid; unfortunately, very little is known about what precisely occurs within the hole. But note that by the above definition $\ell$ is the diameter of the "key hole" formed by the beam, and not the width of the molten metal which, by the usual definition, gives the weld width.

The electrons penetrate the hole in an unknown and extremely complicated manner, although some x-ray photographs give information about the spatial distribution of the absorption.[2] We shall assume (a) that x-rays remove only a negligible fraction of the total power, and (b) no matter how the energy loss of the electrons by interaction with the vapor and the walls of the hole is distributed spatially, this energy is rapidly transported within the hole, so that the wall is of uniform temperature.

The energy which is delivered by the beam is dissipated by various mechanisms: by heat conduction into the solid, by energy transported away by vapor, and by radiant energy.

If the hole is deep and narrow, conduction becomes most important. The temperature gradient at the solid-liquid interface is of order $T_m/\ell$, so that the heat carried away by conduction of of order $\varkappa(T_m/\ell)\pi\ell D$, where $\varkappa$ is the thermal conductivity. The heat flow is thus roughly independent of the hole diameter, but proportional to the hole depth $D$. Therefore, as long as the other energy loss mechanisms are relatively small, the conduction depends on the depth of the hole, which is therefore proportional to beam power; this result is insensitive to the hole diameter, which must be determined by other considerations.

In greater detail, the heat conduction for a length $D$ through a cylinder of inside diameter $\ell$ and inside temperature $T_m$, and outside diameter $L$ and temperature $T_0$ is given by[3]

$$W_I = 2\pi D \kappa \frac{T_m - T_o}{\ln(L/\ell)} \quad (1)$$

There is thus a weak dependence on $\ell$ . We must now choose the radius $L/2$ outside which the material is at the ambient temperature $T_o$ . We find that strictly speaking the process is not stationary and $L$ increases with time. However, as long as the cylinder is not infinitely long but of finite length $D$ , we expect the conduction to be enhanced by the addition of an extra dimension as soon as $L$ becomes comparable to $D$ ; at that point a stationary state is more closely approached. We therefore identify $L/2$ with $D$ , noting that any error will only enter into (1) logarithmically, so that

$$W_I = 2\pi D \kappa \frac{T_m - T_o}{\ln(2D/\ell)} \quad (2)$$

In many typical cases, $\ln(2D/\ell)$ ranges from 3 to 5 .

Equating $W_I$ to the total power of the beam, $W$ , one obtains for the depth of the hole

$$D = \frac{W \ln(2D/\ell)}{2\pi \kappa (T_m - T_o)} \quad (3a)$$

$$\simeq \frac{4W}{2\pi \kappa (T_m - T_o)} \quad (3b)$$

In a typical case of a 15 kilowatt beam and in a metal for which thermal conductivity $\kappa = 1$ watt-cm-deg$^{-1}$, and $T_m = 1500^oC$ , one would expect a penetration of the order of 6 cm. If the diameter of the hole is 0.2 cm, this makes $\ln(2D/\ell) = 4.2$, consistent with our approximation.

Some typical values of $D$ for various materials deduced from (3a) are shown in Table I.

One must recognize that these values are optimum values deduced on the assumption that other heat loss mechanisms are inoperative. Furthermore, it has been assumed that the hole is long and thin, and of uniform temperature, and that the solid material which had to be removed to form the hole has been removed without inhibiting the entrance of the beam. In the case of the 400 cm hole calculated for rock, this is

certainly a questionable assumption. Limitations due to electron scattering are discussed in an associated paper by D. C. Schubert and B. W. Schumacher.[4]

Let us now consider competing heat loss mechanisms. The material inside the hole is partly in the form of liquid, partly in the form of vapor. The latter probably occupies the major fraction of the volume. The vapor emits electromagnetic radiation, and also streams out of the hole, carrying away energy. The black body radiation out of a hole of area $\ell^2$ is

$$W_r = 6 \times 10^{-12} T_v^4 \ell^2 \text{ watt} \tag{4}$$

and even if $T_v \simeq 3000^\circ K$, this is clearly negligible.

The energy loss by vapor flow is more important. Let us assume the vapor to emerge with the velocity of sound v, at a temperature $T_v$. Let $d_o$ be the density of the solid, C its heat capacity per unit volume, and let d be the density of the vapor. The heat capacity per unit volume of the vapor is thus

$$\frac{d}{2d_o} C \tag{5}$$

the factor 2 being included because the vapor atoms have only translational, not vibrational, energy. The energy flow due to the vapor is thus

$$W_{II} = \ell^2 v C T_v \frac{d}{2d_o} \tag{6}$$

Invoking the perfect gas law, and assuming that the vapor issues at or near atmospheric pressure

$$\frac{d}{d_o} \simeq 3 \times 10^{-4} \frac{T_v}{300} \simeq 10^{-6} T_v \tag{7}$$

so that

$$W_{II} = \frac{1}{2} \times 10^{-6} C v \ell^2 T_v^2 \tag{8}$$

In a typical case, when $C \simeq 3.5$ joule/cm$^3$/deg, $T_v = 3000^\circ K$, and $v = 5 \times 10^4$ cm/sec

$$W_{II} \simeq 8 \times 10^5 \ell^2 \text{ watt} \tag{9}$$

For beam energies of the order of 10 kW, this loss becomes important when $\ell$ exceeds say 0.1 cm. In the case of vacuum welding the pressure in the hole is only about 1/4 atm.,[1] and $W_{II}$ is correspondingly decreased.

We now recognize two possible cases: when $W_{II} < W$ and when $W_{II} > W_I$. In the former case the energy balance is

$$W_I = W - W_{II} \tag{10}$$

where $W_I$ is determined by conduction and proportional to the depth of penetration. The vapor loss $W_{II}$ is proportional to $\ell^2$ or the cross-sectional area of the hole. It is thus advantageous to keep $\ell^2$ as small as possible.

The factors which control $\ell^2$ are obscure, but the minimum requirement is a narrow beam, for $\ell$ cannot be less than the beam diameter. Another requirement is that the beam does not wander, and that it is not broadened by atmospheric scattering. Alternatively it is desirable to have a large beam power. Inasmuch as it is difficult to concentrate a large beam power into a small area, the condition

$$W > W_{II}$$

is equivalent to a requirement on the beam power density, namely

$$\frac{W}{\ell^2} > 5 \times 10^{-7}\ C\ v\ T_v^2 \tag{11}$$

which is the harder to fulfill, the greater the vaporization temperature of the material.

In the typical case quoted above, the critical beam power density below which substantial penetration is certainly impossible is 80 kW/cm$^2$. In actual practice the beam power density should exceed this value by a substantial factor.

If $W < W_{II}$, we have different conditions altogether. The beam does not drill a deep hole, but eats its way into the material gradually, leaving a relatively wide depression. No vapor cloud forms in that depression, but material is removed until $D$ is comparable to $\ell$. Further penetration is governed by the speed with which material can evaporate from a liquid surface of area $\ell^2$ kept at some temperature intermediate between the melting temperature $T_m$ and the vaporization temperature $T_v$. The temperature reached in the steady state depends on the power density $W/\ell^2$. Furthermore, since a large amount of liquid is present, the progress of the erosion will depend upon how that liquid will flow and possibly refreeze; this in turn depends on the

direction of gravity and on surface tension effects.

Moving Beam

It is generally observed that the depth of penetration is less for a moving beam than for a stationary beam, and that this depth decreases as the forward speed of the beam is increased. This is readily understood as a consequence of the additional energy requirement of moving the beam. Since heat is left behind in the wake of the moving beam, less heat needs to be conducted away, so that the penetration decreases.

As the beam is moved forward, material has to be melted at the front of the beam, and material resolidifies at the back. The heat required to do so consists in part of heat required to raise the temperature of the material to $T_m$, and in part of the latent heat of melting. The latent heat of melting is given up and, as we may assume, completely regained at the back face where the liquid metal resolidifies. The moving hole leaves behind a wake of heat. Originally this heat was concentrated in a small region immediately behind the hole, at a temperature $T_m$. The fact that it subsequently spreads out does not affect the amount of heat involved. The additional heat required to move the hole is therefore

$$W_{III} = D \ell V C T_m \qquad (12)$$

where $D$ is the depth of the hole, $\ell$ its diameter, $V$ the forward speed of the moving beam, $C$ the heat capacity per unit volume and $T_m$ the melting temperature.

The energy balance is now

$$W = A_1 D + A_2 + A_3 D V \qquad (13)$$

where $A_1 D$ is $W_I$ of Eq. (2), $A_2$ is $W_{II}$ of Eq. (6) and $A_3 DV$ is $W_{III}$ of Eq. (12). The depth of penetration is now given by

$$D = \frac{W - A_2}{A_1 + A_3 V} \qquad (14)$$

and in the stationary case

$$D_o = (W - A_2)/A_1 \qquad (15)$$

which is given by Eq. (10) and (3) as

$$D_o = \frac{2W - \ell^2 v\, C\, T_v\, d/d_o}{\pi \varkappa T_m} \ln\left(\frac{2D_o}{\ell}\right) \tag{16}$$

Strictly speaking, $A_1$ is not quite constant because it contains the factor $\ln(2D/\ell)$, but we may approximate this by $\ln(2D_o/\ell)$, since it varies only relatively weakly.

While (14) and (15) give the magnitude of D and the manner in which it decreases with speed V, it is also of interest to consider the speed $V_c$ for which the penetration is halved. From (14) we obtain

$$V_c = \frac{A_1}{A_3} = \frac{2\pi \varkappa}{C\, \ell\, \ln(2D/\ell)} \tag{17}$$

In most cases when $\ln(2D/\ell) = \ln(D_o/\ell) \simeq 3$

$$V_c = \frac{2\pi \varkappa}{3C\ell} \tag{18}$$

In the case of a typical metal for which $\varkappa/C \simeq 1\ cm^2/sec$, taking $\ell = 0.2$ cm, one finds

$$V_c = 10\ cm/sec = 240\ inches/minute$$

In stainless steel for which $\varkappa/C = 0.04\ cm^2/sec$

$$V_c = 0.4\ cm/sec = 10\ inches/minute$$

In the case of a poor thermal conductor such as concrete, where $\varkappa/C = 0.005\ cm^2/sec$,

$$V_c = 0.05\ cm/sec = 1.3\ inches/minute$$

Experimental data on concrete[5] indicates that half the penetration is lost at a forward speed of about 2.5 inches/minute. The order of magnitude of the agreement is satisfactory; the discrepancy may be due to a number of factors, in particular the crudeness of our theory, but also the variability in the thermal diffusivity of concrete.

Determination of Thermal Diffusivity

The fact that the penetration of the electron beam decreases with forward speed in a manner which depends on the thermal diffusivity of the solid material makes it possible to measure the thermal diffusivity by means of an electron beam. One would have to measure the penetration at two or more forward speeds, and determine $V_c$ from the relation

$$D = D_o \left[ 1 + V/V_c \right]^{-1} \qquad (19)$$

If one also measures the diameter of the cut, $\ell$ , one can calculate the thermal diffusivity $\kappa/C$ from (18), or better still, from (17).

The interesting point is that this method of determining $\kappa/C$ does not depend upon the detailed assumptions which we have made. All which is really required is that thermal conduction is the only heat loss mechanism which depends on $D$, and that the other mechanisms (vapor flow, etc.) are independent of $D$ . Then an energy balance equation of the form (13) holds, and $V_c$ is independent of $A_2$ .

If the thermal diffusivity depends on temperature, this method will yield the diffusivity in the vicinity of the melting temperature $T_m$. Since thermal diffusivity measurements at elevated temperatures are notoriously difficult to carry out, and subject to large and incompletely understood errors, the electron beam method may well be competitive with other methods. Basically, this method is equivalent to a transient method involving a line source of heat, but it avoids the use of thermocouples embedded in the solid.

It would be interesting to attempt quantitative measurements of thermal diffusivity on materials of known properties.

Some Further Problems

Although the present considerations do give an overall description of the beam penetration which seems to agree with what has been observed, at least in some cases, there are a number of questions which have yet to be answered.

The most important question is to determine the factors which govern the "Key-hole" diameter $\ell$ , an important parameter in our considerations. Clearly the beam diameter sets a lower limit to $\ell$ , but there could be mechanisms which tend to make $\ell$ wider than the beam diameter.

A second question is whether the hole is really of uniform diameter, and whether the temperature within it is uniform. This has been assumed in our considerations, and although the heat conducted away is not very sensitive to variations in diameter along the length

of the hole, there is a need to investigate the mechanism of hole formation in greater detail.

Perhaps the greatest need is to find out what happens when the hole is relatively wide and thermal conduction is only a minor mechanism of heat transport. In that case the present considerations are inapplicable (except possibly that the variation of depth with forward speed is still given correctly). It is unlikely that a simple answer exists in this case, but further investigations are clearly needed.

## References


1. H. Schwarz, Mechanism of high-power-density electron-beam penetration in metal, in "Electron and Ion Beam Science and Technology" (R. Bakish, Ed.) p.158. J. Wiley & Sons, New York 1965.

2. B. W. Schumacher, Some observations on high-power electron beams under water, this conference, to be published.

3. M. Jakob, in "Heat Transfer" p. 132, J. Wiley & Sons, New York 1949.

4. D. C. Schubert and B. W. Schumacher, Effect of electron scattering in the metal vapor on the energy dissipation in the cavity present during electron beam welding, this conference, to be published.

5. B. W. Schumacher, Electron beam cutting of rocks and concrete, this conference, to be published.

TABLE I

Beam Penetration for 15 kW Beam,
$\ell$ = 0.2 cm Optimum Values

| Material | $T_m$ ($^oC$) | $\kappa$ watt-cm-deg$^{-1}$ | D cms |
|---|---|---|---|
| Copper (pure) | 1080 | 4.5 | 1.5 |
| Copper alloy (20$\mu\Omega$-cm) | 1080(?) | 0.8(?) | 10 |
| Iron | 1540 | 0.7 | 9 |
| Stainless Steel | 1600(?) | 0.14 | 50* |
| Tungsten | 3380 | 1.0 | 2.0 |
| Rocks, various | 2000(?) | 0.02(?) | 400** |

*NOTE: The thermal conductivity of stainless steel is a room temperature value; it may be considerably higher near $T_m$, resulting in a substantial reduction of D . The value may thus turn out to be closer to that for the copper alloy.

**NOTE: We have neglected the " dilution" of the beam by electron scattering which causes variations in the temperature of the vapor with depth, and would invalidate the present argument in extreme cases. We have also disregarded the factor of time, which is again of great importance in such extreme cases.

# PRESENT KNOWLEDGE OF THE FUNDAMENTAL PROCESSES OF ELECTRON BEAMS AS MATERIAL WORKING TOOLS

Helmut Schwarz
Rensselaer Polytechnic Institute
Hartford Graduate Center
East Windsor Hill, Connecticut 06028 USA

A critical survey of recent studies in thermal electron beam processes of materials performed in several laboratories will be given. Some emphasis will lie on experimental results and interpretation with an attempt to clarify the basic processes of the so called "deep penetration effect". A high-speed movie (up to 20,000 frames per second) taken by R. E. Kutchera of General Electric and not yet presented publicly will show the welding action. It will confirm earlier results of the author. Of special interest in this movie is the reobservation of the periodically rupturing liquid film at the surface. Its importance for "deep penetration" as a heat shield is pointed out. The observation of J. Pellisier that the material removal does not occur continuously but erupts in steps can easily be explained with the conception of a periodically rupturing film releasing the vapor built up in the closed cavity. A. Visser's investigation confirmed these observations when he viewed the electron beam heated spots with photomultipliers.

Cutting and welding in non-vacuum environment will be discussed.

Electron beam welding in outer space will be mentioned and special problems coming up on the non-gravitational conditions will be discussed.

Applications in microelectronics will be reported where fine spot sizes are required. It will be pointed out that the initial enthusiasm of having obtained with the electron beam a tool that could drill holes and perform cuts, i.e. in thin metal film resistors, of line widths as narrow as determined by the electron optics of the beam has to be dampened by the material interaction effects.

## INTRODUCTION

If I were to only report on well established results, this paper could actually be quite short since there is really not much known about fundamental processes of electron beams as a working tool. For half a century, one is aware of the fact that electron beams can heat materials and thus melt, cut, evaporate, and weld. Many small and large machines are being built and do their job more or less satisfactorily. Industrial enterprises do not bother much with the investigation of the fundamental processes. Only a few research laboratories have investigated the effect with varying success. However, enough material of uncertain interpretation exists so that it will not be possible to go into the details. Only a few points will be discussed.

## GENERAL CONDITIONS FOR ELECTRON BEAMS AS A WORKING TOOL

Except for the laser, the electron beam is a power source which can be focused to the highest intensity of all other heat sources known up to now.

It is due to Steigerwald(1) and Stohr(2) who first introduced this powerful heat source into industrial applications. von Ardenne(3) used the electron beam of his electron microscope to produce diaphrams by drilling holes in thin disks with electron beams in the 1930's. It was near at hand that the electron beam should be very useful for welding and cutting in modern microelectronic technology as this had been suggested by the author in 1958(4).

It had been pointed out by Steigerwald(5) that the electron beam heat source would be most efficient for cutting in case the temperature could be brought up to at least 4000°C. At this temperature the energy actually used would constitute about 90% of the total energy input. At 2000°C only 5% would be useful whereas the rest would be lost by heat conduction, radiation, etc. It was also Stohr and Steigerwald who recognized that a sharp temperature gradient would be necessary in order to overcome the heat conduction effects. This is achieved by pulse operation of the electron beam. Depending on the acceleration voltage of the electrons, the pulse duration should be in the order of several microseconds for the 100 kV range when applying the electron beam to ordinary metals, as for example iron. These numbers originate from the fact that it does not make sense to generate more electron beam intensity than is necessary to reach the melting or evaporation heat respectively for a layer that is of the thickness equal to the penetration depth. For 100 kV electrons the penetration depth for iron is roughly 0.001 inch. The electrons will first transmit their energy to the lattice electrons which takes only about $10^{-13}$ seconds which is

the inverse Debye frequency, see for example Reference 6. But it takes a much longer time to transfer the energy from the electrons to the whole lattice which in the case of electrons that have a range of 0.001 inch is about 1 microsecond. From these numbers one can calculate an optimum intensity for an electron beam from the following formula

$$I = a\rho H_{ev}/t_r \qquad (1)$$

where $a$ means the penetration depth, $\rho$ the density of the material $H_{ev}$ the evaporation heat of the material, and $t_r$ the relaxation time which is of the order of microseconds. For a numerical example

where $a = 0.001$ inch, $\rho = 8 \times 10^3$ kg m$^{-3}$, $H_{ev} = 10^5$ J kg$^{-1}$ and

$t_r = 10^{-6}$ sec., we obtain $I = 2 \times 10^6$ W cm$^{-2}$.

One can also find that by exceeding this electron beam power density, the so-called "deep penetration effect" will show up. At intensities higher than 2 MW cm$^{-2}$, the initially heated surface layer will receive more energy than is necessary to evaporate it; therefore, the heat has to go below the surface and shock wave effects will occur. This deep penetration effect is enhanced in case one applies electron beams of higher acceleration voltages so that the cavity can be covered by a thin metal film which first had been discovered by H. Schwarz[7].

## TEMPERATURE DIFFERENCE BETWEEN BOTTOM AND TOP SURFACE OF CAVITY

We have shown experimentally that the surface does not reach a temperature of 4000°C as this would be the most efficient working conditions, but almost 2000° lower and yet the electron beam process is as efficient as one would expect it to be at the higher temperature postulated by Steigerwald[5]. Due to the thin film covering the cavity for most of the electron beam working duration, quite a large difference in temperature can exist between the surface and the bottom of the cavity. This film ruptures periodically, for example at 100 kV every 70 msec. and remains open for about 1/2 msec. The rupture of this film occurs when the pressure inside of the cavity equals the surface tension or in other words if the pressure built up by the metal vapor times the area becomes equal to the surface tension times the periphery. One can actually calculate a critical vapor pressure inside the cavity which is in a specific example of the 100 keV electrons in iron about 150 torr. The surface temperature was determined[7] from the

from the evaporation rate as measured by collecting the vapor condensing at the inside of the half sphere made of copper covering the cavity. A small hole at the top of the half sphere was left for the passage of the electron beam. The temperature of the surface was about 2600°C at which the evaporation rate changes very rapidly with temperature so that an accuracy of plus or minus 10° could be achieved even if an error in measuring the evaporation rate had been of the order of a factor of 2. The best evidence for the periodically rupturing film can be obtained from a high speed movie as we had done in 1963[7] and which recently was repeated by R. E. Kuchera of General Electric. Figures 1 and 2 show a few frames out of these movies and one can see that most of the time the surface is covered and only is open at short intervals. Also J. Pellisier[8] had observed that the material is removed in steps from which he concluded that the electron beam energy is absorbed below the surface and that an explosion-like evaporation takes place. Already Brasch and Lange[9] had this idea and observed that there was a sub-surface heating which caused a blister formation, and he noted that sometimes this blister ruptured. Also A. Visser[10] could see periodical eruptions by viewing the electron beam heated spot with photo-multipliers. As we published previously[7], we could derive a model which would allow the calculation of the temperature at the bottom of the cavity. It was possible to derive the relationship

$$\alpha p_b T_b^{-\frac{1}{2}} - 2 p_f T^{-\frac{1}{2}} = 0 \qquad (2)$$

between the surface temperature $T_f$ and bottom temperature $T_b$ for different cavity heights h. In Formula 2, $p_b$ and $p_f$ constitute the vapor pressure corresponding to $T_b$ and $T_f$ respectively; $\alpha$ is a factor that takes into account the geometry of the channel and can be calculated applying the cosine law[11]. This formula was derived simply from the fact that the thin film has to reach an equilibrium thickness by taking into account the vapor flux leaving the bottom of the cavity and arriving at the lower side of the foil and the vapor stream leaving the foil towards the outside and inside of the cavity. Figure 3 shows a relationship between the bottom temperature $T_b$ as a function of surface temperature $T_f$. This model can be refined by also taking into account the vapor that condenses at the inside wall of the cavity as well as the vapor leaving this wall. In doing so, one arrives at the following equation:

$$\alpha_o \frac{d_e^2}{h^2} \frac{p_b}{T_b^{\frac{1}{2}}} + b d_e \left(\frac{p_b}{T_b^{\frac{1}{2}}} + \frac{p_f}{T_f^{\frac{1}{2}}}\right) \int_o^h \tan^{-1} \frac{d_e}{x} \, dx - 2 \frac{p_f}{T_f^{\frac{1}{2}}} = 0 \qquad (3)$$

$T_b$ and $T_f$ are again the temperatures of the bottom and the surface respectively and $p_b$ and $p_f$ the corresponding vapor pressures. $d_e$ is the diameter of the electron beam affected zone, or in other words the diameter of the cavity. h is the height of the cavity, and $a_o$ and b are constants determined by the geometry of the cavity. In case one assumes the simple relationship between the vapor pressure and the temperature of the vapor:

$$p = Ae^{-\frac{B}{T}} \tag{4}$$

one can again determine a relationship between surface temperature and bottom temperature of the cavity for different heights h. The diameter $d_e$ is mainly determined by the electron beam current, the acceleration voltage, and the quality of the electron optics. Formula 3 can be solved as follows[12]:

$$d_e^2 = \frac{C\frac{h^2}{d_e^2} - A}{B\frac{h^2}{d_e^2}\left[\frac{h}{d_e}\tan^{-1}\frac{d_e}{h} + \frac{1}{2}\ln\left(1 + \frac{h^2}{d_e^2}\right)\right]} \tag{5}$$

$$\text{where} \quad A = a\frac{p_b}{T_b^{\frac{1}{2}}}\ ;\ B = b\left(\frac{p_b}{T_b^{\frac{1}{2}}} + \frac{p_f}{T_f^{\frac{1}{2}}}\right) \text{ and } C = 2\frac{p_f}{T_f^{\frac{1}{2}}}$$

With the solution 5, one can find the ra tio of cavity depth to cavity diameter as a function of cavity depth. Further analysis shows that with decreasing beam diameter penetration depth will become smaller.

## PENETRATION DEPTH AS FUNCTION OF ELECTRON BEAM VOLTAGE, CURRENT AND POWER DENSITY

Matting and Sepold[13] found that penetration depth is not always a linear function of the total electron beam power density. They showed experimentally that it is only a linear function in case they keep the voltage constant and increase the power density by increasing the electron current only. But there was only an initial linear dependency when they increased the electron beam power density by increasing the voltage and keeping the electron beam current constant. At higher power densities, the linear relationship deviated in such a way that the penetration depth increased less than linear with increasing voltage. It appeared that there was even a leveling off. This apparent discrepancy between findings of E. C. Lary[14] can only be explained with the above

formulation. With increasing voltage, the beam diameter will decrease and the vapor which has mostly been created at the bottom of the cavity has less chance to get out of the channel since the solid angle decreases with the square of the cavity depth. The heat conduction towards the walls of the cavity, of course, goes linear with the depth. By substituting in Eq. 3 the beam diameter $d_e$ as given by beam current and beam voltage, one will arrive at the results as found by Matting and Sepold.

## ELECTRON BEAM REFLECTION AND PENETRATION PARAMETERS

Recently E. C. Lary[14] has done some analysis of the electron beam penetration. He asked himself two questions:

(1) Whether the deep penetration of electron beams is due to simple reflections from the side walls of the hole or whether some other mechanism like gas focusing or scattering is responsible for the deep penetration.

(2) He tried to investigate the relationship between penetration depth of a well-focused beam and such parameters as table speed, beam power and beam voltage.

## THE REFLECTION OF ELECTRONS

The first question was answered negative since even at very well polished mechanically pre-drilled holes there was no observable effect of electron beam reflection. This was verified by aiming an electron beam under a small angle at the inside of such a hole. The electron beam then was completely unaffected by the angle under which it impinges the inside wall and no effect could be observed at the opposite wall of the hole.

This is again in contradiction to what Matting and Sepold have observed[13]. Matting and Sepold found that up to 40% of the electrons at the voltage range observed (100 kV) are reflected. If that were the case, then in E. C. Lary's experiment where he had a pre-drilled hole of a 2mm diameter and very high power density, one should have been able to observe some effects of the reflected electrons. The actually observed maximum reflection was about 20%

## PLASMA FOCUSING AND/OR SCATTERING

From these experiments one has to conclude that plasma focusing and/or scattering of the electrons at the vapor should be responsible for the deep penetration. Gas focusing is well known in plasma physics: in a plasma the electrons have a higher mobility and diffuse

faster outwards than the ions, so that an "electrostatic lens" is created which acts like a focusing device on the ions. In many cases, one can observe a wave shaped cross section of the weld which can be explained by scattering effects but not so well with plasma focusing. The wave shaped cross section is probably due to the fact that the vapor density within the cavity is changing periodically with the rupture of the thin films covering the cavity. Immediately after the rupture, the vapor density within the cavity will be low and therefore, few electrons will scatter at the vapor whereas just before the rupture of the thin metal film we have the largest vapor density which means also quite a large number of electrons being scattered by the vapor. During the maximum scattering the cavity will be wider and of course, during the minimum scattering it will be narrower, which then results in the wave shape of the cavity. If there were predominantly gas focusing, the cavity produced by the electron beam should have been in a vapor state along its entire height with a diameter at least as large as the maximum diameter. But this does not show in the metalurgical cross sections along the walls since the metal next to the narrower parts does not seem to have been affected at all.

## ANALYSIS OF BEAM PENETRATION

The second question that E. C. Lary asked himself was answered partly experimentally. Figure 4 shows a relationship between the depth of penetration as a function of beam power for a welding speed of 35 inches per minute. It shows almost a linear relationship. On Figure 5 we find the relationship between welding speed $v$ in inches per minute as a function of depth of penetration which is indicated on the left ordinate. The right ordinate shows $1/d$ ($d$ = penetration depth). This curve suggests a numerical relationship between electron beam power and welding speed given by

$$d = \frac{aP}{v + c} \quad (6)$$

$a$ and $c$ are constants determined by the properties of the working material and of the beam. $c$ mainly contains an effective heat transfer co-efficient which represents the heat lost to the cavity walls. Its value turned out to be 40 inches per minute. Figure 5 follows very well this relationship. Figure 6 shows the variation of the beam diameter with the distance from the lens indicating the geometric nature of the electron beam. Figure 7 shows the linear dependence on beam voltage at constant current which actually means the same as Figure 5, namely that the penetration depth is proportional to the power and not the power density. This somewhat also contradicts Matting and Sepold's

findings that the penetration depth increases less than linear at constant current with changing voltage. However, the two results cannot be compared since E. C. Lary studies the dependence of the total power whereas Matting and Sepold discussed the dependence on the intensity of the electron beam - in other words power density. If one tries to convert Matting and Sepold's results to power values rather than intensities by applying Eq. 3, one will actually find that there is not a real discrepancy.

## THERMAL ELECTRON BEAM PROCESSES IN NON-VACUUM ENVIRONMENT

Since the electrons have to be produced in vacuum, a "window" has to be installed at the vacuum system to let the beam enter the higher pressure working area. For the power density required, this cannot be a real window made of metal foil (Lenard-window). For electron beam processes in gasses, a differentially pumped system has to be designed. B. W. Schumacher[15] could reduce the number of stages of his differential pumping system by a device which he calls "dynamic pressure stages". The idea consists mainly in the fact that a gas rushes through an orifice into vacuum as a shock wave and does not have uniform density in its flow cross section. The pick-up nozzle for the vacuum stage is positioned at the point of lowest gas density within this shock wave. Thus vacuum pumps with much lower pumping speeds are sufficient. Schumacher used the same system for his underwater experiments [16].

## PENETRATION DEPTHS FOR THE NON-VACUUM ELECTRON BEAM PROCESSES

It is to be expected that welding penetration cannot be as deep as in vacuum with the same beam power. J. W. Meier[17] and J. Lempert, J. Lowry, F. Seaman, and C. Williams[18] established experimentally that the acceleration voltage should be in excess of 100 kV. This results from the following facts:

(1) The electron beam has to travel through a space of higher gas density between "window" and work piece. In the gas it will lose additional energy.

(2) The evaporation of the material to be processed is slowed down by the presence of higher pressure background gas. But for deep penetration, evaporation is necessary as we pointed out previously. Beam energy losses to the gas can be derived from the curves of Figure 8 as calculated by L. V. Spencer[19]. They give the range of electrons for energies up to 250 keV in helium and nitrogen in units of atmosphere-inches at NTP. In comparison, the classical range in

aluminum is plotted in inches (right side ordinate). From Spencer's theory one can calculate the gas-thickness in atmosphere-inches at NTP along which the electron beam has lost a certain fraction, for example 10% of its energy for a range amounting to for example 10% of its total range, see Table I.

TABLE I
"Gas Thickness" in atmosphere-inches for 10% electron energy loss.

| Electron Beam Energy in keV | 50 | 100 | 150 | 200 | 250 | 300 |
|---|---|---|---|---|---|---|
| "Gas Thickness" for $N_2$ in atmosphere-inch | 0.16 | 0.52 | 1.0 | 1.6 | 2.27 | 3.0 |

One can see that below 100 keV the electron energy is seriously affected by atmospheric nitrogen. However, there should not exist any basic difference between the electron beam process in vacuum and in non-vacuum. Also in the non-vacuum case, naturally the material density along the electron beam path has to be lowered for penetration depths larger than the classical range. Therefore, all material has to be in a vapor phase of low density which means evaporation has to take place. But evaporation is drastically reduced when the non-vacuum environment exerts a pressure much larger than the vapor pressure of the material to be processed at the working temperature. Penetration will be less. J. W. Meier[17] has compared the welding depth in stainless steel at a welding speed of 35 inches per minute. His results are shown on Figure 9. It appears that penetration depth in the non-vacuum is about 1/4 of that obtained in vacuum under the same conditions.

## ELECTRON BEAM PROCESSES IN OUTER SPACE ENVIRONMENT

Since in outer space ideal vacuum is encountered, this then seems to be just right for electron beam welding as no vacuum pumps are required. However, other problems may show up that do not play a role on earth. Electrostatic charges will be built up. Also in the non-gravitational field certain forces due to reaction forces of the vapor leaving the work piece and due to the pressure of the electrons might influence the movement of the spaceship to be worked on while being free in space. The reaction forces $F_r$ due to evaporation had been discussed by O. C. Wells[20] as applied to electron beam welding and cutting. It is given by:

$$F_r = \nu m \bar{c} A \quad (7)$$

where $\nu$ is the evaporation rate given in the number of atoms leaving the area A during unit time, m the mass of one vapor atom, and $\bar{c} = (8kT_v)^{\frac{1}{2}}(\pi m)^{-\frac{1}{2}}$

In approximation one can write Formula 7 as

$$F_r = 2p_r A/\pi \quad (7a)$$

where $p_v$ is the vapor pressure of the material at the working temperature. For example, at a working temperature of 3000°K and an area of $A = 10^{-6}$ m$^2$ (approximately spot diameter 1 mm) a force of $F_r \approx 3 \times 10^{-2}$ Newton is being exerted on the work piece.

The electron pressure is given by the momentum of the electrons transferred to the work piece. Neglecting back scattering, it is easily calculated by

$$F_e = i(2m_e U/e)^{\frac{1}{2}} \quad (8)$$

where i is the electron current, $m_e$ the mass of the electron, e its charge, and U the acceleration voltage. In terms of electron beam power P, Formula 8 reads:

$$F_e = P(2m_e)^{\frac{1}{2}}(eU)^{-\frac{1}{2}} \quad (8a)$$

which means that for a given electron beam power P, the electron beam force $F_e$ decreases with increasing acceleration voltage. For example, at an electron beam power of P = 10 kW and an acceleration voltage of U = 100 kV we shall have an electron force of at least $F_e \approx 10^{-4}$ Newton.

The reaction force due to evaporation in the example given here is by 2 orders of magnitude higher than the force due to the electron pressure. For practical cases, $F_r$ will always be larger than $F_e$.

F. R. Schollhammer[21] has experimentally established that

neither the work piece nor the operator will be noticeably affected by electrostatic charges.

## ELECTRON BEAM PROCESSES IN MICROELECTRONICS

The initial enthusiasm of having obtained with the electron beam a tool that could drill holes and perform cuts, i.e. in thin metal film resistors, [22] of line widths as narrow as determined by electron optics of the beam has to be dampened by the material interaction effects. In order to obtain fine spots and high power densities, high voltages have to be applied so that the space-charge and thermal-velocity spreading effects of the beam will be less effective. But higher voltages mean deeper initial penetration and sub-surface heating. This will lead to blister formation and result in larger areas affected by the beam which are more extensive than electron optical calculations would yield.

Only in the case of non-thermal processes like the decomposition and carbonization of cellulose nitrate films as demonstrated by Möllenstedt and Speidel[23] really small spot sizes can be achieved since one is not limited by the space charge effects of the electron beams at the low powers needed for such processes. Möllenstedt and Speidel achieved line widths of the order of 100 Å.

## ACKNOWLEDGMENTS

I would like to thank the program committee of the Third International Conference on Electron and Ion Beam Science and Technology for having invited me to present this paper. My thanks are due to Sterling Newberry of General Electric's Research and Development Center, who arranged the high-speed electron beam welding movie made by R. E. Kutchera and Lloyd Winters of General Electric's Jet Engine Department. I greatly appreciate the permission of E. C. Lary of United Aircraft Research Laboratories to report on his unpublished research. I am also grateful to A. Matting and G. Sepold of the Technical University, Hannover, West Germany, for the private communication in regard to their experimental results, which partly constitute a yet unpublished doctoral thesis of G. Sepold. I also acknowledge the assistance of B. R. Onuf of Rensselaer Polytechnic Institute, Hartford Graduate Center, in solving the Eq. 3a.

REFERENCES

1. K. H. Steigerwald, Verhandl. deut. Physik. Ges. 4, 123(1953); Proc. 3rd Symposium on Electron Beam Processes, Boston, Mass. March 1961, pp. 269-290.

2. J. A. Stohr, Fuel Element Conference, Paris, November 1957, TID-7546, Book I, pp. 9-17, US Atomic Energy Commission.

3. M. von Ardenne, Naturwiss. 26, 562 (1938).

4. H. Schwarz, RCA Invention Disclosure Docket #47,360 (1958), "Pattern Writing or Printing by Electron or Ion Beam Guided by Electron Optics".

5. K. H. Steigerwald, 4th Internat. Congress for Electronmicroscopy, Berlin 1958, p. 276.

6. H. Schwarz, Vacuum Deposition by High Energy Laser with Emphasis on Barium Titanate Films. To appear in Rev. Sci. Instr. 1968.

7. H. Schwarz, J. Appl. Phys. 35, 2020 (1964).

8. J. Pellissier, Revue M. Tijdschrift 9, 82 (1962).

9. Brasch and Lange, as reported in J. Dosse and G. Mierdel, "Der Elektrische Strom im Hochvakuum und in Gasen" (S. Hirzel, Leipzig, 1945), p. 46.

10. A. Visser, Werkstoffabtrag mittes Elektronenstrahlen. Dissertation, Technical University, Braunschweig, Germany-West, 1966.

11. See for example L. Holland, Vacuum Deposition of Thin Films (Chapman & Hall, Ltd., London, 1958), p. 143.

12. B. R. Onuf, Private communication, Rensselaer Polytechnic Institute, Hartford Graduate Center 1968.

13. G. Sepold, Dissertation Technical University Hanover, Germany-West 1968, in print.

14. E. C. Lary, UAC Research Laboratories, Private communication 1968.

15. B. W. Schumacher, AVS Symposium 1961 Transactions, Pergamon Press 1962, p. 1192.

16. B. W. Schumacher, Some Observation on High Power Electron Beams under Water. This Conference.

17. J. W. Meier, 1st Internat. Conference on Electron Beam Science and Technology, Toronto, Canada 1964, p. 634.

18. J. Lempert, J. Lowry, F. Seaman, and C. Williams, Proc. Electron and Laser Beam Symposium, edited by A. B. El-Kareh, Penn State University 1965, p. 393.

19. L. V. Spencer, Nat. Bureau of Standards Circular #577, 1956.

20. O. C. Wells, 3rd Electron Beam Symposium, March 1961, p. 291.

21. F. R. Schollhammer, Records of IEEE 9th Annual Symposium on Electron, Ion, and Laser Beam Technology, Berkeley, Cal. 1967, p. 215.

22. H. Schwarz, J. Appl. Phys. 33, 3464 (1962); RCA Invention Disclosure 1958, see Ref. 4 this paper.

23. G. Moellenstedt and R. Speidel, Physikalische Blaetter 4, 192 (1960); Abstract International Solid-State Circuits Conference, Philadelphia, Pa. 1961.

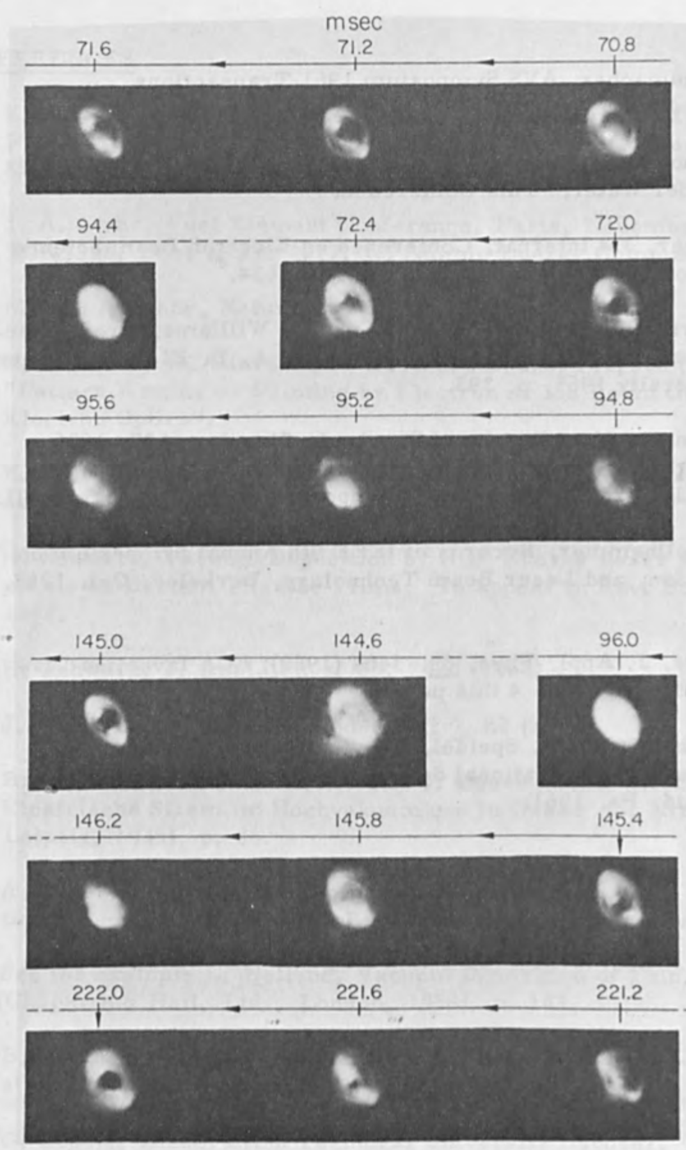


Fig. 1: High speed cinematographs; metal film ruptured at 72.0, 145.4, and 222.0 msec (from Ref. 7) Time magnification 100 x.

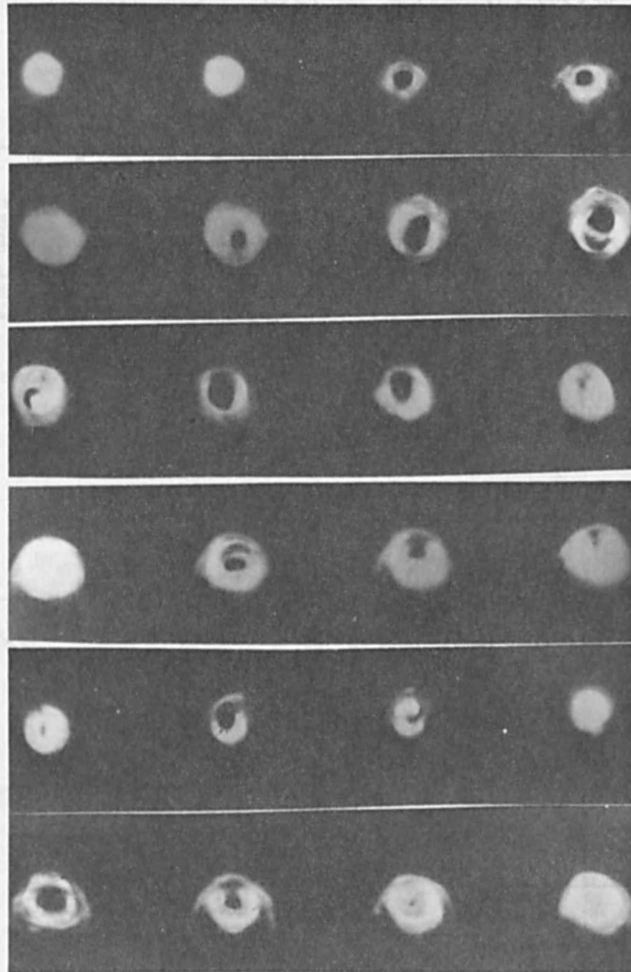

Fig. 2: High-speed cinematographs; courtesy General Electric (see acknowledgment). Time magnification varying between 320 and 1,200.

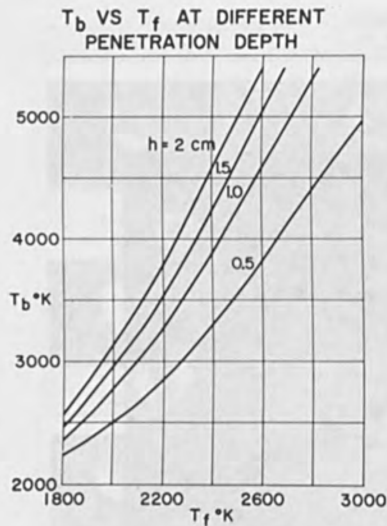


Fig. 3: Bottom temperature $T_b$ as a function of surface temperature $T_f$ at different penetration depths h for pure iron. (Ref. 7)

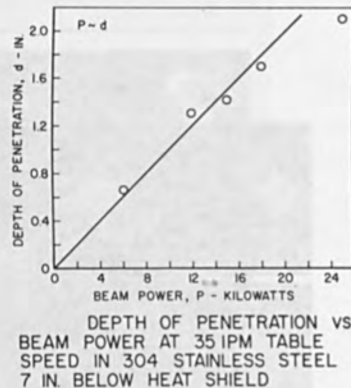


Fig. 4: Courtesy of E. C. Lary, UAC Research. (Ref. 14)

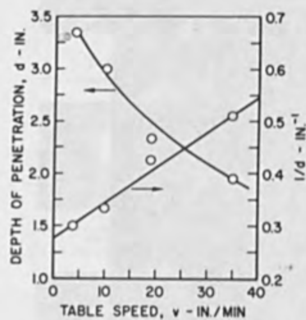


DEPTH OF PENETRATION VS TABLE SPEED AT 150 KV, 160 MA 6 IN. BELOW HEAT SHIELD ROGOWSKI GUN WITH 12 MIL. FILAMENT

Fig. 5: Courtesy of E. C. Lary, UAC Research. (Ref. 14)

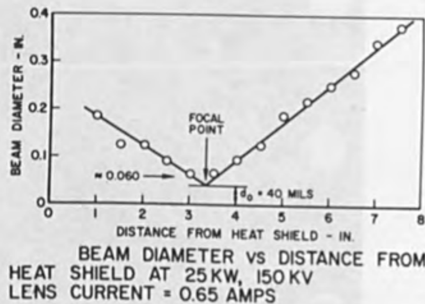


BEAM DIAMETER VS DISTANCE FROM HEAT SHIELD AT 25 KW, 150 KV LENS CURRENT = 0.65 AMPS

Fig. 6: Courtesy of E. C. Lary, UAC Research. (Ref. 14)

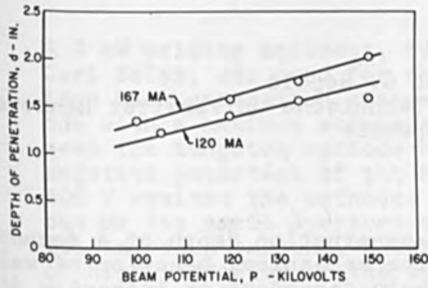


Fig. 7: Courtesy of E. C. Lary, UAC Research. (Ref. 14)

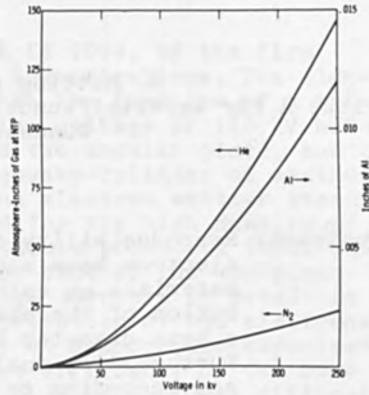

Fig. 8: Range in He and $N_2$ gases and in solid Ae as function of acceleration voltage. (Ref. 18)

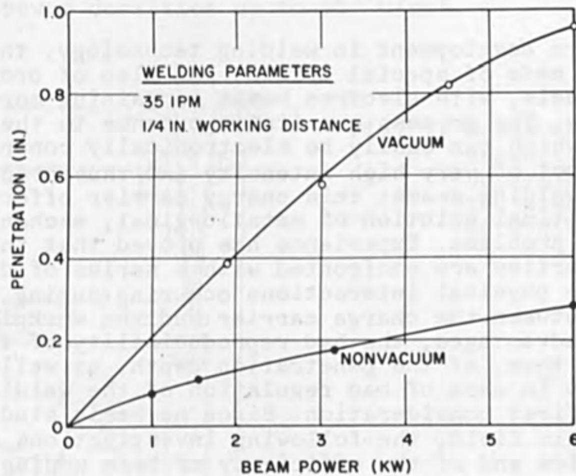


Fig. 9: Vacuum and non-vacuum weld penetration as function of electron beam power at a welding speed of 35 inches/minute in stainless steel. (Ref. 17)

BASIC RESEARCH ON WELDING WITH
ELECTRON BEAMS OF HIGH INTENSITY

by

A. Matting und G. Sepold
Institut A für Werkstoffkunde, Technische Universität Hannover
Bundesrepublik

Abstract: Reproducibility of penetration depth of a focussed electron beam and the mechanical behavior of welded materials are extremely dependent on intensity distribution of the electrons. This has been measured and a beam diameter has been defined.
Furthermore, inelastic backscattering of electrons and according to their primary energy the efficiency is shown to be of large influence on the choice of optimal parameters.

## 1. Introduction

As a modern development in welding technology, the assembly of pieces made of special metals, and also of ordinary low-carbon steels, with electron beams is gaining more and more importance. The process ows its importance to the energy carrier, which can easily be electronically controlled, having a focal spot of very high intensity and thus produces thin and deep welding seams; this energy carrier offers itself for the optimal solution of metallurgical, mechanical and corrosion problems. Experience has proved that these excellent properties are confronted with a series of disadvantages due to the physical interactions occuring during the welding process between the charge carrier and the workpiece. Among these disadvantages, the bad reproducibility of the electron beam and, thus, of the penetration depth, as well as its low efficiency in case of bad regulation of the welding data must be given first consideration. Since no basic studies have been made in this field, the following investigations of beam characteristics and of the efficiency of beam welding should contribute to the achievement of better welding results.

2. Measuring Device for the Regulation of Reproducible Welding Data

A 3 kW welding equiment, type ES 1013, of the firm Carl Zeiss, was used for the investigations. The electron beam generation system has the function of a triode with a maximum acceleration voltage of 150 kV between the tungsten cathode and the annular plate, and a negative potential of the Rogowsky-cylinder of maximum 800 V against the cathode. The electron emitter stands out for its small aperture and for the high density of its emission current, which should produce a focal point of high intensity on the upper side of the workpiece. The penetration depth of charge carriers in metals is dependent on the density distribution of the electrons, which had to be determined by an appropriate experimental setup. Because of the high efficiency of the beam and its small diameter, appr. 500 µm , it was difficult to record the electron density distribution; diaphragms or metal edges for integral records of the distribution form were, for example, destroyed. Important measuring errors were due to this difficulty. With the aid of the device shown in fig. 1, it was eventually possible to record the intensity distribution of electronic beams with power densities up to $10^7$ W/cm².

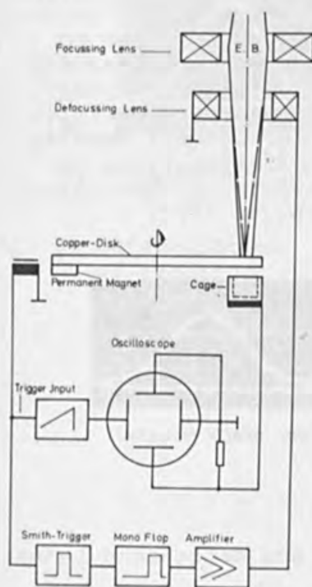


Fig. 1. Measurement assembly for the determination of the electron density distribution.

A copper disk, driven by a d.c. shunt-wound motor controlled from the outside of the chamber, rotates under the electron beam at the level of the workpiece surface. A generator, mounted on the rotating disk, induces a signal in a laterally fixed coil. This signal is, on the one hand, converted into a square sided pulse having to be amplified and is, on the other hand, routed as an external signal to the measuring device, an oscilloscope.

A broad slot covered by a tungsten diaphragm is milled out of the copper disk. A catcher is mounted underneath the diaphragm in the direction of the electron beam axis. The size and the distribution of the electrons per disk revolution, represented as the voltage drop on a known resistor, can be read from the image of the oscilloscope. Even high radiation efficiencies cannot destroy the disk, because the beam remains defocussed till it almost reaches the tungsten slot. Defocussing is obtained by a coil below the magnetic lens, which focusses the beam for a short time at every revolution, then, when the beam is just in front of the slot diaphragm on the tungsten cover plates, it passes over it and is then again defocussed.

The measuring device permits to record the intensity distribution in the x and y direction; the charge carriers are always registered as a sum in one direction because the slot is very long, as compared to the beam diameter. Different values are obtained for the x and y axis in the focal spot. This fact leads to the conclusion that the beam diameter is elliptical. Therefore, the behaviour of the current density does not correspond to a Gaussian distribution, as was often suggested (1,2). The Gaussian distribution is only obtained below the focal plane (fig. 2).

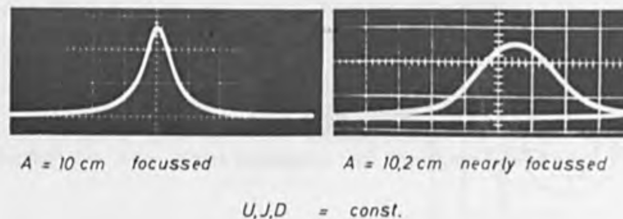


Fig. 2 Distribution of focussed and defocussed beams

Since there is no fundamental difference between these two distributions, the Gaussian distribution - which is simpler from the mathematical point of view - has been used for further considerations. Proceeding on these premises, the electron beam diameter is assigned to the $\pm 2\sigma$ range, which includes 95,45 % of the negative particles. It can be obtained by plotting the function values of the distribution on probability paper, representing them as a straight line and reading off the $\sigma$-values, see fig. 3.

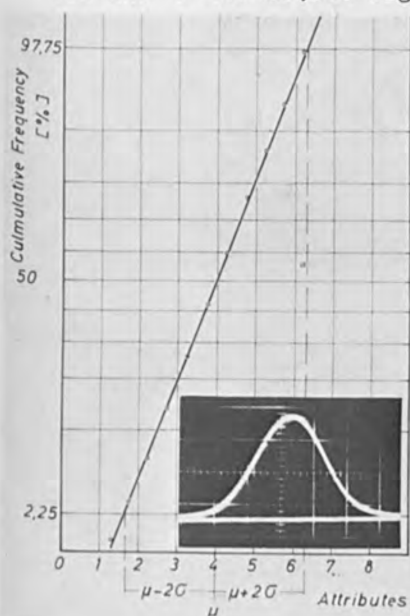


Fig. 3. Determination of electron beam diameter

The electron beam diameter follows from the circumferential speed of the disk at the impact point of the electrons, and from the time t corresponding to the $\pm 2\sigma$ range.

The total current $\dot{I}_t$ can be calculated with the following relation:

$$\dot{I}_t = \int_{-\infty}^{+\infty} \dot{I}_{max} \cdot e^{-t^2/2\sigma^2} \, dt \quad (1)$$

$\dot{I}_{max}$ = maximum current of the distribution per time unit in mA/sec.

This value must correspond to the current value which can be taken up by a Faraday's cage.

The result of the beam diameter measurements as a function of the beam current and the accelerating voltage is represented in fig. 4. and fig. 5.

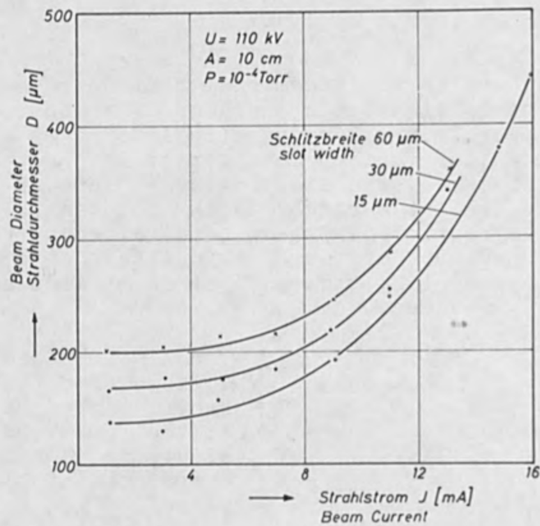


Fig. 4. Beam diameter as a function of I.

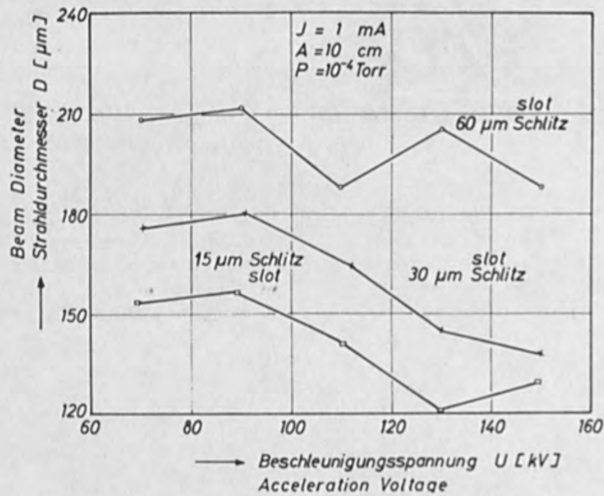


Fig. 5. Beam diameter as a function of U.

In this connexion, the slot width is another parameter. The distance between the curves allows to make conclusions as to the fault due to the slot width. In the main, the statements of Bas and Cremosnik (3), who propose a slot width of appr. 1/10 of the beam radius, can be confirmed.

The set of curves in fig. 4 take the course of a parabola with ascending tendency of beam diameter towards higher beam currents and thus approximately reach the mathematical result (4):

$$d_{min} = 4{,}3.10^6 . Z^{0{,}14 \pm 0{,}06} (C.f)^{0{,}86 \pm 0{,}06} \left[ \frac{i^{1{,}36 \pm 0{,}06}}{V^{2{,}05 \pm 0{,}08}} \right]$$

$$Z = \frac{d_r}{2\alpha}$$

$d_r$ = diameter of the beam cross section just after leaving the effective field of focuseng lens

$\alpha$ = beam aperture

C = spherical aberration constant

f = focal length (m)

$d_{min}$ = theoretical minimum spot diameter

If there is a voltage drop, the dependence of the beam diameters is less obvions (see fig. 5), as it is expressed by the equation. The tendency of falling values at increasing voltages has to be ascertained.

The influence of vacuum conditions was investigated in a similar way, a slight broadening of the distribution could be determined in the range between $5.10^{-3}$ and $1.10^{-4}$ Torr. The influence of the annealing time of the tungsten cathode has shown to be of much greater importance. The surface vaporization, the ion bombardment and particularly the thermic tensions have a critical influence on the distribution form in the focal spot and, thus, a considerable influence on the depth of penetration in welding.

## 3. Efficiency Determination in Electron Beam Welding

The efficiency of electron beam welding is the ratio between the energy required for the melting process and the kinetic energy of the beam. Values of 95 to 98 % (5,6) have been mentionned, but up to now there has been no thorough energy determination.

### 3.1 Backscattered Electrons

Measurements of Brand (7) and Bothe (8) on the losses of charge due to backscattering from solids

have already shown values of 30 % and more. These results, however, do not allow to draw conclusions as to welding circumstances, since in that case, due to the electron bombardment, the material is changing over to the liquid or even to the vaporous phase. In the course of our own measurements with a test setup similar to that of Sternglass (9), backscattered electrons, representing a specific amount of energy, could also be detected during the welding process. This energy is lost for the melting process. The test setup shown in fig. 6. was used for the detection of backscattered electrons.

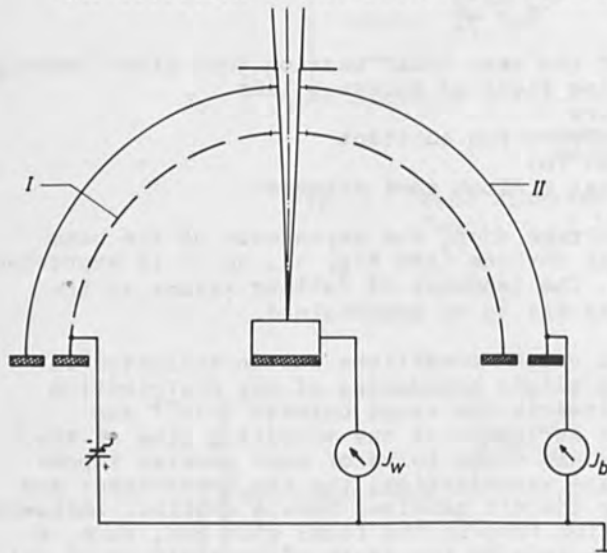


Fig. 6.
Test setup

Primary electrons impinge on an isolated workpiece, some are reflected and have to run back against the variable negative potential of a catcher (I), consisting of extremely thin wire, in order to get into the cage (II). The reflexion current $I_b$ is registered by a recorder and can be represented as a function of the current and of the voltage. The test setup is complicated since a good isolation of the cage, the workpiece, the welding chamber openings and the measuring devices is necessary; this complication renders it difficult to record energy distribution curves of highly accelerated electrons in the 100 keV-range. Therefore, another experimental method was chosen to determine the average energy losses by backscattering.

### 3.2 Energy Balance

The measuring method is based on an energy balance of the physical reactions of the electrons impinging on a metal. The following energy components have to be taken into consideration for the calculation :

$$Q_t = Q_{th} + Q_{ion} + Q_v + Q_r + Q_{el} \qquad (4)$$

$Q_t$ = total energy

$Q_{th}$ = energy required to heat and melt a solid

$Q_{ion}$ = ionization energy

$Q_v$ = vaporization energy

$Q_r$ = radiation energy

$Q_{el}$ = secondary energy, including losses by backscattering $Q_b$.

If the different amounts of energy can be estimated as a function of the welding parameters - except the backscattering term -, an approximation solution for $Q_b$ is obtained. This estimate can be obtained mathematically and experimentally.

#### 3.2.1 Energy of Radiation

When an electron beam impinges on a solid, an increase in temperature can be noted on the solid at the point of impact and at a distance r from this point. The temperature range in consideration extended from the boiling point of the specimen in the centre of the focal spot to a range of appr. 300° C at the distance r = 5 mm from the beam axis. Due to the extremely short melting, vaporization and solidification times of the material, an average temperature course per unit time has to be taken into account, it sets in after appr. 1/10 sec.

It can be assumed with sufficient accuracy that the radiation of the metal surface bombarded with electrons is similar to that of a black body. Therefore, the amount of energy reflected per time and surface unit is, according to Stefan-Boltzmann's radiation law :

$$Q_{radiation} = C_r \left( \frac{T_m}{100} \right)^4 \qquad (5)$$

In this equation, $C_r$ is the radiation coefficient of a completely black body and Tm is the average temperature of the point of impact with the radius r=2mm

The above-mentionned equation covers the spectrum of all wave lengths, from the extremely short wave, energetic X-radiation to the comparatively long wave radiation of the visible light.

The following equation was laid down for the local radial temperature course at the point of impact :

$$T(r) = A \cdot e^{\lambda r} \quad \text{in } {}^\circ K \qquad (6)$$

The constants A and $\lambda$ can be determined by square law compensating computation of the temperature measurements at distances r from the focal spot with the aid of thermoelectric elements. Thus :

$$T(r) = 2600 \cdot e^{-0.457\, r} \qquad (6.1)$$

This equation determines the changing temperature course at definite spots of a solid. The average temperature reflected by an average surface is therefore as follows :

$$Tm^4 \cdot Fm = \int_0^r T(r)^4 \, 2r\pi \, dr \qquad (7)$$

Tm can be determined by the insertion of equation (6.1) into equation (7); thus, for welding data as for example

U = 100 kV, I = 5 mA,

a welding time of 0.1 sec and a radiative surface with r = 2 mm, a radiation loss of 0.5 % is obtained for steel. This value is an approximation.

3.2.2 Vaporization and Ionization Energy

The energy required for the vaporization of a certain quantity is :

$$Q_v = m \cdot s \qquad (8)$$

m = evaporated quantity
s = heat of vaporization

The evaporated quantities of aluminium and steel have been specified in a test with U = 100 kV and I = 8.5 mA. Compared to the total energy of the beam, which is equal to the product $U \cdot I \cdot t \cdot 0.239$ , loss factors of 2.3 % were obtained for aluminium, and of 1.7 % for steel.

Because of their smallness, energy losses caused by the ionization of metal gases can be neglected according to Koch and Neubert (10).

### 3.2.3 Losses by backscattering

The amount of energy $Q_{el}$ of every electron can have different values, according to the kind of physical reaction caused by the impact on the metal surface. They can be expressed by the following equation:

$$Q_{el} = Q_{el\ elastic} + Q_{el\ inelastic} + Q_{el\ secondary} \quad (9)$$

$Q_{el\ elastic}$ is negligible because of the high impact potentials, i.e. the high accelerating voltage is unlikely to produce elastic collisions.

Similarly, the loss of energy caused by thermionic emission is negligible in comparison with the other amounts of energy (10).

$Q_{el}$ is therefore only the energy of backscattered electrons.

The energy loss of these backscattered electrons can be calculated with the following relation :

$$Q_{backscattering} = Q_g - (Q_{th} + Q_k) \quad (10)$$

$Q_k$ is composed of the radiation and evaporation losses. As mentionned above, it amounted to 2.2 % for steel but, as a whole, never exceeded 5 % of the total energy, with a maximum energy of the primary beams of 2.5 kW.

If the thermal energy required for melting in the welding process can be determined in dependence of the welding parameters U,I and v by an appropriate test setup, statements can be made on the amount of backscattering energy.

The test setup is shown in fig.7. The whole setup is mounted on a mobile stand in the welding chamber; the properties of the electron beam are shown in pos. I to III. In position I the distribution form of the electrons for reproducible results is recorded by the measuring device which was described in section 2. The beam current is measured in position II. In position III, the beam passes over tungsten plates and imparts for a short time a certain quantity of heat to the isolated specimen.

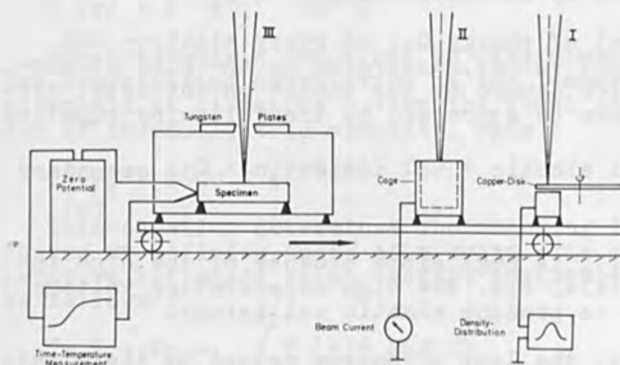


Fig.7. Test setup

After a certain time, due to thermal conduction, a constant temperature is reached in all parts of the specimen.There are no heat losses due to convection in the vacuum; radiation losses of the surface outside the focal point are negligible. A constant temperature per time unit was reached in all parts of the testpiece when the rise in temperature at the ends of the solid reached a maximum and remained constant for a certain time. The rises in temperature were measured with pasted on thermoelectric elements. The thermo-voltages were recorded by a flying spot recorder with low damping resistance.

The experiments are limited to steel and aluminium test pieces.

The thermal energy imparted to the specimen can be determined by the following relation :

$$Q_{thermal} = m \cdot c \cdot \Delta\vartheta_{max} \text{ in cal} \quad (11)$$

c = specific heat of the solid

$\Delta\vartheta_{max}$ = maximum rise in temperature of the solid

The dependence $Q_{el} = Q_b$ on the welding parameters is shown in the following diagrams (fig. 8 - 10).

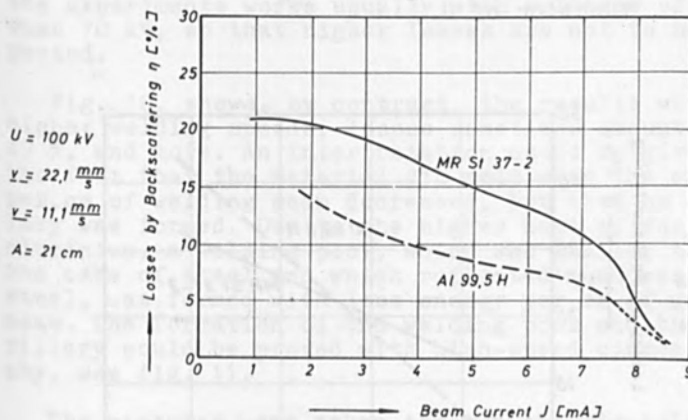


Fig. 8. Losses by backscattering as a function of I.

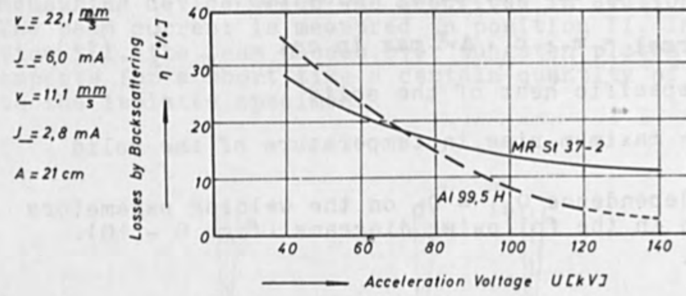


Fig. 9. Losses by backscattering as a function of U.

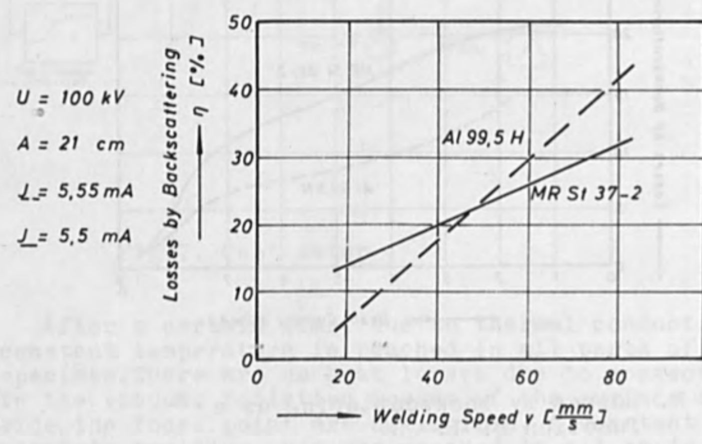


Fig. 10. Losses by backscattering as a function of v.

On principle, the statement that at a constant welding speed the backscattering decreases when the energy U · I per cm of welding seam increases, applies to the first 2 graphs. This indicates a broader and deeper capillary formation in the piece, i.e. the transmission of the electron energy to the capillary by plural scattering in the plasma gas. The welding capillary acts in this case as an electron trap, in which the electrons transmit their energy and their charge by collision to the walls.

The reflexion losses of aluminium were less important than those of steel St 37, i.e. due to the higher rate of evaporation a larger capillary was formed in aluminium.

Fig. 9. shows the backscattering as a function of the acceleration voltage. Losses were relatively small, from about 0 to 15 %, when the accelerating voltages exceeded 80 kV. The welding machine used for the experiments works usually with voltages of more than 70 kV, so that higher losses are not to be expected.

Fig. 10. shows, by contrast, the results with higher welding speeds; losses sometimes amounted to 40 %, and more. An interpretation could be given by the fact that the material did melt when the energy per cm of welding seam decreased, but that no capillary was formed. Due to the higher heat of fusion of aluminium, a welding pool, which was smaller than in the case of steel and which reflected much more than steel, was formed with less energy per cm of welding seam. The formation of the welding pool and the capillary could be proved with high-speed cinematography, see fig. 11.

The pictures were taken through the viewhole of the installation. The larger molten pool of steel can easily be distinguished. The supply of energy is the same in both cases.

It was possible to proove the existence of the relationship between an increasing reflexion loss and higher atomic numbers. Additional tests with Ti, V, Cu and W confirmed this result, which is also mentionned in the technical literature (11), for electron beam welding.

Al

Fe

Fig. 11. Molten pool formation in Fe and Al.

## 4. Summary

A new test method was used for the determination of the backscattered energy in the case of electron beam welding; it was thus possible to record the distribution of the charge carrier density and to obtain reproducible welding results. The following results can be specified :

1. Practical experiments prooved, in the case of electron beam welding, the existence of the theoretically determined relationship, that means that the size of the electron beam diameter is a function of current and voltage.

2. In the case of electron beam welding too, there is a relationship between the backscattered energy and the backscattered electrons, detailed studies have not yet been made on this subject.

3. Efficiencies of more than 90 % could be obtained with beams of higher energy per unit of length of the welding seam.

   However, higher energies are only required for thicker workpieces. The highest degree of efficiency is obtained by the formation of a steam cpaillary. In the case of light- gage sheet steel welding, energetical conditions are less favourable, the efficiency rate may fall below 60 %, so that the values of 95 % and 98 % mentionned in the technical literature can no longer be maintained.

4. There is a dependence between losses by backscattering and the atomic number. Further investigations in this field are going on

REFERENCES


(1) v.Ardenne, M: "Tabellen der Elektronenphysik, Ionenphysik und Übermikroskopie", Vol. 1, p. 136, 1965

(2) Haschimoto, T., Matsuda, F. and Suzuki, H.: "On the Characteristics of Electron-beam Current in Electron-beam Welding, Trans. of Nat.Res. Inst. for Metals, Vol. 6, Nr. 1 (1964) p. 26-39.

(3) Bas, E.B. and G. Cremosnik: "Experimental Investigation of the Structure of High-Power-Density Electron Beams", First International Conference on Electron and Ion Beam Science and Technology, John Wiley & Sons, Inc., New York, p. 111

(4) Schwarz, H.: "Power Density of Optimally Focused Space-Charge-Limited Electron Beams", J.of Appl. Phys., Vol. 33, Nr. 12, 3464-3470

(5) Steigerwald, K.H.: "Elektronenstrahlen als thermisches Werkzeug", Neue Zürcher Zeitung 1963, Nr. 763/66.

(6) Hashimoto, T. and F. Matsuda: "Effect of Welding Variables and Materials upon Bead Shape in Electron Beam Welding", Transactions of Nat.Res. Inst.for Mat., Tokyo, Vol 7. (1966) Nr. 3, p. 96/103

(7) Brand,F,Jacobs,A. and J.Freely:"Mechanism of Field Dependent Secondary Emission", rep.12th Annual Conf. Physics Electronics,p.74.

(8) Bothe,W.:"Zur Rückdiffusion schneller Elektronen", Zeitschr.Naturforsch.,4a,542.

(9) Sternglass,E.J.;"Backscattering of Kilovolt Electrons from Solids", Phys.Rev.95,p.345.

(10) Koch,F.,and G. Neubert:"Wirkungsgradberechnung beim Elektronenstrahlschweissen",ZIS-Mitteilungen, Halle,vol.9 (1967), Nr.5, p.818/827.

(11) Kollath,R.:"Sekundärelektronen-Emission fester Körper bei Bestrahlung mit Elektronen",Handbuch der Physik,vol.21,p.232/303,Springer Verlag 1956.

# MATERIALS REMOVAL PROCESSES IN LASER AND ELECTRON BEAM MACHINING*

by
G. Pahlitzsch and A. Visser

Institute for Machine Tool
and Manufacturing Technology,
T. H. Braunschweig, Germany

## 1. Introduction

In the majority of the literature references about materials removal by means of electron beams or laser beams, it is stated that the process proceeds in the same manner in both cases, namely by evaporation of the material. Some investigators believe in a steady quiet evaporation whereas others are inclined to believe in an explosive process. But these conclusions were the result of rather isolated observations and not the result of a direct comparison of the two processes. Looking at it somewhat closer it seems rather improbable that the process should proceed in the same manner in view of the fact that the energy input is provided by energy carriers which are as different as electrons on the one hand and photons on the other hand.

## 2. Physical Nature of Electron and Laser Beams

The electron beam consists of corpuscles with an inert mass, whereas in a laser beam we have an electromagnetic wave, and no mass. In Table I some of the essential data of the two energy carriers are listed. For electrons mass and elementary charge are the inherent

*Paper to be presented at the Third International Conference on Electron and Ion Beam Science and Technology, Boston, Mass., May 6-9, 1968.

quantities, for photons they are energy and wavelength. However, because of the principle of equivalence of mass and energy one can derive an equivalent energy for the electrons and an equivalent mass for the photons. For a photon-quantum of visible light the mass is only about one five-millionth part of the electron mass. The energy of the quant depends upon the frequency of the wave. For the wavelength of the ruby laser, 6943 Å the quantum energy is approximately $3 \times 10^{-19}$ Ws which would correspond to the kinetic energy of an electron accelerated through a voltage of 2 V. However the commonly used accelerating voltages for electron beam machining are in the range of 20 to 200 kV. While it is easily possible to change the energy of the electrons by changing the acceleration voltage it is not possible to change the photon energy which has a fixed value for the laser material which is being used. One would have to exchange the laser light source, for instance the ruby rod against a neodym rod, to obtain another photon energy.

3. Energy Transfer from the Beam to the Workpiece

There is no question that in both cases the beam energy is finally converted into heat. In a solid body heat is kinetic energy of the crystal lattice. The transfer of the energy cannot occur in a single step. In case of an electron beam the mass difference between the beam electrons and the atomic nuclei is much too big for a direct exchange of impulse or kinetic energy. The electrons of the atomic shell and the beam electrons are however collision partners of about

equal mass. Since equivalent mass of the photons is even small compared with the electrons they do not have the capability for excitation by collision. For them the only possibility left is that of resonance excitation, for which the mass difference is of no consequence. A review of the possible resonance spectra is shown in Fig. 1. There is an essential difference in the resonance behavior of the outer electron shell for nonconductors and for metals. The nonconductors show only a narrow resonance band in the ultraviolet, whereas the resonance band of the conduction electrons in metals stretches over more than 10 orders of magnitude from the ultraviolet to the radiowaves. For the photons of ruby laser light (6493 Å, hν = 1.87 eV) falling on a metal target, the first step in the energy transfer will therefore be an interaction with the conduction electrons. Many nonconductors are transparent for visible light, which means no beam energy is absorbed, because they possess a resonance gap between the lattice vibrations and the electron vibrations. For semiconductors the resonance range of the outer electron shell is shifted to somewhat lower values and laser light is absorbed. However, in the infrared even germanium and silicon are completely transparent.

Contrary to what one finds in the case of photons electron beams of medium velocity, $10^4$ to $10^5$ eV, can dissipate their energy gradually, and in small portions, as the target material is able to accept it. It is not so, as one might naively assume, that the electrons can only exchange energy with the inner shell or the atomic nucleus. Medium velocity electrons passing through thin films of metal will suffer discrete

energy losses between approximately 4 and 60 eV, or approximately integral values of these numbers, which is due to the excitation of the electrons in the outer shell of the atoms. Besides some discrete energy losses in the order of 300 eV are found due to excitation processes in the inner L and K shells. However, the excitation probability diminishes very quickly towards the inner shells and is for the K shell only proportional to $1/Z^5$ (Z = atomic number).

So far only the first step in the energy transfer has been described but the beam energy has not yet been transmitted to the crystal lattice. It proceeds differently depending upon the target material, whether nonconductor, semiconductor, or metal. The relaxation of the excited atom back to the ground state proceeds in the case of nonconductors mainly (to approximately 99%) via collisions of the second kind. There, the stored energy will be transmitted to another nonexcited atom without radiation being emitted, leading to an increase in the kinetic and therefore thermal energy of the collision atom. In the case of semiconductors and metals the energy stored in the conduction electrons is transmitted to the lattice via the lattice photons. Since the equivalent mass of the lattice photons is very small, because of their relatively small energy, many collisions are required. Much larger amounts of energy can be exchanged between the conduction electrons themselves, and thereby dissipated. This is one reason why for metals the heat conduction by electron conduction exceeds by far the one by lattice conduction. One must assume that a considerable part of the beam energy is

transported from the absorbing layer into lower regions of the target before its conversion into heat is completed.

The penetration process for the two kinds of beam is, because of their different physical nature, completely different. On account of their mass and high kinetic energy the electrons penetrate relatively far into a target. Yet a light or laser beam is already absorbed in the surface layer of a metal target. The intensity of the lightwave decays according to an exponential function as shown in Fig. 2a. In Fig. 2b the range R is shown for which the intensity of the lightwave has decayed to 1/e of the initial value. The practical range in which about 99% of the incoming energy is absorbed is approximately 3 R. Monochromatic ruby laser light with a wavelength of 6943 Å penetrates into tungsten not more than .025 μm. For insulators and semiconductors the penetration depths is somewhat larger. For silicon and germanium it is roughly .1 μm.

Electron beams penetrate much deeper into a target, because, for the fast electrons only a very small part of the atom is impenetrable. Yet because of the collisions with the atomic electrons they are slowed down, gradually losing their energy, Fig. 3a. The practical range $R_{pr}$ is shown in Fig. 3b as a function of the accelerating voltage. 150 keV electrons penetrate into a tungsten target approximately 25 μm, about 1000 times as deep as the photons.

## 4. Models of the Materials Removal Process

It follows from the above discussion that in case of a laser

beam the complete beam energy is converted on the surface of the workpiece as shown in Fig. 4. In case of an electrom beam, because of the deeper penetration depths of the electrons, a larger volume below the target surface will be heated directly. For this reason the heating under influence of an electron beam proceeds slower, as can be seen from the values in Fig. 5, although the power density of the electron beam with approximately $10^{10}$ W/cm$^2$ has been assumed to be 100 times bigger than that of the laser beam.

Under laser bombardment a temperature will be reached already at the beginning of a laser spike, within a fraction of a hundredths of a microsecond, at which most materials begin to evaporate even at normal pressures. Because of the inertia of the mass of the target matter, to which later also a high gas kinetic repulsion force is added, the directly heated layer will after melting still be heated more and more without an increase in volume, and will soon reach an overheated state. Ready[1] has observed that during materials removal with giant laser pulses the expansion of the target material begins only after about 40 ns. Within this time interval even a normal laser spike deposits many times the evaporation energy on the target, hence most target materials may be considered superheated to near their critical point.

Besides, a considerable amount of the laser energy will be transported by electron conduction into the interior of the target, at least for metal targets. Fig. 6 gives an impression of the order of magnitude of this effect; it shows the temperature relaxation in a semi-infinite

block of copper, the surface of which has been raised to evaporation temperature at time T = 0. Already after 50 ns melting temperature has been reached at a distance of 2 μm below the surface. Considering the extremely short range of the laser beam this depth effect is remarkable

Most likely the materials removal under laser bombardment begins in a explosive manner with a rarefaction wave traveling with the velocity of sound into the target. At the same time a certain target volume is melted. If a successive laser spike impinges on such a melt zone an explosive eruption of the melt is produced because of the gas pressure of the components with higher vapor pressure. How strong such photo-hydraulic effects can be show the very instructive experiments of Prokhorov et al[2] about the effects of laser beams in liquids. When the absorption of normally transparent water was increased by dissolving copper sulphate bombardment led to a concentrated ejection of the water from the experimental vessel with the ejection reaching a height of up to one meter. It is therefore very probable that materials removal under normal laser bombardment does not proceed exclusively by evaporation but partly by removal of molten material, the process changing more and more from pure evaporation to the molten-liquid-mode with increasing pulse duration.

The hydraulic effect will be even more pronounced in the case of electron beam heating because, according to the above discussed model, a much deeper cone in the target is heated directly by the beam and melted. One must therefore assume that the removal process proceeds in this case mainly in the liquid phase. It has generally been assumed that in the

case of electron beam machining the necessary vacuum has a favorable effect on the vaporization process because the boiling point is reduced under reduced pressure. But apart from the fact that the reduced pressure in the work chamber is not equal to the effective pressure on the treated target spot, the required energy does not change very much because the change in pressure influences only the external energy of evaporation, which is required to bring the molten target volume to the corresponding vapor volume, but the internal binding energy is not affected, and it is by far bigger.

5. Experimental Results

To test the above developed theoretical models about the materials removal processes in case of laser and electron beam machining some experiments were conducted. First, the time dependence of the removal process was observed by means of photoelectric observations of the luminescence of the ejected material, which is luminous because of its high temperature. Then photographs of the removal process were made with a streak camera. Then an energy balance sheet was developed for both methods comparing the utilized beam energy with the theoretically required energy for either liquid-phase or vapor-phase removal of the target material. Finally, the workability of different target materials was compared for laser and electron beams, considering the working speed, the hole diameter, and the amount of material removed.

5.1 Photoelectric Observations of the Time Dependence of the Removal Process. The measuring apparatus for the photoelectric observation of the time dependence of the removal process is shown schematically in Fig. 7. The field of observation of the photodiode is restricted to a region approximately 5 mm above the target point, and on the center line of the cone of the metal ejection; thereby we avoid falsification of the observation by the relatively long lasting luminescence of the edge of the crater at the work spot. An optical system consisting of two lenses of fluorite is used. Light from other points in the system will not be focused in the same plane and is stopped by an aperture in the rear focal plane of the lens system. When the laser beam is used a spectral filter is also inserted into the light path in front of the photodiode to eliminate stray light from the laser beam. In the second channel of the dual beam oscillograph the pulse shapes are recorded, ascertaining exact synchronization, and measuring the pulse shape in case of the laser beam with a photomultiplier, and in case of the electron beam by means of an aperture in the electron beam path.

Fig. 8 shows some oscillograms obtained with this system. It can be clearly seen that under bombardment by the laser, the target material is ejected with the same frequency with which the individual laser spikes follow one another. From this result we see most clearly how fast the energy transfer takes place. Therefore one should not, as is generally done, treat the "normal"-laser pulse as a continuum, but should treat it as a series of consecutive spikes with an additive material removal effect.

On the other hand it would also be wrong to treat these short time heat inputs as completely independent of one another, because the workpiece will not cool down to the initial temperature in the short time interval between the spikes. Every successive spike will find a more and more preheated area.

The oscillograms of the materials removal in case of electron beams were recorded with a much higher sweep rate; they show, especially in the case of silver, that removal begins with full intensity nearly instantaneously at the beginning of the pulse; this may be considered as further proof for the extreme fast energy transfer. The irregular removal rate indicates a pulsating materials ejection. In comparison the removal of carbon proceeds much "quieter." This is most likely due to the required much higher removal energy, and due to the fact that carbon changes practically instantaneously from the solid into the gaseous phase; it sublimes, because of the very small difference between melting and boiling point.

5.2 Streak Camera Pictures of the Time Dependence of the Materials Removal. To get a better insight into the time dependence of the materials removal in the case of laser beam machining, the process was recorded with a streak camera. Fig. 9 shows the position of the streak camera. The maximum recording rate is approximately 100 m/s. We have purposely avoided to record the process in a high speed motion picture film, as it has been done by others,[3] since the process is self-triggering because of the rapid succession of the spikes (approximately 200 kHz); dissecting the process into a series of pictures interferes with the natural sequence inherent in the process, making the coordination difficult.

Fig. 10 shows the removal process recorded with different velocity v. In the picture taken with v = 0, we see a gleaming cloud of steam surrounded by traces of glowing metal particles emerging from the target point. In the streak pictures, recorded with v > 0 an asymmetry is visible between the front and the rear of the target and represents a measure for the time required by the laser beam to penetrate the target.

The higher the time resolution the more it becomes evident that the steam cloud emerging from the target point consists of a superposition of clearly separated successive plasma torches which are triggered by the separate spikes. Only a certain distance from the surface a continuous steam cloud is formed. The velocity of ejection of these torches muct be very high since in spite of the high resolution of nearly 75 m/s they rise nearly perpendicular to the target surface. From the inclination of these torches and the velocity of the film the evaporation velocity may be calculated. Its magnitude is in the order of several km/s. This allows an estimate of the evaporation temperature; between the evaporation velocity $v_d$ and the emission energy 2 kT the following relation exists (provided $v_d$ is equal to the atomic velocity $v_a$):

$$v_d = v_a = \sqrt{\frac{2kT}{m_a A}}$$

$m_a$ is the mass of the proton and A is the atomic weight, k is the Boltzmann-constant. Hence the temperature of evaporation for, e.g., steel

under laser bombardment is higher than 10,000 °C, which is much higher than the evaporation temperature of 2500°C under normal conditions.

As expected, the materials removal does not proceed exclusively in the vapor phase. In addition to the plasma torches, the streak pictures show show some brighter lines, straight, but under an oblique angle to the target surface, indicating a much slower speed than that of the plasma torches. They are obviously produced by the much heavier, liquid, and inert particles. The creation of the plasma torches is due to the direct heating under laser bombardment, whereas the materials removal by molten liquid is connected with the indirect heating of the target by heat conduction whereby a target volume which is increasing with the pulse duration is thermally heated and melted. The photographs show clearly that the removal process is everything but regular or, as suggested by Ready[4], a continuously proceeding process.

5.3 Energy Balance for Materials Removal by Electron and Laser Beams. The theoretical models for the materials removal process, as discussed in paragraph 4, namely a vaporization process in the laser case, a molten-liquid-process in case of electron beams, where checked by an energy balance calculation on the basis of the experiments. Fig. 11 shows the result of this balance. The connecting lines between the separate points are shown only for orientation and are as arbitrary as the correlation of the target materials with the melting temperature on the abscissa. As one can see the difference between electron beam and laser beam is considerable. The energy per unit of volume is always higher in case of the

laser. If the enrgy per unit volume required for materials removal is compared with the theoretical melting and evaporation energies under normal pressure one can see that the laser process tends much more to evaporation than the electron beam process.

To check the theoretical models further experimental results were used. Fig. 12 shows the time required by the laser beam to penetrate a number of target platelets of equal thickness but of different materials and also shown is the number of pulses required to penetrate a target of given thickness with an electron beam. The latter number is proportional to the working time if the pulse frequency is constant. The penetration times for the laser beam were calculated from the streak pictures taking the difference between the beginning of the removal at the front face and the first sign of penetration on the rear face of the target platelet. The required number of pulses of the electron beam was counted electronically. Plotted were the working time in case of the laser, and the number of pulses in case of the electron beam, versu the evaporation or melting energy to obtain the relationship with the removal processes postulated above. In view of the uncertainty in the measurements, and in view of the fact that the removal process proceeds neither in case of the laser nor in case of the electron beam under normal conditions, one obtains a quite unambiguous coordination between the work time, respectively the impulse number, and the evaporation and melting energy. A clear exception from this relationship are, in case of the laser process only the metals Cu, Ag, Au, and in case of the electron beam process the elements Al and Si. The fact that in the first case these metals are

the three best heat conductors and in the second case they are some of the lightest elements, which means materials of very low density, indicates a particularly strong relationship of these properties with the respective processes.

The above was confirmed by measuring the diameter of the holes produced in the different workpieces. Fig. 13 shows schematically the sequence of the workability as determined by the diameter of the holes. Increasing workability means a bigger hole diameter. Average values from many experimental runs, including such with different energy, were plotted to obtain a reasonable representative result. Again, the metals Cu, Ag, and Au form an exception in case of the laser process, and the elements C, Be, Si, and Al are the exception in the electron beam process insofar as their position does not agree with that according to the required melting and evaporation energy.

The reason that in case of the laser process the heat conduction is of special importance and that in the case of the electron beam process the density is of special importance is lastly the result of the difference in the heating mechanism in the two processes. Under laser bombardment only a thin surface layer is heated regardless of the density of the target material, and the lower layers are heated indirectly, the faster the higher the heat conduction. Under electron bombardment the penetration of the particles is the higher the lower the density of the target material, and a much larger volume of the target material is directly heated. In the first case it is heat conduction, in the second case it is the density which is essential for the thermal heating of the

target material prior to the removal. If the heat conduction is small or if the density is high the energy concentration is higher for the laser or the electron beam respectively and enhances the thermal removal process; inversely, the high thermal conductivity or a low density reduce the temperature concentration and thereby make thermal removal more difficult.

## 6. CONCLUSIONS

The predictions made on the basis of the theoretical considerations about the energy transfer, the heating, and the ejection of the material in the case of electron beam and laser beam machining showed a surprisingly good agreement with the experimental results in view of the simplifications which had to to introduced into the theoretical models. The materials removal on the laser bombardment proceeds partly in the vapor phase, partly in a superheated molten liquid phase. In case of the electron beam process however, the molten liquid removal is dominant. This difference is due to the difference in the physical nature of the two kinds of radiation one of which, namely the electron beam is copuscular in nature, whereas the laser beam is electromagnetic and free of mass. This leads in particular to a difference in penetration into the matter. The laser beam penetrates only microns converting its total energy practically in a surface layer, whereas the electron beam, because of the high kinetic energy of the charge carrier particles, pushes deep into the workpiece, heating a higher volume element directly. For equal beam energy density at the target point the energy transfer per unit of volume is therefore much higher in the first case, for the laser, and therefore the tendency to evaporation is stronger.

REFERENCES

1. Ready, J. F., Development of plume of material vaporized by giant-pulse laser, Appl. Phys. Letters 3 (1963) 1, p. 11-13.

2. Prokhorov, A. M., The effects of a laser beam in a liquid, Soviet Physics Jetp, 7 (1963) 6, p. 1463-1465.

3. Kacamarek, J., Untersuchungen über den Prozeß der Evaporations- und Liquidations-Photonenerosion. CIRP-Annalen 1967/68.

4. Ready, J. F., Effects due to absorption of laser radiation, J. Appl. Phys. 36 (1965) 2, p 562-468.

Table I Characteristic Properties of Electrons and Photons

| | Elektronen | Photonen |
|---|---|---|
| Eingeprägte Größen | **Masse** $m_e = 9{,}108 \cdot 10^{-31}$ kg<br>**Elementarladung** $e = 1{,}602 \cdot 10^{-19}$ As | **Energie** $E_{ph} = h \cdot \nu = \frac{c \cdot h}{\lambda}$<br>$h \cdot \nu_R^* = 1{,}87$ eV $= 3 \cdot 10^{-19}$ Ws<br>**Wellenlänge** $\lambda = \frac{c}{\nu}$ $\lambda_R^* = 6943$ AE |
| Äquivalenzprinzip von Masse und Energie | $E = \frac{m}{2} v^2$ | |
| Abgeleitete Größen | **Energie** $E_{kin} = \frac{m_e}{2} v_e^2 = e \cdot U_B$<br>$= 1{,}602 \cdot 10^{-19} \cdot U_B$ Ws<br>$U_B$ = Beschleunigungsspannung V<br>**De Broglie Wellenlänge** $\lambda_e = \frac{h}{m_e \cdot v_e} \sqrt{1 - (\frac{v_e}{c})^2}$ | **Masse** $m_{ph} = \frac{E_{ph}}{c^2} = \frac{h \cdot \nu}{c^2} = \frac{h \cdot \nu}{c \cdot \lambda}$<br>$\frac{h \cdot \nu_R^*}{c \cdot \lambda_R} = 5 \cdot 10^{-36}$ kg<br>* = Gültig für Rubinlaser<br>h = Plank'sches Wirkungsquantum<br>c = Lichtgeschwindigkeit<br>ν = Frequenz |

Charakteristische Eigenschaften von Elektronen und Photonen

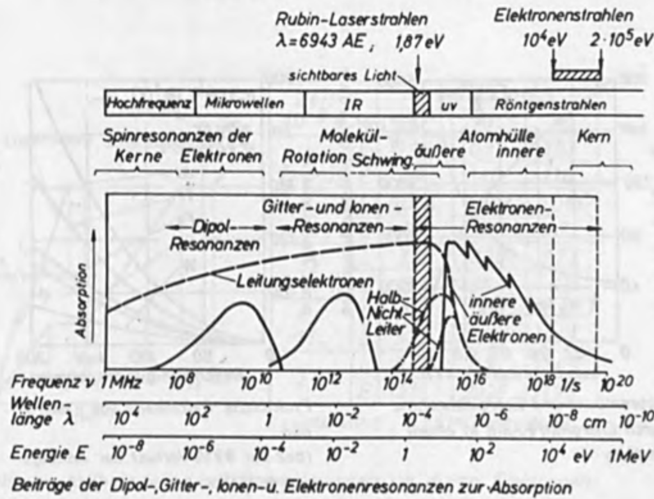


Beiträge der Dipol-, Gitter-, Ionen-u. Elektronenresonanzen zur Absorption

Fig. 1 Contribution to the Absorption by Dipol-, Ion-, Lattice-, and Electron-Resonances

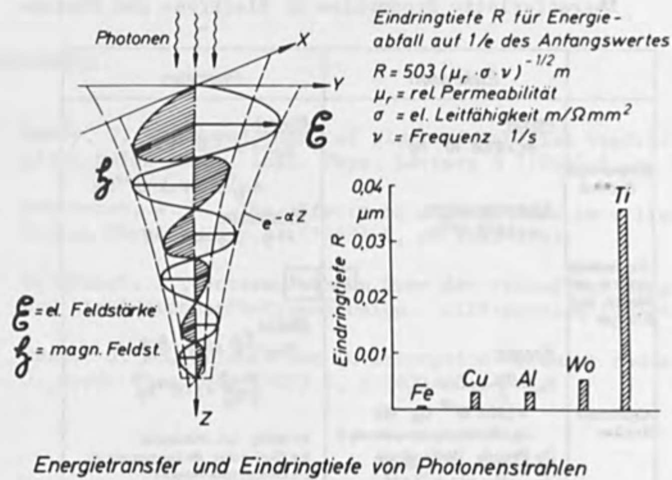


Fig. 2 Left (2a): Exponential Decay of the Light Intensity; Right (2b): Penetration Depth R.

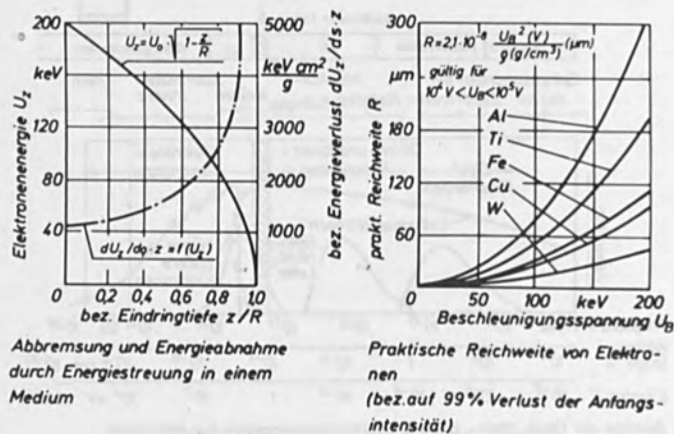


Fig. 3 Left (3a): Deceleration of Electrons and Energy Decay Due to Energy Scattering in a Target; Right (3b) Practical Range of Electrons

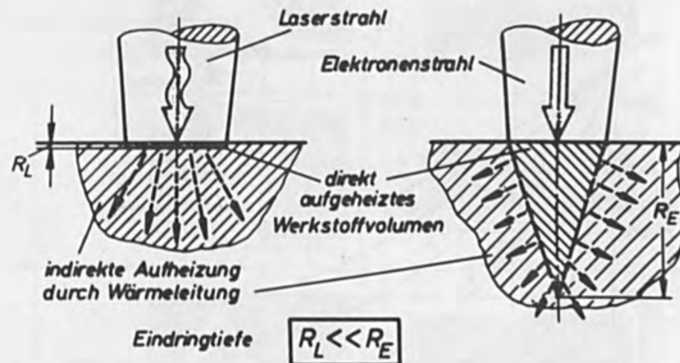


*Vom Laser- bzw. Elektronenstrahl direkt aufgeheiztes Volumen (Modellvorstellung)*

Fig. 4 Volume which is Heated Directly by the Laser or Electron Beam (Theoretical Model)

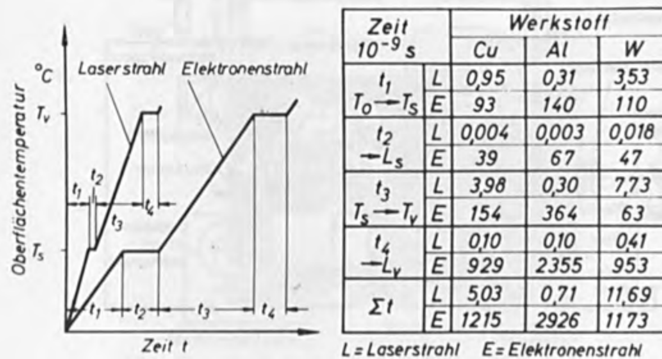


| Zeit $10^{-9}$ s | | Werkstoff Cu | Al | W |
|---|---|---|---|---|
| $t_1$ $T_0 \rightarrow T_S$ | L | 0,95 | 0,31 | 3,53 |
| | E | 93 | 140 | 110 |
| $t_2$ $\rightarrow L_S$ | L | 0,004 | 0,003 | 0,018 |
| | E | 39 | 67 | 47 |
| $t_3$ $T_S \rightarrow T_V$ | L | 3,98 | 0,30 | 7,73 |
| | E | 154 | 364 | 63 |
| $t_4$ $\rightarrow L_V$ | L | 0,10 | 0,10 | 0,41 |
| | E | 929 | 2355 | 953 |
| $\Sigma t$ | L | 5,03 | 0,71 | 11,69 |
| | E | 1215 | 2926 | 1173 |

L = Laserstrahl E = Elektronenstrahl

*Theoretische Aufheizzeiten bei Energieeinspeisung durch Elektronen- bzw. Laserstrahlen*

Fig. 5 Theoretical Temperature vs. Time Relationship for Energy Input by Laser or by Electron Beam

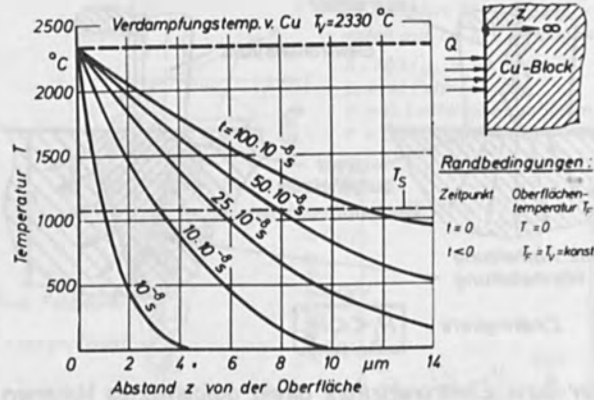


*Temperaturausgleich in einem einseitig unendlich ausgedehnten Körper aus Kupfer*

Fig. 6 Temperature Distribution as Function of Time in a Semi-infinite Block of Copper

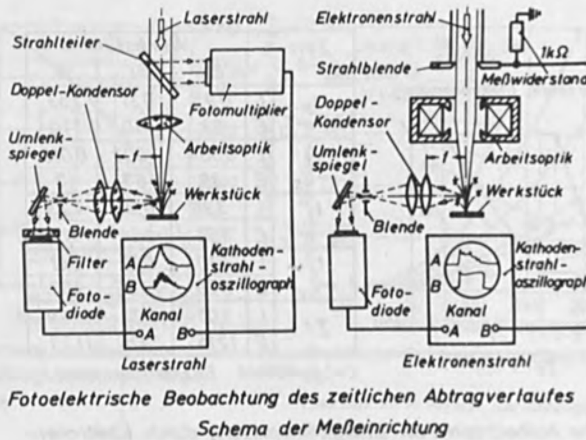


*Fotoelektrische Beobachtung des zeitlichen Abtragverlaufes Schema der Meßeinrichtung*

Fig. 7 Photo-electric Observation of the Materials Removal Process; Schematic of the Measuring System

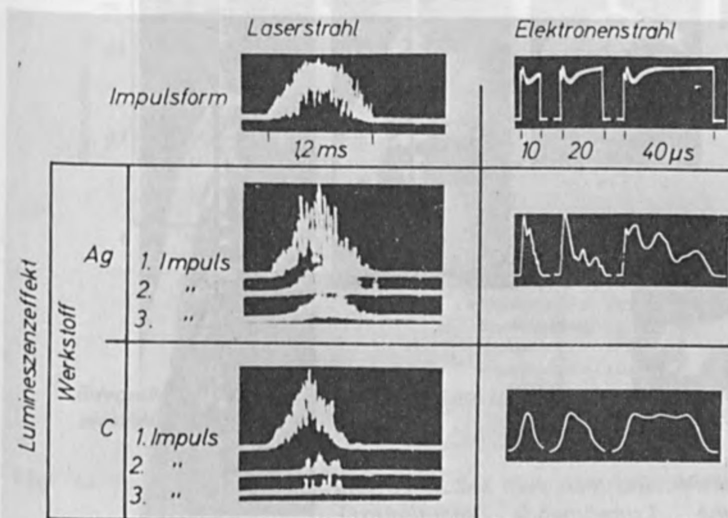


Fig. 8 Observed Luminosity during Materials Removal with Laser and Electron Beam

Fig. 9 System for Observing the Materials Removal Process with a Streak-Camera (= TrommelKamera)

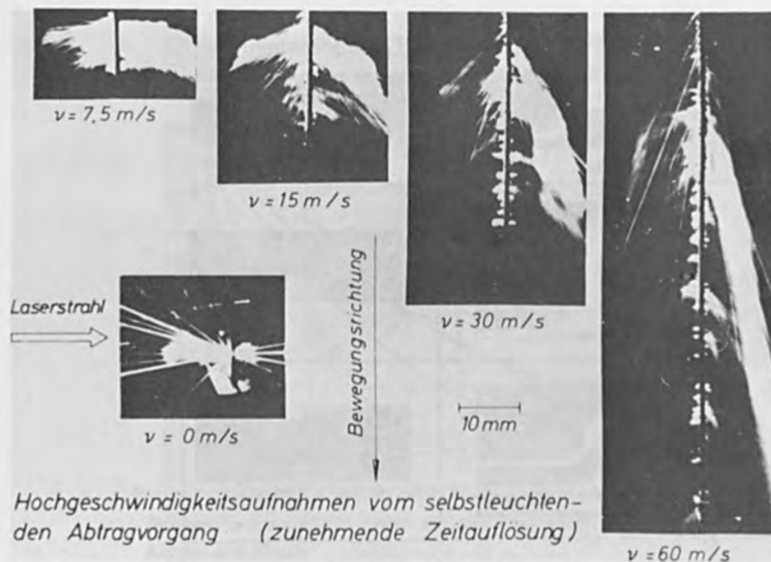


Fig. 10 Streak-Camera Photographs of the Self-luminous Materials Removal Process (with Increasing Time Resolution)

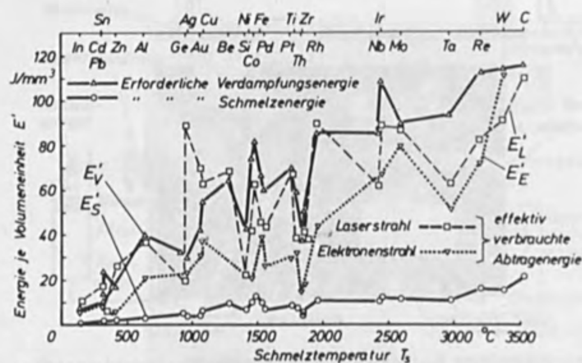


Fig. 11 Comparison of the Theoretically Required Melting and Evaporation Energies and the Actually Expanded Energy in the Removal Process

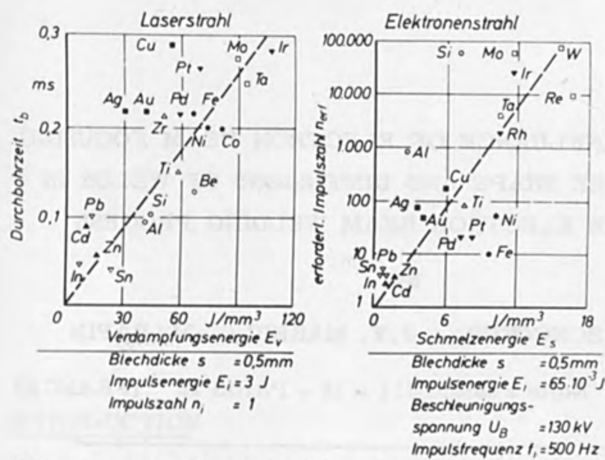


Fig. 12 Drilling Speed for Laser and Electron Beam Process

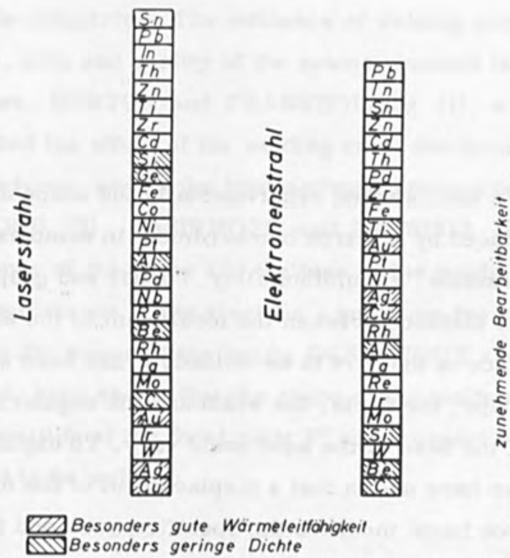


Fig. 13 Sequence of Workability of Different Materials with Laser and Electron Beam (the Hole Diameter used as Criterium)

# THE INFLUENCE OF ELECTRON BEAM FOCUSING ON THE SHAPE AND DIMENSIONS OF WELDS IN THE ELECTRON BEAM WELDING PROCESS

by

M. BONCŒUR - J.Y. MARHIC - M. RAPIN

C.E.A. Boîte Postale 511 - 15 - PARIS 15 ° (FRANCE)

ABSTRACT

We have studied experimentally the shape and the size of welds produced by electron bombardment in samples of stainless steel, uranium, aluminium alloy, copper and graphite, as a function of the distance between the focal point of the electron beam and the surface of the part to be welded. It has been established that the shape, the depth, the width and the regularity of the surface and of the base of the weld could vary. To explain these variations we have shown that a displacement of the focal point of the electron beam modifies the specific power and the convergence of the beam at the surface of the part, as well as the length of the active beam immersed in the sample and the fusion process in the metal.

## I - INTRODUCTION

The industrial applications of welding by electron bombardment are constantly increasing ; electron beam welding equipment is used by the nuclear, aeronautical , electronic and automobile industries. The influence of welding parameters on the shape, size and quality of the seams obtained is, however, little known. BURTON and FRANKHOUSER (1), and MEIR (2) have studied the effect of the welding rate, the acceleration potential of the electrons, and of the bombardment current on the size of the weld. STOHR (3) HASHIMOTO and MATSUDA (4) have contributed a study of the shape and the size of the welds as a function both of the distance of the electron - gun from the sample, and of the specific power of the beam. OLSHANSKIY and NAZARENKO (5) have shown that the shape of the molten zone varies with the position of the focal point P' with respect to the surface of the part to be welded.

The object of our work was first of all to verify experimentally the variations of the shape, the size and the quality of the welds as a function of the distance of the image P' from the surface of the sample.

For this we carried out a series of welding operations in conditions such that the image P' was at various heights above and under the surface of the sample, all other welding parameters being constant. We carried out this series of tests at different welding rates and powers, as well as on materials having different physical properties, e.g. stainless steel, uranium, aluminium alloys, graphite and copper.

## II - EXPERIMENTAL METHOD

### II.1. Electron bombardment welding machine

This machine is equipped with a SCIAKY gun of the SV3 Type built on the PIERCE (6) principles. We give a diagram of such a gun in figure (1). It is made up of three main parts :

a filament, a negative electrode or cathode surrounding the latter, and the anode through which a hole is pierced. The tantalum filament is heated directly by means of the Joule effect. The emitted electrons are accelerated between the two electrodes and are concentrated beyond the anode hole, at a surface P usually called the cross-over. An image P' of P is formed at a sufficient distance from the anode by means

of an electromagnetic lens. The welds are obtained by placing the samples on the position of the image P'. The filament and the electromagnetic focusing coil were supplied with stabilized currents. The first tests were carried out with a non - stabilized high voltage supply and the most recent with a stabilized supply giving an accuracy of 1 % for a given value of the voltage. We have checked that this modification has only a negligible effect on our results. As far as the welding rate is concerned, a variation of ± 5 % could occur during an operation. Under these conditions, we have verified that the depth of a weld could vary by about 5 % if the welding parameters remained constant.

II.2. Samples .

We have chosen metals whose physical properties liable to affect the electron bombardment welding process are very different : copper, uranium alloy (7), stainless steel and aluminium alloys. We have also used graphite which sublimes and forms a cavity under the effect of the impact of an electron beam.

II.3. Welding conditions

We have used beam powers and welding rates of between 2,5 kW and 10,5 kW, and of between 1m/min. and 2.2 m/min. respectively. The distance between the median plane of the focusing coil and the sample was 10 cm unless otherwise stated. The tests were carried out on cylinders and on plates.

### II.4. Determination of the position of the image P' with respect to the sample surface.

During a welding operation, the vapours produced by the molten metal are ionized by the electron beam, with emission of electromagnetic radiation, a fraction of which has a wavelength corresponding to visible light. The electron beam is thus seen by the operator who can bring the narrow part of the beam into the surface of the sample by varying the focusing current. We have arbitrarily decided that the image P' is situated in this case on the surface sample. We have varied the current in the electromagnetic coil so as to have values both above and below the value of the focusing current corresponding to this case. We have assumed that the point P' was situated above the sample when the focusing current was greater than this value ; whilst it was below when the focusing current less.

## III - RESULTS

### III.1. Shape and size of the molten metal zone

#### III.1.1. Shape

The macrographs in figure (2) show, for different materials, how the shape of the molten or sublimated zone varies with the position of the image P', for constant power and constant rate of welding. When P' is situated above the sample, the molten zone is a triangle whose base is on the surface of the metal. If P' is at the metal surface, the molten zone is made up of a deep and narrow zone together with a trapezoidal zone on top of the former. The depth and the

fineness of the weld increase up to maximum values when the point image penetrates inside the metal. When the maximum values are attained, the molten zone is made up of a narrow and deep band topped by a trapezium of small size. If the image P' is still further inside the metal, the depth of the narrow band decreases whereas the size of the trapezoidal zone increases.

In figure (3) it can be seen that the shape of the molten zone changes with the position of P', as we have just described, whatever the power of the beam or the rate of welding.

III.1.2. Depth

Figure (4) gives the depth of the welds obtained in stainless steel as a function of the position of the image P' and for different powers and rates of welding. The curves obtained for other materials have similar shapes as can be seen in figure (5).

It can be remarked that at constant power and constante rate of welding, the depth of the weld varies as a function of the position P' according to a bell-type curve which has a maximum.
Whatever the power or the rate of welding the form of the curves remains the same (8).

In each of them four parts can be distinguished :

1. When P' is above the sample, the penetration is slight

2. When P' is at the surface, the depth is slightly greater

3. The penetration is a maximum when P' is below the surface of the sample

4. The depth decreases as P' penetrates into the metal beyond the level corresponding to the maximum penetration.

In order to confirm these results, we have carried out several welds using the same beam (constant high voltage, bombardment current, and focusing and correction currents), but with the sample surface at different distances, above or below the image P'. In figure (6) we have plotted the curve giving the depth of the welds obtained in stainless steel as a function of the distance between the sample surface and the image P'. The form of this curve is similar to that of the curves given in figures (4) and (5).

The slope of the curves plotted in figure (4) increases in absolute value as the power of the electron beam increases. For stainless steel, an increase of 5 % in the focusing current leads to a maximum variation of 25 % in the depth of the weld.

### III.1.3. Width

Previously, we have described the shape of the molten zone. In particular we have shown that it is made up of two parts : one narrow and deep, the other trapezoidal above the former. We characterized the former by measuring the width of the large base, i. e. the width of the weld at the

surface of the sample, and the latter by the width measured at the half height of the weld.

In figure (7) we have plotted the curves giving the width of the weld on the surface of stainless steel samples as a function of the position of the image P'. It can be remarked that at constant power and rate of welding, the base of the trapezium is a minimum when the depth of the weld is a maximum. This is true for all the materials which we have studied. In figure (8) we have plotted the width of the molten zone measured at the half height of welds in stainless steel. It can be noted that the width remains more or less constant as long as the image P' is situated inside the metal. The width is a minimum for the position of P' which makes it possible to obtain maximum weld depth. When P' is situated above this position the width of the molten zone increases. This increase corresponds to the disappearance of the narrow and deep part of the weld, and to the appearance of the single triangular zone. The width at half depth varies at the most 75 % in the case of stainless steel and 100 % in the case of uranium for an increase of 5 % in the focusing current.

## III.2. Weld quality

### III.2.1. Surface aspect of the weld seam

We have noticed that the surface of welds made in the same material, in constant power and weld rate conditions could be either smooth and without a break, or else

In this figure, we can see that the specific power of the beam varies with the position of point P'. It is interesting to note that the convergence of the beam when it enter the solid varies with this same parameter.

However, in each of these diagrams in figure (12) in which we show the shape of the weld obtained with the type of focusing adjustment which it represents, we can see that the weld obtained is not deepest when the specific power on the sample is a maximum. The greatest depth is obtained when the image P' is situated inside the metal despite the fact that the specific power on the sample surface is lower.
The specific power of the beam on the sample surface is thus not the only parameter influencing the shape and size of the welds ; other beam characteristics must be involved.

## IV.2. Variations in the shape and size of welds as a function of the convergence and of the length of the active beam in the metal.

The specific power of our electron beam is a maximum at the image P' and it keeps this same value over a distance l and l' on either side of P' (l and l' are approximately equal to 1 cm) (9). The weld of maximum depth should be obtained when the whole of the distance l + l' is used to melt the metal. This should happen when the part of the beam corresponding to l + l' is situated just below the sample surface. The diagrams shown in figure (12) confirm this hypothesis. In effect, when the high electron density l + l' of the beam is placed just below the surface of the part to

be welded, the depth of the weld is a maximum (figure 12 c). The use of the part of the beam corresponding to the length l' makes it possible to obtain a more shallow weld (figure 12 a). Use of other part than l + l' of the beam makes it possible to obtain only wide and shallow welds (figure 12 b). In order to characterize the part of the beam corresponding to the length l + l', it will be called " length of the active beam ".

The three characteristics of the beam which we have defined - specific power, convergence and length of the active beam - make it possible to predict the shape of a weld according to the position of the image P' with respect to the sample surface. In figure (12) we show four positions of the impact surface P" of the electrons with respect to the position of the image P'.

1 - $OP'' > OP' + l'$

The specific power of the beam is sufficiently low for metal fusion to be due mainly to heat conduction from the source constituted by the impact surface. The divergence of the beam on entry in the metal increases the extent of the molten zone. The weld is wide and fairly shallow.

2 - $OP'' = OP'$

The length of the active beam leads to the formation of a narrow and deep molten zone characteristic of electron bombardment welding. As soon as it enters the metal however the beam tends to diverge , this leads to a slight widenning of the upper part of the molten zone.

3 - $OP'' = OP' - l$

Over the maximum active length $l + l'$, the beam has a specific power which is sufficient for creating the deep zone characteristic of electron bombardment welding. The deepest and most narrow weld is obtained, and the molten zone formed by heat conduction is almost inexistent.

4 - $OP'' < OP' - l$

The electron beam is converging on arrival but strikes the sample surface with a specific power which is too low to cause unidirectional melting of the metal. As a result the metal melts first by conduction, this leading to the large trapezoidal zone seen on welds made under these conditions. It is probable that part of the electron beam crosses this molten metal layer and that the specific power under the latter is sufficient to melt the metal in a zone having a narrow shape.

### IV.3. Variation in the weld quality as a function of the position of image P'

If the specific power of the electron beam is high, the metal of the target is melted to a great depth by the " electron bombardment effect ". If not, the electrons' energy is given to the sample surface and the thermal energy necessary to melt the metal is transmitted by conduction. Metal fusion by the electron bombardment effect is a rapid and transient phenomenon which leads to the appearance of defects in the surface and of notches at the base of the weld.

Fusion by conduction is a slower phenomenon which attains very rapidly a steady state. As a result, the welds obtained by the single effect is not pitted superficially and has no notches at the base of the seam (figure 13). Generally speaking, the two processes occur simultaneously during the fusion of a metal by electron beam impact. The melting effect produced by electron bombardment is a maximum when, with the power and rate of welding constant, the weld is finest and deepest. In this case it is normal to obtain a seam having an irregular surface and base. If the beam is defocussed, fusion by conduction increases it the expense of that produced by the electron bombardment effect and the defects characteristic this latter process become less numerous.

## V - CONCLUSIONS

We have established that the welds obtained by electron bombardment in various metals at constant power rate and distance of welding have a fused zone whose shape size (depth, width, area) and quality vary according to the position of the focal point P' with respect to the sample surface.

We have shown that any displacement of the image P' leads to a change in the specific power of the beam on the sample surface but that does not suffice to

explain the changes of shape and size observed in the fused zone. We have shown the influence of the convergence and of the length of the active beam immersed just below the metal surface, the active beam being made up of that part of the beam which is on either side of the image P', along which the specific power is more or less equal to that at the image P'. In order to explain the influence of the position of P', on the quality of the welds (surface aspect, notches along the weld base), we have considered that the fusion of the metal under the effect of electron bombardment is the result of two phenomena :

fusion by the electron bombardment effect which favorizes the appearance of these defects and fusion by heat conduction which inhibits them.

**References**


1 - G. BURTON - W. L. FRANKHOUSER, Electron beam Welding, Welding: J. 38 Research supplement 401-409 s (1959)

2 - J. W. MEIR, Electron beam welding characteristics of several materials, Proc. third symp. electron beam tech. BOSTON (1961)

3 - J. STOHR, Contribution à l'étude de la soudure des métaux par faisceaux d'électrons. Rapport CEA - R 2507 (1964)

4 - T. HASHIMOTO - F. MATSUDA, Effect of welding variables and materials upon bead shape in electron beam Welding. Trans. Nat. Res. Inst. for Metals, 7(3) 96-109 (1965)

5 - N. A. OLSHANSKIY - O. K. NAZARENKO, The current status of electron beam Welding in the USSR. First international conference on electron and ion beam science and technology. p 587-605 R. Bakish éditeur Toronto (1964)

6 - J. R. PIERCE, Theory and design of electron beam chapitre 10

7 - M. BONCOEUR, La soudure par bombardement électronique: application à la soudure des alliages d'uranium. Bulletin de Métallurgie Spéciale (Février 1968)

8 - M. BONCOEUR - M. RAPIN, Contribution a l'étude des facteurs modifiant la forme et les dimensions des soudures obtenues par bombardement électronique. Mem. Scient. Rev. Métallurgie LXIV n°11 (1967) 953-964

9 - M. BONCOEUR, Influence de la géométrie du faisceau d'électrons d'une machine à souder sur la forme de la soudure. Non publié.

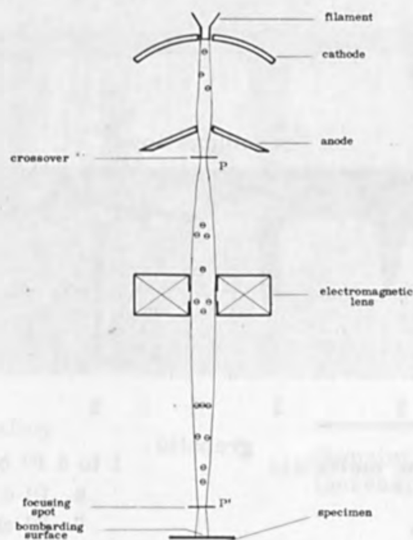


PIERCE type gun

Figure 1

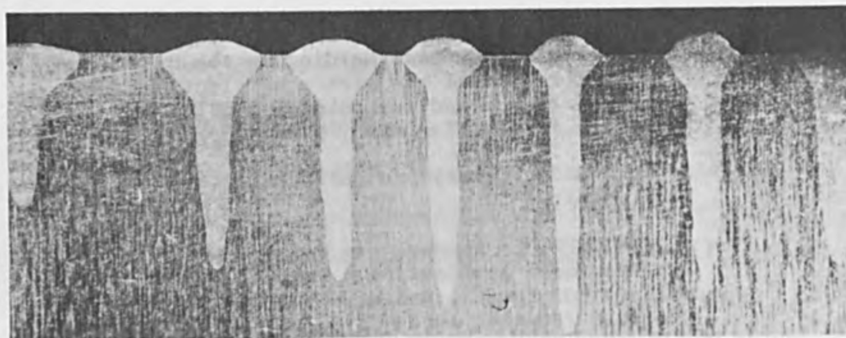


stainless steel

uranium alloy

x3,5

graphite

Welding in different materials

P = 4 kW
v = 1 m/mn

1 to 5 P' below the surface
6 P' on the surface
7 P' above the surface

Figure 2

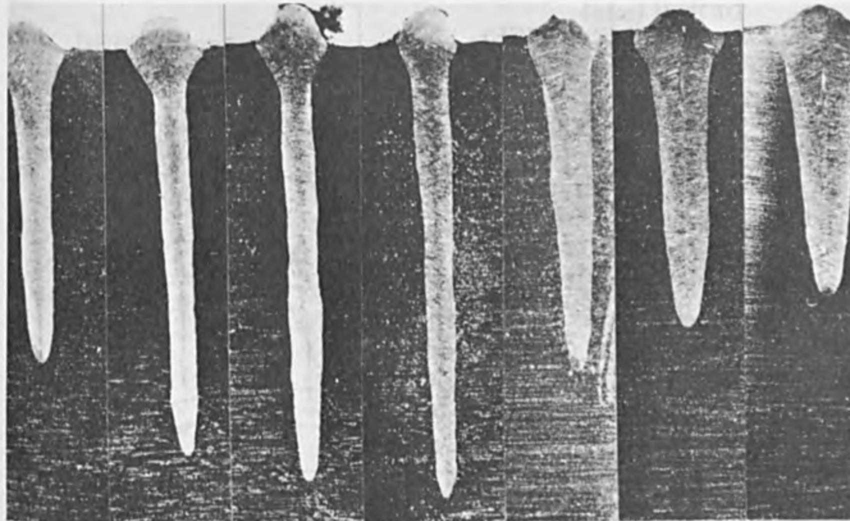

stainless steel

focusing current increasing

P = 7,5 kW

v = 1 m/mn

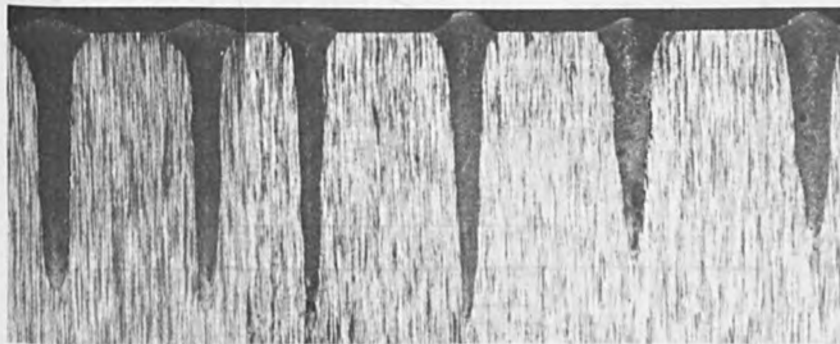

Aluminium alloy

focusing current increasing

P = 9,6 kW

v = 2,2 m/mn

Figure 3 x 3,5

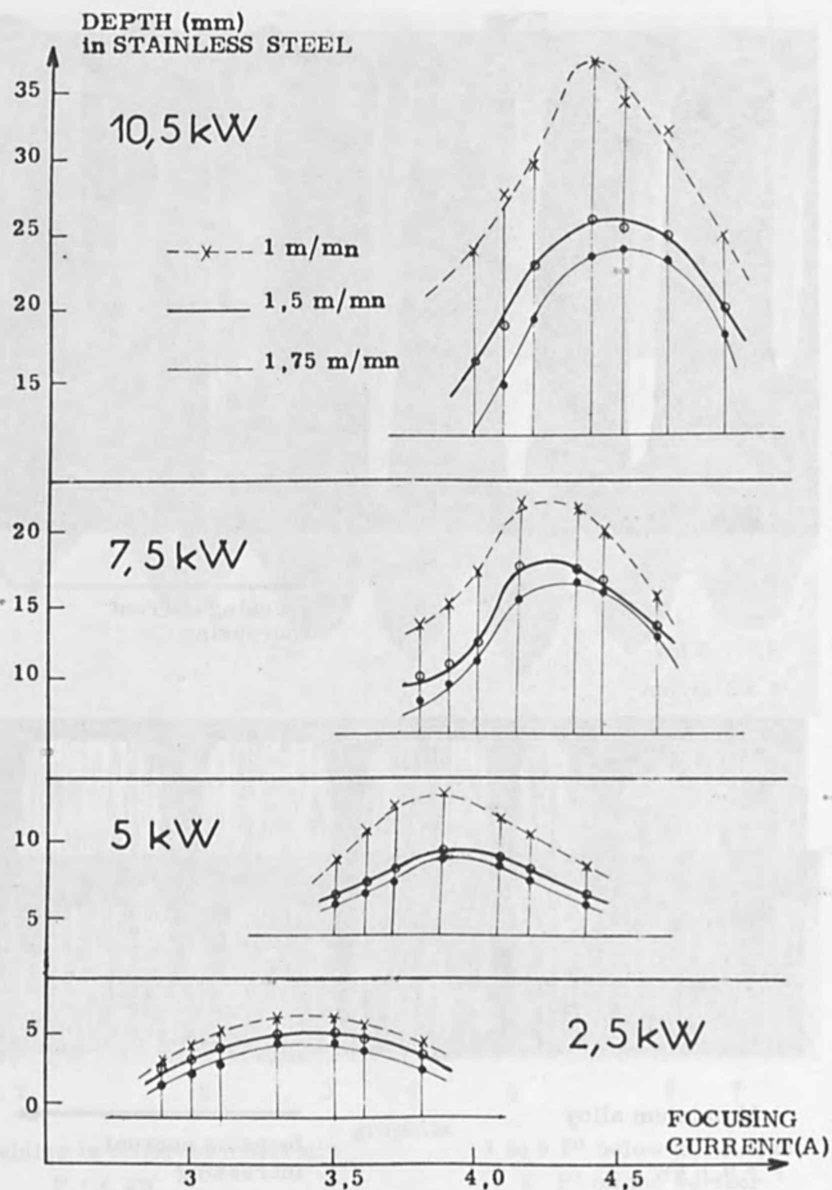


Figure 4

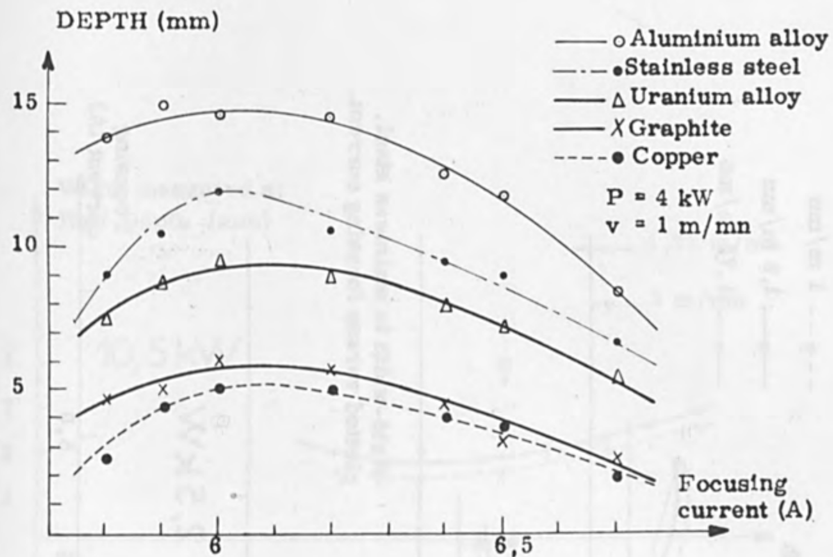


Figure 5

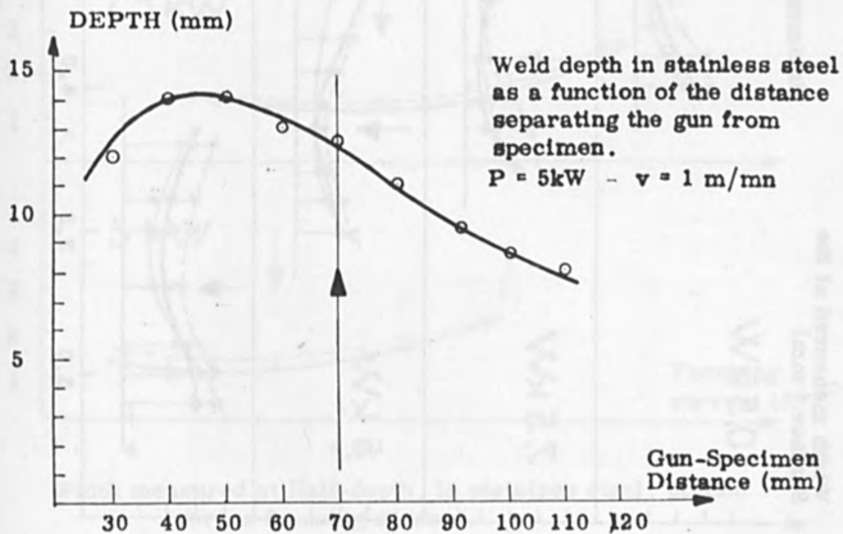


Figure 6

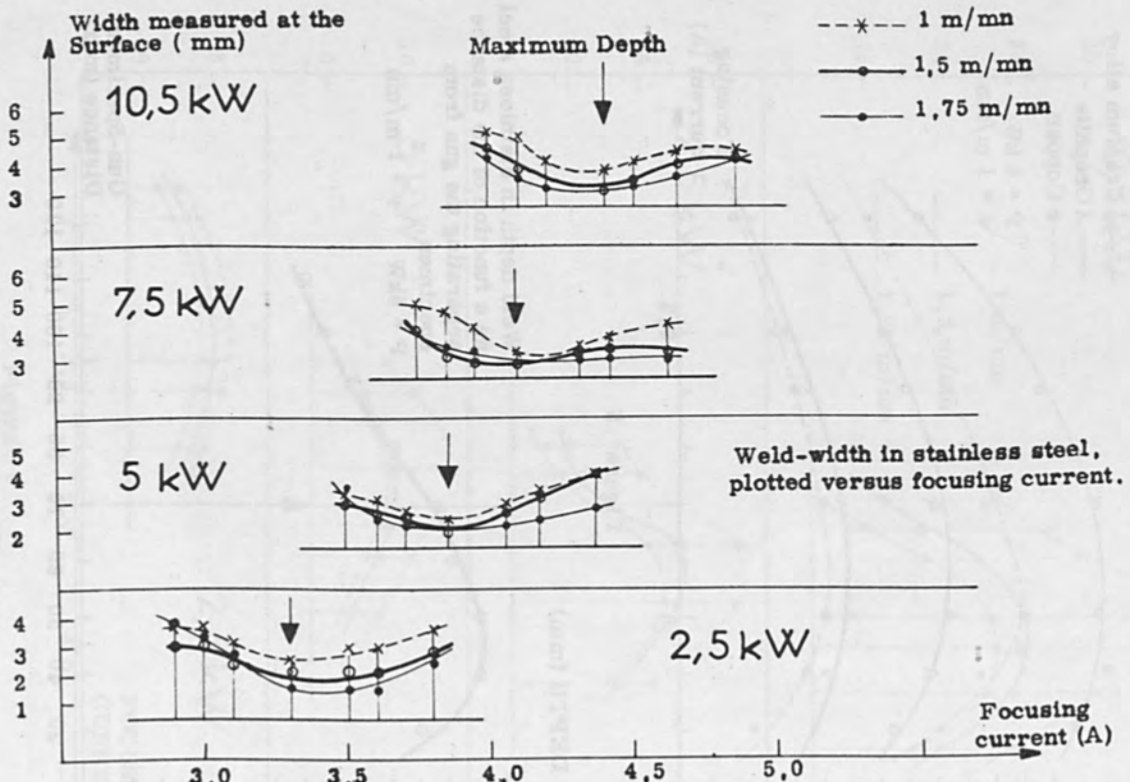


Figure 7

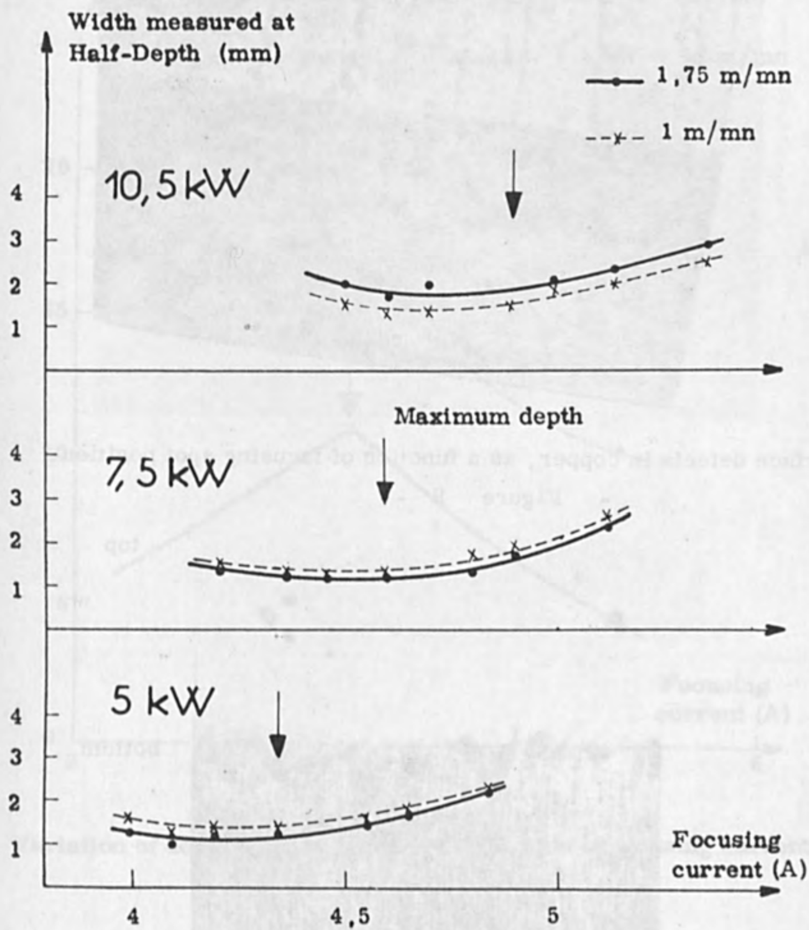


**Width measured at Half-depth, in stainless steel, plotted versus focusing current.**

**Figure 8**

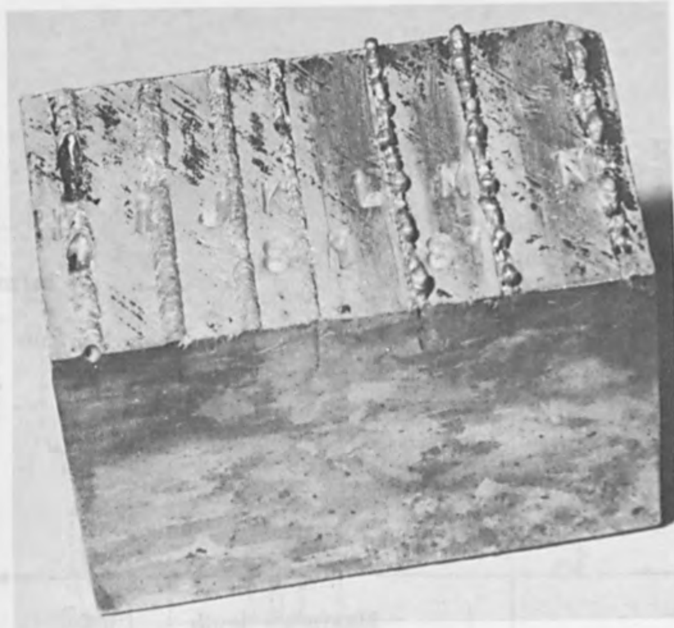

Surface defects in copper, as a function of focusing spot position.

\- Figure 9 -

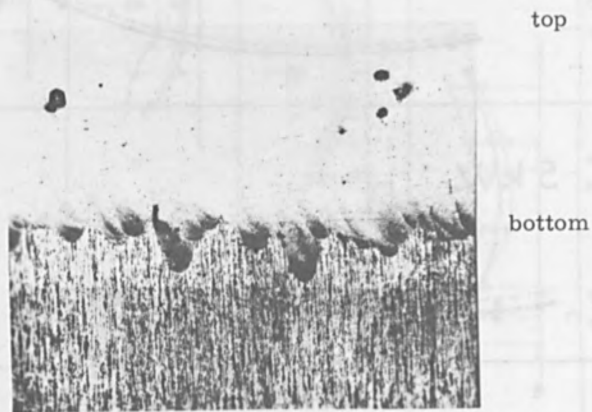


\- Figure 10 -

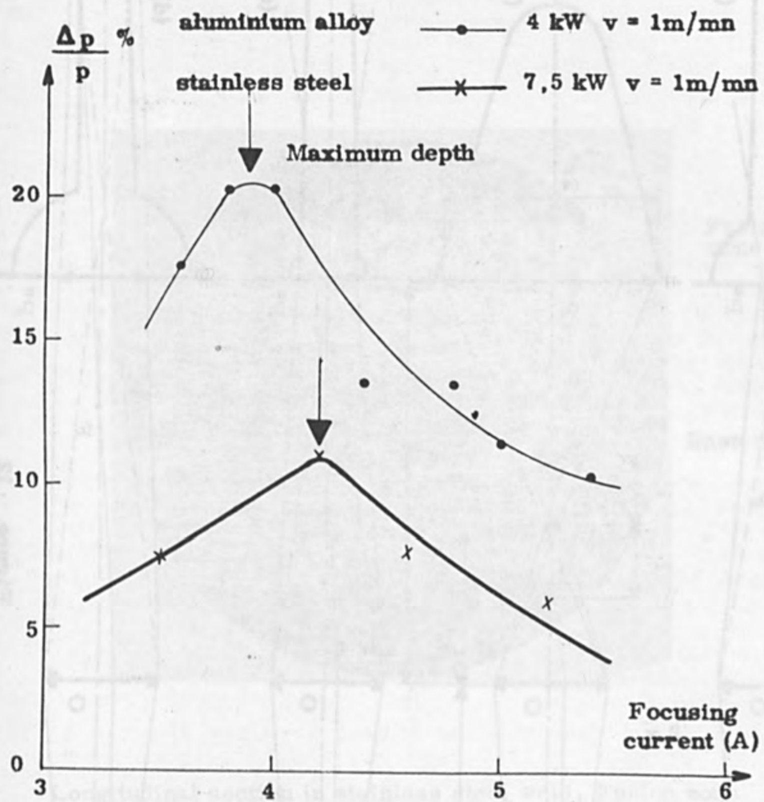


Variation of depth p, in percent, as a function of focusing current

Figure 11

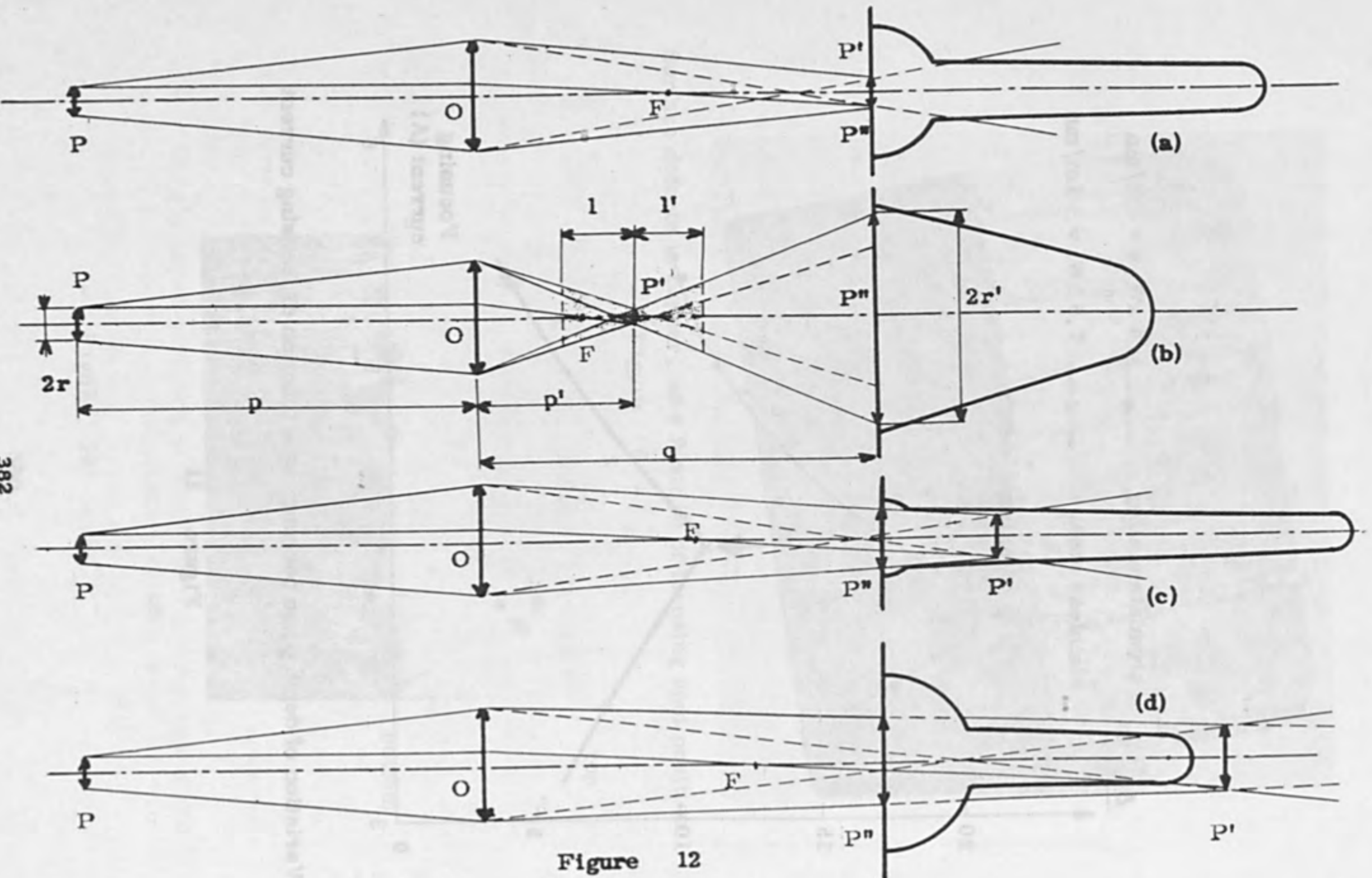

Figure 12

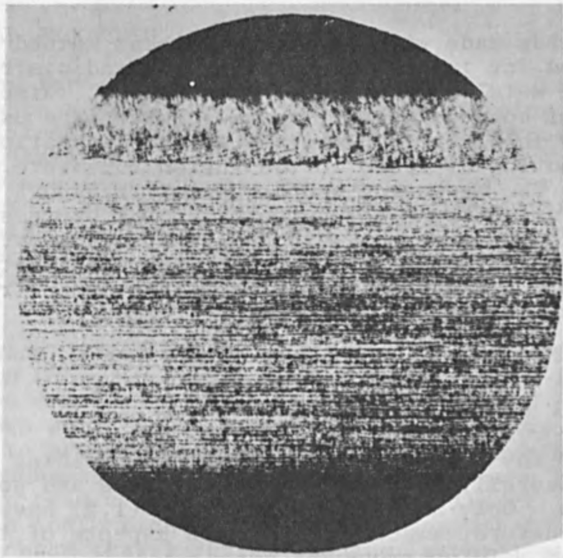


x 6

Longitudinal section in stainless steel weld. Fusion zone produced by heat flow the specimen surface. Note the bottom of fusion zone without " teeth ".

- Figure 13 -

# METAL MIXING DURING ELECTRON BEAM WELDING

P. Shahinian, J. T. Atwell, and E. J. Brooks
Metallurgy Division
Naval Research Laboratory
Washington, D. C. 20390

## ABSTRACT

Welds made with the electron beam method were analyzed for information on the flow and distribution of metal during the fusion process. Wire inserts of copper, nickel, and columbium were used as tracers in titanium plate and the concentration and distribution of these in the fusion zone were determined. The direction and degree of transport of metal during the electron beam welding process was indicated by the post weld analyses. In general, mixing occurred; the presence of the added metal was found throughout the weld but the concentration was not uniform.

## INTRODUCTION

Most of the interest in electron beam welding to date has quite naturally been in its capabilities and possible applications. Only a few investigations (1,2) have been made of the nature, kinetics, or other aspects of the electron beam welding process.

Ordinarily this welding method does not require a filler metal in the weld, unlike many other welding processes. There may be exceptions however, particularly when joining dissimilar metals or metals, such as tungsten, which yield brittle welds. A filler metal may be employed to impart ductility to the weld and, also, in the welds of certain metals may be used to prevent microcracking (3). Furthermore, in instances where incomplete filling of the joint takes place it may be necessary to make a metal addition.

In those cases where a filler metal is required it is of interest to know the distribution of the added metal in the fusion zone because the local composition would be an indication of the strength and ductility in those areas of the weld. However, very little attention has been given to the uniformity of composition in such joints made by electron beam welding.

This study was undertaken to examine the nature and extent of metal mixing that takes place in the electron beam weld. Welds were made in titanium plate in which were embedded various metals and the distribution and concentration of the added metal in the fusion zone were determined. Also, it was thought that the distribution and the indicated transport of filler metal, which would act as a tracer, would provide information on the kinetics of the electron beam welding process.

## EXPERIMENTAL PROCEDURE

Samples for examination were prepared by making simulated welds in a single plate rather than joining two separate plates. Titanium plate of 1-in. thickness was used as the base material in which, for the major part of the study, were embedded 1/16-in. or 1/8-in. diameter wires of copper, nickel, and columbium, Table 1. In addition, in several plates the filler wire was placed in surface grooves. These filler or tracer metals had melting points and vapor pressures ranging from below to above those of the base metal.

A drawing of the plate specimen with the indicated wire locations is shown in Fig. 1. Wires were placed in horizontal holes drilled in the plate and on several plates in 1/16-in. deep surface grooves. This technique had been used previously to produce brittle, crack starter regions for fracture toughness testing (4). Welds were made by passing the electron beam along the length of the insert. In order to obtain an indication of the metal transport in the direction of the beam travel during welding, several wires were inserted vertically in the plate, perpendicular to the beam travel.

The welds were made with a low voltage machine operating at 30 KV and 280 to 350 ma at a pressure of approximately $4 \times 10^{-5}$ Torr. The focal point of the electron beam was at the top surface of the plate for the various welds. Travel speeds of 18 and 30 ipm were employed in order to observe the effect of dwell time on mixing of the metal in the fusion zone.

The plates containing the simulated welds were sectioned in several directions; those with the horizontal inserts being cut approximately at their mid length. The sections were analyzed by means of x-ray spectrochemical techniques to determine the distribution of the metal addition in the fusion zone. In the analysis, scans were made on the sectioned surfaces by an x-ray beam of 0.5 mm diameter. Several analyses

were made across the width of the weld at intervals of 0.5 mm between beam centers, and normal to this direction, along the depth of the weld, at intervals of up to several millimeters, as dictated by the concentration gradient. Also, to determine the concentration gradient in the weld boundary a scan was made with the electron probe microanalyzer. The samples were mechanically polished and then etched with a solution of 1 part HF, 2 parts $HNO_3$ and 30 parts $H_2O$.

## RESULTS

In the observations and analyses of the welds, attention was given to the transport of metal from one region to another within the weld, the effect of beam-dwell time on mixing, the presence of concentration zones due possibly to mixing in gaseous and liquid regions, and the general distribution of the filler metals as a function of their melting temperature.

In the titanium plate which contained horizontal 1/8-in. diameter inserts (plate A), the welds made at the slower travel speed, 18 ipm, fully penetrated the plate while those made at the faster speed of 30 ipm achieved approximately 80 percent penetration. The metal inserts of copper and nickel melted completely whether at the top, center, or bottom of the plate, but about one-half section of the columbium wire remained intact at all three positions. The unfused piece of columbium wire was, for the most part, within the fusion zone adjacent to the weld boundary, Fig. 2. It is difficult to determine the exact size of the electron beam but if it is presumed that the inner edge of the high melting point columbium insert indicates the approximate position of the edge of the beam, then the weld boundary in the titanium appears to extend approximately 1/32-in. beyond the apparent edge of the electron beam.

In most of the welds the etched structure did not appear to be homogeneous, indicating most likely some degree of segregation. At the original location of the copper and nickel inserts, which had fused, the weld zone usually contained a bulge, a consequence of the 1/8-in. insert diameter being about the same as the weld width, Fig. 3. Because of this non-uniformity, most of the analytical work was done on plates containing 1/16-in. diameter wires. Other than the bulge and the presence of the columbium wire segment there was nothing else in the appearance of the welds that could be related to the original position of the wire. With all three filler metals the welds were similar in appearance

except for the unfused portion of the columbium, as noted earlier. In the partial penetration welds made at the faster travel speed, the depth of penetration was usually about 80% for all of the metals. The increase in speed reduced the time the beam dwelled on a spot by one-third from that of approximately 0.21 seconds at the slower speed.

That the distribution of copper in the fusion zone is uneven is shown for the top insert position in Fig. 3. The concentration is a maximum of 5.5 wt. % at the insert position and gradually decreases to slightly less than one-half of that at the top and bottom surfaces. Except at the top of the plate the lateral concentration of copper was uniform to the weld boundary, within the limits of measurement imposed by the 0.5 mm x-ray beam. Near the top surface the copper tended to concentrate close to the weld boundaries, leaving a slightly lower concentration at the middle.

Welds made with the 1/16-in. diameter wire inserts, unlike those with the larger inserts, usually showed no remnants of the original wire. However, several exceptions were noted and will be shown.

The filler metals were distributed unevenly through the depth of the pool, as indicated by the concentration curves in Figs. 4-8, taken along the centerline of the welds. Through the plate thickness the concentration ranged from 2 to 6% for copper, 3 to 13% for nickel, and 2 to 10% for columbium when the insert was at the top of the plate. However, across the welds laterally the concentration was constant to the weld boundary where it dropped sharply to zero. Actually, the concentration transition zone at the weld boundary, measured on a copper-containing weld with the electron microprobe, was about 40 microns. The peak concentrations were slightly below the original insert position, the peak being farther away for the metals with lower melting temperatures. Except for the copper-containing weld, a region of nearly constant concentration or plateau existed at the lower end of the fusion zone. A more even distribution occurred with the lower melting temperature metals. The maximum concentration showed no consistent trend with melting temperature, being higher for the nickel than for the copper and columbium.

An increase in travel speed by a factor of 1.7 yielded a higher concentration peak and a steeper gradient along the depth of the weld as may be seen from a comparison of the copper curve in Fig. 7 with that in Fig. 4. Another consequence of the shorter beam dwell time was incomplete mixing of the copper insert. As shown in Fig. 7, a region of high

copper, about 30%, with a distinct two-phase structure was present at the top. It appears that this material did not become a vapor but remained a liquid. Only in this sample was such a heterogeneous structure observed. The weld zone with nickel made at 30 ipm, although of less penetration, had a more homogeneous structure.

With the columbium insert at the bottom of the plate the peak concentration was again at the insert position, Fig. 8. Only the midsection of the wire was melted by the beam which apparently was very narrow at this point. The incomplete melting may have contributed to the presence of the double peak. Perhaps the temperatures in the region were not sufficiently above the melting point of columbium to insure good mixing. Laterally the distribution was generally uniform.

When the nickel filler wire was placed in a surface groove the concentration curve had the maximum at the top and then declined to a low level plateau at the lower half of the weld, Fig. 9. A similar curve resulted from the weld of the columbium wire in a surface groove except several peaks were present indicating less complete mixing, Fig. 10. The peak concentrations were slightly less than those in plates containing the inserts.

Metal flow parallel to the beam travel was indicated by the post weld distribution of a nickel insert placed vertically in a plate, as illustrated in Fig. 1(b). As shown in the horizontal section in Fig. 11, taken 0.30-in. below the top surface, the nickel was transported in a direction opposite to that of the beam travel as well as along with it. The contour of the molten zone when the beam is at the insert is revealed by the structure of the nickel-enriched material. Nickel had diffused to approximately 1/4-in. behind the beam at this depth. This lag of the boundary of the molten zone behind the beam was greater at the surface and gradually decreased toward the bottom of the fusion zone, as indicated by the vertical section of the weld in Fig. 12. The nickel concentration curve in Fig. 11 reaches a sharp peak about 1/4-in. behind the beam. As the beam passed along the plate, nickel was carried for a distance of about 1/2-in. Despite the tendency of the metal to deposit behind the beam the total nickel content is only slightly higher behind the rod position than ahead of the rod. A zone of high nickel concentration appears, in the vertical section of Fig. 12, to rise from the rod to a region which would be behind the beam. This would indicate that metal flows around and to the rear of the electron beam.

## DISCUSSION

A plausible explanation of the electron beam welding process appearing in the literature has been deduced on

basis of the nature of the weld; however, supporting evidence for the details are lacking. This explanation, as generally given, is that a cavity is formed by the dense electron beam through vaporization of the metal and, as the beam moves along the material, molten metal around the periphery of the cavity flows into it (5).

In the analyses of welds made in this study, zones in which vapor had existed could not be delineated from zones in which only liquid had been present. It appeared that the metal vaporized by the beam mixed well with the surrounding liquid before refilling the cavity. The high nickel concentration at the solid liquid interfaces, about 1/4-in. behind the beam when the beam is at the insert, indicates that the metal just vaporized flows to the rear of the then molten zone and does not immediately fill the void left by the beam. While there is a tendency for the metal to flow to the rear of the beam, much of it is carried in the direction of the beam travel.

In the welding theory the cavity formation is often attributed to electron pressure exerted by the impinging beam or the upward momentum of the metal vapor toward the surface exerting a downward force on the liquid. These factors did not receive support in this study because the concentration gradient was about the same in the downward or electron flow direction, when the insert was in the top of the plate, as it was in the upward direction, when the insert was in the bottom position. The transport of metal was essentially the same whether downward, in the direction of electron flow, or upward. It does not appear that the transport of metal and mixing depend upon the beam direction.

## SUMMARY

The findings from this study are:

1. A filler metal is distributed throughout the depth of an electron beam weld, but the concentration is not uniform.

2. In the vertical distribution of the horizontally positioned insert the peak concentration of the filler metal is at or near the original position of the insert. The distribution of filler metal away from the position of peak concentration followed a characteristic pattern, irrespective of the location of the insert. The higher melting temperature inserts gave sharper peaks and less even distribution.

3. Concentration of the filler metal was generally constant laterally across the weld and dropped abruptly to zero at the weld boundary.

4. An increase in travel speed resulted in a higher peak concentration and steeper gradient along the depth of the weld. Also, the higher speed increased the possibility of incomplete mixing.

ACKNOWLEDGEMENTS

The authors wish to thank Dr. M. R. Achter for his helpful suggestions and review of the manuscript and Messrs. O. R. Gates and D. H. Price for assistance in certain phases of the work.

REFERENCES

1. A. G. Povod, "Mixing of the Metal during Electron-Beam Welding with Dagger-Shaped Penetration," Automatic Welding, No. 8, 1963, p. 76.

2. Helmut Schwarz, "Mechanism of High-Power-Density Electron Beam Penetration in Metal," Journal of Applied Physics, Vol. 35, No. 7, 1964, p. 2020.

3. J. R. King, "Electron Beam Welding," Assembly and Fastener Engineering, March, 1963.

4. W. S. Pellini, R. J. Goode, P. P. Puzak, E. A. Lange, and R. W. Huber, "Review of Concepts and Status of Procedures for Fracture-Safe Design of Complex Welded Structures Involving Metals of Low to Ultra-High Strength Levels," NRL Report 6300, June 1965.

5. G. Burton and W. L. Frankhouser, "Electron-Beam Welding," Welding Journal, Vol. 38, 1959, p. 4015.

TABLE 1

Weld Plate Conditions

| Plate Code | Insert Material | Insert Dia.-in. | Insert Location | Speed ipm |
|---|---|---|---|---|
| A | Ni (1453°C m.p.) | 1/8 | Top | 18, 30 |
| | Cu (1083°C m.p.) | | Center | 18 |
| | Cb (2468°C m.p.) | | Bottom | 18 |
| B | Ni | 1/16 | Top | 18, 30 |
| | Cu | | Center | 18 |
| | Cb | | Bottom | 18 |
| C | Ni | 1/16 | Groove | 18 |
| | Cb | | | |
| D | Ni | 1/16 | Vertical | 18 |

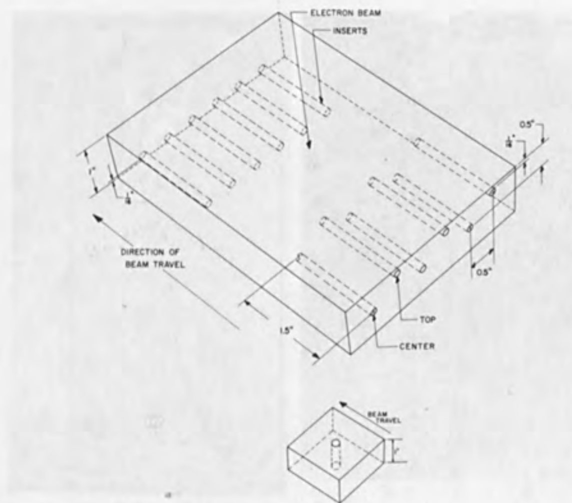


Fig. 1 - Diagram of weld plates showing insert positions.

Fig. 2

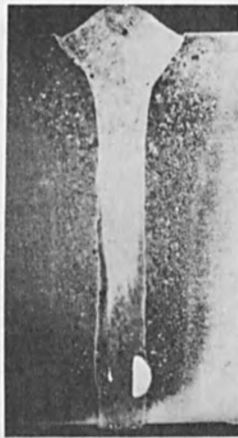

Fig. 3

Fig. 2 - Fusion zone in titanium plate which contained 1/8-in. diameter columbium insert near bottom of plate. 3X.

Fig. 3 - Concentration of copper in fusion zone in titanium plate which contained 1/8-in. diameter insert near top of plate. 3X.

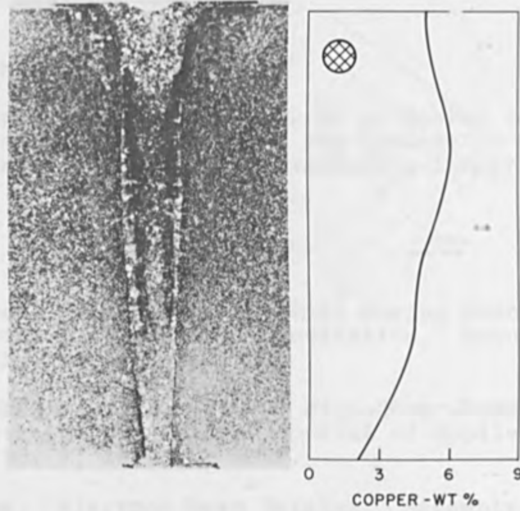


Fig. 4 - Distribution of copper along centerline of weld zone with 1/16-in. insert at top of titanium plate and travel speed of 18 ipm. 3X.

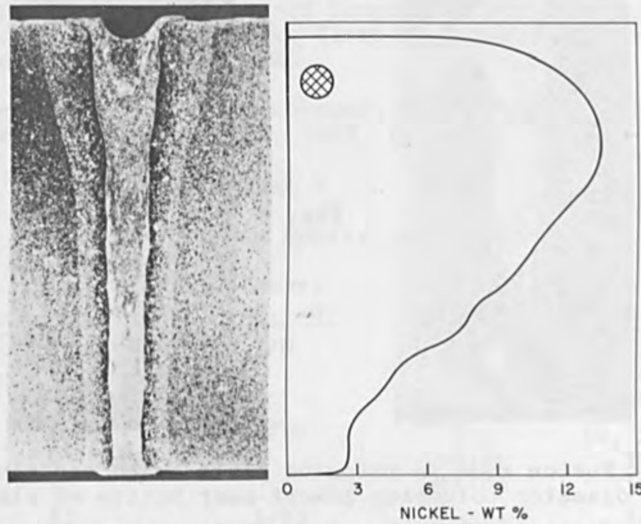


Fig. 5 - Distribution of nickel in weld zone with 1/16-in. insert at top of titanium plate and travel speed of 18 ipm. 3X.

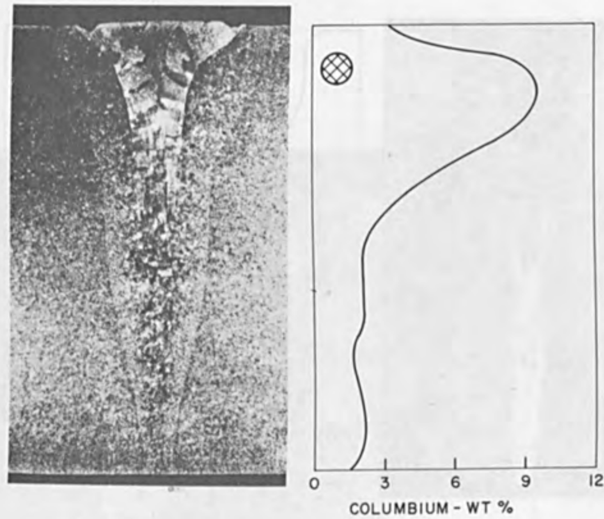


Fig. 6 - Distribution of columbium in weld zone with 1/16-in. insert at top of titanium plate and travel speed of 18 ipm. 3X.

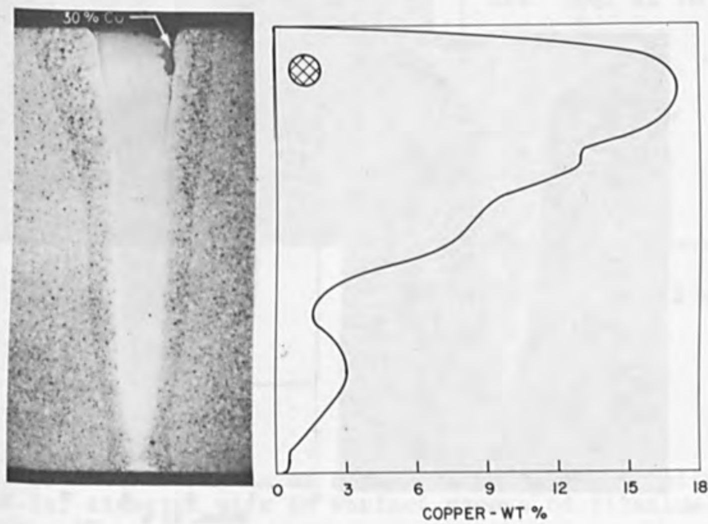


Fig. 7 - Copper concentration along centerline of weld zone made with 1/16-in. insert at top of titanium plate and travel speed of 30 ipm. 3X.

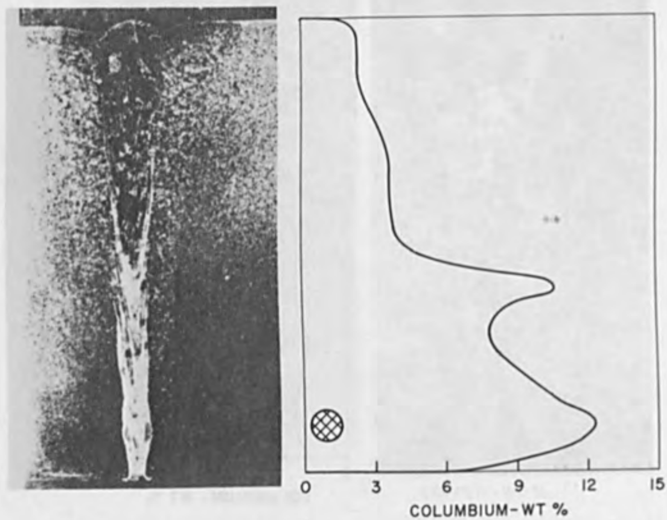


Fig. 8 - Distribution of columbium in weld zone with 1/16-in. insert at bottom of titanium plate and travel speed of 18 ipm. 3X.

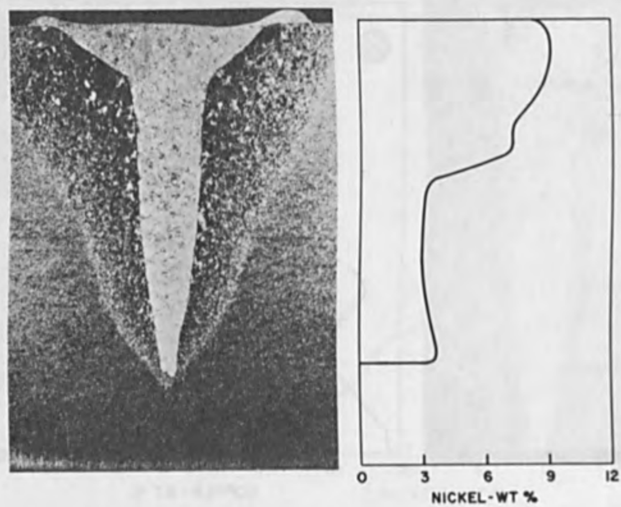


Fig. 9 - Distribution of nickel in weld zone with 1/16-in. wire in surface groove of titanium plate. 3X.

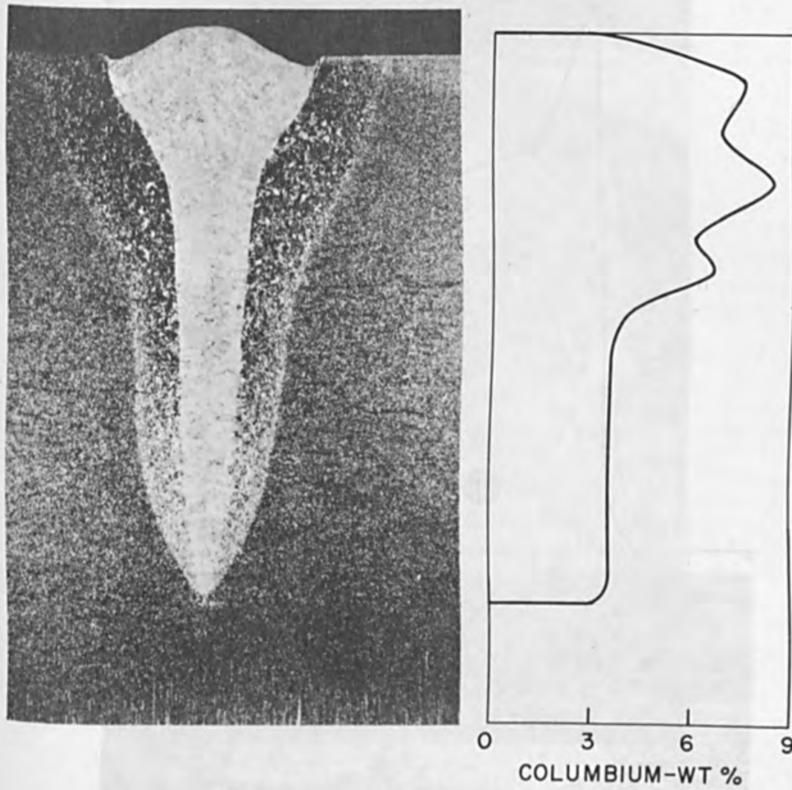


Fig. 10 - Distribution of columbium in weld zone with 1/16-in. diameter wire in surface groove of titanium plate. 5X.

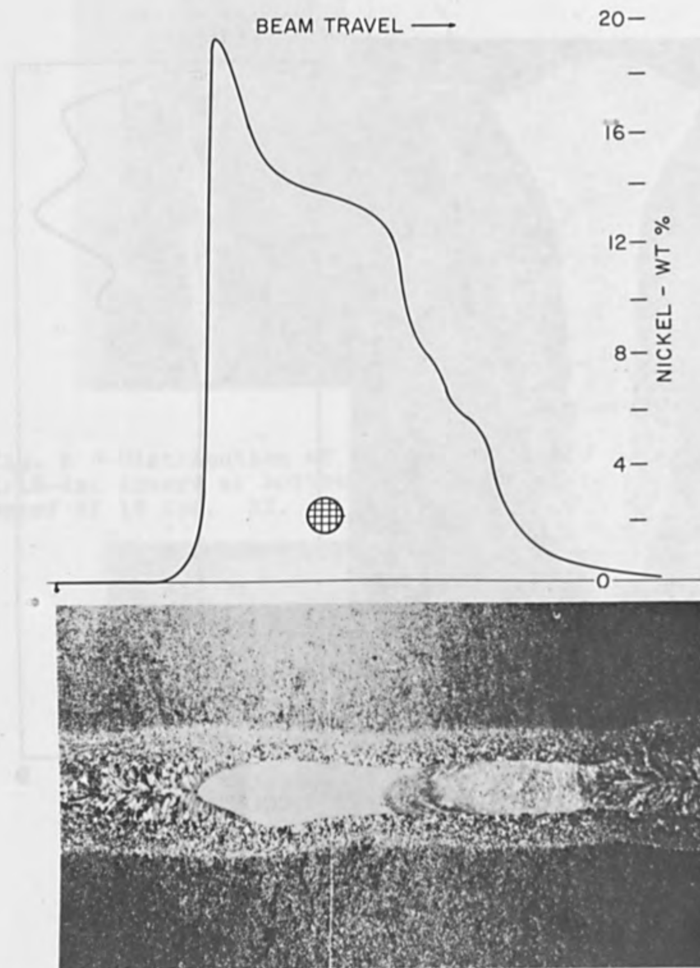


Fig. 11 - Fusion zone in section taken horizontally 0.30-in. below top surface of titanium plate in which nickel wire was inserted vertically. 3.5X

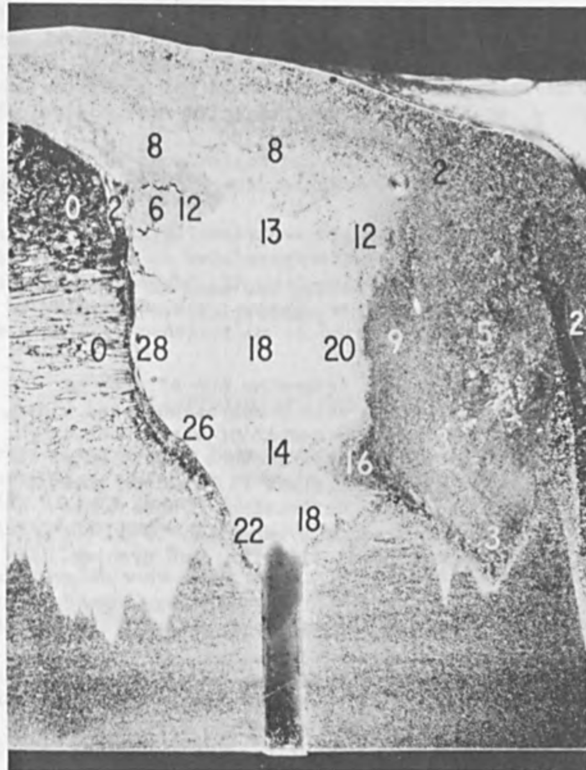


Fig. 12 - Longitudinal section through center of weld in titanium plate containing nickel insert. Nickel concentration in wt. % measured on sample surface. 5X.

PENETRATION VARIATIONS IN ELECTRON BEAM WELDING

G. K. Hicken

W. G. Booco

THE DOW CHEMICAL COMPANY
Rocky Flats Division
Golden, Colorado
80401
U. S. Atomic Energy Commission
Contract AT(29-1)-1106

ABSTRACT

A high voltage electron beam welder was used to conduct experiments on the mechanism of penetration variations in electron beam weldments.

Experiments were conducted to determine the effects of several welding parameters on weld penetration, bead width, penetration variations, and the number of variations in penetration per inch. The weld parameters investigated were: (1) beam power, (2) spot size, (3) welding speed, and (4) frequency of circular deflection. These tests were conducted on aluminum alloy types 1100, 5083, 6061, 7039; commerically pure copper; titanium; and uranium.

The results show that penetration variations are associated with alloying in the base metal. Penetration spikes decrease as the beam spot size increases. Deflection frequency can be obtained which results in a minimum variation in penetration. The data indicates only minor effects of power density variations on the variable investigated, while total power input has a significant effect.

We feel that penetration variations are associated with "gas-focusing" of the beam and hydrodynamic forces in the molten weld pool.

## INTRODUCTION

Electron beam welding has proved to be a valuable asset to the welding industry since its conception 10 years ago. Electron beam welding moved from the laboratory to the production floor in a short period of time. This has resulted in a great many questions about electron beam welding going unanswered. One such question is the cause and cure of electron beam weld penetration variations.

These changes in penetration may take the form of either a wavy weld root or sharp "spikes" penetrating below the normal fusion depth.

The purposes of this investigation were: (1) Determine the effects of equipment variables on weld penetration. (2) Investigate the cause of abrupt changes, "spikes", in weld penetration. (3) Develop suitable techniques by which aluminum, copper, uranium and titanium could be joined with a uniform penetration in partial penetration welds.

## EXPERIMENTAL PROCEDURE

Penetration variations have been observed in most materials when partial penetration welds are made in thicknesses greater than 0.100 in. The mechanism of weld penetration and the causes of the variations in penetration were the primary objectives of the research program.

Initially welds were made over a wide spectrum of conditions in a high voltage electron beam welder. Attempts were made to arrive at a set of welding conditions which resulted in severe weld spiking.

Once this set of conditions had been obtained a creeping random type experiment was designed to determine which of the variables - voltage or amperage - had the greatest effect on decreasing the severity of weld penetration variations.

During this portion of the experiment welds were made on different materials using the welding conditions that resulted in the worst condition of uneven penetration.

Following this portion of the investigation a four factor three level rotable design statistical experiment was conducted.

The factors and levels were as follows:

| | | | |
|---|---|---|---|
| Power | 1200 KW | 2000 KW | 2800 KW |
| Speed | 20 ipm | 30 ipm | 40 ipm |
| Spot size | 0.040 in. | 0.070 in. | 0.100 in. |
| Frequency | 200 hz. | 400 hz. | 600 hz. |

This program was conducted to determine the effect of the variables on penetration. Six responses were measured for various combinations of

factors and their levels. The responses were bead width, weld penetration, depth and width ratio, spike length, and the number of spikes per inch of weld.

To measure the response for all possible combinations of four factors at each of three levels would have required 81 experimental units. Instead, 25 combinations were measured with the center point repeated three times making a total of 27 runs. Coefficients were determined for the equation. The remaining 56 combinations were calculated from equation (1). Replication of the center point provided an estimate of the experimental error. The standard deviation of these three points will be used as the experimental error throughout this report.

$$\hat{y} = b_0 + \sum_{i=1}^{K} b_i x_i + \sum_{i=1}^{K} \sum_{j=1}^{K} b_{ij} x_{ij} \qquad (1)$$

Where k is the number of factors
$\hat{y}$ is the response
$x$ is the level of the factors

WELDING EQUIPMENT

The majority of the welds made during this program were produced on a high voltage electron beam welder. This machine has a maximum output of 150 Kv, 40 ma, in a high vacuum environment. The high voltage welder is equipped with a deflection coil and power supply that makes it possible to oscillate the beam in various shapes at frequencies as high as 1000 hertz.

During the course of the program welds were made on a low voltage electron beam welder. The low voltage equipment has maximum operating characteristics of 60 Kv, 500 ma operating in a high vacuum environment.

MATERIALS

Several materials were investigated during the course of the program. The majority of the welds were made in aluminum alloy type 6061. Welds were also made in: aluminum alloy type 1100, 5083 and 7039, uranium, commercially pure titanium and copper.

These materials were chosen because of the wide range of physical and chemical properties which they possess. All coupons were 1/2-inch thick by 3-inch wide and 6 inches long.

## WELDING PROCEDURE

The welding procedure consisted of cleaning the coupons by mechanical or chemical methods depending on the particular material. The coupons were then placed in a fixture with the 1/2 x 6 inch surfaces butted together. The fixture and coupons were aligned under the beam so the beam spot split the joint interface. Welding was then accomplished using pre-determined parameters in a vacuum of $5 \times 10^{-4}$ torr.

During the statistical plan, spot size was varied using the welder deflection system. The size of the spot was measured optically using the viewing optics in the welder.

## TESTING

Following welding, each joint was visually inspected and the bead width was measured. Once this was completed the weld was fractured through the center or ground to the center of the bead in the longitudinal plane. Both these methods proved satisfactory in obtaining a longitudinal section of the weld centerline. This section was then used to measure the weld penetration, variations in penetration (spikes) and the number of spikes per inch.

For the purpose of this report an abrupt change in penetration is called a "spike". The "spike" length is the difference in penetration between the normal depth of fusion and the depth of areas of excessive penetration. Figure 1 shows a sketch of a spike and the method used in measuring its length.

## "RESULTS AND DISCUSSION"

The creeping random experiment indicated that the worst spiking condition would result when welding at 90 Kv, 20 ma and 10 ipm on aluminum alloy type 6061 - varying accelerating voltage from 70 to 150 Kv and beam current from 2 to 25 ma did not affect the penetration variations in a significant manner. Figure 2 shows the surface and fracture appearance of the weld with the most severe spiking. The spikes produced with the above conditions were very cyclic and repeatable. This made us believe that the mechanical and/or electrical system in the welder may have been responsible for the large periodic increases in penetration. A complete monitoring of the electrical and mechanical portions of the welder that may have caused such a problem showed that these were not connected to the weld spiking.

We then simultaneously welded four sets of aluminum coupons at the same power level. The aluminum coupons were alloy types 1100, 6061, 5083 and 7039. The welds showed a significant difference in the penetration patterns that resulted. The 1100 alloy had an excellent surface

appearance and a uniform penetration to one-third the material thickness. The 6061 alloy had a surface bead width similar to that of 1100 material, but the surface had small craters evenly spaced along the weld centerline. These surface irregularities could be related to the large "spikes" in penetration. The weld in this material had more penetration than the 1100 alloy weld. The welds made in the 5083 and 7039 alloys were very similar in appearance. The surfaces were rough and irregular with small craters evident along the length of the weld. These welds had the greatest amount of penetration. The bottom third of the weld had been fused but many spikes and cold shuts were evident. Figures 2, 3, and 4 show the typical surface and fracture appearances of the welds made in the aluminum alloy.

Welds were also made in uranium, titanium, and copper using the same welding conditions. The uranium weldment had an excellent surface appearance with no surface irregularities. The penetration pattern in this material was wavy with large abrupt changes in penetration. The weld in the titanium had a smooth root appearance although, several craters were present at the surface. Sectioning the material again revealed that the craters were associated with increases in the weld penetration. The titanium showed features of both the wavy root appearance typical of the uranium, and the spikes more typical of the aluminum. A general waviness existed with small spikes protruding below the root fusion line. The uranium, and titanium welds are shown in Figure 5 and 6. The weld in the copper had a good surface appearance. Very little penetration resulted from the weld made in this material, therefore, little information could be determined concerning the penetration pattern, although many small spikes were present.

From the observations of the penetration patterns observed in the different materials we have concluded that penetration irregularities are caused by high energy density beams impinging on materials that contain volatile constituents. We came to this conclusion after observing welds made on aluminum alloys containing varying amounts of alloying elements. Movies of the welds as they were being made showed that the highly alloyed 6061 material appeared to be welded with a pulsing beam, although no electrical evidence of pulsing was found. The 5083 and 7039 alloys showed a similar flickering of the beam. The movies of the weld made on the 1100 aluminum alloys showed no variation in beam appearance.

We have concluded that the penetration spikes are caused by gas focusing in the beam. Linder and Hernquist[1] have shown that electron beam current density can be increased by a factor of 30 by neutralizing

---

[1] Linder, E. G., Hernquist, K. G., "Electron Space Charge Neutralization by Positive Ions", Journal Applied Physics, Vol. 21, November 1950. pp. 1088-1090

space-charge forces. We feel that the mechanism of initial beam penetration is that proposed by Schwarz[2].

We feel that after initial penetration the weld progresses by vaporizing a hole in the metal at the leading edge of the beam. The molten metal then flows around the hole by capillary forces filling the hole and forming a weld. Gas focusing results when a non-equilibrium number of ions are produced in the weld zone. These excess ions neutralize the space charge of the beam causing a large increase in the power density, which results in penetration spikes. We feel that the excess ion concentration is caused by a gradual heat build-up in front of the weld which causes periodic vaporization in excess of the normal amount.

Our assumptions on the cause of spiking led us to make a weld in a low voltage electron beam welder using the same power input that caused the severe spiking when using the high voltage equipment. The welding parameters were 59 Kv, 25 ma and 10 ipm. These parameters resulted in a weld with an excellent surface appearance and uniform penetration. Although the penetration was uniform many small spikes were evident. Figure 7 shows the fracture appearance.

The difference between the welds made in the same material using different types of electron beam welders must be a result of the differences in weld power densities. The low voltage machine has a lower power density, therefore, the weld would not be affected as greatly by equal changes in the density.

The statistical program revealed a great deal of information about the effect of weld parameters and the bead width, depth to width ratio, spike length, and the number of spikes per inch.

Bead Width

As would be expected the electron beam spot size has the most significant effect on bead width. The effects of the parameters on bead width are listed in decreasing order of magnitude.

1. Spot size
2. Speed
3. Frequency
4. Power X spot size interaction
5. Power

With the exception of travel speed all the weld parameters investigated increased the bead width as the parameters increased. The

[2] Schwarz, Helmut, "Electron Beam Processes at Different Voltage", Transactions of the Eight Symposium and Second International Congress American Vacuum Society, Vol. II, Permagon Press, New York, 1962. pp. 699-707

bead width decreased as the welding speed increased. Figure 8 shows a plot of bead width vs deflection frequency. This graph is very similar to those produced by varying spot size and power input.

No significant parameter interactions existed except between power input and spot size; this interaction is shown in Figure 9.

## WELD PENETRATION

Of the four weld variables investigated, power, spot size and welding speed had the greatest influence on weld penetration. As the welding power input was increased from 1.2 to 2.8 Kw penetration increased from .100 to .350 inch. Penetration decreased as speed and spot size increased. These curves are similar to penetration curves presented by Passoja[3].

### Depth/Width Ratios

Power input and spot size were the only variables that had a significant effect on the weld depth to width ratio. Figure 11 shows depth to width ratio as a function of power input. Increasing spot size decreased the depth to width ratio.

All the variables reported above exhibited excellent agreement between experimental and calculated data using equation (1).

### Spike Length

The data on weld spike length were somewhat erratic and hard to fit to an equation. The data were then transformed by taking the square root of each response. The estimated equation resulting from this transformation was acceptable in fitting the data. The function for the spike length data, therefore is:

$$\sqrt{\hat{y}} = b_o + \sum_{i=1}^{K} b_i x_i + \sum_{i=1}^{K} \sum_{j=1}^{k} b_{ij} x_{ij}$$

Beam power had the most significant effect on weld spike length. Figure 12 shows spike length vs power input. Welding speed and deflection frequency had a less significant effect on spiking.

---

[3] Passoja, D. E., "Penetration of Solids by High-Power-Density Electron Beams", British Welding Journal, January 1967. pp. 13-16

The frequency of circular beam spot rotation influenced the amount of weld spiking. The deflection frequency that resulted in minimum penetration variations increased as the total welding power decreased. Figure 13 shows a plot of penetration variation (spike length) vs deflection frequency for three different weld powers.

It is puzzling that the statistical results show no correlation between spot size and spike length; while other work has indicated that varying spot size for a constant power input has affected spiking. **Figure 14 shows some welds made with the same power input but varying power densities. Similar effects have been seen at several other power input levels.**

The data on the effect of power density indicates that there is certain power density required for specific materials to accomplish deep narrow welds. Indications are that power densities greater than this certain level do not significantly affect weld penetration, although there are some contradictions in the data. When the power density is below the threshold level, weld penetration is primarily due to thermal conduction. This results in wide shallow welds which have uniform weld penetration.

Spike Frequency

The number of penetration variations per inch is related to both the beam spot size and the deflection frequency. The spike frequency decreases as the deflection frequency increases from 200 to 600 hertz. Figure 15 shows a plot of spikes/per inch vs deflection frequency. The effect of beam spot size was similar to that of deflection frequency. As the spot size increased, resulting in a lower power density, the number of spikes decreased.

The deflection frequency has a significant effect on the number of spikes per inch. For a given power input there is a frequency at which spiking is minimized. Figure 16 shows a plot of spikes per inch vs frequency for three weld powers. This frequency is probably related to the hydrodynamic action of the molten weld pool.

## CONCLUSIONS

This investigation has not answered all the questions that exist concerning penetration variations in electron beam welds, although some observations have been made as follows:

1. Aluminum alloys are more susceptable to spiking than pure aluminum, titanium, copper or uranium.
2. For a given power input spiking will decrease as the spot size increases.
3. Gas focusing seems to be a possible explanation as to the cause of weld spiking.
4. Weld spiking can be related to deflection frequency and welding power.

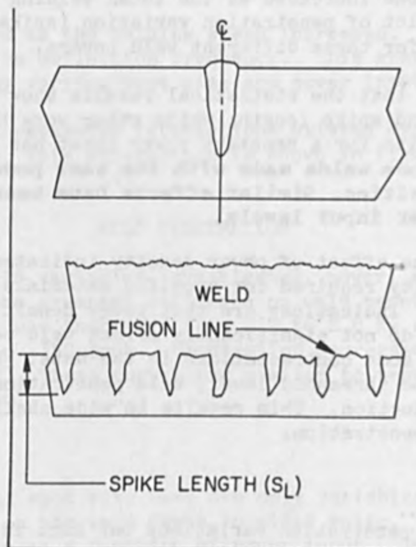


Figure 1. Schematic Showing Method of Determining Spike Length.

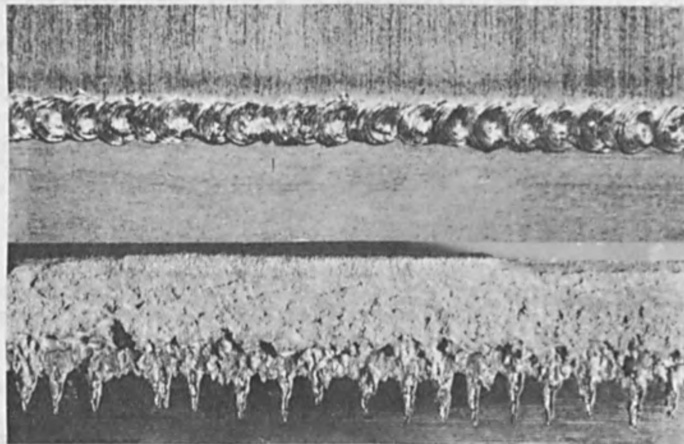

Figure 2. Surface and Fracture Appearance of an Electron Beam Weld in Aluminum Alloy Type 6061. Welded at 90 Kv, 20 ma, 10 ipm.

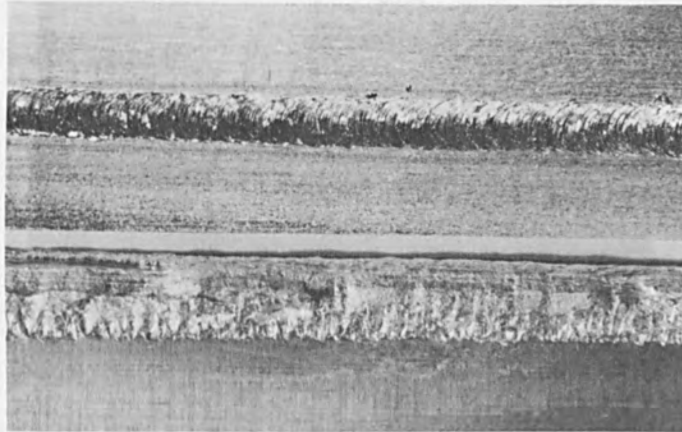

Figure 3. Surface and Fracture Appearance of Weld Made In Aluminum Alloy Type 1100.

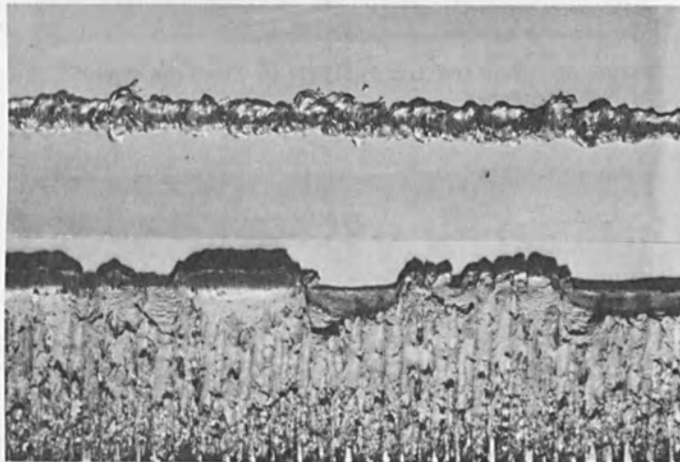

Figure 4. Surface and Fracture Appearance of Weld Made in Aluminum Alloy Type 5083.

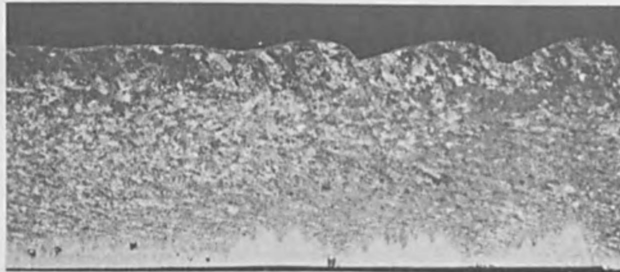

Figure 5. Penetration Pattern Titanium Weldment.

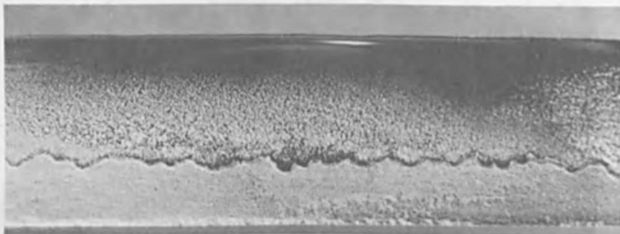

Figure 6. Penetration Pattern in Electron Beam Welded Uranium.

Figure 7. Fracture Appearance Showing Penetration in Aluminum Alloy Type 6061 Weldment Made Using Low Voltage Welder.

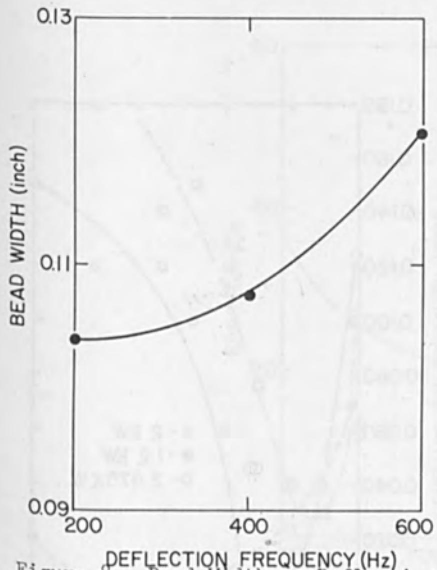


Figure 8. Bead Width vs Deflection Frequency

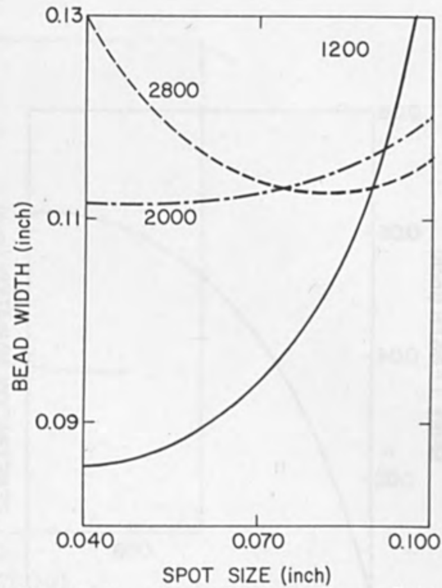


Figure 9. Bead Width vs Power Input and Spot Size

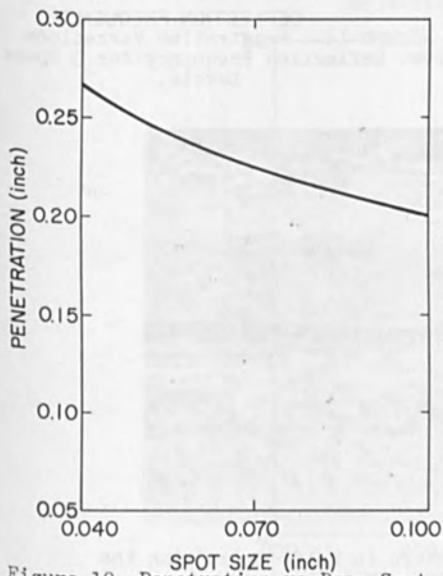


Figure 10. Penetration vs Beam Spot Size

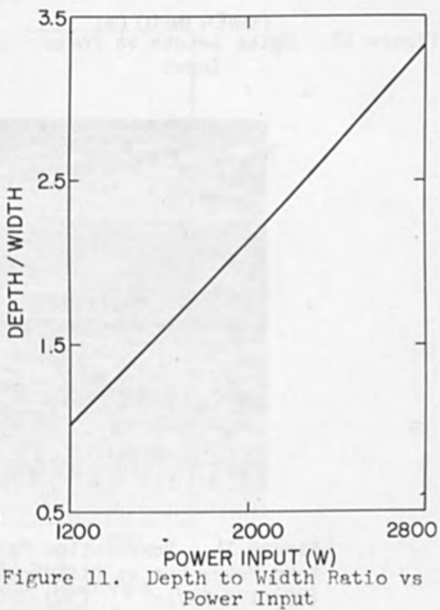


Figure 11. Depth to Width Ratio vs Power Input

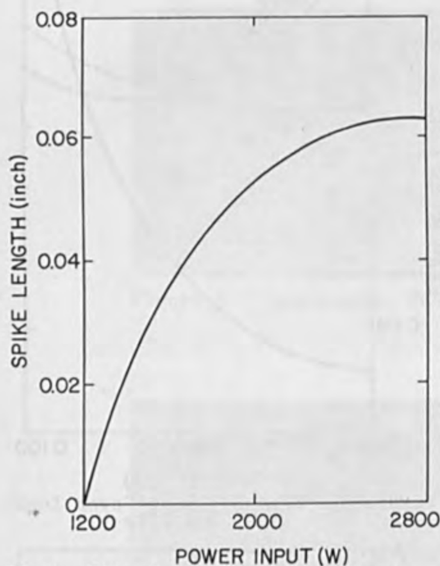

Figure 12. Spike Length vs Power Input

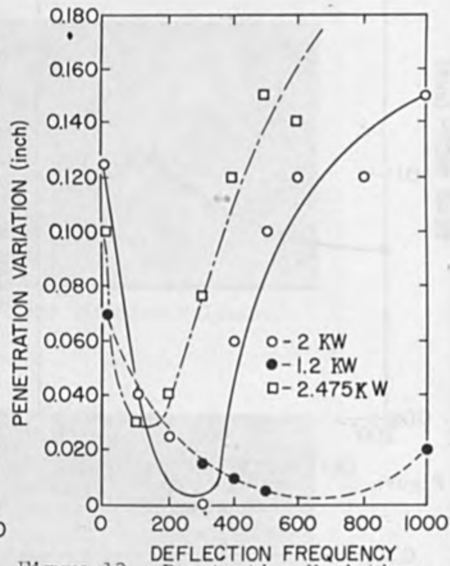

Figure 13. Penetration Variations vs. Deflection Frequency for 3 Power Levels.

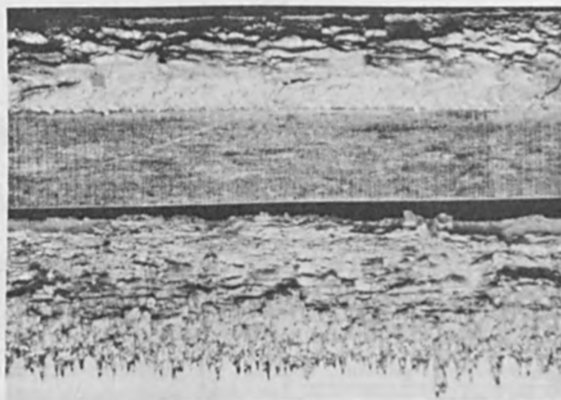

Figure 14. Penetration Pattern in Welds Made Using the Same Power but at Different Power Densities.
(35)-177 $KW/in^2$ (36)-420 $KW/in^2$

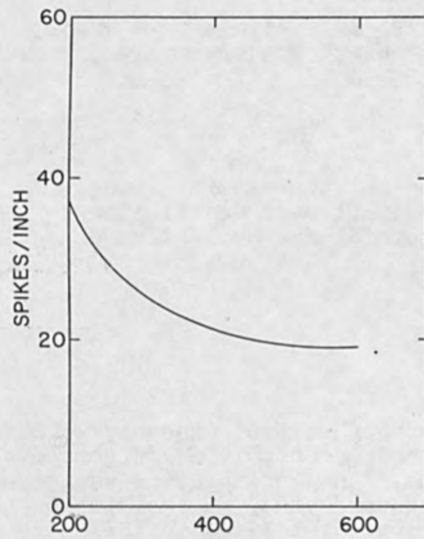

Figure 15. Spikes Per Inch vs Deflection Frequency

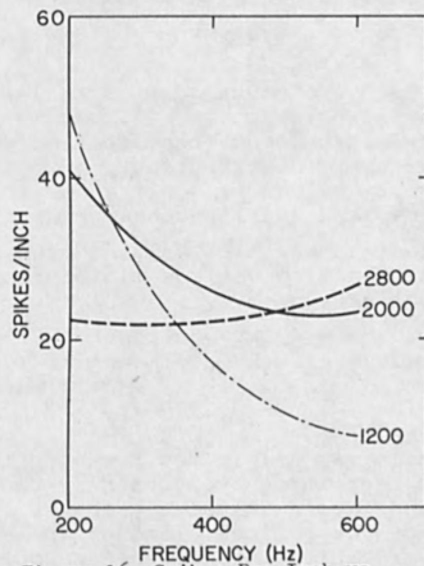

Figure 16 Spikes Per Inch vs Frequency for 3 Power Levels

NEW DEVELOPMENTS IN ELECTRON BEAM WELDING TECHNIQUE
OF NUCLEAR REACTOR STRUCTURE COMPONENTS

by

P. Thomé and R. Roudier
Département de Métallurgie
Centre d'Etudes Nucléaires de Saclay
France

ABSTRACT

Further to E.B. assembly of OSIRIS reactor core and for solving structure assembly problems, a new orientation was given to E.B. welding technology at the French Atomic Energy Commission, leading to the adjustment of two types of units :

- "clamp - on chambers" units
- internal welding machines

Therefore first type units were developped as follows :

a) an "S.L.B.1" prototype adapted to large thickness structures,
b) special electron guns (beam section study, current density distribution),
c) an "S.L.B.2" welder presenting new features as long as handiness is concerned.

The internal E.B. welding problems were solved thanks to various miniaturised components. Applications :

- 10 kW - 40 kV equipment (Ø 150 mm)
- 5 kW - 20 kV equipment (Ø 75 mm)

INTRODUCTION

Since it was originated the electron beam welding process has been intensively used by the French AEC. Initially, it was almost exclusively applied to the welding of various prototype fuel elements [I] . Then, while it was put in fabrication line for these applications, researches were devoted towards assembly problems of nuclear structural parts.

This new direction led-due to difficulties found in using the conventional welding processes-to design new apparatuses [2] and to demonstrate the capability of this technology for welding rather thick pieces such as these used for a linear accelerator of the "cross bar"type (figure 1) and the vessel for the experimental OSIRIS reactor (figure 2). The main advantage, well known in the labs is the negligibility of deformation actually reduced to a very slight shrinkage of a few mils.

However, as we are contemplating the application of the electron beam welding to very large and heavy parts,it seems very important for economical and pratical reasons to stick to the following principles.

a) The electron gun must be moved upon the joint

b) The vacuum chamber is of the clamping type, as rugged and as small as possible.

c) It should be possible in a later stage to weld in the field since this non deformation process links much more to a mechanical process than to a welding one.

Now,for the first development,we aimed at problems which could be solved with the existing power supply equipement, i.e. welding of plates not thicker than 2 inches.

Regarding the accelerating voltage, it is very convenient to use the lowest one, would it be only for reducing gun' size and its associated optics as far as beam characteritics are acceptable for welding. By using accelerating voltage below 60 kV, we could work with local clamping chamber under secundary vacuum without a separate pumping stage for the gun ; However,we have been very soon aware of the advantages of using primary vacuum (pressure $\leqslant 5.10^{-2}$ Torr). This pressure range while giving contamination protection equal to the one given by gas shielded processes generally used, greatly simplifies sealing problems for field welding. In such work,we had to verify the behaviour of an electron gun under various gases and pressures with the same experimental device as for routine checking of the electron guns.

Moreover, we did strain at evaluating the possibilities of internal welding of thick tubes, as it opens the way to new conception and design in assembling with no deformations and reduced residual stresses. The fact that the welding apparatus has to be adapted to each specific problems originated the development of new components which

might be utilized in different cases; we expect that this trend will give rather light weight and universal tools in a near future.

The aim of this paper is to exemplify the problems we have just pointed out.

## I. "S.L.B.1" EQUIPEMENT*:

The anticipated realisation of a moderator tank of about 8 meter diameter for a pressure tubes reactor, put the problem of welding a number of tube stubs in a close lattice patch on a 50 millimeters thick 304 stainless steel end-plate. In a previous realisation (EL.4 reactor, 60 MWe prototype gas cooled reactor) the hand welding process was actually a technical performance and a limitation for further bigger construction because of the catastrophic addition of all weld deformations.

For such a thickness, we generally used a beam power near 30 kW. At the beginning of this study, we had no high power gun with separate pumping available and were obliged to pay special attention to air-tightness of the working chamber [4] .

### 1. 1. Apparatus description

The equipement comprises three parts (figure 4)

- gun and working chamber
- pumping unit
- gauges, controls and securities

The working chamber is mechanically independent from the gun and its appliances. It is a simple cylindrical vessel covering the joint and provided with a top opening for entering the gun and for visual observation.

The vacuum seal is of the hydraulic inflatable type which can allow rather bad plate-surface preparation.

Underneath the joint, a TIG welding pass makes the seal on the other side of the plate.

The gun and its supporting-arm is centered on the machined bore of the stub and then moves with an easily obtained accuracy above the joint. Means are provided in order to have a radial positioning when under vacuum.

* S.L.B. : Soudage Local par Bombardement.

Special care has been taken for reducing the overall dimensions, for completely shielding all the high voltage parts and then eliminating glow-discharge problems,and for being able to change easily the cathode part of the gun which constitutes a plug-unit. The distance,between the concentrating lens and the work,can be adjusted between 80 and 100 mm. All the high and low voltage lines come through the rotating axis. Inside the stub,a double sealing system is used, one between the stub and a centering static piece through an inflatable seal, the other between this piece and the rotating arm,with a conventional Wilson seal.

A primary and a Roots pumps (of respectively 80$m^3$/h and 500 $m^3$/h capacity) are connected with a flexible pipe to the apparatus; a diffusion pump with cooled baffle (3500 l/s) is rigidly connected to the chamber. In the device used for our research,the diffusion pump is parralel to the axis of the welder but some modifications related to the pumping design should be necessary in order to use this apparatus for welding of very large plates.

General controls, commands and securities are grouped in two racks, one for the high and low voltage controls of the gun, the other for pumps,securities,and programming radial and circumferential displacement of the gun.

## 1. 2. Results

This kind of apparatus can be used either on horizontal or vertical test-pieces; however,we have just worked on horizontal ones. We tried to be close to practical shop conditions (figure 3) and in order to demonstrate the process, we proceeded to the welding of "eight holes" test-pieces after having determined the welding parameters on elementary one-weld samples.

The main point was to know general deformation and to check if shaped welds could be ultrasonically examined notwithstanding the fact that it was stainless steel whose weld are not generally relevant of this non destructive testing method.

Regarding the apparatus performances there have been no special difficulties but some usual minor improvements for a prototype equipment. Welding parameters have been fixed up trying to use as low a voltage as possible, because the compactness of the apparatus makes it more sensitive to pressure variations,which can give glow dicharges and affect the stability of the electron beam.

On a first set of experiments, with 52 mm thick plates in 304 stainless steel,the parameters were :

. accelerating voltage 51 kV
. electronic current 770 mA
. working distance 100 mm
. welding speed 112 cm/mn
. energy 21 kj/cm
. vacuum when finishing welding 2. $10^{-4}$ Torr

The focalisation current was function of the high voltage value.

However,we got some cavities in this one pass welds and resumed our experiments on new test pieces 48 mm thick, on which good results were obtained (figures 5 and 6). In this second run,the parameters were :

. accelerating voltage 50 kV
. electronic intensity 760 mA
. working distance 100 mm
. welding speed 140 cm/mn
. energy 16,3 kj/cm
. vacuum 2. $10^{-4}$ Torr

The deformations were a 8 mils (0,2 mm) shrinkage for a bore diameter of 152 mm, a bow of 7 to 8 mm for the total length of the sample (2. 4 meter).

With this apparatus,it seems to be some limitations for welding more than 50 mm in one pass when the voltage is increased above 50 kV; improvements are to be seeked in the stability of the high voltage power supply, or in providing a better pumping on the cathodic part of the gun. We had also some perturbation with an abnormally high nitrogen content of the steel.

## 2 - MEDIUM VACUUM E.B WELDING

Medium vacuum does not affect the beam efficiency for welding so far all the inside of the gun itself is maintained in a secondary vacuum. Now, the problem of residual gas contamination has no signifiance for a great number of applications. On an other and, there is a good technological impact to work in medium vacuum regarding the sealing problem, simplification of the apparatus and then increasing the fiability of the apparatus, reducing the pumping units ...

A study has been made of the dispersion of electron beams used for welding. For this purpose, we used an experimental apparatus; by means of the X-rays,it is possible to reconstruct the beam section as to shape and dimensions, and to have a densitometric analysis of the X-rays picture obtained. This picture visualizes directly the current density distribution across the beam. (3)

The experimental bench is shown in figure 7.

On top of the experimental bench were mounted the gun and an annular pump: this bench presents itself in the shape of several chambers put one on top the other, each with a port-view and different tight fluid pipes.

Through a focusing coil the electron beam is directed vertically to the inclined profile of the revolving target; this profile forms a cone frustrum with an angle of 140° at the top. The target is driven into a revolving speed of 9000 R.P.M by a generator fed motor, trebling the frequency of the network. A beryllium window is placed in the direction of the highest X-ray emission : 20° with respect to the anode surface.

In order to avoid excessive heating of the target, it has been necessary to use short time-exposure ($\leqslant$3 sec.). However, the beam does not show immediately its definite shape : a delay of 0,5 to 2 seconds,starting from the interlock of high voltage,is necessary for its fashioning. During this time, the beam does not have its definite energy distribution,and first measurements showed a very great scattering of results, as long as this phenomenon was not considered. Therefore, we decided to "shape" the beam on a spare target at a distance of about 200 mm, long enough for its defocusing. Afterwards by an electro-magnetic device, the beam is turned back to the anode surface for the duration of the chosen exposure time.

The lecture of X-ray photographs was entirely done on a quick photometer ZEISS type G II, with a recorder. In this type of apparatus, the light beam with an adjustable intensity used for photometric measurements is limited within a "measuring slit" adapted to the exploration to be made. After crossing of the film,a photoelectric cell absorbs the light beam and transforms it into a current proportional to the light intensity received and transmits it to a standard recorder Gl ZEISS of high sensibility.

The blackening of the X-ray photographs to be analysed corresponds to the logarithm of the reciprocal of D transmission of the measured light. The blackening, which

in our case corresponds to a density of the electron beam is given by

$$S = \log \frac{1}{D}$$

figure 8 shows an example of beam analysis for a fixed distance of 345 mm, as well as a range of results obtained in Helium, Nitrogen and Argon atmospheres.

## 3 - "S.L.B.2" WELDER

As a result of the preceding works and in front of the problems raised by different cases of tube stubs on tube plate assembly, we developped a device enabling to take the advantage offered by E.B welding while trying not to suffer its disadvantages (large and inert unit, heavy chamber and tooling, high cost).

We endeavoured to look after some new particulars of this welder, such as :

a) movableness (use in field or shop)
b) production rate
c) site-welding with horizontal gun, on heat exchangers

Therefore this machine constitutes a prototype which is to be considered as a first step to an E.B portable welding machine (figure 9).

Data :

The following points formed the study basis :
- Perfectly maneuverable machine assembly
- Low weight and size, comparable with those of portable devices (for instance portable spot welding machine).
- Welding on vertical wall
- Thickness to be welded : 20 mm
- Time allowed for welding (all included) $\leqslant$5 minutes
- Use of available power supply.

Finally strength and safety standard should be close to those which occur in ordinary boiler-work practice.

### 3. 1 - Description

(see figure 10)

The expandable mandrel (1) adjusts and locks the machine

in the stub to be welded; the chamber applies against the tube plate around the welding joint,through an ordinary "O" ring (2); the movable part (4) bears the electron gun (5) which concentrically rotates around the mandrel with an adjustable diameter.

Gun-to-work distance has been determined by keeping on one hand building needs and,on the other hand,by taking into account the tests carried out in medium vacuum.

We know that regarding the used steel, nitrogen is the most important part of gas emitted during melting (300 ppm $N_2$ ; 100 ppm $O_2$ ; 5 ppm $H_2$). If we consider the preceding works (see figure 8),we can see that as long as nitrogen is the residual gas and for a pressure of $1. 10^{-2}$ mm Hg, we observe, for a distance of 350 mm, a loss of 25% in density with regard to the measures taken in high vacuum; if we admit a proportionality between density loss and distance,and if about 6% is taken as density loss in the case of our machine, we find a distance of :

$$\frac{350 \times 6}{25} = 84 \text{ mm}$$

Density loss in our case is verified by the difference between depth of penetration obtained in testing the gun in high vacuum (25 mm) and depth of penetration obtained during normal operation of the machine (20 mm) with identical settings. (30 kV ; 250 mA ; 80 mm distance).

Front part pumping is performed by a 500 $m^3$/h Roots pump,while vacuum ($< 1.10^{-5}$ Torr) in the cathode chamber is obtained by a 650 l/s diffusion pump; a water-cooling valve insulates the gun chamber during displacements between each welding. In order to avoid any electrical wire torsion we studied with CLOVER Corporation (VILLEJUIF - FRANCE) a rotatable feed throughout (7) enabling high voltage supply of the filament (50 Amps A.C, 30.000 V). The movable part of the feed throughout is driven in rotation together with the gun while the cable remains motionless. This new device works perfectly and gives large possibilities regarding future applications.

3. 2 - Operation

After the machine has been centered for each welding directly in the tube stub, no more adjustment is required and the gun revolution diameter remains identical for each type of tube.

In these conditions the operator, after having placed the "O" ring on the plate and locked the expandable mandrel (figure 11), puts the front part in vacuum and starts the welding cycle. This cycle is computed (high voltage variation and servo coil current) in order to obtain the best recovering. The machine can be displaced as soon as vacuum is released,this operation is performed immediately after welding.

In these conditions,welding time for 1 tube is lower than 2 minutes as follows :

- starting .................................. 30 sec
- primary pumping (1. $10^{-3}$ mm Hg) .......... 10 sec
- welding ................................... 30 sec
- valve plut-off, vacuum release, extraction the machine .............................. 20 sec

Welding parameters,for 20 mm penetration depth,are as follows :

- voltage (initial and final) .............. 8 kV
- voltage (welding) ........................ 30 kV
- beam current ............................. 250 mA
- focus current ............................ 1,9 A (high voltage servo applied)
- welding speed ............................ 50 cm/mn

3. 3 - Results

After having used this apparatus for several months we consider that such a device constitutes an appreciable development of welding process as far as handiness, simplification and net cost are concerned.

If in its present configuration some minor modifications appear to be required for an actual use in a field, no doubt that such a welder can be placed in a boiler shop exactly as for any other portable unit as ordinarily used.

4. ELECTRON GUNS FOR INTERNAL WELDING

Important efforts have been devoted to estimating the possibilities of welding thick tubes from inside.

2 types of guns have been developped; the purpose of the first one is to carry out remote welding with a depth of penetration $\leqslant$35 mm (stainless steel) in tube of diameters $\geqslant$150 mm. The second one enables penetration

$\leqslant$20 mm in tubes $\geqslant$75 mm of diameter.

4. 1 "10 - 40" equipment

This gun, described in figure 12, shows the following particulars :

- voltage (max) : 40 kV
- beam current (max) : 250 mA
- E.B. indirect heating
- gun-to-work distance : from 10 to 30 mm
- beam concentrical view by removable mirror
- size (Ø ) : 140 mm

Such a volume reduction has been possible by adapting low accelerating voltage and optics especially designed for available distances. Moreover the use of refractory metals, cooling systems and the shield of all the parts subject to high voltage, give a compact assembly, entirely adapted to the anticipated use.

Figure 13 shows an example of internal welding on a test-piece of 150 mm inner diameter, the piece being steady during welding.

4.2. "5 - 20" equipment

This second type of gun, the power of which being half of the preceding one, can weld inside a tube of 75 mm Ø, with depth of penetration reaching 20 mm (stainless steel)

In this type, maximum accelerating voltage is reduced to 20 kV on electronic current of 250 mA. The very low gun-to-work distance requires cooling of the lower part of the focus coil (5) (figure 14).

The gun is entirely shielded (figure 15) and a movable endoscope, parallel to the axis, enables the view.

CONCLUSION

These realisations clearly show the feasability of electron beam welding for the assembly of large structures. They just are first steps demonstrating that new and convenient small components open the way to a great number of practical uses as for example in the boiler making industry, and that the advantages of this non-deformation welding process could be actually available for shop and for field welding.

We do hope that the attractiveness of portable E.B apparatus will promote new interest and development work in this technology.

REFERENCES

1 . Stohr. J. A - Fuel Element Conference - PARIS, Nov 1957 TID - 7546, Book I pp 9-17, U.S A.E.C Also : Nuclear Power, 272 (1958)

2 . Solomon J. L and Thomé. P - Proc. of the 7 th elect. and laser beam symp, EL-KAREH Ed. pp 191-218, (1965)

3 . Roudier. R - Thesis, (1968) - To be published

4 . Thomé. P and Roudier. R - SCHWEISSTECHNIK 16, pp 459-462, (1966)

FIG. 1 : BUTT-WELDED 70 cm DIAMETER LINEAR ACCELERATOR COMPONENT

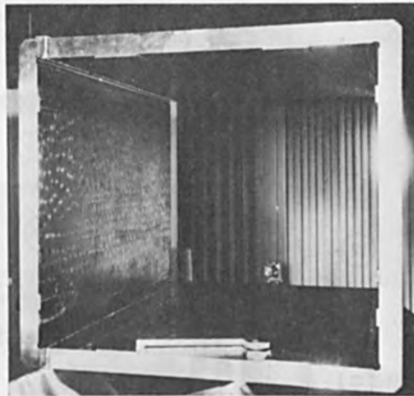

FIG. 2 : CORE VESSEL OF THE NUCLEAR REACTOR OSIRIS

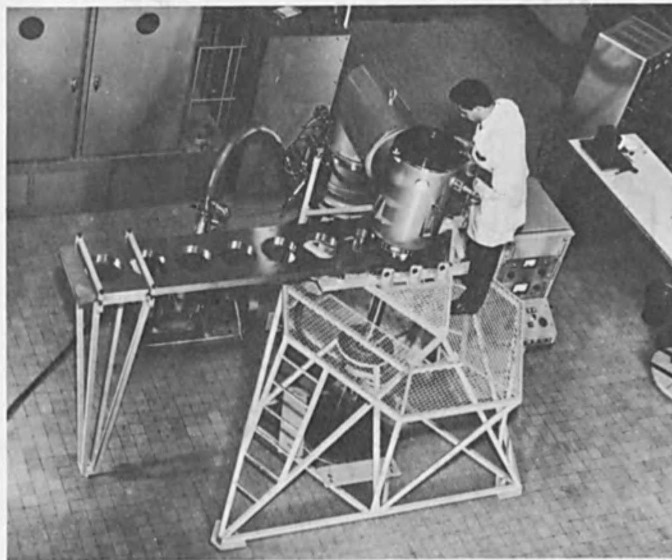

FIG. 3 : S.L.B.1 EQUIPMENT - GENERAL VIEW

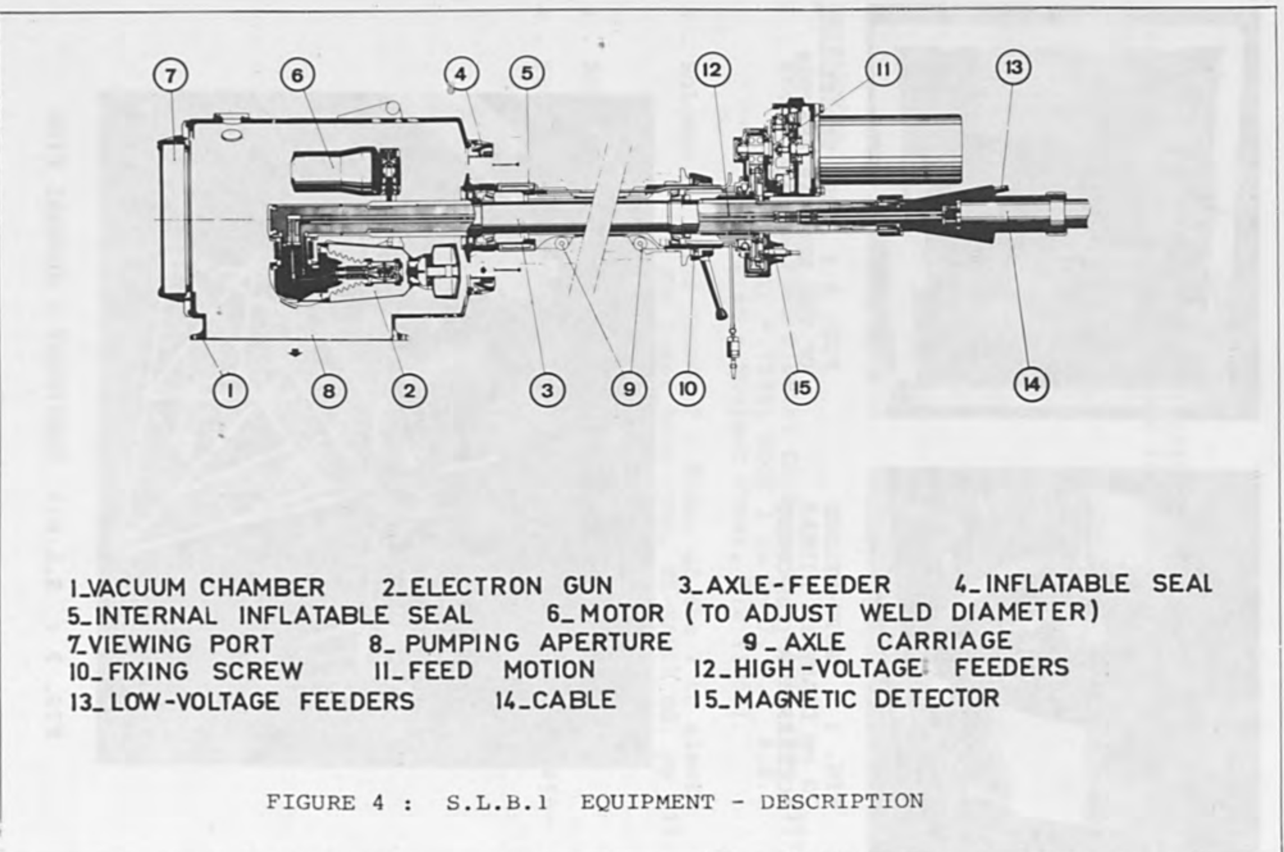


FIGURE 4 : S.L.B.1 EQUIPMENT - DESCRIPTION

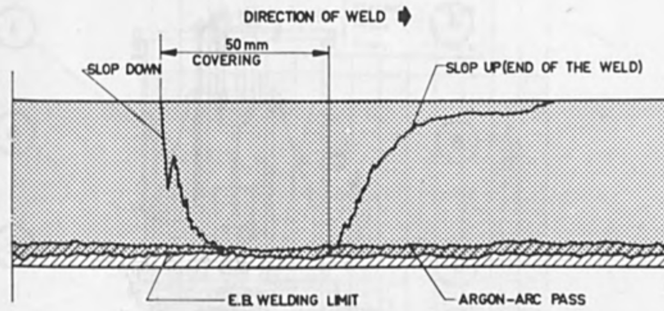


FIG. 5 : SPREADING OF A CIRCULAR WELD

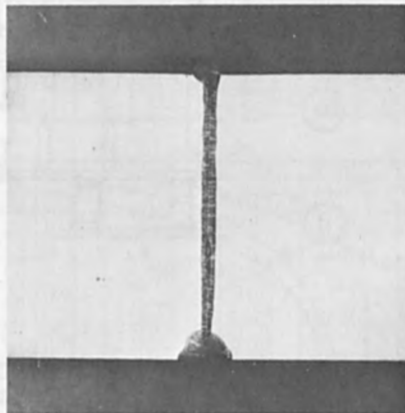


FIG. 6 : CROSS SECTION OF A S.L.B. 1 WELD

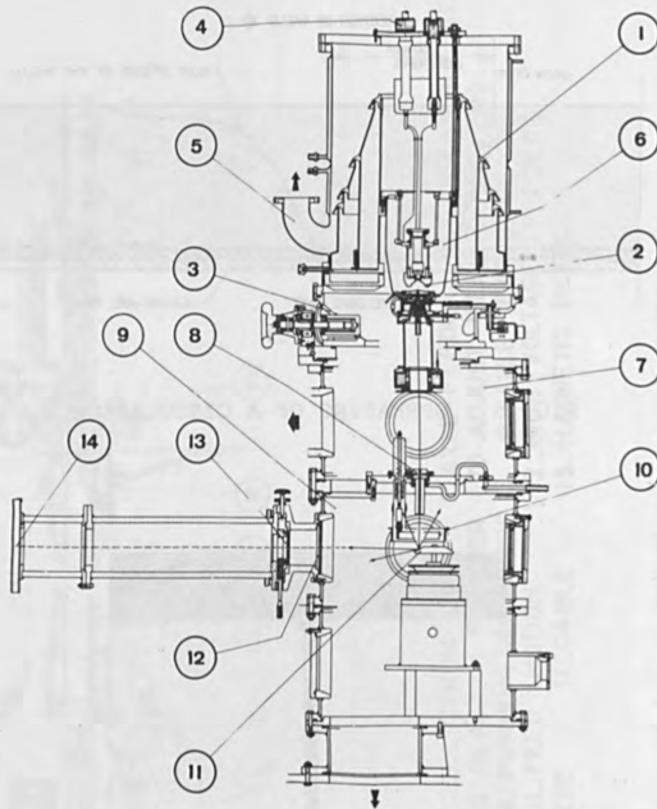


1_ ANNULAR DIFFUSION PUMP 2_ ELECTRON GUN
3_ CARRIAGE 4_ HIGH VOLTAGE FEED 5_ PRIMARY PUMPING
6_ $1.10^{-5}$ mm Hg VACUUM 7_ $1.10^{-5}$ TO $1.10^{-1}$ mm Hg VACUUM
8_ THROTTLING 9_ $10^{-1}$ TO 10 mm Hg VACUUM
10_ SHIELDED ANNULAR HOLLOW CATHODE 11_ ROTATING ANODE
12_ BERYLLIUM WINDOW 13_ PIN-HOLE 14_ X-RAYS FILM

FIGURE 7 : MEDIUM VACUUM EXPERIMENTAL APPARATUS

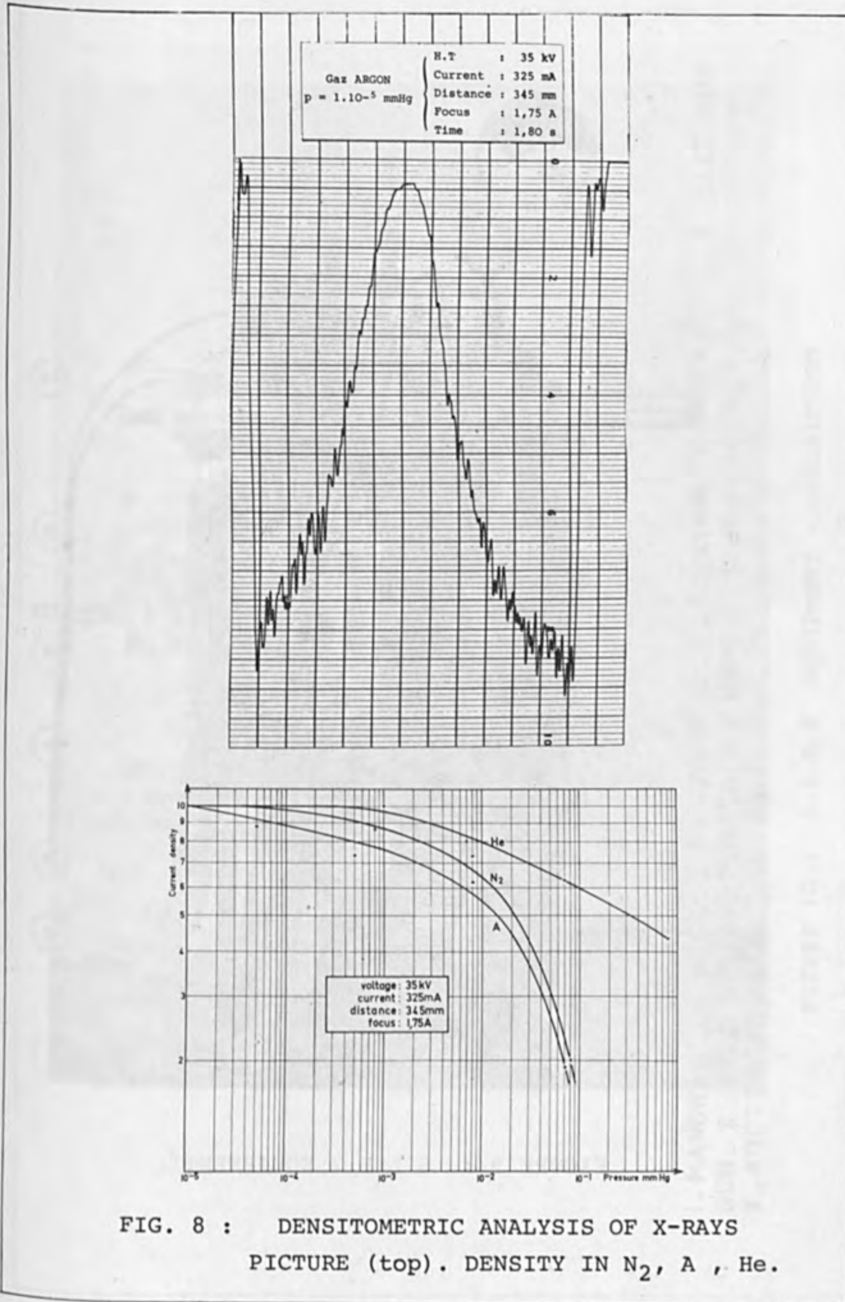


FIG. 8 : DENSITOMETRIC ANALYSIS OF X-RAYS PICTURE (top). DENSITY IN $N_2$, A , He.

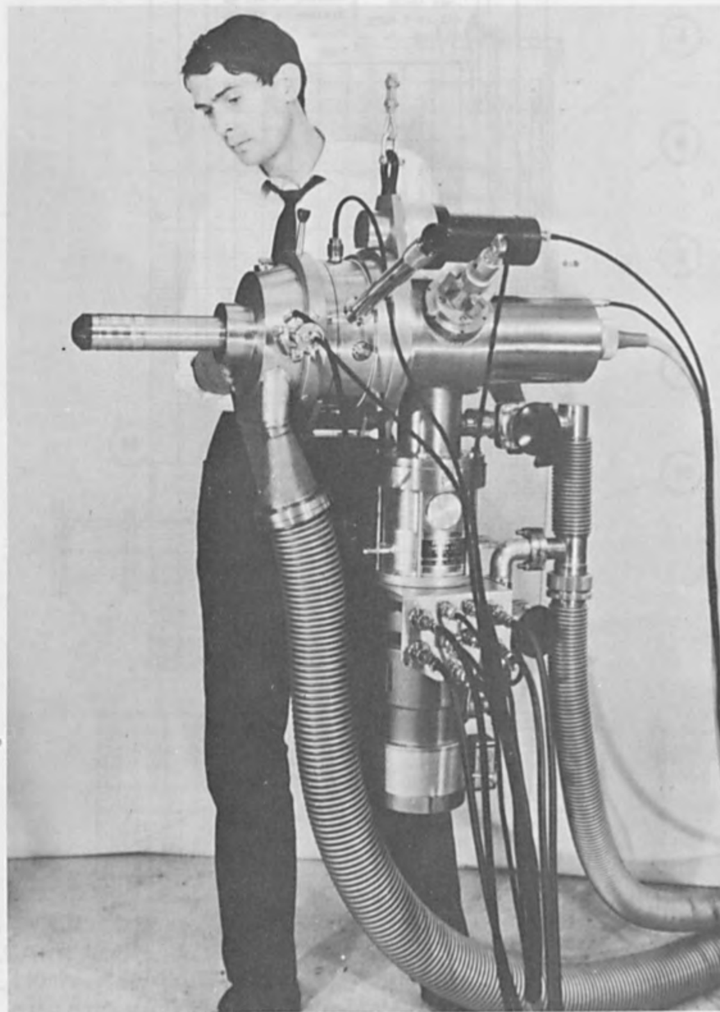

FIGURE 9 : S.L.B.2 EQUIPMENT

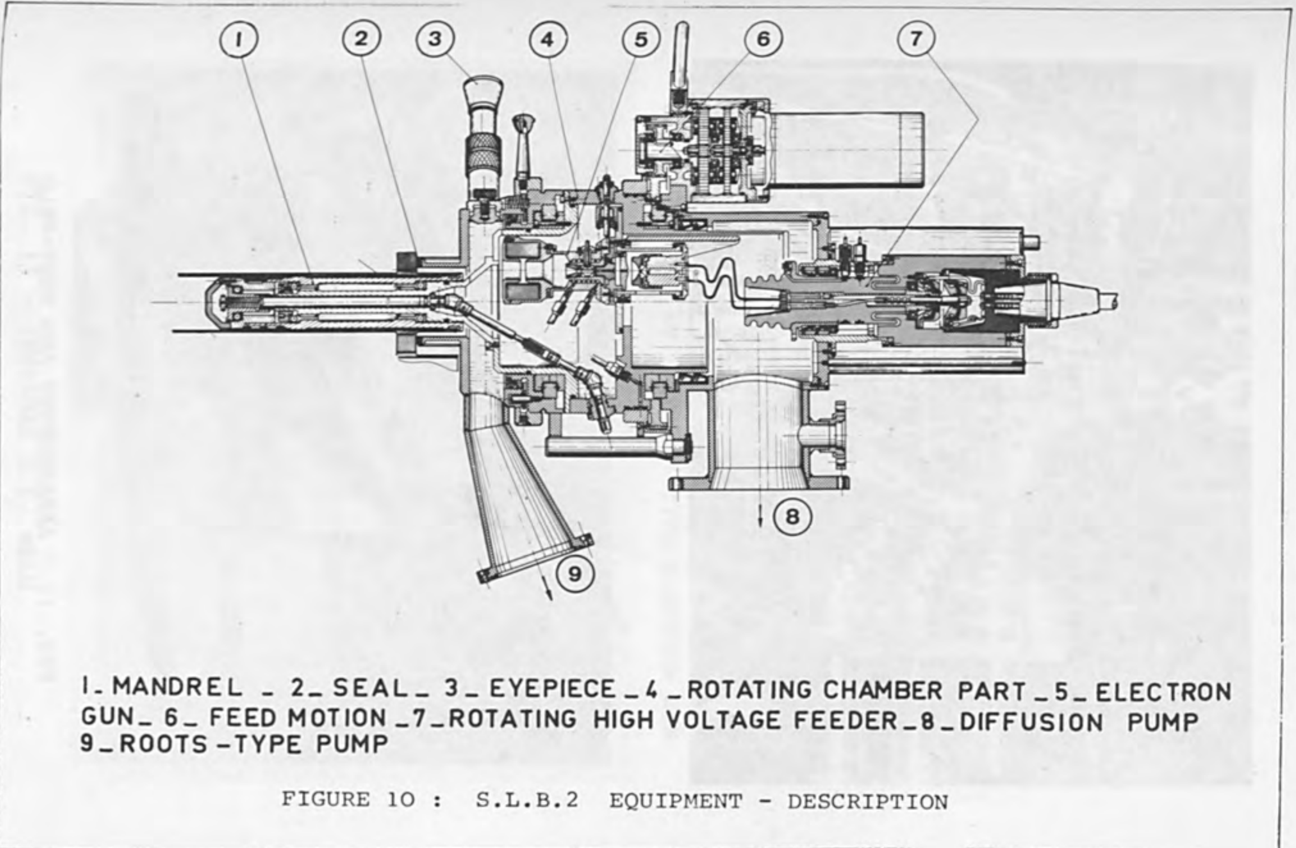


FIGURE 10 : S.L.B.2 EQUIPMENT - DESCRIPTION

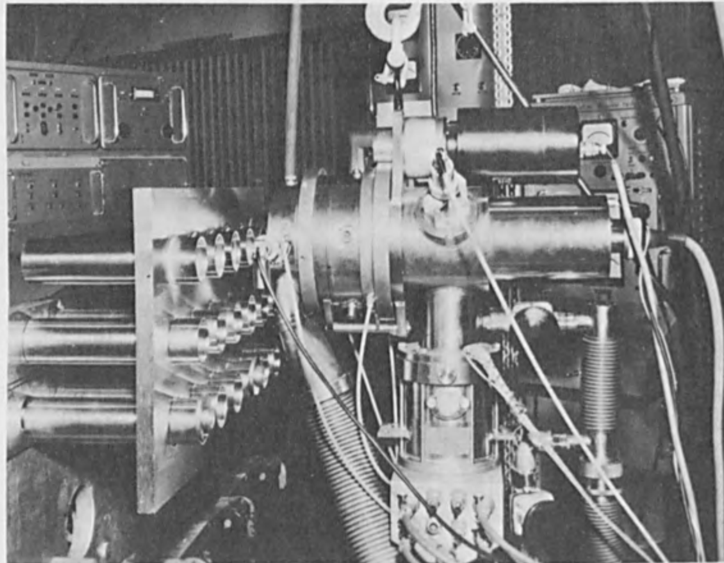

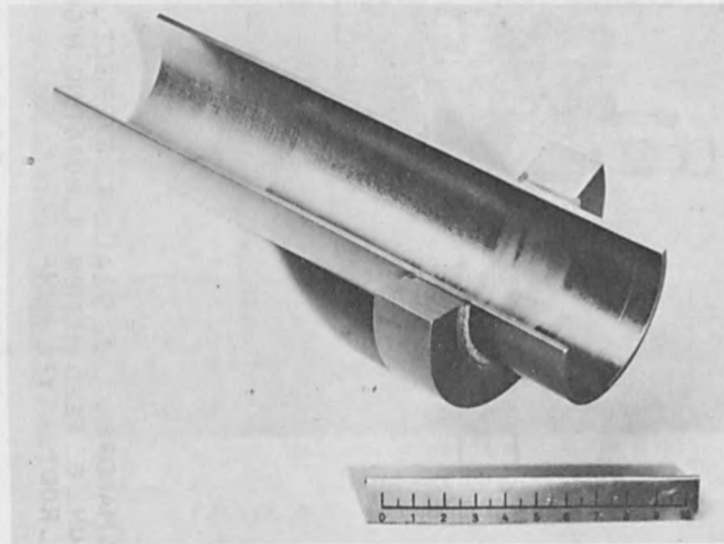

FIG. 11 - ARRANGEMENT AND TEST-WELD

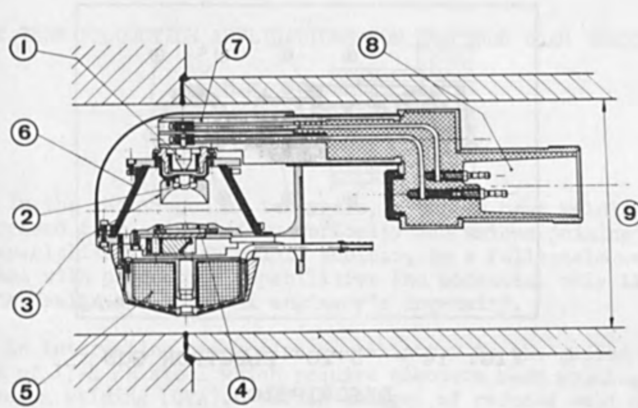


1.FILAMENT 2.CATHODE 3.CATHODE ELECTRODE 4.ANODE 5.MAGNETIC LENS
6.INSULATOR 7.HIGH VOLTAGE FEED INSULATOR 8.PLUG 9. 6" DIAMETER TUBE

FIG. 12 - "10 kW - 40 kV" TYPE ELECTRON GUN

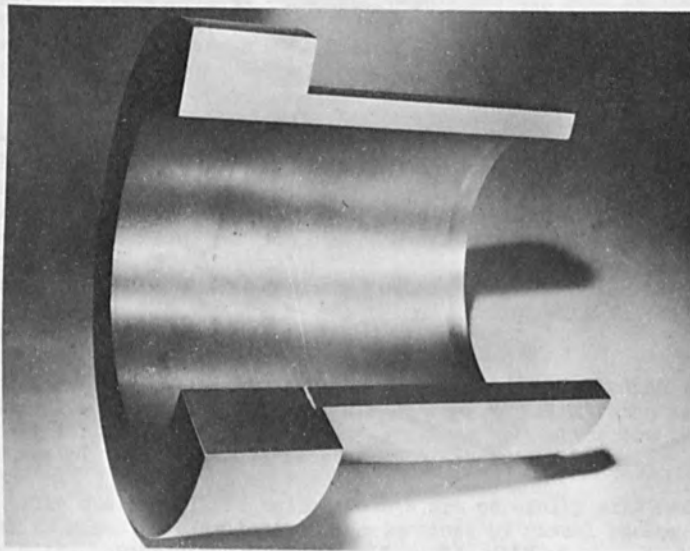

FIG. 13 - INTERNAL E.B. WELD

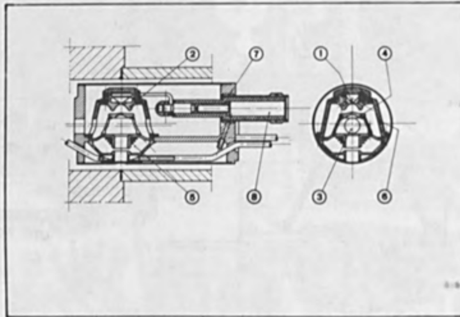

FIG. 14 - "5-20" ELECTRON GUN
DESCRIPTION

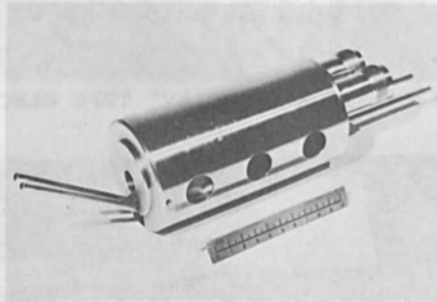

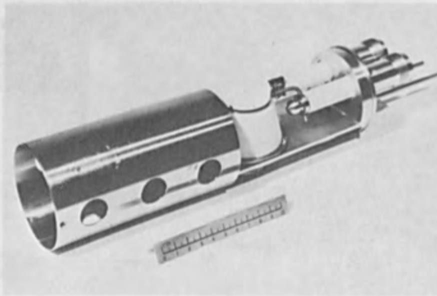

FIG. 15 - "5-20" ELECTRON GUN
ASSEMBLY

## SHORT TERM PRODUCTION APPLICATIONS FOR ELECTRON BEAM WELDING

M.M. Schwartz
Martin Marietta Corporation
Baltimore, Maryland 21203

In the short span of ten years, electron beam welding has progressed from a laboratory curiosity and unique joining media for specialized metals, mainly nuclear, to a full-scale welding process with production capabilities and potential only limited by the design and material engineer's ingenuity.

An interesting production case history is the guided missile vanes of 17-4 PH steel which require electron beam welding in lieu of fusion welding (GTA). The advantages of reduced weld bead build-up, subsequent machining operations and minimum distortion have prompted the mass production of the aforementioned vanes.

Typical weld mechanical properties obtained have averaged 195 ksi tensile and 175 ksi yield strength with 5% elongation.

In most instances, individuals only see the final product thus forgetting and neglecting to realize some of the most important steps leading to the excellent results seen in the finished part. Two important processes, cleaning and demagnetization, which occur prior to electron beam welding have contributed to the achievement of the aforementioned strengths.

The first is the cleaning of the details. All greases, oils, inks, wax markings and shop soil particles are removed by safety solvents, vapor degreasing, hot alkaline cleaners, warm and cold water, and a nitric acid-dichromate solution. This last solution which is agitated most vigorously is most important since it dissolves off free iron and other metallic particles. Subsequently, the vane is soaked in running cold water, a nitric-hydrofluoric acid solution followed by another water rinse and brisk scrubbing to remove smut, a deionized water rinse, drying with filtered air, demagnitization and a final oven bake at 300°F.

The forged vane and the necessary fixturing including the very critical weld run-off tabs and clamps will be illustrated as well as the various joint designs that are used to produce the twelve sequential welds that are necessary to produce the vane.

The quality of the welded joints are carefully examined and quality acceptance criteria are determined by visual radiographic and ultrasonic means. Checks are made for weld width, cracks, gas pockets or porosity and weld penetration. In addition, weld test coupons are prepared prior to the welding of any vane and are

evaluated for mechanical properties and by non-destructive methods described above.

Consistency of acceptable welds doesn't occur at all times. Weld repair techniques and procedures using GTA methods have been developed and the acceptance criteria for these weld repaired assemblies will be discussed.

In order to achieve maximum mechanical property requirements, a series of test programs were necessary to obtain optimum welding parameters, especially the problem of gap size limitations between the detail parts.

The fabrication welding of various types of bellows which range from .001" to .005" gage and cover steels as well as refractory metals has become a production application for electron beam welding. Due to the thinness of material, fusion welding by GTA techniques have not been considered or tried unsuccessfully. The joint design on most bellows has now been tailored for electron beam and the tooling and fixturing made to suit. Examples of bellows configurations and the exactness of detail tooling necessary are described.

Another production application for electron beams are fuel capsules. The material, TZM, doesn't lend itself to fusion welding due to excessive cracking and brazing is not suitable since the temperature of brazing (above 2500°F) has an adverse effect on the fuel within the capsule. The use of electron beam welding solved the various problems which included cracking, restricted heat control therefore, the fuel wasn't overheated, small uniform weld beads which required no post machining and minimum distortion.

Several other short term production applications will be shown in order to exhibit the overall versatility which is offered by electron beams.

In the short span of ten years, electron beam welding has progressed from a laboratory curiosity and unique joining media for specialized metals, mainly for nuclear applications, to a full-scale welding process with production capabilities and potential only limited by the design and material engineer's ingenuity.

An interesting production case history is the guided missile vanes of 17-4 PH steel which require electron beam welding in lieu of fusion welding (GTA), Fig. 1. The advantages of reduced weld bead build-up, subsequent machining operations and minimum distortion have prompted the mass production of the aforementioned vanes.

Metallographic examinations of representative cross-sections of welded panels has revealed 100% penetration, satisfactory grain structure and negligible porosity in all cases. In a joint combining .171 inch and .500 inch gage the weld width was .080 inch to .082 inch at the face, and .028 inch to .032 inch at the back while the width of the heat affected zone (measured encompassing the weld bead) was .115 inch to .117 inch at the face and .047 inch to .057 inch at the back. In a .125 inch to .500 inch gage weld joint, weld width was .071 inch to .078 inch at the face and .030 inch at the back of the weld. The heat affected zone width was .108 inch to .117 inch at the face and .062 inch to .064 inch at the back. The typical weld contour is shown in Fig. 2.

Typical weld mechanical properties obtained have averaged 195 ksi tensile and 175 ksi yield strength with 5% elongation as shown in Table I below.

TABLE I

| Gage (inches) | Gap (inches) | Ftu (Ksi) | Fty (Ksi) | e % |
|---|---|---|---|---|
| .171 | .005 | 199.4 | 185.5 | 4 |
| .171 | .003 | 189.3 | 173.5 | 5 |
| .171 | .000 | 187.0 | 173.5 | 5 |

In most instances, individuals only see the final product thus forgetting and neglecting to realize some of the most important steps leading to the excellent results seen in the finished part. An important process; cleaning, which occurs prior to electron beam welding has been a major factor and contributed to the achievement of the aforementioned strengths.

All greases, oils, inks, wax markings and shop soil particles are removed

by safety solvents, vapor degreasing, hot alkaline cleaners, warm and cold water, and a nitric-acid-dichromate solution. This last solution which is agitated most vigorously is most important since it dissolves off free iron and other metallic particles. Subsequently, the vane is soaked in running cold water, a nitric-hydrofluoric acid solution followed by another water rinse and brisk scrubbing to remove smut, a deionized water rinse, drying with filtered air, and a final oven bake at 300°F. Since the electron beam welding in this instance involves a magnetic steel, a demagnetization operation is performed prior to the final oven baking step above. This demagnetization must be performed otherwise the beam would be deflected away from the joints to be welded.

A second aspect of producing acceptable welded joints is fixturing. The forged vane is placed in a holding fixture and the side panel in the forging is assembled and checked for proper location and fit-up and punch marks in the side panels, locating the weld position in the center web, must be placed up, see Fig. 3. This figure also includes the weld run-off tabs which are securely clamped in place. Fig. 4 shows the vane and tooling in the electron beam chamber.

The sequence of welding is extremely critical, namely, from a shrinkage consideration as well as an economical standpoint. The number of times the vane must be removed from the chamber to perform different welds must be held to a minimum. In Fig. 5, the sequence of welding is shown. Joints 1, 2 and 3 are butt welded in the tool shown in Fig. 6. The vane is then turned over and joints 4, 5 and 6, as well as 7 and 8, are welded. The vane is again turned and welds 9 and 10 are made. The tooling required to perform the spike weld on joints 7, 8, 9, and 10 is shown in Fig. 7. A machining operation is necessary to prepare the ends of the vane prior to welding joints 11 and 12 which are an end butt type of joint and this is shown in Fig. 8. The various joint designs and certified weld parameter settings are seen in Fig. 9.

The quality of the welded joints was carefully examined and quality acceptance criteria was determined by visual, radiographic and ultrasonic means. Checks were made for weld width, cracks, gas pockets or porosity and weld penetration. In addition, weld test coupons were prepared prior to welding of any vane and were evaluated for mechanical properties and by non-destructive methods described below. The angle beam or pulse echo shear wave mode vibration was the most reliable method for ultrasonic testing the electron beam welds. Other ultrasonic methods found metallurgical imperfections, however, these were not able to be confirmed by metallography. These imperfections could have been the presence of partially dissolved delta ferrite stringers in the high temperature edge of the heat affected zone adjacent to the electron beam weldment and the possible opening up of propagated small microscopic fissures and might explain the reflectoscope's transmission pattern. Fig. 10 illustrates the radiographic positive of one of the weld joints which appears sound.

The criteria for acceptable welds was:

1. Full weld penetration
2. No cracks in the weld or the area surrounding the weld
3. Porosity was not acceptable when any 2 cavities were closer than 2 times the greatest dimensions of the larger cavity, or the total accumulated lengths of the greatest dimensions of all cavities in any 5T length of welds exceeded 4%. (T = material thickness)

When a welded vane was rejected for one of the above reasons, one of two weld repair methods were instituted. Electron beam was utilized if the weld defects were:

1. Lack of sufficient penetration
2. Insufficient bead width
3. Cracks and voids

Gas tungsten arc was utilized if the weld defects were:

1. Voids
2. Undercuts and cracks

Test results on continuous stringer pass repairs with GTA and with electron beam techniques (see Fig. 11), indicated that re-welding with electron beam where feasible was preferable to the GTA method. Tables II and III illustrate the aforementioned test results.

In order to achieve maximum mechanical property requirements, a series of test programs reflected the optimum welding strengths especially the problem of gap size limitations between the detail parts. As shown in Table IV, mechanical properties met equipment qualification minima of Ftu: 176.7 and Fty: 159.8 regardless of gap size.

Other applications have been as thoroughly investigated and placed in production as the vane above.

The fabrication welding of various types of bellows which range from .001" to .005" gage and cover steels as well as refractory metals has become a production application for electron beam welding. Due to the thinness of material, fusion welding by GTA techniques have not been considered or have been tried unsuccessfully. The joint design on most bellows is tailored for electron beam and the tooling and fixturing made to suit. Examples of bellows configurations and the exactness of detail tooling necessary are seen in Fig. 12.

Another production application for electron beams are fuel capsules. The material, TZM, doesn't lend itself to fusion welding due to excessive cracking and brazing is not suitable since the temperature of brazing (above 2500°F) has an adverse effect on the fuel within the capsule. The use of electron beam welding solved the various problems which included

cracking; restricted heat control, therefore, the fuel wasn't overheated, small uniform weld beads which required no post machining and minimum distortion. The electron beam welds are seen in Fig. 13.

The above three electron beam assemblies are only a few of many current short-term production applications being welded today.

TABLE II

EFFECT OF CONTINUOUS BEAD GTA REPAIR

| SPECIMEN NO. | NOMINAL GAGE | Ftu | Fty | e |
|---|---|---|---|---|
| H1 | .171 | 166.7 | 162.4 | 7 |
| H2 | | 164.2 | 159.6 | 7 |
| H3 | | 163.7 | 155.6 | 7 |
| H Average | | 164.87 | 159.27 | 7 |

TABLE III

EFFECT OF CONTINUOUS BEAD ELECTRON BEAM REPAIR

| SPECIMEN | NOMINAL GAGE | Ftu | Fty | e |
|---|---|---|---|---|
| 2G-1 | .171 | 185.0 | 174.0 | 4 |
| 2G-2 | | 187.8 | 172.2 | 4 |
| 2G-3 | | 185.9 | 171.5 | 5 |
| 2G Average | | 186.23 | 172.5 | 4.3 |

TABLE IV

EFFECTS OF GAP VARIATION ON 17-4PH

| SPECIMEN NO. | GAGE COMBINATION (in.) | GAP SIZE (in.) | Ftu (Ksi) | Fty (Ksi) | e % |
|---|---|---|---|---|---|
| C1 | .171 - .500 | .005 | 189.9 | 180.4 | 3.5 |
| C2 | | | 188.5 | 177.5 | 4 |
| C3 | | | 189.3 | 177. | 4.5 |
| C Average | | | 189. | 178.36 | 4 |
| A1 | .171 - .500 | .003 | 186.8 | .175.8 | 4.5 |
| A2 | | | 187.5 | 176.6 | 4 |
| A3 | | | 187.3 | 176.0 | 4 |
| A Average | | | 187.2 | 176.13 | 4.17 |
| B1 | .171 - .500 | .000 | 187.4 | 177.4 | 2.5 |
| B2 | | | 178.6 | 174.1 | 2 |
| B3 | | | 190.2 | 177.8 | 3 |
| B* Average | | | 184.4 | 175.95 | 2.5 |
| 5D1 | .125 - .500 | .005 | 177.6 | 175.8 | 3 |
| 5D2 | | | 176.7 | 174.0 | 3 |
| 5D3 | | | 179.4 | 177.6 | 3 |
| 5D Average | | | 177.9 | 175.8 | 3 |
| 3E1 | .125 - .500 | .003 | 179.2 | 175.4 | 2 |
| 3E2 | | | 184.6 | 179.4 | 3 |
| 3E3 | | | 180.2 | 176.8 | 2.5 |
| 3E Average | | | 181.8 | 177.2 | 2.5 |
| 1A1 | .125 - .500 | .000 | 185.1 | 177.6 | 4 |
| 1A2 | | | 186.7 | 178.6 | 3.5 |
| 1A3 | | | 185.9 | 177.9 | 4 |
| 1A Average | | | 185.9 | 178.13 | 3.83 |

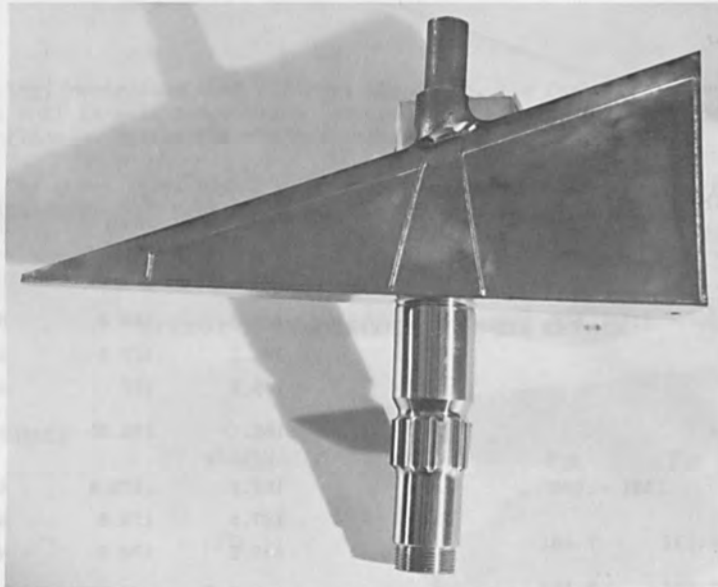

Figure 1. 17-4PH Guided Missile Vane.

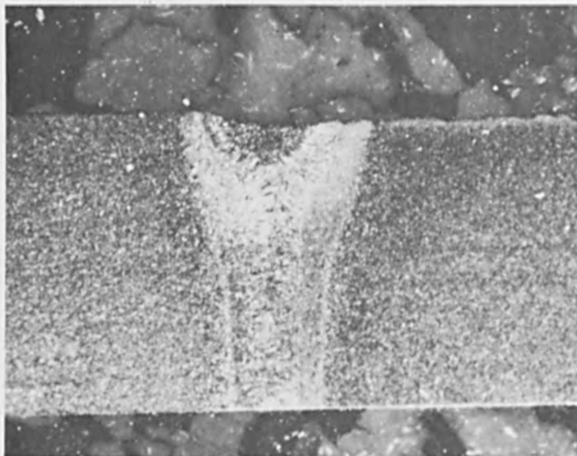

Figure 2. Typical weld configuration in .171 gage with .005" gap of 17-4PH weldment.

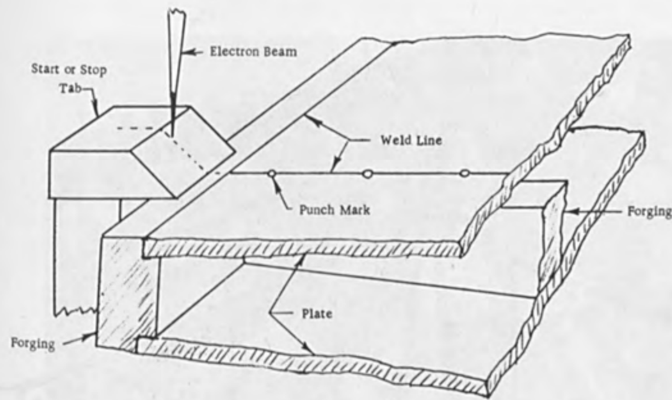


Figure 3. A typical view of the runoff tab.

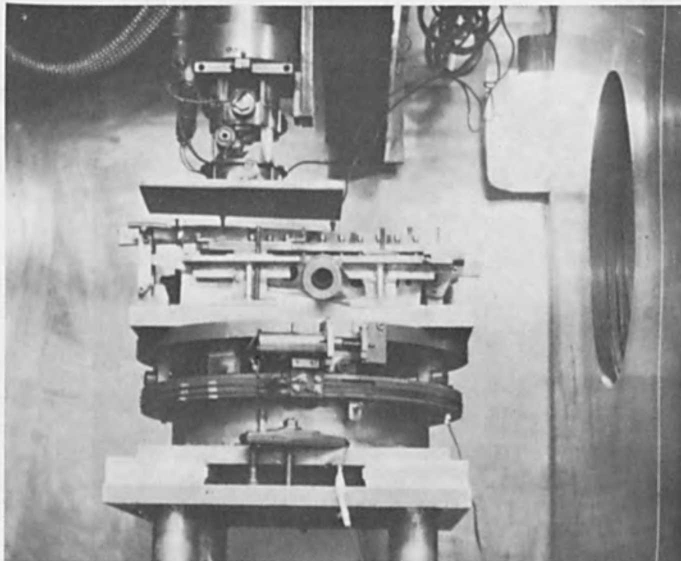

Figure 4. View of welding chamber with welding fixture and vane in welding location under the electron beam welding head.

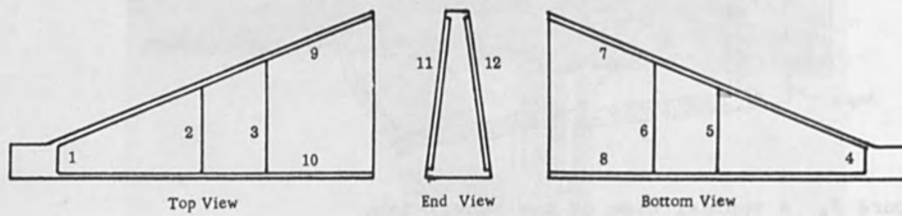


**Figure 5. Sequence of welding missile vane.**

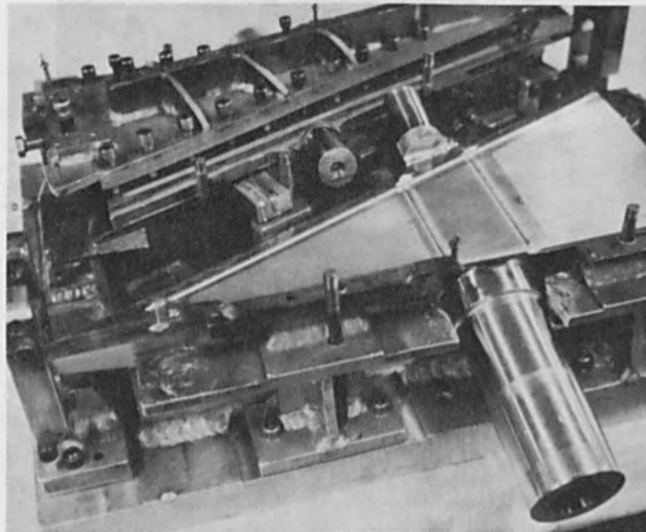

**Figure 6. Weld holding fixture with one vane clamped in position and the second vane positioned in holding fixture.**

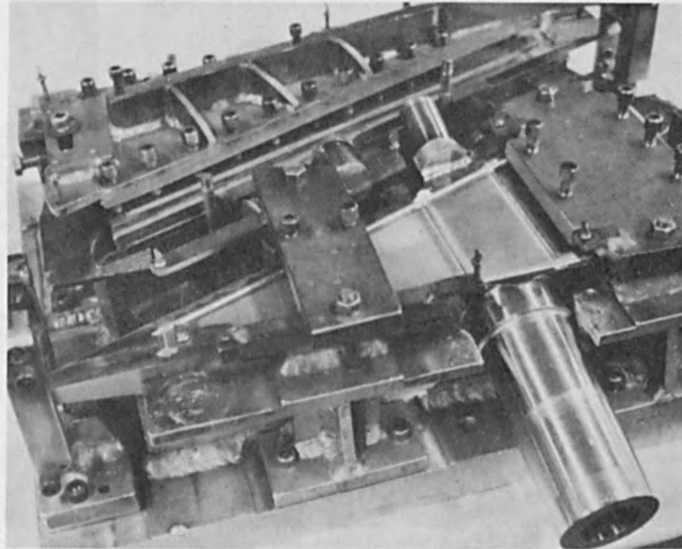

Figure 7. Weld holding fixture with hold down tooling in place to show part of tooling for spike weld.

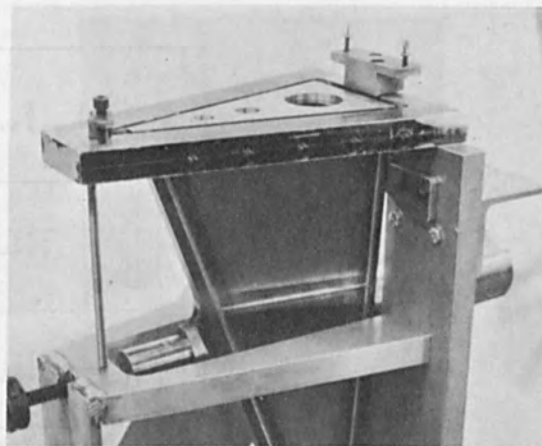

Figure 8. Weld holding fixture for end butt weld with one vane in proper welding location.

| Certified Weld Settings | | | |
|---|---|---|---|
| Weld Parameters | Butt | End Butt | Spike Weld |
| Milliampers | 90 | 90 | 96 |
| Kilovolts | 27.5 | 27.5 | 30 |
| Travel Speed | 45 ipm | 45 ipm | 23 ipm |
| Focal Setting | 52.4 | 52.4 | 48 |
| Distance of Head | 3" | 3" | 3" |

Figure 9. Weld parameters required and joint designs which are welded on vane.

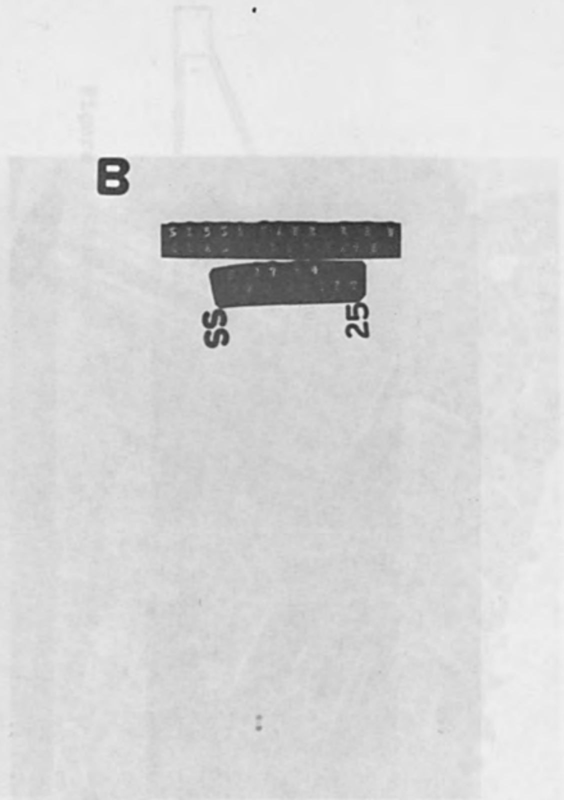


Figure 10. X-Ray shows sound weld joint.

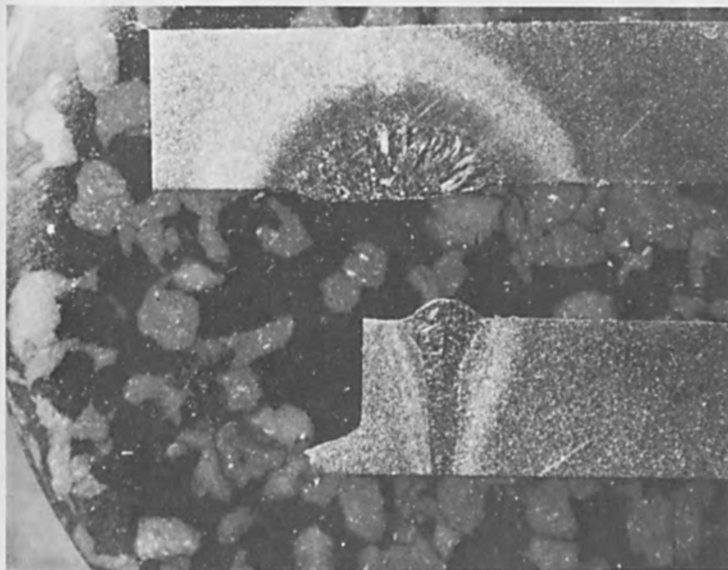

Figure 11. Upper specimen represents typical continuous bead GTA weld repair. Lower specimen is a representative continuous bead electron beam reweld.

Figure 12. Electron beam welding of bellows.

Figure 13. Fuel containers electron beam welded.

# ELECTRON BEAM CUTTING OF ROCKS AND CONCRETE

B. W. Schumacher

Westinghouse Research Laboratories
Pittsburgh, Pa. 15235

## INTRODUCTION

Some time ago Westinghouse had completed the development of a high power electron gun which delivers an electron beam into the atmosphere. This unit is light weight and mobile; it has been developed and is presently used as an out-of-vacuum electron beam welder. With the same machine we have now carried out laboratory studies of rock cutting by means of electron beams.

## THE ATMOSPHERIC ELECTRON GUN

In the atmospheric electron beam machine the electron gun proper forms a structural unit with its power supply, which is rated for 12 kW at 150 kV, and mounted in a tank filled with insulating gas at a pressure of 3 atmospheres. No external high voltage cables are needed between gun and power supply. The input to the power supply comes from a remote 200 V, 400 Hz motor generator set. Power supply and gun weigh less than 300 lb. They can therefore be used as a mobile cutting head.

The electron beam is transferred to the atmosphere through a series of differentially pumped chambers as schematically shown in Fig. 1. The beam is focused on the work piece by a magnetic lens and kept aligned by a magnetic deflection system (not shown in Fig. 1). The beam emerges from the gun through a small orifice with a diameter of .060". To prevent debris

from the work area from being drawn into the gun, a small overpressure chamber which produces a protective gas flow out of the gun is located at the exit end of the beam transfer system. Gas which is flowing into the gun through the beam orifices is continuously pumped out by a set of vacuum pumps. The diffusion pumps (see Fig. 1) are affixed to and ride with the mobile gun; the mechanical pumps are stationary and connected by flexible pump lines. A full description of such guns and their design principles has been given elsewhere[1,2,3].

In Fig. 2 we show a picture of the laboratory electron gun installation with which the present experiments have been made.

WORKING CHARACTERISTICS OF ELECTRON BEAMS

Bringing the electron beam into the air allows one to apply it to processes which could not be considered for in-vacuum work. Not only have we gained the convenience of having the work piece under atmospheric pressure, we can also operate on material which will not only melt but vaporize, boil and sputter, or emit large amounts of gases, all of which would interfere with the electron beam in vacuum. In the atmospheric electron gun we have a perfect decoupling between the beam generating system and the working region.

All the electron beam processes have gained their importance because of certain special features of the electron beam. The power level in an electron beam can be very high; our apparatus and the following experiments were made with a total power of 9 kW. But guns for 100 kW beam power could be built with present day technology. The beam diameter at 1/2" from the gun exit nozzle is in the order of .060". The resultant

high power density produces effects which lead to a penetration of the electron beam into the target material far beyond what is known as the so-called "range" of a weak electron beam impinging on the same material. Speaking very loosely, we may say the high power beam vaporizes the material and drills its own hole in the form of a vaporized zone. This effect of the power level in an electron beam on its "range" was noted already in 1953[4]. Because of the high concentration of the power the losses due to heat conduction etc., are very small and the power efficiency of all electron beam processes is very high, compared with processes using flames, electric arcs, or plasma jets. Furthermore, the power input into deeper layers of the work piece is not limited by heat conduction parameters or by radiation absorption in "black" surface layers, or in steam and vapor clouds; the electrons will penetrate such layers and respond only to the overall mass per unit area.

Because of this special mechanism of energy transfer we can use the electron beam like a cutting knife, melting and vaporizing a narrow slit into the rock. We do not need to restrict ourselves to ablation or spalling processes as in the case of flames. On the other hand, of course, when it is desired the electron beam can be utilized to heat a surface without cutting by moving it across the surface fast enough.

When the electron beam from the electron gun enters the atmosphere the electrons spread out due to scattering by the gas molecules. This is shown at the **left** of Fig. 3, by the blue fluorescence of the air molecules in the region of the electron beam. Fortunately, in a beam of high power this spread due to scattering is not very marked for the first inch or so

of travel. At a distance of 1/2" from the exit nozzle the power density in the beam is still high enough to make a narrow deep melt cut in rock. Even at 3" distance a rock surface can still be melted but no cut is produced anymore. The conditions for producing spallation (minimum energy input) are discussed in another paper[5].

EXAMPLES OF CUTTING ROCK

The **right** picture of Fig. 3 shows a piece of granite on a carrier under the electron gun.

We can switch on the electron beam and then move the rock into the beam. As soon as the rock face intercepts the beam the rock begins to melt and the melting region appears as a brilliant white light source. This process is shown in Fig. 4.

The top picture of Fig. 4 shows the electron beam switched on and the granite block approximately 3/4" behind the axis of the beam. Stray electrons illuminate the face of the granite block slightly. In the middle picture the block has moved toward the electron beam but the axis of the beam is still in front of the block at a distance of about 1/16". About half of the scattered electrons are hitting the face of the granite block causing a brilliant white fluorescence and in addition, spalling (which can not be seen in the picture). In the lower picture the electron beam has made a melt-cut traveling about 1" into the solid granite. The depth of the cut is about 2" and molten rock material is flowing out through the front face of the cut. The region between the granite and the electron gun is filled with vapor which glows under the influence of the electron beam. This granite block was supported on the left and after the cut had

proceeded a bit further than shown in Fig. 4 the right part of the granite block fell down, although the melt-cut itself went only half way through the thickness of the block. Breakage occurred because of the induced thermal stresses.

The top picture of Fig. 5 shows once more the electron beam making a melt-cut, this time through a slab of concrete. The beam can be clearly seen as a narrow bright line between the top face of the concrete slab and the end of the electron gun. Again molten material is flowing out through the front face of the cut; it is also evident that some incandescent droplets shoot out leaving glowing traces behind.

We may also place the rock stationary under the electron gun and then switch on the electron beam. In this case the electron beam will drill a cavity into the rock. The liquified matter will overflow at the upper rim of this cavity. In the case of sandstone this liquified matter shows a very high fluidity and flows rapidly in big droplets. This is shown in the lower picture of Fig. 5. In the case of limestone the liquified matter showed a very high viscosity and was rather tacky; it did not flow but filled up the gap between the limestone and the electron gun as shown in the upper picture of Fig. 6. The lower picture of Fig. 6 shows the cavity drilled into the limestone. Its maximum depth is reached after about 30 to 40 secs. In this case plenty of resolidified matter was found in the cavity but could be broken loose easily. It was also noted that the limestone showed little or no thermal stress cracking. In contrast, the sandstone shown in Fig. 5 lower picture later shattered while still under the electron beam.

Fig. 7 shows several views of a block of sandstone in which a circular cut was made with a 5 kW electron beam at a speed of 4"/min. Also a cavity was drilled with a stationary beam. In addition to the cut, the block shows thermal cracks; a top layer about as thick as the circular cut, 1.3", was cleanly lifted off the block by thermal stresses. In the left row of pictures residues of molten matter can be seen on the interface of the cut. However, in spite of the resolidification of some of this matter, the rock broke apart easily. The right row of pictures shows mainly the cavity drilled by the stationary beam. In the top picture large drops of the overflown glassy "lava" can be seen. These drops are extremely brittle and at times burst by themselves because of the high internal stresses. These glassy drops are partly greenish, partly clear white.

Fig. 8 shows the effect of an electron beam cut on a block of granite. The top picture shows the block under the electron gun after the cut had been completed. One can see a large drop of dark, nearly black, lava type of material which flowed out the front face of the cut. Thermal cracks can be seen all over the block and the lower pictures show how the block broke apart when taken from the machine and lightly tapped with a hammer.

The behavior of limestone was completely different as already mentioned. Fig. 9 shows a cut through a block of limestone. No great amount of "lava flow" was noticed.

When cutting with 9 kW beam power at a speed of 4"/min, a clean cut was achieved which was 2-1/16" deep and 3/16" wide. No glassy material was noticed in the cut and the block which had a total thickness of 3-1/2"

broke apart clean when a light wedging force was applied. Small thermal cracks were observed on both sides of the electron beam cut but were not as pronounced as in the sandstone or in the granite.

In the cavity formed by the stationary beam, Fig. 6, resolidified material was found which was black and did not break as easily as the glass drops formed by the sandstone. It was firmly wedged into the cavity but did not adhere to its wall; it could be broken loose easily once the block was broken apart.

CUTTING OF CONCRETE

A block of reinforced concrete was obtained from a building site. It has some rather coarse pebbles embedded. But we have not any further classification of the material. Its mean specific density was 2.45 g/cm$^3$. In Fig. 10 the appearance of the cut is shown. The left two pictures in Fig. 10 show the entrance face, the right pictures show the exit face where the electron beam left the block. The cut intersected two iron reinforcement rods. The cutting speed was 4"/min at 9 kW, 145 kV. The depth of the cut at the highest point of the block, where the block came closest to the electron gun, is 2". Where the cut was made the block could be broken apart easily. It made no difference whether the electron beam went through the concrete or the embedded coarse pebbles or the iron rods. As one would expect in case of such a coarse material the cut face is rough and rugged.

Slabs of concrete as used for sidewalks, typically 2' x 2-1/2' x 2", were cut by the 9 kW beam at 4"/min. The upper picture in Fig. 5 shows an example. Two slabs were placed on top of one another; the cut went clean through the top one and barely grazed the lower one.

In a standard concrete block 7-1/2 x 3-5/8 x 15-5/8 inches, 2.2 $g/cm^3$, we investigated the depth of the cut as a function of cutting speed and beam power. Fig. 11 shows the block under the electron gun after the cuts had been completed. It also shows the entrance face for a cut made with 5 kW and another cut made with 9 kW of beam power. The lower picture shows the cutting face of the 5 kW cut after the block has been broken apart. In Fig. 12 the cutting face of the 9 kW cut is shown. As indicated on the figure the cutting speed was varied from 1"/min to 32"/min. As depth of the cut we measured the distance to the root of the actual electron beam penetration, marked by the appearance of molten matter on the walls of the cut. The actual breakage, when the block was broken apart by force, went deeper, as the pictures show. From this experiment one can plot a curve for cutting depths versus cutting speed, and also a curve for the cross section cut-out by the electron beam versus cutting speed. These curves are shown in Fig. 13. The higher the cutting speed the shallower is the cut, as one would expect. However the cross section of material sliced by the electron beam increases with the cutting speed. This is also to be expected because at the higher cutting speed the utilization of energy is more efficient since heat conduction losses are reduced. There is, of course, a practical limit; since a very shallow cut is no longer useful. For a cutting depth of 3/4" the cutting speed with a 9 kW beam is 20"/min. This means we slice through a cross section of 15 sq in./min. If we run with only 5 kW beam power the cutting depth is reduced from 3/4" to 9/16". The cutting rate for other rocks was not significantly different.

BULK CUTTING EFFICIENCY

In order to remove large amounts of rock by means of the e.b. cutting process one may cut out prismatic sections from the face of the rock. Initially a triangular prism with a side of 1" may be cut and from there on prismatic sections 1" square. In rocks which show thermal cracking in addition to the pure cutting effect, it seems well possible to remove an even larger prismatic section by making two cuts at right angles.

If one calculates how much bulk material can be removed per unit time by cutting prismatic sections (multiplying the square of the cutting depth by the cutting speed) one finds an increase with a reduction in speed and its associated greater cutting depth. This "bulk cut" curve is also shown in Fig. 13, assuming the cutting is done with a pair of beams of 9 kW each. The values scatter considerably because our preliminary experiments were rather crude. At a speed of 4"/min a bulk removal rate of 18 cu in./min can certainly be maintained with 20 kW beam power (assuming two 10 kW beams working as a pair). If we audaciously extrapolate this figure to 1 MW beam power we obtain a bulk removal rate of 31 cu ft/hr. But at the assumed higher beam power the actual cutting efficiency may be even better; in addition thermal stress cracking, which would also work in our favor, has not been considered.

For comparison we may mention that typically an oxygen jet drill can remove 15 cu ft/hr of rock (9.4" diameter hole, 30.2 ft/hr) with a burning rate equivalent to 1 MW of power. A mechanical drill with 1 MW drive power will remove about 26 cu ft/hr of sedimentary rock, and much less in hard rock. It appears that electron beam cutting of rock is very well competitive.

Of course, this comparison would also have to consider fuel costs, tool replacement, costs for auxiliary equipment, transportation problems, etc. No such studies have been made at this time.

CUTTING CERAMICS, COAL AND WOOD

A few exploratory experiments have been made cutting various materials other than rock by the electron beam. It is, of course, known from the previous welding studies that metals can be cut if proper care is taken to blow the liquid metal out of the cutting slot.

In a quartz plate a clean, narrow cut with smooth surfaces is obtained. This was to be expected from previous experiences with electron beam drilling of quartz. Flakes of quartz wool were found around the electron beam cut, in appearance similar to very fine cotton wool.

A slab of zirconia, which may be considered to be a high temperature ceramic, was placed under the electron beam and a clean narrow cut with nearly parallel sides was obtained. The cutting faces were smooth, save for some resolidified material in the middle section of the cut. In this material no thermal stress cracking whatsoever was noticeable.

In an alumina brick, which can also be considered a high temperature ceramic, a narrow deep cut was obtained; however, the surfaces were not as smooth as in the case of the zirconia. Large amounts of liquified material were flowing out of the cutting slot.

When a piece of natural coal was placed under the electron beam it was immediately ignited as one would expect. Large amounts of smoke filled the room. With the piece of coal traveling under the beam a narrow deep cut

was obtained; when the beam was left stationary a cavity was drilled and some rather spongy-looking material produced. Wood can be cut by the electron beam but catches fire just as coal.

## CONCLUSIONS

The above described experiments have proven the possibility of cutting rocks and concrete by means of an electron beam. It is believed that an electron beam machine of much higher power than our laboratory machine can be built, especially for rock cutting, and no technological difficulties will be experienced with this machine. The economics of the electron beam cutting process should be studied and compared with the economics of existing processes; extrapolations from the present data look very favorable. One should also explore some unique applications where none of the existing methods can compete with the electron beam. An example may be the cutting of narrow trenches for laying pipe lines or cutting open the concrete layers of city streets; the special attractive feature of the electron beam method may be the avoidance of blasting operations and the realization of tailored-to-measure size for a particular trench. The electron beam process may be particularly attractive for work in very hard rock where the usual mechanical cutters and drills show only short life. The hardness of a material will in no way influence the cutting action by the electron beam, the beam will cut easily through hard and soft materials, and the presence of water will not affect the cutting process either. Indications are that the process is economically competitive with existing methods.

## REFERENCES


1. B. W. Schumacher, OPTIK 10, 116, 1963.

2. B. W. Schumacher, Dynamic Pressure Stages for High-Pressure/High-Vacuum Systems; 1961 Transactions of the Eighth Vacuum Symposium and Second International Congress, Pergamon Press, 1962.

3. J. Lempert, The Nonvacuum Electron Beam Welder as a Welding Tool, IEEE Electric Welding Conference, Nov. 15-17, 1966, Detroit, Mich. (Westinghouse Scientific Paper 66-1C2-EWELD-P2, Dec. 1, 1966).

4. B. W. Schumacher, Ann. Phys. 13, 404, 1953 (p. 405).

5. B. W. Schumacher, Power Density Limits for the Particle Penetration Laws and the Onset of Energy Phenomena in Electron Beam Targets. In print (this conference).


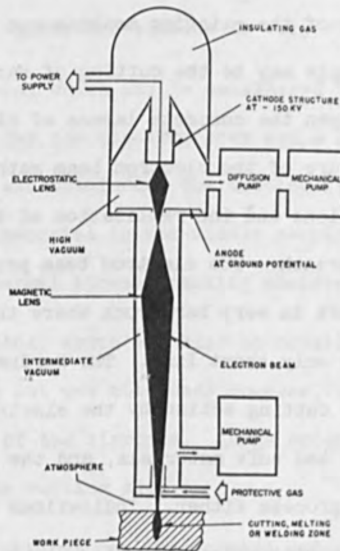


**Fig. 1 Simplified schematic atmospheric electron beam gun.**

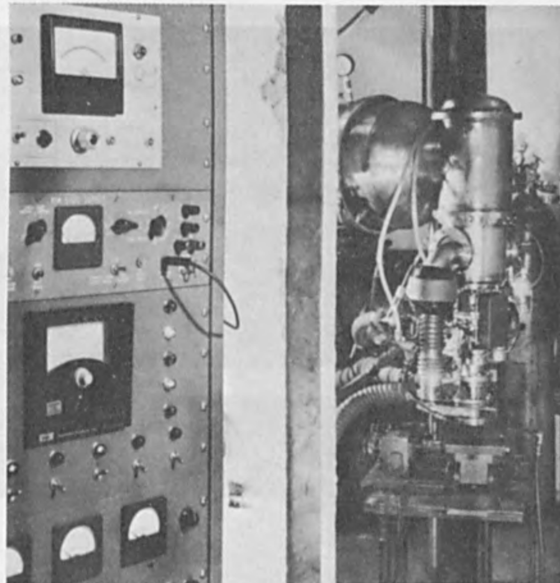

Fig. 2. Experimental installation of atmospheric electron beam gun; power supply, gun, vacuum pumps, work table and control panels are visible.

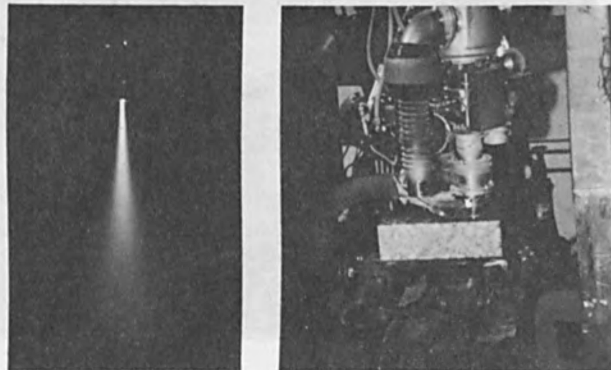

Fig. 3. Left picture: Electron beam in air without work piece. Right picture: Granite block on movable work table under the electron gun.

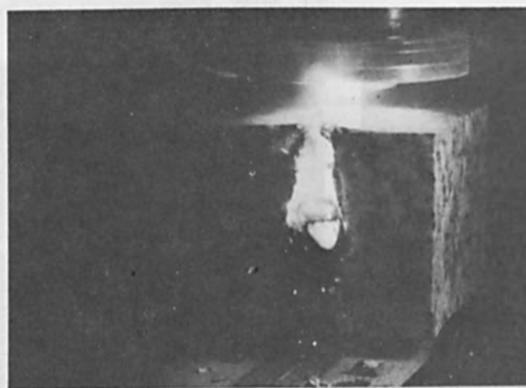

Fig. 4. Granite block moving into the electron beam;
Top: Beam 3/4" from front face of block;
Middle: Beam 1/16" from front face of block;
Lower: Beam cutting slot into the solid rock.

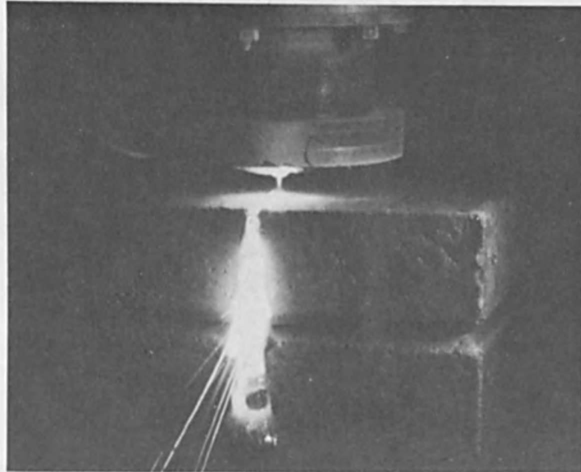

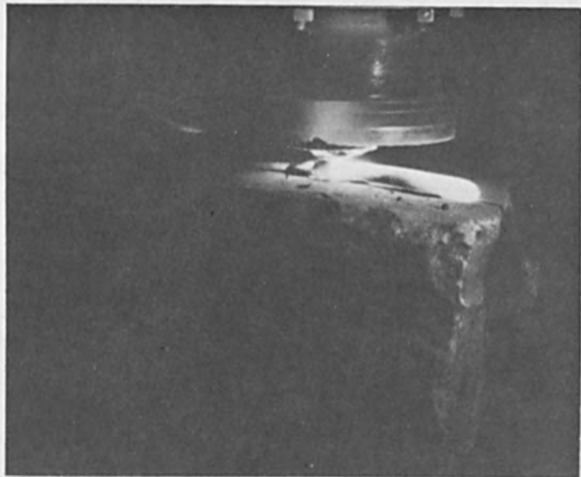

Fig. 5. Top: Electron beam cutting through concrete slab. Lower: Stationary electron beam drilling a cavity in sandstone (Belgian Block), molten rock overflowing to the right.

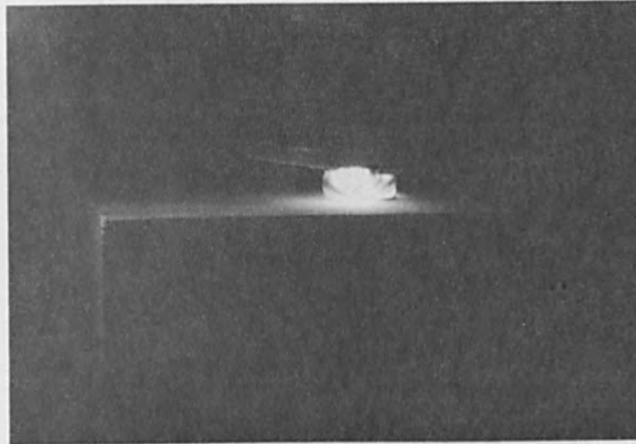

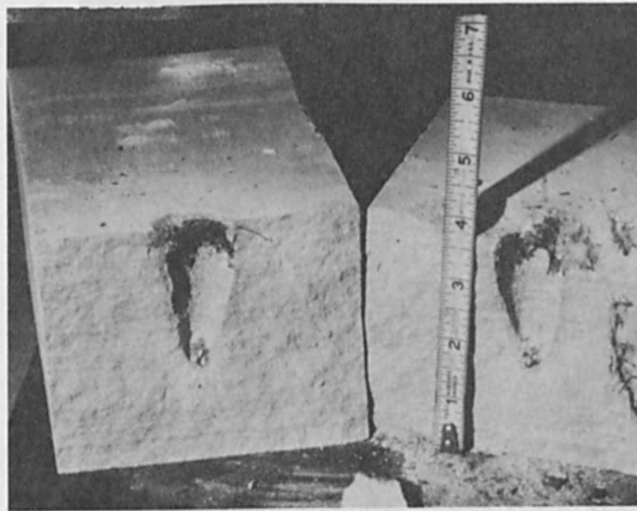

Fig. 6. Top: Electron beam drilling a cavity in limestone; tacky mass is accumulating between rock and electron gun, not flowing. Lower: Cavity formed; little or no thermal cracking.

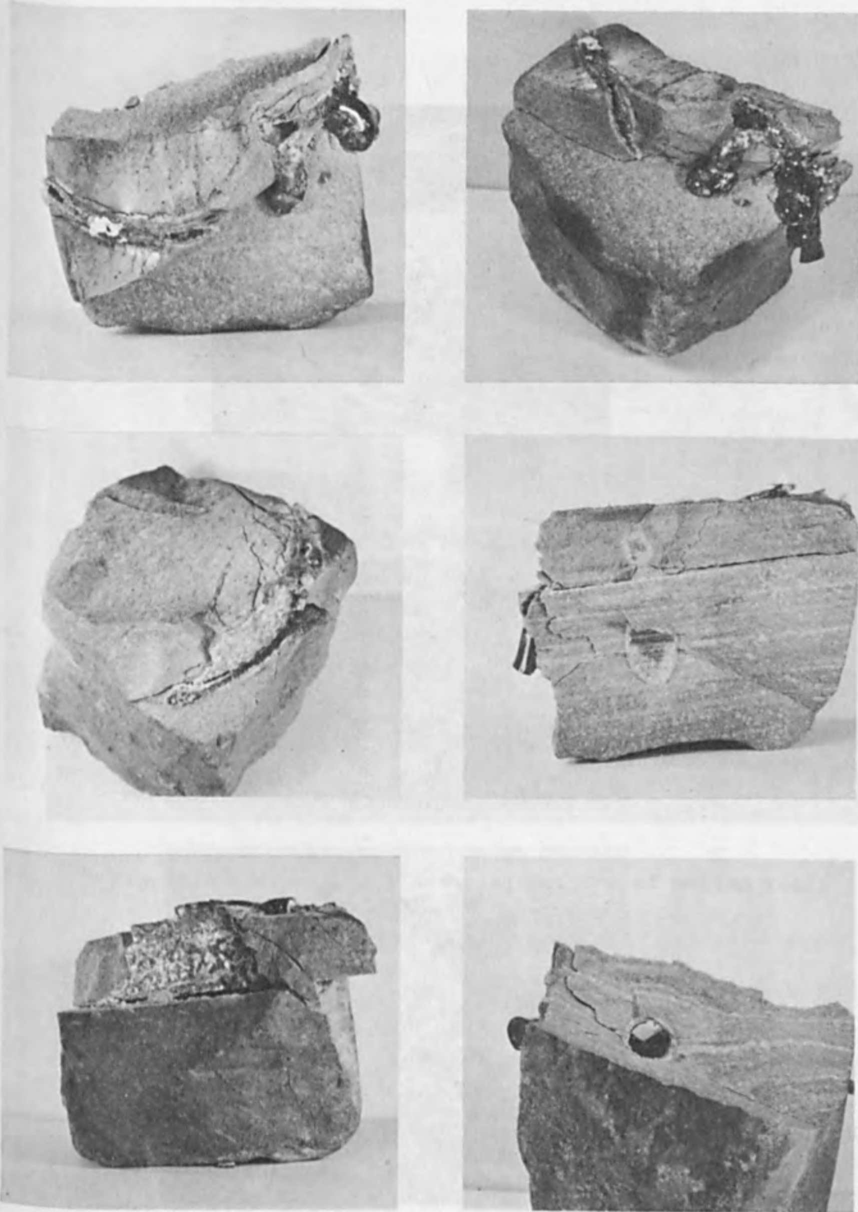

Fig. 7. Circular cut, and cavity drilled with stationary electron beam in sandstone (Belgian Block).

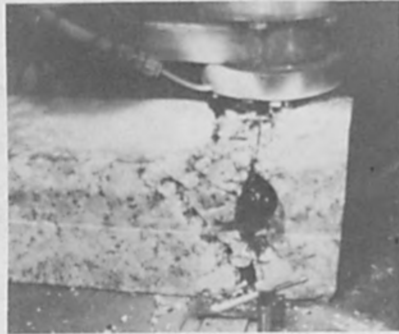

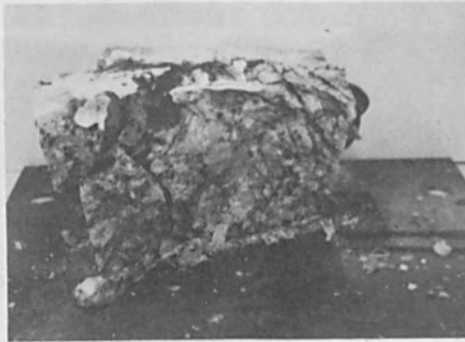

Fig. 8. E.B. cut of granite block producing thermal cracking.

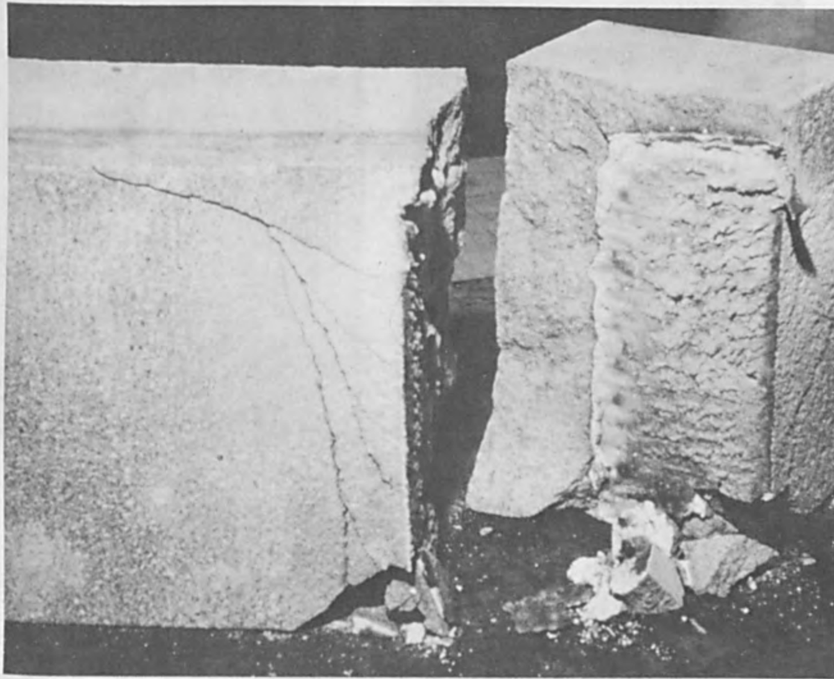

Fig. 9. E.B. cut in limestone; no flow of molten rock; little thermal cracking.

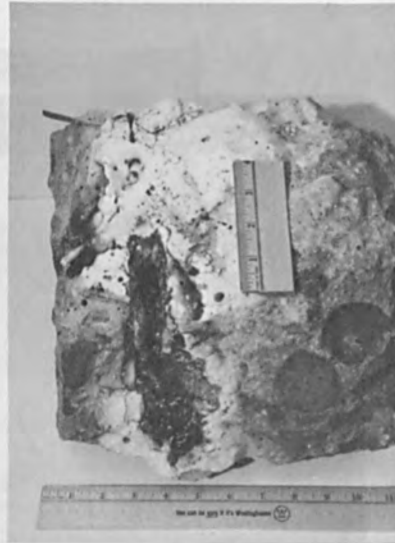

Fig. 10. E.B. cut through block of reinforced concrete.

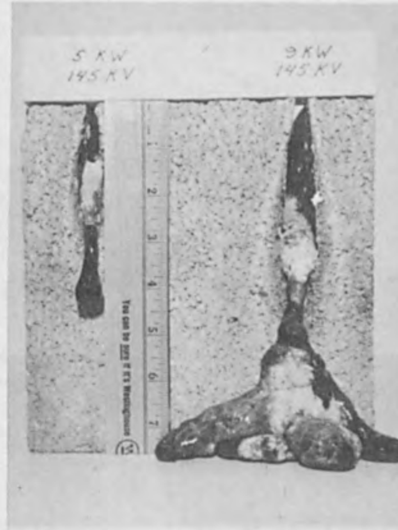



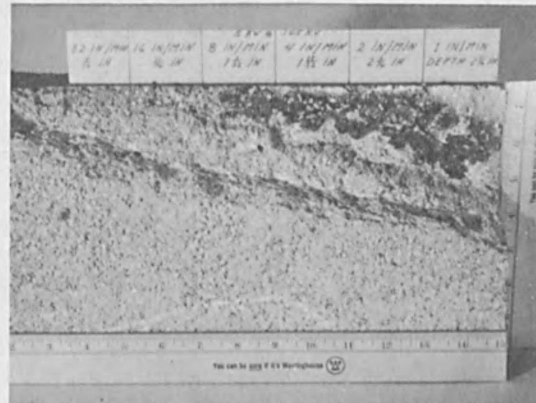



Fig. 11. E.B. cuts in concrete block; with 5 and 9 kW cutting speeds; Lower picture shows break of 5 kW cut.

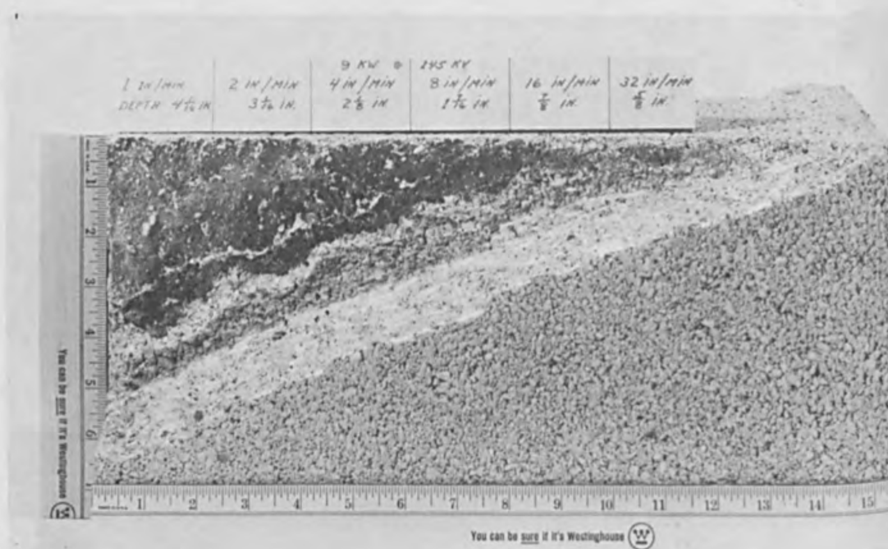


Fig. 12. E.B. cut in concrete block; 9 kW beam power and various cutting speeds.

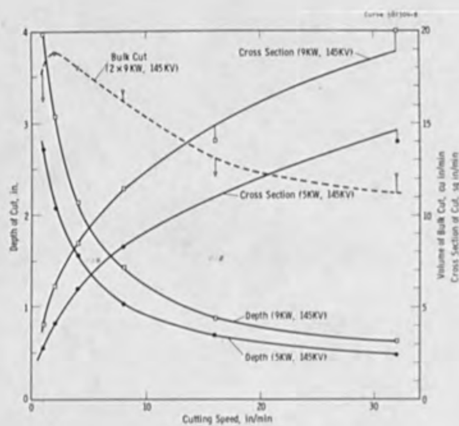


Fig. 13. Electron beam cutting of concrete; depth and cross section as a function of cutting speed and beam power.

# ULTRAHIGH-VACUUM ZONE PURIFICATION OF ZIRCONIUM WITH ANALYSIS OF PARTIAL PRESSURES*

D. S. Easton and J. O. Betterton
Metals and Ceramics Division, Oak Ridge National Laboratory
Oak Ridge, Tennessee 37830

ABSTRACT

An electron-beam zone refiner was developed to produce high-purity zirconium and other refractory metals for use in high-field galvanomagnetic studies. A quadrupole gas analyzer was used to monitor the gas composition over various metals during zoning. Resistance ratios ($R_{300°K}/R_{4.2°K}$) and chemical analysis provided indications of purity levels. Zirconium was successfully zone refined up to 65 zone passes for oxygen removal. The low partial pressures in the system made these lengthy operations possible without contamination. Resistivity ratios of up to 1300 in zirconium and 300 in hafnium were achieved.

## INTRODUCTION

Pure zirconium with low electrical resistivity at low temperatures is needed for studies of the Fermi surface and other fundamental physical properties of this metal. However, preparation of pure zirconium by zone refining is particularly complicated by the well-known affinity of zirconium for gaseous impurities such as oxygen, nitrogen, and carbon. Prior work by Kneip and Betterton [1] had shown that iron and nickel impurities could be purified by floating zone refining at speeds of 2.5 mm/min in a static atmosphere of argon. However, the resistance ratio ($R_{300°K}/R_{4.2°K}$) of 128 was lower than that of the initial crystal bar zirconium, 150, because of gaseous contamination inherent in the silica-walled system used to contain the argon atmosphere in this experiment. On the other hand, Billion and Langeron [2] zone refined zirconium in a dynamic vacuum system, obtaining resistance ratios of 260 and the removal of impurities by a combination of zone refining at 60 mm/hr and evaporation of volatile impurities. Wilson and Picklesimer [3] prepared zirconium with resistance ratios of 400 to 450 by zone refining crystal-bar zirconium using a few passes with electron-beam heating in $10^{-7}$ to $10^{-8}$ torr vacuums provided by a large oil diffusion pump with liquid nitrogen trapping. Wilson also showed that large grains occurred frequently in zone-refined zirconium prepared in this manner. The present investigation describes results of

*Research sponsored by the U.S. Atomic Energy Commission under contract with the Union Carbide Corporation.

zone refining in higher vacuums, provided by ion pumping, liquid-nitrogen-cooled titanium sublimation pumping, and with baking of the zone-refining apparatus. We wished to examine the question whether in sufficiently high vacuums the gaseous impurities could be segregated by zone refining so that pure zirconium with low resistivity could be made. The following variables were studied: total number of passes, the speed of zone refining, annealing temperature, and deliberate additions of carbon, hydrogen, and air. To study the distribution of impurities, we determined the low-temperature resistivities, $\rho_{4.2°K}$, and the resistance ratio, $R_{300°K}/R_{4.2°K}$, for all the zone-refined rods. For development of resistivity as an impurity indicator, the various factors that affect the resistivity of zirconium were observed and are discussed in some detail. The impurity contents were also analyzed by combustion, vacuum fusion, mass spectrometry, and neutron activation. By comparison of these results to the resistance ratios we will show that the refining of zirconium in an ultrahigh vacuum proceeds according to predictions of zone refining theory with allowance for evaporation of volatile impurities.

The zone refining was carried out with simultaneous measurements of the approximate partial pressures by a residual gas analyzer. This information was useful in estimates of the amount of transport of impurities to and from the sample through the vacuum and to determine whether this transport was significant relative to the transport of material by zone refining. In some cases the partial pressures served as indicators of the impurities in the liquid zirconium. Finally, partial pressure analysis showed the specific benefit of various pumping components in the vacuum system.

Krauss and Winkler [4] have discussed the purification of liquid iron by electron-beam heating in vacuum and have shown convincingly that only when the ratio of impurities atoms/solvent atoms in the gas is substantially greater than the ratio in the liquid will the purification proceed without too great loss of the solvent. Krauss and Winkler point out that oxygen is more likely to be removed from liquid iron in combination with other elements. In this paper we will attempt to find similar ternary combinations in liquid zirconium leading to a greater concentration of compounds in the gaseous phase as means to reduce the oxygen and carbon content of the zirconium.

## EXPERIMENTAL APPARATUS

### Vacuum System

The zone refiner (Fig. 1) consists of an 8-in.-diam stainless steel chamber containing the zoning mechanism. The chamber is connected to the pumps by "Con-Flat" flanges with copper gaskets. The system has

no elastometers; aside from a minimum of ceramic insulators, type 304 stainless steel was used for the construction.

A cylindrical collar was used to introduce electrical connectors, rotary motion, ion gage, a quadrupole gas analyzer tube, and a vacuum roughing line. The collar was connected directly to a 140 liter/sec ion pump with a 4-in.-ID port. Above the main chamber was a second assembly containing a liquid-nitrogen cryopump and titanium-tungsten filaments, providing sublimation pumping by evaporation of the titanium on the 77°K walls. The entire system is cooled by pumping liquid nitrogen into 1/4-in.-OD copper tubing brazed to the outside of the chamber. An oven shroud, which surrounded the entire system, provided bakeout temperatures of approximately 200°C. The system under the above conditions would reach approximately 1 to 2 $\times 10^{-10}$ torr. Pressures less than 5 $\times 10^{-11}$ torr were reached after more lengthy pumping and zoning, which further outgassed the system.

### Electron Gun and Refining Mechanism

The sample to be zoned was vertically supported by independently movable clamps driven by a chain drive (Fig. 2). In the original design the electron gun was also driven by a chain hoist with stainless steel linear ball bearings on stainless steel support rods. This was satisfactory until a large number of passes were found to be necessary to segregate oxygen. Under these conditions sticking sometimes occurred, causing freeze-offs and thus making uniform refining difficult. The problem was solved by the replacement of the stainless steel by sapphire balls in the linear bearings and the chain drive by a sapphire ball bearing screw assembly (Fig. 3). With the present mechanism as many as 65 consecutive zone passes have been made without difficulty. The sapphire balls also acted as insulators between the gun and support rods allowing the latter to be utilized to carry the filament current, thus simplifying the apparatus. A tungsten plate optically shielded the entire mechanism from the hot sample and protected it from contamination evaporated from the zoned materials.

### Power Supply

A commercial 5-kw-dc high-voltage power supply and a low-voltage dc filament power supply provided adequate power for zoning. Constant beam current was maintained by controlling the filament current with a feedback arrangement through a saturable reactor.

Zirconium samples ranging from 0.090 to 0.75-in. diam have been zoned in this unit, which proved to be very effective using only 60-w power to provide a molten zone in 1/8-in.-diam zirconium. Filament temperatures were held below the sample temperature; analytical results indicated that the sample was not contaminated from volatilization of the filament or focusing shields.

### Resistance-Ratio Measurements

Along with analytical methods, the resistance ratio ($R_{300°K}/R_{4.2°K}$) was used to test the purity of the material. A potentiometric method was used to measure the resistance. With a known current (from the emf across a standard resistor immersed in oil) the potential drop across the sample was measured. A 6-dial thermal-free potentiometer coupled with a photocell galvanometer provided a precision of $10^{-9}$ v. Current was provided by a regulated dc power supply and was reversed to eliminate any thermal emf. Copper wire probes were attached to the sample with Fiberglas tape. With this method we were able to reproduce resistance ratios to within 1%.

### Pressure Measurements

The total pressure in the chamber was measured by a nude Bayard-Alpert ionization gage. The x-ray limit was approximately $1.3 \times 10^{-12}$ torr, which is small enough to require no correction to the measured pressure. The low value was apparently the result of placing the nude gage within a $1\frac{1}{2}$-in. stainless steel tube and creating reverse x-ray currents [5]. Ion-gage readings and the sum of the partial pressures measured in the residual gas analyzer are compared in Table I. Both types of readings have been normalized to equivalent nitrogen pressure and show good agreement.

Table I

Bayard-Alpert Type Ion Gage Readings vs the Sum of the Partial Pressures Indicated by Residual Gas Analyzer

| Ion Gage (torr) | Corrected[a] Ion Gage (torr) | Total Partial Pressures,[b] (torr) | Approximate Composition of Gas Vol % | | |
|---|---|---|---|---|---|
| | | | $H_2$ | He | CO |
| $2 \times 10^{-8}$ | $4.5 \times 10^{-8}$ | $4.6 \times 10^{-8}$ | 94.0 | 2.9 | 2.2 |
| $5 \times 10^{-9}$ | $1.11 \times 10^{-8}$ | $1.05 \times 10^{-8}$ | 86.2 | 4.5 | 6.9 |
| $2 \times 10^{-9}$ | $4.5 \times 10^{-9}$ | $4.41 \times 10^{-9}$ | 89.0 | 4.41 | 4.12 |
| $6 \times 10^{-10}$ | $1.33 \times 10^{-9}$ | $1.61 \times 10^{-9}$ | 88.1 | 3.6 | 6.8 |
| $6 \times 10^{-10}$ | $1.31 \times 10^{-9}$ | $1.37 \times 10^{-9}$ | 90.6 | 2.9 | 4.3 |
| $4 \times 10^{-10}$ | $9.07 \times 10^{-10}$ | $1.03 \times 10^{-9}$ | 90.0 | 3.9 | 4.2 |
| $6 \times 10^{-11}$ | $1.72 \times 10^{-10}$ | $2.62 \times 10^{-10}$ | 60.0 | 24.8 | 13.7 |

[a] Normalized to $N_2$; see for example, S. Dushman, Scientific Foundation of Vacuum Technique, 2nd Edition, J. M. Lafferty (Ed.), John Wiley and Sons, New York, 1962, p. 14.

[b] By residual gas analyzer.

Residual Gas Analyzer

Partial pressures of various gases in the zone refiner were monitored by a Varian quadrupole residual gas analyzer (R.G.A.). An electron multiplier amplified the ion current, which was then fed into an electrometer with a sensitivity of $1 \times 10^{-13}$ amp. Both an oscilloscope and a recorder were used for readout. With a multiplier gain of $1 \times 10^{5}$ the minimum detectable partial pressure for nitrogen was about $2 \times 10^{-14}$ torr. The R.G.A. tube and multiplier were baked out along with the system, and a bakeable valve prevented exposure to atmosphere when the system was opened.

Partial pressures were extracted from the peak heights by incorporating cracking patterns, sensitivity corrections, ionization constants to normalize to $N_2$, and mass dependence of the electron multiplier into a computer program. A typical analysis of a set of data is shown in Table II.

Table II

Typical Analysis of Residual Gas Within the Zone Refiner

Ionizing current: 1 ma
Ionizing voltage: 120 v
Multiplier gain: $1 \times 10^{5}$
Resolution ($M/\Delta M$ at 1/2 peak height) at mass 28; approximately 55

| Mass Spectra | | Gas Composition | | |
|---|---|---|---|---|
| m/e | Peak Heights (amp) | Gas | Partial Pressure (Torr) | Volume % |
| 2 | $8.0 \times 10^{-10}$ | Hydrogen | $1.57 \times 10^{-10}$ | 69.05 |
| 4 | $6.5 \times 10^{-11}$ | Helium | $3.25 \times 10^{-11}$ | 15.70 |
| 12 | $1.3 \times 10^{-11}$ | Carbon monoxide | $2.55 \times 10^{-11}$ | 12.32 |
| 13 | $1.5 \times 10^{-12}$ | Carbon dioxide | $3.08 \times 10^{-12}$ | 1.49 |
| 14 | $5.5 \times 10^{-12}$ | Methane | $1.2 \times 10^{-12}$ | 0.58 |
| 15 | $1.6 \times 10^{-11}$ | Neon | $7.13 \times 10^{-13}$ | 0.34 |
| 16 | $2.9 \times 10^{-11}$ | Nitrogen | $5.93 \times 10^{-13}$ | 0.29 |
| 17 | $1.2 \times 10^{-12}$ | Argon | $1.43 \times 10^{-13}$ | 0.07 |
| 18 | $1.3 \times 10^{-12}$ | Water vapor | $1.08 \times 10^{-13}$ | 0.05 |
| 20 | $3.0 \times 10^{-12}$ | Oxygen | $8.33 \times 10^{-15}$ | 0.003 |
| 28 | $3.4 \times 10^{-10}$ | $C_2$ and $C_3$ hydrocarbons | $2.2 \times 10^{-13}$ | 0.1 |
| 29 | $4.0 \times 10^{-12}$ | Total | $2.07 \times 10^{-10}$ | 100 |
| 30 | $1.8 \times 10^{-12}$ | | | |
| 32 | $1.0 \times 10^{-13}$ | | | |
| 40 | $2.0 \times 10^{-12}$ | | | |
| 44 | $5.0 \times 10^{-11}$ | | | |
| Total | $1.33 \times 10^{-9}$ | | | |

The effects of bakeout and performance of the various pumps on partial pressures of some gases are seen in Fig. 4. The partial pressure data are shown by bar graphs with letter symbols, representing the operating stages of the vacuum system, arranged along the abscissa. In the unbaked system (A) the major gases are $H_2O$, $H_2$, CO, and $CO_2$. Since all of these gases (except $H_2$) are oxidizing agents towards zirconium [6], this demonstrates the disadvantage of using an unbaked system for experiments involving reactive metals. Baking (B) greatly reduced the $H_2O$, $CO_2$, CO, and $CH_4$. Titanium sublimation pumping (C) had its greatest effect on $H_2$, whereas addition of a liquid-nitrogen cryopump (D) reduced the $H_2O$, $CH_4$, He, and Ar. In Fig. 4 the primed symbols A′, B′, C′, and D′ indicate the rise in pressure after the ion pump was turned off for 20 min. With only ion pumping all gases except $H_2O$ increase rapidly. With the addition of titanium sublimation pumping, the inert gases, $CH_4$, and CO still show large increases after the ion pump is turned off. It is interesting to note that the first gas to increase immediately upon turning the ion pump off is $CH_4$. After a liquid-nitrogen cryopump is added only He and Ne show any increase after 20 min. These pressures reach maximum values and remain constant for long periods of time. The system has been shut down for periods of 4 days and showed a pressure increase of only approximately $6 \times 10^{-10}$ torr.

The authors feel that the partial pressures given are about as accurate as ion gage readings, as shown previously in Table I, and with errors of the order of 25%. The pressures obtained for successive experiments are more reproducible than this, although we do not claim them to be absolute pressures under static equilibrium conditions because a correction was not made for pumping speed and because of various systematic errors involved in the process of calibration and resolution of each partial pressure.

## EXPERIMENTAL RESULTS

### Residual Gas Analysis

Tracings of spectra from the R.G.A. exhibited on an oscilloscope before zoning and over a zirconium sample during various zone passes are shown in Fig. 5. The atmosphere of the base system is seen in Fig. 5(a) with a total pressure of $5 \times 10^{-11}$ torr. Peaks from $H_2$ and CO are predominant with smaller contributions seen from $CH_4$ and $CO_2$. Peaks of higher mass values than $m/e = 44$ were sought but not found. To a certain small extent the spectrum may have been influenced by the quadrupole tube itself (i.e., CO evolving from the filament and walls). The pressures during the first zone pass are shown in Fig. 5(b) at a total pressure of $2 \times 10^{-7}$ torr. The peaks have increased by several magnitudes, and in addition, peaks due to water

vapor along with $C_2$ and $C_3$ hydrocarbons can be seen.* By the 10th pass [Fig. 5(c)] with a total pressure of $3 \times 10^{-9}$ torr, the only peaks that can be seen are due to $H_2$, $CH_4$, CO, and $CO_2$. The total pressure was down to $3 \times 10^{-10}$ torr by the 35th pass and the partial pressure peaks show a corresponding decrease, with the $CO_2$ peak at $m/e = 44$ essentially disappearing [Fig. 5(d)].

A more complete analysis of partial pressures as a function of zone passes is shown by the bar graphs in Fig. 6. The partial pressure of various gases, normalized to equivalent nitrogen pressure, over a zirconium sample zoned 20 passes at 20 cm/hr are given at various stages. The inert gases are shown collectively; helium constitutes approximately 90% of the total. Hydrogen was the predominant gas present in all stages of zone refining. The large drop in pressure following the 20th zone pass in $H_2$, $CH_4$, and $C_2$ and $C_3$ hydrocarbons and the lack in change in the pressure before and after zoning imply that these gases were truly being evolved from the molten sample. This would seem to indicate the possibility of carbon reduction by hydrogen in zirconium. The nitrogen pressure also showed a large decrease but this may be related to the large reduction in $N_2$ pressure from before-zoning to after-zoning due to the outgassing of the system. Likewise, CO, $CO_2$, and $H_2O$ showed decreases in pressure after-zoning when compared to the before condition, which illustrates system outgassing. However, the rise in pressure of these gases during the first zone pass was too large to be accounted for by system outgassing and to some extent must come from the sample itself.

Pressures above a zirconium sample with carbon added to the head of the sample are shown in Fig. 7. The pattern is very similar to that of the sample without carbon except for rather higher initial pressures of $H_2$, CO, $CH_4$, $H_2O$, and the $C_2$ and $C_3$ hydrocarbons. Apparently the pressures in general were so low that any reactions were so small that they were difficult to observe.

The predominance of hydrogen in the system is shown in Fig. 8, which compares the gas with the total pressure of the system. During zoning the hydrogen constitutes over 90% of the total pressure. This is not an undesirable condition in zone refining of zirconium, as there may be some carbon reduction occurring, as shown previously.

Different metals showed different partial pressure patterns, as seen in Fig. 9, which compares pressures over zirconium, hafnium, and molybdenum during the first zone pass. The difference in patterns also

---

*The notation $C_2$ and $C_3$ denotes $C_2H_4$, $C_2H_6$, and $C_3H_8$ hydrocarbons. This notation is used because we were unable to make reliable separations of these components at the pressures involved.

indicates that the pressures observed are truly a result of the sample and not just outgassing of the system. Although the pressures over hafnium are much greater than over zirconium and molybdenum, the pressures dropped rapidly after the first zone pass and actually became lower than those over zirconium in subsequent passes.

In summary, the partial pressure over molten zirconium, after two passes of zone refining, are such that only hydrogen is present in sufficient quantity to be transported significantly in the gas phase. All other gases have pressures less than $1 \times 10^{-10}$ torr, and it seems unlikely that any transport in the gas phase could occur.

## Effect of Number of Zone Refining Passes

During zone refining [7] small shifts in concentration should occur with each pass as the solidified material becomes enriched in impurities which raise the melting point ($K > 1$), and depleted in impurities which lower the melting point ($K < 1$). Thus a strong influence of the total number of passes is normally observed, where impurities of K greater or less than unity concentrate at opposite ends of the sample. In electron-beam zone refining at low pressure, impurities may also transported in the gas phase to the cold walls of the apparatus, and particularly in the initial stages of the purification when appreciable partial pressures of impurities occur, this gas transport should dominate the purification process. Ultimately as the purification proceeds, zone refining should continue undisturbed by gas transport, other than when the enrichment at either end of the sample should cause gas transport to reoccur. This effect should create an upper limit to the concentration of each impurity when the zone refining is done in vacuum conditions.

The present experiments are an example of the vacuum zone refining process. Zirconium was zone refined at 20 cm/hr for 1, 5, 10, and 20 total passes, and the resulting resistance ratio, $R_{300°K}/R_{4.2°K}$, is plotted against percentage of sample length in Fig. 10.

As shown by the increase in the resistance ratio profile over the whole sample length, the first stage of zirconium zone refining appears to consist of an evaporation of the volatile impurities such as H, Fe, Al, Ni, Cr, and Si. With further passes a second stage of purification occurs, and the resistance ratios of the final ends of the samples rose to progressively higher values. The shape of the curves suggested zone segregation of oxygen, since oxygen as an impurity in zirconium has a K-factor of nearly two [8]. A third stage of the purification process occurs throughout the zirconium refining, and consists of chemical reactions such as the reduction of carbon with hydrogen. These processes and additional evidence for the segregation of oxygen will be discussed below in sections dealing with the chemical analysis of impurities.

Effect of Zone Refining Speed

In discussing the theory of zone refining Pfann pointed out [7] that a relatively slow zone velocity is desirable to avoid entrapment of impurities in dendrites and other nonplanar freezing surfaces and to keep the compositional gradient small in the liquid. Other metals have been zone refined at rates varying from 1.3 cm/hr for platinum [9] to 12 to 25 cm/hr for tungsten, molybdenum, and tantalum [10]. In prior work on zirconium, refining was reported [3,11,12] between 3 and 15 cm/hr, although Mills and Craig [13] observed that they could refine oxygen only at rates near 0.4 cm/hr. In contrast, our results showed desirability of higher rates.

The data are shown in Fig. 11 for zone refining identical samples ten passes each at various speeds in the range 5 to 20 cm/hr. The highest resistance ratios in the final portion of the sample length were with the highest speeds (10 to 20 cm/hr), whereas in the central portion of the sample the ratios were the same for all three speeds. At the starting end of the sample the lowest ratio was observed in the 5-cm/hr experiment. Similar results were found in our work with other lots of zirconium. These results showed that zoning speed was not as strong a variable in zirconium zone refining as would be expected from theory. A possible interpretation is that with all impurities reduced to a low level by evaporation and with only oxygen, carbon, and hafnium remaining, faster zone refining is possible than would be true for less pure material. Pfann [7], citing a result of Rutter and Chalmers [14] concerning freezing tin liquid with lead impurity, notes that the maximum travel rate for which the solidus/liquidus factor K will differ appreciably from unity increases as the impurity concentration decreases. As a result of this effect and a rapid diffusion of oxygen in liquid zirconium, zone segregation of oxygen at 20 cm/hr could be understood. On the other hand, in slower passes at 5 cm/hr, solid state diffusion from the oxygen-rich handle could reduce the resistance ratio at the ends of the bar and restrict the efficiency of oxygen separation by diffusion of oxygen from the enriched starting end to the purified final end of the sample. In this way the peculiar differences in resistance ratios shown on Fig. 11 can be explained.

An alternate interpretation of speed effects is that impurities may collect on dislocations formed during solidification. In the present work, polygonization was much more prevalent after zone refining at 10 to 20 cm/hr than at 2 to 5 cm/hr, probably due to the larger numbers of dislocations and vacancies being formed at the liquid/solid interface. The higher ratios with faster zoning then suggest that the polygonized structure, which forms in this case, collected the impurity atoms in such a way that the resistivity was lowered. In support of this hypothesis a drop in the ratio after annealing has sometimes been noted. This effect could be due to dispersion of the impurities into random solution by the annealing. This is probably not the major cause of higher ratios in the samples zoned at higher speeds but can contribute to the results and should be considered.

Effect of Heat Treatment on the Resistance Ratio of Iodide and Zone-Refined Zirconium

Table III compares the impurity contents and their contributions to electrical resistivity for the as-received iodide zirconium with the material after six-pass zone refining. The resistivity contributions were calculated from the use of resistivity coefficients of Betterton and Easton [15] and the impurity contents. A better picture of the actual purification achieved in zone refining is seen in Table IV

Table III

Results of Chemical Analysis with Comparison to Electrical Resistivities[a]

| Solute | $\partial\rho/\partial x$ μohm-cm (at. %)$^{-1}$ | As-Received Iodide-Zirconium: Concentration (at. %) | As-Received Iodide-Zirconium: Resistivity contribution (μohm-cm) | Zoned Zirconium[a]: Concentration (at. %) | Zoned Zirconium[a]: Resistivity contribution (μohm-cm) |
|---|---|---|---|---|---|
| O | 6.7 | 0.0123 | 0.0824 | 0.0063[b] | 0.0422[b] |
| N | ~7.0 | 0.0029 | 0.0203 | <0.0003 | <0.0021 |
| C | 7.29 | 0.0090 | 0.0657 | 0.0061[c] | 0.0442[c] |
| H | 0.6 | 0.3394 | 0.2036 | <0.0091 | <0.0054 |
| Al | ~20.0 | 0.0010 | 0.0200 | 0.0001 | 0.0020 |
| Ca | ~4.0 | 0.0005 | 0.0020 | 0.0002 | 0.0008 |
| Cr | ~20.0 | 0.0005 | 0.0100 | 0.00001 | 0.0002 |
| Cu | ~17.0 | 0.0001 | 0.0017 | 0.000004 | -- |
| Fe | 8.05 | 0.0065 | 0.0527 | 0.00001 | -- |
| Hf | 0.45 | 0.0010 | 0.0005 | 0.0010 | 0.0005 |
| K | ~5.0 | 0.0005 | 0.0025 | <0.00002 | -- |
| Mo | 20.2 | <0.0001 | <0.0020 | <0.0001 | <0.002 |
| Nb | 5.1 | 0.0001 | 0.0005 | <0.0001 | -- |
| Ni | ~8.0 | 0.0012 | 0.0096 | 0.00002 | -- |
| Si | ~22 | 0.0007 | 0.0154 | 0.0002 | 0.0040 |
| Ta | ~3.9 | 0.0002 | 0.0008 | 0.0002 | 0.0008 |
| W | ~20 | 0.00001 | 0.0002 | 0.00001 | -- |
| Zn | ~19 | 0.0003 | 0.0057 | 0.00002 | 0.0004 |
| Others | ~10 | 0.0002 | 0.0020 | -- | -- |
| Total | | 0.3764 | 0.4956 | 0.01417 | 0.0951 |

[a] Six passes

[b] 0.0023 at. % and 0.0154 μohm-cm after 20 passes

[c] 0.0006 at. % and 0.0043 μohm-cm after 20 passes

Table IV

Effect of Successive Stages of Purification on Zirconium

| Condition of Zirconium | Zirconium Assay (at. %) | Impurity Resistivity Contribution (μohm-cm) | Resistivity Ratio $\rho_{300°K}/\rho_{4.2°K}$ Calculated | Measured |
|---|---|---|---|---|
| As-received | 99.62 | 0.4956 | 90 | -- |
| Heated to remove $H_2$ | 99.96 | 0.2920 | 153 | 152 |
| Zoned 6 passes | 99.98 | 0.0951 | 470 | 450 |
| Zoned 20 passes | 99.995 | 0.0308 | 1376 | 1340 |

which compares calculated and measured resistivity ratios. The first heating of the unzoned material removed the hydrogen, and additional passes gave further reduction of the carbon and oxygen contents, essentially the only impurities remaining after six passes.

The low-temperature resistivity and the resistance ratio, $R_{300°K}/R_{4.2°K}$, are thus useful indicators of the overall purity of the samples, while the impurities are in a uniform solid solution in the sample. In the following we will discuss the effect on the resistance ratio of heat treatments at different temperatures for both crystal-bar and zone-refined zirconium since such annealing operations have effects that reflect on the impurity content of the samples and show certain limitations on the use of resistance ratios.

The changes in resistance ratio with annealing temperature from 200 to 900°C are shown in Fig. 12. The impurities in the iodide zirconium have been summarized by the analysis in Table III. When the impurities in iodide zirconium are in solid solution, the product of the concentration of the individual impurities and their respective resistivity coefficients can be added to give a resistance ratio of 153. This value agrees fairly well with the experimentally determined ratio for annealing temperatures of 800 to 900°C. A large increase in resistance ratio was observed for lower temperatures to 500°C, which suggests precipitation and restricted solubility of most all the impurity elements. Study of the Zr-O, Zr-N, and Zr-Hf phase diagrams at 500 and 800°C shows that oxygen, nitrogen, and hafnium are soluble at both temperatures, but the other impurities including carbon could be nearly insoluble. If we assume that this is the case, the resistance ratio due to a solid solution of only the oxygen, nitrogen, and hafnium gives a calculated ratio 450, in reasonable agreement with the experimental ratio 410 after a 500°C anneal as shown in Fig. 12.

The annealing of the zone-refined zirconium, on the other hand, produced the same experimental ratio, 450, after annealing at 800 and 500°C which compares to the calculated ratio of 470 in Table IV for the case of six passes of zone refining. The assumption that all

impurities become insoluble except oxygen, nitrogen, and hafnium in zone-refined zirconium permits a ratio of 1057 to be calculated. This illustrates what we believe is an important property of carbon that can be deduced from the resistivities. Carbon appears to precipitate at 500°C when present with other impurities such as Fe, Ni, Al, and Si but remains soluble at least to 0.006 at. % in zirconium if the only impurities present are O, N, and Hf. On this basis the calculated resistivity ratio is 516, in better agreement with the experimental values.

## Zone Refining with Chemical Additives

The analysis of partial pressures showed that carbon can be transported through the vacuum as hydrocarbons, CO, and $CO_2$. In the hope that we could increase the transport of carbon and oxygen through the vacuum by such effects, we prepared samples with additives of carbon, hydrogen, and air.

### Carbon Additions and Determination of the Carbon Resistivity Coefficient

A rod of zirconium was painted with a stripe of colloidal graphite suspended in distilled water and zone-refined six passes. The low-temperature resistivity was determined and found to have a constant value 0.956 μohm-cm along the whole sample. The microstructure showed no signs of the presence of a second phase, indicating that the carbon was apparently in solid solution. An analysis by combustion showed 0.12 at. % C to be present from which we calculated a resistivity coefficient of 7.29 μohm-cm/at. % C, very similar to that for oxygen. The constancy of the resistivity content along the rod would indicate that the carbon content does not vary and that carbon has an effective K factor close to unity.

Two other experiments are illustrated by Figs. 13 and 14, which show the resistance ratios of samples with and without carbon additions plotted against sample length. The carbon in this case was a small piece of graphite added at the starting end. Comparison of the two figures shows results that would be expected from zone-refining theory with a starting zone addition of impurity for $K \geq 1$. The carbon is gradually diffused toward the center of the rod without reaching the final end.

The experiments with carbon additions showed that zone refining of carbon did not occur at the speeds employed here, and secondly, that carbon addition was not beneficial. However, we still know that carbon purification is occurring from the amount of carbon initially in zirconium. This was shown by the partial pressures of hydrocarbons, CO, and $CO_2$ during the initial passes, and by the carbon analysis and electrical resistivities discussed previously.

## Hydrogen Addition

As shown earlier in this paper, hydrogen was the dominant component of the gases in the vacuum over molten zirconium, but the pressure was appreciable only in the first several passes of zone refining. To investigate the effects of larger quantities of hydrogen present through all passes of the zone melting, we turned off the ion and titanium sublimation pumps and allowed the hydrogen pressure to remain high throughout this operation. There was no appreciable effect on the resistance ratio along the sample, the values after a total of 12 passes rising from 380 at the starting end to 890 at the final end, in good agreement with similar values obtained at much smaller hydrogen pressure. This would indicate that under our conditions no further gain could be made by having hydrogen present in larger amounts during all the passes.

## Zone Refining with Air Leaks

We calculated the mass of oxygen molecules absorbed by an exposed 3-mm cylinder of hot solid using the kinetic theory of gases and the assumption that all the colliding molecules stick and dissolve. A formula given by Dushman [16] for molecules striking a flat surface was modified to give concentrations of contaminating atoms w(ppm) in solid solution in a metal cylinder of density $\rho$(g/cm$^3$) and diameter d(cm). The concentration of impurities in solid solution is

$$w = 2.33 \times 10^5 \, tP(M/T)^{\frac{1}{2}} d^{-1} \rho^{-1}$$

where

T = temperature (°K)
t = time (sec)
M = molecular weight of the gas (g/mole)
P = pressure (torr).

For the special case of oxygen molecules: [M = 32 g/mole, d = 1/8 in., $\rho$ = 6.5 g/cm$^3$ (zirconium), T = 300°K] and expressing oxygen concentration as n = 5.70 w (atoms/million), this formula becomes $n = 2.11 \times 10^5$ tP. Curves for oxygen contamination from the vacuum are given in Fig. 15 for various times at five different oxygen pressures from $2 \times 10^{-7}$ to $1 \times 10^{-10}$ torr. Similar behavior would be expected for nitrogen. The results of the kinetic theory calculation can also be applied to contamination during zone refining. For zirconium we estimate that the reaction would occur over a hot liquid and solid cylinder which is about ten centimeters long. The total time of contamination of any point on the sample during zone refining can then be calculated from the estimated reaction length. For example, 10 passes at 20 cm/hr correspond to heating for 5 hr. On the basis of the above,

which overstates the contamination (since the sticking factor was assumed to be unity), and on the basis of the partial pressure results discussed earlier, the gas transport of all gas components except hydrogen in our vacuum system is not significant as far as the impurity content of the liquid is concerned after two passes of zone refining.

We deliberately added air to the system in an effort to determine the pressure at which contamination could be observed by decreases in the resistance ratio of zirconium. Further, this experiment was intended to seek possible benefit in increasing the nitrogen and oxygen content of the gas phase in the hope that the carbon content could be reduced by association with the other impurities. In the results shown in Fig. 16, significant gas transport occurred first at $2.9 \times 10^{-7}$ torr, which would agree with the value indicated in Fig. 15 only if the sticking factor were reduced to 0.3 to 0.4.*

Sticking factors of the same order were reported by Pasternak [17] in his study of niobium, but in our case we cannot carry the zirconium analysis too far because the effective length for reaction during zone refining is very uncertain. The absorption of the gas present at $2.9 \times 10^{-7}$ torr by the hot sample and the outgassing of the hot sample at pressures $2 \times 10^{-8}$ torr and lower supports the resistance ratios in that an abrupt change in the role of the liquid from a pump to a source occurs in this pressure range. This is shown in Table V where in experiments A, B, and C the sample acted as a source of gas and in experiment D, a getter.

As indicated in Fig. 16, the higher ratios in the starting half of the bar zone refined in an atmosphere containing $2 \times 10^{-8}$ torr air may be due to reductions in the carbon content through the interaction of the oxygen or nitrogen with this impurity. In the final and purer end of the bar there was no improvement with this amount of air addition, but in this region the zone refining keeps the oxygen content depleted.

---

*We can show this as follows. The composition of the vacuum gases in the experiment illustrated by Fig. 16 is given in Table V. For a $2.9 \times 10^{-7}$ torr air leak and a cold sample, the oxygen and nitrogen total 71% of the pressure of $2 \times 10^{-7}$ torr. For the conditions of zone refining for 10 passes at 20 cm/hr and reaction over a 10-cm length, the assumption of sticking probability of 1 leads to 760 atoms/million oxygen increase. We ignore differences between oxygen and nitrogen here and read the dotted line at $2 \times 10^{-7}$ torr. On the other hand, Fig. 16 shows the resistance ratio to be 150 for the starting end of the $2.9 \times 10^{-7}$ torr sample after zone refining. For a pure alloy (zirconium plus oxygen) this corresponds to 0.0445 at. % O. The ratio 400 for the $2.6 \times 10^{-10}$ torr sample corresponds to 0.0166 at. % O and the difference between them is 280 atoms/million for a sticking factor of 280/760 = 0.37.

Table V

Effect of Air Leaks on the Composition and the Pressure of Gas ($P_H$) Over the Hot Sample on Last Pass and Over the Cold Sample ($P_C$) After Zone Refining

| Experiment | Total Pressure (torr) | Pressure Change (%) $\left(\frac{P_H - P_C}{P_C} \times 100\right)$ | Composition of the Gas (Vol %) | | |
|---|---|---|---|---|---|
| | | | $H_2$ | $N_2$ | $O_2$ |
| **Over Cold Sample** | | | | | |
| A | $2.6 \times 10^{-10}$ | | 60 | 0.2 | 0.1 |
| B | $2.1 \times 10^{-9}$ | | 55 | 40 | 0.1 |
| C | $2.0 \times 10^{-8}$ | | 33 | 56 | 1.5 |
| D | $2.9 \times 10^{-7}$ | | 4.5 | 66 | 5.0 |
| **Over Hot Sample** | | | | | |
| A | $1 \times 10^{-9}$ | +285 | 90 | 0.4 | 0.03 |
| B | $1.4 \times 10^{-8}$ | +576 | 93 | 5.1 | 0.01 |
| C | $2.43 \times 10^{-8}$ | +22 | 46 | 46 | 0.5 |
| D | $2.2 \times 10^{-7}$ | −24 | 7 | 66 | 3.5 |

Zone Segregation of Oxygen and Determination of the Oxygen Resistivity Coefficient

In Fig. 17 we show the results of an oxygen analysis by vacuum fusion of samples from a bar that had been zone refined for 63 passes at speeds 10 to 30 cm/hr. In this experiment a successful zone refining of oxygen was clearly observed. The vacuum fusion analysis showed a similar variation of the nitrogen content from 0.5 ppm at the final end of the bar to 1 to 3 ppm at the starting end. With a slight correction for this nitrogen, the residual resistivity at 4.2°K can be associated entirely with the oxygen content. This comparison is shown by curve I on Fig. 18, for which the resistivity is nearly linear in oxygen content. The slope of curve I is 6.7 μohm-cm/at. % O which is in good agreement with slopes determined at 300°K by Treco [18] (7.3 μohm-cm/at. % O) and Renucci and Langeron [19] (7.1 μohm-cm/at.% O). The intercept of curve I at zero oxygen concentration shows that an additional oxygen-independent component of resistivity is present. This large intercept (0.064 μohm-cm) was unusual in that after 63 passes in a very good vacuum we did not expect to find such a large resistivity. Carbon appears to be the only impurity detected chemically in sufficient amounts to account for the high intercept. The results of an experiment pertinent to this effect where higher resistance ratios were involved are indicated in curve II on Fig. 18. A carbon addition was made at the start of the zone in this sample, but as was explained

before in the section on Chemical Additives, the solidus/liquidus factor of carbon has an apparent value $K \geq 1$, and thus the carbon additive in the starting zone did not extend to the final zone. The smaller intercept of the curve II results from a lower carbon content,* which in turn arose from a lower, uniform carbon content in the original bar. Assuming that they are entirely due to carbon, the intercepts of curves I and II correspond to 85 and 10 at. ppm C, respectively, and we have the unusual situation that the sample with carbon additive ended up with the smallest carbon content. Carbon did not zone refine or did not evaporate below about 85 at. ppm, and in this range the zoned values depend upon initial material.

We have concluded from the experiments shown previously that carbon has an effective K factor near unity, and from the experiment immediately above that carbon is the impurity responsible for the variation in zirconium resistance ratios between 700 and 1300 under seemingly identical experiments with different lots of zirconium.

## Chemical Analysis of Impurities

The impurity contents determined by chemical analysis of iodide zirconium, before and after zone refining six passes, and the resistivities due to these impurities were shown previously in Table III. Segregation of a typical volatile impurity, iron, is illustrated in Fig. 19. The original iron content of 11 at. ppm in the handle of the rod is reduced to 0.1 to 1.0 at. ppm in the zone refined region of the same rod by six passes. As shown in Table III, similar evaporation of essentially all the impurities occurs with the exception of Hf, Ta, Mo, Nb, and W. We can conclude from combined neutron activation and mass spectrometry that concentrations of Mo, Nb, Ta, and W after zone refining did not exceed 1, 1, 2, and 0.01 at. ppm, respectively. The latter are not present in large enough quantities in zirconium to be an important factor in the resistance of the zone-refined zirconium.

Table III shows appreciable reductions in oxygen and carbon through evaporation and reaction. The numbers in the table are characteristic of central locations on the zone refined bar, which would be unaffected by oxygen from zone refining after six passes. The principle impurities remaining at this state were oxygen, carbon, and hafnium; no others exceeded 5 at. ppm. Since hafnium has relatively small effects on resistivity, the resistance ratio profiles of zone-refined zirconium must represent mainly changes in oxygen and carbon contents, and the ideas expressed earlier in connection with volatilization of impurities and zone refining from oxygen in Fig. 10 are consistent with chemical analysis.

---

*Actual analysis of this material was <6 atoms carbon per million. At this level, however, the combustion analysis for carbon is not reliable, and we must rely mainly on the small value of resistivity.

Hafnium and Molybdenum Purification

Although this work was concerned primarily with zirconium, a preliminary investigation was made with hafnium and molybdenum to see if the techniques could be extended to other metals. Principal impurities in the as-received iodide hafnium, which had a resistance ratio of 19, were: 0.16 at. % C, 0.06 at. % Fe, 0.0080 at. % Mo, 0.02 at. % O, 0.04 at. % Si, and 0.1 at. % Zr. A gradual increase in resistance ratio is observed with increased number of zone passes, as seen in Fig. 20. Since zirconium in hafnium increases the resistivity by only 0.1 to 0.2 μohm-cm/at.% and iron and silicon would be expected to volatilize readily, the increase in resistance ratio (19 to 300) would indicate that carbon and oxygen are being volatilized. The change in slope of the curves from 16 passes to 35 passes indicates the stage at which purification by zone refining becomes the predominant refining mechanism. We propose that this resistance ratio profile arises from oxygen zone refining with oxygen segregating to the final end of the sample. This fact would agree with the hafnium-oxygen phase diagram of Rudy and Stecher [20], which shows oxygen having a $K < 1$, but disagrees with the hafnium-oxygen phase diagram of Domagala [21] which shows oxygen having a $K > 1$. The volatilization of oxygen and carbon would agree with the previously shown residual gas analysis, which showed large amounts of $CH_4$, CO, and $CO_2$ being evolved in the initial zone passes.

Molybdenum, like tungsten, has an extremely low vapor pressure and is much more easily purified by vacuum zone refining. Only two zone passes increased the resistance ratio for 25 to 3300. The starting material had the following typical impurity analysis: <0.0480 at. % O, <0.0171 at. % Si, <0.0086 at. % Fe, <0.0080 at. % C, and <0.0069 at.% N. Since the analysis does not preclude the presence of significant oxygen, the purification may be due to oxygen volatilizing as a molybdenum suboxide and not depend upon reduction by carbon as reported by Gerrchyshen and Barr.[22].

SUMMARY

The development of a baked, stainless steel vacuum system with refrigerated walls and combining ion, titanium sublimation, and liquid nitrogen pumping permits zone refining of reactive metals such as zirconium at partial pressures below that which impurity transport in the gas phase is significant.

The use of sapphire ball bearings in the electron-gun elevator permitted the large number of zone passes that were found to be necessary to segregate oxygen by zone refining. With a quadrupole gas analyzer, partial pressures could be measured as accurately as total pressure could be measured by ionization gage readings in the range $1 \times 10^{-6}$ to $5 \times 10^{-11}$ torr. These partial pressures showed that hydrogen and hydrocarbons were evaporating from the liquid zirconium throughout the zone

refining, while $CO$, $CO_2$, $N_2$, and $H_2O$ evaporated mainly during the initial passes. Studies of the partial pressures also showed that when air leaks were introduced during zoning, liquid zirconium changed abruptly from a getter at pressures $2.9 \times 10^{-7}$ torr to a source of gas at pressures lower than $2 \times 10^{-8}$ torr.

The vacuum zone refining process in zirconium can be characterized as follows: The first stage consists of evaporation of volatile impurities such as Fe, Ni, Al, Si, which meet the condition that they enrich in the gas phase compared to the liquid. After the first stage and the evaporation of these impurities, the principal impurities in zirconium are O, C, and Hf and $<7$ at. ppm of other impurities are present. The second stage consists of zone purification, in accord with zone refining theory, of nonvolatile impurities. An oxygen gradient in zirconium was established after 63 zone passes showing a change from 0.0022 wt % in the original material to 0.0045 wt % at the head of the bar to 0.0004 wt % at the tail of the zoned bar.

A third process occurs throughout the refining and consists of chemical reactions such as the reduction of carbon with hydrogen. The difficulty of obtaining accurate carbon determination in very low concentrations made the definition of these reactions less than desired; however, partial pressure analysis and the correlation of resistivity measurements with impurity analysis indicated that reactions of this type did indeed occur. Carbon did not zone segregate in our experiments and apparently is responsible for variations in resistance ratios between 700 to 1300 in the highest purity zoned material with different batches of starting material.

Summation of resistivities due to measured impurities agreed well with the total residual resistivity of zirconium as experimentally determined. Given the history of zone refined zirconium, a fairly accurate analysis for its impurities can be predicted from the measurement of the residual resistivity.

Zirconium, hafnium, and molybdenum were refined significantly as indicated by the resistance ratio changes in Table VI. The zirconium and hafnium samples with ratios of 1340 and 300, respectively, are thought to be the purest samples of these metals that have yet been produced.

Table VI

Purification of Zirconium, Hafnium, and Molybdenum

| | | Resistance ratio, $R_{300°K}/R_{4.2°K}$ | |
|---|---|---|---|
| | | Initial Material | Zone refined |
| Zirconium | 20 | 150 | 1340 |
| Hafnium | 35 | 20 | 300 |
| Molybdenum | 2 | 25 | 3300 |

## REFERENCES


1. G. D. Kneip, Jr., and J. O. Betterton, Jr., J. Electrochem. Soc. 103, 684 (1956).
2. M. Billion and J. P. Langeron, C. R. Acad. Sc. Paris 259, 4671 (1964).
3. J. C. Wilson and M. L. Picklesimer, First International Conference on Electron and Ion Beam Science and Technology, R. Bakish (Ed.), John Wiley and Sons, New York, 1965, pp. 502–520.
4. T. Krauss and O. Winkler, "The Reactions Occurring in Electron Beam Melting of Metals," Chap. 6 in Introduction to Electron Beam Technology, R. Bakish (Ed.), John Wiley and Sons, New York, 1962, pp. 145–167.
5. W. H. Hayward, R. L. Jepsen, and P. A. Redhead, "Reverse X-ray Currents in Bayard-Alpert Ionization Gauges," 1963 Transactions of the Tenth National Vacuum Symposium, American Vacuum Society, pp. 228–233.
6. J. P. Guerlet, J. Debrigue, and P. Lehe, "Study of the Oxidation of Zr and Certain of Its Alloys in Carbon Dioxide," Study of Corrosion and Protection of Zr and Its Alloys, Presses Universitaires de France, Paris, June, 1965, pp. 27–37.
7. W. G. Pfann, Zone Melting, John Wiley and Sons, New York, 1958.
8. Rodney P. Elliott, Constitution of Binary Alloys, 1st Supplement, McGraw-Hill, New York, 1965, p. 708.
9. W. P. Allred, R. C. Hines, and H. L. Goering, Proceedings First Symposium on Electron Beam Technology, J. Hetherington (Ed.), Boston, Massachusetts, 1959, p. 38.
10. R. Bakish, Introduction to Electron Beam Technology, John Wiley and Sons, New York, 1962, p. 195.
11. G. D. Kneip, Jr., and J. O. Betterton, Jr., J. Electrochem. Soc. 103, 684 (1956).

12. Jean-Paul Langeron, Application of the Method of Zone-Melting to the Purification of Zr, Thesis, ORNL-TR-781, 1965, p. 37.
13. D. Mills and G. B. Craig, Trans. AIME 236, 1228 (1966).
14. J. W. Rutter and B. Chalmers, Can. J. Phys. 31, 15 (1953).
15. J. O. Betterton and D. S. Easton, manuscript in preparation.
16. S. Dushman, Scientific Foundation of Vacuum Technique, 2nd ed., John Wiley and Sons, New York, 1962, p. 14.
17. R. A. Pasternak, High Temperature Oxidation and Nitridation of Niobium in Ultra-High Vacuum, 1964, SRI Project PAU-4151, SRIA-132.
18. R. M. Treco, Symposium Am. Soc. Metals on Zirconium and Zirconium Alloys, Cleveland, 1953, p. 254.
19. Louis Renucci and Jean-Paul Langeron, Compt. Rend. 264, 673 (1967).
20. E. Rudy and P. Stecher, J. Less Common Metals 5, 78 (1963).
21. R. F. Domagala, A Study of the Hafnium-Oxygen System, ARF-B194-17, Armour Research Foundation, 1963.
22. M. Gerrchyshen and R. Q. Barr, Arc-Cast Molybdenum and Tungsten-Base Alloys, Climax Molybdenum Co., contract NONR-2390(00), Project NR039-002, p. 139.

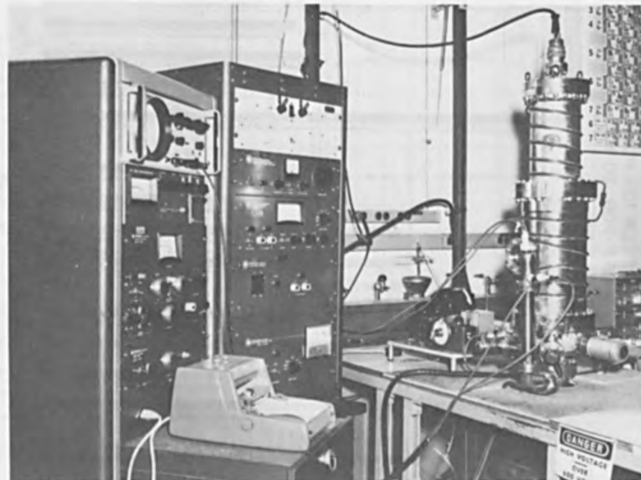

Fig. 1. Electron-Beam Zone Refiner and Related Instrumentation.

Fig. 2. Zone Refining Apparatus Showing Chain Driven Sample Supports.

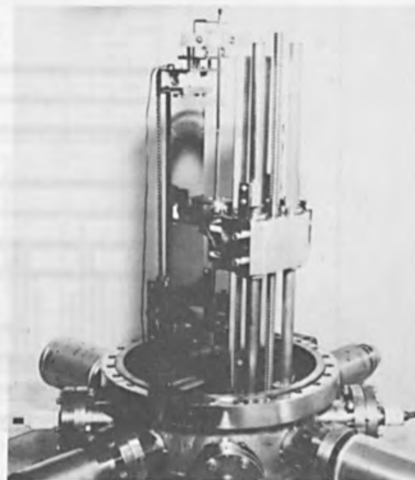

Fig. 3. Electron-Beam Gun Elevator Mounted on Sapphire Ball Bearing Screw Driver.

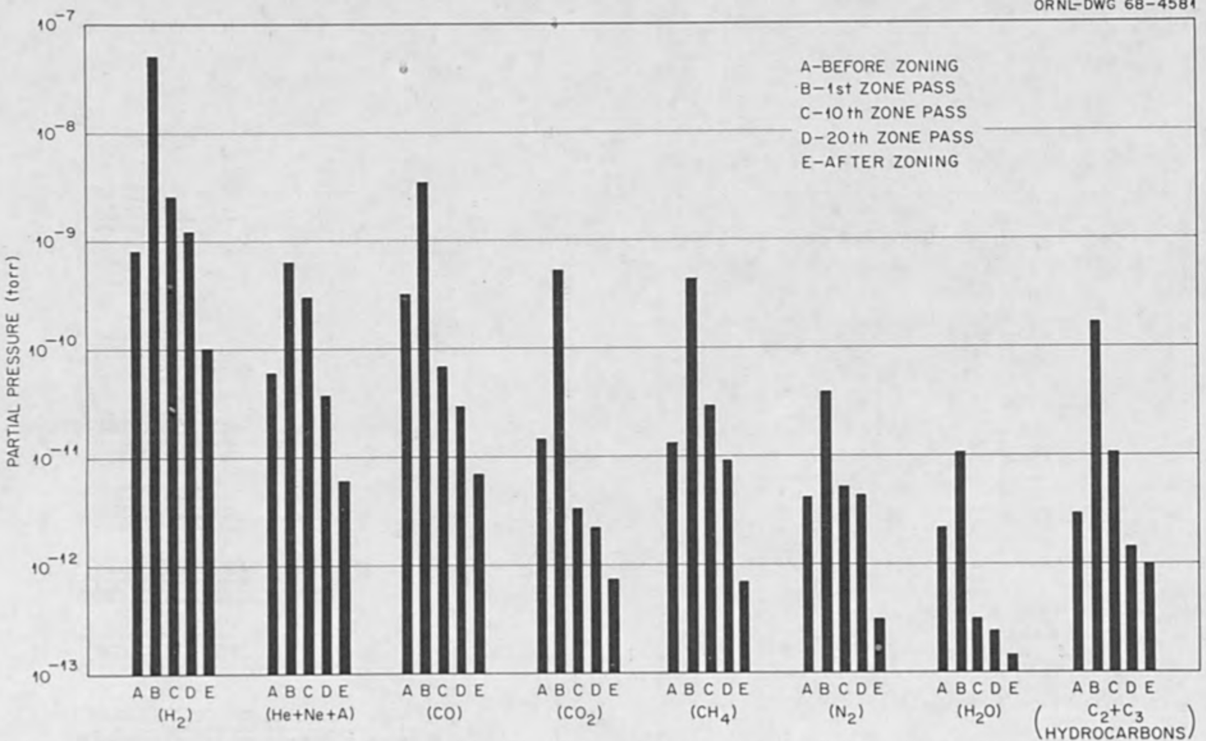


Fig. 7. Partial Pressures over a Zirconium Sample with Carbon Addition.

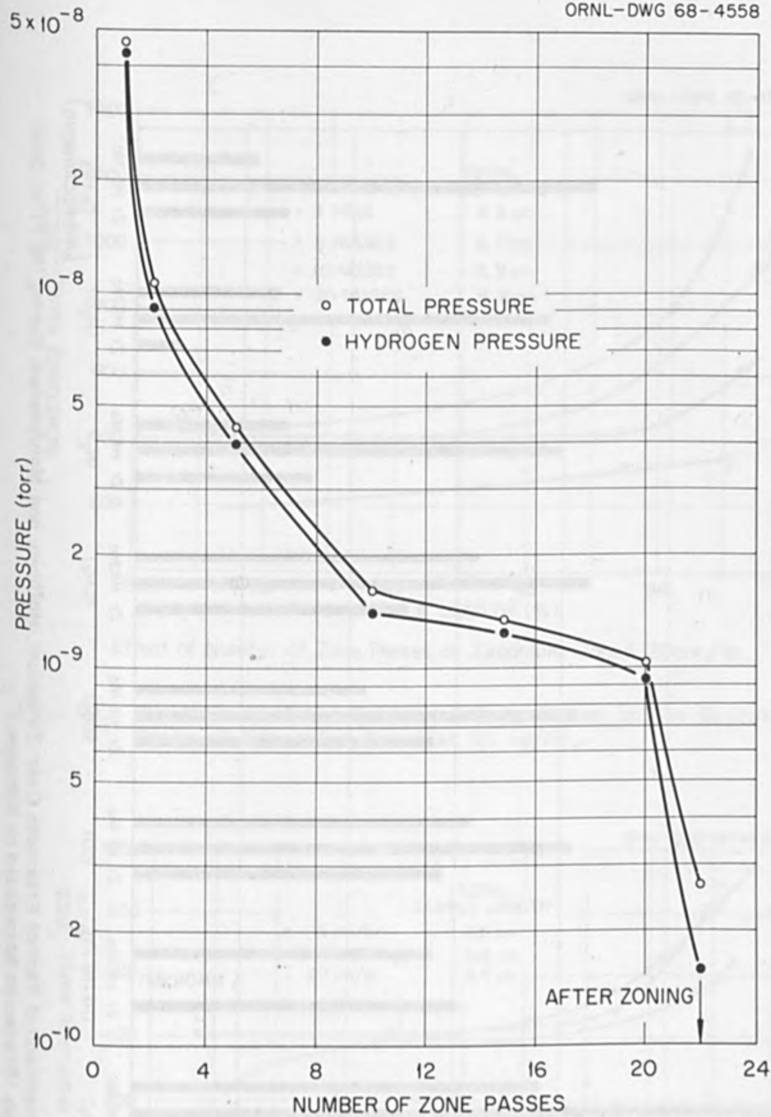


Comparison of the Total Pressure with Hydrogen Partial Pressure over a Zirconium Sample Zoned 20 Passes at 20 cm/hr.

Fig. 8. Comparison of Total Pressure in the System with Hydrogen Partial Pressure over Zirconium during Zoning.

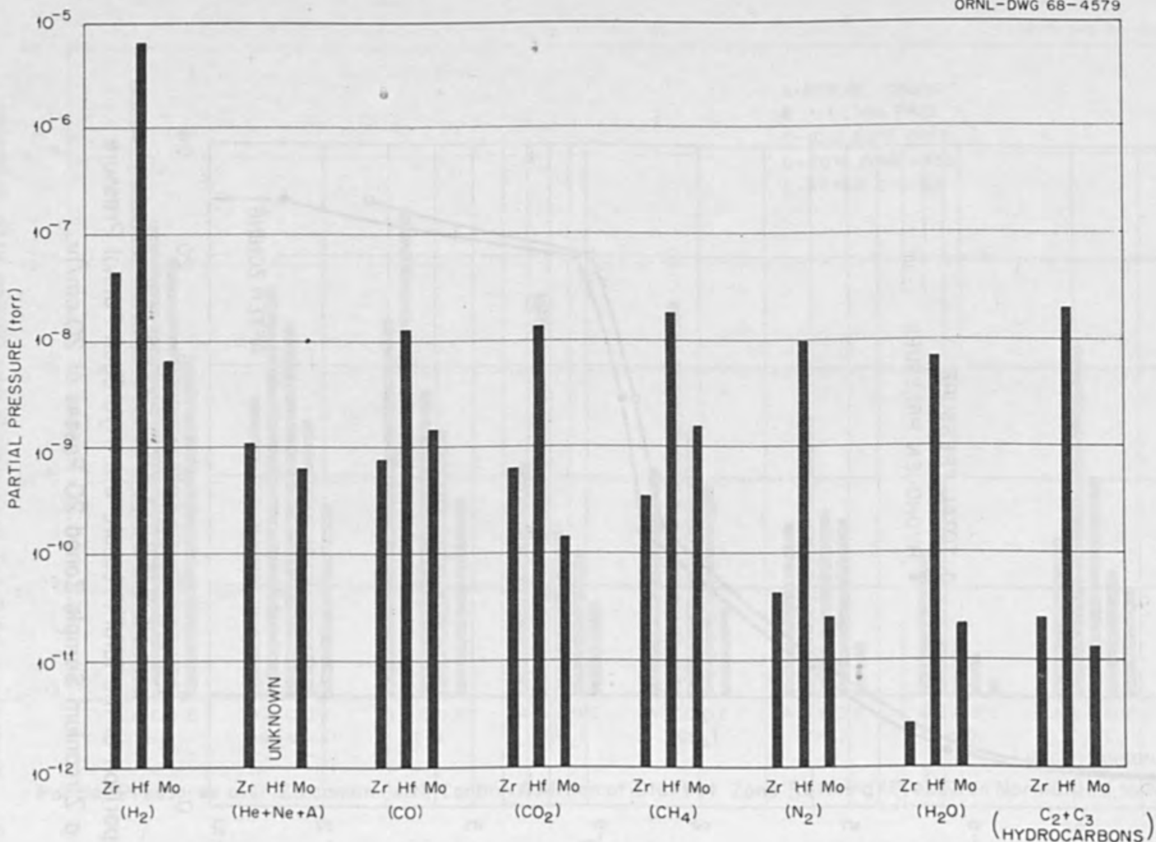


Comparison of Partial Pressures Over Zirconium, Hafnium, and Molybdenum During the First Zone Pass (Pressures Normalized to Nitrogen.)

Fig. 9. Comparison of Partial Pressures over Zirconium, Hafnium, and Molybdenum during the First Zone Pass.

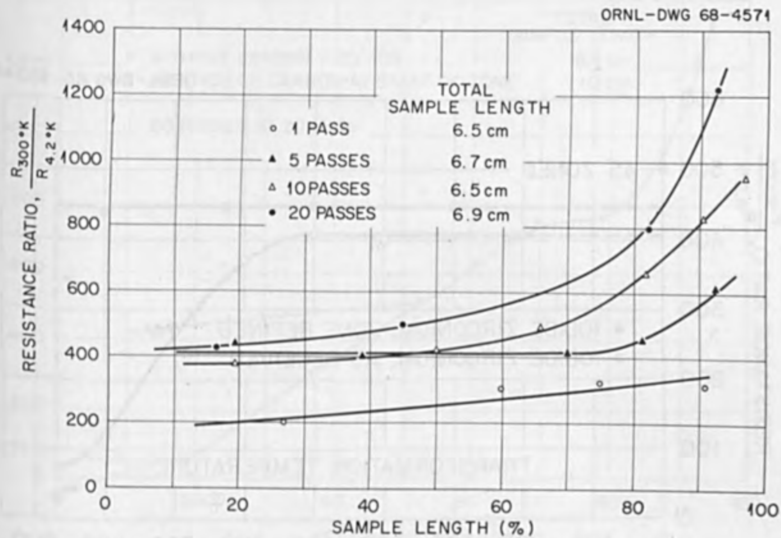


Effect of Number of Zone Passes on Zirconium Zoned 20cm/hr.

Fig. 10. The Effect of the Number of Zone Passes on the Resistance Ratio of Zirconium Zoned at 20 cm/hr.

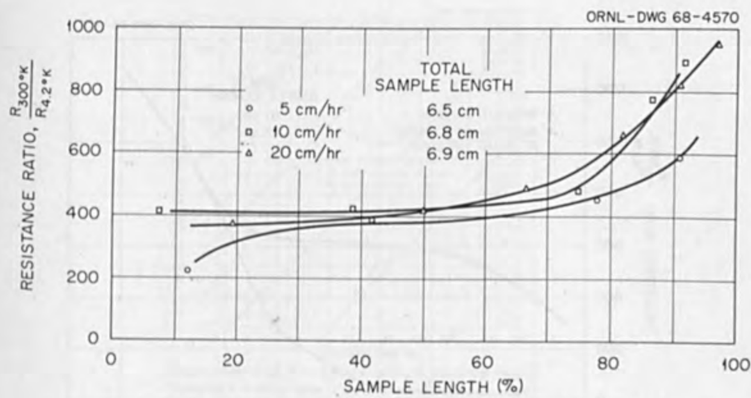


Resistance Ratio as a Function of Zoning Speed of Zirconium Zoned 10 Passes.

Fig. 11. The Resistance Ratio of Zirconium Samples Zoned 10 Passes Each as a Function of Zoning Rate.

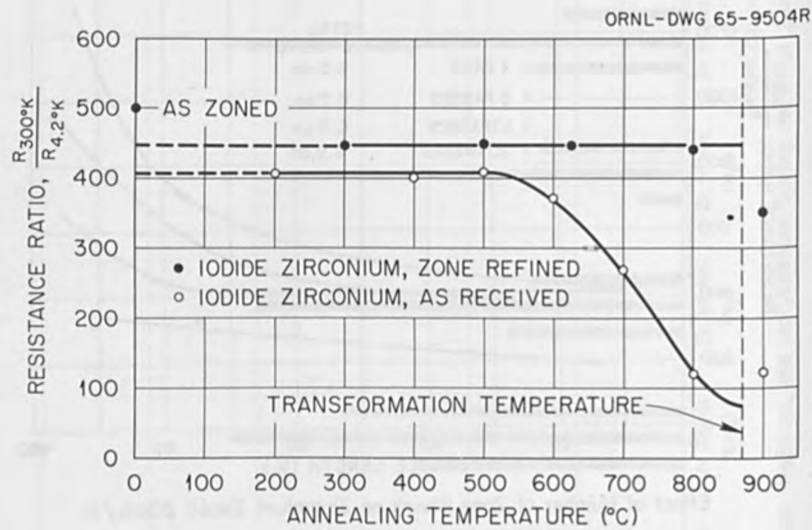


Fig. 12. The Effect of Annealing Temperature on the Resistance Ratio of Zoned and Unzoned Zirconium.

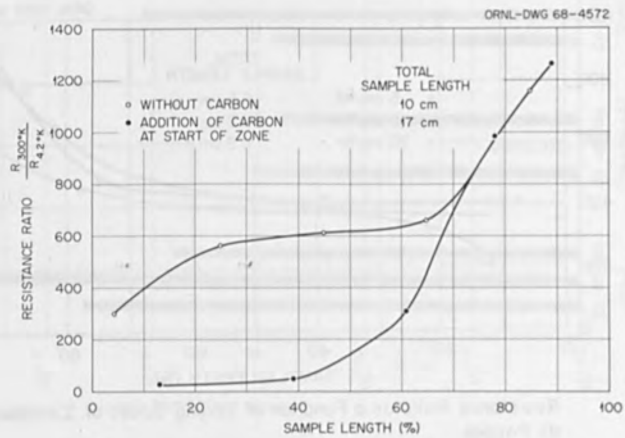


Fig. 13. The Comparison of Zirconium Samples Zoned 25 Passes with and Without Carbon Addition Showing the Effect of Carbon Extended to only 70% of the Sample Length.

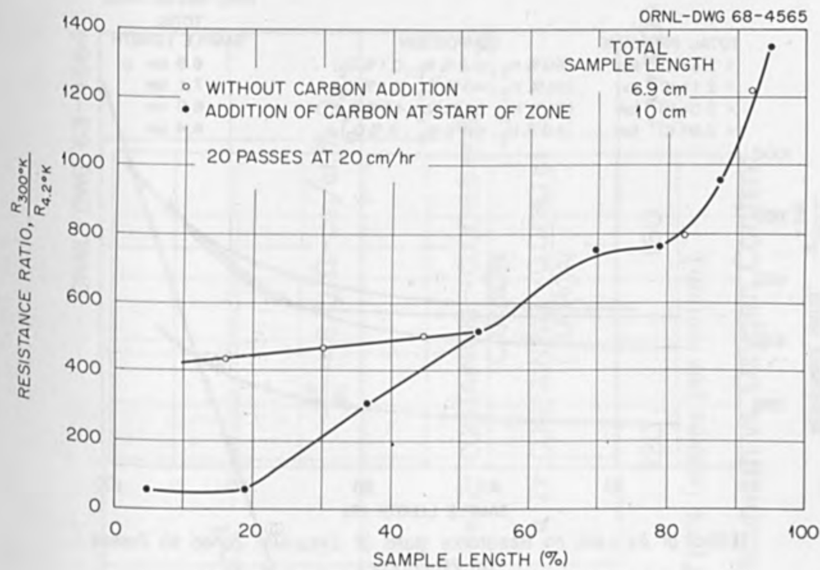


Fig. 14. The Effect on the Resistance Ratio of Zirconium with and Without Carbon Addition.

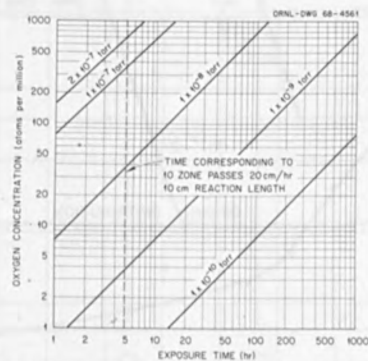


Fig. 15. Oxygen Contamination as a Function of Time and Pressure According to the Kinetic Gas Theory and Assuming a Sticking Factor of Unity and Complete Solution of the Contaminating Gas.

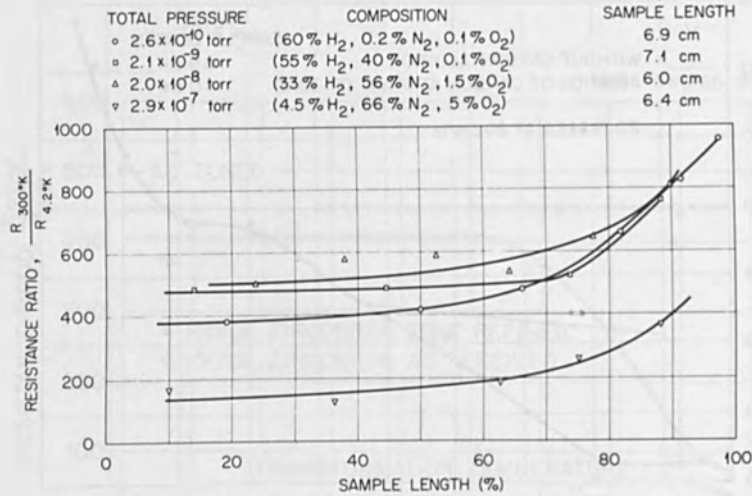


Effect of Air Leak on Resistance Ratio of Zirconium Zoned 10 Passes at 20 cm/hr.

Fig. 16. Resistance Ratio Changes Due to Introduction of Air Leaks at Different Pressures in Zirconium Samples Zoned 10 Passes at 20 cm/hr.

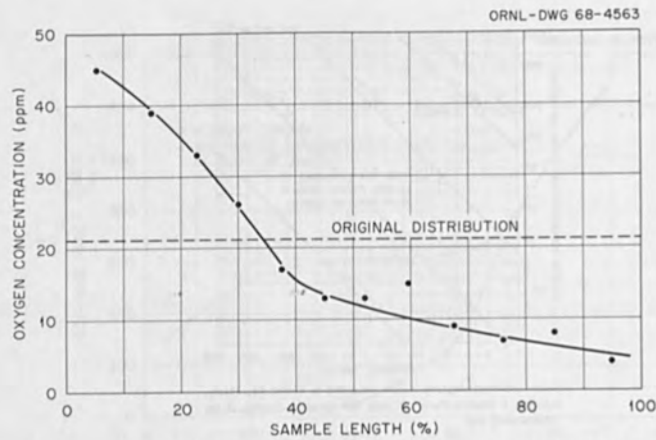


Oxygen Distribution after Zoning 63 Passes and Annealing 48 hr at 800°C.

Fig. 17. Oxygen Distribution in a Zirconium Sample after Zoning 63 Passes.

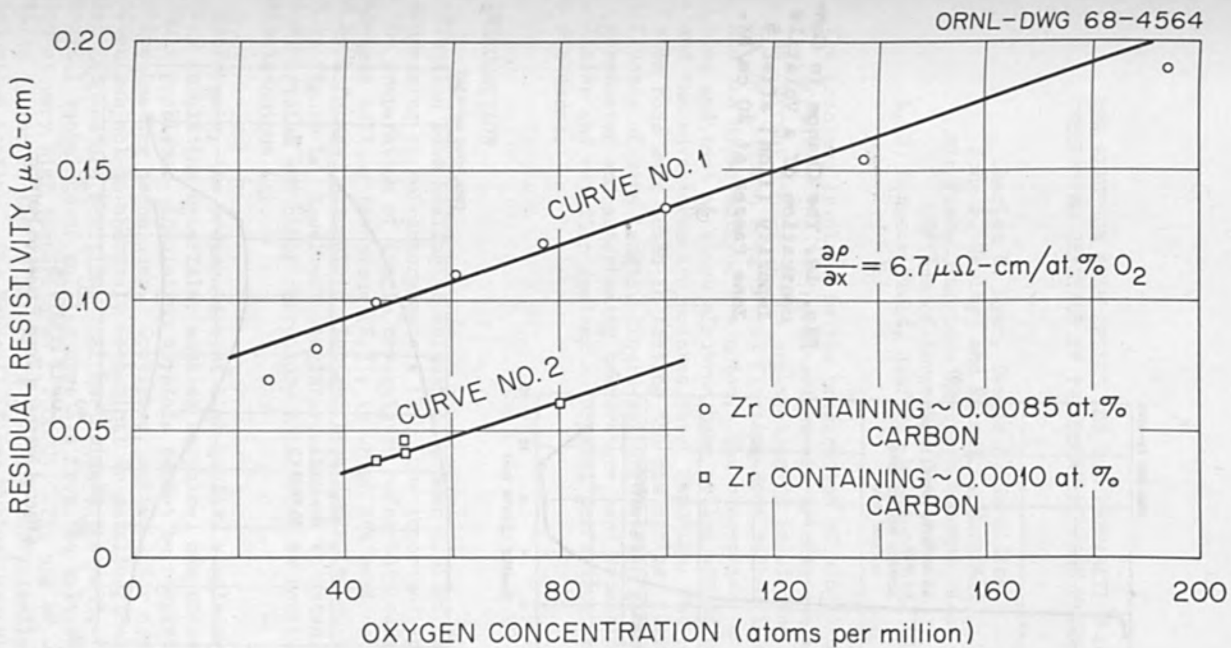


Fig. 18. The Change in Residual Resistivity of Two Lots of Zone-Refined Zirconium as a Function of Oxygen Contamination.

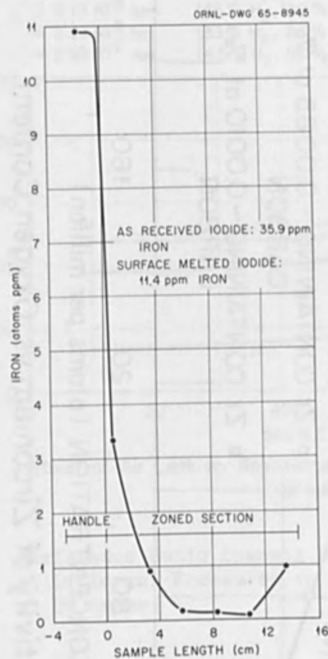


**Fig. 19. The Change in Concentration of a Volatile Impurity (Iron) after 6 Zone Passes at 20 cm/hr.**

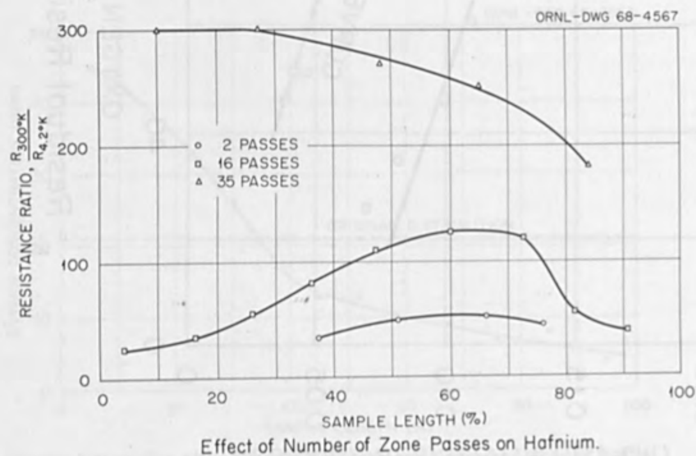


Fig. 20. The Effect of the Number of Zone Passes on the Resistance Ratio of Hafnium.

# NEW ELECTRON BEAM OPTICS FOR THE PREPARATION OF INSULATING CRYSTALS BY THE FLOATING ZONE METHOD

Charles E. Ryan, Dennis P. Considine,
John J. Hawley, and Robert C. Marshall
Air Force Cambridge Research Laboratories
Office of Aerospace Research
L. G. Hanscom Field, Bedford, Massachusetts 01730

The problems involved in the preparation of single crystals of refractory insulating materials are briefly outlined. The current status of the preparation of insulating crystals by the electron beam heated floating-zone method is reviewed, and the disadvantages are noted. The conception, construction and test of a new electron beam optics are described, and the advantages are pointed out. Sapphire, ruby and tungsten rods were zoned in testing the new optics. The influence of zone length, liquid-solid interface geometry, foreheater and afterheater temperature, and mechanical translation and rotation systems on crystal perfection are discussed.

## 1. INTRODUCTION

Electron beam heating techniques have been applied extensively to the processing of refractory metals (1). One important application has been the preparation of single crystals of refractory metals by a vacuum-zone melting technique (2,3), in which the heat source is provided by a focused concentric electron beam impinging on the work as shown in Figure 1. Excellent single crystals of tungsten, tantalum, rhenium, iridium and other refractory metals can be routinely prepared by this technique (4).

Conversely, the preparation of high-quality single crystals of refractory insulating materials, such as sapphire, has presented many difficult problems. Insulating crystals cannot be coupled readily by induction-heating techniques. Crucibles, suitable for use above 2000°C, are often subject to chemical, mechanical or metallurgical failure, or to high temperature reactions that contaminate the melt. Hence, the Czochralski technique of pulling crystals from the melt becomes quite limited at very high temperatures (>2000°C). The use of water-cooled crucibles is restricted to materials that are sufficiently conductive for induction heating. The Verneuil (flame fusion) technique (5) imposes severe limitations on the chemical and structural perfection of crystals grown by this method.

2. PREVIOUS EFFORTS

In its original form for zoning metals, the electron beam technique was unsuitable for zoning insulators for two reasons: (1) there was no way of accelerating electrons to an insulating work piece, and (2) a charge building up on the insulating material would defocus an electron beam. Neuman and Huggins (6) and others (7) overcame these disadvantages by inserting a positive high-voltage accelerating electrode between the cathode and the work shown in Figure 2.* The electrons from the cathode are accelerated by the positive grid. (More accurately, this grid is a perforated anode.) Many of these electrons miss the grid and give up their energy as heat when they impinge on the work. The charge, which would normally build-up on the insulating work, is dissipated to the positive grid in a manner which is not clearly understood but may be akin to secondary emission or thermionic emission.

Although the arrangement shown in Figure 2 demonstrated the physical effects by which electron beams could be used to refine insulators, several difficulties remained that limited the practical preparation of high-quality single crystals. First, the grid (made of tungsten) became sufficiently hot so that it sagged before a zone could be passed along a sapphire rod which melts at 2050°C. This sag caused loss of control of the zone, and sometimes destruction of the grid if it touched the molten zone. Second, with this type of grid it became difficult to keep the zone narrow enough to be sustained by surface tension without loss of visibility due to closely spaced focusing electrodes. Third, there was little hope of scaling up this electron optics system to handle larger rods. Fourth, it was difficult to adapt an afterheater to this system so that the effects of annealing during growth on crystal imperfections could be studied.

Dr. W. Class, and his associates at Materials Research Corporation (8), ameliorated these problems by the ingenious design of a water-cooled single-turn grid from a 50 mil-diameter tantalum tubing as shown in Figure 3.** This arrangement required the use of an afterheater which was composed of an alumina tube with a conductive outer surface. The energy to heat the afterheater to about 1300°C was derived from a portion of the electron beam that melted the work. Since the grid was water-cooled, it had to run at a temperature of less than 100°C or the water would vaporize and provide a hazard of rupturing the tube, thus leaking water into the vacuum system. An insulating deposit (probably $Al_2O_3$) gradually grew on the grid, which was the coolest part of the system, and caused instabilities. Nevertheless, a considerable advance was achieved by these modifications over the original grid structure (9).

* Figure 1 of Materials Research Corporation Report No. 477.

** Taken from Figure 4 of Materials Research Corporation Report No. 477.

## 3. AFCRL APPROACH

At AFCRL, the approach was originally aimed at the design of an inert-gas cooled grid which would run a few hundred degrees cooler than the uncooled grid, and thus avoid sag, and its resultant electrical and thermal assymetries and failures. It was also thought that it might be possible to have a vernier control on the zone temperature by varying the gas flow through the grid. However, before attempting the gas cooling, it was felt that the electron optics could possibly be improved, resulting in more energy being dissipated in the work and less in the grids. Since the electrons are accelerated perpendicular to the equipotential lines, it appeared possible to design a "virtual grid" in the position of the zone to be melted by using two shielded grids as shown in Figure 4. The correctness of this concept was experimentally verified; in fact, the grid temperature could be controlled by adjusting the position of the focusing or shield electrode.

The success of this arrangement was obscured during the first several experiments because tantalum wire was used to fabricate the grid. A reaction between the tantalum and vapors from the molten $Al_2O_3$ zone caused a heavy black deposit (probably tantalum oxide with a melting point of 1960°C) on both the grid and the zone, resulting in early failure of the grid. When a tungsten grid structure was substituted for the tantalum grid, the only contamination visible was a slight tungsten deposit on the cooler part of the rod. It is believed that this deposit came from cathode rather than from the grids.

## 4. DESIGN AND CONSTRUCTION

At this point, it became obvious that the grids and focusing electrodes could be extended in the vertical directions, permitting the design of mechanically-strong structures. Because of these mechanically-strong structures and the electron optical arrangement (in which more electrons hit the work and less electrons hit the grid, resulting in more efficient zone heating), gas-cooling of the grid was no longer required. Nevertheless, if desired either gas or water-cooling of the extended grid structure would be relatively simple. A sectional view of the resulting configuration is shown in Figure 5.

After some months delay in unsuccessfully attempting to have a satisfactory electron optical system constructed by a local company (skilled in the fabrication of tungsten parts), it was decided to fabricate an experimental unit in the laboratory by using conducting parts made of high-density carbon and insulating parts made of boron nitride. A somewhat similar electrode configuration composed of tungsten parts has recently been called to our attention (10).

Figure 6 shows the electron optics without the cathode in place. The accelerating grids and focusing electrodes are fabricated from

high-density carbon*, and the supporting and insulating structure is made of boron nitride.** (11) This structure has several advantages in fabrication and use. The carbon is easy to machine, is relatively very strong at very high temperature, and can be readily purified after fabrication by outgassing the parts in a partial vacuum at temperature of the order of 2500°C. It is also dimensionally very stable with heat treatments. The boron nitride has corresponding advantages, except that it should not be outgassed at temperatures higher than about 1800°C. It is the best insulating material that we have found for use at high voltages in a high-vacuum situation. The lack of any requirement for heat treatment after fabrication together with its mechanical, electrical and thermal compatibility with carbon over a wide temperature range, makes boron nitride a very convenient and useful material as a high-temperature insulator. Both carbon and boron-nitride parts can be easily cleaned after repeated use by scraping or abrading any deposits from the surface with, for example, steel wool. The threaded structure shown in Figure 6 was designed to provide easy adjustment of grid-separation and grid-electrode position relative to the cathode. Similarly, the focusing electrodes can be readily adjusted independently of the grid electrodes. This particular structure also has the advantage of shielding the high-voltage insulating surfaces from deposits which may arise by outgassing or volitalization of the material being zoned.

Figure 7 shows a sketch of the electron optics assembled into the MRC type EBZ-93A electron beam zone-melting apparatus.

## 5. TEST AND EVALUATION

The first test on the optics was made with the grids separated 1/4-inch and the focusing electrode, level with the grid, as shown in Figure 8A. At approximately 500 watts, the sapphire rod melted, forming a molten zone, while the grids remained black; that is, their temperature, as viewed by the optical pyrometer, was not above 700°C. With the focusing electrodes withdrawn, as shown in Figure 8B, the grids reached a temperature of 1800°C and it was difficult to maintain a stable zone because the zone extended inside the orifice of the grids. A series of experiments showed that the optimum position for the grids and focusing electrodes for 1/8-inch ruby or sapphire rods, was the position shown in Figure 8C. In this position, the temperature at ends of the grids was about 1600°C. Power of about 1 kilowatt was necessary to melt a zone 3/16-inch long in the 1/8-inch ruby rod and to heat the grids for the foreheater and afterheater.

The advantage of having an easily-adjustable electron optics can be clearly seen in Figure 9. The curved rod was grown with the grid

---

* Type "G" Carbon from Basic Carbon Corporation, Sanborn, New York.

** Grade "HBN" Boron Nitride from Carbon Products Division, Union Carbide Corporation, New York.

electrodes separated slightly more than 1/4-inch. This led to a zone length of approximately two diameters of the ruby rod. Because of the relatively low surface tension of this material ($Al_2O_3$), it is difficult to maintain a zone of more than about one and one-half diameters. When the zone is too long, the molten material tends to flow down the zone, and to enlarge the diameter of the lower rod. If the zone is then run cooler to prevent its loss, the liquid becomes much more viscous and tends to resist the rotation of the lower rod, causing misalignments resulting in an irregular bar as shown in Figure 9A. The grid separation was reduced to 3/16-inch (one and one-half diameter zone length) and the focusing electrodes set back 1/4-inch from the grid edges, leading to foreheater and afterheater temperatures of about 1600°C. At this setting, the zone was very stable and was run hotter (more than 100°C) than the previous run (Pyrometer reading 2250°C rather than 2100°C). This higher temperature reduced the viscosity of the zone, permitting the growth of a constant diameter crystal as shown in Figure 9B. The complete loss of chromium from the ruby rod indicates that the zone temperature was higher, and the zone mixing was more uniform.

In order to grow high-quality crystals, it is necessary to control the growth interface at the freezing end of the molten zone. The liquid-solid interface should be perpendicular to the axis of the rod being zoned, and either straight or slightly convex towards the growing solid. It is believed that the split-grid configuration with both foreheater and afterheater and the correct length zone, establish the conditions necessary for a flat-zone interface and correct vertical and horizontal-temperature gradients to produce relatively strain-free crystals. As far as can be seen by visual observation of the crystals during growth and after growth, the interface appears to be both flat and perpendicular to the rod axis. Moreover, the zone length appears to be accurately determined by the accelerating grid separation.

The striations that show up clearly on Figure 9B are associated with irregularities in the drive mechanism and the rotation mechanism. This is clearly shown in Figure 10, which shows the same two crystals that were shown in Figure 9 together with another crystal shown in Figure 10C. The crystal in Figure 10C was grown with the same rotation rate but with a different growth rate and a gear adjustment in the drive train of the growth-travel mechanism. Near the middle of the growth section, the rotation was stopped for about five minutes, and then started again with the same speed but with the opposite direction of rotation. Figure 11 shows the third crystal (Figure 10C) in more detail. Here, several of the different superimposed patterns are evident. The light striations are due to planes of imperfections (like very small bubbles) sometimes known as veils. While similar imperfections probably occur in opaque crystals, they show up dramatically in transparent crystals. In optical crystals, these veils are a very serious defect and clearly show the importance of smooth drive and rotation mechanisms in crystal growth.

Figure 12 gives some idea of the control of the molten zone. At point A of Figure 13 (which is a sketch of Figure 12), the molten zone was formed. At point B, the rotation of the lower rod was started and increased to 48 rpm, and the scanning mechanism was started and adjusted so that the cathode scanned down the rod at a rate of approximately 1-inch in 16 minutes. At point C, the molten-zone diameter was decreased by jogging downwards on the lower half of the rod. At point D, the zone diameter was increased by jogging upward on the lower rod. In practice, it is better to keep the rod diameter constant by slight adjustments of the pulling rate or of the zone temperature. If the zone temperature is too high, the zone diameter tends to shrink. Similarly, too low a zone temperature tends to increase the zone diameter. A constant-diameter grown crystal indicates that the growth interface was planer, even though the molten zone is slightly necked-in as it travels up the rod.

Since there is no reason why the same electron optics or electrode structure should not work for metals as well as insulators, the ruby rods were replaced with 1/8-inch tungsten rods. It was reasoned that the efficiency of the electron optics could be measured by plotting temperature versus power in two cases: (1) where the high voltage was attached to the carbon grids as in the case of sapphire, and (2) where the high voltage was attached to the tungsten metal rods and the carbon grid left unconnected (that is, floating rather than grounded). Figure 14 shows the data for these two cases. The data are unreliable above approximately 2700°C because the vapor pressure at this temperature, in a vacuum of about $5 \times 10^{-5}$torr is such that appreciable evaporation of tungsten from the tungsten rod takes place. The evaporated tungsten coats the insulators, creating leakage paths leading to very large increases in power. It also coats the viewing window rendering the pyrometer readings inaccurate. Hence, as the power was increased, the pyrometer readings decreased. Nevertheless, the tungsten bar was melted and zoned as shown in Figure 15, indicating that temperatures of well above 3000°C were reached. The ratios of powers at given temperatures are, at best, only a fair indication of the efficiency of the new electron optics, because the power consumed is proportional to the length of the molten zone which is not necessarily the same in both cases. Moreover, in the insulator case, part of the power is used to intentionally heat the grids acting as foreheaters and afterheaters, which help control crystal interface shape.

## 6. ADVANTAGES OF NEW DESIGN

In summary, a new electron optics (or electrode configuration) has been described which has the following advantages over previous systems:

(1) The electrodes can easily be adjusted for the experimental determination of optimum conditions.

(2) The molten-zone length is determined primarily by the separation between the upper and lower accelerating electrodes.

(3) The grids can serve as foreheater and afterheater; then temperature can be adjusted over a wide range (<700°C to >1700°C) by simply adjusting the separation of the focusing electrodes relative to the separation of the grid electrodes.

(4) The component parts can be easily machined using carbon and boron-nitride parts. The tolerances are well within the range of good machine shop practice. The parts can be readily cleaned; by vacuum heating after machining, and by simple abrading techniques after use. (After every few experiments, we used steel wool to clean the boron-nitride surfaces from deposited films, and a pipe cleaner to clean the inside of the accelerating grids.)

(5) The molten zone and the grids are accessible for visual observation and pyrometer readings during crystal growth.

(6) The carbon parts could be replaced by tungsten or other refractory metals (in special cases) to avoid specific high temperature reactions.

(7) The entire electrode structure should scale up easily for the processing of larger diameter bars. This feature could be very important for the preparation of high-quality sapphire substrates for deposition of single crystal semiconductors like silicon. It could also be very important for any optical, laser or insulating crystals.

(8) The same structure can be used for insulators, semiconductors and metals.

## 7. FUTURE EFFORT

It is planned to scale up the present optics to handle 1/4-inch rods, and to improve the mechanical systems in order to eliminate the veils. A separate report will be written on the quality of the crystals prepared with this electrode structure after the mechanical drive and rotation defects are eliminated. A still larger system capable of about 1/2-inch rods is visualized. In this system, a split cathode will be designed so that visibility will be better, and zone control will be improved by independent control of the two annular cathodes. Some experiments will be attempted on the control of the growth interface by adjustment of the focusing-electrode potential during operation. In essence, it is hoped to provide a fine adjustment of the foreheater and afterheater temperatures in this way.

## 8. CONCLUSION

It is concluded that a new and useful electron optics has been devised for the purification of refractory insulating materials and their

growth into single crystals, starting with pressed or sintered powdered bars which do not have volatile components that would evaporate excessively at the order of $10^{-5}$ mm/Hg vacuum.

## ACKNOWLEDGMENTS

The authors have benefited by discussions with many members of CRW, by chemical analyses performed by CRWD, the fabrication of the device and modification of the MRC float zoning apparatus by the group shop under Mr. Walter Jackson and, particularly, by discussions with Dr. Walter Class, Materials Research Corporation, who was actively engaged on related work under AFCRL Contract No. AF19(628)-4089.

## REFERENCES

1. R. Bakish, Ed., Introduction to Electron Beam Technology, John Wiley and Sons, New York (1962).

2. H. W. Schadler, The Art and Science of Growing Crystals, ch. 17, pp. 343-364, J. J. Gilman, Ed., John Wiley and Sons, New York (1963).

3. M. S. Brooks, E. O. Fisk and B. Rubin, Semiconductor Products and Solid State Technology, 8, No. 12, p. 34 (1965).

4. I. Drangel and G. Murray, "Parameters pertinent to electron beam zone refining of refractory metals", presented at AIME meeting, New York (1964).

5. W. H. Bauer and W. G. Field, The Art and Science of Growing Crystals, ch. 20, pp. 398-407, J. J. Gilman, Ed., John Wiley and Sons, New York (1963).

6. L. Newman and R. A. Huggins, Rev. Sci. Instr., 33, pp. 433-434 (1962).

7. Materials Research Corporation, Rept. No. 463 - Qtrly. Rept. No. 4, Contract AF49(638)-1241, (1964).

8. Materials Research Corporation, Rept. No. 477 - Qtrly. Prog. Rept. No. 1, Contract AF19(628)-4089, (1964).

9. Materials Research Corporation, Final Rept. Contract AF19(628)-4089 (1966).

10. A. I. Somov, A. P. Svinarenko and A. G. Tyutyunnik, Izv. Akad. Nauk SSSR, Neorganicheskie Materialy, 2, No. 10, pp. 1892-1894 (1966)

11. J. E. Frederickson and W. R. Redanz, "Boran Nitride for Aerospace Applications", Union Carbide Corporation, New York (1964).

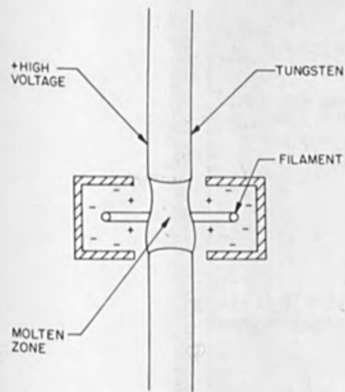


Figure 1. Typical Electrode Configuration for Zone Melting Metals

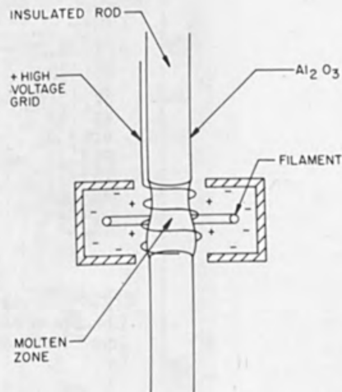


Figure 2. Accelerating Electrode for Zoning Insulators

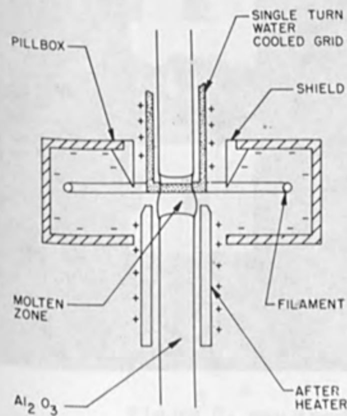


Figure 3. Sectional View of Cold-Grid and Afterheater Arrangement

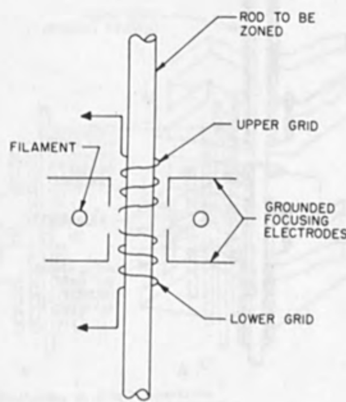


Figure 4. First Design of Shielded Split Grid

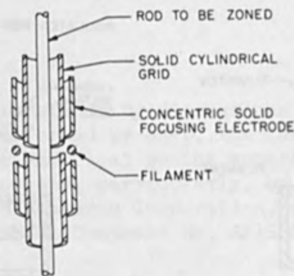


Figure 5. Sectional View Illustrating Concept of Solid Cylindrical Concentric Electrodes

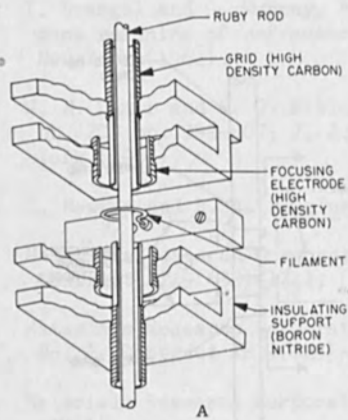


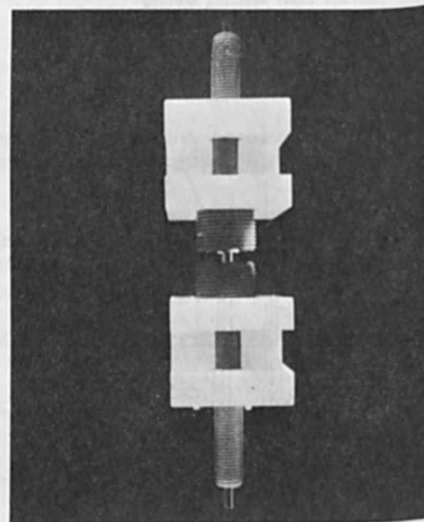


Figure 6. First Carbon-Boron Nitride Split Grid Electron Optical System for Zoning Insulators.

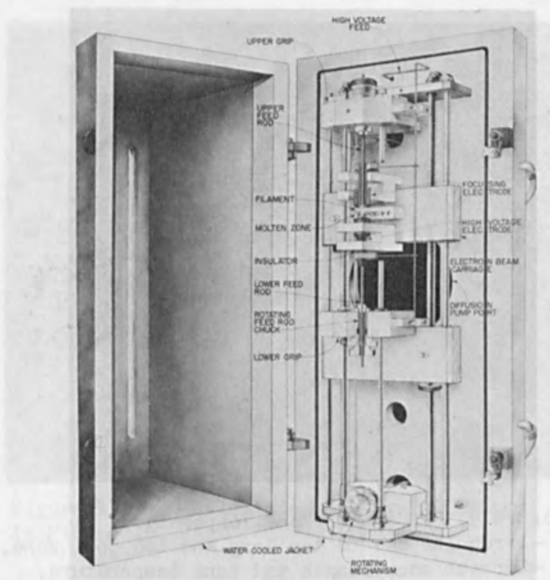


Figure 7. Illustrator's Sketch of New Electrode Structure Mounted in MRC Type EBZ-93A Electron Beam Zone Melting Furnace

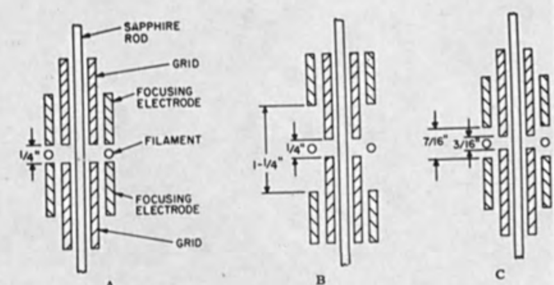


Figure 8. Effect of Varying Focusing Electrodes on Grid Temperature. A-Grid cool (<700°C). B-Grid hot (>1800°C). C-Grids normal (~1600°C)

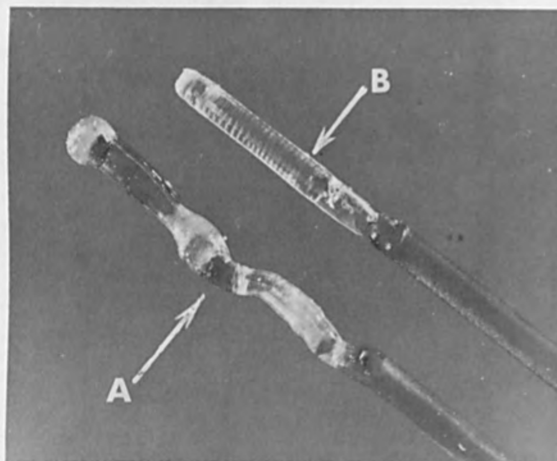


Figure 9. Effect of Zone Temperature.
A - Irregular due to too long and too cool zone.
B - Correct zone length and zone temperature.

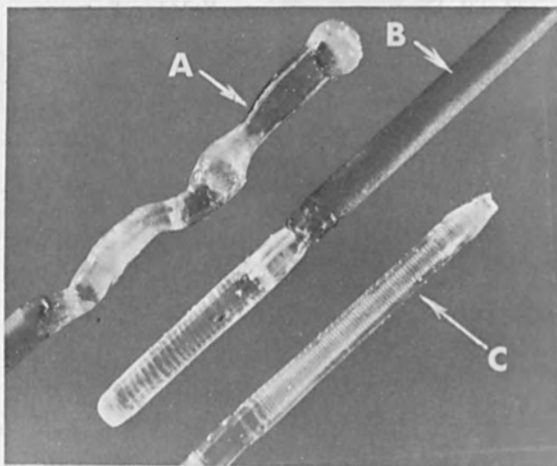


Figure 10. Influence of Mechanical Drive Adjustments or Striations and Veils in Crystals. A and B - Same as Figure 9A and 9B. C - Shows effect of mechanical adjustments on striations

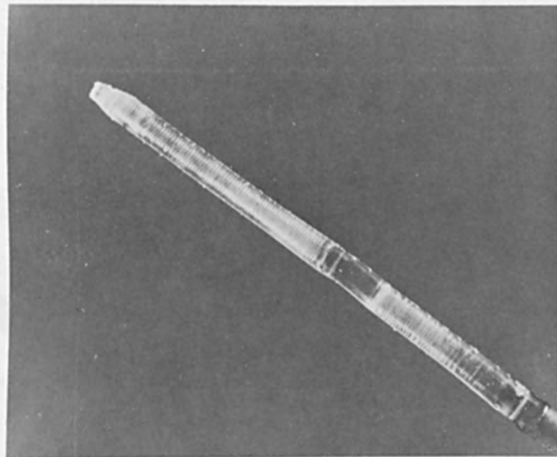

Figure 11. Detailed View of Crystal Shown in Figure 10C

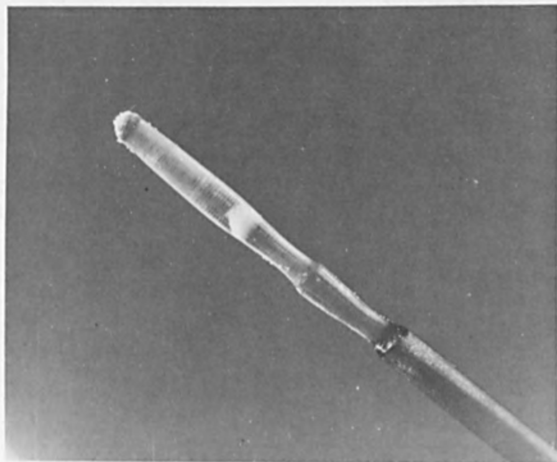

Figure 12. Effect of Growth Conditions on Crystal Diameter

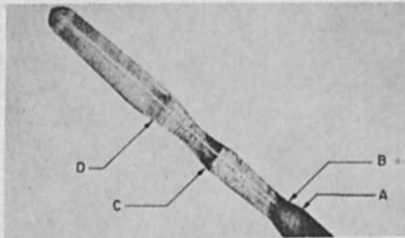


Figure 13. Sketch of Crystal Shown in Figure 12. A-Molten zone formed. B-Rotation and translation started. C-Molten zone diameter decreased by "jogging down" on lower grip (stretching zone). D-Molten zone diameter increased by "jogging up" on lower grip

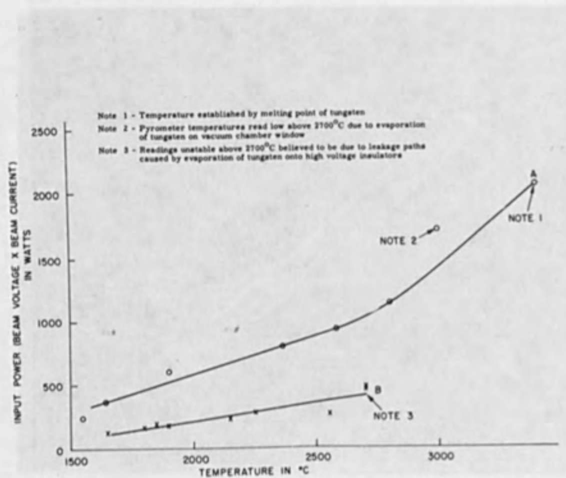


Figure 14. Input Power Versus Zone Temperature. Curve A-New electrode configuration for tungsten bar using concentric optics. Curve B-Standard electrode configuration for tungsten bar connected to high voltage with grids floating

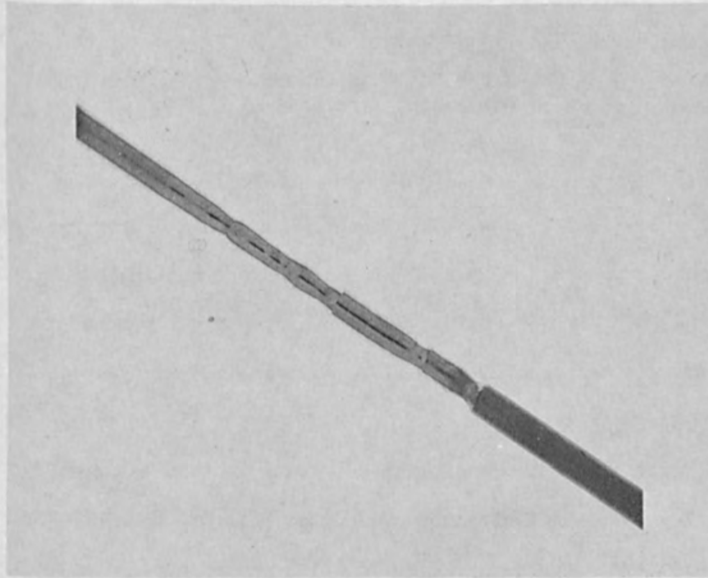

Figure 15. Tungsten Bar Welded and Zoned with New Electron Optics Configuration

SOURCES OF CONTAMINATION DURING ELECTRON-BEAM MELTING*

R. E. Reed
Solid State Division

C. W. Dean and R. E. McDonald
Metals and Ceramics Division

J. F. Emery
Analytical Chemistry Division

Oak Ridge National Laboratory
Oak Ridge, Tennessee

ABSTRACT

High-purity niobium was electron beam melted and drop cast at a furnace chamber pressure of $5 \times 10^{-6}$ torr. Before melting, a neutron activation analysis showed: 84 ppm Ta, 4 ppm W, and < 1 ppm hafnium. After melting, using a tantalum (T-111 alloy) emitter, the analysis showed: 564 ppm Ta, 50 ppm W, and 413 ppm Hf.

At first it was believed that the contamination was coming from the emitter. New batches of niobium were melted using niobium and thoriated tungsten emitters. However, all melts still showed considerable contamination. An investigation revealed that the contamination was being volatilized from the furnace walls by the radiant energy from the beam. After cleaning the chamber, another melt using a T-111 alloy emitter resulted in a metallic impurity content of 115 ppm Ta, 5 ppm W, and < 10 ppm Hf. The purpose of this paper is to show the various sources of contamination during melting and to illustrate the importance of keeping the furnace chamber clean.

*Research sponsored by the U. S. Atomic Energy Commission under contract with the Union Carbide Corporation.

## INTRODUCTION

In the production of high purity single crystals for basic research on the effects of neutron irradiation upon the physical and mechanical properties of niobium, it was necessary to have starting material low in Ta and W impurities. This was important for two reasons: (a) the electron beam floating zone technique used for the production of single crystals did not reduce the Ta and W impurity content[1]; and (b) the subsequent gamma emission after neutron irradiation of the samples was largely due to activation of the Ta and W impurities and hence low levels of radiation necessary for normal laboratory handling depended upon low Ta and W impurity contents.

The best starting material was found to be a dendritic powder produced by electrodeposition from molten salts.[2] This material could be obtained with Ta less than 100 wt. ppm and W less than 10 wt. ppm. However, the powder had to be consolidated into rod form for the electron beam floating zone technique.

The first method attempted was arc melting. The usual sources of contamination to metals melted in this manner are gases from the chamber atmosphere and materials from the mold and electrode. This may be minimized by having a vacuum tight chamber with a good vacuum pumping system, by using a high purity back fill gas, by using water-cooled copper molds that are frequently cleaned and etched, and by using electrodes which have tips made of high melting point materials. However, it was found that niobium drop castings produced by arc melting picked up both W and Ta from the electrode tip and striking peg respectively.[1]

The development of an electron beam melting furnace capable of drop casting high purity metals at ORNL[3] made it possible to consolidate the powder directly into rod form. It was expected that electron beam melting would produce an ingot with little Ta or W contamination. However, metallic impurities were introduced into the melt during this process. The purpose of this paper is to describe the amount and source of contamination of metallic impurities during electron beam drop casting of high purity niobium and to show how it can be minimized to acceptable levels.

## EXPERIMENTAL PROCEDURE

The electron-beam furnace used in this study was an original NRC Equipment Corporation design that had undergone considerable modification by ORNL. Although originally equipped with only one electron gun and one hearth, the furnace had been modified to accommodate two guns and double hearths. This latter configuration permitted two melts to be made without opening the furnace chamber. Hearth covers and manipulators had been installed to prevent the melt being made in one hearth from contaminating the melt in the other hearth. The modified furnace is shown in Fig. 1.

The original Varian electron beam guns, made for use on power clystrons, were modified to permit easy disassembly and assembly of the guns so that cathodes could be easily replaced. The Kovar seals were replaced with engineering flanges which could be bolted together, and a vacuum seal was maintained by the use of O-rings. Each gun column had a separate 4-inch "short series" diffusion pump which maintained column pressures of $5 \times 10^{-7}$ torr during melting. Figure 2 shows the gun components. The assembled gun is shown in Fig. 3.

The original cathodes had been replaced with "drop-in" type cathodes. These cathodes were approximately 1 inch in diameter and 1/8 inch thick with a highly polished concave face to aid in the initial focusing of the beam. A new and a used cathode is shown in Fig. 4. These easily removable cathodes were ameanable to conducting numerous studies of a research and developmental nature. Among these studies were: increasing cathode life by fabricating cathodes from different materials; increasing cathode life and efficiency by varying machining and lapping techniques; and studying amount of cathode contamination to melts.

A removable, interior water-cooled copper shield was fabricated to protect the furnace shell from radiant heat, metal splatters, and volatile impurities being evolved from the melts. This shield was easily removed from the furnace for cleaning. This feature was found to be highly desirable.

The niobium metal used in this study was a dendritic powder obtained from CIBA Limited, Basle, Switzerland. It was first dry compacted into disks. The disks were then placed on the water-cooled copper drop casting hearth in the electron beam furnace. This mold had a cavity to cast a 1/2-inch dia. rod, 5" long. After melting and drop casting at a furnace chamber pressure of $5 \times 10^{-6}$ torr, the ingots were sectioned in half longitudinally. Figure 5 shows such a polished and etched ingot section of a niobium drop casting using a niobium emitter. The other ingot half was further sectioned to obtain samples for neutron activation analysis for Ta, W, and Hf impurities. Samples were taken from the top, middle, and bottom of the as-cast rod plus some samples from the ingot "head".

Niobium powder was electron beam melted under the following conditions:

a. T-111 alloy (Ta base - 8 wt. % W, 2 Wt. % Hf) emitter, uncleaned chamber walls.

b. Thoriated W emitter, uncleaned chamber walls.

c. Niobium emitter, uncleaned chamber walls.

d. T-111 alloy emitter, all chamber components cleaned and etched.

Prior to melt conditions, a, b, and c, records showed that unalloyed Hf and a T-111 alloy had been melted in the furnace.

The niobium samples taken for impurity analyses were chemically polished with a mixture of $HNO_3$ and HF acids to remove any impurities from the cutting saw. The samples ranged in weight from 50 to 500 mg. The samples along with 20 μg W, 100 μg Ta, and 300 μg Hf were irradiated for 4 hours in the $D_2O$ tank of the Bulk Shielding Reactor. The thermal neutron flux in this position is $1.2 \times 10^{12}$ n/cm$^2$ sec. The samples were allowed to decay for 24 hours so any short lived impurities would not interfere in the analysis of Ta, W, and Hf.

The impurities Ta, W and Hf when exposed to a neutron flux undergo the following reactions:

1. $^{181}Ta\ (n,\gamma)\ ^{182}Ta$
2. $^{186}W\ (n,\gamma)\ ^{187}W$
3. $^{180}Hf\ (n,\gamma)\ ^{181}Hf$
   $^{174}Hf\ (n,\gamma)\ ^{175}Hf$

The above radioactive nuclides decay with their characteristic half life ($T_{1/2}$) by the emission of gamma-rays to stable nuclides. Table I

summarizes the nuclear data for each nuclide

Table I

Nuclear Data for Ta, W, Hf

| Radio-Nuclide | Type Decay | Stable Nuclide | Gamma Ray Energies (Mev) |
|---|---|---|---|
| $^{182}Ta$ | $\beta^-$ | $^{182}W$ | 1.13, 1.22, others |
| $^{187}W$ | $\beta^-$ | $^{187}Re$ | .48, .67, others |
| $^{175}Hf$ | K | $^{175}Lu$ | .34, others |
| $^{181}Hf$ | $\beta^-$ | $^{181}Ta$ | .48, others |

The gamma-ray spectrum of this mixture was obtained using a 40 cc lithium drifted germanium coaxial detector in conjunction with a 400 channel pulse height analyzer.

The spectra of the Ta, W and Hf standards were used as "library spectra", i.e., a pure spectra of the individual radioisotope with a known intensity (activity/gm), to analyze the sample spectra by a least-squares computer program, ALPHA.[4] ALPHA resolves the sample spectrum into the individual components, computes the concentrations and standard deviations. The input parameters required by ALPHA are the weights of the standards and samples, the counting time intervals, and the decay time of each sample.

## EXPERIMENTAL RESULTS

Table II summarizes the neutron activation results for the niobium material.

Table II

Neutron Activation Analyses

| Ingot No. | Melting Conditions | Number of Samples | Average Impurity Content in Weight ppm | | |
|---|---|---|---|---|---|
| | | | Ta | W | Hf |
| - | As Received Powder | 4 | 84 | 4 | ≦ 1 |
| T | T-111 Alloy Emitter;Uncleaned Chamber Walls | 16 | 564 | 50 | 413 |
| N | Nb Emitter Uncleaned Chamber Walls | 16 | 424 | 27 | 302 |
| W | W Emitter Uncleaned Chamber Walls | 16 | 477 | 25 | 287 |
| TC | T-111 Alloy Emitter Cleaned Chamber | 7 | 115 | 5 | ≦ 10 |

In addition, a small amount of Cu contamination was detected. This evidently came from the water cooled copper mold. Cu impurity contents from 2 to 40 wt. ppm were detected in the as cast ingot. It was predominately located on the outer surface of the casting since neutron activation samples with large amounts of original outer ingot surface area on them indicated the largest copper contents. The outer rim of the "head"

of the ingot tended to show the most copper contamination. The as-received powder had essentially no copper.

The ingots exhibited an equiaxed grain size. However, there were voids in the casting which evidently were caused by gas evolution during solidification. Small voids were present near the surface of the casting. Large voids approaching 1/4-inch in size were occasionally present in the center of the casting more frequently near the "head". Figure 5 shows some of these features.

DISCUSSION

The emitters used in the electron beam furnace did lose metal. A graphic illustration of this is Fig. 4 which is a picture of T-111 alloy emitters before and after using in the electron gun. This loss was on the order of a few grams total. Thus the emitter can be a source of metallic impurity contamination to the melt. However, the amount of contamination was small when you compare the as-received niobium powder analysis to the ingot analysis after melting with a T-111 alloy emitter in a clean chamber. About 30 ppm Ta, 10 ppm Hf, and 1 ppm W was transferred to the melt. The ideal case would be to use a niobium emitter to melt niobium in a clean chamber. However, it was found that the niobium emitter was partially melted under the conditions used in the earlier drop casting. Lower emitter temperatures would require higher voltages on the gun for the same power level.

A much more serious source of contamination was found to be metal deposited on the chamber walls from previous melts. In the furnace used in this study, melt records showed that prior to the niobium drop castings

two Hf and one T-111 alloy (Ta-8W-2Hf) melts had been made. A total weight loss of about 100 gm was noted. Thus the chamber walls had Hf, Ta, and W deposited in some form on the surface. Table II shows that the uncleaned chamber walls contributed about 400-500 ppm Ta, 300-400 ppm Hf, and 25-50 ppm W to the electron beam melted drop castings of niobium. The total weight of a drop casting was about 400 gm so this level of contamination meant a transfer of metallic impurities on the order of tenths of a gram.

The metallic impurities Ta, W, and Hf would not be expected to transfer in the metal vapor form since they all have rather low vapor pressures at the temperatures encountered in drop casting niobium. However, all three have very volatile monoxides. Table III is a compilation of calculated ratios of metal monoxide to metal vapor pressures at 2000°K as done by Smith _et al._[5] In fact, the weight loss noted in the prior melts of Hf and T-111 alloy may have been by the evolution of the monoxide form of these metals from the melt. Thus much of the chamber wall deposit was probably HfO, WO, and TaO. From Table III, the vapor pressures of the metal monoxides of Hf and Ta are $10^4$ larger than the metal while WO is $10^2$ larger than W. If it is assumed that the relative rate of vaporization of the metal oxide compared to that of the metal as calculated at 2000°K is independent of temperature, then it is evident that HfO, TaO, and WO are probably vaporized in appreciable quantities from the chamber walls during a melting operation.

Table III

Ratio of the Vapor Pressures of the Metal Monoxides to the Metal at 2000°K

| Metal | Ratio |
|---|---|
| Y | $10^5$ |
| Mo | $10^5$ |
| Hf | $10^4$ |
| Ta | $10^4$ |
| Th | $10^3$ |
| W | $10^2$ |
| B | $10^2$ |
| Zr | $10^2$ |
| Nb | 10 |
| Ti | 1 |
| V | $10^{-2}$ |
| Be | $10^{-3}$ |
| Cr | $10^{-4}$ |
| Mn | $10^{-5}$ |
| Fe | $10^{-6}$ |
| Ni | $10^{-7}$ |

How the metal monoxide would interact with the melt in order to introduce metallic impurities is not readily apparent. The presence of high temperatures, an electron beam, residual gases in the vacuum environment, and gas evolution from the melt all combine to form a complex system for chemical reactions. However, this study showed that removal of the prior

metal or metal monoxide deposits from the chamber walls and other components markedly reduced metallic impurity contamination of Hf, Ta, and W to electron beam melted drop castings of niobium.

## CONCLUSIONS

This study shows that melts may be contaminated by volatilizing material from furnace walls. In the case cited here, this material is probably in the form of volatile metal monoxides. Thus when high-purity melts are required, care must be taken to insure that the furnace chamber and associated components are clean. Since a small amount of contamination is picked up from the emitter, it should be made either of the same metal as that being melted, or of a high melting point material with a low electron emission temperature. Equipment should be designed for ease of cleaning and should have easily replaceable emitters.

## REFERENCES

1. R. E. Reed, "Electron Beam Floating Zone Refining of Niobium," Proceedings of the 2nd International Conference on Electron and Ion Beam Science and Technology, R. Bakish, Editor, Gordon and Breach Publishers, to be published 1968.

2. G. W. Mellors and S. Senderoff, "Electrodeposition of Coherent Deposits of Refractory Metals. I. Niobium," J. Electrochem. Soc. 112, 266 (1965).

3. C. W. Dean, R. E. McDonald, and C. F. Leitten, "High Purity Shape Casting with an Electron Beam Furnace," Record of the IEEE 9th Annual Symposium on Electron, Ion, and Laser Beam Technology, R. F. W. Pease, Editor, San Francisco Press, 1967, pp. 262-267.

4. E. Schonfeld, Oak Ridge National Laboratory Report, ORNL-3975, 1966.

5. H. R. Smith, C. d'A. Hunt, and C. W. Hanks, "The Development of Large Scale Electron Bombardment Melting and its Effect on the Composition of Metals and Alloys," in Reactive Metals, W. R. Clough, Editor, Interscience, New York, 1959, pp. 131-146.

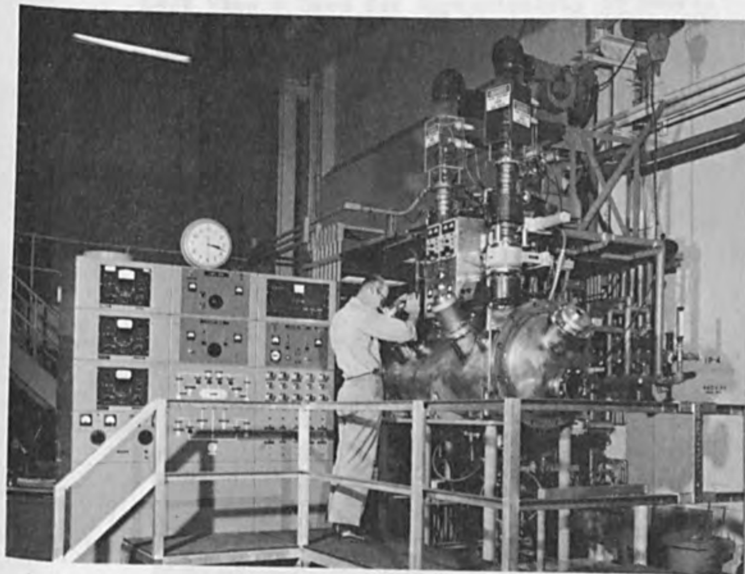

**Figure 1. Over-all View of the Dual Hearth Electron Beam Drop Casting Furnace.**

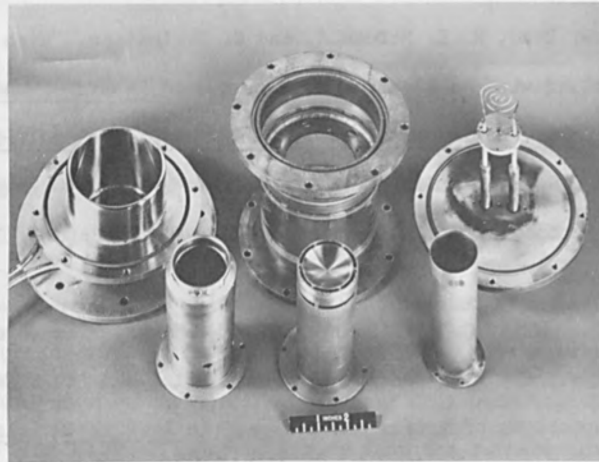

**Figure 2. The Electron Gun Disassembled to Show Component Parts.**

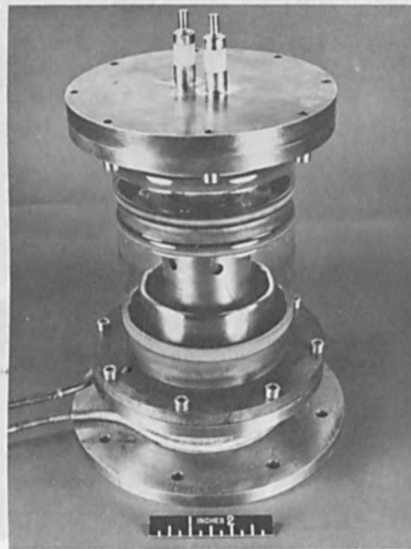

**Figure 3. The Electron Gun Completely Assembled.**

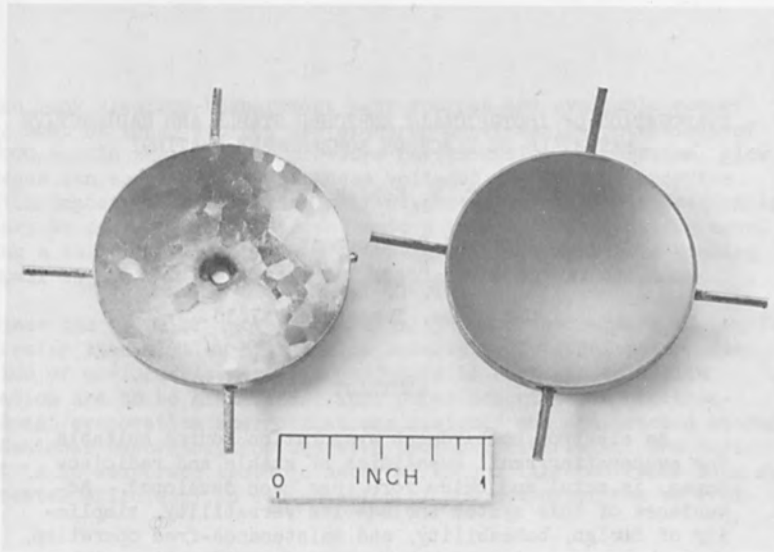


**Figure 4. A T-111 Alloy Replaceable Emitter: Right View - Unused; Left View - Used for Approximately 60 Hours.**

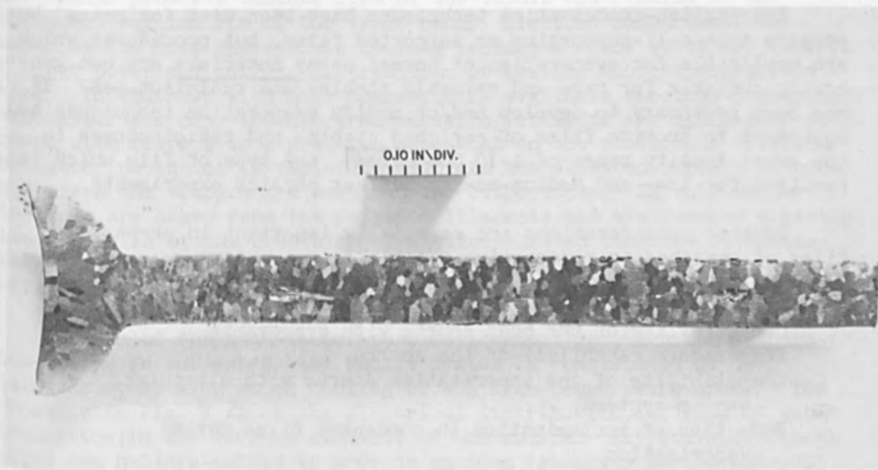


**Figure 5. A Sectioned and Etched Niobium Electron Beam Drop Cast Ingot Using a Niobium Emitter.**

# EVAPORATION OF ISOTOPICALLY ENRICHED STABLE AND RADIOACTIVE MATERIALS BY ELECTRON BOMBARDMENT HEATING*

H. L. Adair, E. H. Kobisk, F. R. O'Donnell

Isotopes Development Center
Oak Ridge National Laboratory
P. O. Box X
Oak Ridge, Tennessee 37830

## ABSTRACT

An electron bombardment evaporation source suitable for evaporating small quantities of stable and radioisotopes, in metal and oxide form, has been developed. Advantages of this system include its versatility, simplicity of design, bakeability, and maintenance-free operation. When the evaporation source is used in conjunction with a suitably designed crucible, a collimated vapor beam is obtained which allows efficient condensation of the evaporant on a substrate. Other applications of the evaporation source are described.

Evaporation-condensation techniques have been used for years[1] to prepare thin self-supporting or supported films, but procedures which are applicable for evaporation of normal assay materials are not generally suitable for rare and valuable stable- and radioisotopes. It has been necessary to develop and/or modify evaporation techniques and equipment to provide films of enriched stable- and radioisotopes in the areal density range of 1-10,000 $\mu g/cm^2$, the type of film which is required for low- and medium-energy nuclear physics experiments.

Several considerations are especially important in preparing films of enriched or radioactive materials:

Conservation of valuable isotopes,
Compatibility of the heat source with evaporants,
Temperature capability of the source,
Compatibility of the vaporization source with ultrahigh vacuum systems,
Reduction of contamination in condensed films during vaporization,
Low cost of equipment.

---

*Research sponsored by the U. S. Atomic Energy Commission under contract with the Union Carbide Corporation.

Although many electron-bombardment heat sources are available commercially, most of these sources use electron acceleration potentials of 4000-6000 v. In the event of pressure bursts during evaporation, glow discharges can occur readily at these voltages and will destroy the thin-film deposit. In preparing self-supported films, it is frequently necessary to condense the evaporant onto a water-soluble parting agent covering a solid substrate. Glow discharges can destroy this coating and impair separation of the condensed film from the substrate.

Since the value of isotopes is usually one or two orders of magnitude greater than similar high purity materials of normal assay, conservation of enriched isotopes is mandatory if costs in thin-film fabrication are to be minimized. This paper describes an electron-bombardment evaporation source that was designed and constructed at Oak Ridge National Laboratory for use with isotopic materials. The basic concept is to evaporate isotopic material as a collimated vapor beam so that greater efficiency in condensation of the evaporant can be realized.

## EVAPORATION SOURCE DESIGN

The source (see Fig. 1) is designed to produce vapor-beam collimation by evaporating small quantities ($<$100 mg) of material from a cylindrical crucible whose length is much greater than its inside diameter. This design promotes laminar flow of the vapors and results in the subsequent collimation of the vapor beam. Electron bombardment was chosen as the most appropriate heating technique since it offers control of input power and uniform distribution of heating along the crucible walls. In contrast with most commercially available electron-bombardment evaporation sources, the electron emission filaments are maintained at ground with respect to a positive potential on the conducting crucible. The latter potential is varied to regulate the electron current in order to achieve the temperature required for evaporation. In this manner electrons are drawn from the emission filaments and are focused directly onto the walls of the crucible. Resistance-heated tungsten filaments are employed, and electron acceleration potentials of 100-1000 v are sufficient to produce crucible temperatures up to 3000°C.

Because of the high-temperature environment to which the evaporation source is subjected, the entire system is constructed of 304L stainless steel with water cooling of all high-temperature areas. The schematic in Fig. 1 shows the electrical distribution and mode of water circulation in the various elements of the source. All stainless steel joints are heliarc-welded to provide maximum integrity during bakeout and evaporation. Bakeout temperatures of the evaporation source are limited only by the ceramic-to-metal braze joints (required for electrical isolation of the various conductors) which are beyond the mounting flange of the source. Experience has shown that bakeout temperatures exceeding 400°C will not damage the source.

Cooling water can be circulated through the tubes leading to the filament holders and the hearth. Coaxial tubes are used in the conductors (both water and electrical) leading to the filament holders. Since all electrical and water connections are made outside the vacuum system, this arrangement provides maximum flexibility for mounting and makes it possible to seal the source into the vacuum chamber by either elastomer or metal-to-metal seals. The evaporation source has been operated at vacuum levels of $10^{-10}$ torr.

Electrical power requirements are moderate, and a bridge-type full-wave mercury rectifier with 0-1000-v output is used (constructed at Oak Ridge National Laboratory using design shown in Fig. 1). Crucible heating requires electron currents of 0-3 amp between the emission filaments and the crucible. Solid-state rectifier components are not recommended for this system since occasional pressure bursts from impure evaporants can cause surges of electron current at two to three times the rated power of the rectification system. Unless overdesigned solid-state components are used, damage is immediate and permanent. Type 872A mercury rectifier tubes do, however, provide surge capabilities which are compatible with such bursts.

The most sensitive component of the evaporation source is the crucible. The crucible must be an electrical conductor and is most frequently fabricated from a high-melting-point refractory metal such as tungsten, tantalum, or molybdenum. (Carbon and platinum have also been used for this purpose.) If the crucible material is not compatible with the evaporant, the interior of the crucible can be coated with some refractory oxide, not necessarily an electrical conductor, so that a corrosion-resistant barrier is created. Ceramic liners of zirconia, magnesia, or thoria can be used, but the thermal gradient between the crucible wall and the liner (usually 300-700°C) requires that care be taken not to exceed the melting point of the refractory metal crucible while reaching the required evaporation temperature inside the liner. Contamination of vapor-condensed films can usually be held to $<100$ ppm by careful choice of materials for crucible construction.

As illustrated in Fig. 2, the electron-bombardment evaporation source can be mounted on quick-close flanges[2]. Use of these flanges (see Fig. 3) on glass-T evaporator systems provides an advantage for the preparation of radioisotope deposits. This entire vacuum system and evaporation source can be constructed for <\$1000 and, if unduly contaminated during use, it can be discarded without excessive capital loss.

## OPERATIONAL CHARACTERISTICS

In evaluating the evaporation source, the degree of vapor collimation was the main criterion. To examine this characteristic, the deposition of gold from a cylindrical tungsten crucible was compared

with a similar deposition from a flat, resistance-heated molybdenum filament. The tungsten crucible had a length-to-diameter ratio of 5.6 and was located 2 in. below a planar glass substrate onto which the gold vapors condensed. The same distance was employed for the flat vapor source. In both cases, a known quantity of gold was evaporated, and the thickness distributions of condensed gold on the glass plates were measured with a light microdensitometer.

Figure 4 illustrates the mass distribution on the flat substrates as a function of the distance from the center of the deposits. It is evident from the figure that an increased quantity of gold vapor was condensed using the cylindrical crucible. (The deposit resulting from crucible evaporation was calculated to be ~2.6 times greater at the center than that from the alternate source.) The quantity of material deposited was more localized about the intersection of the vertical axis of the crucible and the substrate than about a comparable intersection using the flat vapor source. There is less uniformity of deposition with the crucible source because of collimation (see Fig. 5), but conservation of the evaporant is achieved by this technique. Both of these effects increase as the length-to-diameter ratio of the crucible increases up to a value of at least 10. This characteristic is useful since most practical evaporations cover only a small area where, with proper choice of source-to-substrate distance, the beneficial features of the crucible source can be fully exploited. Rotation of the substrate in the collimated vapor beam permits larger areas to be coated uniformly.

The electron bombardment source is not limited to operation with cylindrical crucibles, but has been employed with many configurations which are required for unusual evaporation geometries. A boat-type tungsten crucible was used to evaporate $PuO_2$ onto the inside and outside of cylindrical substrates which were used in construction of a fission chamber (see Fig. 6). The evaporation boat was formed by Elox-cutting from a 1/4- x 3-in. tungsten bar. A hairpin configuration of the electron emission filament was used for good heat distribution down the length of the boat. Because of the small physical size, the entire heat source could be inserted into cylinders having an inside diameter of 0.75 in. When evaporating on the external surfaces of the cylinders, a tantalum heat shield surrounded the crucible and filament to restrict thermal losses by radiation since evaporation of $PuO_2$ requires temperatures of ~2400°C. Coatings having an areal density of 1 mg/cm$^2$ were achieved in this operation.

As can be seen in Figs. 1, 2, and 3, crucibles used in the electron bombardment source are mounted on a 0.040-in.-dia tungsten wire supported in the center of a water-cooled hearth. The purpose of this wire is to limit thermal conductivity and permit high temperatures to be attained at low power input. A crucible temperature of 2500°C was achieved with as little as 750-w input by using a tungsten crucible 1 in. long with an OD of 1/8 in.

The source design can be used with no modification for evaporation of bulk solids by placing them directly on the water-cooled hearth, a technique which is similar to that employed in commercially available sources. Figure 7 shows two $^{10}B$ pellets (prepared by pressing powdered elemental boron) before and after evaporation by electron bombardment. In this case, boron was evaporated from a molten pool in the center of the pressed pellet. The electron source was a circular, pure tungsten filament (formed in a single turn) with a diameter which was two-thirds the diameter of the pellet to be evaporated. The only contamination in the resulting film was that introduced by the tungsten filament and the vacuum environment.

The electron bombardment heater can also be used for melting refractory metals to form homogeneous beads suitable for cold-rolling into thin foils. Molybdenum isotopes in 20- to 100-mg quantities have been melted into homogeneous masses directly on the hearth of the electron source. Successive rotation of the resulting bead permits complete melting, but less than half the mass is melted at any one time. Contamination from the hearth as a result of this operation does not exceed 100 ppm. "Beaded" metals formed in this manner have excellent ductility and malleability as a result of the reduction in occluded contamination, especially gases such as oxygen and nitrogen.

## SUMMARY

An electron-bombardment heat source was developed at Oak Ridge National Laboratory for the preparation of thin films of isotopic materials by vacuum evaporation-condensation techniques. The unit can produce evaporation temperatures up to 3000°C, and, when used with a cylindrical crucible, the efficiency of evaporation-condensation is greater than that obtainable from a flat-filament heat source. The advantages of low-cost construction and vapor collimation make this unit practical for thin-film preparations using expensive stable- and radioisotopes. Electron acceleration voltages of <1000 v permit the source to be operated at vacuum levels as low as $5 \times 10^{-4}$ torr without glow discharge. Since crucible and filament designs can be changed at will, the unit has versatility in coating unusual surface geometries. The stainless steel and ceramic materials used in construction enable the vapor source to be used in ultrahigh vacuum systems ($10^{-10}$ torr) with bakeout temperatures in excess of 400°C. The small size of the vapor source permits its use in almost any type of vacuum chamber with only minimum modification of the system. Between a few tenths of a milligram and 20 g of material can be evaporated efficiently, and contamination of the condensed film does not exceed 100 ppm.

## REFERENCES

1. L. Holland, Vacuum Deposition of Thin Films, John Wiley and Sons, Inc., New York, 1958.

2. Bendix-Balzers Vacuum, Inc., Bulletin Micro-BA 3, Blank BA 3 Flange, p. 4.


ORNL-DWG 68-5164

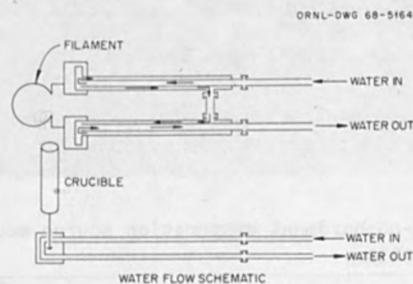


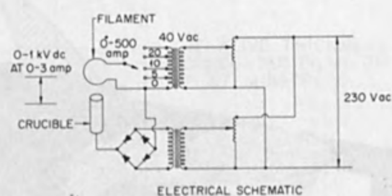


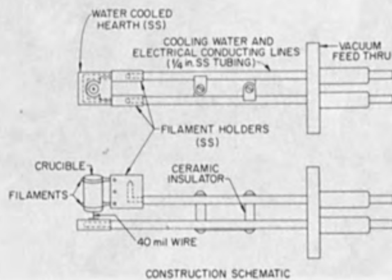


Electron Bombardment Evaporation Source.

Fig. 1. Electron-bombardment evaporation source schematic.

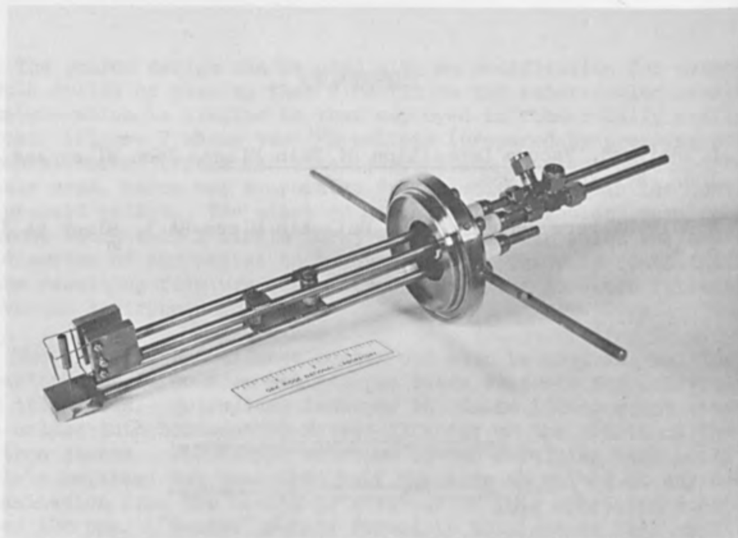

Fig. 2. Electron-bombardment evaporation source mounted on a quick-close flange.

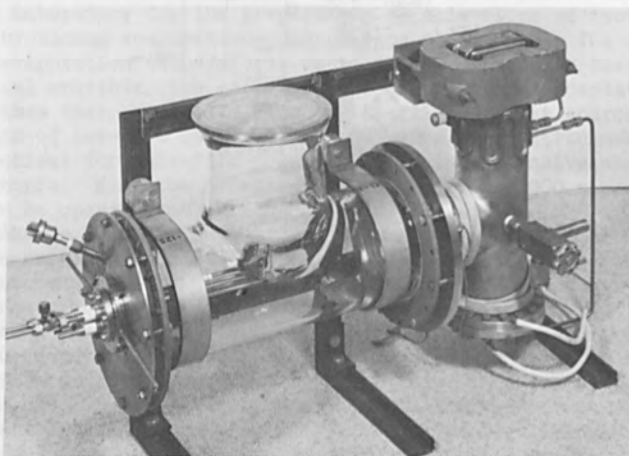

Fig. 3. Glass-T evaporator system with the electron-bombardment evaporation source mounted on a quick-close flange.

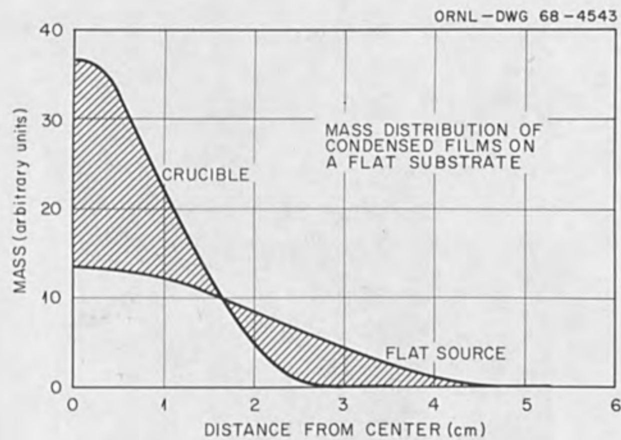


Fig. 4. Mass distribution of gold films condensed on a flat substrate 2 in. above a cylindrical crucible (L/D = 5.6) and a flat filament source.

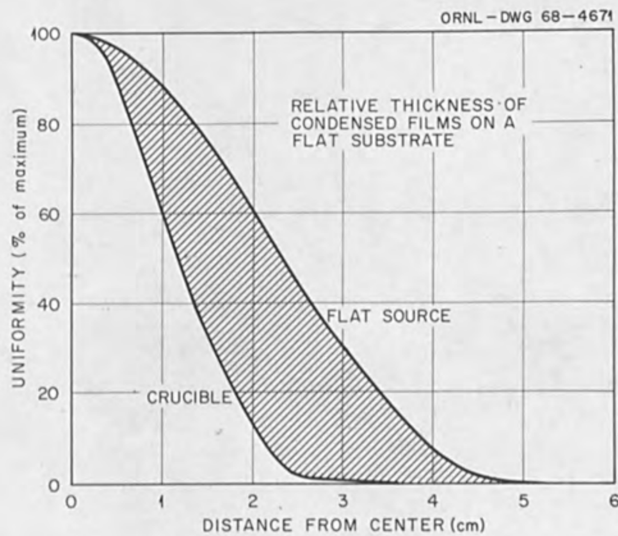


Fig. 5. Relative thickness (compared with center of deposit) of gold films condensed on a flat substrate 2 in. above a cylindrical crucible (L/D = 5.6) and a flat filament source.

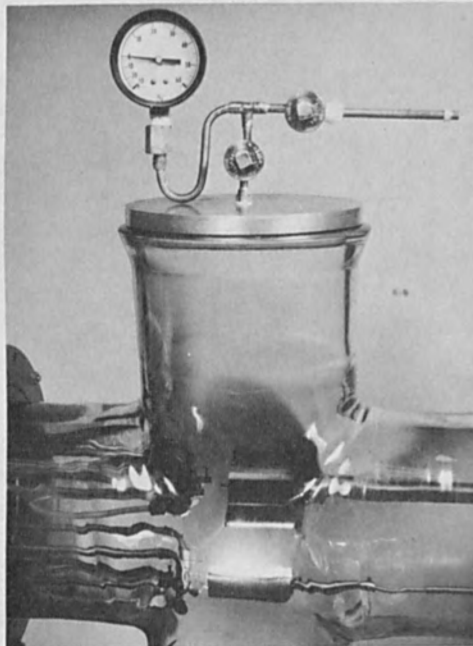

Fig. 6. Evaporation-condensation of $PuO_2$ onto a cylindrical titanium substrate.

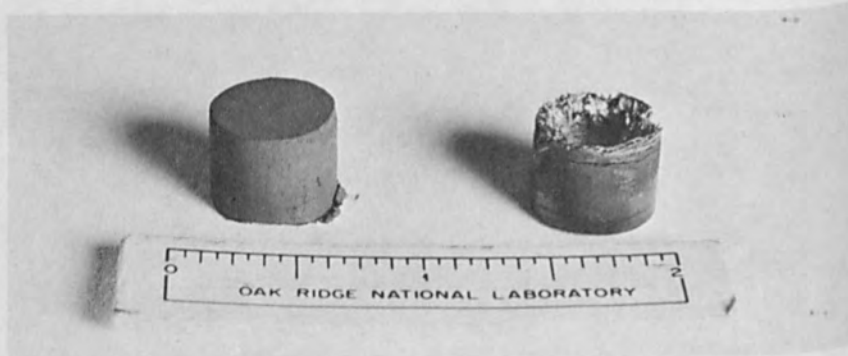


Fig. 7. Boron-10 pellets before and after evaporation by electron bombardment.

# APPLICATION OF VAPOR DEPOSITION TECHNIQUE IN THE METALLURGICAL INDUSTRY

**S. Schiller, H. Förster, P. Lenk, and B. Wenzel**
**(Forschungsinstitut Manfred von Ardenne, Dresden/GDR)**

## 1. Introduction

A number of institutions **have**, in the past several years, worked in the field of coating continuous strips by means of vapor deposition of aluminium [1,2,3]. The development of high power electron beam guns made it possible, to face the realization of industrial plants, for only with these guns one can achieve the deposition rates necessary for large scale production.

The advantages of strip coating by electron beam vapor deposition have been repeatedly reported in the past, also at the Second International Conference on Electron- and Ion beam-Technology in New York [1].
This presentation deals with the efforts, which have been realized according to this problem at the Manfred von Ardenne Research Institute in close cooperation with VEB LEW Hennigsdorf and VEB Stahl- und Walzwerk Hennigsdorf (GDR).

## 2. The Principle of Strip Processing

Figure 1 shows for remembrance the schematic drawing of an industrial processing line for electron beam vapor deposition. A vapor deposition installation includes various functional elements, which are in the same form constituent part of tin coating lines.

One important requirement for oeconomic production is the continuous operation of the plant.

Figure 1 shows the reel, the cutting and the welding equipment in front of the storing section.

We know from experiments, that a reproducible cleaning is the basic demand for the production of commercial aluminium vapor deposited steel strip.
We have used electrolytic cleaning followed by pickling.

After washing and drying the strip passes a lock system with rolls, enters the vacuum part of the line, consisting of a preheating chamber and the deposition chamber, and leaves it through a second lock system similiar to the inlet system. Just here have to be considered higher temperatures.

It has been experienced, that the strip should to be cooled before it rolling up, since its temperature reaches 300°C and more, dependent on strip thickness and layer thickness. This cooling is followed by the exit storing section.

## 3. The Employment of Axial Electron Guns for strip heating and vaporisation

### 3.1 The Electron Guns

It may be mentioned, that those firms are busy with the development of aluminium vapor deposition plants, which have employed high power electron beam technology for melting and casting. There have been used mainly transverse gun systems for strip heating and deposit material vaporisation. [1,2] The Research Institut Manfred von Ardenne employs axial guns for both heating and vaporisation.

We have developed axial gun systems in the power range from 5 kW to 1200 kW, applicable for vaporization and melting [4,5].

The scheme of an electron beam gun of the power of 60 kW is to be seen in figure 2.[6]

The beam generating chamber is evacuated by an oil diffusion pump of 500 l $s^{-1}$. Between this generating chamber and the process chamber an intermediate chamber is placed, which enables the functionship of the beam generating system up to pressures of $10^{-2}$ Torr in the process chamber. The chambers are connected by water cooled copper tubes, the

diameters of which fit the beam diameter.

Figure 3 shows the practical performance of a gun of 60 kW electrical power.

### 3.2 Preheating station

The pressure at the preheating chamber is about $10^{-3}$ Torr during line operation. The strip is heated up in the range of 150°C to 300°C in this chamber in order to obtain a good adherence of the Al.

In the case of axial guns the beam is time linearly oscillated over the whole strip, perpendicular to the strip motion. For equal temperature distribution over the steel strip width the frequence f of oscillation must not exceed a lowest limit:

$$f \geq k \cdot \frac{v_{[mm\ s^{-1}]}}{d_{F[mm]}} \qquad [s^{-1}] \qquad (1)$$

There means

k a form faktor, taking into consideration the inhomogeneous power distribution over the beam cross section, which is commonly chosen of the order 5 to 10,

v the strip speed,

$d_F$ the beam diameter direct on the strip.

Because of the width of the electron beam cross section and because of the deviations from time linear behavior at the turning points the amplitude of the oscillating beam must be greater than the strip width. Out of the strip the beam power is absorbed by water cooled areas. These facts and the consideration of the back diffusion of beam electrons result in an efficiency of the preheating power of about $\eta$ = 0,7.

In a typical example one has:
Strip width $b = 400$ mm, strip thickness $d = 0{,}3$ mm, preheating temperature $t_v = 300°C$, strip speed $v = 2000$ mm $s^{-1}$ and in consequence beam power $p = 500$ kW.

Between the preheating chamber and the processing chamber there occurs only a little temperature lowering by thermal radiation, because of the distance is just some m and the strip speed is about several m $s^{-1}$.

3.3 <u>About our deposition station</u>

In the processing chamber the strip passes two deposition stations, where one after another both sides are to be coated. Each deposition station consists of a single electron beam gun, the magnetic deflection and the magnetic turning system for the electron beam, and the crucible for the evaporant.

Figure 4 shows a possible arrangement with an axial gun. The beam is shot horizontally between the crucible and the strip and is turned to the evaporant material by magnetic deflection. In order to get a controllable beam power distribution at the surface of the evaporant, especially in the case of larger strip width, the magnetic field is produced by separated pol pieces, being driven by a suitable program.

Figure 5 demonstrates theoretical deposit distributions on the steelstrip, resulting from different beam power distributions in the crucible. The strip width is 400 mm, the distance between the crucible and the strip 200 mm. Diagramm a shows the distribution, if you have a constant temperature over the whole surface of the evaporant, in diagramm b you see the layer thickness distribution, produced by four point sources, whereby the outside sources have double the richness than the inside sources.

Since the duration of the electron beam on a place determines the richness of vapor production at this place, the deposit distribution may be corrigated by the beam deflection program.

The experimentally obtained layers are more uniform than theoretically predicted. This is explained by deviations from the Lambert characteristic at higher pressures of some torrs, which pressures occur directly over the evaporant material.

The necessary surface temperatures of the aluminium range from 1400°C to 1500°C.

Because of the thermal contact between the aluminium and the water cooled crucible is good, hot crucibles are to be used, as thesehave a thermally isolating effect. Aluminium is very aggressiv at these high temperatures and only special ceramic materials have the required resistance.

Theoretically one needs an energy input of $e = 2{,}5$ kWh kg$^{-1}$ for heating the aluminium up to 1500°C. The real values for the energy input are $e = 6 \ldots 12$ kWh kg$^{-1}$.

The discrepancy is as well due to losses by thermal radiation and thermal conduction as due to the back diffusion of beam electrons from the aluminium.

Figure 6 is a photograph of an experimental installation for handling 100 mm wide steelstrips. It has only one deposition station with an axial gun of 60 kW.

Figure 7 shows the model of a large scale production plant for handling of 400 mm wide steel strips. There are used two axial guns, each with 250 kW, for heating and two guns of 250 kW for evaporation.

By thermal radiation from the crubibles and by the sublimation heat of the coating a temperature rise of the steel strip results.

Figure 8 is a schematic diagramm of the progress of temperature in the deposition plant.

4. Results of the technological investigations

The above mentioned experimental installation at the Manfred von Ardenne Research Institute serves to perform technological investigations, in collaboration with the VEB Stahl- und Walzwerk Hennigsdorf. These investigations aim at the best processing parameters. Criterions for comercial application are for instance tests of food ware industries.

In the packing industries the aluminium deposited steel strip has to withstand strong mechanical stresses, when used for production of packing, whereby the aluminium depositimust not burst off.

Figure 9 is the photograph of a bottle lid with sharp coinings. Our aluminium vapor deposited steel strips withstand these deformations without burst off.

Figure 10 shows other packings, produced of aluminium vapor deposited steel strip.

We have found, that the aluminium deposited steel strip withstands the mechanical stresses but not the chemical food tests, when the deposition parameters are not exactly kept. For this purpose special conditions are to be kept.

5. Conclusion

The achieved results allow the conclusion, that aluminium vapor deposition will be a competitive process in comparision to the processes used up to now.

The difficulties, the firms in the field have to overcome yet presently, are to be regarded as naturally.
Further investigations will show, to which extent vapor deposition as production technique can be employed.

The authors are indebted to Professor Dr.h.c. Manfred von Ardenne for his special support of this work and for stimulating discussions.

References:

[1] SMITH,H.R. and HUNT,C.D.A.:
Advances and the Future of Electron Beam Processes.
II. Intern.Conf. on Electron and Ion Beam Technol., New York, April 1966

[2] REICHELT,W.; DIETRICH,W.; HAUFF,A.:
Das großtechnische Aufbringen von Schutzschichten auf Stahlbändern durch Bedampfen im Vakuum
Metalloberfl., 20 (1966) p. 474-478

[3] von ARDENNE,M.; SCHILLER,S. and FÖRSTER,H.:
On problems of Industrial-scale Electron Beam Vaporization
Int.Z.Elektrowärme 25 (1967) p. 216-218

[4] von ARDENNE,M.:
Tabellen der Elektronenphysik, Ionenphysik und Übermikroskopie
Dtsch. Verlag d. Wiss., Bd.2, Berlin 1956

[5] von ARDENNE,M.; SCHILLER,S.; LENK,P.:
Electron Guns with Powers of between 5 kW and 1200 kW and Their Technical Applications
Kernenergie 1968 (to be publ.)

[6] SCHILLER,S.; FÖRSTER,H.; LENK,P.; SCHMIDT,K.; ALTMANN,W.:
Ein neuer 60-kW-Elektronenstrahlmehrkammerofen.
Elektrie 20 (1966) p. 60-63

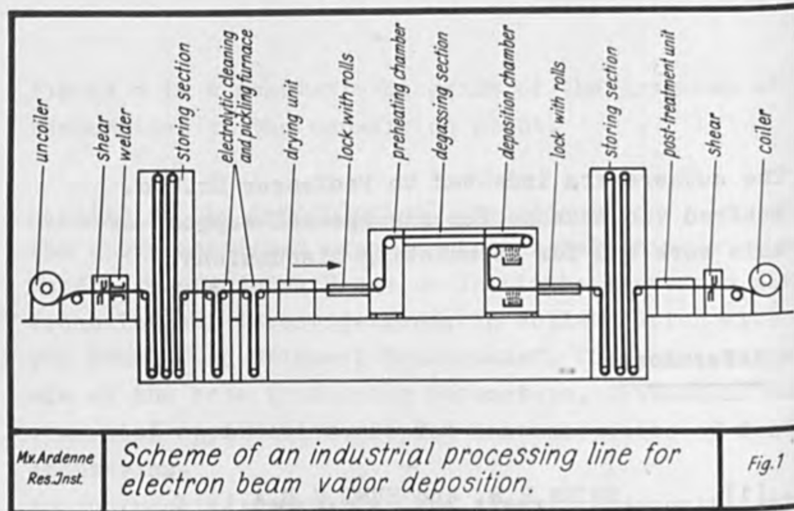

Scheme of an industrial processing line for electron beam vapor deposition.

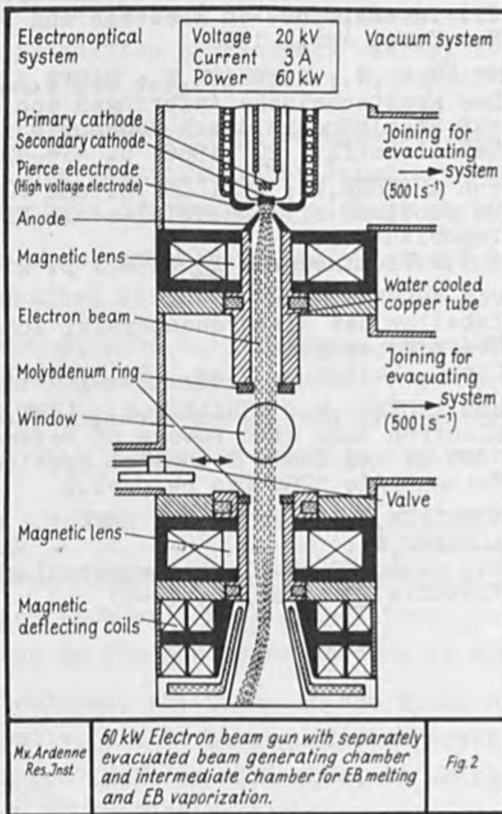

60 kW Electron beam gun with separately evacuated beam generating chamber and intermediate chamber for EB melting and EB vaporization.

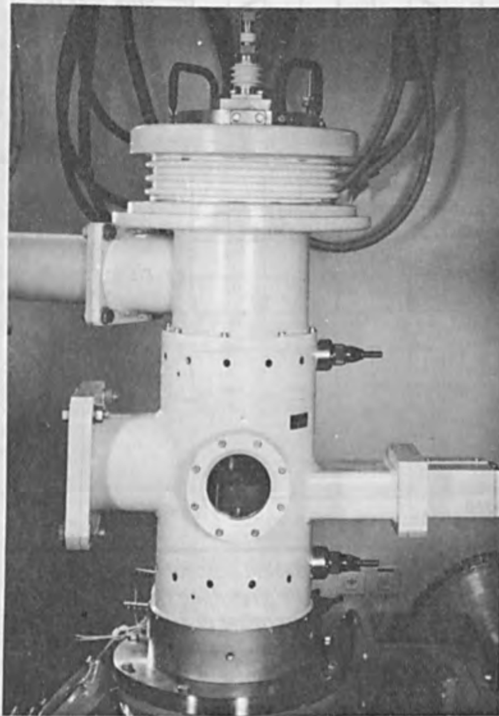

Fig. 3: Practical performance of a 60 kW electron beam gun

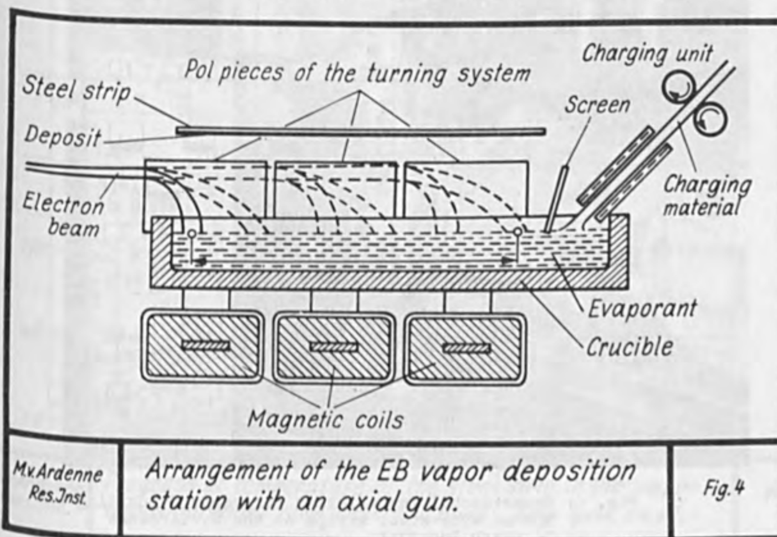

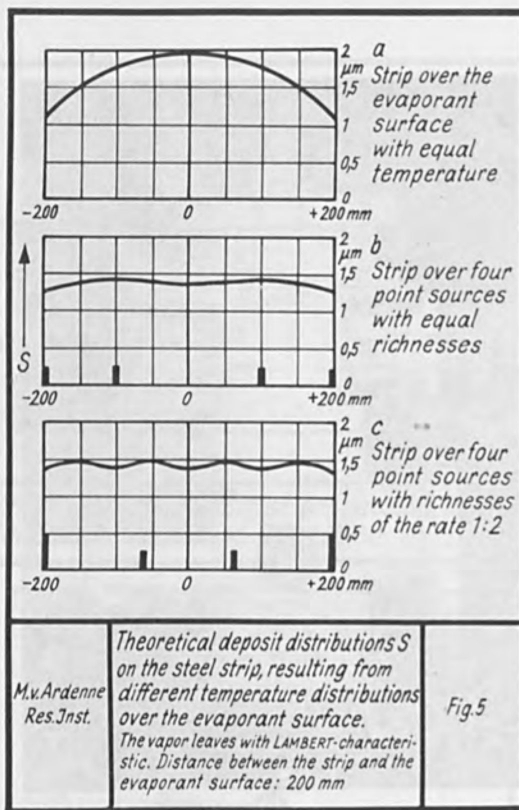


Theoretical deposit distributions S on the steel strip, resulting from different temperature distributions over the evaporant surface.
The vapor leaves with LAMBERT-characteristic. Distance between the strip and the evaporant surface: 200 mm

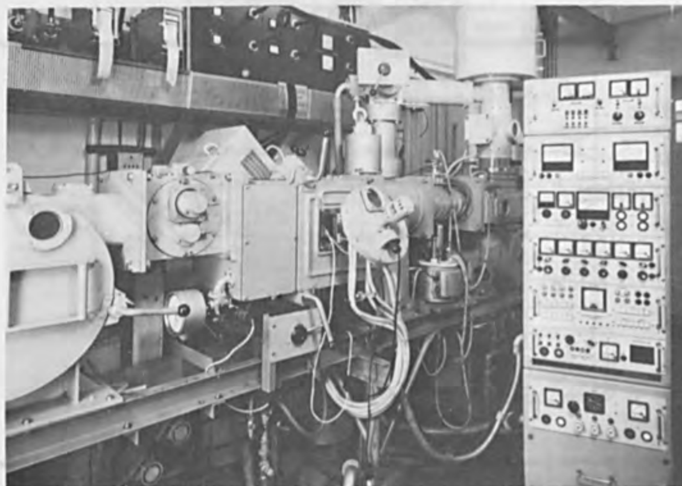

Fig. 6: Experimental installation for vapor depositing 100 mm wide steel strips at the M.v.Ardenne Research Institute

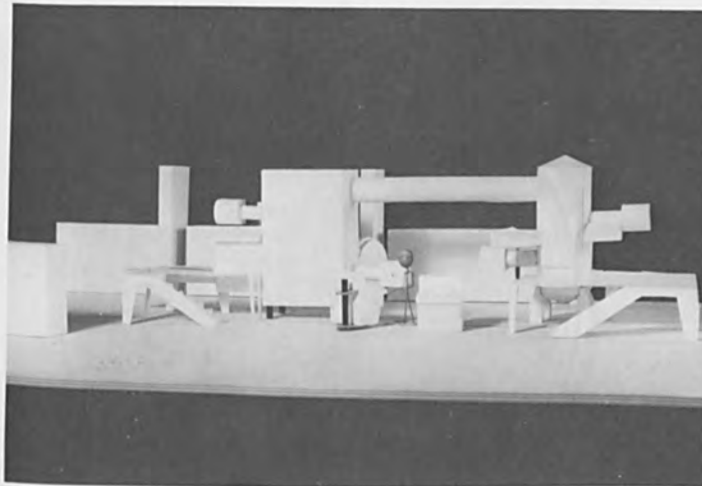

Fig. 7: Model of a large scale production plant for vapor depositing 400 mm wide steel strips;
Maximum EB input for preheating: 2 x 250 kW
(Two axial guns with time linear deflection perpendicular to strip movement)
Maximum EB input for vaporization: 2 x 250 kW
(Two axial guns with programmed deflection).

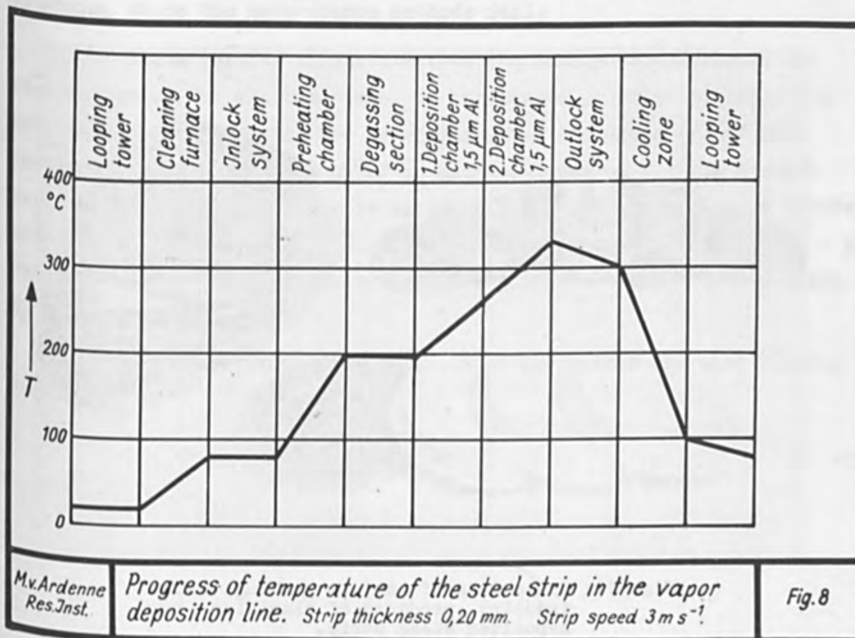


Progress of temperature of the steel strip in the vapor deposition line. Strip thickness 0,20 mm. Strip speed 3 m s$^{-1}$.

Fig. 9: Bottle lid with sharp coinings from aluminium vapor deposited steel strip. There occures no burst off.

Fig. 10: Collection of various packings for industry, produced of aluminium vapor deposited steel strip.

MEASURING THIN ALUMINUM COATINGS ON STEEL
BY MEANS OF AN ELECTRON PROBE

Eldon L. Keller and Berthold W. Schumacher
Westinghouse Research Laboratories
Pittsburgh, Pennsylvania 15235

ABSTRACT

Coating thickness measurements can be effected by detecting characteristic X rays produced in the substrate material by an electron beam which penetrates the coating. The lowest electron energy at which X rays are detectable ($E_o$) is indicative of the energy loss in the coating and can be combined with the range-energy relationship for electrons in matter to yield the coating thickness. An experiment, designed to be demonstrative in scope, was conducted and extends the readily measurable thicknesses to the sub-mg/cm$^2$ range, i.e., 0.13 to 0.78 mg/cm$^2$ of aluminum, where the more-common methods fail.

These results illustrate that the energy dependence of the stopping power for electrons must be considered in order to apply the range-energy relationship for determining the thickness (X) of thin coatings from the measurement of $E_o$ and knowledge of $E_K$, the K-shell binding energy of the substrate material. The thickness is more accurately given by $X = R(E_o) - R(E_K)$, R being the range, rather than $X = R(E_o - E_K)$ which is a useful approximation only for thick coatings or cases where $E_K$ is negligible.

The sensitivity and precision of the method are also briefly discussed.

## INTRODUCTION

The recent advances in electron beam and probe technology, particularly atmospheric microprobes,[1] have led to considerations of their application to thickness gauging problems. Specifically, Schumacher and co-workers[2-5] devised a method for measuring plating, or coating thicknesses by directing an electron beam of variable energy at the sample and determining the electron energy ($E_o$) at which characteristic X rays are produced in the coating substrate. Because a minimum energy equal to the K-shell binding energy ($E_K$) must be delivered by each transmitted electron to the substrate material in order to produce these X rays, ($E_o$ - $E_K$) is the energy lost in traversing the coating and this is a sensitive function of the coating thickness because of the well-known range-energy relationship for electrons in matter.[6,7]

Kriegler and Schumacher[3] demonstrated the method for 1.1 to 3.4 mg/cm$^2$ (0.05 to 0.15 mil) coatings of nickel on iron and also for chromium-plated nickel. Very thin coatings on glass, working with visible fluorescence rather than X rays ($E_K$ being therefore negligible), were measured by Schumacher and Mitra.[4] The method was also shown to be applicable to multiple coatings. This paper presents experimental results which extend the range of coating thicknesses to 0.13 to 0.78 mg/cm$^2$, i.e., 0.019 to 0.11 mil of aluminum on steel using Fe X rays from the steel substrate. The results demonstrate the feasibility of the

---

*Paper to be presented at the Third International Conference on Electron and Ion Beam Science and Technology, May 6-9, 1968 in Boston, Massachusetts.

method for this range of thicknesses which cannot readily be measured by other methods; a critical evaluation was not intended.

## EXPERIMENTAL TECHNIQUE

The experiment was conducted using an electron probe microanalyzer equipped with a non-dispersive flow proportional counter. The detector subtended a solid angle of ~ $3 \times 10^{-3}$ sr at the beam spot on the sample. Standard pulse counting electronics together with a 400-channel pulse height analyzer were used to monitor the yield of Fe and Al $K_\alpha$-X rays emitted from the samples in a reflection geometry (see Figure 1). Measurements were made at 7.5-keV intervals for electron energies between 7.5 and 45 keV on Al vacuum depositions 0.13, 0.27, and 0.78 mg/cm$^2$ thick as determined interferometrically. All data were obtained with 30-sec integrations and an electron current of $8.7 \times 10^{-9}$A. Typical pulse height spectra are shown in Figure 2.

## EXPERIMENTAL RESULTS

The data are shown in Figure 3. Even though the number of datum points is limited, a linear yield curve can be readily fit to each set. Extrapolations to zero yield defines $E_o$ of 22.5, 14.0, and 11.1 keV for Al thicknesses of 0.78, 0.27, and 0.13 mg/cm$^2$, respectively. Some of these data are shown replotted in Figure 4 as a function of thickness for two electron energies. Again a linear fit is applicable, notwithstanding the limited data. The slopes of these curves, $1.3 \times 10^5$ and $1.2 \times 10^5$ counts/mg cm$^{-2}$ for E = 30 and 35 keV, respectively, are indicative of the sensitivity of the method. It is particularly important to note that it is <u>not</u> necessary to measure absolute X-ray intensities since an extrapolation to zero X-ray signal (and the related electron beam energy) is made.

## DISCUSSION OF RESULTS

A first approximation to the coating thickness as calculated using the range-energy relationship consists of obtaining the range (R)

for the energy difference $(E_o - E_K)$, as this is the energy loss of the electrons in the coating. This approximation is useful for thick coatings on steel for which $E_o \gtrsim 200$ keV and thicknesses $(X) \gtrsim 50$ mg/cm$^2$. Because the stopping power for electrons in solids is energy dependent, the more nearly correct expression for the coating thickness is

$$X = R(E_o) - R(E_K). \quad (1)$$

An absolutely correct expression would have to take into account the fact that at $R = X$ the electrons are no longer monoenergetic (as they originally were). But this may be considered a second-order correction, and electron scattering theory is presently not even good enough to derive a value for this correction.

Numerical values for the electron stopping power were tabulated by Berger and Seltzer[8] and can be approximated by

$$dE/d\xi = 0.95 \times 10^5 \ E^{-0.7} \quad \text{keV/gcm}^{-2}, \quad (2)$$

where E is in keV units and $\xi$ represents the true electron path length (for a fuller discussion, see Schumacher[7,9]). This expression could be integrated from the initial electron energy to $E_K$, but this would leave us with the above-mentioned second-order correction because of electron scattering. By working with the range values $R(E_o)$ and $R(E_K)$, we have implicitly taken care of the integration and some of the corrections for scattering. A comparison of Equation 1 and the $R(E_o - E_K)$ approximation is shown in Figure 5. This vividly illustrates that this approximation is quite useless for thin coatings and high values of $E_K$.

The use of Equation 1, the experimental $E_o$ values, and $E_K = 7.11$ keV yields X = 0.80, 0.26, and 0.13 mg/cm$^2$ for the 0.78, 0.27, and 0.13 mg/cm$^2$ Al coatings, respectively. This agreement is very good and is indicative of the inherent potential of this electron probe, range-energy method.

From Figure 4 we can obtain an estimate of the precision with which the thickness can be determined. The 30-keV data, for example, are described by a slope of $1.3 \times 10^5$ counts/mg $cm^{-2}$. At 0.13 mg/$cm^2$, the number of Fe X-ray counts (c) is 139,000 and the statistical uncertainty ($c^{1/2}$) is 372 counts. This uncertainty, when combined with the slope, corresponds to a thickness uncertainty of $372/1.3 \times 10^5 = 0.00286$ mg/$cm^2$, or a statistical precision of 2.2% for the 0.13 mg/$cm^2$ coating. The precision improves with increasing coating thickness where $E_K$ is a smaller fraction of $E_o$; it is 0.23% at 0.78 mg/$cm^2$. If we could use the Fe L - X rays ($\lambda = 14.6$ Å) with $E_L = 0.85$ keV, the accuracy for thinner coatings would increase, provided the x-ray absorption in the aluminum is not excessive and dominant.

A considerable flexibility is available for improving the speed and/or precision of this thickness measurement. Recall that the present results were obtained using an electron probe current $I_e = 8.6 \times 10^{-9}$ A, an X-ray detector $\Omega$ of $\sim 3 \times 10^{-3}$ sr, and t = 30 sec. For this type of measurement, $I_e$ could be increased by four orders of magnitude and $\Omega$ by a factor of ~10. Consequently, the measurement time could be decreased substantially, in keeping with the coating thickness of interest and the desired precision. The method is therefore potentially capable of fast-response thickness monitoring for aluminum on steel in a continuous plating mill.

## CONCLUSIONS

The present experiment has adequately demonstrated that the electron probe, range-energy gauging method is useful for measuring coating thicknesses in the sub-mg/$cm^2$ range, even on a non-transparent metallic base. The speed and precision should be adequate for a wide variety of applications. Because the method is perfectly general and can be applied for microspot sampling, a wider implementation is undoubtedly foreseeable.

## REFERENCES


1. B. W. Schumacher, Optic 10, 116 (1953).
2. B. W. Schumacher, Canadian Patent No. 665, 613 (June 25, 1963).
3. R. Kriegler and B. W. Schumacher, Plating 47, 393 (1960).
4. B. W. Schumacher and S. S. Mitra, Electronics Reliability and Microminiaturization 1, 321 (1962).
5. B. W. Schumacher, Plating 53, 1235 (1966).
6. H. Kanter and E. J. Sternglass, Phys. Rev. 126, 620 (1962).
7. B. W. Schumacher, "A Review of the (Macroscopic) Laws for the Electron Penetration through Matter" in Electron and Ion Beam Science and Technology edited by R. Bakish (J. Wiley and Sons, Inc., New York, 1965).
8. M. J. Berger and S. M. Seltzer, "Tables of Energy Losses and Ranges of Electrons and Positrons," NAS SP-3012, 1964 (available from the Office of Technical Services, Dept. of Commerce, Washington, D. C. 20230).
9. B. W. Schumacher, "Power Density Limits for the Particle Penetration Laws and the Onset of Energy Phenomena in Electron Beam Targets" (in print - this conference).


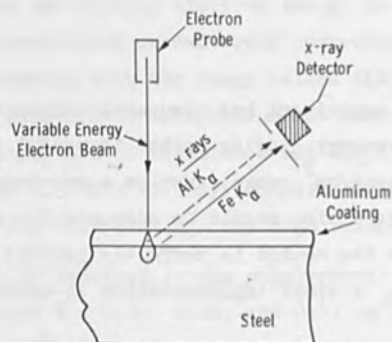


Fig. 1—Diagram of component arrangement for coating thickness measurement using electron probe, range-energy technique

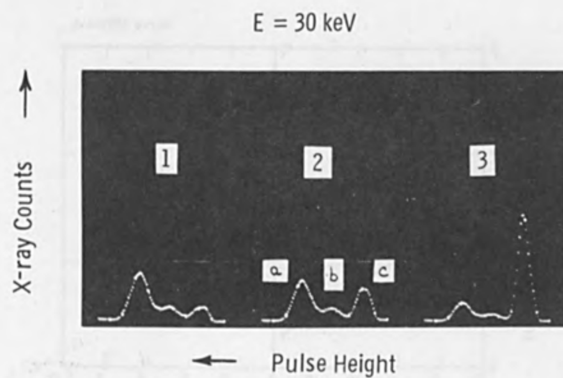


Fig. 2—Pulse height spectra of iron and aluminum $K_\alpha$ —x rays for $X_{Al}$ = 0.13 (1), 0.27 (2), and 0.78 (3) mg/cm$^2$. Peaks are identified as (a) Fe x rays, (b) Argon escape peak produced by Fe x rays, and (c) Al x rays

Curve 583340-A

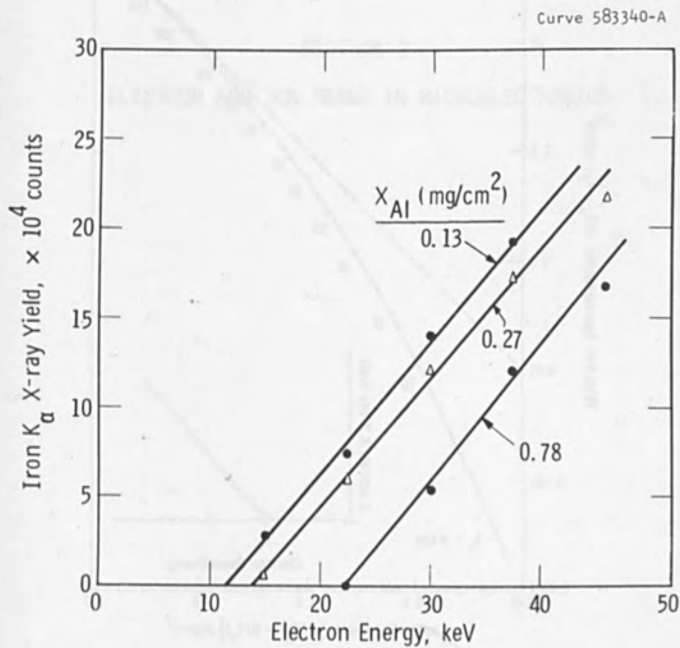


Fig. 3—Iron $K_\alpha$ x-ray yield versus electron energy

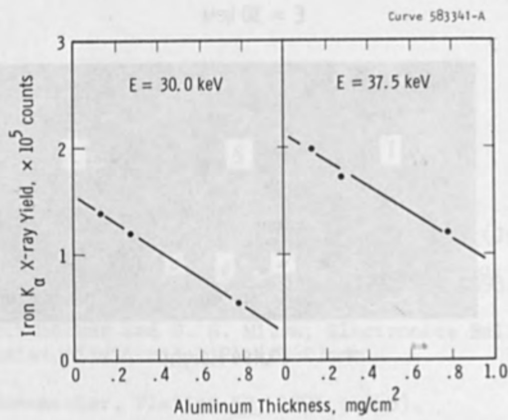


Fig. 4—Iron $K_\alpha$ x-ray yield versus aluminum thickness for two electron energies

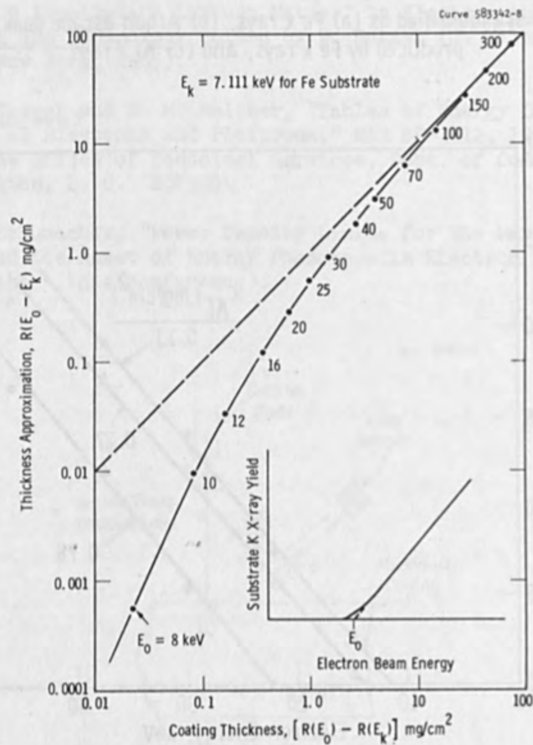


Fig. 5—Comparison of $R(E_0 - E_k)$ thickness approximation with $R(E_0) - R(E_k)$ thickness. See text for discussion

## SECTION 3

## ELECTRON AND ION BEAMS IN MICROELECTRONICS

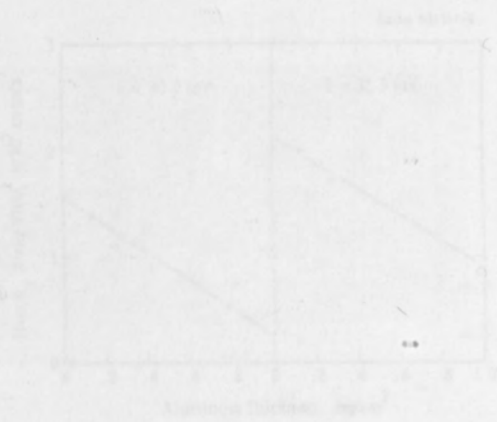

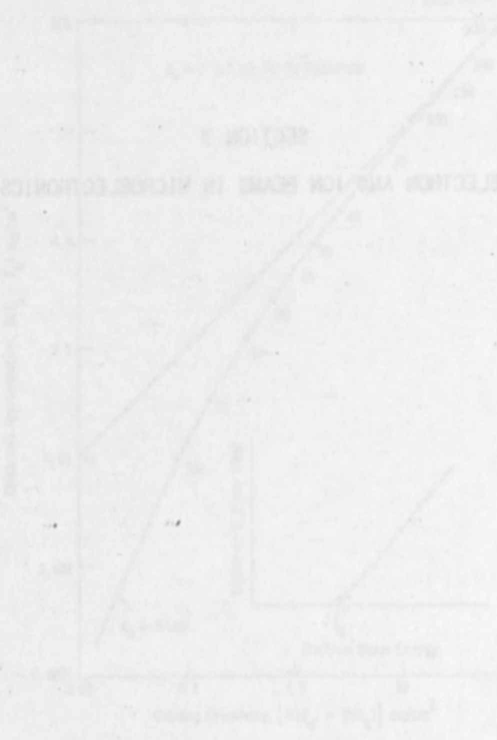

## HIGH RESOLUTION ELECTRON BEAM TECHNIQUES FOR TRANSISTOR FABRICATION

J.M.S. Schofield, H.N.G. King, and R.A. Ford

Mullard Research Laboratories, Redhill, Surrey, England.

The paper describes the fabrication of transistor devices with submicron accuracy using high resolution electron beam techniques. The electron beam may be used to produce diffusion barriers, protective film over the p-n junctions directly on the silicon substrate and also to define the aluminium connections through the exposure of the photoresists. Accurate positioning with respect to other features already present is by scanning electron microscopy. Some characteristics of M.O.S. transistors made this way are presented and a critical assessment of the techniques is given.

### Introduction

The demand is increasing, particularly in the computer industry for high speed silicon integrated circuits with response times $\sim$ 1 nsec. Transistor devices are limited at high frequencies by the transit time of the current carriers and by series resistance and parasitic capacity. These lower the available current gain necessitating an increase in drive current and result in a significant voltage drop within the device. If the size of the device is made too large the voltage will be lowered sufficiently at the extreme ends to cut off these parts electrically, and although they will not be working they will still continue to contribute to the parasitic capacity. To overcome this micron size devices are needed, highly doped but with shallow junction depths and they must be made to submicron tolerances. The last requirement cannot be met consistently using conventional photolithography because of the diffraction limitations of the optical wavelength. However, this target can be achieved by electron lithography because the resolution of a focused electron beam is at present limited rather by the lens aberrations and with existing lens designs it is not difficult to obtain sufficiently high current, $\sim 10^{-7}$A, within a spot of submicron diameter. We have used the beam to define diffusion barriers and the insulating layers around the aluminium connection areas.

The beam can readily be controlled electronically and so is easily automated with a computer, which may be servo-controlled by scanning electron microscopy, so as to align and focus the beam with respect to the substrate before exposing the desired pattern. At present

however, in our work, these processes are controlled and adjusted manually. Ultimately, when fully automated we expect to find improved yields because they will be no longer a matter of the subjective judgement of the operator. Also the direct definition of the barrier layers eliminates the uncertain wet chemical etching processes and avoids having to use up the more highly conducting silicon surface layers in growing oxide for the barriers. In the large scale integration of devices, yield is a vital factor,the final yield being merely the product of that of the individual components.

Lastly and most important of all the electron beam lithography promises to be an economic process. New materials highly sensitive to exposure by electrons have been developed recently and are reported in the following paper by E.D. Roberts.[1] The sensitivity is such as to allow an area of 1 mm square to be exposed with submicron resolution in under 8 seconds. This is about the area which can be scanned electrically without significant defocusing, and could contain an integrated circuit with about a hundred transistors. Mechanical stepping of the silicon wafer is used to cover a larger area. This, together with the alignment and refocusing, is estimated to require less than 2 seconds. Five separate electron beam exposures are required for the complete processing, that is under a minute for each integrated circuit.

## Electron Beam Apparatus

The system used to focus the electron beam to a submicron spot diameter and with a current density of $\sim 30\ A/cm^2$ is substantially the same as that described at the previous meeting[2]. In addition the beam can now be switched on and off in less than 1 μsec by electrostatic deflection. The plates to do this are immediately below the electron gun as shown in Figure 1. The beam is initially defined by a 100 μm diameter stop in the anode, and when blanked off, is deflected from the 1 mm diameter final stop in the objective lens. Two pairs of double deflection coils for x and y scans are mounted within the objective lens, above the stop but outside the vacuum system, and can be rotated together for orientating the pattern with the substrate. Astigmatism correcting coils are also mounted here. The substrate is mounted on a table which is moved mechanically. It has a total movement of one inch in each direction and can be repositioned to within 10 μm. To see the surface detail on the substrate by scanning electron microscopy, the Everhert-Thornley system[3] of scintillator detector and photomultiplier is used. This monitors the variations in secondary electron current from the substrate as the focused beam is scanned and provides a television display of the surface. The surface appears in relief because the detector is placed to one side of the substrate.

Active Materials

The beam is used to define diffusion barriers or insulating and protective layers directly on a silicon substrate, by introducing into the vacuum system either as a vapour or as a solid predeposited layer, a suitable organo-silicon compound. This is cracked and re-polymerised by the action of the beam on the surface to form a stable film. The film is satisfactory as a diffusion barrier against boron, phosphorus and arsenic, and is converted into something akin to silica during the diffusion temperature cycle. Similar films can also be made resistant to hydrofluoric acid etch and with good insulating properties which should prove useful to define the contact windows of high frequency bipolar transistors. The electron beam may also be used to expose conventional photoresists and hence to define the aluminium connections with high resolution. By scanning a finely focused beam films of fine geometry may be produced.

(a) Film formation from the vapour is simpler because it is possible to line up and focus directly on the regions to be worked before the vapour is admitted. However, the deposition occurs a monolayer at a time and is slow, taking a few minutes to deposit the diffusion barrier of a single transistor. To build up sufficient film the pattern must be accurately retraced many thousands of times because the spot must be moved sufficiently fast to avoid using up a significant fraction of the vapour adsorbed on the surface. In this way the rate of formation of film is proportional only to the time averaged current and therefore has the same resolution as the beam. The deposit has the same gaussian profile as the beam but scattered electrons also produce a thin deposit elsewhere which has been observed to reduce the diffusion with an increase in the measured sheet resistivity of the devices. This can, however, be removed by etching, and the profile may be further improved if up to half of the original deposit is etched away. M.O.S. transistors have been made successfully using this method to define the diffusion barrier and are described in detail later. The application to bipolar transistors has proved more difficult. The method has been used for making the diffusion barriers for a device with an array of 3 μm wide emitter stripes, and after phosphorus diffusion and cleaning to outline the aluminium connection areas. However, the connections have been poor with Schottky barrier characteristics, even though test diodes with the same geometry had previously given good results.

(b) Film formation from the Solid has not yet been tested in making devices and techniques are still being developed to enable this method to be applied to making bipolar transistors. The resolution is improved since only one sweep of the beam is required, obviating any retracing errors, and besides all material is subsequently dissolved off which has not been sufficiently exposed, giving the edge of the film a sharp profile. The technique is fast, a typical device area of a hundred thousand square microns can be exposed in a second. However, it is now necessary to align and focus on a marker outside the device area, but which is accurately positioned relative to it.

The nature of the marker is critical. It must be

(i) Accurately defined so as to give the orientation and scale information.

(ii) Able to survive undamaged all the various diffusion and cleaning processes to which the silicon slice is subjected during transistor manufacture.

(iii) Clearly visible by scanning electron microscopy even when coated with up to 1 μm of the electron resists.

The most suitable marker found so far is one made in the silicon itself and is created during the boron diffusion of the base when an oxide grows over the unmasked silicon about 0.2 μm thick. The silicon accounts for about half this thickness, ∿ 0.1 μm, and a pit in the surface is left after the oxide is removed, which is accurately preserved through the subsequent processing.

However, when the marker is covered with resist it is initially very difficult to find. It now seems that an additional electron exposure and diffusion process will be needed in order to grow marker steps about 0.5 μm deep. This will make a total of five separate electron exposures to make the bipolar transistors.

## Pattern Generation

(a) Triggered Signal Generators can be used to give the x and y deflections and simple patterns can be scanned repeatedly at a constant speed necessary to produce the required uniform exposure. This method of generating patterns is preferred when the process of deposition is slow, such as when using the vapour technique, because only the areas on which a deposit is required need be scanned.

(b) Flying Spot Pattern Readout is simpler where more complex patterns are needed. A pattern mask is provided and read out by a photomultiplier and a flying spot scanner in synchronism with the beam, the output of which provides the beam unblanking pulses. Although much unwanted area may be scanned in this way, the extra time taken may not be significant where, for instance, deposition takes place by exposure of a sufficiently sensitive solid material. One such system which has been used is outlined in Figure 2. The flying spot is produced by a short persistence oscilloscope and is focused with a camera carrying a film strip on which are the sequence of pattern masks required. A photomultiplier detects the light transmitted through the film. The output is then used to actuate a Schmitt trigger set to discriminate between on and off. An adjustment of the trigger level allows for variations in the brightness of the spot and is set to obtain the

sharpest readout. Distortions in the optical system may be reduced if the same camera is used to produce the film from accurately cut stencils.

The substrate and pattern are aligned by scanning electron microscopy. Holes are provided accurately positioned on the mask relative to the central pattern. These switch on the beam and thus behave as windows through which the corresponding markers provided on the substrate may be viewed and aligned without exposing the central pattern. Pairs of markers are selected alternately to set the x and y scales and the orientation. The pattern is exposed in a single scan after the alignment procedure has been completed.

## Design of the M.O.S. Transistors

The M.O.S. transistor is the simplest vehicle on which to prove these techniques. It requires only a single diffusion process, which may be done using the high resolution electron beam deposited barrier. The improvement in performance can be quickly assessed by making conventional devices with coarser geometry on the same silicon wafer. The design is such that all remaining processes may be done conventionally and accurate registrations are not required. A schematic of the design is shown in Figure 3. The source drain separation or channel length L is determined by the diffusion mask. We adopted an interdigital structure of source and drain with up to 16 cycles within the 100 μm width of the device. The fingers are 35 μm long 1 μm wide and spaced 2 μm apart to give a total channel width of ∿ 1 mm. The length of the fingers W is slightly longer than the gate width, by ∿ 5 μm, so that accurate registration of the gate on the channel is not necessary. Also half the width of the drain fingers, ∿ 0.5 μm, is the effective (averaged all round) gate to drain overlap, L', which introduces an unwanted feedback capacity. This is predetermined in the design by the electron beam process. The fingers cannot be made much narrower than 1 μm because of lateral diffusion, ∿ 0.25 μm, of the diffusant. Arsenic was chosen for this because of its low diffusion coefficient. The beam oxide is subsequently removed and a thermal gate insulating oxide grown and during this process the lateral diffusion must be small. Thermal oxide is the better because of its electrical stability. The length of the fingers W is determined by the sheet resistivity there (∿ 50 ohms per square) and is such that the additional series resistance is $\sim g_m^{-1}$, $g_m$ being the transconductance. The frequency response is improved by decreasing the channel length L until it is of the same order as the overlap L' when stability rather than transit time limits the response.

## Characteristics of M.O.S. Transistors

The static characteristics of two different devices are shown in Figures 4a and 4b. The drain current I is plotted as a function of drain voltage V for gate voltage $V_G$ as parameter. The locus of maximum slopes gives the total series resistance of the source and drain fingers.

The minimum slope is the leakage resistance, see Figure 4a. This is probably due to a break in the channel and comes from over etching the mask before diffusion. The measured $g_m$ is observed to saturate with gate voltage. This is attributed to a critical field for saturation of the electron drift velocity in the channel having been exceeded (∿ 20 KV/cm). The drain voltage cannot be increased beyond that for the breakdown to the substrate shown here, or that of punch-through to the source. Proper choice of substrate doping ensures that for a given channel length these occur together and enable the maximum operating voltages to be used.

The effect of resistance in the fingers is to lower the effective gate and drain voltages. The applied gate voltage may always be increased even if, the $g_m$ becomes independent of it. However, the applied drain voltage is limited by the breakdown and so will prevent the pinch-off voltage being attained everywhere at sufficiently high currents. The effect is to lower $g_m$ and increase the shunt drain conductance.

The measured transconductance can be corrected for the finger resistances and from this the channel geometry may be deduced. The corrected pinch off voltage is also needed in the calculation. Both devices are shown to have channel length ∿ 2.5 μm. Series resistance is higher in the 8 cycle device shown in Figure 4b but so is the leakage resistance.

M.O.S. transistors with up to 10 cycles of channel have been made and show proportional increase of the measured $g_m$. Compared with a conventionally made device of the same area this corresponds to nearly a factor four improvement in $g_m$. However, as the number of cycles was increased series resistance due to an increased sheet resistivity in the fingers caused the $g_m$ measured to decrease rapidly.

A device with 16 cycles of channel is shown by scanning electron microscopy in Figure 5. The electrical details of the channel junctions are revealed by reverse biasing the source and drain with respect to the substrate and collecting the charges induced by scanning the beam. The gate and its oxide have been removed and surface detail of the channel is revealed by voltage contrast. Various imperfections can be seen in the channel which is shown at greater magnification in the lower set of photographs. Note the channel is out of focus in the electrical picture due to electron scattering within the silicon, while a speak of dust on the surface is sharp. The channel dimensions are however ∿ 2 μm, as intended, showing that series resistance is limiting the $g_m$ attained.

A $5^{\circ}$ angled section has been taken through a completed device with 8 cycles of channel, a photograph of which is shown in Figure 6. Here the channel length has been increased to 4 μm so as to reduce the finger width to 2 μm. The junction depth of the diffusion is about 0.25 μm. Thermal oxide has been grown over the device; it is thinner over the channel than it is over the source and drain regions. This is partly

beneficial in that the effective gate-drain capacity is reduced in comparison with the channel capacity. However, more of the arsenic doped silicon has been used which may account for the high finger resistance.

## Conclusions

Methods have been described for making transistors economically at high resolution using electron beam techniques. The way in which the geometry and doping levels determine the characteristics have been described and illustrated from experience in making M.O.S. transistors. Measurements show that while the geometry is as intended the sheet resistivity in the source and drain becomes too high as the spacing is reduced.

## Acknowledgements

This paper describes work done under a C.V.D. contract and is published by permission of the Ministry of Defence (Navy Department). The authors wish to thank the Directors of Mullard Research Laboratories for permission to publish this paper, and to acknowledge helpful discussions with Messrs. E.D. Roberts, J.R.A. Beale and Dr. P.J. Daniel, and the technical assistance of Mr. R.C. Barclay.

## References

1. ROBERTS, E.D. "Rapid Direct Formation of Siliceous Diffusion Barriers by Electron Beams", Third International Conference, Electron and Ion Beam Science and Technology, Boston 1968.

2. BEER, A.F., et. al., "The Formation of High Resolution Silica Films by an Electron Beam Process", Second International Conference, Electron and Ion Beam Science and Technology, New York 1966.

3. EVERHERT, T.E. and THORNLEY, R.F.M., "Wideband Detector for Micro-micro-ampere Low Voltage Electron Currents". J. Sci. Inst. Vol. 37, p 246-8, July 1960.

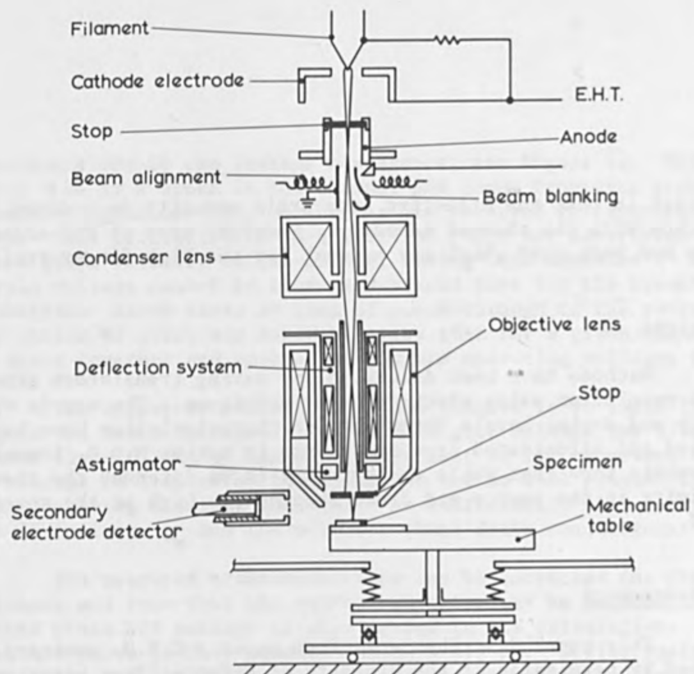

Fig. 1. ELECTRON BEAM MACHINE.

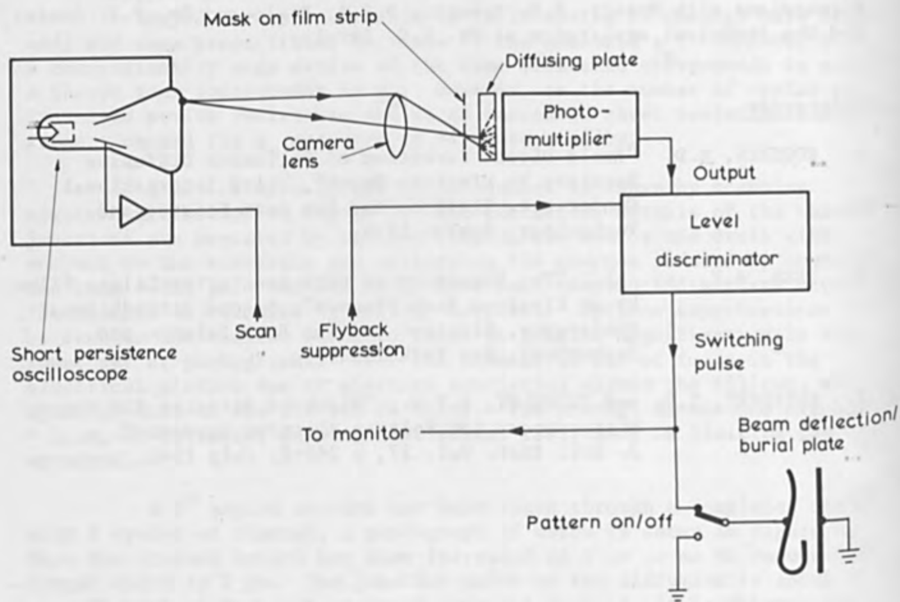

Fig. 2. PATTERN READOUT SYSTEM.

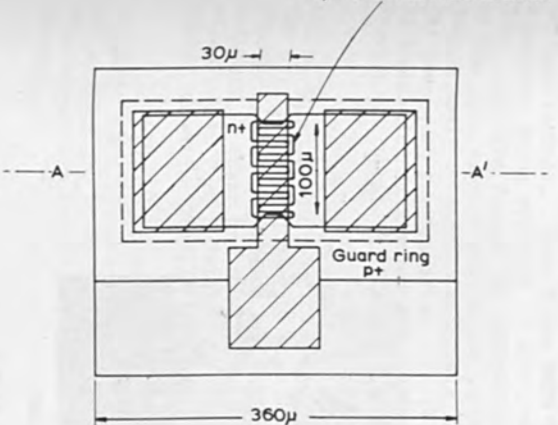


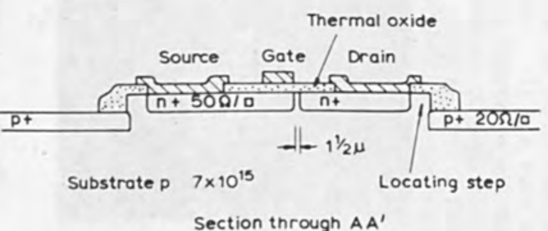


FIG.3. SCHEMATIC OF M.O.S.T. WITH ELECTRON BEAM DEFINED SOURCE/DRAIN SEPARATION

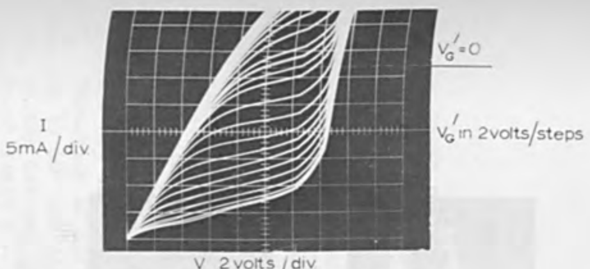


a) Channel: 6 cycles $W = 30\mu$ $L = 2{\cdot}5\mu$
Best $g_m'$ 1·8 mA/volt at $I = 25$ mA
Turn on voltage $V_T' = -30$ volts
Pinch off voltage $V_P' = 8$ volts
$R_S + R_D = 220\,\Omega$, $R_L = 1{\cdot}3\,k\Omega$

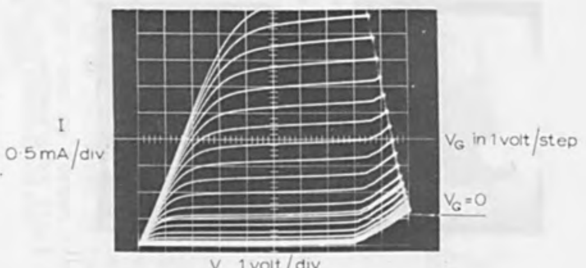


b) Channel: 8 cycles, $W = 30\mu$ $L = 2{\cdot}5\mu$
Best $g_m' = 0{\cdot}7$ mA/volt at $I_1 = 16$ mA
Turn-on voltage $V_T' = -5$ volts
Pinch off voltage $V_P' = 14$ volts
$R_S + R_D = 810\,\Omega$, $R_L = 70\,k\Omega$

FIG. 4 STATIC CHARACTERISTICS OF INTERDIGITATED M.O.S.T. STRUCTURES

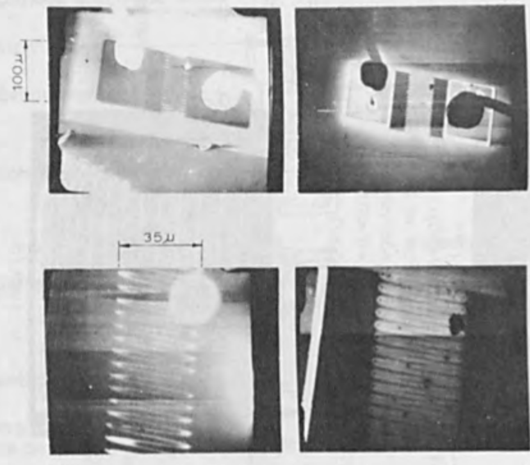


SURFACE DETAIL
with voltage contrast at 7V bias

ELECTRICAL DETAIL
Residual bias by beam

$g_m' = 0.22$ mA/volt $\quad V_T' = -12$ V
Punch through voltage $\quad V_{pt} = 35$ V

**FIG. 5** SCANNING ELECTRON MICROGRAPH

16 cycle M.O.S.T. with gate removed
p/n junctions equally biased

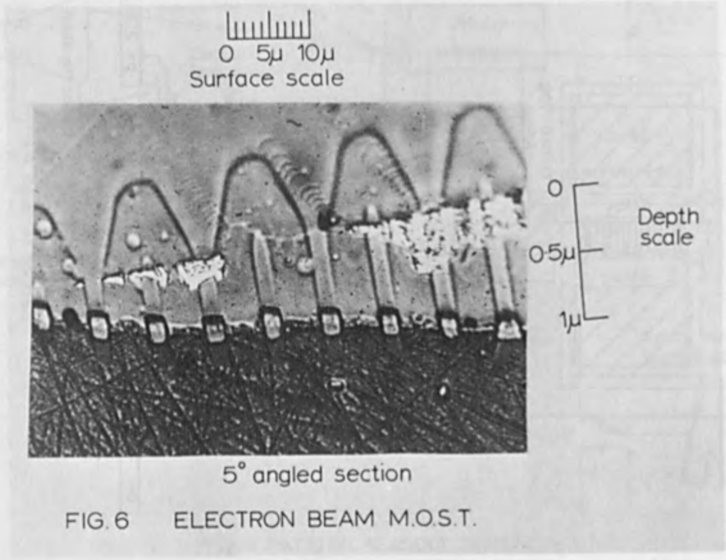


FIG. 6 ELECTRON BEAM M.O.S.T.

# RAPID DIRECT FORMATION OF SILICEOUS DIFFUSION BARRIERS BY ELECTRON BEAMS

E.D. Roberts

Mullard Research Laboratories, Redhill, Surrey, England.

Silica-like films for use as diffusion barriers in transistor technology can be made by bombarding surfaces with an electron beam in the presence of the vapour of suitable silicon compounds, but the process is slow. The preparation and use of solid silicon compounds, enabling the rate of formation of diffusion barriers to be increased by factors up to $10^6$ are described. Barriers can be formed directly in any desired configuration and patterns with lines down to at least 1 μ in width can be made.

## Introduction

It has been known for a number of years that when an electron beam strikes a surface within a vacuum system, a solid film is formed on that surface. Such films were first observed as contamination on specimens being examined in electron microscopes. It was soon shown[1-3] that they were formed by interaction between the electrons and molecules of residual vapours within the system, such as those of pump oil, vacuum grease, volatile materials from rubber gaskets, etc. This effect has been used for preparing thin films of both insulators and conductors, by bombarding substrates with electrons in the presence of suitable vapours deliberately introduced into the system [4-8].

In such processes, molecules of the vapour are adsorbed on all surfaces within the vacuum system, including the substrate on which the film is to be formed. When an adsorbed molecule is struck by an electron, it is activated and may break down forming ions and/or free radicals. These may react with each other or with other adsorbed molecules to form a larger, less volatile molecule, and a layer of solid, non-volatile film is gradually built up.

This paper describes the use of electron beams for producing directly the siliceous diffusion barriers required in certain stages in the manufacture of transistors. The barriers may be made in any desired pattern by deflecting the electron beam to trace out that pattern.

Preparation of Films of Large Area

Experiments on the rate of film formation and the preparation of large films for preliminary tests as diffusion barriers were carried out in the apparatus shown in fig. 1. The inner and outer chambers are evacuated and a suitable chemical vapour is introduced via one of the vapour tubes passing through the base to produce the required partial pressure in the outer chamber which contains the substrate. The other vapour tube allows another vapour or gas to be introduced concurrently if required. The electron beam produced by the gun assembly is normally accelerated by 10 kV, and focused by a system of lenses on to the substrate. The latter is clamped into a holder through which water or other fluid can be passed to maintain the substrate at constant temperature. This apparatus produces films of diameters up to about 15 mms, and which are large enough to be weighed, analysed or otherwise examined.

The solid materials described later are applied as a film to the substrate. The coated substrate is supported in the holder and bombarded by the beam in the evacuated apparatus, no vapours or gases being introduced.

Preparation of Films from Volatile Silicon Compounds

Tetraethoxysilane (TEOS) vapour was used in the first experiments and the process of film formation was found to be very inefficient. The introduction of oxygen with the tetraethoxysilane vapour increased the efficiency by a factor of two or three [9], but even then, with substrates maintained at 20°C, and a current density about 3 $mA/cm^2$, only one electron from every thirty arriving at the substrate incorporated a molecule into the film. Further, only one molecule from every eighty adsorbed on the substrate was converted to film [9]. This effect is thought to be due to local heating of the substrate as each electron strikes it, resulting in molecules being desorbed around the site of impact. The efficiency can be further increased by cooling the substrate, but at -30°C a gain of only two or three is achieved, and the process is rather inconvenient. Using tetraethoxysilane under typical operating conditions, a film about 2000 Å thick, which is adequate to mask silicon against the diffusion of arsenic, phosphorus or boron, requires an exposure of about 1 $Coulomb/cm^2$.

Other silicon compounds were prepared in attempts to improve the efficiency of film formation. These compounds were chosen to have the largest possible existing silica-like structure while still retaining sufficient volatility for introduction into the vacuum chamber. Three apparently suitable compounds were 2,4,6,8,-tetramethyl-cyclo-tetrasiloxane (TCTS), 2,4,6,8,10,-pentamethyl-cyclo-pentasiloxane

(PCPS), and 2,4,6,8,10,12,-hexamethyl-cyclo-hexasiloxane (HCHS). The rates of film formation under identical conditions, and diffusion barrier properties of films prepared with these materials are shown in fig. 2 and are compared with films from tetraethoxysilane. The rates of film formation are approximately proportional to the number of silicon atoms in the molecule, but the resistance to diffusion of arsenic becomes worse as this number increases, presumably because the larger rings result in a more porous structure. The best results were obtained with TCTS, a barrier which masked adequately against arsenic diffusion being formed by an exposure of 0.15 Coulomb/cm$^2$.

It was clear that in order to increase further the rate of film formation, it was necessary to use compounds containing larger numbers of silicon atoms. The structure of the molecule must also be suitable both to maintain ability to prevent diffusion, and to give increased efficiency in deposition rate. For example, although TCTS enables film to be formed at four times the rate obtainable with tetraethoxysilane, the structurally similar octamethyl-cyclo-tetrasiloxane, in which the active hydrogen atoms are replaced by methyl groups, deposits film only at the same rate as tetraethoxysilane.

However, usually as the number of silicon atoms in the molecule is increased, the compound becomes less volatile, and it becomes increasingly difficult to introduce the vapour into the apparatus. (Fig. 3 illustrates this for the series of cyclic siloxanes used in this work). Consequently the maximum rate of film formation which can be achieved must fall because insufficient molecules are available to maintain it. The optimum condition appears to be achieved when TCTS is used.

A further disadvantage of using vapours became apparent when diffusion barriers of very fine geometry were made with an electron beam of about 1 μ diameter. It was found that the thickness profile of the films was Gaussian, corresponding with the distribution of current density in the beam (fig. 6a). To approach more nearly to the rectangular thickness profile desirable for the ideal diffusion barrier, it was necessary to prepare films nearly twice as thick as the minimum required and to remove the excess by a controlled etching process. This procedure effectively reduced the efficiency by a factor two.

## The Use of Non-Volatile Silicon Compounds to Form Diffusion Barriers

It was thought that non-volatile silicon compounds used in the manner of photoresists to form diffusion barriers directly could result in the following advantages:-

1. Loss of material by desorption due to local heating by the electrons arriving at the substrate should be practically eliminated.

2. Using vapours, film can be formed only by the addition of successive monomolecular layers. With non-volatile materials, however, layers thousands of molecules thick could be predeposited on the substrate. The electron beam must be able to penetrate right through, but in doing so, it could cause many molecules to react, for example, by cross-linking.

3. The absence of added vapours enables lower working pressures to be used, allowing better focusing of the beam to be achieved. Contamination of lenses and other components should be reduced, thus extending the periods between cleaning operations.

## Preparation of Non-Volatile Silicon Compounds

A range of solid, soluble siloxane type polymers was prepared by the hydrolysis of organotrichlorosilanes in a medium of ether cooled by ice. The resulting ether solution, which has contained the intermediate organosilan-triols, yields gummy polymers if the ether is removed directly, but if the solution is treated first with about 1-3% saturated aqueous ammonia solution (based upon the weight of organotrichlorosilane), condensation of the silan-triols occurs to give polymers which, after removal of the ether, are solids of crystalline appearance. The polymers are soluble in ethers and ketones, and some are also soluble in aromatic hydrocarbons. Their melting points range from 50°C upwards, depending upon the precise conditions of condensation and upon the organic groups attached to the silicon atom. No attempts to optimise the yield have been made and it has varied between about 50 and 85% of the theoretical yield, depending upon the ease with which the silan-triols form three-dimensionally cross-linked polymers. These insoluble materials tend to be formed in greater quantity the smaller the organic group attached to silicon.

Polymers prepared from methyl-, vinyl- and ethyl- trichlorosilanes have been used to make diffusion barriers directly by the use of electron beams. The molecular weights of the ethyl and vinyl polymers are 1370 and 1460 respectively, while that of the methyl polymer is 422. The structures of the polymers have not yet been determined, but the differences in molecular weights suggest that the methyl polymer may have a different type of structure from the other two.

## Formation and Properties of Diffusion Barriers from Non-Volatile Silicon Compounds

General considerations and early experiments suggested that

the methyl polymer may be more suitable than the others for making diffusion barriers, so most work has been done with this. The polymers are used as a solution in any convenient solvent. Methyl isobutyl ketone is specially suitable. Solid films on the substrate are made by coating it with the solution and drying. Any coating process such as spreading, dip-coating or spinning may be used to prepare films of predetermined thickness. The dried film is bombarded by the electron beam, scanned if necessary to form the required pattern, and the polymer becomes cross-linked and insoluble in solvents when it has received a sufficient dose of electrons. The pattern is developed by rinsing for a few seconds in a solvent such as acetone, when unirradiated material rapidly dissolves.

The change which renders the polymer insoluble occurs sharply at the minimum exposures shown in fig. 4. Over-exposure, when resolution of the pattern becomes degraded, begins to become apparent at about four times the minimum exposures. The minimum exposure required to form the pattern appears to be independent of film thickness, though the pattern adheres to the substrate only when the electrons can penetrate the film completely. The exposures required to form diffusion barriers from tetraethoxysilane and TCTS vapours are also shown in fig. 4.

The results of diffusion tests on large area films made by electron bombardment of the solid methyl polymer are shown in fig. 5. The patterns were all formed by an exposure of $150 \times 10^{-6}$ Coulomb/cm$^2$, followed by development in acetone. The arsenic diffusion cycle produced a resistivity of 50 ohms per square n-type in unmasked 1-3 ohm cm p-type silicon. Satisfactory barriers against arsenic diffusion can be made by the simple irradiation and development procedure described above, but a considerable improvement can be obtained if further irradiation or conventional densification is carried out after developing the pattern. The ethyl and vinyl polymers need to be used as rather thicker films to act satisfactorily as diffusion barriers.

## Diffusion Barriers of Fine Geometry from Non-Volatile Silicon Compounds

Patterns of fine geometry, having lines about 1 μ wide, have been made in the high resolution electron beam machine described by Ford, King and Schofield [10]. Photomicrographs of patterns made from the solid methyl compound and from TCTS vapour are shown in fig. 6. The films from the solid (figs. 6b and c) are 7000 Å thick and can be used directly as diffusion barriers. That from TCTS (fig. 6a) is 3000 Å thick and must be etched to improve its thickness profile before use as a barrier. The variation in thickness of the film from TCTS due to the Gaussian distribution of current density in the electron

beam is apparent, while the films from the solid polymer are of uniform thickness. This is due to the sharp conversion from the soluble to insoluble condition at the minimum exposure given in fig. 4. It can be seen that this effect also enables finer patterns to be made from the solid polymer (fig. 6c) than are possible when vapours are used. The width of lines formed by the beam in the solid polymer is independent of film thickness at least up to 8000 Å, the maximum which has been used. The exposure times, using a beam current of $10^{-7}$ A, required to form the film patterns shown in fig. 6, were (a) 3 mins. (b) 14 msecs. (c) 18 msecs.

## Conclusion

By using predeposited solid siloxane polymers for producing siliceous diffusion barriers by electron beam techniques, an increase in rate of film formation over that obtainable with tetraethoxysilane vapour by factors of $10^4$ to $10^6$ can be obtained, together with much improved resolution of fine geometrical patterns. The solid polymer obtained by hydrolysis and condensation of methyltrichlorosilane is preferred for general use.

## Acknowledgements

This paper describes work done partly under a CVD contract and is published by permission of the Ministry of Defence (Navy Department). The author also wishes to thank the Directors of Mullard Research Laboratories for permission to publish this paper, and to acknowledge helpful discussions with Mr. H.N.G. King and Mr. J.M.S. Schofield and assistance with the experimental work by Mr. R.A. Ford and Mr. B.F. Martin.

## References

1. ENNOS, A.E., Brit. J. Appl. Phys. 1953 Vol. 4, 101
2. POOLE, K.M., Proc. Phys. Soc. (London) 1953 Vol. B66, 541
3. ENNOS, A.E., Brit. J. Appl. Phys. 1954 Vol. 5, 27
4. HLAVIN, J.M. and FOTLAND, R.A., "The Fabrication of Electronic Components Using Low Energy Electron Beams". First International Conference, Electron and Ion Beam Science and Technology, Toronto 1964
5. CHRISTY, R.W., J. Appl. Phys. 1960 Vol. 31, 1680
6. BEER, A.F. et al. "The Formation of High Resolution Silica Films by an Electron Beam Process". Second International Conference, Electron and Ion Beam Science and Technology, New York 1966

7. BAKER, A.G., and MORRIS, W.C., Rev. Sci. Instr. 1961, Vol.32, 458
8. CHRISTY, R.W., J. Appl. Phys. 1962, Vol. 33, 1884
9. FORD, R.A., et al. "The Preparation of High Resolution Silica Diffusion Barriers by an Electron Stimulated Chemical Reaction". Proceedings of Joint IERE-IEE Conference on Applications of Thin Films in Electronic Engineerings. Suppl. Vol. London, July 1966
10. SCHOFIELD, J.M.S., KING, H.N.G., and FORD, R.A., "High Resolution Electron Beam Techniques for Transistor Fabrication". Third International Conference, Electron and Ion Beam Science and Technology, Boston 1968


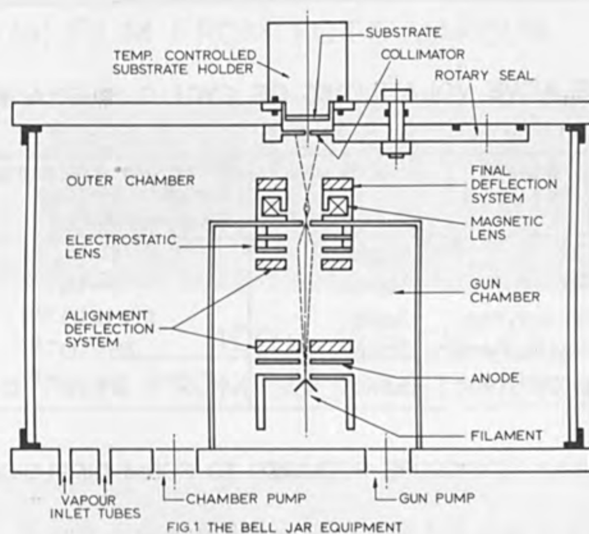


FIG.1 THE BELL JAR EQUIPMENT

| Vapour | No. Si atoms in molecule | Wt. of film / Wt. of film from TEOS | No. Si atoms / No. Si atoms from TEOS | Resistance to diffusion of As |
|---|---|---|---|---|
| TEOS | 1 | 1·0 | 1·0 | Satisfactory >2000Å |
| TCTS | 4 | 3·86 | 4·0 | Satisfactory >1300Å |
| PCPS | 5 | 4·38 | 4·6 | Satisfactory >2700Å |
| HCHS | 6 | 5·78 | 5·6 | Unsatisfactory at 6000Å |

Pressure of vapour in chamber = 0·3 μ Hg.
Current density = 0·5 mA/cm²
Time of exposure = 30 mins
Ratio $P_{O_2}/P_{vapour}$ = 3·0
Diameter of films = 15 mms

FIG.2 RATES OF FILM FORMATION AND DIFFUSION TEST RESULTS

| Compound | No. of Si atoms in molecule | B. Pt. (760 mms.) °C | Maximum pressure attainable in electron beam machine μ Hg. (Pirani gauge.) |
|---|---|---|---|
| TCTS | 4 | 133 | 0·7 |
| PCPS | 5 | 165 | — |
| HCHS | 6 | 189 | 0·3 |

FIG. 3 RELATIVE VOLATILITIES OF CYCLIC SILOXANES.

| Compound | Form used | Minimum exposure to form diffusion barrier Coulomb / $cm^2$ |
|---|---|---|
| TEOS | Vapour | 1 |
| TCTS | Vapour | 0·15 |
| Ethyl polymer | Solid | $250\times10^{-6}$ |
| Methyl polymer | Solid | $75\times10^{-6}$ |
| Vinyl polymer | Solid | $2\times10^{-6}$ |

FIG.4 MINIMUM EXPOSURE REQUIRED TO FORM DIFFUSION BARRIER

All films irradiated by $150\times10^{-6}$ C/$cm^2$ and developed in acetone

| Subsequent treatment of film | Thickness required to mask against As |
|---|---|
| None | 5000 Å |
| Flooded by $1000\times10^{-6}$ C/$cm^2$ | 2500 Å |
| Densified by heating 15 mins at 1230°C in nitrogen. | 2000 Å |

FIG.5 DIFFUSION TESTS ON FILMS FROM SOLID METHYL POLYMER

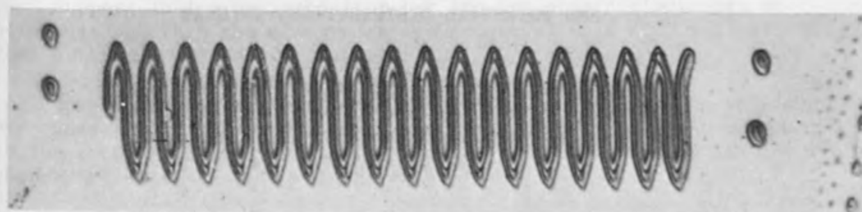

100μ = 12½ CYCLES

(a) FILM FROM TCTS VAPOUR

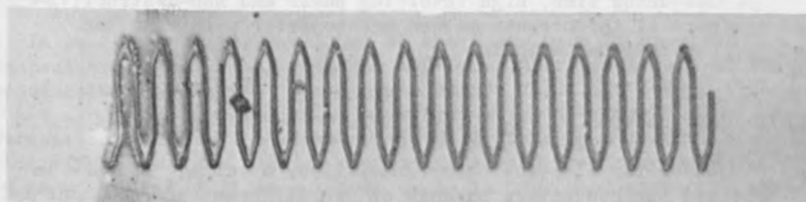

100μ = 12½ CYCLES

(b) FILM FROM SOLID METHYL POLYMER

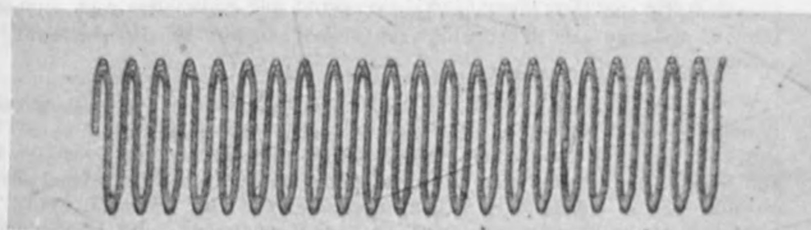

100μ = 16 CYCLES

(c) FILM FROM SOLID METHYL POLYMER

FIG. 6

# APPLICATION OF ELECTRON-BEAM-INDUCED CONDUCTIVITY TO MEASUREMENT OF RESISTIVITY, ELECTRIC FIELD AND POTENTIAL DISTRIBUTIONS IN GaAs

Chusuke MUNAKATA

Central Research Laboratory, Hitachi Ltd.
Kokubunji, Tokyo

A focused electron beam was used to measure resistivity, electric field and potential distributions in GaAs crystals by means of detecting the signal due to the electron-beam-induced conductivity. The electron beam was pulsed. Two specimen bars were cut out of an oxygen-doped GaAs ingot, and the beam scanned the bar along its long axis. Short measuring time, high resolving power and non-destructiveness of the present method are superior points to the conventional methods.

## 1. Introduction

Under the electron beam irradiation, a voltage appears in unbiased semiconductors because of two different effects; one is the ohmic drop due to the irradiating beam current and the other the induced voltage due to the bulk electron voltaic effect[1]. The ohmic drop has been already applied to measuring the resistance[2][3], and the bulk electron voltaic effect to measuring the resistivity distribution in Ge crystals[4].

In such a high-resistivity semiconductor as the GaAs crystals examined in the present experiment, however, the ohmic drop and the induced voltage are often comparable and can not be independently measured.

In a biased semiconductor, a signal due to the electron-beam-induced conductivity[5], which Zareba named $\beta$-conductivity for short[6], appears in addition as a change in the terminal voltage of the biased semiconductor. According to the analyses[7] by the present author, the $\beta$-conductive signal depends upon the electric field strength at an irradiated point in a semiconductor, and it can be increased much more than the ohmic drop and the induced voltage. The $\beta$-conductive signal can be thus separated from other voltage signals, and it has recently been applied to measuring the resistivity distribution in Ge and CdS crystals[8].

In this paper the $\beta$-conductivity method is experimentally proved to be applicable to the measurement of the potential distribution in GaAs crystals as well as the resistivity distribution in them.

## 2. Principle of β-conductivity method

Suppose that a semiconductor bar has two ohimic electrodes at both ends and that the electrodes are connected to a d.c. voltage source through a detecting resistor r.

Under the beam irradiation, the terminal voltage of the specimen bar changes with the conductivity increment $\Delta\sigma$ over a length $\Delta x$ owing to the excess carriers created by the electron beam[9]. The voltage change $\delta V$ detected with r is given by[7) 8)]

$$\delta V = \frac{r R_t}{r + R_t} E^2 \frac{S_o}{V_s} \Delta\sigma\Delta x \ , \qquad (1)$$

where $R_t$ is the resistance of the specimen bar, E the electric field at the irradiated point, $S_o$ the cross-sectional area of the conductivity-modulated region and $V_s$ the terminal voltage or specimen voltage of the bar.

In eq.(1) all factors except $\delta V$ and E are usually constant irrespectively of the beam position and hence the square-root of the β-conductive signal, $\sqrt{\delta V}$, gives the electric field E. Integration of $\sqrt{\delta V}$ along the current path, therefore, gives the potential distribution*. Since the electric field is given by a product of resistivity $\rho$ and the biasing current density J, $\sqrt{\delta V}$ also gives $\rho$ if J is known or/and if it is constant as is in the one-dimensional case.

## 3. Experimental arrangements

### 3.1. Specimens

A GaAs single crystal ingot, from which the specimen bars were cut out, was made with the horizontal Bridgmann method, and its resistivity was very high because of oxygen-doping.

Dimensions of the first specimen denoted as GaAs(1) in this experiment were 0.5(thickness), 1(width) and 5.8(length) mm. The second one, GaAs(2), was similar to the first, but was 6.6 mm long. The specimen bars were chemically etched in a solution composed of $H_2SO_4$:$H_2O_2$:$H_2O$=1:1:1 for 2 minutes. Indium was alloyed on both ends of each bar in $H_2$-atmosphere at 500°C for 5 minutes to make ohmic electrodes.

### 3.2. Conventional methods of measuring resistivity and potential distributions

---

* A preliminary experiment was already reported[10], where $\delta V$ instead of $\sqrt{\delta V}$ was integrated to get the potential distribution because the change in E was comparatively small.

Resistivity and potential distributions in the specimen bars were measured with two conventional methods before the measurements with the present $\beta$-conductivity method.

The resistivity distribution was obtained from the current-voltage relations of forwardly biased Au-contacts made upon the cross-section of the GaAs ingot, as is schematically shown in Fig. 1, before the specimen bars were cut out of the ingot.

The potential distribution along the long axis of the bar, to which a biasing voltage of 47 V was applied, was measured in the dark with a tungsten probe. The measuring circuit is shown in Fig. 2, where the potential is obtained by means of finding the null point of the galvanometer G.

The electric field distribution can be deduced in principle from the potential distribution, but the result was ambiguous.

### 3.3. Electron beam and measuring systems

The measuring system, whose main part is schematically shown in Fig. 3, has already been reported elsewhere[11]. Energy, frequency, current and diameter of the pulsed electron beam were 20 KeV, 1 KHz, a few pA and about 10 $\mu$m, respectively. The signal of smaller than a few mV was detected with the detecting resistance of 1 M$\Omega$. The measuring time was shorter than 10 seconds.

### 3.4. Calibration of resistivity and electric field

Mean value of the $\beta$-conductive signal, $\overline{\sqrt{\delta V}}$, is obtainable along the specimen, and it corresponds to the mean resistivity $\overline{\rho}$ of the specimen, or to the mean electric field $\overline{E}$ in the specimen. $\sqrt{\delta V}$ curves were thus calibrated refering to $\overline{\rho}$ or $\overline{E}$, while the potential distribution was normalized to the specimen voltage.

## 4. Results

### 4.1. Resistivity distribution (Au-contact method)

Figure 4 shows the resistivity contours in a cross-section of the GaAs ingot. The contours are based on the results obtained with the Au-contact method. Since the measurement was done under the room-light illumination, the values attached to the contours are relative. It is seen that the resistivity varies in an extensive range from $10^{-2}$ to $10^{6}$.

### 4.2. Rectifying characteristic of the specimen

Figure 5 shows the current-voltage relations of GaAs(1) measured in the dark. They show the rectifying characteristic which is

probably due to a H-L junction in the specimen. GaAs(2) also showed a rectifying characteristic, but it was weak.

### 4.3. Potential distribution (one-probe method)

Circles in Fig. 8 show the potential distribution in GaAs(1) measured with the tungsten probe. It is seen that the contacts at both ends are ohmic. Accuracy of the measurement is not so good.

### 4.4. Detection of the $\beta$-conductive signal

#### 4.4.1. GaAs(1)

Figure 6 shows the resistivity $\rho(\delta V)$ or electric field distribution obtained with GaAs(1) in case of forward bias. Calibrated peak resistivity and electric field are 14.5 M $\Omega$cm and 0.77 KV/cm. The resistivity distribution agree well with the results shown by triangles obtained with the Au-contact method.

Figure 7 shows the electric field distribution $E(\delta V)$ in case of reverse bias, and an equivalent resistivity scale is also given. The peak electric field attains to 3.6 KV/cm.

To get the potential distribution, $\sqrt{\delta V}$ was integrated and the resultant curves are shown in Fig. 8 by solid lines. These results agree well with those obtained with the conventional one-probe method.

## 5. Discussions

### 5.1. Mobility and lifetime for holes

The present GaAs crystal is believed to be highly doped with Si before the oxygen-doping. Therefore the lifetime for holes $\tau_p$ in the present specimen is considered to be very short[12] as is

$$\tau_p \sim 5 \times 10^{-10} \text{ sec} \quad , \tag{2}$$

while the mobility $\mu_p$ is given by[13]

$$\mu_p \sim 300 \text{ cm}^2/\text{Vsec} \quad . \tag{3}$$

If the lifetimes and mobilities for holes and electrons are position-dependent, the present result is erroneous because $\Delta\sigma\Delta x$ in eq.(1) is not constant along the specimen[6]. For example, the step-like change at $x = 2.8$ mm on the negative potential distribution curve in Fig. 8 would deviate from the result measured with the probe if the characters of the newly created carriers were not constant. From

the good coincidence shown in Fig. 8, however, the anxiety should be denied.

5.2. Resolving power

Since the diffusion length for holes is estimated to be 0.6 μm by using the values in eqs.(2) and (3), the resolving power is mainly limited by the beam diameter of about 10 μm in this experiment[6].

With a high electric field, however, the carriers are swept away by the field. Then the resolving power should be somewhat lower at $x = 3.2$ mm of GaAs(1) in case of reverse bias, where the drift length due to the electric field is 5.4 μm.

5.3. Comparisons with conventional methods

As for the resistivity distribution the Au-contact method is more suitable than the present method to get a resistivity map in a broad area and in a wide range of resistivity. In a one-dimensional case, however, high resolution, short measuring time and non-destructiveness of the present method are greatly advantageous points over the former method which needs many Au-contacts and is a kind of destructive method.

As for the field distribution the conventional method hardly compete with the present method. In case of the one-probe method, a process of differentiation is required, which sometimes gives erroneous results, while the present method directly gives E distribution even in a two-dimensional case[7] in a short time.

As for the potential distribution the present method is more convenient than the one-probe method, which is generally laborious and often erroneous especially in GaAs because of high contact resistance between the probe and the specimen.

It is well known that a light beam can be used for the same purpose of measuring the electric field[14]. However, it is reported[15] that the accuracy or resolving power is poorer probably because of diffusive scattering of the light beam in the specimen crystal.

6. Conclusion

The electron-beam-induced conductivity was experimentally proved to be applicable to measuring resistivity, electric field and potential distributions in GaAs crystals. The present method is superior to the conventional ones on the points of short-measuring time, high resolution and non-destructiveness.

Acknowledgements

The author wishes to thank Drs. H. Watanabe, H. Kimura and M. Migitaka for their useful suggestions and discussions. Thanks are also due to Mr. J. Shirafuji for his discussions and efforts to prepare the specimens for this experiment and Miss K. Imuta for her help in preparing the manuscript.

References

1) C. Munakata: Japan. J. appl. Phys. 4(1965)697.
2) H. Watanabe & C. Munakata: Japan. J. appl. Phys. 4(1965)250-258.
3) C. Munakata & H. Watanabe: Japan. J. appl. Phys. 5(1966)1157-1160.
4) C. Munakata: Japan. J. appl. Phys. 6(1967)963-971.
5) N. C. MacDonald & T. E. Everhart: Appl. Phys. Letters 7(1965)267-269.
6) A. Zareba: Acta Phys. Polon. 21(1962)371-381.
7) C. Munakata: Japan. J. appl. Phys. (to be published).
8) C. Munakata: J. sci. Instrum. (in press).
9) C. Munakata: Japan. J. appl. Phys. 5(1966)756-763.
10) C. Munakata: Japan. J. appl. Phys. 6(1967)548-549.
11) C. Munakata: Microelectron. & Reliab. 6(1967)27-33.
12) T. Kinsel & I. Kudmann: Solid-St. Electron. 8(1965)797-801.
13) N. B. Hannay: Semiconductors (Reinhold-Maruzen, Tokyo 1959) p.415.
14) D. C. Northrop et al.: Solid-St. Electron. 7(1964)17-30.
15) A. Lempicki: J. Opt. Soc. Amer. 46(1956)611-614.

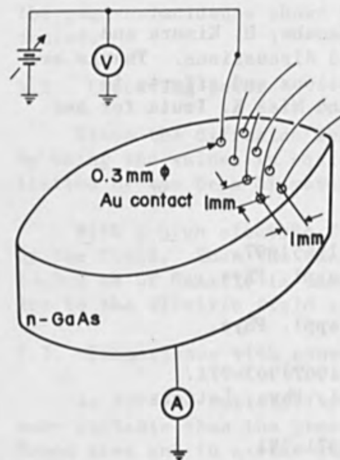


Fig. 1 Au-contact method. The resistivity derived from the current-voltage relation of the contact.

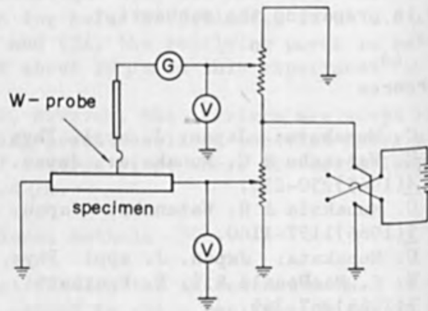


Fig. 2 One-probe method. An electronic ammeter was used as the galvanometer G to detect an electric current of 1 nA or less.

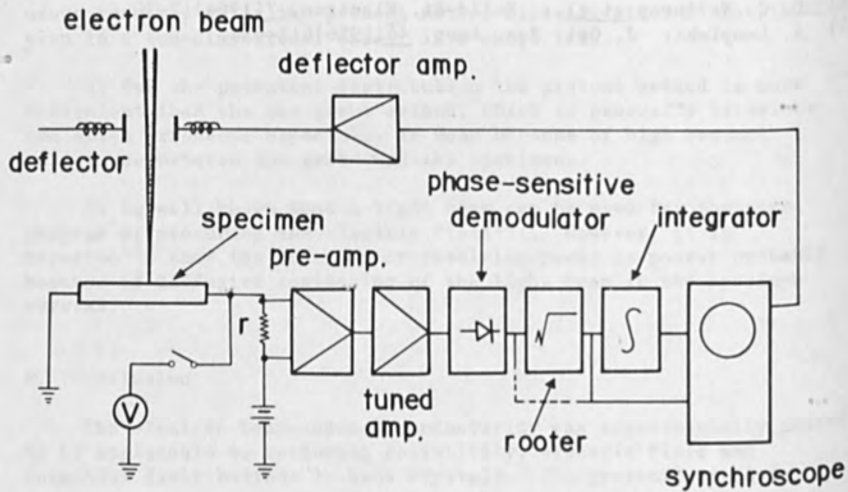


Fig. 3 Measuring system.

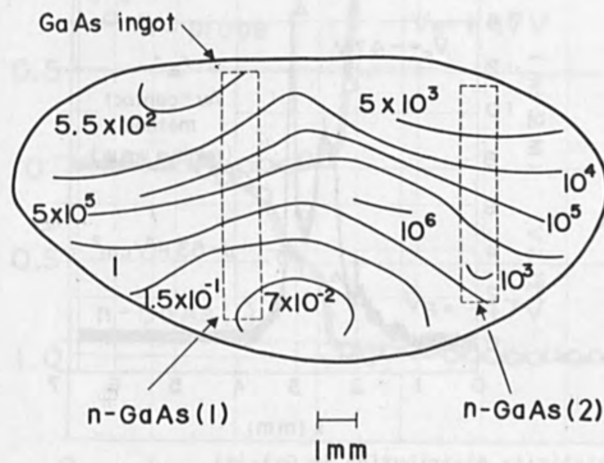


Fig. 4 Relative resistivity contours in a cross-section of the GaAs ingot.
The specimen bars were cut out from the places shown by dotted lines.

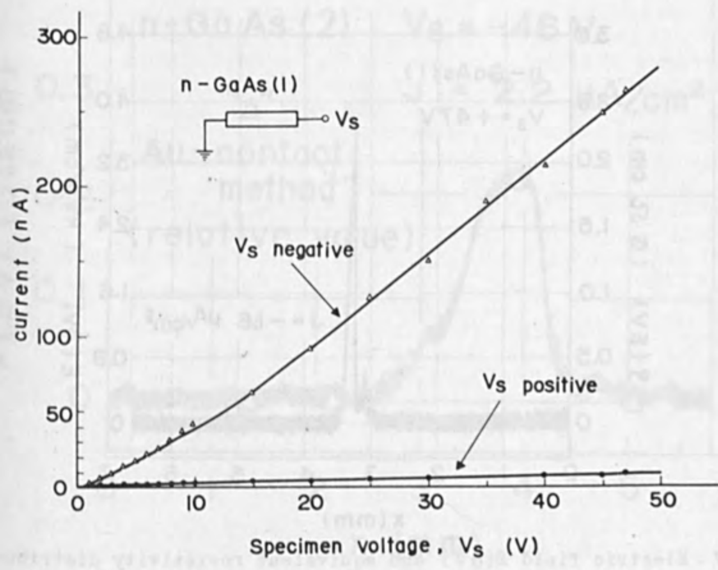


Fig. 5 Rectifying characteristic of GaAs(1).

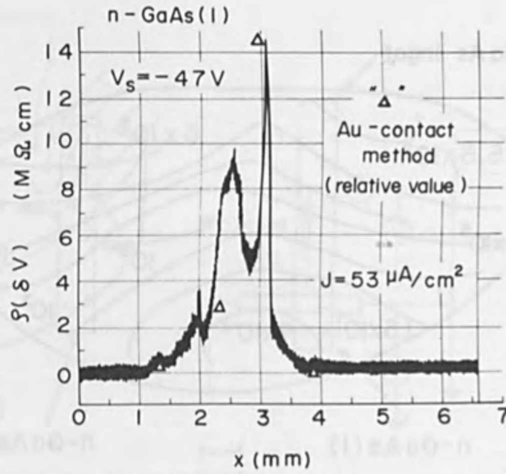


Fig. 6 Resistivity distribution in GaAs(1).
The field strength is given by the product of the resistivity $\rho(\delta V)$ and the biasing current density J. These curves in Figs. 6, 7, 8 and 9 were all traced from the synchroscopic photographs.

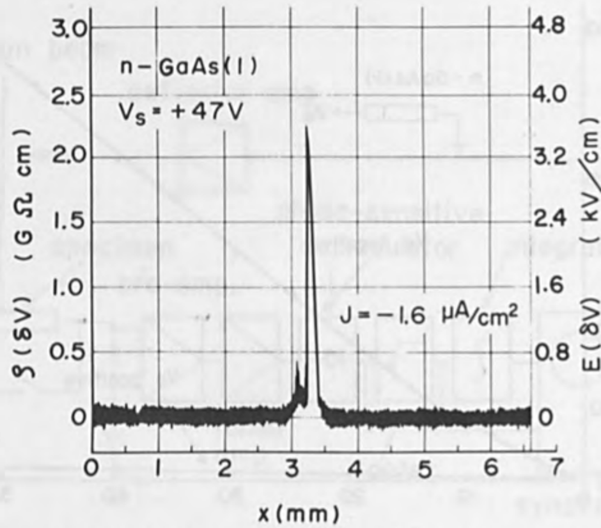


Fig. 7 Electric field $E(\delta V)$ and equivalent resistivity distributions in GaAs(1) in case of reverse bias.

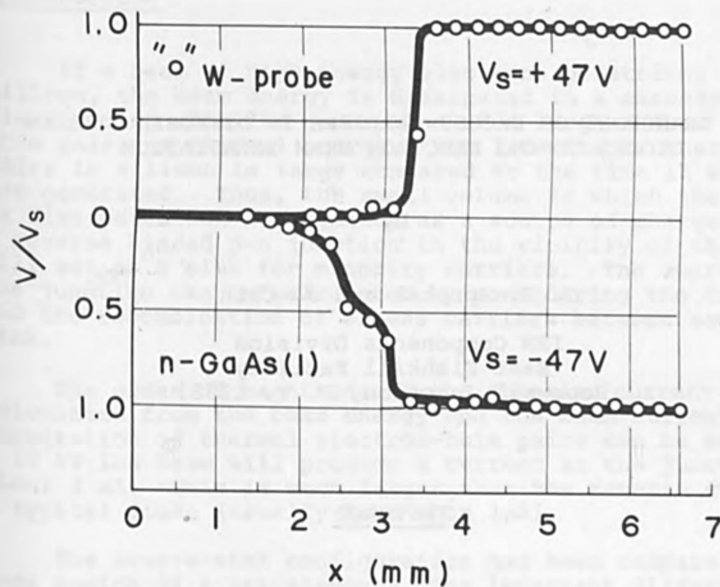


Fig. 8 Potential distributions in GaAs(1).

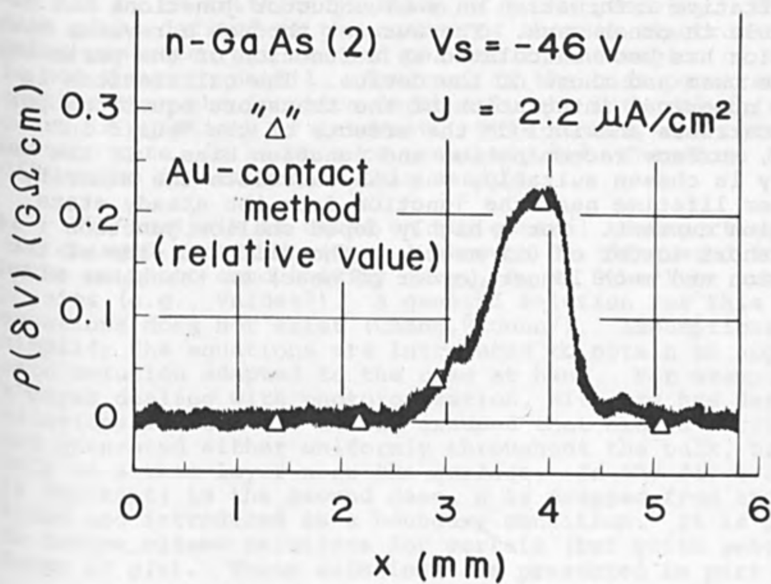


Fig. 9 Resistivity distribution in GaAs(2).

THE TRANSPORT OF EXCESS CARRIERS IN DIFFUSED SILICON DIODES DURING ELECTRON BEAM IRRADIATION

by

G. J. Sprokel and J. Chin

IBM Components Division
East Fishkill Facility
Hopewell Junction, N. Y. 12533

ABSTRACT

A scanning electron microscope can be used to obtain quantitative information on semiconductor junctions not attainable in other ways. The current through a reverse biased junction has been calculated as a function of the parameters of the beam and those of the device. The calculations involve numerical integration of the transport equations for both carriers and include the effects of the "build in" field, surface recombination and junction bias. If the beam energy is chosen suitably, one can calculate the minority carrier lifetime near the junction from the steady state junction current. For a highly doped shallow junction $\tau$ is very short (order of 0.1 nsec) on the diffused side of the junction and much longer (order of nsec) on the other side.

## INTRODUCTION

If a beam of high energy electrons penetrates into silicon, the beam energy is dissipated in a cascade of ionizations ending with the generation of a large number of electron-hole pairs of thermal energy. The lifetime of thermal e-h pairs in silicon is large compared to the time in which they are generated. Thus, the small volume in which the beam energy is dissipated can be regarded as a source of charge carriers. A reverse biased p-n junction in the vicinity of this source will act as a sink for minority carriers. The current through the junction can be calculated by considering the transport and the recombination of excess carriers between source and sink.

The order of magnitude of the junction current is readily calculated from the beam energy and the beam current. If recombination of thermal electron-hole pairs can be neglected, a 10 kV-1μA beam will produce a current at the junction of about 3 mA. This is much larger than the reverse current of a typical diode (usually less than 1μA).

The source-sink configuration has been compared with the base region of a transistor.[1] The important difference is that the source is described by a distribution function, $g(x)$, and not by an emitting junction of known geometry. The function $g(x)$, defined as the number of thermal electron-hole pairs generated per $cm^3$ and per sec in the region of the beam, is not known in detail. However, if the beam penetration is smaller than the junction depth only the integral $\int g(x)dx$ appears in equations of interest. This number, the total generation rate, is known more precisely.[2,3] Therefore this discussion is limited to this case.

The analysis is based on the general transport equations for charged particles (Eqs. 1 through 5), discussed in textbooks on photo conductivity (e.g., R. H. Bube[4]) or transistor physics (e.g., Valdes[5]). A general solution for this set of equations does not exist (Chang,[6] Gunn[7]). Assumptions which simplify the equations are introduced to obtain an approximate solution adapted to the case at hand. For example, in a paper dealing with photoionization, Rittner[8] has derived solutions for $E = 0$. It was assumed that excess carriers are generated either uniformly throughout the bulk, or limited only to a thin layer near the surface. In the first case, $g$ is constant; in the second case, $g$ is dropped from the equations and introduced as a boundary condition. It is possible to derive closed solutions for certain (but quite general) forms of $g(x)$. These solutions are presented in part I of

this paper. They are applicable at best to homogeneous media; for diffused structures, it is necessary to include the field term even outside of the depletion layer. In the main part of this aper, a numerical solution is presented and the two are compared. The reason for discussing the field free case at all is that these results are used to shorten the computer time needed for the general case.

Solutions of Eqs. 1 through 5, including the space charge field but excluding generation and recombination terms have been discussed in many papers on transistor physics.[6,7,9,10,11] Recent papers by Y. F. Chang[6] and by D. P. Kennedy and R. R. O'Brien[11] discuss much of the earlier work. Therefore, such review is omitted here.

Chang's solution is based on the assumption that the net charge density is zero everywhere. For homogeneous media, this is equivalent to equating the gradients of the minority and majority carrier concentrations. The solution presented here is not based on charge neutrality although advantage is taken of the fact that the net charge density is small compared to the carrier concentrations.

Kennedy and O'Brien apply the basic equations to a linearly graded junction and neglect the generation and recombination terms. In the present paper, the current through the reverse-biased junction is calculated from the excess carrier concentration near the junction determined mainly by the recombination process outside of the depletion layer. But, since the beam energy is limited so that no carriers are generated within the depletion region, generation and recombination within this region is neglected. The current must be limited to avoid avalanche multiplication at the junction. There is a practical aspect to this since the device is usually irreversibly changed if avalanche multiplication is allowed to occur.

Czaja[12] discussed the response of p-n junctions to electron beam irradiation. The analytical part of this paper is rather incomplete, no attempt was made to solve the transport equations with the appropriate boundary conditions. The field is neglected; the expressions for the carrier concentrations apply to homogeneous, semi-infinite regions but not to regions bounded by a source and a sink. An attempt is made to account for surface recombination but from the data it appears that the "front layer" must extend to about 1/3 of the junction depth. Finally, there is nothing in the equations to account for the junction bias.

Recently Kyser and Wittry[13] discussed the spacial distribution of excess carriers for a homogeneous, electrically isolated system (field and current zero). The generation function is assumed to be Gaussian.

## EXPERIMENTAL

Experimental techniques will be discussed elsewhere. However, before proceeding with the analysis, some experimental results are presented to justify the approximations made in the analysis.

In Fig. 1 the diode current is plotted against bias for selected values of beam current. The example chosen refers to a deep junction (3.5μ) and low doping levels ($10^{16}$ $cm^{-3}$ at the junction). For forward bias the effect of the beam is negligible; for reverse bias, the current depends only weakly on the junction bias.

In Fig. 2, the diode current is plotted against beam current using the beam energy as parameter. The diode current is proportional to the beam current over a wide range but it depends strongly on the beam energy. The device chosen shows current cut off near 5 kV. At 10 kV, the beam penetrates deep enough to make the source to sink (junction) distance less than the diffusion length. At 5 kV, the distance is much larger than L. Although at 5 kV, the number of carriers has decreased by a factor of 2, the number arriving at the junction is about 300 times smaller.

## ANALYSIS

The model is specified in Fig. 3. A junction is located at $X_j$. The junction is reverse-biased and the depletion layer extends from $X_1$ to $X_2$. The electron beam is directed perpendicular to the surface. The beam diameter is smaller than the dimensions of the diffused area but large compared to the penetration depth. Hence, one dimensional analysis is used. The current densities for holes and for electrons are given by Eqs. 1 and 2:

$$J_p = q(p\mu_p E - D_p p') \tag{1}$$

$$J_n = q(n\mu_n E + D_n n') \qquad (2)$$

The continuity equations are:

$$\dot{p} = g - \frac{p - po}{\tau_p} - \frac{1}{q} J'_p \qquad (3)$$

$$\dot{n} = g - \frac{n - no}{\tau_n} + \frac{1}{q} J'_n \qquad (4)$$

Since the equations will be used in heavily doped material, the simplified, rather than the complete Shockley-Read expressions for the recombination rates are used. We neglect trapping and therefore the recombination rates must be equal. Also, $\tau_p$ is considered an average over the region of integration.

The field is determined by Poisson's equation:

$$E' = \frac{q}{\varepsilon} (N_d - N_a + p-n) \qquad (5)$$

To specify this set of equations, five boundary conditions are required.

In the steady state case, $J'_p + J'_n = 0$, or $J_p + J_n = J$, and $J$ is constant. At the front surface, $J_p(x=0) = 0$ and thus $J_n(x=0) = J$. If it is desired to take surface recombination into account, the hole current near the surface should be just large enough to supply the needed carriers. At the junction, neglecting the quiescent current we have $J_n(x=x_1) = 0$ and $J_p(x=x_1) = J$. Two other conditions are required, preferably containing either $p_o$, $n_o$ or $p_1$, $n_1$. Chang[6] supplies these conditions by assuming that the junction is at equilibrium and the minority carrier concentration is given by the Boltzmann equation. This is true only for $J = 0$ but not during irradiation.

In part 1 of this section, an approximate solution is obtained neglecting the field terms in Eqs. 1 and 2. Only two boundary conditions are required since the equations are now

decoupled. In part 2, the field is re-introduced and the minority carrier concentrations calculated in part 1 form an upper limit for the desired solution. Thus, since the range of $p$ is determined, the computer program merely iterates. It was found advantageous to re-write the equations using $p$ and $\Delta$ rather than $p$ and $n$. $q\Delta$ is the net charge density and it may be assumed to be small compared to either $qp$ or $qn$. It is still not possible to use the Runge Kutta technique for simultaneous differential equations because these solutions depend critically on the starting values and as yet $\Delta(0)$ and $\Delta'(0)$ are unknown. But it was found that an iteration scheme quickly leads to a self consistent solution. First, $p$ is calculated taking $\Delta = 0$, then $\Delta$ is calculated using these values for $p$. A new $p$ is calculated using these $\Delta$'s, etc. The reason why the process converges rapidly will become apparent from the numerical results.

## Part 1 - Field Free Approximation

Neglecting the field term, Eq. (3) may be written as

$$\dot{p} = g - \frac{p}{\tau_p} + D_p p'' \qquad (6)$$

in which $p = p - p_o$.

The function $g$ is represented by trial functions

Case 1 $\quad g(x) = g_o e - \frac{x}{\ell} \quad \ell<0.2x_1$

and

Case 2 $\quad g(x) = g_o$ for $\quad o<x<a$

$\quad g(x) = 0$ for $\quad a<x<x_1$

Solutions of Eq. (6) are subjected to the following boundary conditions

$$p(x = x_1) = p_1 \qquad (7)$$

and

$$-D_p p'_o + s p_o = 0 \tag{8}$$

Equation (7) maintains the minority carrier concentration at the edge of the depletion layer at some value $p_1$, to be determined later.

Equation (8) states that the minority carrier current at a small distance from the surface be equal to the surface recombination current. The surface recombination velocity $s$ is assumed to be constant in this layer.

The steady state solution Eq. (6) subjected to the boundary conditions, Eqs. (7) and (8) can be written as

$$p = g_o \tau \cdot U(x, x_1, \ell, L, s) + p_1 V(x, x_1, \ell, L, s) \tag{9}$$

From Eq. (9), the following expression for the current density is obtained:

$$J = q g_o \ell \cdot W(x_1, \ell, L, s) - \frac{q p_1 D_p}{L} \cdot Z(x_1, \ell, L, s) \tag{10}$$

The derivation of these equations is given in Appendix 1. The functions U, V, W, and Z are listed in Table 1.

For zero beam current, Eqs. (9) and (10) reduce to the well-known equations for a reverse-biased junction in equilibrium. Experimentally the diode current under irradiation is 2 or 3 orders of 10 larger than the quiescent diode current. Thus the second term in Eqs. (9) and (10) can be neglected. Note that $q g_o \ell$ represents the maximum diode current density for the particular beam parameters.

Thus:

$$W = \frac{J}{q g_o \ell} \leq 1. \tag{15}$$

The functions U and W are independent of $g_o$ but they do contain the beam penetration parameter $\ell$. Figures 4a and 5 illustrate the functions U and W for $Ls/D = 10^{-3}$ and $\ell/x_1$ as indicated. From Fig. 5, it is apparent that the residual effect of $\ell/x_1$ is not large. In Fig. 6, the current

TABLE 1. Steady State Solution.

Case 1 $g(x) = g_o e^{-x/\ell}$

$$U = \frac{\frac{L}{\ell}\sinh\frac{x_1-x}{L} + e^{-x_1/\ell}\cdot\cosh\frac{x}{L} - e^{-x/\ell}\cdot\cosh\frac{x_1}{L} - \frac{Ls}{D}\left[e^{-x/\ell}\cdot\sinh\frac{x_1}{L} - \sinh\frac{x_1-x}{L} - e^{-x_1/\ell}\cdot\sinh\frac{x}{L}\right]}{\left(\frac{L^2}{\ell^2} - 1\right)\left(\cosh\frac{x_1}{L} + \frac{Ls}{D}\sinh\frac{x_1}{L}\right)} \tag{11}$$

$$V = \frac{\cosh\frac{x}{L} + \frac{Ls}{D}\sinh\frac{x}{L}}{\cosh\frac{x_1}{L} + \frac{Ls}{D}\sinh\frac{x_1}{L}} \tag{12}$$

$$W = \frac{1 - e^{-x_1/\ell}\left(\cosh\frac{x_1}{L} + \frac{\ell}{L}\sinh\frac{x_1}{L}\right) + \frac{Ls}{D}\left[\frac{\ell}{L} - e^{-x_1/\ell}\left(\sinh\frac{x_1}{L} + \frac{\ell}{L}\cosh\frac{x_1}{L}\right)\right]}{\left(1 - \frac{\ell^2}{L^2}\right)\left(\cosh\frac{x_1}{L} + \frac{Ls}{D}\sinh\frac{x_1}{L}\right)} \tag{13}$$

$$Z = \frac{\sinh\frac{x_1}{L} + \frac{Ls}{D}\cosh\frac{x_1}{L}}{\cosh\frac{x_1}{L} + \frac{Ls}{D}\sinh\frac{x_1}{L}} \tag{14}$$

Case 2 $g(x) = g_o$ for $o < x < a$, $g(x) = 0$ for $x > a$

$$U = \frac{\sinh\frac{a}{L}\sinh\frac{x_1-x}{L} + \frac{Ls}{D}\sinh\frac{x_1-x}{L}\left(\cosh\frac{a}{L} - 1\right)}{\cosh\frac{x_1}{L} + \frac{Ls}{D}\sinh\frac{x_1}{L}} \tag{11a}$$

$$V = \frac{\cosh\frac{x}{L} + \frac{Ls}{D}\sinh\frac{x}{L}}{\cosh\frac{x_1}{L} + \frac{Ls}{D}\sinh\frac{x_1}{L}} \tag{12a}$$

$$W = \frac{\frac{L}{a}\left[\sinh\frac{a}{L} + \frac{Ls}{D}\left(\cosh\frac{a}{L} - 1\right)\right]}{\cosh\frac{x_1}{L} + \frac{Ls}{D}\sinh\frac{x_1}{L}} \tag{13a}$$

$$Z = \frac{\sinh\frac{x_1}{L} + \frac{Ls}{D}\cosh\frac{x_1}{L}}{\cosh\frac{x_1}{L} + \frac{Ls}{D}\sinh\frac{x_1}{L}} \tag{14a}$$

density is plotted as a function of Ls/D. It is apparent that for $s < 10^4$ cm $sec^{-1}$ the effect of surface recombination is small.

If surface recombination can be neglected, the time dependent solution of Eq. (6) can be obtained directly using Laplace transformation. The results are collected in Table 2. Details of these calculations are given in Appendix 2. It is seen that the time independent parts of these expressions are identical to those of Table 1 for s = 0, as it should be. Figure 7a illustrates the shape of the transient curve for case 1.

## Part 2 - General Solution

### 2.1 Steady State

In the steady state the partial differential equations change to ordinary differential equations. Runge-Kutta subroutines exist to solve a set of ordinary differential equations[15], however initial values are required. It is not feasible to determine four starting values by trial and error. Therefore the set of equations 1 through 5 is transformed to a new set for which the choice of initial values is more obvious.

Add Eqs. (1) and (2), and solve for E

$$E = \frac{\frac{J}{q} - D_n n' + D_p p'}{p\mu_p + n\mu_n} \tag{20}$$

and

$$E' = \frac{D_p p'' - D_n n''}{p\mu_p + n\mu_n} - \frac{\frac{J}{q} - D_n n' + D_p p' (p'\mu_p + n'\mu_n)}{(p\mu_p + n\mu_n)^2} \tag{21}$$

TABLE 2. Time Dependent Solution for $s = 0$.

Case 1 $g = g_o e^{-x/\ell}$

$$\frac{p(x,t)}{g_o \tau} = \frac{\frac{L}{\ell}\sinh\frac{x_1 - x}{L} + e^{-x_1/\ell}\cosh\frac{x}{L} - e^{-x/\ell}\cosh\frac{x_1}{L}}{\left(\frac{L^2}{\ell^2} - 1\right)\cosh\frac{x_1}{L}} - 2\sum_k (-1)^k \frac{\frac{\ell}{x_1}\sin(2k+1)\frac{\pi}{2}\frac{x_1 - x}{x_1} + (2k+1)\frac{\pi}{2}\frac{\ell^2}{x_1^2} e^{-x_1/\ell}\cos(2k+1)\frac{\pi}{2}\frac{x}{x_1}}{\left[1 + \left((2k+1)\frac{\pi}{2}\frac{\ell}{x_1}\right)^2\right]\left[1 + \left((2k+1)\frac{\pi}{2}\frac{L}{x_1}\right)^2\right]} e^{-a_k t}$$

$$\frac{J}{q g_o \ell} = \frac{1 - \frac{\ell}{L} e^{-x_1/\ell}\left(\sinh\frac{x_1}{L} + \frac{L}{\ell}\cosh\frac{x_1}{L}\right)}{\left(1 - \frac{\ell^2}{L^2}\right)\cosh\frac{x_1}{L}} - 2\sum_k (-1)^k \frac{\frac{L^2}{x_1^2}(2k+1)\frac{\pi}{2}\left(1 + (-1)^k (2k+1)\frac{\pi}{2}\frac{\ell}{x_1} e^{-x_1/\ell}\right)}{\left[1 + \left((2k+1)\frac{\pi}{2}\frac{\ell}{x_1}\right)^2\right]\left[1 + \left((2k+1)\frac{\pi}{2}\frac{L}{x_1}\right)^2\right]} \cdot e^{-a_k t} \qquad (17)$$

Case 2 $g = g_o$ for $o < x < a$, $g = 0$ for $x > a$

$$\frac{p(x,t)}{g_o \tau} = \frac{\sinh\frac{a}{L}\sinh\frac{x_1 - x}{L}}{\cosh\frac{x_1}{L}} - 2\sum_k (-1)^k \frac{\sin(2k+1)\frac{\pi}{2}\frac{a}{x_1} \cdot \sin(2k+1)\frac{\pi}{2}\frac{x_1 - x}{x_1}}{(2k+1)\frac{\pi}{2}\left[1 + \left((2k+1)\frac{\pi}{2}\frac{L}{x_1}\right)^2\right]} \cdot e^{-a_k t} \qquad (18)$$

$$\frac{J}{q g_o a} = \frac{\frac{L}{a}\sinh\frac{a}{L}}{\cosh\frac{x_1}{L}} - 2\frac{L^2}{a x_1}\sum_k (-1)^k \frac{\sin(2k+1)\frac{\pi}{2}\frac{a}{x_1}}{1 + \left((2k+1)\frac{\pi}{2}\frac{L}{x_1}\right)^2} \cdot e^{-a_k t}$$

$$\text{in which } a_k = \frac{1}{\tau}\left[1 + \left((2k+1)\frac{\pi}{2}\frac{L}{x_1}\right)^2\right] \qquad (19)$$

in which $J = J_p + J_n$ and $J' = 0$.

Substitute Eqs. (1) and (2) into Eqs. (3) and (4) respectively, then substitute Eqs. (20) and (21). The result is:

$$0 = g - \frac{p}{\tau_p} + bD_p \frac{\left(\frac{J}{qD_p} + p'-bn'\right)(pn'-np')}{(p + bn)^2} + bD_p \frac{np'' + pn''}{p + bn} \qquad (22)$$

in which

$$b = \frac{\mu_n}{\mu_n} = \frac{D_n}{D_p}$$

If we put

$$N_D - N_A + p - n = \Delta(x) \qquad (23)$$

Eq. (5) can be written:

$$E' = \frac{q}{\varepsilon}(N_d - N_a + p - n) = \frac{q}{\varepsilon}\Delta(x) \qquad (24)$$

$\Delta$ is far smaller than any of the terms on the left of Eq. (2[illegible]) Use Eq. (23) to eliminate $n$ from Eq. (22). The result is abbreviating $N_D - N_A = N$:

$$0 = g - \frac{p}{\tau_p} + bD_p \frac{\left\{\frac{J}{qD_p} + p'(1-b) - bN'\left(1-\frac{\Delta'}{N'}\right)\right\}\left\{pN'\left(1-\frac{\Delta'}{N'}\right) - p'N\left(1-\frac{\Delta}{N}\right)\right\}}{\left\{p(1+b) + bN\left(1-\frac{\Delta}{N}\right)\right\}^2}$$

$$+ bD_p \frac{p''N\left(1-\frac{\Delta}{N}\right) + pN''\left(1-\frac{\Delta''}{N''}\right) + 2pp''}{p(1+b) + bN\left(1-\frac{\Delta}{N}\right)} \tag{25}$$

Equation (5) changes to

$$\Delta(x) = \frac{\varepsilon}{q} \cdot \frac{kT}{q}\left[\frac{(1-b)p'' - bN''\left(1-\frac{\Delta''}{N''}\right)}{(1+b)p + bN\left(1-\frac{\Delta}{N}\right)} - \frac{\left\{\frac{J}{qD_p} + (1-b)p' - bN'\left(1-\frac{\Delta'}{N'}\right)\right\}\left\{(1+b)p' + bN'\left(1-\frac{\Delta'}{N'}\right)\right\}}{\left\{(1+b)p + bN\left(1-\frac{\Delta}{N}\right)\right\}^2}\right] \tag{26}$$

Equations (25) and (26) form a set of simultaneous, second order differential equations in $p$ and $\Delta$, equivalent to Eqs. 1 through 5. If starting values for Eqs. 1 through 5 were known, there would be no need for these transformations.

Note that in Eqs. (25) and (26) $\Delta$ occurs only as $(1 - \Delta/N)$ terms and $\Delta/N \ll 1$. Therefore, to circumvent the initial value problem, neglect $\Delta/N$ as compared to 1 and solve (25). Then, using this solution obtain $\Delta$ from (26)

and iterate between the two until a self consistent set $p$ and $\Delta$ is found.

The two boundary conditions for Eq. (25) are, as before:

$$J_p(x=x_1) = J \tag{27}$$

$$J_p(x=0) = 0 \tag{28}$$

With Eqs. (1), (20), and (23), these equations change to:

$$\frac{J}{qg_o \ell} = b \cdot \frac{L^2}{\ell} \cdot \frac{1}{g_o t} \cdot \left( N' - \Delta' + p' \left( \frac{N - \Delta}{p} + 2 \right) \right) \Bigg|_{x=0} \tag{29}$$

$$\frac{J}{qg_o \ell} = - \frac{L^2}{\ell} \cdot \frac{1}{g_o t} \left( p' + \frac{N' - \Delta' + p'}{N - \Delta + p} \cdot p \right) \Bigg|_{x=x_1} \tag{30}$$

Starting values for $p(o)$ and $J/qg_o\ell$ are obtained from the functions $U(x=0)$ and $W$ in part 1. Introducing the field will decrease $p(o)$ and increase the current density.

Thus:

$$0 \le P(0) \le U(x=0) \tag{31}$$

$$W \le \frac{J}{qg_o \ell} \le 1 \tag{32}$$

Values for the surface concentration and the normalized current density are assumed within their respective ranges, and $p'(o)$ is calculated from Eq. (29). The Runge-Kutta scheme supplies $p(x)$ and $p'(x)$ for each step up to $p(x_1)$.

Equation (30) is now evaluated, and the numerical result is compared with the assumed current density. The process is repeated until the two agree to within a determined interval. Next $\Delta$ is evaluated from Eq. (26), and the whole sequence is repeated until the boundary conditions agree.

It is helpful to normalize all equations. We have introduced

$$u = x/x_1$$

$$p(x) = P(u) * g_o \tau_p$$

$$N_D = N_{D^o} \operatorname{erfc}\left(u * \frac{x_1}{2\sqrt{Dt}}\right)$$

The normalized equations and further details are given in Appendix 3.

Table 3 is an excerpt of a 100 point computer run for the parameters indicated. Three iterations were required to establish the starting value (0.217560-1) for $\Delta = 0$. The numerical value of $\Delta/N_{D^o}$ is of the order of $10^{-5}$, indeed much smaller than 1. The second approximation for $\Delta$ differs at most 0.3% from the first, further iteration is not necessary. The change in $P(I)$ is about 0.1% and the change in $J$ is about 1 in $10^{+5}$. Experimental accuracy is estimated at 5%.

The customary checks on the Runge-Kutta method were made; doubling the number of steps or inverting the direction of integration produces the same results.

## 2.2 Time Dependent Solution

The Laplace solution, Eq. (16) in part 1, consists of a time independent part $P(x,\infty)$ and a harmonic series with coefficients exponentially decreasing in time. For the general case, assume a solution of similar form:

$$p(x,t) = p(x,\infty) - \sum_{k=0} A_k \cos kx \exp-\alpha_k\frac{t}{\tau} + B_k \sin kx \exp-\beta_k\frac{t}{\tau} \qquad (33)$$

TABLE 3. Excerpt of Computer Output for X1L = 1; $N = 10^{19}$ erfc x/0.48; $N_A = 2.10^{16}$ $cm^{-3}$; $x_j = 1.05$ $\mu$; 10V bias; $g_0\tau = 10^{17}$ $cm^{-3}$; CON (0) = 0.2208600 -3. Computer time 1.2 minutes

| | Before Iteration | | After 1st Iteration | |
|---|---|---|---|---|
| $x/x_1$ | P (I) | $\Delta$ (I)/$N_D$o | P (I) | $\Delta$ (I)/$N_D$o |
| 0.00 | 0.217560-1 | 0.953872-5 | 0.217560-1 | 0.953916-5 |
| 0.05 | 0.223619-1 | 0.980227-5 | 0.223619-1 | 0.980277-5 |
| 0.10 | 0.219783-1 | 0.100602-4 | 0.219784-1 | 0.100608-4 |
| 0.15 | 0.212075-1 | 0.103100-4 | 0.212076-1 | 0.103107-4 |
| 0.20 | 0.203069-1 | 0.105508-4 | 0.203070-1 | 0.105516-4 |
| 0.25 | 0.193852-1 | 0.107827-4 | 0.193854-1 | 0.197836-4 |
| 0.30 | 0.184867-1 | 0.110062-4 | 0.184870-1 | 0.110074-4 |
| 0.35 | 0.176285-1 | 0.112223-4 | 0.176288-1 | 0.112237-4 |
| 0.40 | 0.168145-1 | 0.114321-4 | 0.168159-1 | 0.114338-4 |
| 0.45 | 0.160477-1 | 0.116370-4 | 0.160483-1 | 0.116390-4 |
| 0.50 | 0.153233-1 | 0.118387-4 | 0.153240-1 | 0.118412-4 |
| 0.55 | 0.146396-1 | 0.120395-4 | 0.196404-1 | 0.120425-4 |
| 0.60 | 0.139934-1 | 0.122418-4 | 0.139946-1 | 0.122455-4 |
| 0.65 | 0.133820-1 | 0.124489-4 | 0.133836-1 | 0.124536-4 |
| 0.70 | 0.128025-1 | 0.126651-4 | 0.128045-1 | 0.126709-4 |
| 0.75 | 0.122522-1 | 0.120957-4 | 0.122547-1 | 0.129030-4 |
| 0.80 | 0.117284-1 | 0.131473-4 | 0.117314-1 | 0.136567-4 |
| 0.85 | 0.112282-1 | 0.134291-4 | 0.112322-1 | 0.134413-4 |
| 0.90 | 0.107496-1 | 0.137529-4 | 0.107547-1 | 0.137688-4 |
| 0.95 | 0.102899-1 | 0.141346-4 | 0.102965-1 | 0.181557-4 |
| 1.00 | 0.984706-2 | 0.145956-4 | 0.985545-2 | 0.146242-4 |
| CON(1) | 0.2212231-3 | | 0.2208517-3 | |

As before, we neglect the minority carrier concentration in the quiescent state compared to the concentration upon irradiation. Thus:

$$p(x,t=0) = 0 \tag{34}$$

and therefore

$$p(x,\infty) = \sum_{k=0} A_k \cos kx + B_k \sin kx \tag{35}$$

which determines the coefficients $A_k$ and $B_k$.

To determine the $\alpha_k$ and $\beta_k$'s rewrite Eq. (33) as

$$p(x,t) = \sum_{k=0} A_k \cos kx(1-\exp-\alpha_k\frac{t}{\tau})+B_k \sin kx(1-\exp-\beta_k\frac{t}{\tau}) \tag{36}$$

and substitute Eqs. (36) and (1) in Eq. (3). This leads to

$$\sum_{k=0} A_k\alpha_k \cos kx + B_k\beta_k \sin kx = gt \tag{37}$$

This determines all products $A_k\alpha_k$ and $B_k\beta_k$ and therefore $\alpha_k$ and $\beta_k \cdot J(t)$ can now be calculated using Eq. (30).

The function $p(x,\infty)$ has been tabulated as the normalized function $P(u,\infty$ for $u = 0, 0.01, 0.02.....1$.

If we set

$$P(I) = \sum_{k=0}^{50} A_k \cos k\frac{2\pi}{101}(I-1) + B_k \sin k\frac{2\pi}{101}(I-1) \tag{38}$$

for I = 1,2,.....101.

Then

$$A_k = \frac{2}{101} \sum_{I=1}^{101} P(I) \cos \frac{2\pi}{101} k(I-1) \tag{39}$$

and

$$B_k = \frac{2}{101} \sum_{I=1}^{101} P(I) \sin \frac{2\pi}{101} k(I-1) \tag{40}$$

for k = 1,2.....50,

$$A_o = \frac{1}{101} \sum P(I) \tag{41}$$

and

$$B_o = 0. \tag{42}$$

Similar expressions hold for the products $A_k \alpha_k$ and $B_k \beta_k$.

Finally:

$$\alpha_k = \frac{\sum_{I=1}^{101} \exp\left(- \frac{x_1}{\ell} \cdot \frac{I-1}{100}\right) \cdot \cos \frac{2\pi}{101} k(I-1)}{\sum_{I=1}^{101} P(I) \cos \frac{2\pi}{101} k\ (I-1)} \tag{43}$$

and

$$\beta_k = \frac{\sum_{I=1}^{101} \exp\left(-\frac{x_1}{\ell} \cdot \frac{I-1}{100}\right) \sin\frac{2\pi}{101} k(I-1)}{\sum_{I=1}^{101} P(I) \sin\frac{2\pi}{101} k(I-1)} \tag{44}$$

for $k = 1, 50$

$$\alpha_o = \frac{\sum_{I=1}^{101} \exp\left(-\frac{x_1}{\ell} \cdot \frac{I-1}{100}\right)}{\sum_{I=1}^{101} P(I)} \tag{45}$$

and

$$\beta_o = 0. \tag{46}$$

A standard subroutine is available to evaluate the expressions, see reference 15.

The method breaks down if any one of the $\alpha_k$ or $\beta_k$ are negative. It is easy to show that the enumerator approaches the expression

$$\frac{\frac{\ell}{x_1}\left(1 - e^{-\frac{x_1}{\ell}}\right)}{1 + \frac{2\pi k\ell}{x_1}^2}$$

which is positive since $x_1/\ell > 1$. No direct proof has been found to show that the denominator is always positive. However numerical calculation has shown this to be the case. As an illustration, the coefficients $A_k$, $B_k$, $\alpha_k$, and $\beta_k$ are

listed in Table 4. The $\alpha_k$'s are of the order $10^2$ - $10^3$ for all k except k = 0. This means that the expenonential term is small compared to 1 for all $t/\tau > 0.01$. Thus $p(x,t)$ increases in time almost as a single exponential. This exponent is the ratio of the number of carriers generated per unit time and the number of carriers at equilibrium. There is a small contribution of the $\beta_k$ term.

TABLE 4

Excerpt of Computer Run. Coefficients $A_k$, $B_k$, $\alpha_k$, and $\beta_k$ for k = 50. All Parameters as in Table 3

| $A_k$ | $B_k$ | $\alpha_k$ | $\beta_k$ |
|---|---|---|---|
| 0.15829D-01 | 0.0 | 0.40743D 01 | 0.0 |
| 0.64500D-03 | 0.45159D-02 | 0.17745D 03 | 0.85967D 01 |
| 0.90706D-04 | 0.22168D-02 | 0.95330D 03 | 0.25599D 02 |
| 0.43737D-04 | 0.14169D-02 | 0.14379D 04 | 0.41444D 02 |
| 0.52430D-04 | 0.10278D-02 | 0.89587D 03 | 0.53047D 02 |
| 0.66158D-04 | 0.80268D-03 | 0.55442D 02 | 0.60981D 02 |
| 0.77495D-04 | 0.65702D-03 | 0.38620D 03 | 0.66384D 02 |
| 0.86003D-04 | 0.55525D-03 | 0.29486D 03 | 0.70136D 02 |
| 0.92305D-04 | 0.48007D-03 | 0.24008D 03 | 0.72808D 02 |
| 0.97017D-04 | 0.42216D-03 | 0.20462D 03 | 0.74762D 02 |

This is in agreement with the equations listed in Table 2. The first coefficient for the field free case is 3.47, and if the field is included one finds 4.07 for the parameters indicated in Table 4. Including the field decreases the risetime as one would expect.

For $t/\tau < 0.01$ and $x/x_1 \approx 1$, the numerical values of $p(x,t)$ are very small and inaccurate because of accumulated errors. Thus for small t, $J(t)$ can not be calculated. At the other end of the range, $J(t \to \infty)$ agrees with the steady state value to within 1%.

DISCUSSION

Figure 4b illustrates some steady minority carrier profiles calculated for the same parameters as in Fig. 4a. The average concentration is lower in Fig. 4b as it should be

since the field aids the transport of minority carriers toward the junction. In Fig. 4a $P'(0) = 0$ but in Fig 4b $P'(0) > 0$. Thus the graphs in Fig. 4b show a maximum. As XlL increases this maximum is more pronounced and moves toward the surface. For L infinitesimally small the curves would represent the function $g(x)$.

In Fig. 4a $P(1)$ is assumed to be determined only by the junction bias but in Fig. 4b it is seen that $P(1)$ depends on XlL.

In both Fig. 4a and 4b the concentration is normalized by the factor $g_o\tau$. The profiles in Fig. 4b remain essentially constant as $g_o\tau$ is changed. Calculations have been made up to $g_o\tau = 10^{18}$ $cm^{-3}$ (for beam currents as normally encountered $g_o \leq 10^{17}$ $cm^{-3}$). The $g_o\tau$ term is contained in the expression GTN, GTNA, and GTNB. For $g_o\tau = 10^{18}$ $cm^{-3}$ the terms GTN*P are about 1% of EN thus a change in $g_o\tau$ affects $P(1)$ very little. Physically this means that the electron beam does not change the field near the junction. The field is determined essentially by the impurity profile.

In Fig. 5 the normalized diode current is plotted versus $x_1/L$ for the same parameters as used in Fig. 4. For the field free case it has already been mentioned that the residual effect of $\ell/x_1$ is small. However the addition of the field increases the current markedly. Using the program outlined above, graphs like Fig. 5 are calculated for the device being analyzed. The impurity profile must be known but it need not be as simple as a complementary error function. The ordinate, the normalized diode current, is readily calculated from the observed current and the electron beam parameters. The corresponding abscissa is $X_1/L$.

Figure 7a indicates the order of magnitude of the risetime of the junction current for an infinitely fast switching beam. It is seen that the risetime is approximately equal to the carrier lifetime $\tau$ if L is less than $x_j$ and smaller than $\tau$ is L is larger than $x_j$. For highly doped shallow junctions, such as emitter junctions, the calculated risetimes are of the order of 0.1 ns, far too short for accurate measurements. For deep and lightly doped junctions the calculated risetime increases to a few ns which can be observed. The observed risetimes agree roughly with the expected risetime. However, pulse type measurements are as yet rather inaccurate. Figure 7b shows that if the field is included the transit time is shorter, as it should be.

Figure 8 illustrates the minority carrier profile for successive time steps.

Figure 9 illustrates the effect of junction bias on diode current for constant beam parameters. Calculations were made for a 1μ junction, the normalized diode current is plotted against L. If L is approximately equal to $x_j$, an increase in bias from 1 to 10 V increases the current by a few percent. But if $L \approx 0.2\ X_j$ (typical for an emitter junction), the current increases by a factor of 2.

Finally, in Fig. 10, the field is plotted for the example used in Fig. 8. The field does not depend on $x_1/L$.

SUMMARY

The theory accounts for the observations: the diode current is proportional to the beam current and depends on the beam energy through the total number of carriers generated. The diode current depends very little on junction bias if L is about the same as $x_j$, but it depends markedly on the bias if L is much smaller than $x_j$. Surface recombination for carefully prepared surfaces does not have an appreciable effect. However any numerical value for s can be introduced into the calculations. The excess hole concentration near the surface, caused by secondary electron emission, has been neglected.

The method was used to calculate L near a junction. For highly doped junctions, L was found to be quite small (0.1 or 0.2μ) corresponding to carrier lifetimes of a fraction of a nanosecond. Lifetimes of this order can not be measured by a pulse technique. L is an average over the source to sink distance. Apparently, it depends on the doping level. More experimental data are needed to describe L more accurately.

Trapping has been neglected. There is as yet no experimental evidence to suggest a large trapping cross section near the junction.

The mobility ratio is taken constant, but again a known b(x) curve can be introduced into the calculations.

For very small L, the minority carrier profile approaches the generating function. However, the profile can not be determined experimentally. If L were known accurately

one could increase the beam energy allowing carriers to be generated within the strong field region. From the diode current, one could possibly obtain more information about the function $g$.

ACKNOWLEDGMENT

The experimental part of this work was carried out in cooperation with R. N. Schiavone. Figure 2 is taken from his work.

APPENDIX 1. STEADY STATE SOLUTION OF EQUATION 6.

A closed solution of Eq. (6) can be obtained for certain functions $g(x)$. As an example take case 1:

$$g = g_o e^{-x/\ell} = g_o \sum_{n=0}^{\infty} \frac{(-1)^n}{n!} \cdot \left(\frac{x_1}{\ell}\right)^n u^n$$

in which $u = x/x_1$.

Expand $p$ in a power series

$$p = p_o \sum_n A_n u^n$$

and substitute both series in Eq. (6). One obtains the recurrent relation:

$$A_{n+2} = \frac{A_n}{(n+2)(n+1)} \cdot \left(\frac{x_1}{L}\right)^2 - \frac{g_o \tau_p}{p_o} \cdot \frac{(-1)^n}{(n+2)!} \cdot \left(\frac{x_1}{\ell}\right)^n \left(\frac{x_1}{L}\right)^2$$

$$n = 0,1,2\ldots.$$

The recurrent relation determines all coefficients $A_n$ except $A_0$ and $A_1$ which must be obtained from boundary conditions. One repeated application of the recurrent relation it is seen that the coefficients $A_n$ can be written as

$$A_n = \frac{1}{n!} \cdot \left(\frac{x_1}{L}\right)^n - \frac{g_o \tau}{p_o} \cdot \frac{\frac{1}{n!}\left(\frac{n_1}{L}\right)^n - \frac{1}{n!}\left(\frac{x_1}{\ell}\right)^n}{1 - \frac{L^2}{\ell^2}} \quad \text{for } n = 0,2,4\ldots$$

These are the coefficients of the expression

$$\cosh \frac{x}{L} - \frac{g_o \tau}{p_o} \left[ \frac{\cosh \frac{x}{L} - \cosh \frac{x}{\ell}}{1 - \frac{L^2}{\ell^2}} \right]$$

For the odd numbered terms, one finds

$$A_n = C_1 \frac{L}{x_1} \frac{1}{n!} \left(\frac{x_1}{L}\right)^n + \frac{g_o \tau}{p_o} \frac{\frac{L}{\ell} \cdot \frac{1}{n!}\left(\frac{x_1}{L}\right)^n - \frac{1}{n!}\left(\frac{x_1}{\ell}\right)^n}{1 - \frac{L^2}{\ell^2}} \quad n = 1,3,5\ldots$$

These are the coefficients of the expressions.

$$C_1 \frac{L}{x_1} \sinh \frac{x}{L} + \frac{g_o \tau}{p_o} \frac{\frac{L}{\ell} \sinh \frac{x}{L} - \sinh \frac{x}{\ell}}{1 - \frac{L^2}{\ell^2}}$$

On combining the two expressions the general form of p is obtained

$$\frac{p}{p_o} = \cosh\frac{x}{L} \cdot C_1 \cdot \frac{L}{x_1} \sinh\frac{x}{L} + \frac{g_o\tau}{p_o} \cdot \frac{\frac{L}{\ell}\sinh\frac{x}{L} - \cosh\frac{x}{L} + \exp - \frac{x}{\ell}}{1 - \frac{L^2}{\ell^2}}$$

The arbitrary constants $C_1$ and $p_o$ are eliminated by substituting the general form of p in Eqs. (7) and (8), solving for $C_1$ and $p_o$. The result is Eq. (9) as used in the text.

If the series expansion technique is applied to the general equations one obtains a set of simultaneous indicial equations. Four parameters have to be determined. We programmed these equations to obtain the numerical values of the coefficients but the approach was abandoned. The numerical values of the coefficients of the higher terms are meaningless numbers.

## APPENDIX 2. TIME DEPENDENT SOLUTION NEGLECTING SURFACE RECOMBINATION

The Laplace transform of Eq. (6) is:

$$\frac{\partial^2 \bar{p}}{\partial x^2} - \bar{p} \cdot \frac{1 + s\tau}{L^2} + \frac{g_o\tau\, e^{-x/\ell}}{sL^2} = 0$$

$$\bar{p} = \int_0^\infty p(x,t)e^{-st}\, dt$$

Assume a solution of the form:

$$\bar{p} = u(x,s)e^{-x/\ell}$$

Then $u(x,s)$ satisfies:

$$\frac{\partial^2 u}{\partial x^2} - \frac{2}{\ell} \cdot \frac{\partial u}{\partial x} + u\left(\frac{1}{\ell} - \frac{\sqrt{1 + s\tau}}{L^2}\right) + \frac{g_o\tau}{sL^2} = 0$$

which has a general solution of the form

$$u = A \exp\left(\frac{1}{\ell} + \frac{\sqrt{1+s\tau}}{L}\right)x + B \exp\left(\frac{1}{\ell} - \frac{\sqrt{1+s\tau}}{L}\right)x - \frac{g_o\tau}{s\left(\frac{L^2}{\ell^2} - (1+s\tau)\right)}$$

Hence

$$\bar{p} = A \exp \frac{x}{L}\sqrt{1+s\tau} + B \exp \frac{x}{L}\sqrt{1+s\tau} - \frac{g_o\tau}{s\left(\frac{L^2}{\ell 2} - (1+s\tau)\right)}$$

A and B are determined from the boundary conditions. After some arithmetic, it is seen that $\bar{p}$ may be written as

$$\frac{\bar{p}}{g_o\tau} = \frac{f(s)}{g(s)}$$

in which

$$g(s) = s \cdot \cosh \frac{x_1}{L}\sqrt{1 + s\tau}$$

$$f(s) = \frac{\exp - \frac{x_1}{\ell} \cdot \cosh \frac{x}{L}\sqrt{1 + s\tau}}{\frac{L^2}{\ell^2} - (1 + s\tau)}$$

$$+ \frac{\frac{L \sinh \frac{x_1 - x}{L}\sqrt{1 + s\tau}}{b\sqrt{1 + s\tau}} - \exp - \frac{x}{\ell} \cosh \frac{x_1}{L}\sqrt{1+s\tau}}{\frac{L^2}{\ell^2} - (1 + s\tau)}$$

The poles are $s = 0$ and $\cosh x/L\sqrt{1 + s\tau} = 0$. Note that the term $L^2/\ell^2 - (1 + s\tau)$ is common and not a pole.

$$\frac{p(x,t)}{g_o\tau} = L^{-1}\frac{\bar{p}}{g_o\tau} = \sum_n \frac{f(s_n)}{g'(s_n)} e^{s_n t}$$

$$g'(s) = \cosh \frac{x_1}{L}\sqrt{1 + s\tau} + \frac{s\tau x_1}{2L\sqrt{1+s\tau}} \cdot \sinh \frac{x_1}{L}\sqrt{1+s\tau}$$

$$g'(s = 0) = \cosh \frac{x_1}{L}$$

$$g'\left(\cosh \frac{x_1}{L}\sqrt{1+s\tau} = 0\right) = (-1)^k \frac{-1-\left((2k+1)\ \frac{\pi}{2}\cdot\frac{L}{x_1}\right)^2}{2\cdot(2k+1)\frac{\pi}{2}\cdot\left(\frac{L}{x_1}\right)^2}$$

$$f(0) = \frac{\exp-\frac{x_1}{\ell}\ \cosh\frac{x}{L} + \frac{L}{\ell}\ \sinh\frac{x_1-x}{L}\ -\exp-\frac{x}{\ell}\ \cosh\frac{x_1}{L}}{\frac{L^2}{\ell^2} - 1}$$

$$f\left(\cosh \frac{x_1}{L}\sqrt{(1+s\tau)=0}\right) = \frac{\sin\ (2k+1)\cdot\frac{\pi}{2}\cdot\frac{x_1-x}{x_1}}{(2k+1)\cdot\frac{\pi}{2}\cdot\frac{\ell}{x_1}\left[\frac{L^2}{\ell^2}+\left[(2k+1)\frac{\pi}{2}\ \frac{L}{x_1}\right]^2\right]}$$

$$+\frac{(2k+1)\frac{\pi}{2}\cdot\ \frac{\ell}{x_1}\cdot\exp-\frac{x_1}{\ell}\cdot\cos(2k+1)\frac{\pi}{2}\ \frac{x}{x_1}}{(2k+1)\cdot\frac{\pi}{2}\cdot\frac{\ell}{x_1}\left[\frac{L^2}{\ell^2}+\left[(2k+1)\frac{\pi}{2}\ \frac{L}{x_1}\right]^2\right]}$$

Upon collecting all terms:

$$\frac{p(x,t)}{g_o\tau} = \frac{\frac{L}{\ell}\ \sinh\frac{x_1-x}{L}\ +\exp-\frac{x_1}{\ell}\cdot\cosh\frac{x}{L}-\exp-\frac{x}{\ell}\ \cosh\frac{x_1}{L}}{\left(\frac{L^2}{\ell^2}-1\right)\ \cosh\ \frac{x_1}{L}}$$

(continued on next page)

$$-2\sum_k (-1)^k \frac{\frac{1}{x_1}\sin(2k+1)\cdot\frac{\pi}{2}\cdot\frac{x_1-x}{x_1}}{\left[1+\left((2k+1)\,\frac{\pi}{2}\,\frac{\ell}{x_1}\right)^2\right]\left[1+\left((2k+1)\,\frac{\pi}{2}\,\frac{L}{x_1}\right)^2\right]}\cdot \exp^{s_n t}$$

$$-2\sum_k (-1)^k \frac{(2k+1)\frac{\pi}{2}\cdot\frac{\ell^2}{x_1^{\,2}}\cdot \exp-\frac{x_1}{\ell}\cdot\cos(2k+1)\,\frac{\pi}{2}\,\frac{x}{x_1}}{\left[1+\left((2k+1)\,\frac{\pi}{2}\frac{\ell}{x_1}\right)^2\right]\left[1+\left((2k+1)\,\frac{\pi}{2}\frac{L}{x_1}\right)^2\right]}\cdot \exp^{s_n t}$$

in which:

$$s_n = -\frac{1}{\tau}\left[1+\left((2k+1)\,\frac{\pi}{2}\,\frac{L}{x_1}\right)^2\right]$$

APPENDIX 3. PROGRAMMING DETAILS

The following normalizations are introduced:

$$u = x/x_1$$

$$p(x) = P(u) * g_o\tau_p$$

$$N_d = N_do \; \mathrm{erfc}\, u\cdot\frac{x_1}{2\sqrt{Dt}}$$

$$N = N_d - N_a$$

$$N(1-\frac{\Delta}{N}) = N_do\left[1-\mathrm{erf}\, u\cdot\frac{x_1}{2\sqrt{Dt}}-\frac{N_a}{N_do}-\frac{\Delta}{N_do}\right] = N_do * EN(u)$$

$$N'\left(1-\frac{\Delta'}{N'}\right) = \frac{N_d^o}{x_1}\left[-\frac{2}{\pi}\cdot\frac{x_1}{2\sqrt{Dt}}\exp - u\cdot\frac{x_1}{2\sqrt{Dt}}^2 - \frac{\delta}{\delta u}\frac{\Delta}{N_D^o}\right] = \frac{N_d^o}{x_1} * \mathrm{DEN}(u)$$

$$N''\left(1-\frac{\Delta''}{N''}\right) = \frac{N_d^o}{x_1^2}\left[-\frac{4}{\pi}\cdot u\cdot\frac{x_1}{2\sqrt{Dt}}^3 \exp - u\cdot\frac{x_1}{2\sqrt{Dt}}^2 - \frac{\delta^2}{\delta u^2}\frac{\Delta}{N_D^o}\right]$$

$$= \frac{N_d^o}{x_1^2} * \mathrm{DDEN}(u)$$

also write:

$$g_o\tau/N_d^o = \mathrm{GTN}$$

$$\frac{g_o\tau}{N_d^o}\left[1+\frac{1}{b}\right] = \mathrm{GTNB}$$

$$\frac{g_o\tau}{N_d^o}\left[1-\frac{1}{b}\right] = \mathrm{GTNA}$$

$$\frac{x_1}{L} = \mathrm{X1L}$$

$$\frac{\ell}{x_1} = \mathrm{SLX1}$$

$$\mathrm{CON} = \frac{J}{qg_o\ell} * \mathrm{X1L} ** 2 * \mathrm{SLX1} * \mathrm{GTN/SB}$$

Equation (25) can be written as

```
DDP = X1L**2*(P-EXP(U*X1SL))*(GTNB*P+EN)/(EN+2*GTN*P)

     - (CON-GTNA*DP-DEN)/(EN+2*GTN*P)*(P*DEN-DP*EN)/

     (EN+GTNB*P)

     - DDEN*P/(EN+2*GTN*P)
```

In this form, Eq. (25) can be programmed directly using the 4th order Runge-Kutta technique, see reference 13.

Equation (26) changes to

```
DELTA = B3*((-GTNA*DDP-DDEN)/(GTNB*P+EN)-

     (CON-GTNA*DP-DEN)*(GTNB*DP+DEN)/(GTNB*P+EN)**2))
```

in which

$$DELTA = \Delta / N_{D}o$$

$$B3 = \frac{\varepsilon}{q} \cdot \frac{kT}{q} \cdot \frac{1}{x_{1}^{2}} \cdot \frac{1}{N_{D}o}$$

The Field is calculated from the normalized Eq. (20):

```
FIELD = B8*(CON-GTNA*DP-DEN)/(GTNB*P+EN)
```

in which

$$B8 = \frac{kT}{q} \cdot \frac{1}{x_1}$$

The boundary condition Eqs. (29) and (30) change to:

```
DP0 = P0*(CON) - (DEN0)/(EN0 + 2*GTN*P0)

CON1 = -GTN/SB*(DP1+(DEN1+DP1*GTN)*P1/(EN1+P1*GTN))
```

The indices 0 and 1 refer to the beginning and the end of the interval.

REFERENCES


1. A. V. Brown, IEEE Trans. El. Dev. 10, 8 (1963).
2. K. G. McKay, Phys. Rev. 84, 829 (1951).
3. F. E. Emery, T. A. Rabson, IEEE Trans. Nucl. Sci. NS 13, 1, 48 (1966).
4. R. H. Bube, Photoconductivity of Solids, J. Wiley, 1960.
5. L. B. Valdes, Physical Theory of Transistors, McGraw-Hill, 1961.
6. Y. F. Chang, J. Appl. Phys., 38, 539 (1967).
7. J. B. Gunn, J. Electronics & Control 4, 17 (1958).
8. E. S. Rittner, Photoconductivity Conference, Altantic City, 1954, J. Wiley, 1956, p. 216.
9. W. V. Roosbroeck, Phys. Rev., 91, 282 (1953).
10. W. V. Roosbroeck, J. Appl. Phys., 26, 380 (1955).
11. D. P. Kennedy, R. R. O'Brien, IBM J. Res. Rev., 11, (3) 252, (1967).
12. W. Czaja, J. Appl. Phys., 37, (11) 4236 (1966).
13. D. F. Kyser, D. B. Wittry, Proc. IEEE 55, (5) 733 (1967).
14. J. B. Scarborough, Numerical Math. Analysis, Oxford, 1962, Art. 116.
15. IBM System/360 Scientific Subroutine Package, Version II.

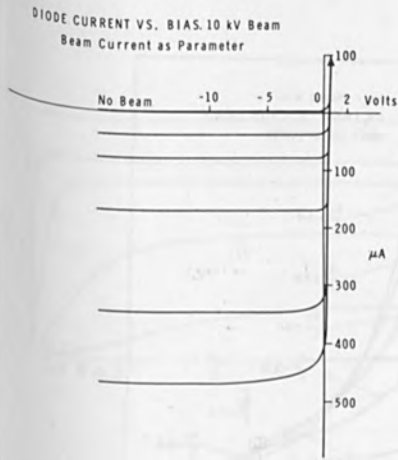


Fig. 1. Diode current vs. bias. 10 Kv beam. Beam current as a parameter.

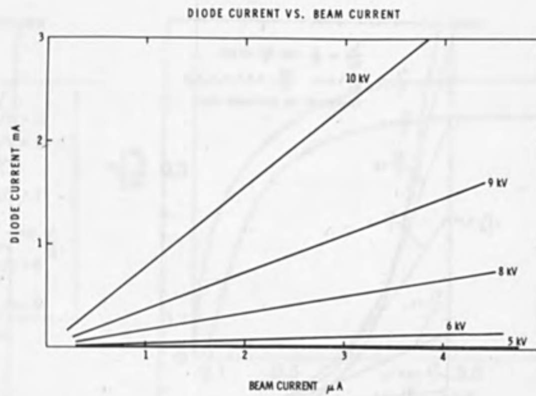


Fig. 2. Diode current vs. beam current.

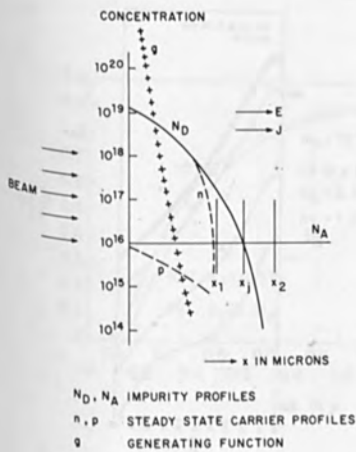


Fig. 3. Concentration profiles.

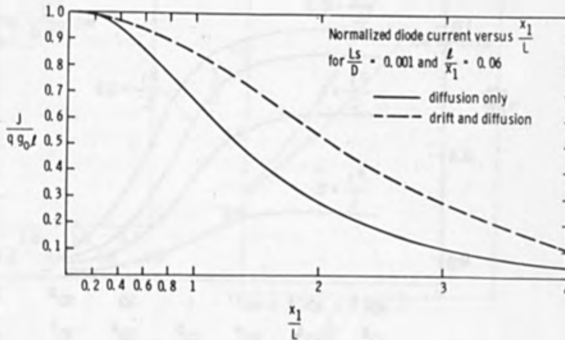


Fig. 5. Normalized current density vs. $x_1/L$.

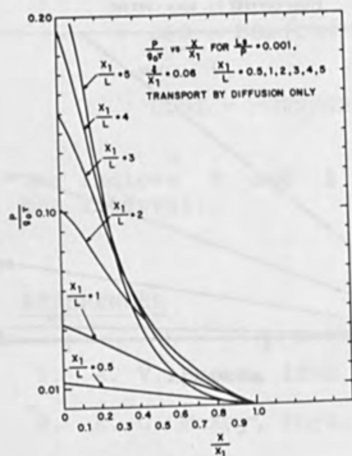

Fig. 4a. Minority carrier concentration profiles.

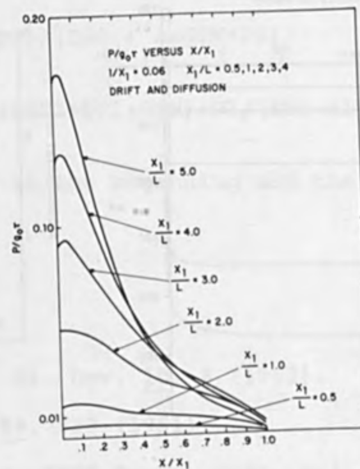

Fig. 4b. Minority carrier concentration profiles.

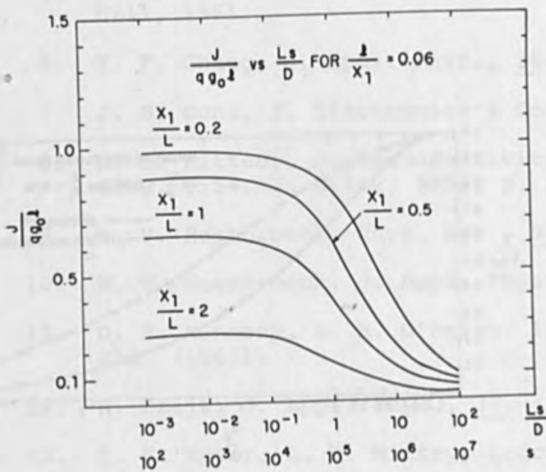

Fig. 6. Normalized current density vs. surface recombination velocity.

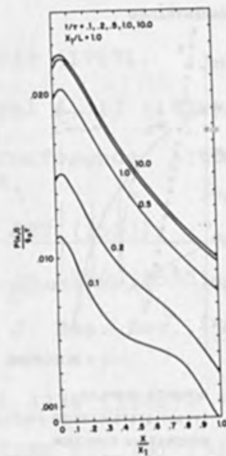

Fig. 8. Minority carrier concentration profiles for successive time steps.

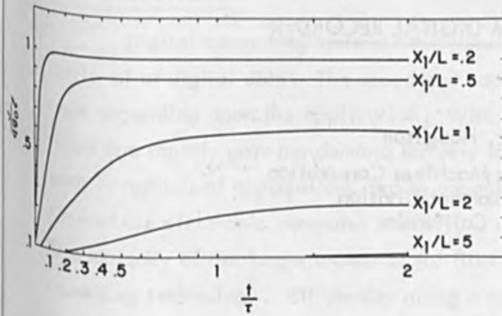


Fig. 7a. Risetime of diode current for an infinitely fast switching beam calculated from Eq. (17).

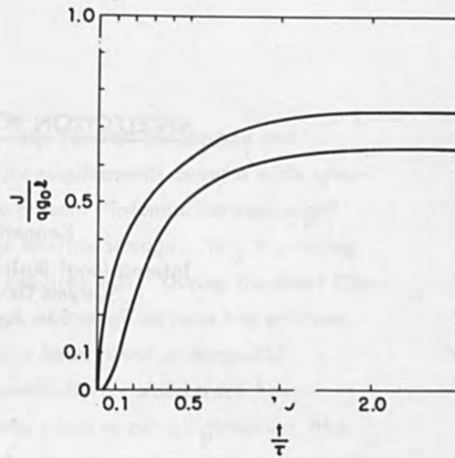


Fig. 7b. Risetime of diode current, comparison of general solution and field free approximation.

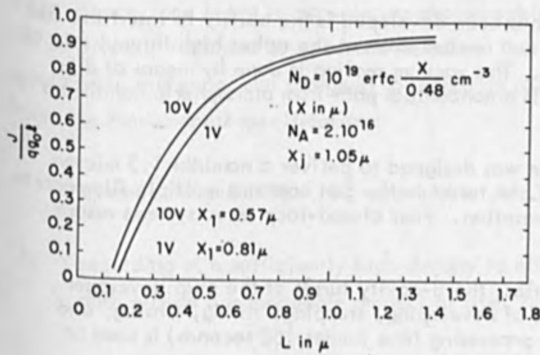


Fig. 9. Effect of reverse bias - normalized diode current vs. L for a 1μ junction.

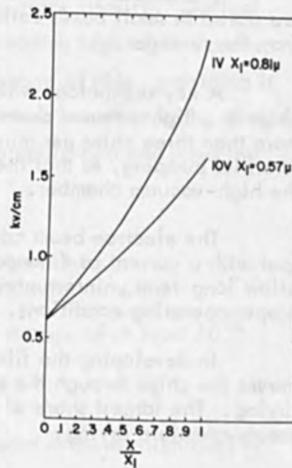


Fig. 10. Field outside the depletion layer. Same parameters as in Fig. 8. Field is independent of L.

# AN ELECTRON BEAM DIGITAL RECORDER

Kenneth E. Haughton

International Business Machines Corporation
Systems Development Division
San Jose, California

## ABSTRACT

To capitalize on the high-density recording capabilities of an electron beam, an electron beam recorder has been developed to write digital data on silver-halide photographic film. While the bit density is of the same order as magnetic systems, the track density is more than order of magnitude greater.

The data are stored on 35mm by 70mm photographic film chips. These chips are stored in small boxes called cells which are transported pneumatically to and from the recorder.

A key technology which has been developed is the ability to insert the film chips in a high-vacuum chamber and remove them at the rather high thruput rate of more than three chips per minute. The vacuum sealing is done by means of differential pumping, so that there is a noncontact path from atmospheric conditions to the high-vacuum chamber.

The electron beam column was designed to deliver a nominal 1.3 micron spot with a current of 4 nanoamp. A turret in the gun contains multiple filaments to allow long-term uninterrupted operation. Four closed-loop servo systems assure proper operating conditions.

In developing the film chips, the 8-cavity turret of the chip developer moves the chips through the steps of developing, stopping, fixing, rinsing, and drying. The largest share of the processing time (under 150 seconds) is used to assure complete drying.

Presented at the Third International Electron and Ion Beams in Science and Technology Conference, Boston, May 5 - 9, 1968.

## INTRODUCTION

Digital computing systems have varying requirements for storage and retrieval of digital data. The speed and capacity requirements cover a wide spectrum depending upon the application. With the present "information explosion" there is a rapidly growing demand for very large on-line storage. This is growing both in number of applications and in capacity requirements. During the short lifetime of the electronic computer industry, a range of storage devices has evolved. The majority of the larger memories (or files) have been based on magnetic recording technology. Bit density along a magnetically recorded track has increased at a significant rate and should for some years to come. However, the improvements in track density have not been as great, nor do they look as promising in the future.

Ignoring the capabilities of a particular technology and looking at present state-of-the-art densities (of the order of $10^3$ linear bits per inch and $10^2$ tracks per inch), one instinctively turns to an attempt at increasing track density. Optical servoing techniques allow some tracking advantages to reading high track density data. Hence, one is led to considering photographic storage of data, providing it can be properly recorded at a reasonable rate. The electron beam recording device described in this paper was designed to record on photographic film and meet the following fundamental specifications:

1. average thruput of $8 \times 10^8$ recoverable data bits per hour,
2. recording at a sufficiently high density to allow storage of at least $10^{12}$ data bits on a manageable amount of film, and
3. film processing that allows the film to meet standard archival-film quality tests.

In addition to these specific recorder specifications, the following system specifications impose restrictions on the performance of the recorder:

1. Upon rereading accepted data, not more than one line (300 data bits) shall be found containing any uncorrectable errors in a sample of $8 \times 10^8$ data bits.

2. The system shall produce not more than one undetected error in $2.7 \times 10^{10}$ data bits read when rereading accepted data.

These system specifications clearly are influenced by data quality in the recording process. Error detection and correction employed by the system will measure the uncorrectable (but detected) error rate. The undetected error rate is determined by two means: first, by a bit-by-bit compare using a standard set of data with a known bit pattern and, second, by statistical calculations based on the error correction activity (for the case where the first method cannot be used).

A requirement of reliable unattended long-term operation forced the solution of some practical and difficult problems. For example, rapid entrance of discrete pieces of photographic film into (and exit from) a high-vacuum environment is accomplished, a stable unattended electron beam column is used, and film is processed to archival quality at a high thruput rate. Other mundane but bothersome problems were also solved; examples are the transport of film from one position to another in an orderly manner, and the accurate positioning of the film before the electron beam so that the recorded data are located within close tolerances of a known position on the film. These functions are all accomplished with a recorder that operates unattended and is serviced by nonspecialists.

## STORAGE MEDIA

Figure 1 illustrates the basic storage unit, a silver-halide film chip 35mm by 70mm. Data is recorded on this chip in 32 discrete frames. Each frame contains 492 tracks, each with 420 bits. Of these 420 bits, 300 are data bits, and the remainder are for error correction and housekeeping tasks. The size of the frames is such that there are 1580 bits per inch and 1790 tracks per inch, representing a

density of 2.82 × $10^6$ bits per square inch. This is a rather ordinary linear bit density, but the track density is more than an order of magnitude greater than available in magnetic systems. The capacity of a single chip, at this density, is slightly less than 5 million data bits.

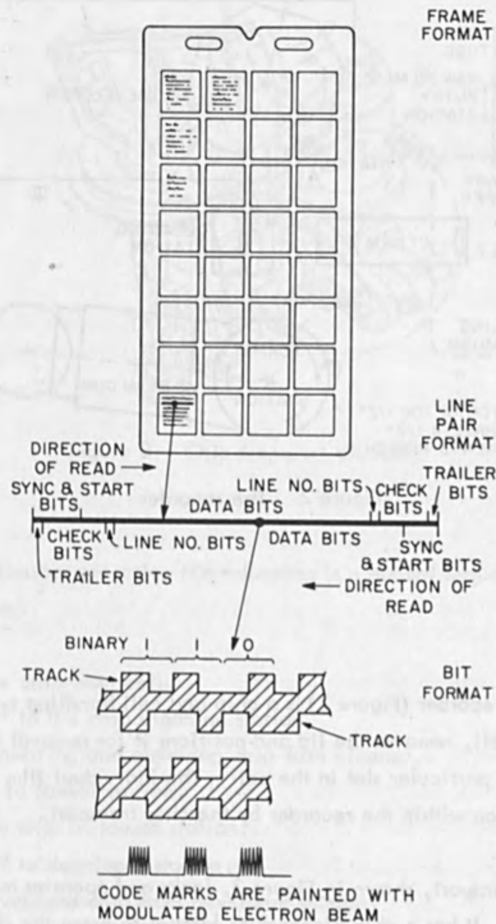


Figure 1 Chip showing data format

A box, called a cell, is used for storing the film chips. Each cell stores 32 chips. Raw film is supplied in cells; film with data in the final form is also stored in them. The cell is transported within the system, from recorder to file to reader, etc., by means of a pneumatic transport system.

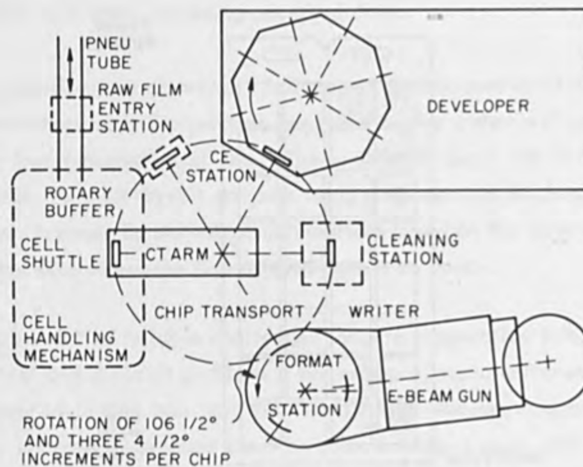


Figure 2 The recorder

## CHIP TRANSPORT

Within the recorder (Figure 2) is a chip and cell handling system. A cell shuttle grasps the cell, removes the lid and positions it for removal or insertion of a particular chip in a particular slot in the cell. The individual film chips are moved from station to station within the recorder by the chip transport.

The chip transport, shown in Figure 3, looks and operates much like a small construction crane. It has a chip picker with latches to grasp the chip. The picker moves up and down as desired to remove or deposit a chip at a given station.

Alignment of the chip guides is accomplished by detenting the transport guides in line with the station guides during the early part of the picker stroke motion. When the picker is in the up position, the transport is rotated from one station to another via a discrete-position stepping-motor drive.

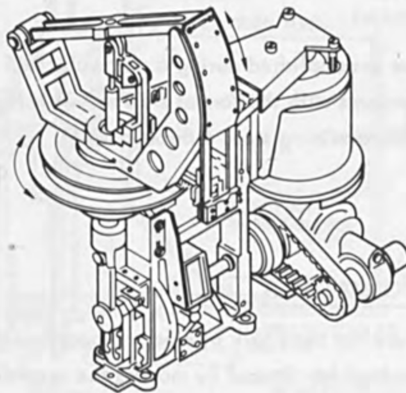

Figure 3 Chip transport assembly

Under continuous operation the following is a normal sequence of activities for the chip transport:

1. Remove raw chip from cell.
2. Rotate 180° to the chip cleaning station.
3. Clean by inserting and removing chip from cleaner.
4. Rotate 60° to format station.
5. Deposit raw chip in format station.
6. Rotate 120° to developer station.
7. Remove developed chip from developer station.
8. Rotate 120° to cell station.
9. Deposit developed chip in cell.

10. Rotate 120° to format station.
11. Remove exposed chip from format station.
12. Rotate 120° to develop station.
13. Deposit exposed chip in developer.
14. Rotate 120° to cell station.
15. Repeat Step No. 1.

Steps 11 through 5 must be accomplished during a particular 4.5 second period due to synchronization requirements with the format station. This leaves a rather leisurely 13.5 seconds for the remaining steps 6 through 10.

## VACUUM ENTRY AND FORMATTING

For some years there has been talk of electron beam recording in one form or another; the task of attaining high thruput by moving the recording media in and out of the high-vacuum environment has been one of the considerations that somewhat reduced enthusiasm. The fact that our system has a recorder and a reader allows the recorder to be a sequential device (no random vacuum entry requirements). With sequential operation, staging of the entry can be arranged. However, a rapid turn-around is still required for the period of time from the completion of recording a chip until the data can be checked on the reader.

The vacuum entry and formatting station (Figure 4) is a multipurpose device. It provides:

1. a platen to hold the film chips in a known plane and position;

2. a transport for moving into the vacuum chamber;

3. an intermediate vacuum position that allows sufficient time for outgassing of the film before it enters the high-vacuum chamber; and

4. a means of placing the chip before the electron beam in a sequence of 32 different positions to allow recording of each of the 32 data frames.

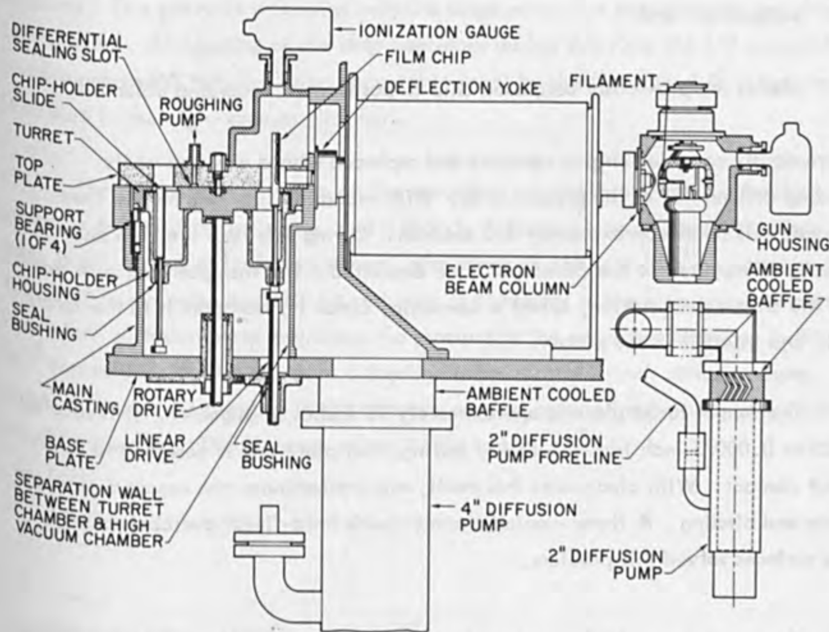


Figure 4 Cross section showing vacuum entry and formatting station

The format turret is a flat plate with three compartments that contain film platens. A mating, nonrotating, flat plate with differential pumping slots accomplishes the sealing between the outside air pressure and the high-vacuum chamber. A 5-cfm mechanical roughing pump is sufficient to handle the leakage such that the pressure in the recording chamber is maintained in the $10^{-5}$ torr range. Upon completion of recording of a chip, the turret rotates 106-1/2 degrees. This accomplishes three things:

1. brings the already recorded chip into position so that it can be removed by the chip transport and be replaced with a new one;

2. moves the previously inserted new chip to a pumping station to begin outgassing; and

3. places the previously outgassed chip in position for recording column "0."

The previously recorded chip is removed and replaced with a new one while recording column "0" of the present chip. With recording time and motion time included, this takes approximately 4.5 seconds. During this time the chip must be removed, transported to the developer, and deposited. The transport arm must then go to the chip-select station, select a new chip, clean it, transport it to the format turret, and insert it in the platen.

The format turret plate is approximately 10 inches in diameter. It is located 0.0005 to 0.00075 inch from the fixed, mating, flat plate and is designed to rotate without contact. With clearances this small, any contaminant can create a problem of wear and binding. A flame-coated chrome-oxide hard-finish overcoat on each of the surfaces solved this problem.

To record the eight frames in column "0," the chip platen within the appropriate compartment is pushed upward (by means of a push rod through a seal) in eight increments, with a pause for recording after each step. The remaining three columns of the chip are reached for recording by successively rotating the format turret in 4-1/2 degree increments. At each column position, the platen moves through the eight vertical positions. Hence, an entire chip is recorded by recording frame by frame down column "0," up column "1," down column "2" and up column "3."

The 106-1/2 degree rotation of a chip cycle places the most recently loaded compartment so that its opening through the flat plate is opposite the differential

pumping slot. Air carried in the compartment is pumped out and outgassing of the film chip begins. The first 4-1/2 degree rotation closes this connection and moves the opening to the foreline pump. The geometry of this connection is such that the conductance to the foreline pump increases with each of the succeeding 4-1/2 degree rotations. This prevents a foreline pressure surge when first connected to the chip compartment. Outgassing of the chip continues during this time (13 1/2 seconds) and the pressure is reduced to an acceptable level by the time the chip compartment is rotated to the high-vacuum chamber.

The total pumping system on the recorder includes two 5-cfm mechanical pumps, a 4-inch diffusion pump, and a 2-inch diffusion pump. One mechanical pump is for sealing as indicated above. The other is used as a foreline pump for the 4-inch diffusion pump and also for reducing the pressure in the chip compartments. The 4-inch diffusion pump maintains the pressure in the recording chamber in the $10^{-5}$ torr range. It also serves as a foreline pump for the 2-inch diffusion pump which maintains the pressure in the cathode area an order of magnitude lower than the chip chamber. There are no valves in the system.

## ELECTRON SOURCE AND ITS CONTROL

Figure 5 shows the electron column and its control systems. These have been described in some detail in previous papers by Loeffler,[2] Kurzweil,[3] et al, and are treated briefly here.

The electron optical column consists of three major functional elements:

1. an electron gun which represents the electron beam source;

2. a system of electron optical elements which demagnify the image and shape the beam to the required diameter; and

3. a deflection system capable of positioning the beam with accuracy within the specified field of view at the target plane.

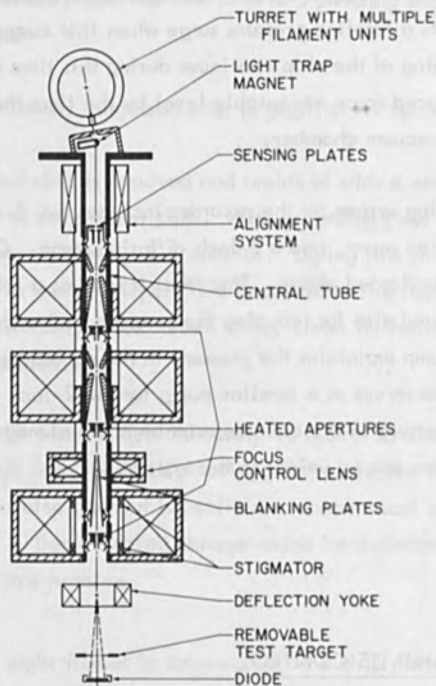


Figure 5 Electron column

Mounted in the turret of the electron gun are sixteen filaments that are changeable under machine control. The cathode is at the negative acceleration potential of 12.0 kV with respect to ground, whereas the grid cylinder is negatively biased against it, producing the focusing action. The anode at a distance of 0.162 inch from the grid is mechanically a part of the structure of the electron optical column and is at ground potential. Included in the design of the electron gun is a

filament operating point servo to optimize the lifetime-brightness relationship. The design goal was an average lifetime of 30 to 35 hours and an assured lifetime of 20 hours for each filament. This has been achieved; hence, each loading of the turret gives an assured operation time of 320 hours. Filament-assembly change time is short, consisting primarily of pump cooling and reheating time.

The electron optical column shapes the electron beam in such a way that a spot two microns or less in diameter with approximately $4 \times 10^{-9}$ amp current is constantly available at the target. To achieve this, the following functions are performed by the column:

1. alignment of the electron beam with the axis of the column;
2. demagnification of the electron source;
3. shaping the electron beam (reducing the diameter) to enable the appropriate spot size and current level to be delivered to the target; and
4. focusing the image of the electron source on the target surface.

To insure alignment of the electron beam, the column contains four symmetric sensing plates that sense the beam position relative to the column axis. The sensing plates generate an error signal for the beam-alignment control system. The alignment servo drives two alignment yokes to center the beam on the sensing plates.

The major demagnification is accomplished with two main lenses (magnetic) and their corresponding pole pieces.

The required beam is cut from the original beam in successive steps by four apertures. One of these is combined with the sensing plates and three others with the three lenses. These apertures are continuously heated to 300 degrees C to avoid contamination by residual organic vapors. Concern over contamination of the elec-

tron optical column and consequent loss of spot-size control was the prime motivation for heated apertures and the concept of an easily replaceable central column that contains all critical elements. This central column can be removed by merely sliding it out of place after pivoting the gun section out of the way. A factory-cleaned column can then be inserted. The entire operation takes about one-half hour, most of which is used in pump cooling and heating. With performance as reliable as it has been, the quick-change feature is not absolutely necessary. For example, columns were installed in two machines in November 1966. They were interchanged during a test in January 1967 and have not been removed since.

Coarse focusing is accomplished by the final lens (also magnetic). This lens is combined with a stigmator to correct the unavoidable astigmatism of the lens. Its current is automatically adjusted to minimize the spot by the spot-size servo.

In addition, the column has blanking plates for deflecting the beam away from the last aperture. The column is enclosed in a magnetic shield for protection against stray magnetic fields.

The electron beam is deflected to scan across the field by means of an electromagnetic deflection coil. In the recording mode, the beam is unblanked, scans across the data field, and then is blanked while it returns to rescan for the next line. Vertical track separation is obtained by a high precision digital-to-analog deflection drive. Data is written by "painting" the bits with an electrostatic deflection of the beam normal to the scan direction.

## CHIP DEVELOPER

The chip developer provides on-line processing of the silver-halide film chips. It accepts chips from the format station at a maximum rate of one chip every 18.5 seconds and automatically processes and returns a dry chip of archival quality

to the chip transport within a total cycle time of approximately 150 seconds. The developer is capable of continuous operation for periods of up to six hours without operator intervention for replenishing the chemicals. Parallel sets of chemical supply containers make indefinite uninterrupted operation possible.

Chip processing is performed in a rotary turret consisting of eight individual processing cavities (Figure 6). The turret is indexed in 45-degree increments to sequentially present a processing cavity to a single fixed load-unload station and seven individual fixed processing stations. The individual turret-mounted processing cavities are open-ended to permit the introduction and removal of chips at the load-unload station and then the introduction and drainage of processing fluids (or drying air) at the seven processing stations. The turret is indexed in one second, providing a dwell of approximately 17.5 seconds at each station. The processing cavities are sealed to the processing stations by means of a vertically reciprocating "cymbal" ring and deformable elastometer seals. Chemicals are gravity-fed from three supply containers of one gallon size placed at the top of the developer. After proper heating, air-driven diaphragm pumps introduce a discrete volume of chemicals into the processing cavities at the two chemical processing stations. Heated fresh water is introduced at two stations to assure complete washing, and heated air is introduced at the final three stations to dry the chip and cavity.

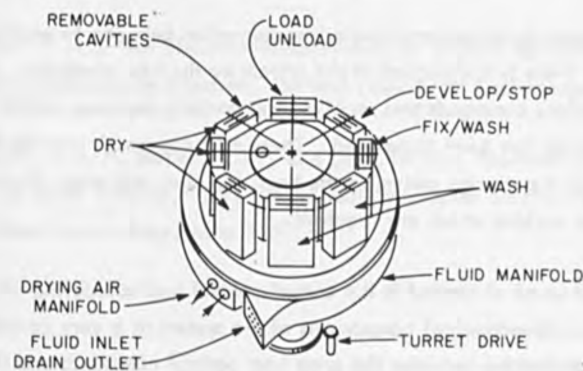


Figure 6 Developing cavities

Two chemical processing stations are provided. The first chemical station introduces developer solution, followed by stop solution. The second station introduces fix solution and rinse water. The third and fourth stations provide heated fresh water for additional chip washing, while stations five, six and seven are drying stations. The chip is loaded and unloaded at the eighth station.

Pump and drain valving and air purging are incorporated into each fluid processing station utilizing air-operated diaphragm valves. Drain and air-pressure purging is also provided at wash stations three and four.

Individual temperature control is provided for the two chemical stations. Independent temperature control is also provided for the wash water and the drying air.

## CONTROL

Control programs for the system schedule the operation of the mechanisms so that the various functions required by the host computer are efficiently executed. They also provide diagnostic capabilities and customer engineer aids.

The programming system provides a transformation between two basic levels of control. First, there is the control of the system by the host computer. At this level the host provides commands and receives appropriate responses which indicate the commanded action has been completed. These host commands provide the functional capability of the storage system to the host, but they are gross relative to the number of detailed actions which are required.

The second level of control is the actual control and scheduling of various electronic and electromechanical components of the system at a very detailed level. To effect the transformation between the gross host control commands and the detailed hardware control, the commands from the host are associated with lists of

actions which control the system subassemblies. The sequence of events required for the proper control of these subassemblies includes:

1. the actual command to set or reset a control point,
2. waiting predetermined lengths of time for completion of various operations,
3. sensing particular conditions in the subassembly, and
4. the logic and branching necessary to communicate with other parts of the program and to sequence the events within the control program.

## ACKNOWLEDGEMENTS

The author gratefully acknowledges the outstanding efforts of members of the team that made this device a reality.

## REFERENCES

1. Kuehler, J.D. and Kerby, H.R., "A Photo-Digital Mass Storage System," Proceedings of the Fall Joint Computer Conference, pp. 735-742 (1966).

2. Loeffler, K.H., "An Electron-Beam System for Digital Recording," IEEE 9th Annual Symposium on Electron, Ion and Laser Beam Technology, May 1967.

3. Kurzweil, Jr., F, Barber, R.R., and Dost, M.H., "Automatic Control of an Electron-Beam Column," IEEE 9th Annual Symposium on Electron, Ion and Laser Beam Technology, May 1967.

# REQUIREMENTS ON BEAM TECHNIQUES AND SYSTEMS FOR ION IMPLANTATION DOPING OF SEMICONDUCTOR MATERIALS AND DEVICES

R. G. Wilson, R. R. Hart, D. M. Jamba, and S. A. Thompson
Hughes Research Laboratories
Malibu, California

Ion implantation doping is just one technique in a newly emerging field of electron and ion beam technologies for processing semiconductor materials, devices, and integrated circuits. Certain requirements are placed on the doping ion beams and implantation systems by the solid state phenomena which occur in the target substrate, by the solid state and device measurements which must be performed, and by the desired device structures. Such requirements and methods of achieving the desired effects and results are discussed.

Ion Implantation is the process of doping semiconductor materials and devices by causing the dopant (impurity) atoms to enter the substrate by accelerating them to high energy as ions in a beam which is directed onto the substrate. The substrate may be as simple as a plain silicon crystal or as complicated as an integrated circuit or passivated and contacted device array. The basic elements in the process (Fig. 1) are an ion source, an ion acceleration system, various beam handling techniques (which may or may not include mass separation, electrostatic deflection, beam sweeping, and focusing to a small diameter with programmed deflection), the semiconductor substrate, and a vacuum system in which to generate and transmit the ion beam and contain the substrate target under the proper conditions. There are two fundamental concepts of applying ion beams for implantation doping (Fig. 2): the use of broad area, rastered beams combined with one of a variety of masking techniques, and programable, deflection-controlled tiny ion beams.

Because many semiconductor materials are sensitive to very small concentrations of impurity atoms and ion implantation is a process of introducing doping impurities, restrictions on the purity of an ion beam result. The ion beam should not contain species, other than the one desired, of a nature and concentration which could cause undesired electrical activity in the substrate. The doping beam may be allowed to contain small parts of impurities which are inert in the substrate or even quantities of more active dopant species which are low enough that they produce concentration less than the base doping level of the substrate and therefore do not affect its electrical properties. Most ion source types produce ion beams which comprise a spectrum of ion species, both in mass and in charge. For example, the complex

mass spectrum of the beam from a simple electron bombardment ion source operated on $CS_2$ vapor is shown in Fig. 3, showing that $C^+$ and $S^+$ components are available. However, the same ion source operated in cadmium vapor produces the simple spectrum shown in Fig. 4, comprising only $Cd^+$ and $Cd^{++}$ and some weak ambient vacuum gas peaks. Sophisticated mass separation systems such as isotope separators and particle accelerators are capable of producing beams of great purity, but they are costly and not always adapted to fulfill some of the requirements for semiconductor doping remaining to be discussed. Simpler, less expensive, mass separation systems are capable of separating elements, are more flexible, and have been shown to be satisfactory for ion implantation doping processes. Studies need to be performed to determine how much the requirements on mass separation can be relaxed for device fabrication with manufacturing in mind, because the capital investment in implantation systems can be reduced as such requirements are relaxed. A properly designed surface ionization source offers a great simplification in the system requirements by eliminating mass separation altogether for some applications. Such a source creates only singly ionized ions of only low ionization potential elements. For example, beams of Al, Ga, or In of suitable intensity (1 to 10 μA) can be generated with from $10^{-5}$ to $10^{-4}$ parts of impurities which are potassium and sodium and which are not substitutional dopants. Sodium is a problem in some passivation structures, however. Even if the alkali impurities were active dopants, a doping concentration of Al, Ga, or In $10^4$ greater than the substrate base doping level can be provided while keeping the alkali level below the base level. The results of implantation studies at these Laboratories indicate no significant difference between unpassivated silicon samples implanted with $Ga^+$ or $Al^+$ beams from surface ionization sources with and without mass separation.

Requirements are placed on the energy of the doping ions by substrate penetration requirements, one of which is junction depth. Penetration decreases as the ion mass increases, and increases with ion energy. While there are a number of other variables which influence the ion penetration depth (e.g., substrate crystallographic orientation, beam-substrate alignment, and sometimes substrate temperature), large ion energies are generally required to achieve deep, high concentration dopant profiles. Research is being carried out in the range from several keV to several MeV of ion energy. As an example of penetration depths, the amorphous (large angle or nuclear scattering) range of 100-keV boron ions in silicon is about 0.4 microns. Curves of calculated range vs energy up to 500 keV for several ions in silicon and $SiO_2$ are shown in Fig. 5. Versatile research and production implantation systems can be built for energies up to about 300 keV. For higher energies, research equipment such as Van deGraaff and Cockroft-Walton accelerators are sometimes used, but these are less practical for production. Specific device applications dictate ion energies (depth). Shallow (low energy) implants are required for emitter-base junctions in bipolar transistors, large area photodetectors, low thermal resistance microwave power sources, ohmic contacts, and other

applications. Fabrication of good ohmic contacts by ion implantation is a very valuable and versatile use for the technique. Deep (high energy) implants are required for the base-collector junctions of bipolar transistors, submerged junction devices, and device junctions made under passivation layers by implanting through the passivation layers. Doping through passivation layers, when done under the proper conditions which do not harm the passivation layer characteristics, may be the answer to making especially good devices by ion implantation.

Hall coefficient measurements are important for ion implanted layers because the carrier mobility may vary as well as the concentration, and sheet resistivity measurements alone are not sufficient. Hall measurement geometries require a sizable uniformly doped region on the semiconductor substrate within which the desired Hall pattern is etched. Even more important and requiring even larger uniformly doped areas is the doping of device arrays and circuits over the entire area of standard wafers (up to 3.5 cm in diameter). To guarantee good uniformity requires that an ion beam be swept in two dimensions over an area at the target greater than that of the target sample. The use of saw tooth sweep signals in perpendicular directions and at significantly different frequencies is a satisfactory method for achieving this result. Work in our Laboratories has utilized 30 and 3000 Hz frequencies. This technique raises a potential problem, however. Sweeping the beam at two frequencies superimposes ac signals of the two frequencies on the dc beam level which must be measured and integrated for ion dose control. For accurate measurement, the current meter or integrator must respond to these ac variations and properly average the total signal. We have found that some meters do not do this; they may follow accurately the lower frequency but tend to be peak-reading for the higher frequency and hence yield too high a value of current (and dose). There may be an advantage in the use of a low impedance current meter, or the higher frequency may be reduced somewhat.

Ion implantation causes lattice damage and results in dopant atoms in both substitutional and interstitial sites. Control of these two effects places requirements on both beam techniques and system design. Both of these effects can be controlled significantly by maintaining the substrate at elevated temperatures during implantation to anneal out lattice damage as it is created and to allow the implanted dopant atoms to move to substitutional sites. The required temperature varies with the substrate material and is greater than 430°C for silicon. Data obtained by L. Eriksson for silicon are shown in Fig. 6. Post annealing of samples implanted at room temperature has been found to be less satisfactory in some cases, but in other cases requiring higher temperature annealing, post annealing produces utilization coefficients near unity and equally good devices. For applications of channeling, temperatures below ambient may be desirable to reduce thermal motion during implantation - followed by post annealing. When hot implantation is favored, a heating technique which maintains all devices or circuits on a wafer at the same temperature is desirable, and an oven in the target chamber has been found to be capable of maintaining

a temperature uniformity within $5^{o}K$ (at up to $1000^{o}K$) over a wafer, as proved by infrared pyrometer scans and alloy dot melt techniques. Contact heating with silicon wafers produces larger temperature variations ($\sim 50^{o}K$).

Another technique for reducing lattice damage is to implant with a parallel beam of ions directed accurately toward an open crystallographic direction of the substrate. Under this channeling condition, the ions lose energy by electronic collisions (small angle) in the surface region and create most of the damage near the end of their path, greatly reducing surface damage. Another requirement for parallel ion beams maintained at the same angle of incidence to the substrate surface over a large area to guarantee uniform penetration depth is imposed by the fabrication of certain devices like large area photodetectors and device arrays which are very sensitive to junction depth.

The general problem of dopant depth distribution or profile control is one of the most serious facing ion implantation. The relative magnitudes of the three distribution-controlling phenomena in ion implantation (see Fig. 7), the amorphous or large-angle scattering peak, the channeling or small-angle scattering distribution, and the enhanced-diffusion tail or vacancy-assisted diffusion distribution, must be controlled in order to be able to control the junction depth and dopant profile requires the ability to govern the presence or absence of the channeling and/or enhanced diffusion distributions. The better the alignment between a parallel beam and an open crystallographic direction of the substrate, the greater the degree of channeling possible. Alignment of about $0.1^{o}$ can produce a significant channeling distribution effect and alignment of $0.01^{o}$ or better gives the maximum effect, a distinct second peak in the distribution at greater depth, in some substrates. Alignment to $0.1^{o}$ or less is best achieved by auxiliary Rutherford scattering measurements employing a beam of light ions ($H^{+}$ or $He^{+}$). A solid state detector monitoring backscattered ions receives a minimum signal when alignment is achieved. There are two methods of utilizing auxiliary light ion beams for alignment as shown in Fig. 8. One is to operate the doping ion source to produce an $H^{+}$ or $He^{+}$ ion beam for alignment, then to switch to the dopant ion species for implantation. The concern with this technique is that sufficient angular resolution, and hence alignment, can be achieved with a proton energy equal to the doping ion energy (say $\sim$200 keV). The other method is to use an auxiliary higher energy ion source, such as a Van de Graaff accelerator to produce a beam of $H^{+}$ or $He^{+}$ of MeV energy through the same channel to the target for alignment only (see Fig. 8), and then to switch to the dopant ion beam from the other source, delivered through an extension of the same channel. This latter technique is being used at Bell Labs, the former by us at Hughes.

Limiting channeling effects to a negligible magnitude for profile control with the amorphous distribution only is also difficult. Channeling effects may be minimized if not eliminated by several techniques (see Fig. 9), viz., (a) implanting through an oxide (passivation) layer

to cause scattering of the beam, (b) misorienting the beam with respect to all crystal axes or planes (e. g., 6 to 8 degrees off the (110) axis), and (c) predamaging the surface layer of the substrate crystal to destroy the crystallinity (channels) there.

Tailored doping profiles are possible by ion implantation but place stricter requirements on beam handling. Combination of ion energy programming and the alignment or randomization techniques described above can be employed to build up a variety of dopant profiles valuable for device concepts. Combinations of amorphous scattering peaks, channeling distributions, and possibly even enhanced diffusion may be utilized to fabricate more complex dopant distributions.

Accurate control and measurement of the total ion dose (the doping concentration) (see Fig. 10) requires current integration at the substrate target, i. e., measuring the instantaneous product of ion current density and time, for cases in which the ion current density is not absolutely constant. Voltage ripple and other high frequency variations and longer term drift can be accounted for in this way. Voltage variations (ripple or drift) on the ion source or accelerator cause variations in the ion energy which are translated into transverse motion by the mass separation magnet. Variations in magnet field strength have the same effect. The problems arising from beam sweeping, and the associated frequencies were discussed earlier. Secondary emission must be suppressed, or known and accounted for, in such measurements. This can become a difficult task when the target is maintained at a high temperature and auxiliary electron beams are employed.

Fabrication of device structures with improved performance has imposed requirements on ion beam techniques in terms of meaningful applications of ion implantation. Several important features have been worked out in studies at our Laboratories. The fabrication of suitably passivated device structures (e. g., MOS field effect transistors) has been achieved by implanting directly through passivation layers under special conditions which maintain the integrity of the passivation layer. Techniques have been found which allow this to be done without creating serious permanent damage or in reducing the breakdown voltage of the passivation layers. This has been achieved by implanting through an $SiO_2$ layer held at an elevated temperature and flooded at the same time by electrons. The system requirements therefore include broad area electron flooding and heating of the device array or circuit surface. It has been found recently that equally good devices can be made by implanting at lower temperatures and followed by post annealing.

Techniques for definition of device array or circuit patterns depend on whether broad area or fine deflected ion beam techniques are to be employed. The use of broad area beams requires a masking technique. The following materials have been shown to be satisfactory for this purpose at these Laboratories: (a) photoresist, (b) thin metal films on the substrate, (c) metal contact masks, and (d) device contacts

and oxide (passivation)layers. Two maskless techniques are fine programmed ion beams and the projected model technique, (plus stepping over a wafer area because of projection area size limitations). The use of fine programmed ion beams imposes severe requirements of high stability in power supplies producing the ion energy, the magnetic field for mass separation (deflection), and the deflection voltages. Small area techniques further impose difficult registration and stepping requirements.

An important system consideration is the vacuum environment. Requirements on the quality in terms of magnitude and type of pumping have not been studied specifically and therefore have not been clearly established. The requirements may vary with the substrate material. Some materials may be more subject to contamination. The minimum requirements for device manufacture need to be established because the capital investment in the facility will be significantly determined by the quality of vacuum system required. We hope to study this vacuum quality requirement in the future at our Laboratories. We presently have systems which are all ion pumped, all oil diffusion pumped (cryogenic trapping), and oil diffusion pumped at the source and ion pumped at the target. This latter case - the combination of the two - may be the best, because high speed is valuable at the ion source, contamination is a lesser problem, and the pressures are higher. The target chamber is the location where cleanness and better vacuum quality are desired. Hydrocarbon vapors which can be cracked on the target face by the incident ion beam are a concern. Implantation systems are often naturally adapted to differential pumping because of collimating apertures and magnet chambers. Mercury diffusion pumps are being employed at SERL. We make extensive use of liquid nitrogen cooled walls in the system channels which is valuable for removing condensables which are the more serious contaminants. Residual gas spectra comprise hydrogen and nitrogen in diffusion pumped systems, plus some argon in ion pumped systems.

In summary, we have discussed the following beam techniques and system considerations related to ion implantation doping of semiconductor materials, devices, and circuits: 1) mass separation or beam purity (What degree is required for production? ), 2) ion energy (related to dopant and junction depth), 3) substrate temperature and dosage uniformity, 4) the need for large implanted areas (for identical device arrays and for Hall measurement geometries), 5) beam sweeping and frequencies (possible problem for accurate dosage measurement), 6) methods for limiting channeling, 7) degree of particle trajectory parallelism, collimation, and alignment with target crystal (of concern for profile control via control of channeling), 8) current stability problems, and power supply stability (especially for tiny beams), 9) use of auxiliary electron beams for neutralization, 10) beam masking techniques and 11) vacuum environment requirements (What degree is required for particular materials and device structures and beam processes? ).

In conclusion, I wish to acknowledge the contribution of ideas to this paper made by my associates, R. W. Bower, G. R. Brewer, and O. J. Marsh. This work is part of a broader program of ion implantation doping techniques which is supported in part by the Air Force Avionics Laboratory.

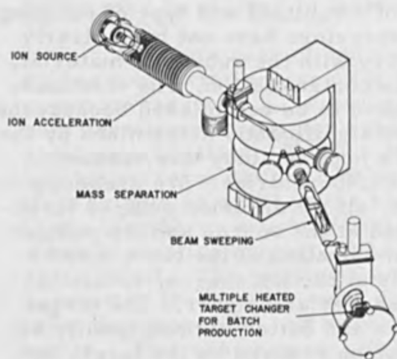


Fig. 1 Ion implantation system basic elements.

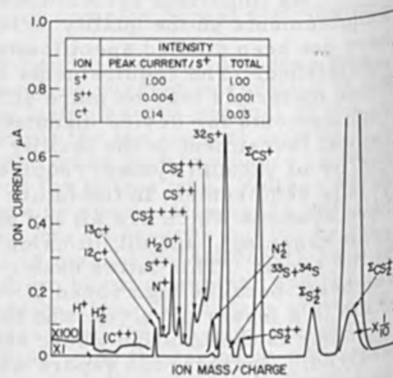


Fig. 3 Mass spectrum of $CS_2$ from an electron bombardment ion source.

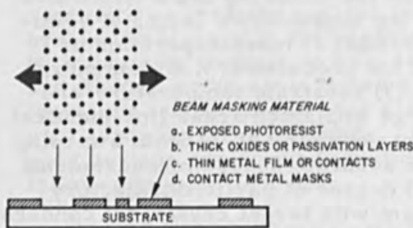


Fig. 2 Ion beam concepts for implantation.

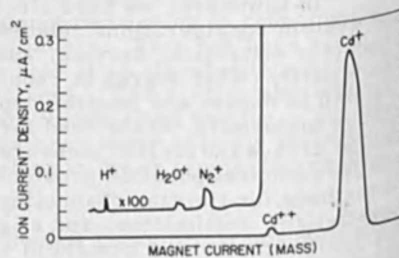


Fig. 4 Mass spectrum of metallic cadmium from an electron bombardment ion source.

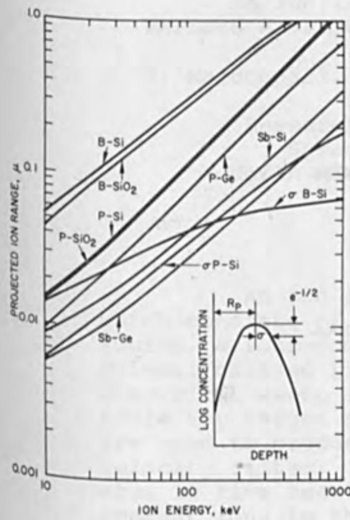


Fig. 5 Calculated range vs energy curves for several ions in Si and $SiO_2$.

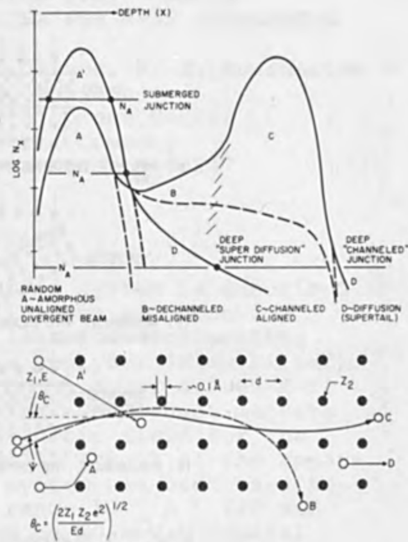


Fig. 7 Depth distribution of implanted ions.

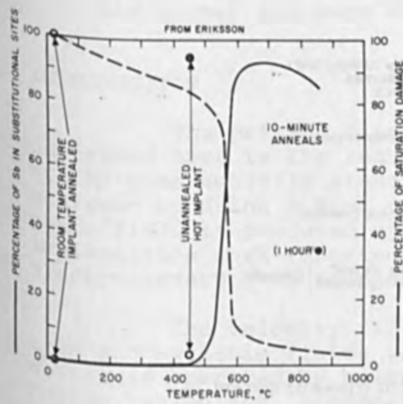


Fig. 6 Eriksson's data for damage and substitutional location for Sb in Si.

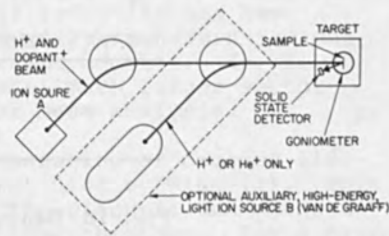


Fig. 8 Beam substrate alignment by Rutherford scattering.

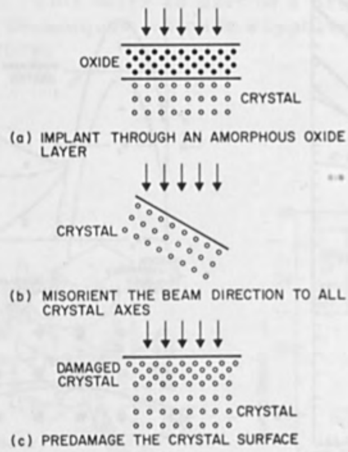


Fig. 9 Methods for preventing channeling.

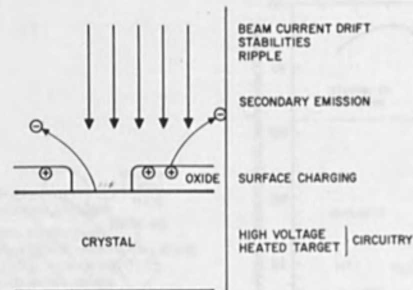


Fig. 10 Beam current measurement

# AN ION IMPLANTATION SYSTEM WHICH EMPLOYS A VELOCITY FILTER FOR MASS SEPARATION

J. D. Macdougall, F. W. Anderson, K. E. Manchester
and P. E. Roughan
Research and Development Center
Sprague Electric Company
North Adams, Massachusetts 01247

## ABSTRACT

An ion implantation system is described which consists of an oscillating electron ion source, a four-component lens and accelerating column, crossed field mass analyser (Wien Filter), electrical sweep system, and a motor driven X-Y table for target positioning. Permanent magnets are used to produce the magnetic field for the velocity filter. The overall length of the apparatus is five feet. This system has been used to implant ions in the mass range $10 \leq A \leq 120$ and in the energy range 10 keV to 70 keV. Typical beam parameters are several microamperes of current focused to a 1 mm diameter spot at the target. With a 30 kV accelerating voltage, the measured mass dispersion is approximately 0.5 mm/mass unit at mass 60. Some advantages of using a velocity filter rather than a conventional sector magnet for mass separation are discussed.

## INTRODUCTION

The primary distinguishing feature of the system described here is the reduction in the cost and complexity of the mass analysis stage. This reduction has been achieved by using a Wien velocity filter wherein the magnetic field is produced by permanent magnets. In all ion implantation work reported to date, much larger sector electromagnets have been used for mass analysis.

The velocity filter consisting of crossed electric and magnetic fields was first used by Wien (1). This device is operated by balancing the electric and magnetic forces, which act in opposition to each other. For a given ratio of the electric and magnetic fields, charged particles of a given velocity and charge can be caused to pass through

the crossed fields with zero deflection. Thus when mono-energetic ions pass through the filter, mass dispersion results.

Since the crossed field velocity filter was first used by Wien, it has found only occasional application as a mass separator. However, the recent construction by Wåhlin (2) of an isotope separator using a Wien filter has brought about renewed interest in this device. Wåhlin obtained a useful mass dispersion and resolving power with an electro-magnet that was considerably smaller than the conventional sector magnet. Since the requirements for mass separation in ion implantation are generally less stringent than those for isotope separation, the system herein described has a smaller geometry in the velocity filter. In addition, the use of permanent magnets in this apparatus eliminates the need for the large, well regulated current supply which is necessary for an electromagnet.

## CONSTRUCTION AND OPERATION

Figure 1 is a schematic diagram of the ion implant-ation system. A self-supporting vertical construction has been used for the ion beam column. Welded steel frame con-struction at the base of the target chamber is used to support the entire system except for the source pumping station, which is supported independently. Apart from the velocity filter, the vacuum system is cylindrically symmetric.

The general operation of the system is as follows. Positive ions are extracted from the source by a 10-35 kV potential. These ions are focused and accelerated by four cylindrical electrodes. The first three electrodes function as extractor and Einzel lens, while the last two electrodes form an accelerating gap with a weak lens action. A voltage drop of 0-40 keV can be sustained across the final acceler-ating gap. The focusing action of the final accelerating gap and the velocity filter which follows is sufficiently weak to allow the focus at the sample to be controlled by small variations in the voltage applied to the Einzel lens.

For initial alignment and focusing of the ion beam, an electrical sweep voltage is applied to the deflection plates located before the entrance to the mass analyzer. This electrical sweep is synchronized with the sweep of an oscilloscope, which views the output of a Faraday cup detec-tor located on the sample holder. The resulting peak is then adjusted to the required current and width by adjusting the

focusing voltages and the source parameters. Mass selection is accomplished by adjusting the voltage applied to the electric field plates of the velocity filter. After the desired ion beam has been obtained, a motor driven table is used to bring the sample under the ion beam. Large area implants are made by sweeping the beam perpendicular to the direction of mass dispersion, while moving the sample across the swept beam.

The construction of the oscillating electron ion source is similar to one described by Nielsen (3) and Almen and Nielsen (4). All metal parts are constructed from stainless steel, while insulators are fabricated from boron nitride or alumina. A four-inch diffusion pump with a liquid nitrogen cooled baffle is used to evacuate the source region.

Under typical operating conditions, the anode voltage is 100 V, the filament emission is 100 mA, and the magnetic field along the axis of the discharge chamber is 200-300 gauss. With a source pressure of approximately $1 \times 10^{-4}$ Torr, and a 30 kV extraction voltage, the total ion current extracted from the 1/16 in. source aperture is typically 15 μA.

The source charge can either be admitted externally as a gas or placed in an internal oven. Experience to date indicates that the oven and discharge chamber are adequate to use solid source charges, which have a vapor pressure of at least $10^{-4}$ Torr at 500°C.

The cylindrical electrodes of the extractor and Einzel lens stage were machined from mild steel. Precision ground quartz spacers form the insulators in the Einzel lens. All quartz to metal seals were made with epoxy resin.

A 1/4 in. source extractor spacing and a 1/16 in. extractor aperture are used. The inner diameter and wall thickness of the Einzel lens electrodes are 3 in. and 1/4 in., respectively. The spacing between electrodes and the length of the electrodes were chosen to correspond to lens No. 4 in a paper by Liebmann (5), where it was shown that this geometry produced particularly small aberrations.

For experiments at energies above 35 keV an accelerating voltage of 0-40 kV can be applied across the second accelerating stage. This final acceleration gap is 2.5 in. As a result of this wide gap, only a weak focusing action occurs and this stage functions primarily as an accelerating gap.

Before entering the mass analysis stage, the ion

beam passes through a moveable aperture and X-Y electric deflection plates. The aperture is normally 3/16 in. diameter and serves to remove the diffuse low intensity shoulder from the ion beam. One set of deflection plates is used to sweep the beam perpendicular to the direction of mass dispersion, while the other set of plates serves to center the beam between the electric plates of the velocity filter.

Figure 2 is a schematic drawing, which shows the geometry and construction of the velocity filter. Alnico V horseshoe magnets and Armco iron pole pieces are used in an "H" configuration. The magnets and pole pieces were assembled first and magnetized as one unit to produce a 4.0 kilogauss field across the 1.25 in. magnet gap. The length of the magnet pole faces and the electric field plates is 2 in., while the separation of the electric field plates is 3/8 in. All vacuum joints and the insulators for the electric field plates were formed with epoxy resin. The overall length of the velocity filter and the drift space for the mass analysis stage is 14 in.

Two 0-3 kV voltage supplies are used to apply up to 5 kV across the plates of the velocity filter. In order to obtain a symmetric electric fringing field, the voltage (V) is applied to the plate approximately as + V/2 and - V/2 on the positive and negative plates, respectively. Wåhlin (2) has shown that the fringing field of a velocity filter can be used to improve the focus of the ion beam. It was found that significant departures from ± V/2 are useful in obtaining an optimum focus at the detector.

The power supplies which produce the accelerating voltage and operate the source are conventional regulated supplies. One less common feature of the electrical system is that the total accelerating voltage is obtained from two 0-50 kV supplies operated in series. One high voltage unit, which operates from an isolation transformer supplies the extractor voltage and operates the Einzel lens by means of a voltage divider. The second high voltage unit supplies the voltage to the final accelerating stage. The use of two supplies in series eliminates the need for a voltage divider or power supply which can sustain the full accelerating voltage.

The detector and sample holder are mounted together at ground potential on an X-Y table* which is operated by external stepping motors via rotary vacuum feedthroughs.

- - - - - - - - - - -

* Transistor Automation Corporation, Woburn, Massachusetts

The target chamber is evacuated by a 6 in. diffusion pump with a liquid nitrogen cooled baffle. Under typical implant conditions, the pressure in the target chamber is $1 \times 10^{-6}$ Torr.

Ions are detected by a Faraday cup located below an aperture in the sample holder. Secondary electron emission from the Faraday cup is suppressed by applying a - 90 V bias to the sample holder. The ion current delivered to the detector is measured with either an oscilloscope or an electrometer before and after implanting a sample. The average current value is combined with the exposure time and area to determine the implanted dose. Electron microprobe examination of a high dose indium implant showed that the absolute dose determination is accurate to better than 20%.

SYSTEM PERFORMANCE

It has been experimentally verified that the system described above is adequate for implantations in the mass range $10 \leq A \leq 124$ and over the energy range 10 keV to 70 keV. As examples of typical ion currents at the detector, approximately 10 μA of $^{40}A^{+}$ and 3 μA of $^{64}Zn^{+}$ over the energy range 20 keV to 70 keV can be obtained. At energies less than 20 keV, the extraction efficiency and transmission decrease such that approximately 2 μA of $^{40}A^{+}$ can be obtained at 10 keV. By decreasing the source filament emission and the relative vapor pressure of the desired species, the current of a given ion can be reduced smoothly to less than $1 \times 10^{-9}$ amperes.

Because of the small size of the mass analysis stage, the mass dispersion and resolving power are very modest when compared to an isotope separator. However, the mass discrimination obtained has proved adequate for a wide range of ion implantation experiments. One determination of the resolving power and dispersion was made using a zinc ion beam. With an accelerating voltage of 30 kV, the ions $^{64}Zn^{+}$ and $^{66}Zn^{+}$ could be clearly separated with a 0.5 mm detector slit. This corresponds to a resolving power ($M/\Delta M$) of approximately 30 measured at the base of the peaks, and a dispersion of 0.5 mm/mass unit. To investigate possible contaminants, the resolving power can be increased to 60 by aperturing the beam and reducing the size of the final slit. A semi-empirical general expression for the mass dispersion (D) of the system is:

$$D = \frac{1.4 \text{ cm}}{\sqrt{VM}} \quad \text{for 1\% mass difference,}$$

where V is the accelerating voltage in keV and M is the atomic mass number of the ion being collected at the detector. It is interesting to note that the observed mass dispersion is 30% larger than the value calculated for the system geometry and magnet field. This difference is attributed to the large extent of the magnet fringing field which was not considered in our calculation.

DISCUSSION

Experience with the small and relatively simple system described herein indicates that it is useful for a wide range of low energy ion implantation experiments. The use of a velocity filter has allowed the replacement of the conventional sector magnet and current supply with permanent magnets, while still maintaining mass selection independent of the ion accelerating voltage. Because of the low power consumption and small size of the mass analysing system, the source, lens and velocity filter arrangement should make a convenient mass analysed ion source and injector for higher energy experiments in which the system described here would be used to feed an accelerating tube.

REFERENCES

1. W. Wien, Ann. Physik., 65, 440 (1898); 8, 260 (1902).

2. L. Wåhlin, Nucl. Instr. and Meth., 27, 55 (1964); 38, 133 (1965).

3. K. O. Nielsen, Nucl. Instr. and Meth., 1, 298 (1957).

4. O. Almen and K. O. Nielsen, Nucl. Instr. and Meth., 1, 302 (1957).

5. G. Liebmann, Proc. Phys. Soc., 62, 15 (1949).

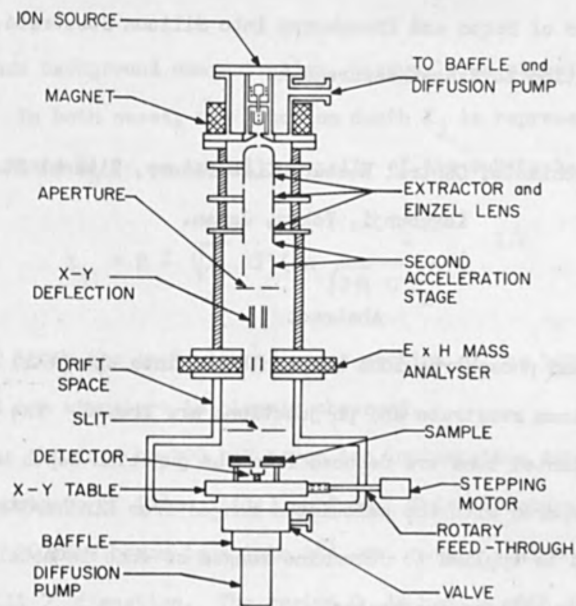


FIG. 1 SCHEMATIC DIAGRAM OF ION IMPLANTATION SYSTEM. THE OVERALL LENGTH IS FIVE FEET.

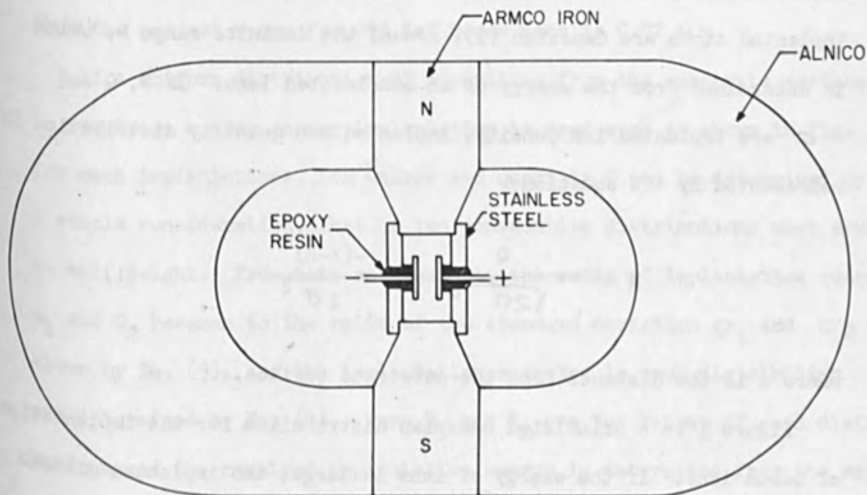


FIG. 2 SCHEMATIC DRAWING SHOWING CONSTRUCTION OF VELOCITY FILTER.

Implantation of Boron and Phosphorus into Silicon Substrate and Its Application to Range Measurement.

Takashi Tsuchimoto, Central Research Laboratory, Hitachi Ltd.
Kokubunji, Tokyo, Japan.

Abstract

Boron and phosphorus ions are implanted into the (111) surface of the silicon substrate and pn junctions are fromed. The ranges of the implanted ions are decuced from the junction depth measurements and are compared with the calculated ranges from Lindhard's theory. This method is applied to determine ranges of ions in metal films deposited on silicon substrates.

The implantation of boron and phosphorus ions into silicon substrate introduces a distribution of these atoms into the substrate and pn junctions are formed. We assume the distribution of implanted atoms are Gaussian (1), around the definite range R, which is determined from the energy of an accelerated ions. If N, Q and $\sigma$ are implanted ion density, implanted ion quantity distribution is represented by the equation

$$N = \frac{Q}{\sqrt{2\pi}\,\sigma} \exp \frac{-(x-R)^2}{2\sigma^2} , \qquad (1)$$

where x is the distance from the substrate surface.

Figure 1 is a calculated Gaussian distribution for the implantation of boron ions. If the energy of ions is large, the implanted distribution will resemble that in Fig. 1, and npn structures would be expected. If the energy of ions is small, the distribution is shifted toward the surface and the concentration of the distribution and the surface may not

be less than background concentration, thus only pn structures are expected. In both cases, the junction depth $X_j$ is represented by Eq. (2). Where $N_B$ is an impurity density of the substrate.

$$X_j = R \pm \sqrt{2}\ \sigma \left(\ln \frac{Q}{\sqrt{2\pi}\ \sigma N_B}\right)^{1/2} \qquad (2)$$

Fig. 2 shows the angle lapped cross section of the boron implanted sample and npn structure is clearly observed.

This is obtained by 200 keV boron ion implantation into a n type silicon substrate of 1Ωcm, (111) surface. This structure was produced by implanting 200 KeV boron ions into 1Ω -cm, n-type silicon oriented in the < 111 > direction. The region $O_a$ is n-type with an np junction at 0.5μm below the surface, and the region ab is p-type with a pn junction at 0.44μm below the np junction. The midpoint of the p-type region is assumed to correspond to the peak of the implanted distribution, thus the project range for 200 KeV boron ions is 0.72μm.

If a uniform distribution of impurities from the substrate surface is required, a step energy implantation is used such as shown in Fig. 3. For each implantations, ion energy and quantity Q can be determined by a simple consideration, that is two consecutive distributions must cross at half height. From this requirement, the ratio of implantation quantity $Q_1$ and $Q_2$ becomes to the ratio of the standard deviation $\sigma_1$ and $\sigma_2$ as shown by Eq. (3), and the implantation energies in each distribution are determined by Eq. (4). Here $R_1$ and $R_2$ are the ranges of each distributions and the required implantation energy is determined from the range R.

$$\frac{Q_1}{Q_2} = \frac{\sigma_1}{\sigma_2} \qquad (3)$$

$$R_1 - R_2 = \sqrt{2}\ \sqrt{\ln 2}\ (\sigma_1 + \sigma_2) \qquad (4)$$

Fig. 4 shows the delineated cross section of the silicon substrate for the above mentioned implantations, and uniform boron distribution is observed. The maximum implanted ion energy is 350 keV in this case, and the junction depth is observed to be 1.5 m. In both cases the range R is determined by the ion energy but the junction depth $X_j$ changes with ion quantity Q. This is shown in Eq. (2).

The results of these junction depth measurements are summarized in Fig. 5. Ion energies were varied from 5 to 350 keV for ion quantities Q of $10^{12}$, $10^{14}$, and $10^{16}$ ions/$cm^2$. The solid lines represent the junction depth calculated from Lindhard's theory[1]. If we assume the distribution is Gaussian, the range is obtained by subtracting the half width. Fig. 6 represent the ranges obtained by thin measurement, and the solid lines represent also calculation from Lindhard's theory. These results show fairly good agreement which may be due to the fact that (111) plane has a closed channel crystallographic structure.

Using these silicon junction formation technique, the ion ranges in various metals can be obtained. The thin metal layers are prepared on the surface of silicon substrates by a vacuum evaporation, and implantations are carried out through these metal layers. The ion passed through the metal film can form pn junction in the silicon substrate, and the junction depth $X_j$ can be readily measured by observing the cross section of the substrate. With the samples having various thickness of the metal films, the junction depth are measured and plotted as shown in Fig. 7. The intersection of the extrapolated point at the abscissa d means just the corresponding point b in Fig. 8 Therefore, one can obtain the range R in the metal by subtracting the distribution width $W_{metal}$ of Eq. (5)

form the value of d. This distribution width is deduced from Eq. (2) and Fig. 8.

$$W_{metal} = \sqrt{2}\,\sigma_{metal} \left( \ln \frac{Q}{\sqrt{2\pi}\,\sigma_{metal} N_B} \right)^{1/2} \qquad (5)$$

In Fig. 9, the measured junction depth $X_j$ in the case of evaporated aluminum film is shown. The implantation was 200 keV boron ions. The extrapolated point shows $0.82\,\mu m$. Subtracting the distribution width from this value, the range of boron in aluminum with the energy of 200 keV is $0.62\,\mu m$.

The measurements of the ranges in metal film of aluminum, chromium, nickel and molybdenum are summarized and compared with the calculated values of Lindhard's theory in Table 1. A small difference is seen in the case of aluminum. These results are applied to the ion beam stopping films for the fabrication of microelectronic device.

The penetration of ions in silicon dioxide film is measured by using the step structures shown in Fig. 10. These steps are formed by repetitive photo-etching of silicon dioxide. When the ions are implanted, some of them stop in the thick $SiO_2$ and some of them pass through the $SiO_2$ and form a pn junction image of step structure of the oxide.

In Fig. 11, the photograph of $SiO_2$ steps and the delineated cross section of 200 keV boron implanted substrate are shown. The interference lines correspond to the thickness of $SiO_2$ steps. The delineation is carried out with Sirtle etch solution.

In summarizing, the ranges of boron and phosphorus in silicon substrate are measured from the junction depth which are formed by these ion implantation. The ranges in metals are also measured by using the junction depth, that is, ranges are measured by using silicon substrate as a detector, and the penetration of ions through $SiO_2$ film is also detected by this method.

The author wishes to express his sincere thanks to Professor Dr. Masakatsu Sakisaka of the Kyoto University and Drs. Toyozo Kanbara, Sachio Takei and Takashi Tokuyama of Central Research Lanoratory, Hitachi Ltd. for their valuable discussions.

References:

(1) J. Lindhard, M. Scharff, H. E. Schoitt: Range concepts and heavy ion ranges. Dan Vid. Sesk. Mat. Fys. Medd. Vol. 33, No 14, (1963)

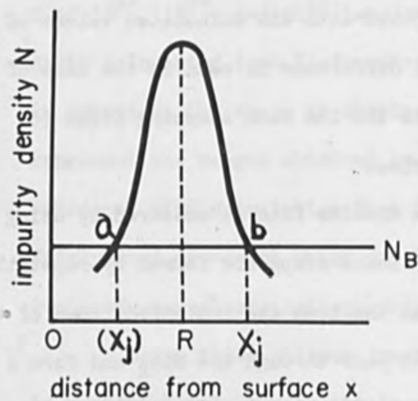


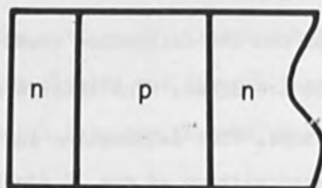


Fig.1 npn Structures

Fig.2 Photograph of npn Structure

substrate ; n type, 1 Ω cm, (111) plane
ion quantity ; $10^{14}$ (atoms/cm$^2$)

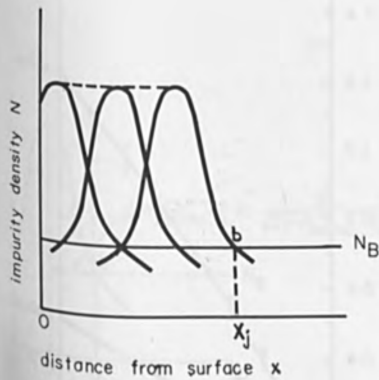


Fig.3 Uniform Impurity Distribution

Fig.4 Photograph of Uniform Impurity Distribution

substrate ; n type, 1 Ω cm, (111) plane
ion quantity ; $10^{16}$ (atoms/cm$^2$)
first step

Table 1 Ranges of Boron and Phosphorus in Metals (implantation energy ; 200 KeV)

| metal \ ion | boron | | phosphorus | |
|---|---|---|---|---|
| | measured (μm) | calculated (μm) | measured (μm) | calculated (μm) |
| aluminum | 0.62 + 0.02 | 0.85 | 0.18 + 0.02 | 0.214 |
| chromium | 0.30 ± 0.02 | 0.325 | 0.09 ± 0.02 | 0.0947 |
| nickel | 0.29 ± 0.02 | 0.294 | | |
| molybdenum | 0.20 ± 0.02 | 0.218 | | |

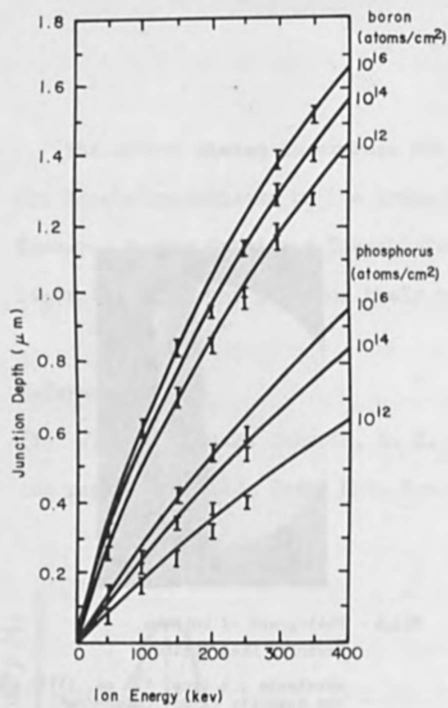


Fig.5 Junction Depth vs. Ion Energy
substrate n and p type, 1 Ω cm, (111) plane
ion quantity ; $10^{12}$, $10^{14}$, $10^{16}$ (atoms/cm$^2$)

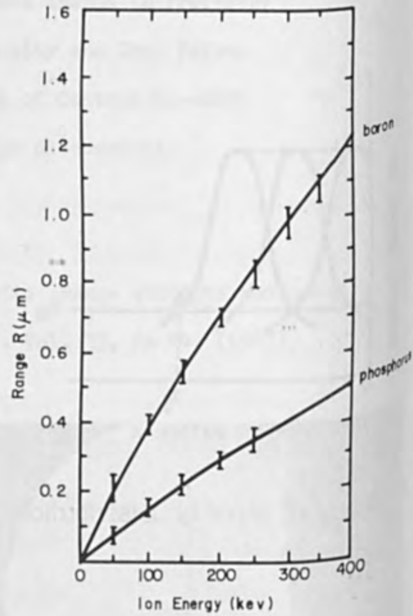


Fig.6 Range-Energy Relations

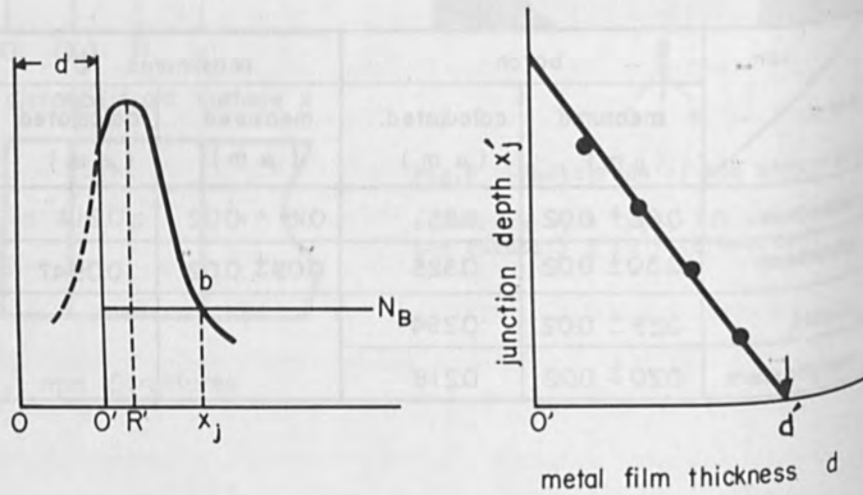


Fig.7 Range Measurement in Metals

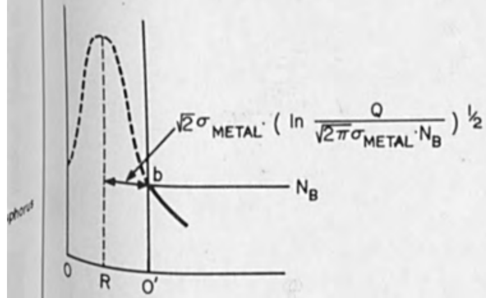


Fig.8 Explanation of d'

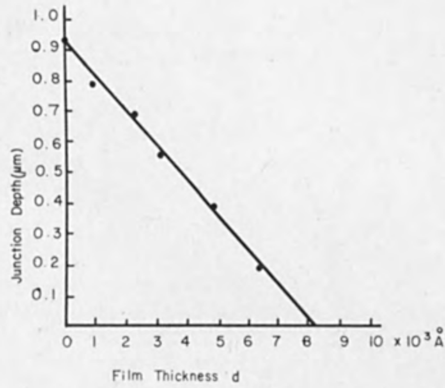


Fig.9 Aluminum Range Measuremet

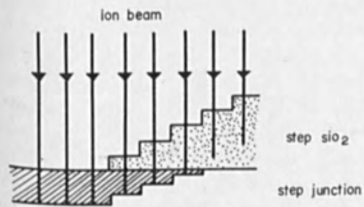


Fig.10 Range Measurement in Silicon Dioxide

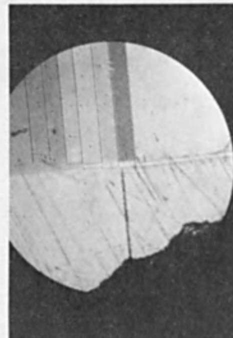

Fig.11 Photograph of Step Structure Junction

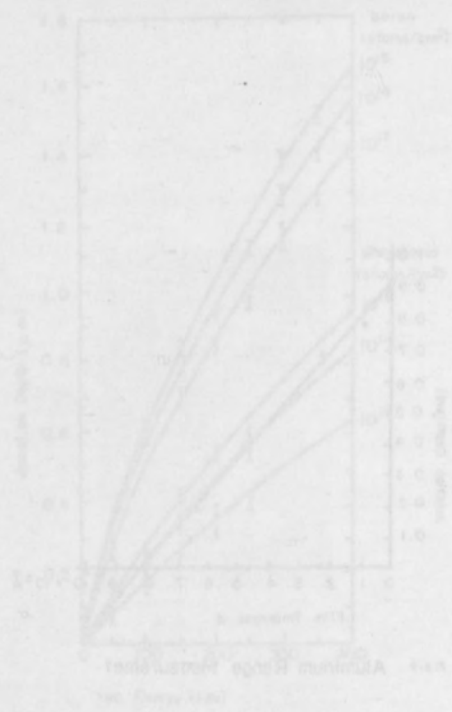
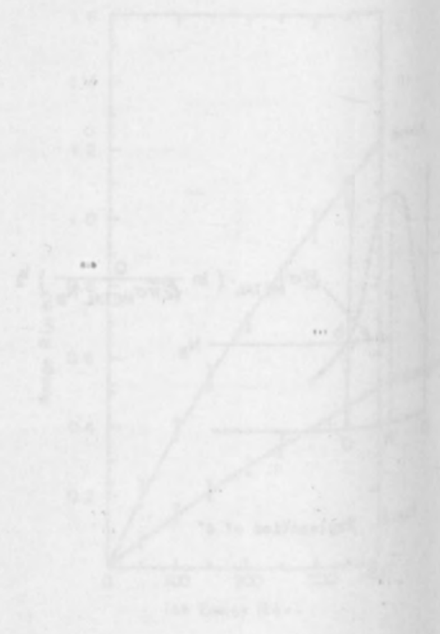

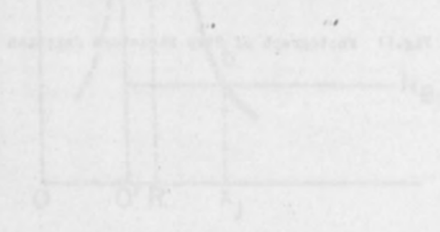
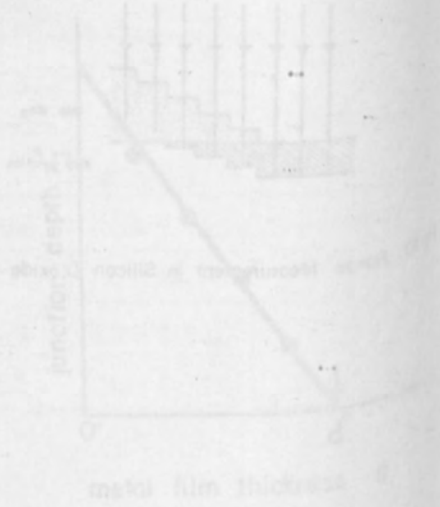

# APPENDIX

## AUTHORS' SUMMARIES

Abstract No. 128

# ON THE MEASUREMENT OF IMPURITY ATOM DISTRIBUTIONS ARISING FROM ION IMPLANTATION IN HIGH-RESISTIVITY SILICON*

D. P. Kennedy, P. C. Murley, and W. Kleinfelder
International Business Machines Corporation
East Fishkill Laboratory
Hopewell Junction, New York

## I. Introduction

It has been reported[1] that 20-kV implantations into high-resistivity silicon (20 to 50 k$\Omega$cm) results in a deep penetration of donors (frequently called a "super-tail"); this deep penetration is suggested to imply the existence of unexplained mechanisms that determine the distribution of implanted ions. The profiles upon which this conclusion is based were measured by the differential capacitance technique. Because no method is available whereby the results of differential capacitance measurements can be experimentally verified at small values of impurity atom density, the need for a rigorous mathematical investigation of this topic is apparent.

The one-dimensional ambipolar diffusion equations for holes and electrons have been applied to a boundary value problem that approximates the differential capacitance method for determining an impurity atom distribution in semiconductor material. Thereby, comparisons were made between the impurity atom distribution inferred from differential capacitance calculations and the impurity atom distribution assumed in the analytical model. In situations where the differential capacitance inferred profile was in error, a study was initiated to determine the source of error. Resulting from this investigation is an understanding of some inherent limitations of the differential capacitance technique for measuring impurity atom distributions; a discussion of these limitations is presented here.

## II. The Differential Capacitance Measurement

An important conclusion of this investigation is that an incorrect interpretation of differential capacitance measurements is possible. An approximate analysis of this measurement produces the equation

$$n(x) = -\frac{C^3}{qK\epsilon_0}\left(\frac{dC}{dx}\right)^{-1}, \quad (1)$$

* This work was supported in part by the Air Force Cambridge Research Laboratories, Office of Aerospace Research, under Contract F19(628)-C0116, Project 4608.

where C is the differential junction capacitance measured at a given reverse biasing voltage.

The mathematical development of Eq. (1) differs from previous publications on this subject;[2] charge neutrality is not assumed within the semiconductor material. Equation (1) shows that differential capacitance measurements imply the distribution of majority carriers within a semiconductor $[n(x)]$, rather than the impurity atom distribution $[N(x)]$. If, instead, the semiconductor material is assumed to be charge neutral, we obtain $n(x) = N(x)$, and the traditional interpretation of this experiment becomes applicable.

## III. Analysis

Semiconductor material of homogeneous conductivity type, containing a discontinuous change of impurity atom density (frequently called an abrupt high-low junction), exhibits an electrostatic double-layer of the type attributable to a p-n junction. Such material contains a region on the high-doped side that is partially depleted of majority carriers, and a region on the low-doped side that contains an accumulation of majority carriers.

It is shown that the differential capacitance inferred profile in the space-charge region of a high-low junction is quantitatively equal to the mobile carrier distribution. This conclusion is consistent with Eq. (1), which is applicable to regions of semiconductor material not exhibiting charge neutrality.

Figure 1 compares the mobile carrier distribution inferred from differential capacitance calculations with the experimental results from Fig. 1 of the forementioned publication on ion implantation.[1] An abrupt high-low junction was assumed in the mathematical model used for these calculations.

From the calculations illustrated in Fig. 1, it is suggested that the observation of a deep donor penetration due to ion implantation is a consequence of the interpretation of differential capacitance measurements. Figure 1 implies that this implantation is sufficiently shallow to be considered an abrupt high-low junction, and that the differential capacitance measurement establishes the mobile carrier distribution associated with this type of structure, rather than the doping profile arising from ion implantation.

---

1. R. W. Bower, R. Baron, J. W. Mayer, and O. J. Marsh, Applied Phys. Letters, 9, 203 (1966).
2. N. I. Meyer and T. Guldbrandsen, Proc. IEEE, 51, 1631 (1963).

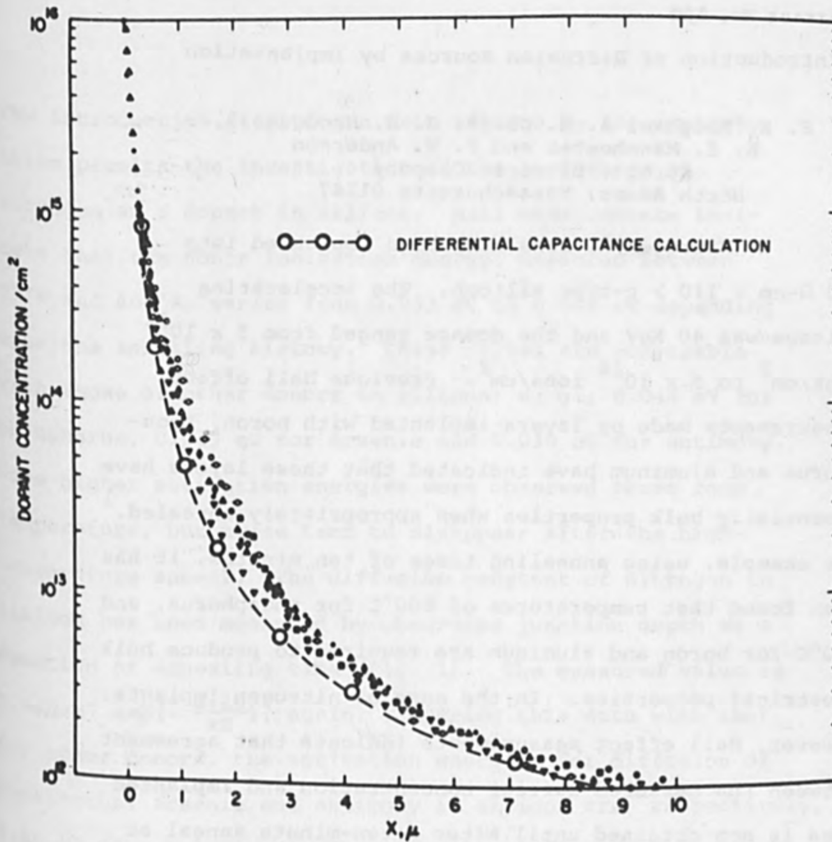


Fig. 1. A comparison between the measured doping profile arising from ion implantation experiments and the results of differential capacitance calculations for an abrupt high-low junction.

**Abstract No. 130**

## Introduction of Diffusion Sources by Implantation

P. E. Roughan, A. H. Clark, J. D. Macdougall,
K. E. Manchester and F. W. Anderson
Sprague Electric Company
North Adams, Massachusetts 01247

Nitrogen-14 ions have been implanted into 100 Ω-cm $\langle 110 \rangle$ p-type silicon. The accelerating voltage was 40 KeV and the dosage ranged from $3 \times 10^{12}$ ions/cm$^2$ to $5 \times 10^{14}$ ions/cm$^2$. Previous Hall effect measurements made on layers implanted with boron, phosphorus and aluminum have indicated that these layers have essentially bulk properties when appropriately annealed.[1] For example, using annealing times of ten minutes, it has been found that temperatures of 600°C for phosphorus, and 950°C for boron and aluminum are required to produce bulk electrical properties. In the case of nitrogen implants, however, Hall effect measurements indicate that agreement between the measured carrier concentration and implanted dose is not obtained until after a ten-minute anneal at 1200°C.

Since it is a Group V element, one expects that nitrogen should act as a donor in silicon. However, it is extremely difficult to introduce into the silicon lattice by ordinary techniques, because of its low segregation coefficient and its tendency to form silicon nitride.

- - - - - - - - -

1. A. H. Clark and K. E. Manchester, Trans. AIME, to be published.

The introduction of nitrogen into silicon by ion implantation permits the investigation of the properties of nitrogen as a dopant in silicon. Hall measurements indicate that the donor ionization energy, measured between 77°K and 400°K, varies from 0.033 eV to 0.044 eV depending upon the annealing history. These values are comparable with those of other donors in silicon; e. g., 0.044 eV for phosphorus, 0.049 eV for arsenic and 0.039 eV for antimony. Some higher activation energies were observed above room temperature, but these tend to disappear after the high-temperature anneal. The diffusion constant of nitrogen in silicon has been measured by observing junction depth as a function of annealing time (Fig. 1). The measured value is $D = 0.87 \exp(-\frac{3.29}{kT})$; again, comparing this data with that for other donors, the activation energies for diffusion of phosphorus, arsenic and antimony in silicon are, respectively, 3.69, 3.56 and 3.96 eV. These results indicate that nitrogen in silicon has essentially the same properties as the other Group V donors. Similar experiments have been carried out with indium and preliminary results will be presented.

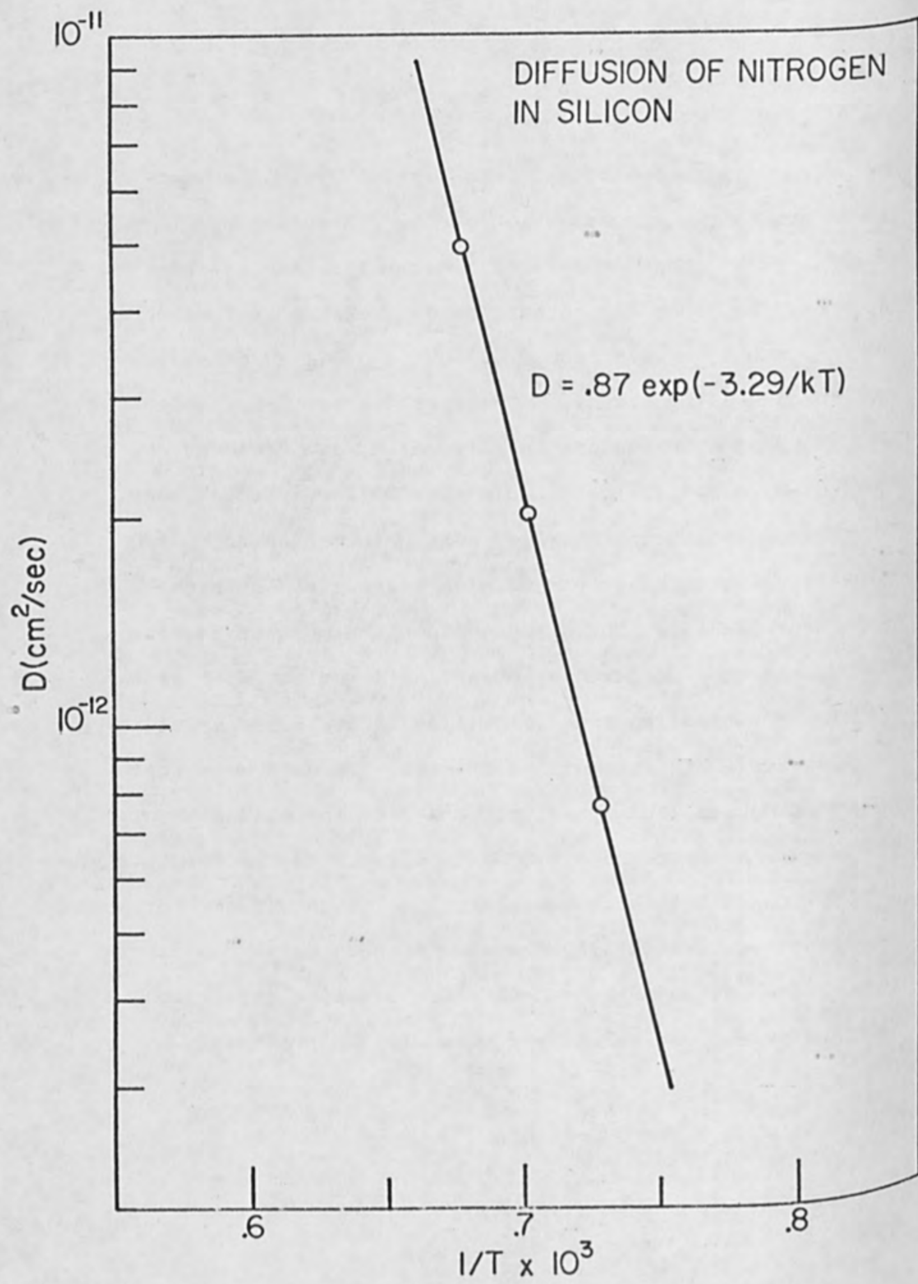

DIFFUSION OF NITROGEN IN SILICON
D = .87 exp(-3.29/kT)
10^-11
10^-12
D(cm^2/sec)
.6
.7
.8
1/T x 10^3

Abstract No. 131

# Evaluation of Ion Implantations into Silicon by Hall Measurements *

G. A. Shifrin, R. Baron, O. J. Marsh, and J. W. Mayer
Hughes Research Laboratories
3011 Malibu Canyon Road
Malibu, California 90265

The dependence of the number of active carriers on implant temperature, anneal temperature, and depth has been studied for implanted silicon crystals. Samples have been implanted with both group III and V dopant elements, at ion energies between 20 and 100 keV, and at temperatures from 23 to 500°C. Among the dopant ions studied were Al, As, B, Bi, Ga, Sb, and Tl.Hall effect and sheet resistivity measurements performed at room temperature were used to determine the total effective number of carriers and the effective mobility as a function of anneal temperature. This measurement technique was subsequently combined with successive layer removal operations to determine the variation with depth of the carrier concentration (n) and mobility ($\mu$). This technique considerably refines the electrical evaluation of the implanted layer. Since the conductivity and the Hall coefficient measured at the original surface are weighted averages of n and $\mu$ with depth, one can then relate the true values of these quantities with the effective values normally measured at the surface.

Combined Hall effect and layer removal measurements show that for low and moderate concentrations in implanted layers the relation between $\mu$ and n is similar to that exhibited in bulk diffused silicon. However, at high concentrations ($\gtrsim 10^{19}/cm^3$) the Hall mobility is found to be significantly lower than the published values for diffused silicon. There is correlation of this fact in that where such lower mobility is observed, the total number of carriers is considerably less than the number implanted. This implies that there is an additional scattering mechanism associated with those implanted atoms which are electrically inactive.

Room temperature implants of B, Al, and Ga show increasing impurity conduction in response to ten minute anneals starting from 300°C. Typically no further increase is observed beyond 500°C to 1000°C, depending on the total implanted dose. In contrast, Sb shows type conversion after a 300°C anneal but relatively little electrical utilization of the implanted atoms until anneal temperatures of 600°C where the activity increases rapidly. The utilization coefficient is defined as the ratio of the electrically active carriers to the number of implanted atoms.

Hot implantations (400°C or more) in light doses ($10^{13}/cm^2$ or less) of column III elements show close to unity utilization coefficient. Heavy doses (more than $10^{14}/cm^2$) show utilization coefficients of from 0.1 to 0.001, decreasing with heavier doses. The utilization coefficient tends to increase with increasing anneal temperature, but for Al and Ga it saturates at far less than unity because of solubility limitations. On the other hand, hot implants of Sb and Bi tend to show high utilization coefficients. For heavy implants these elements can exhibit substitutional solubilities far in excess of that achievable by thermal equilibrium processes such as diffusion or growth.

The results obtained for the electrically active carriers with the Hall effect measurements have been compared with the number of implanted atoms found on substitutional sites using Rutherford scattering techniques** on similarly implanted and annealed samples. Significant correlations have been found between the results from these independent techniques.

* This work was partially supported by the Air Force Avionics Laboratory, Research and Technology Division, Air Force Systems Command, Wright-Patterson Air Force Base, Ohio.

** Measurements performed by J. W. Mayer, L. Eriksson, S. T. Picraux, and J. A. Davies at Chalk River (Atomic Energy of Canada, Ltd), and by J. W. Mayer and S. T. Picraux at California Institute of Technology.

Abstract No. 133

Electrical Characteristics of
Ion Implanted Gallium Arsenide *

R. G. Hunsperger and O. J. Marsh

Hughes Research Laboratories
3011 Malibu Canyon Road
Malibu, California 90265

The technique of ion implantation has been used to dope high resistivity, single crystal gallium arsenide with such impurities as zinc, cadmium and tin. Implants were made with 20 to 70 kV ions, into both heated and room temperature substrates. Electrical characteristics of the implanted layers have been studied as a function of isothermal and also isochronal annealing cycles. The surface resistivity, average mobility and carrier concentration of implanted layers has been determined by Hall measurements, and the spatial distribution profile of electrically active implanted ions has been determined by making surface barrier capacitance-voltage measurements.

Measurements on 20 kV zinc implanted substrates of 1-10 Ω-cm n-type gallium arsenide indicate that a p-type layer is formed when the substrate is heated to 400°C during implantation. This layer initially has very high surface resistivity (typically $3.5 \times 10^4$ Ω/□) and relatively low carrier mobility (~ 1 $cm^2$/V-sec), however annealing causes surface resistivity to decrease and mobility to increase. Isochronal anneal cycles of 10 minutes duration at temperatures from 410°C to 600°C produced a decrease in surface resistivity by a factor of approximately 25, with most of the change occurring below 450°C. Annealing of similarly implanted samples in 20 minute cycles at temperatures up to 700°C increased mobility by a factor of 20, again with most of the change occurring below 450°C. Isothermal annealing of 400°C implanted samples at 500°C and 600°C for various lengths of time up to 30 minutes caused corresponding decreases in surface resistivity and increases in mobility. At 500°C most of the change occurred in the first 5 minutes of anneal and at 600°C most of the change occurred in the first 2 minutes. Some samples were prepared by 20 kV zinc implantation with the substrate held at 500°C during implantation. It was found that these samples had higher carrier mobility and lower surface resistivity than those implanted at 400°C and annealed at 500°C. Also, some samples were implanted at 70 kV, and these samples were observed to have better electrical characteristics than those implanted with 20 kV ions. For example, a sample of high resistivity n-type GaAs was implanted with 70 kV Zn ions at a substrate temperature of 400°C. After annealing for 2 minutes at 600°C

the implanted layer was found to be p-type with surface resistivity $\rho_s = 598\ \Omega/\square$, mobility $\mu = 45.8\ cm^2/V\text{-sec}$, and carrier concentration $N_s = 2.28 \times 10^{14}/cm^2$. The corresponding values for a 20 kV ion implanted sample, similarly annealed, were $\rho_s = 3100\ \Omega/\square$, $\mu = 19.5\ cm^2/V\text{-sec}$, and $N_s = 1.05 \times 10^{14}/cm^2$.

The implantation of cadmium ions into gallium arsenide has also resulted in the formation of p-type layers, but it has been observed that cadmium implants require somewhat more extensive annealing than do zinc implants. Samples of high resistivity n-type gallium arsenide were implanted with 20 kV cadmium ions with the substrate held at 400°C. The "as implanted" samples showed no evidence of the formation of a p-type layer, and annealing these samples at 500°C for up to 1 hour was not sufficient to cause conversion to p-type. However annealing at 600°C for only 5 minutes created a p-type layer with (typically) $\rho_s = 5.2 \times 10^4\ \Omega/\square$, $\mu = 6.8\ cm^2/V\text{-sec}$, and $N_s = 1.9 \times 10^{13}/cm^2$. Additional annealing at 600°C for a total of 60 minutes changed these values to $\rho_s = 2.6 \times 10^4$, $\mu = 45\ cm^2/V\text{-sec}$ and $N_s = 6 \times 10^{12}/cm^2$.

N-type layers have been formed in gallium arsenide by implantation with tin ions. In order to create the desired n-type implanted layer it has been found necessary to protect the surface of the sample during annealing to prevent outdiffusion of tin atoms. Two successful techniques of doing this have been to cover the surface of the sample with a sputtered $SiO_2$ film or to cover the sample wafer with a second, polished wafer of gallium arsenide. Using this method samples of high resistivity p-type gallium arsenide were implanted with 35 kV tin ions at 400°C substrate temperature and annealed for 10 minutes at 700°C. An n-type layer resulted with $\rho_s = 18,000\ \Omega/\square$, $\mu = 5.6\ cm^2/V\text{-sec}$ and $N_s = 6.2 \times 10^{13}/cm^2$. The covering wafer (or $SiO_2$ layer) also served to prevent dissociation of the gallium arsenide during annealing.

* This work supported in part by NASA, ERC, Cambridge, Massachusetts.

Abstract No. 138

# ADVANTAGES OF ELECTRON-BEAM HEATING IN A METALLURGICAL HEAT-TREATING FURNACE*

J. C. Wilson

Metals and Ceramics Division
Oak Ridge National Laboratory
Oak Ridge, Tennessee

High-vacuum furnaces for metallurgical heat treatment usually employ resistance (ohmic) heating. There are a number of significant advantages to using electron-beam heating instead, or, in resistance-heated furnaces, using auxiliary electron-beam heating to speed outgassing, reduce pumpdown times, or to reach lower pressures. In our experience the principal advantage of electron-beam heating is that the heat may be directed to or distributed over selected areas from simple thermionic cathodes. As a result it is possible to apply heat not only to the work but to the furnace structure, radiation shields, or the vacuum enclosure to obtain rapid and efficient outgassing. Also, the distribution of heat on the work can be easily adjusted; and, for special purposes, deliberate temperature gradients may be introduced.

We shall describe the design and operation of several electron-beam furnaces. The largest has a 2-in.-diam by 8-in.-long isothermal hot zone capable of reaching temperatures above 1500°C with pressure in the $10^{-10}$ torr range.

The specimen chamber (anode) is a vertical cylinder surrounded by a cathode of vertical wires. Outside the cathode are concentric tantalum radiation shields. An auxiliary cathode is placed between the shields and the vacuum enclosure. In operation, the radiation shields are quickly heated from outside and inside to outgas them well above their operating temperatures before the work is lowered (by magnetic suspension) into the furnace. In this way the principal obstacle (i.e. radiation shield outgassing) to obtaining low pressures during heat treating (particularly for short times) is overcome.

The entire furnace assembly (except auxiliary cathode) can be removed by lifting out a suspension ring below an 8-in.(ID) flange. Anode and cathode are separately removable, each on its own suspension ring, so that cathodes and anodes with different characteristics may be inserted or removed easily. Pumping is done by a 6-in. orbitron pump supplemented by a sublimation pump in which superheated molten titanium is evaporated by an electron beam.

---

*Research sponsored by the U.S. Atomic Energy Commission under contract with the Union Carbide Corporation.

The performance of the furnace will be compared with a simulated resistance-heated furnace in which the anode is heated from within by electron bombardment from a temporary cathode. Pressure-time comparisons, including residual gas analyses, show the superior speed and lower attainable pressures in the electron-beam configuration. The electron-beam concept is particularly well adapted to heat treatment of ultrahigh purity materials because of its simplicity, ready replacability of potential contaminating components, and ability to achieve high vacua in reasonable times.

Abstract No. 142

# POISONING OF $LaB_6$ CATHODES

H. E. GALLAGHER
Hughes Research Laboratories
Malibu, California

The poisoning of lanthanum hexaboride cathodes by various gases was investigated experimentally. The poisoning gases used were oxygen, nitrogen, carbon monoxide, carbon dioxide, water vapor and hydrogen. The cathode geometry was a long cylinder with one end serving as the emitting surface. The opposite end of the cylindrical cathode was mounted in a copper heat sink which lowered the temperature sufficiently to prevent chemical reactions between the $LaB_6$ and its support. The emitting end was radiation heated with coaxial tungsten coil. A planar cathode-anode geometry was used. The cathode was surrounded by a shield to insure a uniform field. The anode was water cooled for high emission density dc measurements. The vacuum envelope was pumped with sublimation and ion pumps. The system was bakeable, including the leak valve through which the poisoning gases were injected. A mass spectrometer was used to monitor the relative pressures of residual gases, decomposition products, and the poisoning gas. A relatively constant pressure for the poisoning gas was maintained by establishing a constant leak rate against a reduced pumping speed.

The poisoning characteristics were measured by recording the emission current for various pressures of the poisoning gas and for various cathode temperatures. For each poisoning gas pressure, an equilibrium or steady state emission was established. It was found that for a given cathode temperature, a critical pressure existed for each poisoning gas. The emission decayed exponentially with pressure for values above this critical pressure. Also, for each poisoning gas, the critical pressure increased with increasing cathode temperature. The poisoning characteristics of this $LaB_6$ cathode are compared with the poisoning data for oxide, impregnated, and pure tungsten cathodes.

After reaching a steady state emission level for a given poisoning gas pressure, the leak valve was closed and the ion pump speed was increased. The recovery of emission was then recorded in relation to the time required to reduce the pressure below its critical value. Except for excessive poisoning pressures, the emission recovered to its original unpoisoned level. The emission recovery times were used to calculate the desorption energy for oxygen on lanthanum hexaboride.

Abstract No. 147

# COLD CATHODE AS A METALWORKING TOOL

Marvin L. Kohn

**Hamilton Standards Division, United Aircraft Co., Windsor Locks, Conn.**

Cold cathode technology, as developed by United Aircraft Corporation, involves the use of nonthermionic cathodes for the production of electron beams for metalworking. The primary areas of use include welding, brazing, diffusion bonding and heat treating. A secondary use, one not limited solely to metallic materials, is growing single crystals. The applications described in this paper indicate graphically that cold cathode devices will not replace thermionically-produced electron beams for welding, but rather will augment them and make electron beam technology applicable to a wider segment of technology.

In order to apply cold-cathode generated electron beams most effectively, they are shaped as needed by the specifications of the process or the shape of the part, or both. For welding, the beam must be as narrow as possible at the point of impingement upon the workpiece to maximize the beam power density and thereby produce fusion. Conversely, brazing, heat treating, and diffusion bonding all require the application of heat without base-metal fusion. For these cases it is desirable to produce a beam in which the impingement area is wide, and therefore the power density would be insufficient to produce fusion over the time of exposure to the beam.

An extremely basic factor of cold cathode technology allows for geometric control of focal point and also permits shaping of the electron beam to match the workpiece contour. This beam shaping is accomplished by contouring the emitting surface of the cathode. Electrons are accelerated outward from the cathode emitting surface in a direction perpendicular to the tangent to the cathode surface at the point of electron emission. This directionality of electron acceleration provides the ability to shape and focus the electron beam. In addition the beam may be shaped further by placing a shield at ground potential in front of the emitting surface of the cathode which then either blocks the beam, or prevents electron emission. The specific action of the shield depends upon its location with respect to the cathode fall region. If the shield is outside the cathode fall region, the electron emission falls solely on the shield and heats it as for any heat shield; this prevents workpiece heating, but is acceptable only for short time exposures. Placing the shield within the cathode fall region prevents electron emission; this has no adverse effect on the shield but causes aberrations in the beam at the region of the beam most affected by the shield.

Welding experience has involved a variety of workpiece and cathode shapes. Butt welding of tubing has been accomplished using annular cathodes which produce beams focused at the diameter of the tubing. In this case, samples up to 4-inch O.D., 1/4-inch wall have been welded. Butt and lap welding of flat sheet specimens have been accomplished using a cathode designed to produce a focused line. The length of the focal line can be adjusted by shielding to tailor the weld length to the requirements of the application.

Brazing, diffusion bonding, and heat treating can be accomplished using the same cathodes used for welding so long as the workpiece is placed away from the beam focal line or point. In this way, the beam energy is transmitted to the workpiece over a wider area instead of a narrow line and heating without melting is accomplished. The rate at which heat is transmitted to the workpiece controls depth of heating. High heat flux produces shallow heat penetration when the part is exposed for only a short time. This technique is used for surface hardening of steels. Similarly, lower heat flux over long periods results in deeper heat penetration.

The ability to shape the pattern of heat transmitted to the workpiece provides a most versatile heating tool. The versatility is clearly demonstrated by the applications discussed in the paper.

Abstract No. 148

## SOME RECENT DEVELOPMENTS IN E.B. WELDING EQUIPMENT AND ITS APPLICATIONS

J. SOMMERIA - ALCATEL, 98 Avenue de Brogny - 74. ANNECY

The requirements for purity and for security in the metallurgical proceedings of the nuclear technology have given first of all in the area a preponderant place to the electron-beam welding, which represents pre-eminently the vacuum proceeding.
People have then rapidly remarqued that the exceptionnal power density obtained permitted to weld with a low energy input and consequently with the most reduced modifications of the structure of the metals or the alloys.
This features have opened a large access for the electron beam bombardement to the "civil area". It has then become necessary to undertake an important labour tending to reduce the prices of the equipments.
An important step has been accomplished this way by using in certain cases an industrial vacuum as welding surroundings.
This proceeding, however, will require some precautions and studies have been executed for the limitation of the choice of metals or alloys that can be welded with security in a given vacuum. The experimental results are indicated for reactif metals or for metals forming refractory oxides.
Two types of manufactory equipments in medium vacuum are representing two particular directions of the development of welding proceedings.
The execution of great series of small pieces like the welding of stoppers for nuclear fuel element-sheath have lead us to the construction of a relatively simple equipment with a small chamber where vacuum and atmospheric pressure can quickly alternate at each welding.
Details of the performance cycle are given permitting the indication of the production possibilities with this equipment.
For the welding of complicated units of big dimensions such as turbo-jet engine-wheels we have executed an equipment with a chamber of 8 cubic meters with a vacuum of $10^{-2}$, $10^{-3}$ Torr by a group of mechanical pumps.
The use of an electron beam gun with autonomical pumping system in such huge chambers procures movement problems, because some displacing of the workpiece with regard to the welding spot must be transferred to the gun which represents a unit difficult to move.
The gun being situated vertically at the top of the cylinder-shaped chamber of a diameter of 2,20 m, it will be necessary to regulate the altitude of the welding-spot. This has been obtained by the means of two magnetical focalisation-coils one of which can move along the axis of the beam.

The small circular or square weldings can be executed on huge immobilised work-pieces by magnetical deflection of the electron beam.

Some details will be given about the other important parts of the equipment such us the movement of the work piece. The different work times are also indicated with precision.

Finally we find the description of some applications and special studies. The welding of copper of some light alloys and high strength steels have been studied in particular. The given metallurgical and mechanical results lead to the conclusion that electron beam can remove far away the boundaries of the technical possibility in moulding matter.

**Abstract No. 154**

# DYNAMIC VOLTAGE CONTRAST DISPLAY USING THE STROBOSCOPIC SCANNING ELECTRON MICROSCOPE

G. S. Plows * and W. C. Nixon
Engineering Department
Cambridge University
England.

Static display of voltage contrast at p-n junctions and in complete microcircuits has been observed with the scanning electron microscope for some considerable time (C. W. Oatley, W. C. Nixon and R. F. W. Pease, Advances in Electronics and Electron Physics, 21, 181, 1965). In practice, microcircuits operate at high frequencies and this form of static presentation may not reveal the true voltage distribution on a functioning device. Dynamic display has now become possible by using the principle of the sampling oscilloscope. The primary electron beam in the electron microscope column is pulsed with a pulse width of less than 10 nanoseconds at present. These current pulses are used to illuminate the microcircuit and voltage contrast formed with a special detector giving a direct relationship between specimen voltage and detected signal. By varying the phase of the primary beam pulse to that of the applied waveform on the microcircuit, the voltage contrast will be built up of a series of sampled points at the same place in each cycle. By proper choice of frequency ratios the individual dots merge into a complete picture of the microcircuit but now showing the variation of voltage with respect to both space and time as well as the usual three dimensional surface detail seen in any scanning electron micrograph. A 7 megacycle per second waveform applied to the gate of a MOST microcircuit ladder has been studied with respect to phase variation and local voltage distribution during the cycle. The stroboscopic principle has much wider applications to other electrical or magnetic phenomena on a microscale as well as mechanical or structural vibration, micro resonance, fatigue cycling at high frequency or similar dynamic repetitive studies. The additional electronics needed to perform this type of dynamic display amounts to one or two standard racks, and could, in principle, be added to a commercial instrument such as the Stereoscan scanning electron microscope of the Cambridge Instrument Company Ltd.

(* also I. C. T. Stevenage, England.)

Abstract No. 155

## EXAMINATION OF METAL-INSULATOR-SEMICONDUCTOR STRUCTURES BY SCANNING ELECTRON MICROSCOPY

**D. V. Sulway and P. R. Thornton**

**University College of North Wales, School of Engineering Science, Bangor, Caerns, Wales**

Although the conventional electrical methods (CV plots, surface recombination, velocity measurements and surface mobility studies) enable device properties to be understood in considerable detail they do involve an inherent integration over the whole of the device. In situations where local variations (patch effects) exist the results obtained by integration over the whole active area of the device may hide or "cloak" significant observations. There is an indication that this may be occurring during irradiation damage studies of planar transistors because supposedly near identical devices (as indicated by electrical measurements) can behave very differently under irradiation. At present this scatter of the behaviour that is observed upon irradiation is an unresolved question. The SEM has been used to investigate the importance of patch effects in Metal/$Si_3N_4$ Si structures in conjunction with determinations of the CV characteristic, surface recombination velocity and surface mobility. In brief the experiments consist in determining the device capacity, the recombination velocity and surface mobility as a function of surface field both before and after controlled amounts of electron irradiation. Once a satisfactory macroscopic picture of the device behaviour has been obtained the device is annealed and examined inthe SEM. In particular contrast effects are sought which relate to known electrical behaviour and evidence for the existence of patch effects are also sought.

Initial results show that contrast effects can be observed in the SEM which are related to the change from surface accumulation through depletion to inversion. It has also been shown that contrast associated with an "external" inversion layer extending out over the surface away from the metal gate contact. Such an inversion layer has been previously postulated by Hofstein and Warfield (1) and others to explain the hysteresis effects sometimes observed in these structures. Other observations have shown that there are localised variations in device properties. Some of these variations do not change with change in gate voltage others are voltage dependent. At present we have insufficient evidence to state the importance (i.e. frequency of occurrence and electrical properties) of these localised variations, but such data should be shortly available. The use of the SEM to study localised variations in insulator layers which are not covered by metal layers is also illustrated. Here the method employed is to use the charge up effects that can be observed by working near to the beam voltage corresponding to the second-crossover point. Finally the ability of the SEM to do controlled irradiation experiments in which only a prechosen part of the device is irradiated is illustrated.

(1) S.R. Hofstein and G. Warfield, Solid State Electronics, 8, 321,(1965)

Abstract No. 156

## DETECTION OF COMPOSITIONAL VARIATIONS USING THE SCANNING ELECTRON MICROSCOPE

**D. A. Shaw and P. R. Thornton**

**University College of North Wales, School of Engineering Science, Bangor, Caerns, Wales**

An assessment of the usefulness of the scanning electron microscope to investigate variations in composition is described. Two competing detection systems are described. One is the two surface barrier detector system pioneered by Kimoto and Hashimoto (1). The second method uses two channel secondary electron multipliers (2) in a similar manner to that employed with surface barrier detectors. The instrumentation involved in the use of channel multipliers is discussed. In particular various methods of amplifying the signal from the channel multipliers are considered. The relative merits of direct coupling, magnetic and optical coupling are discussed in relation to the sensitivity and bandwidth requirements of the system. A comparison is then made between the two systems as regards sensitivity (beam current required), bandwidth and cost. The versatility of the channel multiplier system, i.e. the inherent ability to detect secondary electrons as well as reflected primary electrons, is stressed.

The use of reflected electrons to study compositional contrast is compared and contrasted with the use of secondary electrons to give information about the specimen composition. The dependence of both methods on beam voltage, beam current and film thickness are considered and the ability to distinguish between adjacent atomic number materials

over the bulk of the periodic table ($Z \geqslant 12$) is illustrated. It is shown that very thin films can be revealed by the technique. It is also stressed that the method is qualitative. Some of the difficulties facing the quantitative development of the method are outlined and it is suggested that the main application will be to give rapid information about the distribution of known impurities in materials science problems and to indicate regions of different chemical composition in a rapid examination of the specimen prior to X-ray microanalysis.

(1) S. Kimoto and H. Hashimoto, 'The Electron Microprobe', Editors, McKinley, Heinrich and Wittry, J. Wiley 480, (1966).

(2) J. Adams and B.W. Manley, Phillips Tech.Rev., 28, 156 (1967).

Abstract No. 157

## TIME RESOLVED SCANNING ELECTRON MICROSCOPY OF ELECTRIC FIELDS IN CdS OSCILLATORS

N. C. MacDonald and R. M. White

Department of Electrical Engineering and Computer Sciences,
University of California at Berkeley, Berkeley, California

A scanning electron microscope (SEM) is used to probe the time varying field distribution in CdS oscillators. Recent measurements of the time varying fields were obtained by monitoring the potential distribution along the sample with a tungsten probe or appropriately spaced, evaporated electrodes. Since the dimensions of the oscillators are usually quite small (1mm x 1mm, 2mm long), these point by point probing methods are quite tedious and may disturb the field distribution along the sample. The SEM method described here uses the fact that the trajectories of the secondary electrons are influenced by changes in the local field distribution. In CdS oscillators small (1-100μm) regions of high field, a domain, traverse the length of the CdS bar from cathode to anode. Hence, a traveling high field domain will alter the collected secondary electron (SE) current.

Detection of the time variation of the electric fields required that the bandwidth of the SE collection system must be of the order of the inverse transit time of the domain; this transit time is approximately 0.2-1μs for the devices used in our experiments. The frequency of oscillation ranged from 1-10 mc. If we are to time resolve this moving domain, the overall time response of the SE collection system should be at least .1μs, or the system bandwidth should be at least 10 mc.

Since the bandwidth of the SE-video amplifier combination in the SEM is usually .2 to 1 mc, the SE signal was taken directly from the output of the photomultiplier tube using a coax cable terminated with a 50Ω resistor; the potential across the resistor was monitored on a high gain, widebandwidth oscilloscope. A deflection modulation display was used to present the relatively wideband SE signal in discernable form.

The bandwidth of the collection system and the photomultiplier tube represent an upper limit for the usefulness of this technique. Secondary electron transit time spread also influences this upper limit, this transit time spread being of the order of 10 ns. The rise time of the scintillator material is approximately 10 ns, and the time spread of the photomultiplier tube is approximately 10 ns. Consequently, the overall bandwidth of the system is of the order of 100 mc. Time solution of better than 50 ns should be possible using the present equipment.

In order to obtain SE signals of sufficient amplitude, beam currents of 10-100 mA were used to obtain the display. The diameter of the electron beam was approximately 0.3-1μm.

The experiment consists of pulsing the CdS oscillator for 4-10μs with a potential in the range 0-1000v; the SE signal is monitored simultaneously as the electron beam is scanned over the surface of the device. The beam is turned "on" for a period of .5-8μs during each line scan. This pulsed-beam technique allows selection of any portion of the time that the oscillator is active. Pulsing the beam also reduces the amount of contamination placed on the surface of the device by electron bombardment.

If the voltage applied to the oscillator is below the threshold voltage for the onset of the oscillations, the secondary electron signal indicates a linear increase in the potential from the cathode to anode. For applied voltages above the threshold voltage, the SE signal shows a distinct oscillating SE electron signal. The DMD's of the SE signal were found to be qualitatively similar to the displays obtained using a tungsten probe.

By the use of photoconducting CdS to make the oscillators, the field distribution along the sample may be changed by a focused light beam. If the light pipe from the SE collector to the photomultiplier tube is properly masked and if optical filters are placed in series with the light pipe, saturation of the photomultiplier tube by the light probe can be avoided. Deflection modulation displays were obtained that illustrate the change in the potential distribution along the length of the CdS oscillator with various illumination patterns.

Abstract No. 158

# FACTORS COVERING CONTRAST IN SCANNING ELECTRON MICROGRAPHS OF THIN OXIDE LAYERS

David Green
Westinghouse Research Laboratories
Pittsburgh, Pennsylvania 15235

Thin oxide films have been examined in the scanning electron microscope, in a manner which allows changes in electron beam induced conductivity of the oxide to appear as contrast variations in the micrographs. In this manner various inhomogeneities of the oxide layer can be observed. Contrast formation in this mode of operation depends on variation in the current which flows through the oxide. Various factors which govern this current in addition to inhomogeneities in the oxide will be discussed.

Samples were made of $SiO_2$ on a silicon substrate. An aluminum pad was formed on the oxide surface and a bias was applied between the pad and the substrate. These samples were examined in two modes: With a 200 micron diameter electron beam which flooded the area of interest, and secondly with a beam of 500Å diameter which was scanned in a raster over a similar area. Both methods of examination yielded similar data on the oxide current. In the scanned mode it was also possible to produce micrographs of the scanned area. Variation in the primary beam energy was found to have a strong effect on the oxide current. The ratio of oxide current to primary beam current (i.e., the "Gain") was a maximum when the primary beam just penetrated to the silicon-$SiO_2$ interface. (Fig. 1) The effects of variation in the aluminum pad thickness can be predicted from the normal penetration formulae for thin films. The sensitivity to such variations is limited by noise in the oxide current amplifier and it was found that thickness variations of 10% in the aluminum would not appear as a contrast change. The method is more sensitive to variations in the oxide thickness and in this case thickness variations of 2 to 5% can be detected. The effect of bias on the gain is found to be relatively symmetrical for the plate positive and negative, for a high energy primary beam. However, when the beam is not sufficiently energetic to reach the interface, more current is observed in the plate negative condition.

The current through the oxide was found to depend on the total electron irradiation to which the sample was exposed. The general trend was for the gain to decrease with increasing exposure but a local maximum is observed in the gain in the region of $10^{-4}$ coulomb/cm$^2$ (Fig. 2). This behavior is reflected in contrast changes in micrographs taken with increasing irradiation in selected regions. A simple model can explain the slow fall in oxide current in terms of a build up of trapped charge in the oxide. This causes most of the bias voltage to be dropped across the charged region. The resulting drop in the field in the remaining oxide causes a decrease of the oxide current. However, this fails to predict the observed local maximum in the gain.

These contrast mechanisms which depend on factors other than inhomogeneties in the oxide necessitate great care in the interpretation of scanning electron micrographs of oxides taken in this manner.

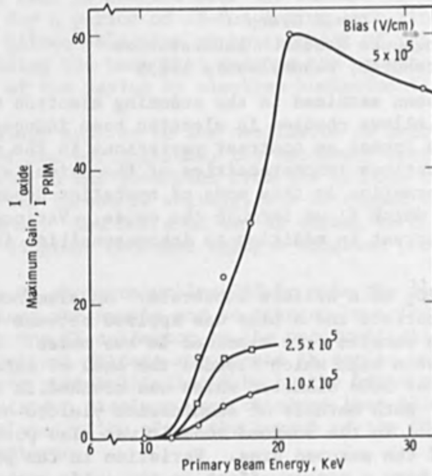


Fig. 1 Effect of Primary Beam Energy on Gain (10,000Å Oxide)

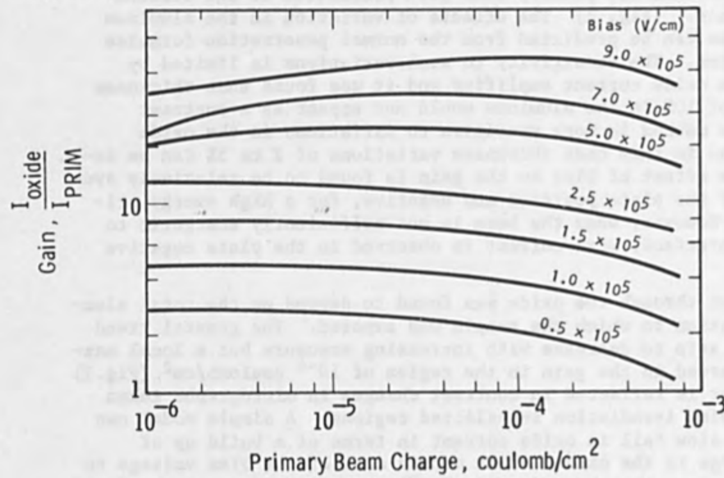


Fig. 2 Effect of Primary Beam Charge on Gain (10,000 Å Oxide)

Abstract No. 161

## ELECTRON MICROPROBE INVESTIGATION OF INTEGRATED CIRCUIT METALLIZATION

James E. Cline, Rosemary P. Beatty and Jon Gerhard

NASA Electronics Research Center, Cambridge, Massachusetts

For integrated circuits with low to medium current densities, the semiconductor industry has generally used aluminum metallization, which is economical to deposit and easy to etch into the interconnection pattern. Electron microprobe techniques for determining the thickness of aluminum metallization by either aluminum or silicon characteristic x-rays were studied in this work. There are many potential advantages of gold-molybdenum metallization, such as higher temperature capability, higher current density operation, minimization of electromigration effects, ease of bonding to gold leads without the formation of brittle intermetallics. The electron microprobe method of determining the gold and molybdenum thicknesses on a point-by-point basis enables the molybdenum barrier layer in the integrated circuit to be inspected for pinholes and for insufficient thickness to retard gold diffusion. A technique was developed for the simultaneous determination of the thicknesses of both gold and molybdenum in integrated circuit laminated metallization as part of a long-range effort to improve device dependability.

Aluminum films were deposited on silicon substrates by vacuum evaporation from a tungsten coil. For the study of gold-molybdenum metallization the molybdenum films were deposited by electron beam evaporation and the gold from a tungsten coil. A linear relationship is found[1] between the thickness t of aluminum on silicon and the intensity function of ($I_t$) during x-ray fluorescence, where

$$f\,(I_t) = -\log_{10}\,(1-I_t/I_0) \qquad (1)$$

$I_t$ represents the intensity of the characteristic aluminum x-rays from the film, and $I_0$ is the limiting maximum intensity from thick films.

The same function $f(I_t)$ in the electron microprobe technique departed significantly from linearity, as shown in Fig. 1, but was considered very convenient for smoothing the data points. The intensity function depends strongly on electron beam voltage. For the study of the gold-molybdenum system the patterns of depositions were arranged to leave four well-defined areas on the silicon substrate; (1) bare silicon (2) molybdenum on silicon (3) gold on silicon, and (4) gold on molybdenum on silicon.

Abstract No. 163

# THE APPLICATION OF ELECTRON BEAM FABRICATION TO LARGE SCALE INTEGRATION

M. W. Larkin, R. K. Matta, and P. R. Malmberg
Westinghouse Research Laboratories
Pittsburgh, Pa.

In order to predict the techniques which are required for the next generation of electronics it is necessary to investigate the types of circuits which will be fabricated. One fairly obvious extrapolation is that, for reasons of reliability and economy, more and more components are being integrated into larger circuits, forming integrated sub systems.

To obtain such large arrays of devices it is necessary to have a high yield. In the planar process it has been found that the yield of an active device is closely related to the active area occupied, the smaller the active area, the larger the yield. This is a result of the random defects which occur both in the initial substrate material and also which are introduced during processing. A limitation on the reduction in size which can be achieved by present methods is imposed by the optical technique used to define the geometrical area of the devices. If the reduction in size introduces difficulties in fabrication, the advantages gained by smaller size may be outweighed by the losses due to the fabrication process.

The substitution of an electron beam method of area definition not only creates a fairly simple method for fabricating micron size devices, but because of the ease with which an electron beam position can be programmed creates a straightforward method for generating discretionary interconnection patterns.

A 0.1 micron diameter electron beam derived from the electron optical system of a scanning electron microscope has been used to delineate patterns on a silicon substrate by means of an electron beam sensitive resist material. An array of 108 transistors each with 1 x 1 micron emitter windows has been fabricated by this method. The transistors have high gain ($\beta \sim 50$) at low input currents $I_{BCO} \sim 5\mu A$ and are suitable for large scale integration. The scanning microscope deflection system has also been modified to accommodate a digital deflection system. The deflection and blanking of the beam is controlled by a computer tape input. A schematic diagram of the control system is given in Fig. 1. This system enables programs generated on a Burroughs B5500 computer to be directly transformed into areas exposed by the scanned electron beam. Programs which are available from the computer enable the flexible interconnection of unit cells of an integrated subsystem avoiding defective components or the generation of a sequence of integrated circuit geometries directly on the slice without recourse to the precise engineering drawings required by conventional techniques.

The various problems involved with combining these applications to generate a maximum density array of micron sized devices utilizing programmed interconnections are discussed, particularly the criteria for alignment and testing of the structures and also the design factors for the unit cell.

Examples of discretionary wiring patterns and individual device patterns made utilizing this system are shown. Some aspects of methods of evaluation and testing utilizing the computer controlled scan are also discussed and the overall systems concept is considered.

The great potential afforded by the combination of the enhanced resolution capability and flexibility of an electron beam exposure system with a computer derived pattern generation system has been demonstrated by this work. The extension of this method to larger, more complex systems is being carried out and the possibility of including computer aided circuit design in the system is being considered.

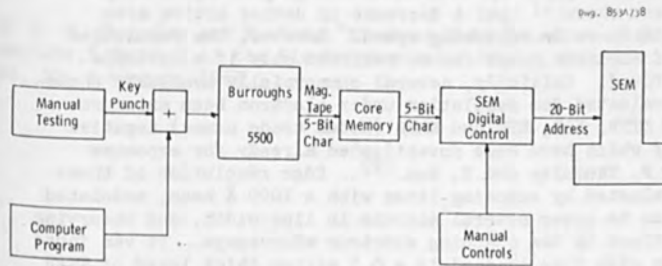


Fig. 1 SEM Computer Control System

**Abstract No. 164**

ELECTRON BEAM TECHNIQUES FOR HIGH RESOLUTION CIRCUIT AND MASK FABRICATION

M. Hatzakis

IBM WATSON RESEARCH CENTER
YORKTOWN HEIGHTS, NEW YORK

The advantages of using electron beam systems rather than light optical systems for the exposure of photoresists for microcircuit fabrication are the resolution, power density, and deflection capabilities of electron beams. It is possible to build an electron beam system that produces a 1000 Å spot at $10^{-9}$ amps that can be deflected over a 50 x 50 mil. field. Such a system is capable of fabricating submicron geometry devices with high packing density. Also, it has been shown[1] that a decrease in device active area results in an increase in switching speed. However, the resolution capabilities of electron beams can be realized only if a suitable resist can be found. Initially, several commercially available photoresists were evaluated for resolution under electron beam exposure. These included KTFR, KOR, KPR and KMER (Kodak trade names) negative resists, all of which have been investigated already for exposure sensitivity by R. Thornley and T. Sun [2]. Edge resolution of these resists was evaluated by exposing lines with a 1000 Å beam, modulated with a fast scan to cover several microns in line width, and observing line cross sections in the scanning electron microscope. It was found that a 2 micron wide line exposed in a 0.5 micron thick layer of KTFR at 12 KV exhibits a sloping edge of about 2 microns on either side after development. KOR, KPR and KMER exhibited similar edge effects, and it was concluded that these resists were unsuitable for high resolution work.

Shipley AZ-1350, a positive photoresist was found to develop correctly only in a narrow range of exposure around $5 \times 10^{-5}$ coul/cm$^2$, and was also considered unsuitable for use in a reliable microcircuit fabrication system.

A methacrylate based positive resist developed in this laboratory was tested and found to exhibit most of the properties desirable for high resolution work. Correct exposure can be obtained in the range of $5 \times 5^{-5} - 5 \times 10^{-4}$ coul/cm$^2$ at 10 - 15 KV. Edge resolution studies indicate a slight undercut in the developed image that can be increased or eliminated by suitable processing after exposure and development. The resist is light insensitive, and it can withstand basic or acidic etch baths for prolonged periods of time. Metalized structures can be formed by evaporating the metal through the developed resist with a demonstrated one-to-one height-to-width ratio down to 3000 Å line widths. An electron beam system has been constructed for experimental

work, capable of producing a 1000 Å spot at $10^{-9}$ amps and covering a 20 x 20 mil. field. The beam is controlled by an optical scanner with 1000 line resolution that scans an 8.5 x 11 inch transparency. Transistors with stripe widths of one micron and one half micron have been fabricated using this system with methacrylate resist on silicon epitaxial wafers. It is believed that higher resolution can be achieved with this resist by using improved electron beam systems and thinner resist layers. Also, the possibility of producing high resolution, durable, contact masks using the electron beam system and methacrylate resist is being investigated.

## REFERENCES


1. V. A. Dhaka, "Subnanosecond Monolithic Current Switch and Design of High Frequency Transistors," presented at the Internationaler Electronik Arbeitskreis Ev., Munich, Germany, October, 1966.

2. R. F. M. Thornley and T. Sun, "Electron Beam Exposure of Photoresists," Journal of the Electrochemical Society, Vol. 112, No. 11, November, 1965.

**Abstract No. 170**

# DESIGN OF ANASTIGMATIC COILS FOR DEFLECTING MICRON SIZE ELECTRON BEAMS

A. Speth

THOMAS J. WATSON RESEARCH CENTER
YORKTOWN HEIGHTS, NEW YORK 10598

In electron beam recording systems, the field size or number of spot diameters over which the electron beam may be deflected with minimal spot growth is a limiting parameter which is often difficult to define. Magnetic deflection is known to introduce smaller aberrations than electrostatic means. A number of analytic approaches have characterized the parameters which influence the various forms of magnetic deflection aberrations and have indicated the general form of field distributions required to minimize the individual effects. The major experimental effort has been in the CRT area. High performance CRT's have center field spot sizes ranging from 10 to 30 microns. There is little experimental information relating to considerably smaller spot sizes in systems which maintain comparable imaging angles.

The present work describes the coil design parameters and experiments used in determining the limits over which a nominal micron diameter beam can be anastigmatically deflected without accessory compensation. The experiments have used small angle ($< 15^{\circ}$) line scans over plane targets with refocusing to compensate for field curvature. Deflection of a one micron beam (half angle = 0.004 radians) over 25,000 spot diameters ($\pm$ 0.5 inch) has been one result. The data demonstrate that optimum operation is possible by matching the sagittal and meridial foci at the extremes of the deflecting field. This result shows that in deflecting small beams, the normally used square law variation of astimagmatic aberration with deflection distance is not adequate. Experiments have also demonstrated anastigmatic deflection within the deflection field, allowing shorter lens working distances and reduced sensitivity to mechanical tolerances.

An approximation technique for defining the relation between the anastigmatic plane and the coil wire placements will be described. These computations are considerably simpler and more intuitive than closed form integral approaches which evaluate errors at the image plane.

The experimental coils have been built in the "saddle" fashion. A 2 inch long - 1 inch diameter ceramic tube is slotted lengthwise on its outside diameter with 16 mil grooves to provide a close fit for enameled wire. The drive current into the single wire in each slot was limited to 6 amps due to heating. This current limit imposed the requirement of 32 slots (8 per quadrant) for deflecting a 20 keV beam through $\pm 10^{\circ}$. Two fitted discs, slotted to match the tube, were placed on either end of the tube. This construction allows for magnetic shrouding which doubles the deflection sensitivity. Details on the coil field distribution and the influence of the closure windings on results will be given.

The beam is formed by a two-lens electron column with the gun potential held at -20 keV. The coil is fixed in a jig which maintains concentricity between the final aperture, the final lens bore, and the coil. The specimen plane holds a 500 mesh nickel grid over which the electron beam is scanned in raster fashion by deflection coils mounted before the final lens. The beam which passes through the grid impacts a grounded sheet of plastic scintillator which is mounted on a light pipe, coupling the light signal to a PMT. A TV type display is used to evaluate spot distortion while line scans are used for detailed spot size measurements.

Abstract No. 170B

# A 10 KEV, 0.5 AMPERE ROCKET-BORNE ELECTRON ACCELERATOR*

W.C. Beggs, R. Elcox, R. Harrison, and F. McCoy

ION PHYSICS CORPORATION
Burlington, Massachusetts

A system has been developed and tested for injecting an electron beam into the upper atmosphere from an Aerobee 350 sounding rocket. The experiment is designed to test the ability of an electron beam to be ejected from an object into the upper atmosphere, to pass through the existing ionospheric plasma without suffering serious losses due to plasma-beam interractions, and to produce adequate excitation and ionization for ground viewing by optical and radar means. To assist in neutralizing the vehicle, an 85 ft diameter conductive screen will be unfolded to "catch" the ambient plasma electrons.

The electron beam will be programmed by an on-board programmer over a large current range from 1.5 to 500 ma in six discrete steps and over an energy range from 1.2 to 10 kev in four discrete steps. The experimental matrix of pulses in a sequence includes 20 pulses of length 100 ms and two signature pulses at the highest voltage and current of length one second. The pulse spacing is 3 seconds and the total experiment time 260 seconds.

The electron beam is produced by ten small ceramic-metal electron guns, spaced on a 13 in. circle, which utilize UHF planar triode technology including quick warmup indirectly heated nickel matrix cathodes, close spaced control grid, pre-accelerator grid and cylindrical anode to produce a beam over the current and voltage range of 10 deg. half angle. The guns are provided in the activated, conditioned and baked out condition and are opened to the space vacuum by a novel technique described in the paper.

Beam current control and pulsing is provided via 10 kv isolated reed relays feeding an electronic controller in the control grid lines. Regulated supplies and batteries are provided at the high voltage potential for the filaments and 800 volt pre-accelerator potential.

The high voltage beam current supply is housed in a separate rfi-emi shielded compartment and is made up of eight individual 1.25 kv supplies with their outputs in series. The supplies utilize a driver oscillator stage, a

*Work supported under NASA Goddard Space Flight Center Contract NAS-5-9326.

transistor bridge inverter, a high voltage transformer, and a bridge rectifier. Turn on of each module is via a reed relay in the driver stage. The number of modules turned on is a function of the programmer voltage command. Short circuit protection is effected by a feedback transformer from the bridge inverter into the driver oscillator. Modified ferrite pot cores are used for the high voltage transformers to reduce weight and contain the generated magnetic fields.

The battery system for supplying the beam current supply as well as the gun opening circuits is made up of two separately encased, high current silver-zinc batteries which are each capable of supplying 120 amperes at 30 volts. The converter-battery system voltage regulation is held to within 0.6 kv of nominal from no load to full load by careful design and by removing the eighth module for the highest power pulse (10 kv, 500 ma).

The gun opening operation requires 70 amperes current at 15v for several seconds. Transistor switching circuits are provided for performing this operation along with circuits to open the guns in groups of four sequentially.

The entire electronics circuits and gun mounts are contained in an insulating gas pressurized container which allows the tight packaging to meet the high voltage requirements at no cost in serviceability.

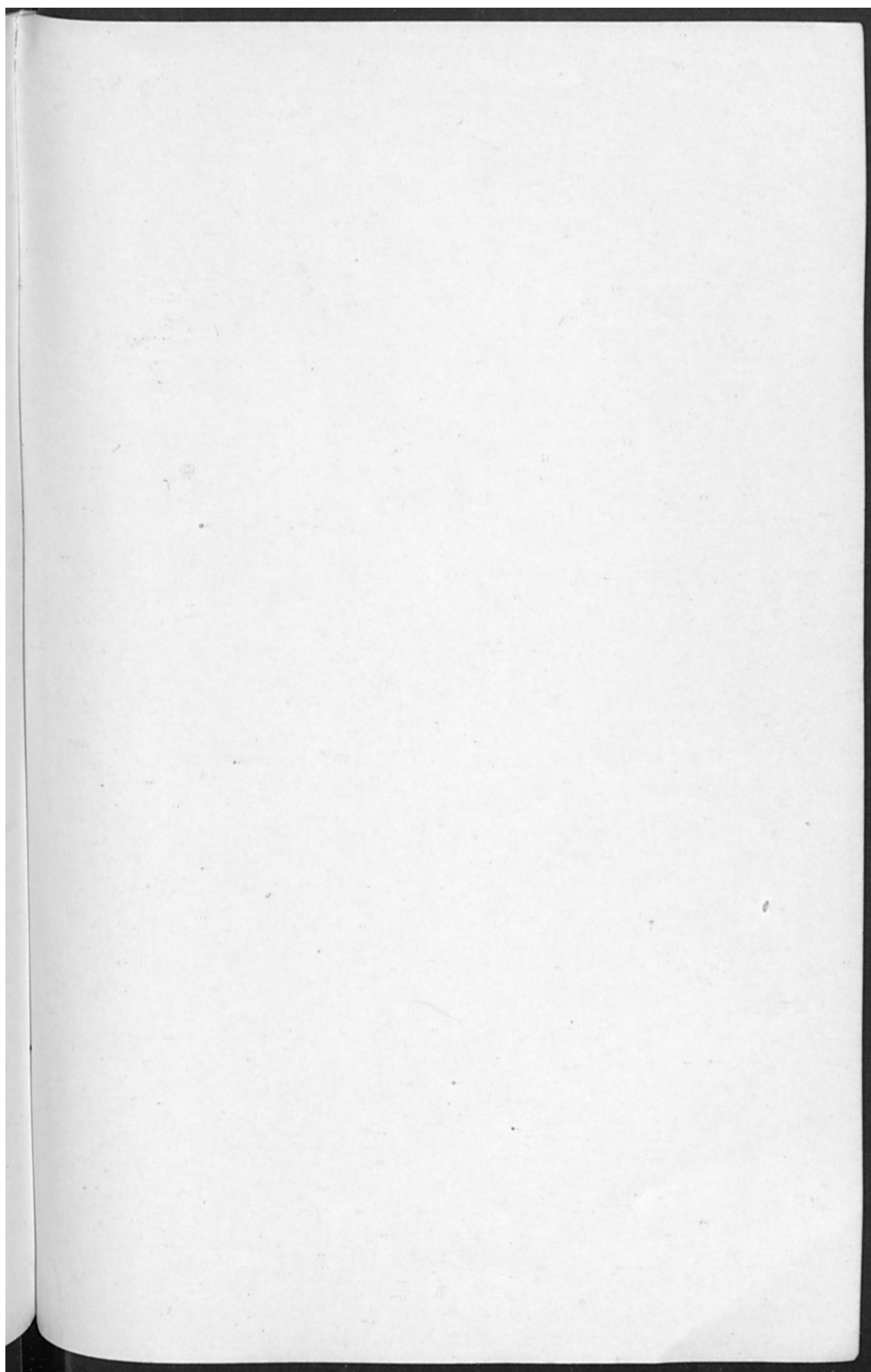

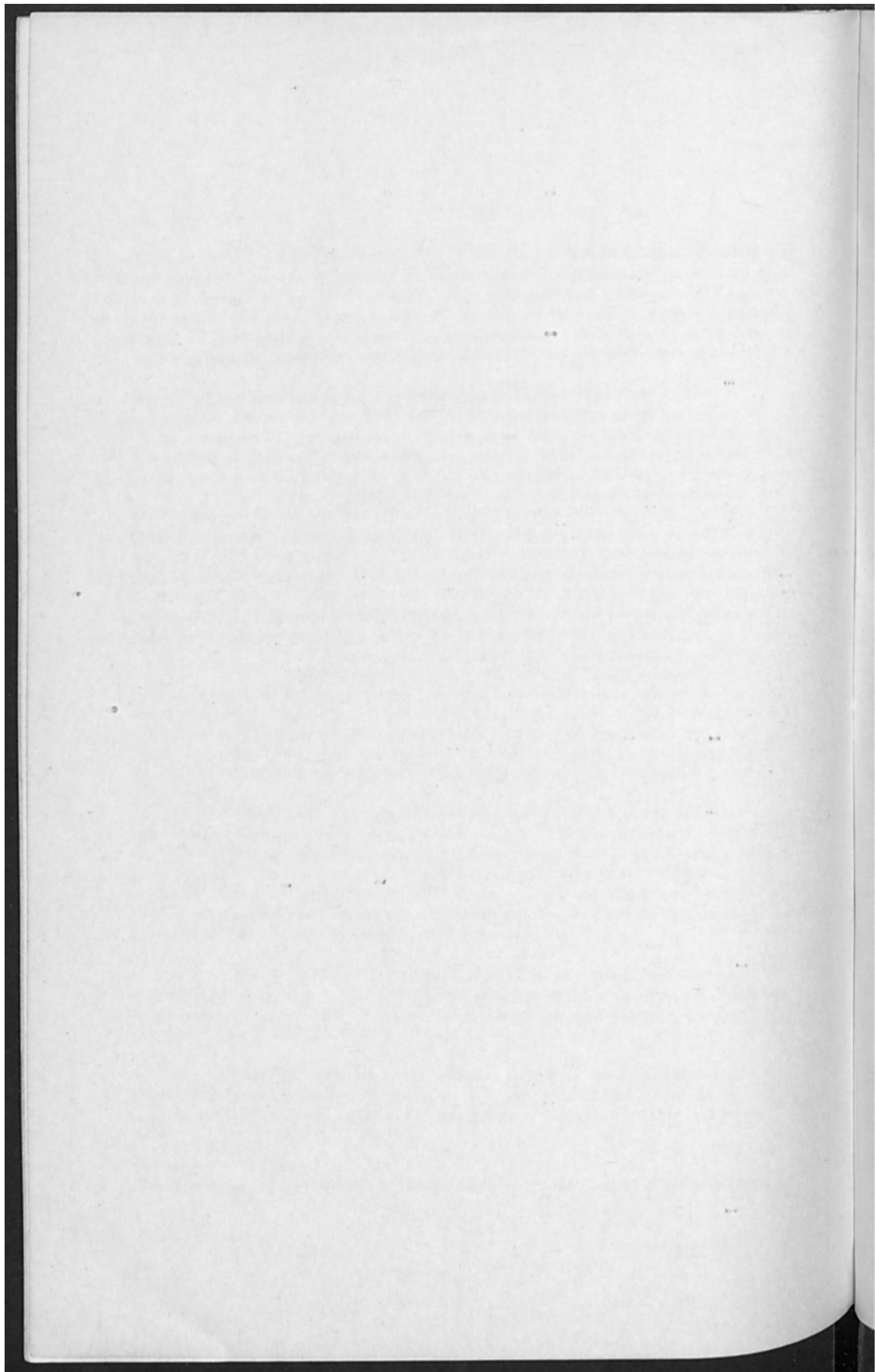

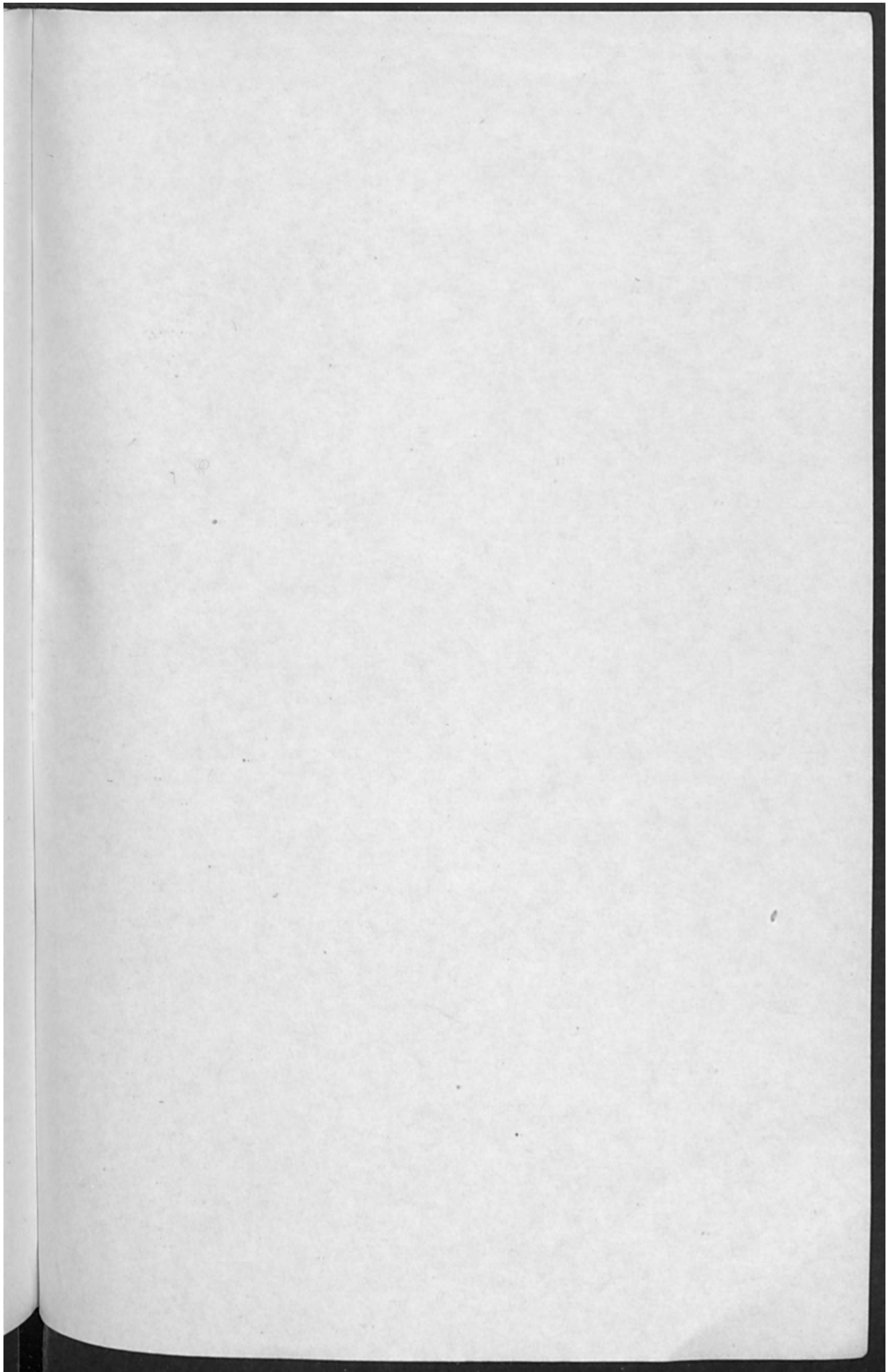

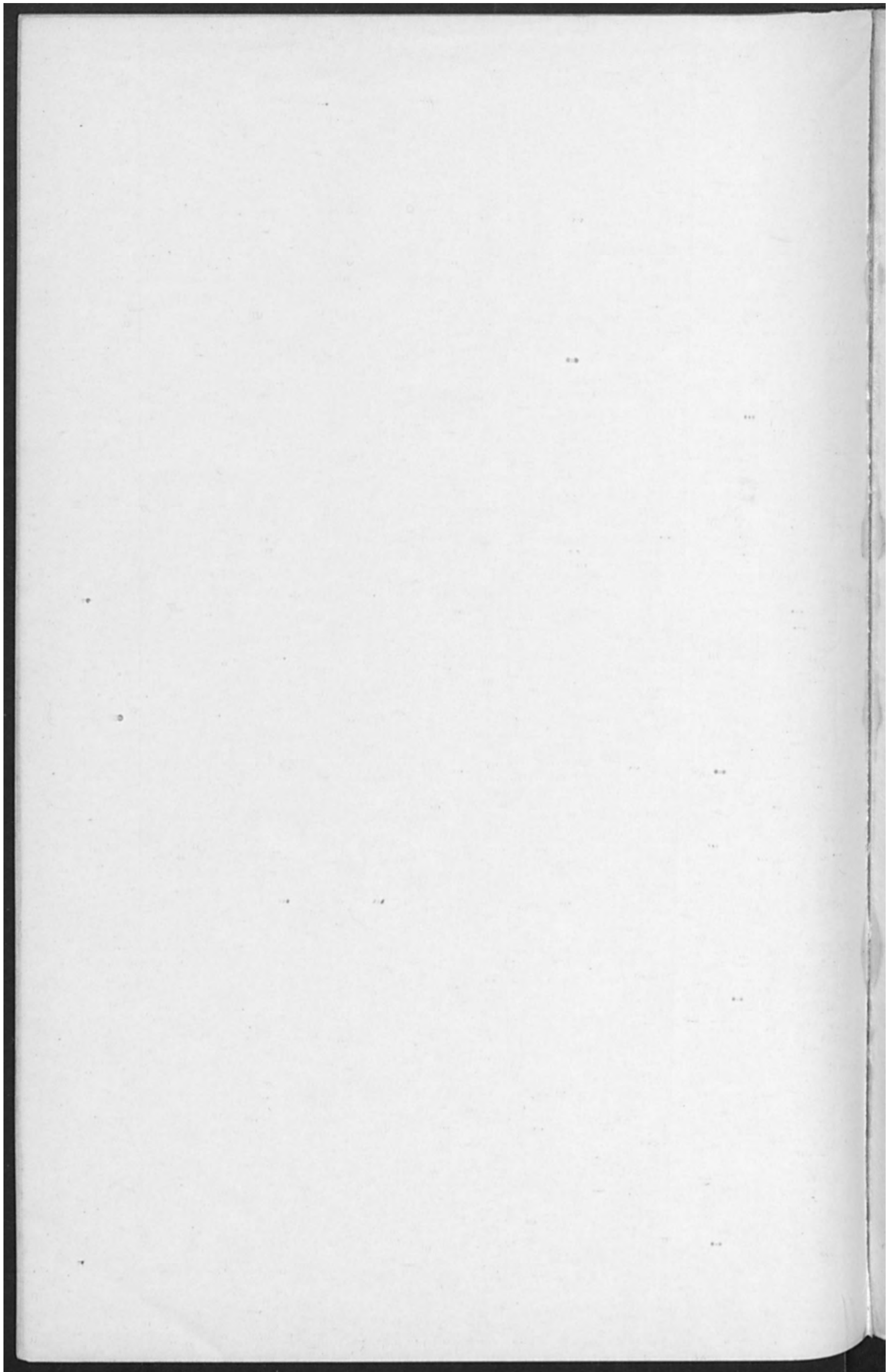

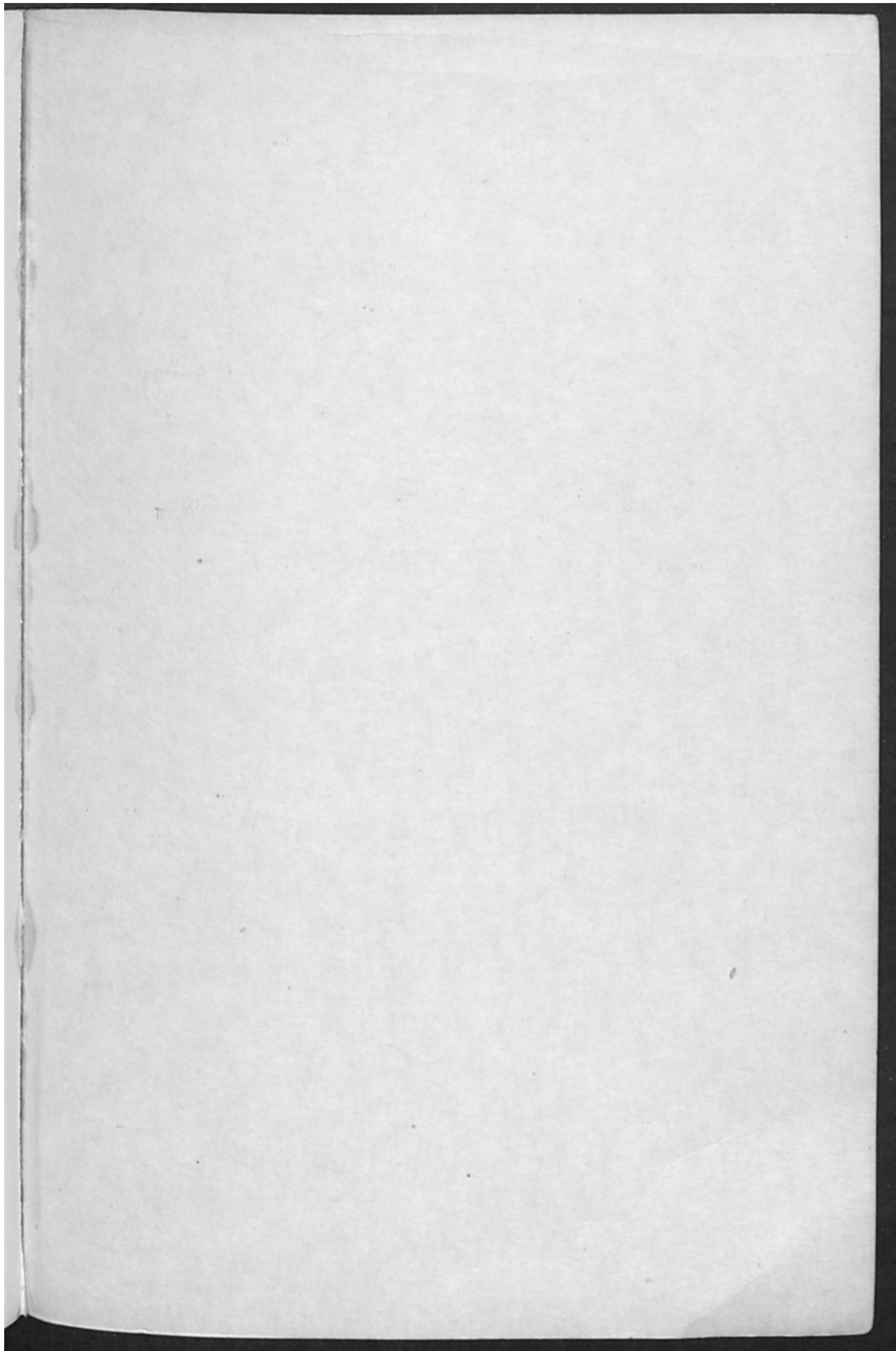

# SOCIETY SOFTBOUND SYMPOSIUM SERIES

[a] **Surface Chemistry of Metals and Semiconductors,**
H. C. Gatos, J. W. Faust, Jr., and W. J. La Fleur, Editors.
A 1959 symposium. 526 p. $21.50.

[a] **Electrode Processes,**
First Conference, E. Yeager, Editor.
A 1959 symposium. 374 p. $15.50

[a] **Mechanical Properties of Intermetallic Compounds.**
J. H. Westbrook, Editor.
A 1959 symposium. 435 p. $17.50

[a] **Zirconium and Its Alloys,**
J. P. Pemsler, E. C. W. Perryman, and W. W. Smeltzer, Editors.
A 1965 symposium. 250 p. $10

[a] **Electrolytic Rectification and Conduction Mechanisms in Anodic Oxide Films,**
P. F. Schmidt and D. M. Smyth, Editors.
A 1967 symposium. 230 p. $7

[b] **Measurement Techniques for Thin Films,**
B. Schwartz and N. Schwartz, Editors.
1965 and 1966 symposia. 374 p.
$12 (softbound) $15 (Hard cover)

[b] **Electrode Processes,**
Second Conference, E. Yeager, H. Hoffman and E. Eisenmann, Editors.
A 1966 symposium. 190 p. $5

[c] **Vacuum Metallurgy,**
J. M. Blocher, Jr., Editor.
A 1954 symposium. 216 p. $5

[c] **Electrets and Related Electrostatic Charge Storage Phenomena,**
L. M. Baxt and M. M. Perlman, Editors.
A 1967 symposium. 150 p. $11

[c] **Dielectrophoretic and Electrophoretic Deposition,**
E. F. Pickard and H. A. Pohl, Editors.
A 1967 symposium. 148 p. $9

[c] **Electron and Ion Beam Science and Technology,**
Third Conference, R. Bakish, Editor.
A 1968 symposium. 725 p. $21

[c] **Optical Properties of Dielectric Films,**
N. Axelrod, Editor.
A 1968 symposium. 325 p. $9

[c] **Electrodialysis,**
W. A. McRae and E. J. Parsi, Editors.
A 1968 symposium. 500 p. To be published

**Iron Ore Reduction,**
R. R. Rogers, Editor.
A 1960 symposium. 359 p. $12.50. Order from the MacMillan Co., 60 Fifth Avenue, New York, N. Y. 10003

**Rhenium,**
B. W. Gonser, Editor.
A 1960 symposium. 225 p. $12.50. Order from American Elsevier Publishing Co., 52 Vanderbilt Ave., New York, N.Y. 10017

[a] Order from University Microfilms, Inc., 300 N. Zeeb St., Ann Arbor, Mich. 48103. Enclose payment with order. Specify an Electrochemical Society volume.

[b] Order from Johnson Reprint Co., 111 Fifth Avenue, New York, N. Y. 10003. Specify an Electrochemical Society volume. Prices subject to change without notice.

[c] Orders filled at the list price given, subject to availability, from The Electrochemical Society, Inc., 30 East 42nd St., New York, N. Y. 10017. Enclose payment with order.